63 /3/ 2025

JOURNAL OF THEORETICAL AND APPLIED MECHANICS

WARSAW 2025, QUARTERLY, VOLUME 63, ISSN 1429-2955 eISSN 2543-6309

POLISH SOCIETY OF THEORETICAL AND APPLIED MECHANICS
ptmts

POLISH SOCIETY OF THEORETICAL AND APPLIED MECHANICS

JOURNAL OF THEORETICAL AND APPLIED MECHANICS

Vol. 63 • No. 3
Quarterly

WARSAW 2025

JOURNAL OF THEORETICAL AND APPLIED MECHANICS
(until 1997 Mechanika Teoretyczna i Stosowana, ISSN 0079-3701)

Beginning with Vol. 45, No. 1, 2007, *Journal of Theoretical and Applied Mechanics* (JTAM) has been selected for coverage in Thomson Reuters products and custom information services. Now it is indexed and abstracted in the following:

- **Science Citation Index Expanded** (also known as SciSearch®)
- **Journal Citation Reports/Science Edition**

Advisory Board

Michał Kleiber – Chairman
Jorge A.C. Ambrosió, Romesh C. Batra,
Alain Combescure, Jüri Engelbrecht, Józef Kubik,
Włodzimierz Kurnik, Zenon Mróz, Wiesław Nagórko,
Ryszard Parkitny, Ekkehard Ramm, Meir Shillor,
Andrzej Styczek, Eugeniusz Świtoński, Hisaaki Tobushi,
Andrzej Tylikowski, Dieter Weichert, Jose E. Wesfreid,
Joseph Zarka, Vladimir Zeman

Editorial Board

Piotr Kowalczyk – Editor-in-Chief
Section Editors: Iwona Adamiec-Wójcik, Piotr Cupiał, Krzysztof Dems,
Witold Elsner, Eric Florentin, Elżbieta Jarzębowska,
Oleksandr Jewtuszenko, Zbigniew Kowalewski, Tomasz Krzyżyński,
Anna Kucaba-Piętal, Stanisław Kukla, Tomasz Łodygowski,
Ewa Majchrzak, Janusz Narkiewicz, Michał Nowak, Piotr Przybyłowicz,
Błażej Skoczeń, Jacek Szumbarski, Krzysztof Tajduś,
Utz von Wagner, Jerzy Warmiński

Language Editors – Ewa Kiczko, Jolanta Romanowska, Karol Matysiak
Technical Editor – Katarzyna Jezierska
Managing Editor – Urszula Kowalczyk

Editorial Office

Al. Armii Ludowej 16, room 650; 00-637 Warsaw, Poland
e-mail: jtam@ptmts.org.pl
www.jtam.pl

Articles in JTAM are published under Creative Commons Attribution 4.0 International. Unported License https://creativecommons.org/licenses/by/4.0/deed.en. By submitting an article for publication, the authors consent to the grant of the said license.

Crossref
Similarity Check
Powered by iThenticate

The journal content is indexed in Similarity Check, the Crossref initiative to prevent plagiarism.

Ministry of Science and Higher Education
Republic of Poland

This issue has been published with financial support from the Polish Ministry of Science and Higher Education under the Excellent Science II programme "Support for scientific conferences".

JOURNAL OF THEORETICAL
AND APPLIED MECHANICS
63, 3, pp. 459–459, Warsaw 2025

FROM THE EDITORS

The present issue of JTAM (Vol. 63, No. 3) is entirely devoted to the 40th Danubia-Adria Symposium on Advances in Experimental Mechanics, held on 24–27 September 2024 in Gdańsk, Poland. The Danubia-Adria Symposium (DAS) was established in 1984 as an initiative of the Danubia-Adria Society. Danubia-Adria Symposia bring together internationally recognized experts and young researchers in an effort to exchange ideas on different topics within the field of experimental mechanics. The conferences also serve as a platform for establishing connections between different research teams and for the development of future scientific collaboration. Apart from the basic problems usually studied within a framework of experimental mechanics, the symposia have covered experimental, theoretical and numerical aspects of the mechanical behaviour of solids at various loading conditions, with special emphasis on the dynamic loading conditions. Lack of knowledge about the behaviour and performance of structures/components against hazardous dynamic loads of human or natural origin may result in catastrophic consequences for human life and structural systems. The experience and knowledge from extensive research, experimental testing and advanced computational techniques can provide feasible solutions to diminish these catastrophic effects.

DAS 2024 was organized by the Danubia-Adria Society, the Institute of Fundamental Technological Research of the Polish Academy of Sciences, and the Gdańsk University of Technology. The meeting was focused on experimental and measuring techniques for a thorough study of the mechanical properties of different materials, engineering structures and systems which are necessary to create the physical bases and provide verification of analytical or numerical methods in engineering design. DAS 2024 attracted more than 120 participants from 21 countries and considerably contributed to the development of experimental mechanics and international scientific collaboration in this field.

This post-conference issue contains 24 articles reflecting research that was presented at the 40th DAS, 2024, in the form of plenary lectures and keynote speeches, as well as poster presentations, later developed to full-size articles. All of them have been reviewed within the standard editorial procedure of JTAM. The topics being presented here indicate problems in mechanics and related disciplines that attract the attention of scientists and are important for technological innovations and their applications in modern industry. We would like to thank all the authors of the articles in this issue for submitting their post-conference papers and thus contributing to the publishing output of JTAM. The organizers are grateful to the Ministry of Science and Higher Education of Poland for its financial support of the 40th DAS, aimed at increasing the scientific quality, impact and international reputation, and a broader participation in DAS 2024 of young scientists.

Guest Editors

Zbigniew Kowalewski
Chairman of the 40th DAS

Mateusz Kopeć
Scientific Secretary of the 40th DAS

JOURNAL OF THEORETICAL
AND APPLIED MECHANICS
63, 3, pp. 461–469, Warsaw 2025
https://doi.org/10.15632/jtam-pl/200388

DURABILITY TESTS FOR THE AUTOMOTIVE INDUSTRY

Tadeusz SZYMCZAK[1]*, Zbigniew L. KOWALEWSKI[2], Adam BRODECKI[2]

[1] *Vehicle Type-Approval & Testing Department, Motor Transport Institute, Warsaw, Poland*
[2] *Department of Experimental Mechanics, Institute of Fundamental Technological Research, Polish Academy of Sciences, Warsaw, Poland*

*corresponding author, *tadeusz.szymczak@its.waw.pl*

This study focuses on component durability testing methods and their application in the automotive industry. These types of tests can be used to assess various objects with simple and complex geometries and a range of dimensions, manufactured using certain structural materials, including 6005 T6 aluminium alloy and S700MC high-strength steel. The test results characterise the component response at 2×10^6 loading cycles, and the crack trajectories are analysed after a high number of cycles. The influence of the welding process on the tensile mechanical parameters of the aluminium alloy and steel is also discussed, and fatigue behaviour of S700MC and its weld is illustrated.

Keywords: durability test; fatigue; cracks; fracture; coupling; vehicles.

1. Introduction

Durability tests have been used to examine the fatigue resistance of different components (Berger *et al.*, 2010; Creager *et al.*, 2015; Szymczak *et al.*, 2022a; 2022b). Generally, they are employed in two branches of industry: aviation (Berger *et al.*, 2010; Creager *et al.*, 2015) and automotive (Szymczak *et al.*, 2022a; 2022b), where many working elements operate under cyclic loading. From an engineering perspective, this indicates that inspections should be performed to capture crack occurrence, as cracks can lead to element's failure.

Different types of testing stands can be used to examine durability. One type uses two-level platforms for mounting the tested objects and for subsequent examinations (Servotest Systems; SSTM, 2019). Depending on their complexity, they enable different types of loading applications such as cyclic and dynamic torsion, dynamic axial loading, and thermal cycles (Servotest Systems). More complex multi-element devices enable biaxial loading (i.e., horizontal and perpendicular) (MTS). Testing stands can be used in conjunction with environmental chambers which control the temperature range from −40 °C to 120 °C and provide special conditions with the application of water, salt and mud. Multiaxial systems are recommended for examining the mechanical resistances of components of different shapes and dimensions (MTS). Multi-servo actuators and closed-loop feedback enable effective testing of vehicles (Instron; Wielton Group).

Research groups have focused on different aspects of durability tests, such as stochastic changes in selected physical quantities during road testing by a target dynamic system comprising a potentiometer, an accelerometer, and a strain gauge, and their analyses (Jung *et al.*, 2003).

Ministry of Science and Higher Education
Republic of Poland

The publication has been funded by the Polish Ministry of Science and Higher Education under the Excellent Science II programme "Support for scientific conferences".
The content of this article was presented during the 40th Danubia-Adria Symposium on Advances in Experimental Mechanics, Gdańsk, Poland, September 24–27, 2024.

This type of data is also analysed using the acceleration time signal and frequency response fraction to calculate the displacement and shock response functions (Halfpenny, 2006). A Weibull analysis was also performed for stochastic cycles (Król & Gasiak, 2018).

In another study, the authors used the stress-strain relationship to determine the limits of the cyclic force (Gowda *et al.*, 2015). If the tests are performed at different operational times, then comparisons can be made (Stembalski *et al.*, 2024).

Typical fatigue tests are directly used in the automotive industry to determine the mechanical resistance of components used for vehicle coupling, such as balls and drawbar beams, as shown in Fig. 1. The coupling components can be used at a constant high level (Fig. 1) or three levels using screws, as shown in Fig. 2. In these cases, the component can operate at permissible loading values determined in the durability testing. Operational loading at values within the defined limit does not cause any deformation or cracks owing to coupling.

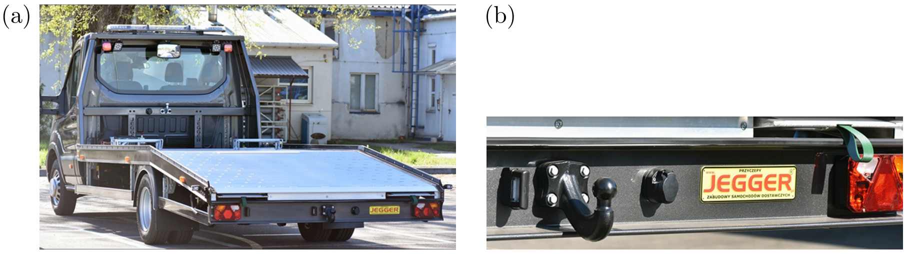

Fig. 1. Car transporter having a JEGGER regular platform with a coupling function using the A50-X ball, made of steel and aluminium alloy.

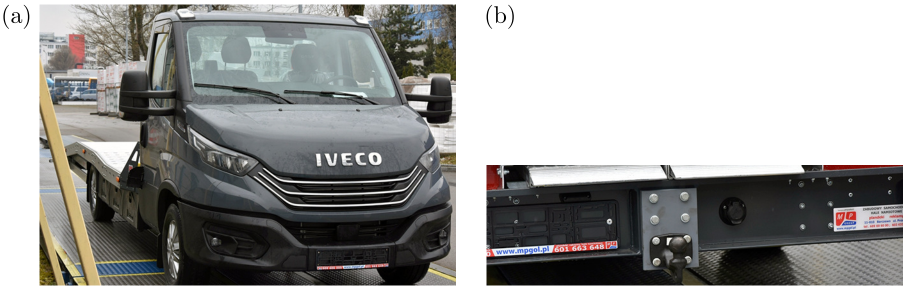

Fig. 2. Car transporter having an MP Group irregular platform with a multi-levelled coupling function using the A50-X ball, made of steel and aluminium alloy.

This kind of test is not trivial but a complex one, because of the weight and dimensions of the tested object, as the values of these physical parameters are often between 200 kg–400 kg and 3.5 m × 2 m, respectively. From the practical point of view, the mounting manner is very important and should be done according to the operation process. This requires a conception and a lot of time to connect the tested object with a platform. Therefore, in the case of towing frames, this kind of component was examined in a reversed position where the platform followed the vehicle mass, while in the case of platforms (6 m × 2 m), it was tested as a complete one with a wheel axis and suspension at an operational orientation. Those approaches can be indicated as the requirements for examining huge components. Moreover, an inspection of the tested object and physical parameters used in the tests should be done every day, while the tests require 2 weeks in continuous mode, i.e., day and night. Another significant feature of the experiment is connected with type approval, because positive results enable applying to the approval authority (TDT – transport technical supervision, Poland) for issuing a certificate of approval. This kind of final result enables the mounting of a component in a vehicle and it can be called “made in Poland” for sale in the EU and other countries of the World. Moreover, the experiment with a component such as a platform for a vehicle for transport vehicles, towing frames to recovery vehicles and coupling adapters can be conducted in a technical service approved by the TDT. Sometimes, the stand test should be supported by static and fatigue experiments if a joining technology is selected for qualification concerning its quality or modelling. Taking this information into consideration, the paper's aim was proposed: a multistage mechanical approach to testing components and their joints enables determining their technical quality and type approval. Therefore, the paper collects a lot of details of experiments on components, specimens of parent materials and their weld covering aluminium alloy and modern high-strength steel.

2. Details of experiments

This kind of experiment requires dedicated research equipment such as a digital controller (Instron Structural Testing for example), software (RSview used in stand tests), computer, mobile servo-actuator (Saginomiya ±30 kN at angular position of piston rod applied for examining) and a huge T-slot platform with a seismic mass (the laboratory section component of the Department of Type-Approval and Testing of Motor Transport Institute). The digital controller should be used to achieve the required technical level for durability tests. Such a device enables the collection of different signal types such as displacement, force, rotation angle, and torque. It is typically equipped with several measurement cards to acquire the digital and analogue signals. A computer with special software for tuning, testing, and data collection supports durability testing.

The main parameters of the durability tests, such as amplitude and frequency, can be established basing on specific requirements. For example, UN Regulation No. 55 (UN/ECE, 2010) was used in the tests on mechanical coupling devices. Information about the direction of the force vector (an angle for the actuator) is also provided in the regulation, as shown in Fig. 3. Additionally, it indicates the basic regime of the mounting components used for the examination. No deviations from the procedure were allowed because durability tests play a crucial role in component qualification concerning its quality, approval, application, and final sale.

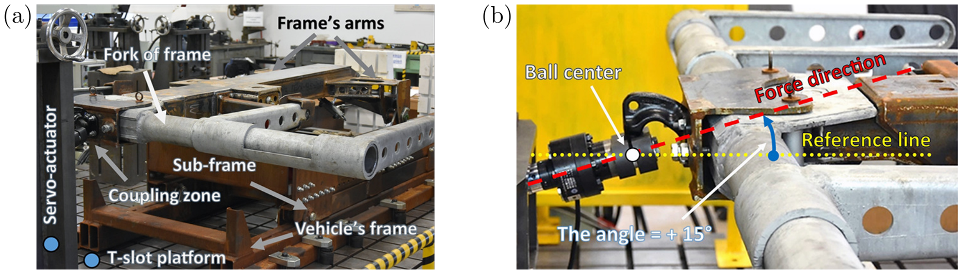

Fig. 3. Towing frame (for recovery vehicles on highways and expressways) on a stand testing platform: (a) a general view; (b) a mechanical connection of the servo-actuator and frame through a spherical grip and A50-X coupling ball.

This approach was supported by mechanical tests on specimens that assessed the base metal and its weld. It is important to determine the following fundamental mechanical parameters: Young's modulus, elastic limit, yield stress, and ultimate tensile strength. These can be used to determine the welding quality, quality of the welding technology, and model the component behaviour under cyclic loading. Therefore, these tests were performed for the 6005 T6 aluminium alloy and its weld. The specimens (Figs. 4 and 5) were cut from an aluminium alloy plate (Fig. 4) using electrical discharge machining (EDM).

All the tests were performed at room temperature using an 8874 Instron servo-hydraulic testing machine and a 2610 Instron extensometer, as shown in Fig. 5. Considering the aim of the test, represented by the automotive component approval, faces and roots of welds were not removed. This enabled the collection of data on the joint and comparison with the base material.

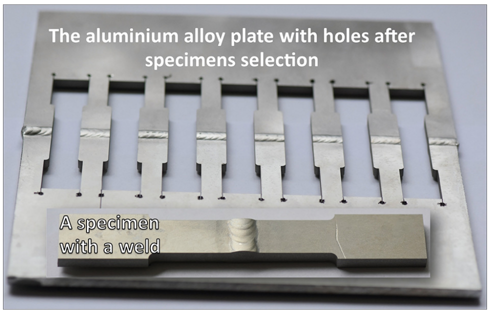

Fig. 4. Aluminium alloy plate after specimens manufacturing for examination of mechanical resistance of the weld.

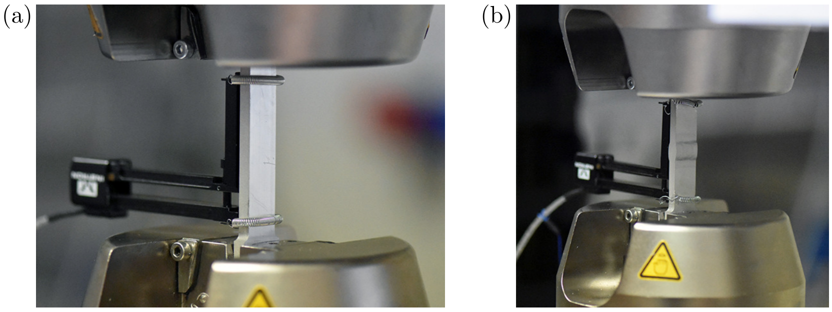

Fig. 5. Aluminium alloy specimen in 8874 Instron servo-hydraulic testing machine: (a) a base material; (b) with a weld.

3. Results

The results of the durability tests were strongly dependent on the type of signal used to control the test stand. If a signal force is applied, the changes in displacement values can be collected. They should be analysed at various stages of cyclic loading, including the last stage, as shown in Fig. 6. Even small differences in the responses of a tested object can be effectively demonstrated by applying this procedure. This is particularly evident in the changes in the minimum values of the captured signal.

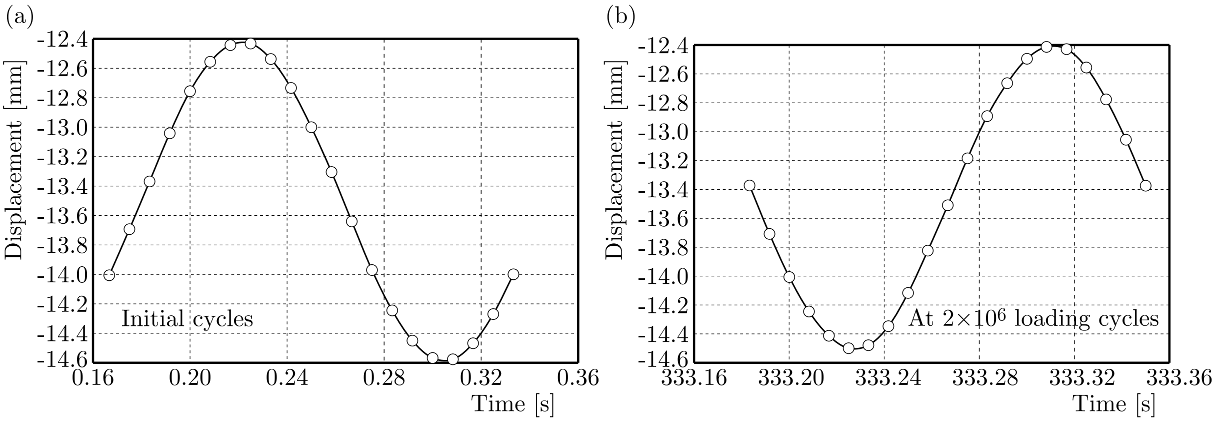

Fig. 6. Displacement captured during the durability test of a towing frame for a heavy recovery vehicle (test carried out at amplitude of ±18.6 kN and frequency of $f = 6\,\mathrm{Hz}$).

The same type of loading signal is used for other mechanical coupling devices such as adapters for SUVs in the USA trade market. Although construction of the components is not complex, a crack occurred in this case. This is visible in the region close to the weld as an effect of the joining technology (Fig. 7).

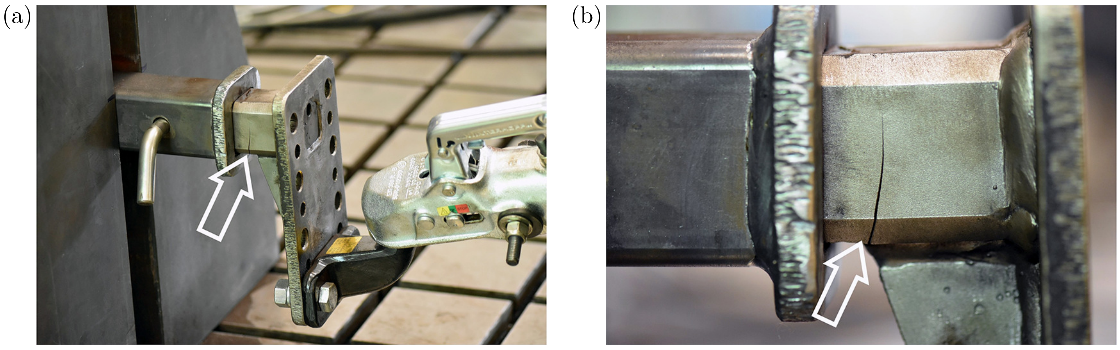

Fig. 7. Cracks in the adapter to SUV from USA market for a coupling after 1.7×10^6 loading cycles under amplitude of $\pm 12.33\,\mathrm{kN}$ and frequency $f = 5\,\mathrm{Hz}$.

This type of results, due to cyclic loading, is visible in the aluminium alloy; however, in this case, hairline cracks were the dominant type of damage, as shown in Fig. 8a. In steel, cracks are typically more visible and easier to detect. These reflect the low quality of the joint and its unfavourable influence on the base material of the vehicle frame, as shown in Fig. 8b.

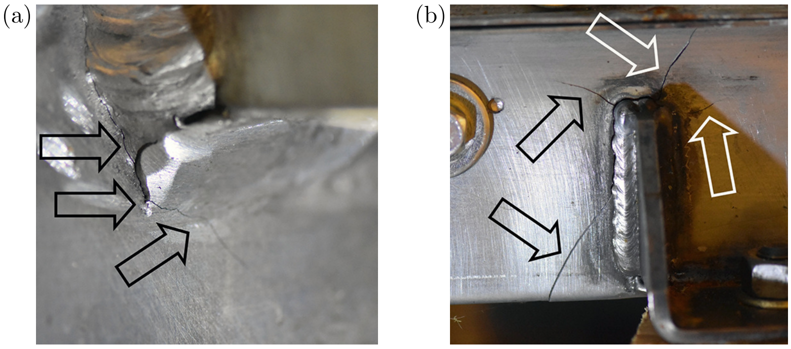

Fig. 8. Cracks in the platform with a coupling function after 2.24×10^6 loading cycles under amplitude of $\pm 10.3\,\mathrm{kN}$ and frequency $f = 4\,\mathrm{Hz}$ for: (a) aluminium alloy; (b) steel.

Notably, visual observations, macrophotographic techniques, and dye-penetrant methods enable identification of cracks. The defect inspection method depends on the applied engineering materials. Thus, in the case of typical steel grades (Figs. 7 and 8), observation or microphotography techniques are very suitable, whereas in the case of aluminium alloy or high-strength grades, these methods are not sufficient because of the occurrence of hairline cracks.

Therefore, if a component is made of an aluminium alloy or a high-strength steel, a macrophotography technique (Fig. 9) at negative and positive loading values, as well as a dye-penetrant technique, are recommended.

Fig. 9. Hair cracks in a component made of high-strength steel (S700MC) using dye-penetrant technique after 2×10^6 cycles.

The second stage of the durability test is determining the causes of cracks. To achieve this goal, tensile tests of welding joints are helpful because the recommended basic mechanical parameters of the object are selected by comparing the tensile characteristics of the base material and its weld, as shown in Fig. 4. Differences in the tensile characteristics of the base metal and welded material can be significant, reaching 120 MPa, as shown in Fig. 10. This also indicates that the fatigue resistance of the joint was lower than that of the alloy. Therefore, this region should be inspected during durability tests and considered for the mechanical parameters for the failure effect analysis approaches. This can also be selected as a feature for the qualification of the welding technology; however, the joining method should be improved.

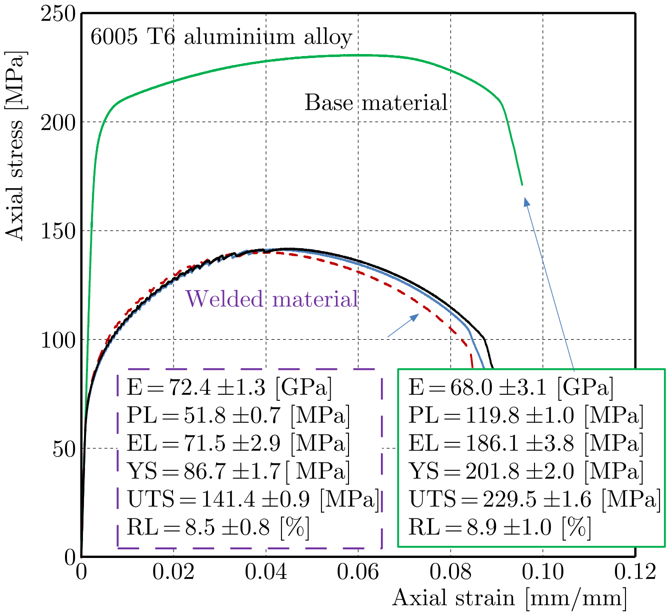

Fig. 10. Tensile characteristics of 6005 T6 aluminium alloy and its weld: E – Young's modulus, PL – proportional limit, EL – elastic limit, YS – yield stress, UTS – ultimate tensile strength, RL – relative elongation.

Differences between the welded and base materials were observed in the fracture zones. The alloy exhibited brittle failure (Fig. 10), whereas the joint exhibited ductile failure (Fig. 11). Moreover, in the case of the weld, a range of heat-affected zones was clearly observed.

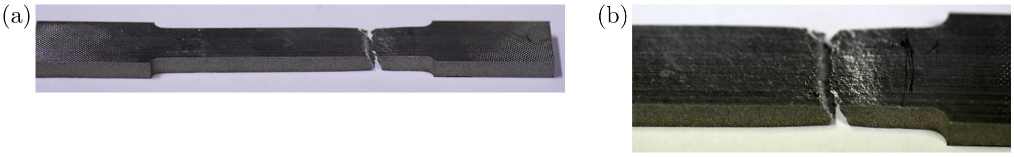

Fig. 11. 6005 T6 aluminium alloy after tensile test.

If the welding technology is suitable for the structural material, then the mechanical parameters of the joint can reach higher values than those of the base metal, as shown in Fig. 12. This can be observed in the fracture regions because, in contrast to the weld in the case of the parent material, a shear stress component occurs, as shown in Fig. 14. This is due to the higher

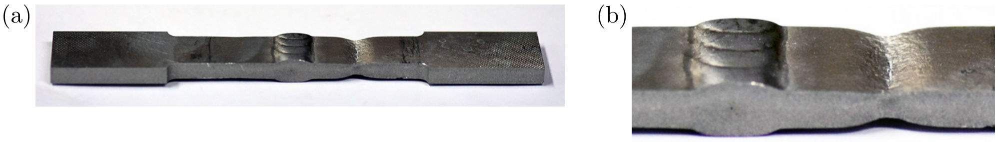

Fig. 12. 6005 T6 aluminium alloy specimen with weld after tensile test.

elongation value of the steel, as illustrated in Fig. 13. This causes the mechanical resistance of the weld to be better than that of steel under static and fatigue loading.

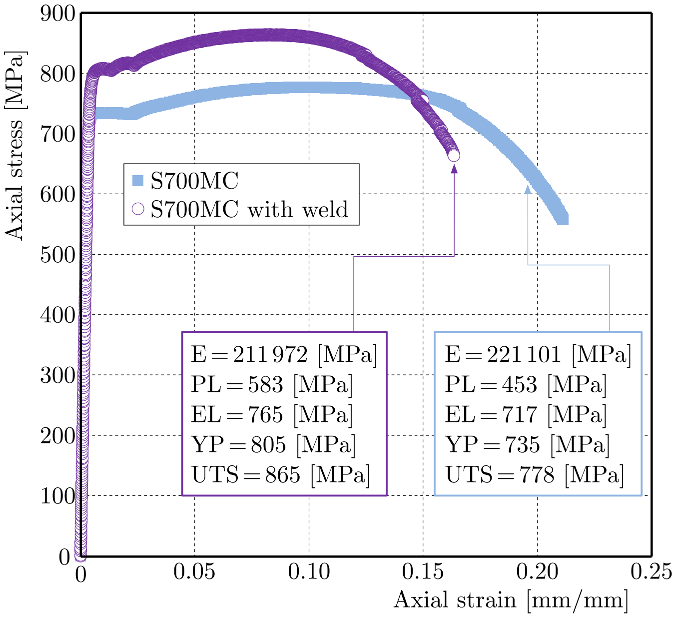

Fig. 13. Tensile characteristic of the S700MC and its weld.

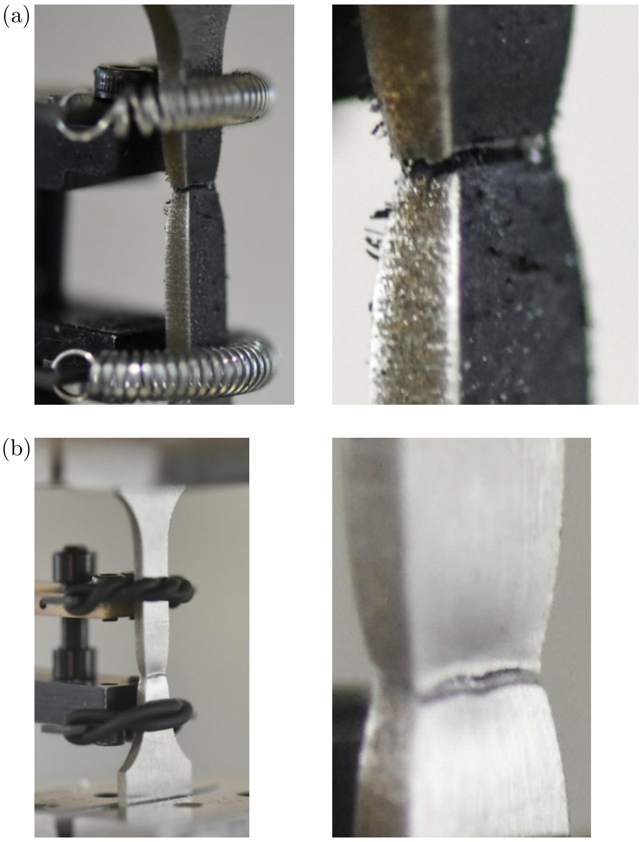

Fig. 14. Flat specimens after the tensile test: (a) S700MC; (b) the welded steel.

Nevertheless, as confirmed by the fatigue test (Fig. 15), the joint behaviour under cyclic loading was worse than that of the base metal. The difference between the fatigue limit values of the material sections was 290 MPa. This indicates that the weld is more sensitive to cyclic loading

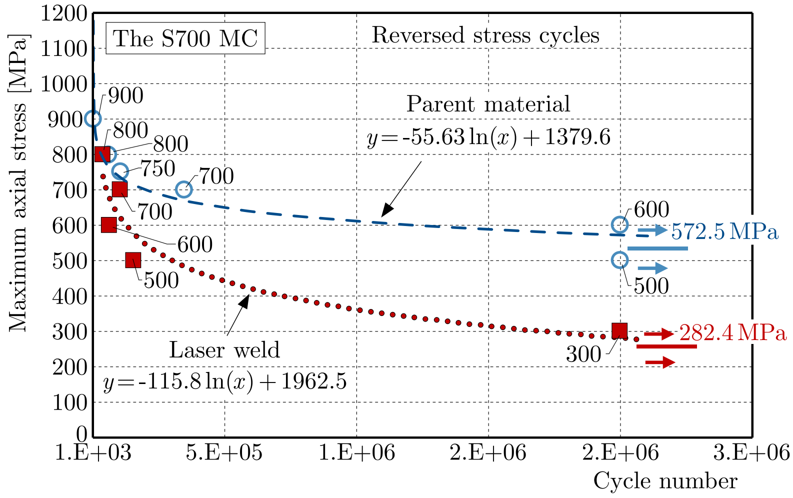

Fig. 15. Wöhler curve of the S700MC and its weld.

than the steel. This conclusion can also be drawn from the proportion of the fatigue limit values and the ultimate tensile strengths, which were 0.66 and 0.36 for the base metal and weld, respectively.

4. Summary

To determine the quality of a given object, durability testing requires the following conditions to be met:

a) an assembly should reflect the operating conditions of the object;
b) tests should be carried out for at least 2×10^6 cycles;
c) the inspection should cover all types of connections;
d) test results must indicate the causes of cracks or deformations;
e) welding technology should be qualified based on tensile and fatigue tests.

Taking into account a component type, its following regions require attention:

a) coupling zone and arms and their welds to a towing frame of a recovery vehicle;
b) a region for welding a coupling hole plate and bar for a coupling adapter to SUVs from the USA market;
c) a weld joining between an overrun section platform's frame and its subframe to auto-transporter.

References

1. Berger, H., Klein, M., Lambert, F., & Levadoux, B. (2010). Optical vibration measurement and frequency response analysis on large structures under multiple excitation load conditions. *Proceedings of ISMA2010 Including USD2010*, 1693–1702.

2. Creager, C., Johnson, K., Plant, M., Moreland, S., & Skonieczny, K. (2015). Push–pull locomotion for vehicle extrication. *Journal of Terramechanics*, *57*, 71–80. http://doi.org/10.1016/j.jterra.2014.12.001

3. Gowda, KG S., Ghai, A.S., Polisetti, S., Tiwari, S., & Ashok, B. (2015). Fatigue life prediction and durability test of passenger car Rheocast aluminium steering knuckle. *Journal of Materials Science & Surface Engineering*, *3*(1), 171–176.

4. Halfpenny, A. (2006). Method for accelerating dynamic durability tests. *9th International Conference on Recent Advances in Structural Dynamics*, Southampton, UK.

5. Instron, www.instron.com.
6. Jung, W.-W., Park, S.-C., Yoon, Y.-J., Park, S.-H., Lee, Y.-J., & Lee, M.H. (2003). Development of durability test system for automobile. *ICCSA*, October 22–25 (pp. 286–291). Gyeongju, Korea.
7. Król L., & Gasiak, G. (2018). Durability test of central differential in automotive industry. *AIP Conference Proceedings*, *2028*(1), Article 020006. https://doi.org/10.1063/1.5066396
8. MTS, www.mts.com, (access date: 07.03.2018).
9. Servotest System, www.servotestsystems.com, (access date: 07.03.2018).
10. SSTM (2019). Anthony Best Dynamics Outline Specification SSTM SP6102, issue 3, 4 pages.
11. Stembalski, M., Czarnuch, A., Szydłowski, T., & Batory, D. (2024). Assessment of the possibility of validating the durability testing method for large-sized vehicles based on changes in shock absorber characteristics – Preliminary tests. *Applied Sciences*, *14*(1), Article 127. https://doi.org/10.3390/app14010127
12. Szymczak, T., Brodecki, A., Kowalewski, Z.L., & Rudnik, D. (2022a). Mechanical investigations supported by DIC of structural components intended for operation. *Scientific Reports*, *12*, Article 19148. https://doi.org/10.1038/s41598-022-22615-0
13. Szymczak, T., Cholewiński, S., Brodecki, A., & Łączyński, J. (2022b). Mechanical coupling devices to various types of vehicles under cyclic loading. *International Journal of Automotive Technology*, *23*(1), 159–167. https://doi.org/10.1007/s12239-022-0013-2
14. UN/ECE, Regulation No 55 of the Economic Commission for Europe of the United Nations, (2010). Uniform provisions concerning the approval of mechanical coupling components of combinations of vehicles. http://data.europa.eu/eli/reg/2010/55(2)/oj
15. Wielton Group (in Polish), https://wieltongroup.com/news-press/aktualnosci/centrum-badawczo-rozwojowe-wieltonu-otwarte/, (access date: 01.07.2019).

Manuscript received December 2, 2024; accepted for publication January 22, 2025;

JOURNAL OF THEORETICAL
AND APPLIED MECHANICS
63, 3, pp. 471–478, Warsaw 2025
https://doi.org/10.15632/jtam-pl/200608

COMPARATIVE STUDY OF DIE MATERIALS FOR HOT ALUMINIUM FORMING USING AN AUTONOMOUS TRIBOLOGICAL TESTING SYSTEM

Vincent WU*, Xiao YANG, Heli LIU, Liliang WANG

Department of Mechanical Engineering, Imperial College London, London, United Kingdom
*corresponding author, *qiunan.wu22@imperial.ac.uk*

This study examines the tribological characteristics of different die materials for hot aluminium forming processes using an autonomous testing system. Four die materials – P20, CR7V, UH1, and RPU – were tested against AA6111 aluminium alloy blanks at elevated temperatures of 300 °C and 350 °C, with lubricant applied to the blank surface prior to each sliding cycle. The investigation incorporates both single-cycle friction behaviour and multi-cycle analysis to simulate industrial forming conditions, using an advanced robotic testing system for consistent and repeatable measurements. A comprehensive analysis of the coefficient of friction evolution during continuous sliding and across multiple cycles was conducted to understand the tribological behaviour under various temperature conditions. The study aims to establish quantitative relationships between die materials, temperature, and friction characteristics for hot forming applications, providing reference data for industrial die material selection.

Keywords: robotic arm; aluminium hot stamping; tribological analysis.

1. Introduction

The hot stamping of aluminium alloys has become increasingly important in the automotive industry due to its ability to form complex components while achieving high strength (Anyasodor & Koroschetz, 2017). The process offers significant advantages including weight reduction and enhanced mechanical properties (Atxaga *et al.*, 2022), making it particularly attractive for manufacturing lightweight vehicle components in automotive and aerospace industries.

The examination of tool-workpiece interfacial interactions in these processes is crucial as it directly influences material flow behaviour and surface quality of the formed components (Pujante *et al.*, 2015). These interactions become particularly complex at elevated temperatures, affecting both the forming process stability and final part quality (Venema *et al.*, 2018).

Various tribological testing methods have been developed and investigated to understand tool-workpiece interactions under different conditions. For general wear and friction studies, pin-on-disc and ball-on-disc tests have been widely employed due to their ability to maintain consistent contact conditions and continuous measurement capability (Ghiotti *et al.*, 2011; Hardell & Prakash, 2008). For sheet metal forming applications, researchers have developed more specialised testing methods. Strip drawing tests simulate the blank holder and die radius regions

---

Ministry of Science and Higher Education
Republic of Poland

The publication has been funded by the Polish Ministry of Science and Higher Education under the Excellent Science II programme "Support for scientific conferences".
The content of this article was presented during the 40th Danubia-Adria Symposium on Advances in Experimental Mechanics, Gdańsk, Poland, September 24–27, 2024.

(Decrozant-Triquenaux *et al.*, 2021; Schwingenschlögl & Merklein, 2020), while twist compression tests evaluate friction under high contact pressures (Kim *et al.*, 2008).

However, these conventional testing methods predominantly focus on lab-scale constant contact conditions, which cannot adequately represent industrial hot stamping processes. In actual forming operations, the interfacial conditions undergo complex evolution due to varying temperature distributions, changing contact pressures, and diverse sliding velocities (Pereira *et al.*, 2010). Die materials experience repeated contact with fresh workpiece surfaces at elevated temperatures. These interactions occur at temperatures typically ranging from 300 °C to 500 °C (Ma *et al.*, 2021), leading to dynamic changes in friction characteristics and potential wear mechanisms. Furthermore, the cyclic nature of mass production introduces additional complexities that are not captured in standard tribological tests, such as cumulative thermal effects and progressive changes in surface conditions.

To address these limitations, Yang *et al.* (2021; 2022) developed the TriboMate system, an advanced friction testing apparatus capable of evaluating various tool-workpiece combinations under hot forming conditions. Building upon this platform, our study incorporates enhanced control measures and data processing techniques to enable a comprehensive multi-cycle analysis, better representing industrial forming conditions.

This study employs this autonomous testing system to evaluate four different die materials – P20, CR7V, UH1, and RPU – against AA6111 aluminium alloy blanks at elevated temperatures of 300 °C and 350 °C. The investigation encompasses both single-cycle friction measurements for detailed friction evolution during continuous sliding and multi-cycle analysis to examine tribological stability under repeated contact conditions. Through this systematic approach, we aim to establish quantitative relationships between die materials and workpiece interactions under conditions representative of industrial hot forming processes.

2. Methodology

An autonomous tribological testing system TriboMate (Yang *et al.*, 2021; 2022) (as shown in Fig. 1) was developed to evaluate die materials under conditions representative of hot aluminium forming processes. The system centres on a UR10 robotic manipulator integrated with a custom-designed pin holder for precise control of the die material samples. A real-time data exchange (RTDE) interface enables a synchronous recording of force and position data throughout testing.

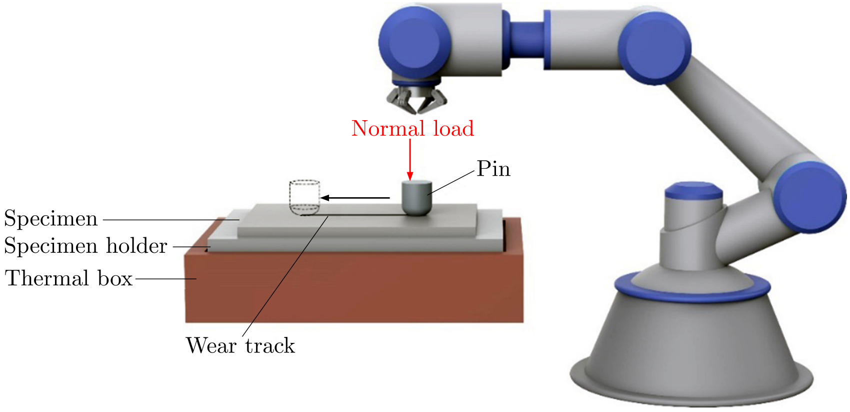

Fig. 1. Schematic diagram of the experimental setup (Yang *et al.*, 2021; 2022).

The test specimens comprised pins made from four die materials: P20, CR7V, UH1, and RPU, all without heat treatment. These materials were tested against AA6111 aluminium alloy blanks in T4 condition. Testing was conducted at two elevated temperatures: 300 °C and 350 °C, chosen to represent typical hot forming conditions. A direct contact heating system was used to heat the aluminium blanks. To compensate for heat losses and maintain stable blank temperatures of

300 °C and 350 °C, the heating system was set to 330 °C and 385 °C, respectively. Temperature was monitored using K-type thermocouples attached to the blank surface, and preliminary testing verified uniform temperature distribution across the blank. A pneumatic spraying system applied lubricant to the blank surface immediately prior to the sliding, with volumes of 35 $\mathrm{g/m^2}$ at 300 °C and 55 $\mathrm{g/m^2}$ at 350 °C to maintain consistent lubrication conditions.

The testing sequence began with heating the aluminium blank to the target temperature. Once the desired temperature was reached, lubricant was applied to the blank surface. The spherical die material pin then engaged with the blank under a constant normal load of 6 N, sliding at a speed of 30 mm/s over a distance of 75 mm. This sliding action represents a single cycle of contact between die and workpiece material (Yang *et al.*, 2024a; 2024b).

To simulate industrial stamping operations where tools repeatedly contact fresh blank surfaces, each test comprised 18 consecutive cycles on different tracks (as shown in Fig. 2). The robotic system maintained a 2 mm spacing between adjacent tracks to prevent overlap. This testing strategy reflects the actual working conditions of die materials in mass production, where tools contact new blank surfaces while experiencing cumulative wear effects. The system maintained consistent testing parameters throughout all the cycles, including temperature, contact load, and sliding speed.

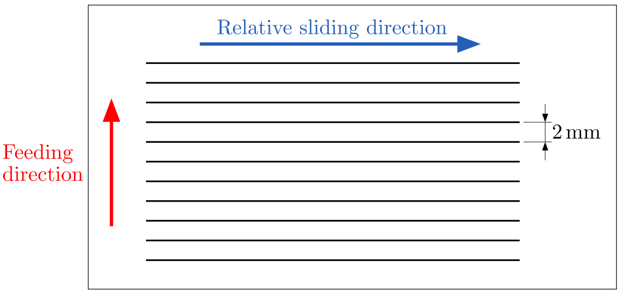

Fig. 2. Schematic of tribological test setup showing sliding and feeding directions.

Data processing occurred in two stages. During testing, the system collected real-time measurements of normal and friction forces along with position data. These measurements enabled the calculation of the instantaneous coefficient of friction values throughout each sliding cycle. The second stage involved the statistical analysis of the collected data to examine both detailed friction evolution within individual cycles and broader trends across multiple cycles.

For a single-cycle analysis, the system tracked the coefficient of friction evolution throughout the entire 75 mm sliding distance, capturing initial contact behaviour, running-in characteristics, and steady-state friction conditions. A multi-cycle analysis examined the evolution of average friction coefficients across all 18 cycles, measuring the tribological behaviour under repeated contact with fresh blank surfaces.

The testing system incorporated several control measures to ensure measurement reliability. Temperature monitoring maintained consistent heating conditions throughout testing. The pneumatic spraying system provided uniform lubricant coverage across all the tests. Position sensors in the robotic manipulator ensured precise control of sliding speed and distance, while the external force sensor attached on the end effector maintained consistent normal load application.

3. Results and discussion

3.1. Effect of a die material on the coefficient of friction evolution at 300 °C

The coefficient of friction (CoF) measurements at 300 °C revealed distinct characteristics for each die material in both single-cycle and multi-cycle analyses. The initial temperature significantly influenced the tribological interaction patterns between the die materials and the aluminium blank.

In the single-cycle sliding tests, P20 recorded the highest average CoF values with notable fluctuations. High-amplitude oscillations persisted throughout most of the sliding distance, indicating continuous variations in the tribological interface. After 60 mm of sliding, P20 exhibited a decreasing trend in CoF, suggesting potential changes in contact conditions during extended sliding. CR7V demonstrated a characteristic U-shaped CoF evolution pattern, with an initial decrease in friction followed by a gradual increase in the latter portion of sliding. In contrast, both UH1 and RPU maintained relatively steady CoF values throughout the sliding distance, with RPU recording the lowest average values. This stability in friction behaviour suggests more consistent tribological interactions at the interface (Fig. 3).

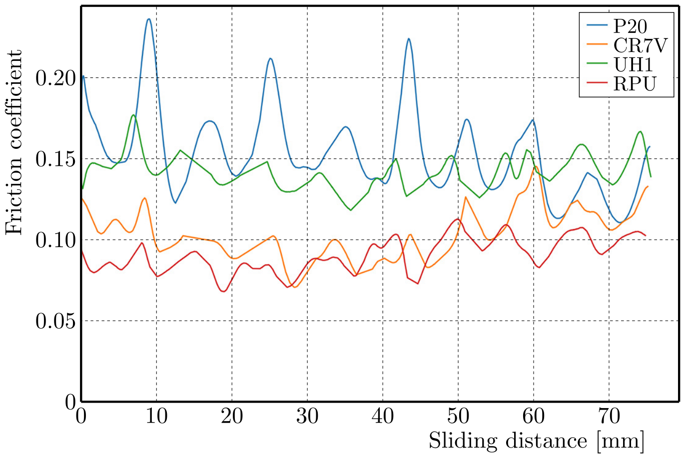

Fig. 3. Comparison of the coefficient of friction evolution on different die materials at 300 °C.

The multi-cycle analysis at 300 °C provided insights into the evolution of tribological characteristics across repeated sliding events. Throughout the 18 test cycles, all the materials maintained CoF values below 0.5, indicating stable tribological conditions. P20 consistently recorded the highest CoF values, ranging from 0.165 to 0.285 across all the cycles, with notable cycle-to-cycle variations. CR7V showed a distinctive behaviour pattern, exhibiting a gradual increase in average CoF until the sixth cycle, with values ranging from 0.104 to 0.217, after which the values stabilised. RPU maintained the lowest and most consistent CoF range (0.081–0.180) throughout the cycles, though its standard deviation increased with a cycle number. For all the materials, the progressive increase in standard deviation with a cycle number suggests growing variability in tribological interactions over repeated sliding events (Fig. 4).

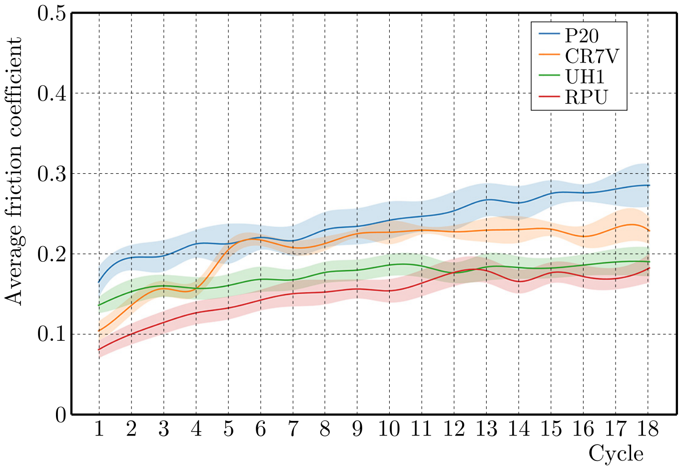

Fig. 4. Comparison of average CoF evolution for a multi-cycle analysis on different die materials at 300 °C, with SD envelopes.

3.2. Effect of a die material on the coefficient of friction evolution at 350 °C

At the elevated temperature of 350 °C, the friction characteristics demonstrated marked differences from the lower temperature tests, revealing temperature-dependent changes in the tribological behaviour of all the die materials.

In a single-cycle analysis, a distinctive feature emerged: all the materials exhibited a pronounced running-in stage within the first 3 mm of sliding. This stage was characterized by high initial CoF values followed by rapid stabilisation, a phenomenon not observed at 300 °C. P20 recorded the highest CoF values during this initial running-in stage. After the running-in period, all four die materials showed similar CoF values, fluctuating within a narrow range between 0.15 and 0.2, with CR7V maintaining its characteristic U-shaped evolution pattern (Fig. 5).

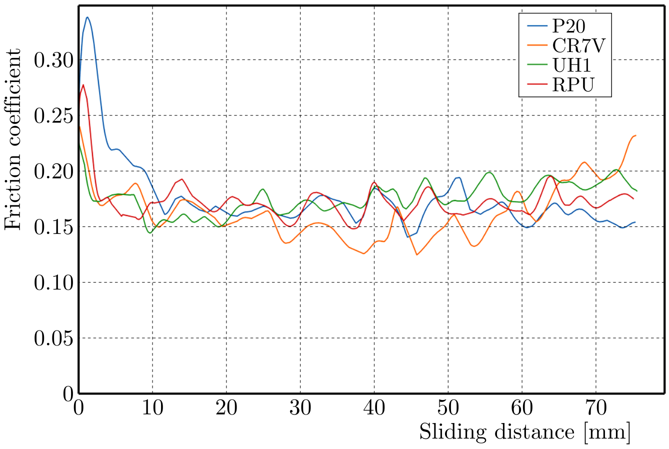

Fig. 5. Comparison of the coefficient of friction evolution on different die materials at 350 °C.

The multi-cycle behaviour at 350 °C revealed distinctive patterns in friction evolution. All the materials exhibited a gradual increase in average CoF across the successive cycles, accompanied by progressively increasing standard deviations. During the initial and middle stages (cycles 1–14), the materials showed similar CoF ranges, varying from 0.18 ±0.02 to 0.3 ±0.01, indicating more uniform tribological behaviour at elevated temperatures. The later stages (cycles 15–18) revealed differentiation in material behaviour, with CR7V and RPU recording notably lower average CoFs, reaching values of 0.273 and 0.312, respectively, at cycle 18. This divergence in late-cycle behaviour suggests the emergence of material-specific tribological mechanisms at extended sliding durations (Fig. 6).

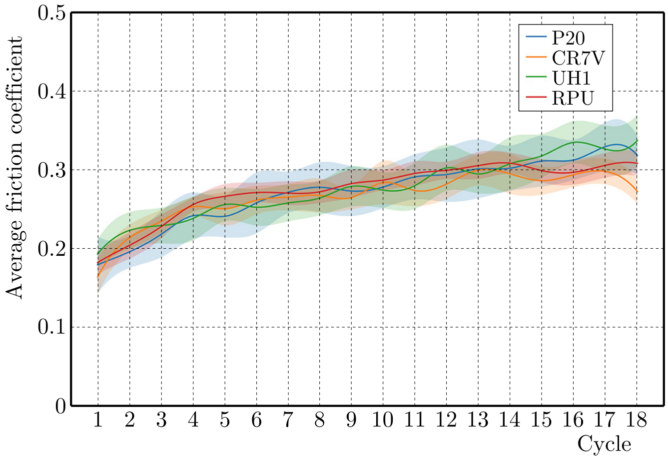

Fig. 6. Comparison of average CoF evolution for a multi-cycle analysis on different die materials at 350 °C, with SD envelopes.

3.3. Effect of lubricant volume on the coefficient of friction evolution at 350 °C

Due to the elevated temperature of 350 °C, a higher lubricant volume was required to compensate for potential evaporation and maintain optimal lubrication performance. To investigate this effect, the UH1 die material was selected for further evaluation, as it exhibited relatively stable tribological behaviour in the previous tests.

Figure 7 presents the single-cycle CoF evolution for UH1 at 350 °C under three different lubricant volumes: 35 $\mathrm{g/m^2}$, 55 $\mathrm{g/m^2}$, and 70 $\mathrm{g/m^2}$. At the lower volume of 35 $\mathrm{g/m^2}$, which was used for the tests at 300 °C, the CoF values were higher, indicating inadequate lubrication at the elevated temperature.

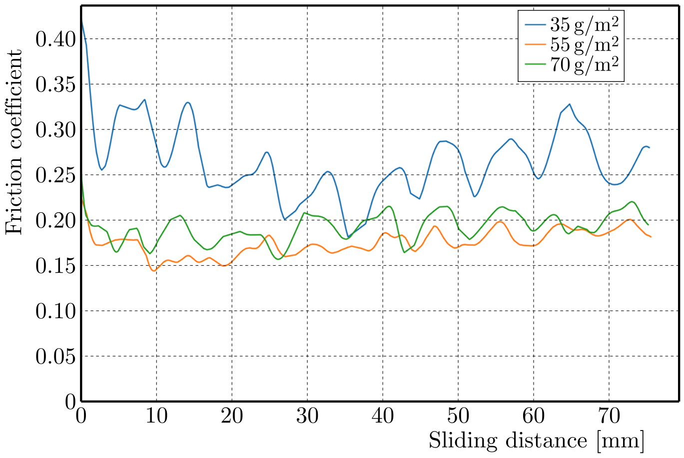

Fig. 7. Comparison of the coefficient of friction evolution on a different lubricant volume at 350 °C.

When the lubricant volume was increased to 55 $\mathrm{g/m^2}$, a significant reduction in CoF was observed, demonstrating the beneficial effect of enhanced lubrication at higher temperatures. The volume of 55 $\mathrm{g/m^2}$ was considered saturated, as a further increase in the lubricant volume to 70 $\mathrm{g/m^2}$ did not lead to a further decrease in CoF. In fact, the CoF values for the 70 $\mathrm{g/m^2}$ condition were slightly higher than those for 55 $\mathrm{g/m^2}$, potentially due to excess lubricant affecting the tribological interactions.

4. Conclusions

In this study, tribological characteristics of various die materials for hot aluminium forming were investigated using an autonomous testing system. The comprehensive evaluation encompassed both single-cycle friction evolution and a multi-cycle stability analysis at elevated temperatures of 300 °C and 350 °C. The autonomous system enabled consistent measurement conditions throughout testing, incorporating real-time data acquisition and advanced processing routines. A systematic comparison between P20, CR7V, UH1, and RPU die materials revealed distinct temperature-dependent friction behaviours and long-term stability characteristics. The following conclusions can be drawn from this investigation:

- at 300 °C, die materials exhibited distinct friction patterns, with P20 recording the highest CoF values (0.165–0.285) and RPU showing the lowest range (0.081–0.180) across 18 cycles. The CoF values increased initially before stabilizing in the middle and late cycles, while standard deviation showed a progressive increase with a cycle number;
- temperature elevation to 350 °C introduced a pronounced running-in stage within the first 3 mm of sliding for all the materials. After this stage, the materials showed uniform friction behaviour with CoF values between 0.15–0.2. A multi-cycle analysis revealed similar CoF ranges (0.18 ±0.02 to 0.3 ±0.01) during the early cycles, with CR7V and RPU recording lower values of 0.273 and 0.312, respectively, in the final cycles;

- the transition from 300 °C to 350 °C demonstrated significant changes in friction characteristics, most notably the emergence of the running-in stage and reduction in friction coefficient differences between the materials. These temperature-dependent changes provide essential insights for die material selection in different temperature ranges;
- lubricant volume optimisation proved critical at elevated temperatures, as evidenced by UH1's reduced friction coefficients when increasing lubricant volume from 35 g/m^2 to 55 g/m^2 at 350 °C, while a further increase to 70 g/m^2 showed no additional benefits.

References

1. Anyasodor, G., & Koroschetz, C. (2017). Industrial based volume manufacturing of lightweight aluminium alloy panel components with high-strength and complex-shape for car body and chassis structures. *Journal of Physics: Conference Series*, *896*, Article 012093. https://doi.org/10.1088/1742-6596/896/1/012093
2. Atxaga, G., Arroyo, A., & Canflanca, B. (2022). Hot stamping of aerospace aluminium alloys: Automotive technologies for the aeronautics industry. *Journal of Manufacturing Processes*, *81*, 817–827. https://doi.org/10.1016/j.jmapro.2022.07.032
3. Decrozant-Triquenaux, J., Pelcastre, L., Courbon, C., Prakash, B., & Hardell, J. (2021). Effect of surface engineered tool steel and lubrication on aluminium transfer at high temperature. *Wear*, *477*, Article 203879. https://doi.org/10.1016/j.wear.2021.203879
4. Ghiotti, A., Bruschi, S., & Borsetto, F. (2011). Tribological characteristics of high strength steel sheets under hot stamping conditions. *Journal of Materials Processing Technology*, *211*(11), 1694–1700. http://doi.org/10.1016/j.jmatprotec.2011.05.009
5. Hardell, J., & Prakash, B. (2008). High-temperature friction and wear behaviour of different tool steels during sliding against Al–Si-coated high-strength steel. *Tribology International*, *41*(7), 663–671. https://doi.org/10.1016/j.triboint.2007.07.013
6. Kim, H., Sung, J., Goodwin, F.E., & Altan, T. (2008). Investigation of galling in forming galvanized advanced high strength steels (AHSSs) using the twist compression test (TCT). *Journal of Materials Processing Technology*, *205*(1–3), 459–468. https://doi.org/10.1016/j.jmatprotec.2007.11.281
7. Ma, Z., Ji, H., Huang, X., Xiao, W., & Tang, X. (2021). Research on high temperature stamping forming performance and process parameters optimization of 7075 aluminum alloy. *Materials*, *14*(19), Article 5485. https://doi.org/10.3390/ma14195485
8. Pereira, M.P., Yan, W., & Rolfe, B.F. (2010). Sliding distance, contact pressure and wear in sheet metal stamping. *Wear*, *268*(11–12), 1275–1284. https://doi.org/10.1016/j.wear.2010.01.020
9. Pujante, J., Vilaseca, M., Casellas, D., & Riera, M.D. (2015). The role of adhesive forces and mechanical interaction on material transfer in hot forming of aluminium. *Tribology Letters*, *59*(1), Article 10. https://doi.org/10.1007/s11249-015-0542-1
10. Schwingenschlögl, P., & Merklein, M. (2020). Characterization of tribological conditions within direct hot stamping. *Journal of Materials Processing Technology*, *278*, Article 116535. https://doi.org/10.1016/j.jmatprotec.2019.116535
11. Venema, J., Hazrati, J., Matthews, D., & van den Boogaard, T. (2018). An insight in friction and wear mechanisms during hot stamping. *Key Engineering Materials*, *767*, 131–138. https://doi.org/10.4028/www.scientific.net/KEM.767.131
12. Yang, X., Liu, H., Dhawan, S., Politis, D.J., Zhang, J., Dini, D., Hu, L., Gharbi, M.M., & Wang, L. (2022). Digitally-enhanced lubricant evaluation scheme for hot stamping applications. *Nature Communications*, *13*, Article 5748. https://doi.org/10.1038/s41467-022-33532-1
13. Yang, X., Liu, H., Wu, V., Politis, D.J., & Wang, L. (2024a). Interactive friction modelling and digitally enhanced evaluation of lubricant performance during aluminium hot stamping. *Lubricants*, *12*(12), Article 417. https://doi.org/10.3390/lubricants12120417

14. Yang, X., Liu, H., Wu, V., Politis, D.J., Yao, H., Zhang, J., & Wang, L. (2024b). Digitally enhanced development of customised lubricant: Experimental and modelling studies of lubricant performance for hot stamping. *Computers in Industry*, *163*, Article 104152. https://doi.org/10.1016/j.compind.2024.104152
15. Yang, X., Zhang, Q., Zheng, Y., Liu, X., Politis, D., El Fakir, O., & Wang, L. (2021). Investigation of the friction coefficient evolution and lubricant breakdown behaviour of AA7075 aluminium alloy forming processes at elevated temperatures. *International Journal of Extreme Manufacturing*, *3*(2), Article 025002. https://doi.org/10.1088/2631-7990/abe847

Manuscript received December 15, 2024; accepted for publication January 29, 2025;
published online June 13, 2025, 2025.

JOURNAL OF THEORETICAL
AND APPLIED MECHANICS
63, 3, pp. 479–489, Warsaw 2025
https://doi.org/10.15632/jtam-pl/200711

DIRECT SEARCH METHODS FOR DETERMINING NEW DESIGNS OF AUXETIC COMPOSITE MATERIALS

Iulian Constantin COROPEȚCHI[1,2], Dan Mihai CONSTANTINESCU[1,3], Alexandru VASILE[1,2], Andrei Ioan INDREŞ[1,2], Ştefan SOROHAN[1], Dragos Alexandru APOSTOL[1]

[1] *National University for Science and Technology Politehnica Bucharest, Bucharest, Romania*
[2] *Military Technical Academy "Ferdinand I", Bucharest, Romania*
[3] *Technical Sciences Academy of Romania, Bucharest, Romania*
*corresponding author, *iulian.coropetchi@mta.ro*

Composite materials have gained significant attention in various engineering applications due to their ability to exhibit unique properties that can be tailored to meet specific design requirements. Among these, auxetic materials stand out for their counterintuitive behavior of expanding in all directions when stretched, as opposed to traditional materials which contract. This property makes auxetic materials promising candidates for applications such as impact protection, energy absorption, and advanced engineering structures. In this paper we investigate the application of direct search methods in determining new designs of auxetic composite materials.

Keywords: auxetic materials; composite materials; direct search methods.

1. Introduction

Structural optimization is a significant area of focus in mechanical engineering and has been continuously evolving over the years. It is commonly applied to reduce the material usage and total deformation energy of structures while ensuring adequate strength and mechanical stiffness (Li *et al.*, 2020). Traditionally, structural optimization can be categorized into three main types: 1) dimensional optimization, which involves determining the optimal distribution of parameters such as plate thickness or cross-sectional areas of truss bars; 2) shape optimization, aimed at identifying the optimal geometry of a specified domain; and 3) topological optimization, which stands apart from the other two as it allows the material to occupy any position within the defined domain (Bendsøe & Sigmund, 2004).

Structural optimization nowadays encompasses a much broader range of topics, extending beyond the previously mentioned classical approaches. Notable examples include, among others, cellular microstructures (Pan *et al.*, 2020; Ptochos & Labeas, 2012), deformable mechanisms (Zhu *et al.*, 2020), spinodal structures (Kumar *et al.*, 2020), multiphysics problems (Yoon, 2021), and composite materials (Casalotti *et al.*, 2020; Gu *et al.*, 2018a). Alongside the diversity of applications, significant attention is also devoted to the mathematical methods used to solve these problems. These methods can generally be grouped into three major categories: gradient-based approaches (Ghiasi *et al.*, 2009; 2010; Luu & Banh, 2023; Sandhu, 1971; Tavakoli, 2014),

---

Ministry of Science and Higher Education
Republic of Poland

The publication has been funded by the Polish Ministry of Science and Higher Education under the Excellent Science II programme "Support for scientific conferences".
The content of this article was presented during the 40th Danubia-Adria Symposium on Advances in Experimental Mechanics, Gdańsk, Poland, September 24–27, 2024.

direct search algorithms (Coropețchi *et al.*, 2022; Sait *et al.*, 2023; Vasile *et al.*, 2022), and artificial intelligence techniques (Gu *et al.*, 2018b; Harish *et al.*, 2020; Yu *et al.*, 2019; Zhang *et al.*, 2019).

In mechanical engineering, the development of efficient methodologies for solving optimization problems remains a continually evolving area of research. The intricate and dynamic nature of structures needs advanced optimization techniques capable of exploring the entire solution space and identifying designs that meet specific performance requirements. As computational capabilities and methodologies progress, researchers have access to a variety of optimization techniques, each offering unique advantages and limitations.

This article focuses on reviewing direct search methods for solving structural optimization problems in the field of composite materials. We investigate the application of these methods in determining new designs of auxetic materials. The methods are valued for their simplicity, versatility, and applicability to a wide range of problems. Unlike gradient-based approaches, direct search methods do not depend on explicit knowledge of the gradient of the objective function. Instead, they explore the optimization space through a structured sequence of trial points, making them particularly well suited to problems with non-differentiable, discontinuous, or computationally intensive objective functions.

The purpose of this article is to compare and assess various direct search methods based on their performance in solving structural optimization problems. For each method, its strengths, weaknesses, and practical considerations are analyzed in the context of the problem being addressed. This analysis aims to highlight the specific advantages and trade-offs associated with each method, providing valuable insights for their application in structural optimization tasks.

2. Problem definition

This study aims to evaluate the performance of various direct search methods in solving structural optimization problems. To facilitate this evaluation, we define an optimization problem involving composite materials, which serves as a benchmark for testing the methods. As the primary focus of the paper is to compare the performance of the methods rather than solving a specific structural problem, the selected problem is largely theoretical but has also practical application in the field of auxetic materials.

Composite materials, known for combining the properties of multiple constituents, introduce a new dimension to structural design. The optimization of structures made from these materials highlights the inherent complexity of balancing material proportions and orientations to achieve desired performance criteria. With their unique combination of strength, lightweight properties, and durability, composite materials present a challenging and yet rewarding domain for optimization methodologies.

We consider a 2D periodic structure consisting of two different materials for which the material domains are defined by triangular pixels in a representative volume element (RVE) which is shaped as a hexagon with 4 pixels on each side. Each pixel can be of hard or soft material. Hexagonal cells are obtained by rotation of the base area, as shown in Fig. 1. In the base triangle

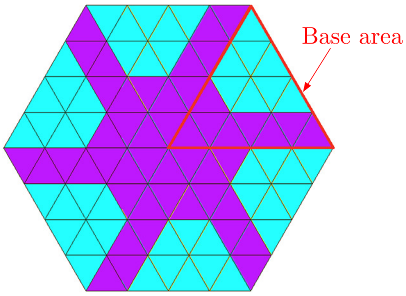

Fig. 1. Base area rotated 6 times with 60°.

area of the hexagon, there are 16 material domains. In our problem, we impose the condition that half of the material domains must be soft and the other half hard.

The RVE can be repeated in a pattern so that it can form the periodic structure presented in Fig. 2. Analyzing the figure, we can identify a rectangular area that contains two RVEs and form the analysis domain that will be used in FEM simulations.

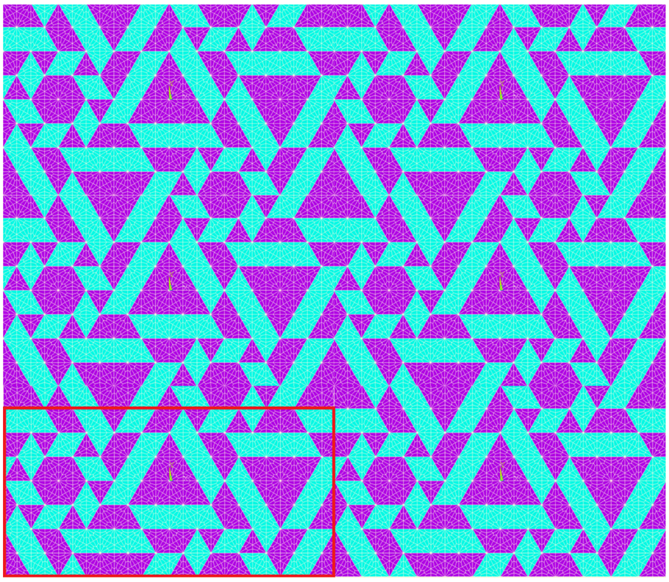

Fig. 2. Periodic structure and analysis domain.

The materials from which the analysis domain is built are represented with magenta and cyan colors. For each material, Young's modulus and Poisson's coefficient are known. The materials properties corresponding to each color are presented in Table 1.

Table 1. Materials description.

Material	Hard	Soft
Color	🟪	🟦
Young's modulus	100000 MPa	1000 MPa
Poisson's ratio	0.2	0.4

In order to simulate the analysis domain in a periodic structure, specific boundary conditions must be applied for every load case to determine Poisson's coefficient. According to (Sorohan *et al.*, 2018) for bidimensional analysis, one should use 3 load cases for determining the specific material properties. These load cases are traction alongside the X-axis, traction alongside the Y-axis and shear in the XY plane. The representation of the boundary conditions for the analysis domain in the first load case is shown in Fig. 3, and the boundary conditions for all three load cases are presented in Table 2. In Fig. 3, the nodes that have 0 displacement are represented with blue arrows alongside the direction in which this constraint is imposed, and the nodes that are coupled in terms of displacement are represented with green arrows alongside the direction in which the coupling of the displacement is imposed.

The finite elements utilized can be quadrilaterals with either four or eight nodes. In a linear elastic analysis, the stress distribution within each finite element may vary unless techniques such as reduced integration for linear quadrilateral elements or stress averaging across the element are applied. However, for practical purposes, constant stresses are often assumed for each finite element to simplify the calculations.

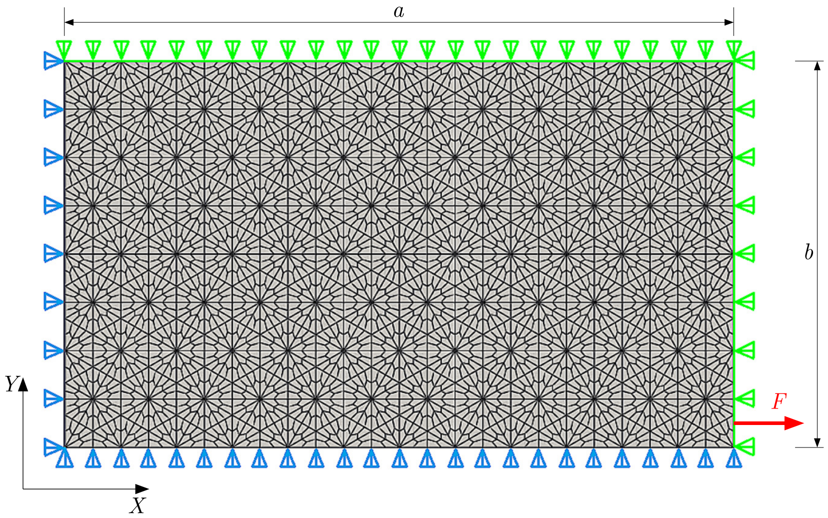

Fig. 3. Representation of load case 1.

Table 2. Periodic boundary conditions for the three load cases.

Load case	Nodes	u_x	u_y	Observation
1 Traction X	1 $(X=0)$	0	Free	Symmetry X
	2 $(X=a)$	$\overline{\varepsilon_{01}}a$	Free	–
	3 $(Y=0)$	Free	0	Symmetry Y
	4 $(Y=b)$	Free	Coupled	–
2 Traction Y	1 $(X=0)$	0	Free	Symmetry X
	2 $(X=a)$	Coupled	Free	–
	3 $(Y=0)$	Free	0	Symmetry Y
	4 $(Y=b)$	Free	$\overline{\varepsilon_{02}}b$	-
3 Shear XY	1 $(X=0)$	Free	0	Asymmetry X
	2 $(X=a)$	Free	0	–
	3 $(Y=0)$	0	Free	Asymmetry Y
	4 $(Y=b)$	$\overline{\gamma_{03}}b$	Free	–

While performing the FEM simulations, we observed that all the solutions are isotropic. This can be explained by the way the periodic model is constructed with the rotation of the base triangle into forming a hexagonal RVE and the repeating of the RVE. In this case, we can use only the first load case in order to determine all the mechanical properties of a configuration.

For the present problem, the parameter of interest is the effective Poisson's coefficient which can be obtained using the relation:

$$\nu_{12eff} = -\frac{\bar{\varepsilon}_y}{\bar{\varepsilon}_x} = -\frac{\frac{1}{V}\sum\limits_{i=1}^{NE} V_i\varepsilon_{yi}}{\frac{1}{V}\sum\limits_{i=1}^{NE} V_i\varepsilon_{xi}}, \tag{2.1}$$

where ν_{12eff} – effective Poisson's coefficient, $\bar{\varepsilon}_y$ – average strain in the y-direction, $\bar{\varepsilon}_x$ – average strain in the x-direction, V – total volume of the analysis domain, NE – number of finite elements in the domain, V_i – volume of element i, ε_{yi} – average strain in y-direction in element i, ε_{xi} – average strain in x-direction in element i.

Validating the performance of an optimization algorithm requires knowledge of the optimal solution. To identify the optimal solution, the brute force method is applied by evaluating all possible configurations. For the described problem with 16 material domains in the base area, there are 12,870 possible solutions.The distribution of Poisson's coefficient values for all solutions is illustrated in Fig. 4 as a histogram. Notably, only 1.2 % of the solutions exhibit a negative Poisson's coefficient.

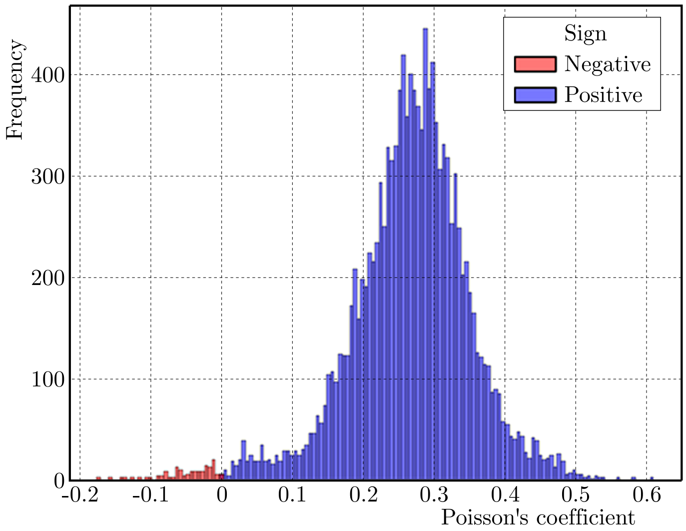

Fig. 4. Histogram of Poisson's coefficient for all solutions.

In evaluating our optimization algorithm, we choose the first three values as optimal solutions, representing almost 0.1 % of all solutions. The periodic model of the chosen best solutions and the value for Poisson's coefficient are presented in Fig. 5.

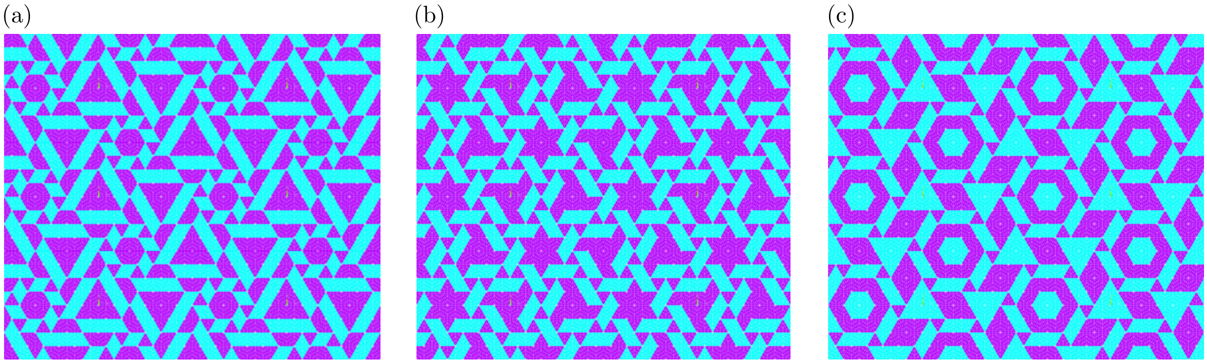

Fig. 5. Optimal solutions for 16 material domains base triangle:
(a) 1st best, $\nu = -0.174072$; (b) 2nd best, $\nu = -0.155901$; (c) 3rd best, $\nu = -0.142588$.

3. Direct search methods

Analytical methods are renowned for their rapid convergence rates. However, direct search methods offer a significant advantage by not requiring gradient information for either the objective function or constraints. This characteristic is particularly beneficial in the field of topological optimization, where computing the gradients of the objective function can be computationally expensive or, in some cases, infeasible. Instead, direct search methods rely solely on the objective function values from previous iterations to identify the optimal solution.

Enumeration, also known as brute force search, is a method that involves exploring and evaluating all possible combinations of the problem's variables to identify the best solution. While this approach guarantees finding the global optimum, it is often impractical or computationally impossible due to the immense number of combinations that must be evaluated. Nevertheless, the brute force method can be valuable for generating data sets in smaller-scale problems. For instance, in (Gu *et al.*, 2018a), this method is employed to create a labeled dataset used to train a neural network. Once trained, the neural network can efficiently identify optimal structures within a larger search space, where the problem size makes the brute force approach infeasible.

The greedy algorithm iteratively evaluates a set of configurations, making incremental changes toward the best configuration at each step, until no further improvements to the objective function are possible. However, a key limitation of the greedy algorithm is its inability to achieve a better solution if it must pass through a suboptimal solution as an intermediate step. To address this limitation, the algorithm requires a well-defined variable space and an appropriately chosen iteration step. In (Coropețchi *et al.*, 2022), the greedy algorithm was applied to design repetitive composite cellular microstructures aimed at maximizing stiffness in two orthogonal directions. The flowchart of the greedy algorithm is presented in Fig. 6.

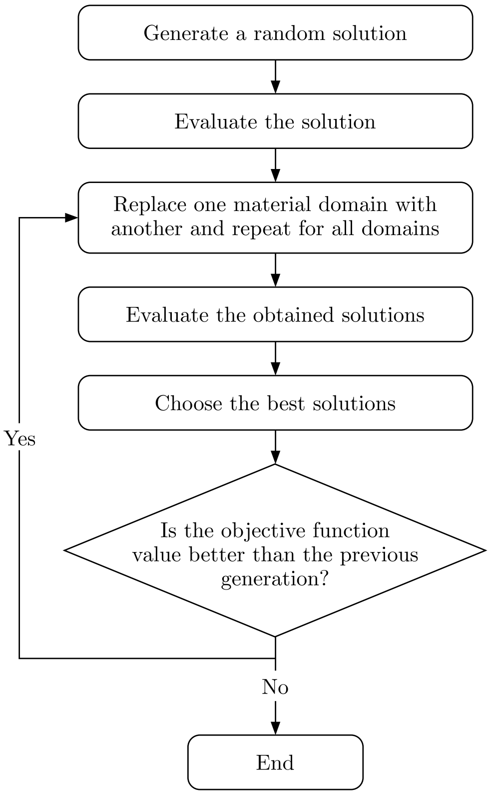

Fig. 6. Flowchart of the greedy algorithm.

As previously discussed, the greedy algorithm evaluates a set of configurations and iteratively makes changes toward the best configuration until no further improvements to the objective function can be achieved. For the described problem, the process begins with a random material distribution. The algorithm evaluates all potential configurations derived from this initial setup by swapping pairs of material domains with different materials. Specifically, in the case of the base triangle, there are 16 material domains – eight of material #1 and eight of material #2. At each iteration, the greedy algorithm examines 64 possible configurations resulting from exchanging pairs of different materials. It selects the configuration with the best objective function and repeats the process in the next step. The algorithm continues this process, selecting the best modification at each iteration, and stops when no further improvements are found, returning the best solution discovered.

The greedy algorithm offers notable advantages, including simplicity of implementation and a relatively small number of objective function evaluations needed to reach an optimal solution. At each iteration, it converges to a local optimum, which, in some cases, may coincide with the global optimum. However, its primary drawback is its inability to guarantee the global optimum. This limitation arises from the possibility that achieving a better solution may require simultaneous changes to multiple pairs of material domains – something the algorithm does not account for.

According to Clerc (2006), particle swarm optimization (PSO) is a collective, iterative, and decentralized optimization method that emphasizes cooperation among solutions. This partially random algorithm operates without a selection operator. To identify the global optimum within a solution space, the algorithm begins with a swarm of particles (potential solutions), which share information such as their current positions and corresponding objective function values.

Inspired by the social behavior observed in bird flocks (Engelbrecht, 2007), the algorithm models individual solutions, referred to as particles, "flying" through a multidimensional solution space. The movement of each particle is influenced by socio-psychological factors, specifically the tendency of individuals to compete and learn from the success of others. As a result, a particle's position updates are guided by its own experience as well as the knowledge and performance of its neighboring particles. The flowchart of the PSO algorithm is shown in Fig. 7.

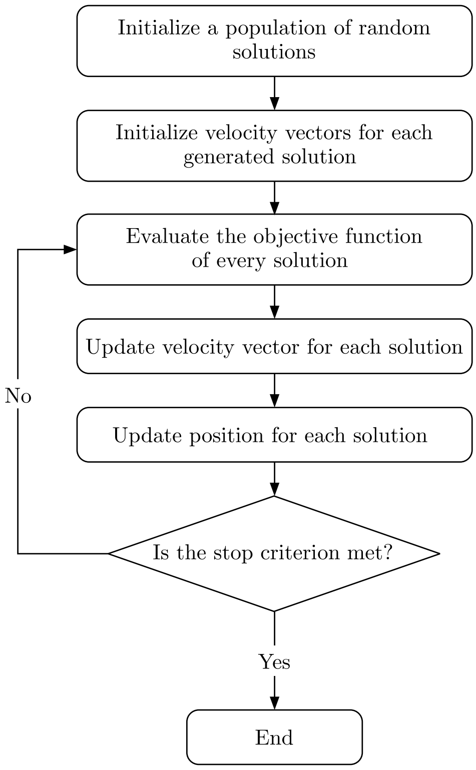

Fig. 7. Flowchart of the PSO algorithm.

This algorithm was proven to be efficient in many optimization problems, among which we can mention Arjomandi *et al.* (2024), Perez and Behdinan (2007).

4. Results and discussions

The optimization algorithms – greedy and particle swarm optimization – were developed using Python, leveraging its simplicity and extensive library support for efficient implementation. The integration of the PyAnsys package facilitated seamless interaction with Ansys for finite element analysis, enabling the algorithms to utilize structural simulations for objective function evaluation. In Table 3 are highlighted key computation times for the brute force method across various configurations. The data presented below was obtained using a computer with the following specifications: Intel® Xeon® W-2104 CPU @ 3.20 GHz, 32 GB DDR5 RAM, and an NVIDIA Quadro P2000 4 GB GDDR5 graphics card.

Table 3. Estimated time necessary for evaluating all solutions in different configurations.

Material domains in base area	Possible combinations	Estimated time
16	12,870	64350 seconds ~**17.87 hours**
36	9,075,135,300	1,522,325,936 seconds ~**2896.35 years**

To assess the success rate – defined as the probability of an algorithm achieving the optimal solution or, in this case, one of the top three optimal solutions outlined in Section 2 – each algorithm was executed 100 times for the problem involving 16 material domains in the base area. Additionally, to evaluate the performance of the algorithms, the number of objective function evaluations required to reach the optimum was also recorded. The results are presented in Fig. 8.

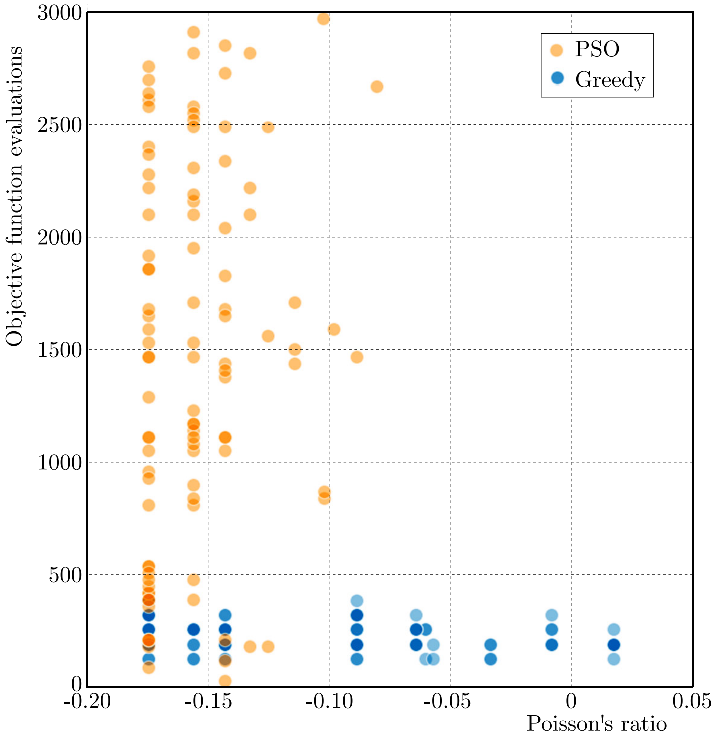

Fig. 8. Final values of Poisson's ratios obtained as depending on number of evaluations – greedy and PSO.

If we analyze this chart, we can see that there is a big difference between how these two optimization algorithms perform. We would like to have an optimization method that would give us a very good objective function value for a small number of evaluations. In this figure, we can see that the greedy algorithm always returns a final solution after a small number of function evaluations but the value is not very good. At the same time, PSO delivers a very good objective function value but with a higher number of evaluations. In this case, the user must make a compromise and should choose which thing is more important: speed or performance. Some summary statistics of these 100 runs are presented in Table 4.

After validating that the two algorithms can find the optimal solutions, we proceeded to the next step in which we performed the optimization process on a problem featuring 36 material domains instead of 16 in the base triangle. For this problem, we showed that it is impossible to apply the brute force method, mainly because there are over 9 billion solutions. We performed 5 runs with each algorithm for this problem and compared the results. To make a direct comparison between these two algorithms, it is necessary to present the evolution of the objective function against the number of evaluations of the function because each algorithm evaluates a different number of solutions at each iteration.

Table 4. Summary statistics of the 100 runs performed on greedy and PSO.

Algorithm	Greedy	PSO
Reached 1st best	27	41
Reached 2nd best	9	26
Reached 3rd best	14	17
Success rate	50 %	84 %
Auxetic	90	100
Mean – objective function value	−0.103819	−0.154334
Mean – number of evaluations	231.04	1470.90
Median – number of evaluations	192	1470
Standard deviation – number of evaluations	67.67	834.05

We can see in Fig. 9 that in the beginning PSO performs better than greedy but then reaches a plateau indicating a blocking in a local minimum. For the greedy algorithm, we can see a steady decrease in the objective function value until it reaches a dead end and for the long run it performs better than PSO in 2 out of 5 runs. The periodic representations of the 3 best obtained configurations are shown in Fig. 10.

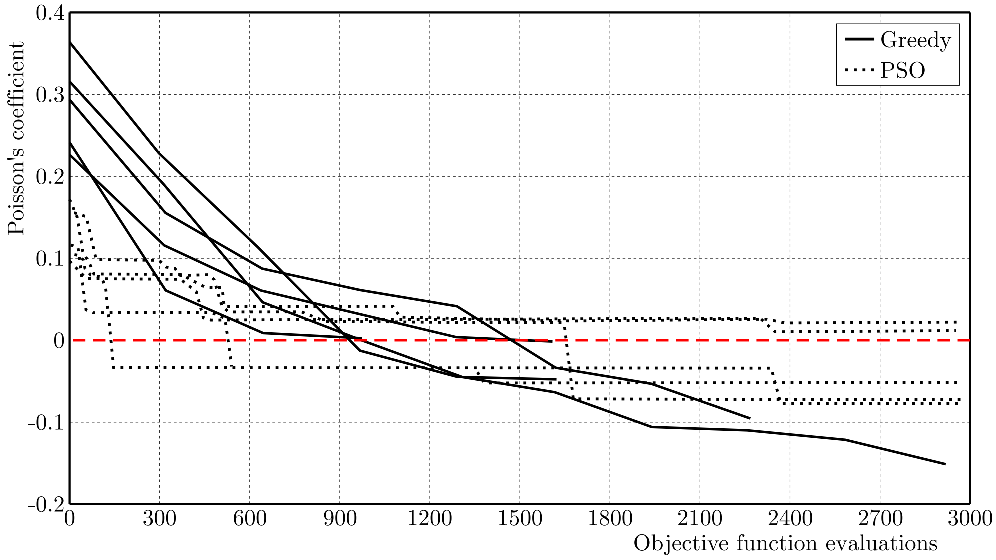

Fig. 9. Objective function evolution vs. the number of evaluations needed for each algorithm – greedy and PSO.

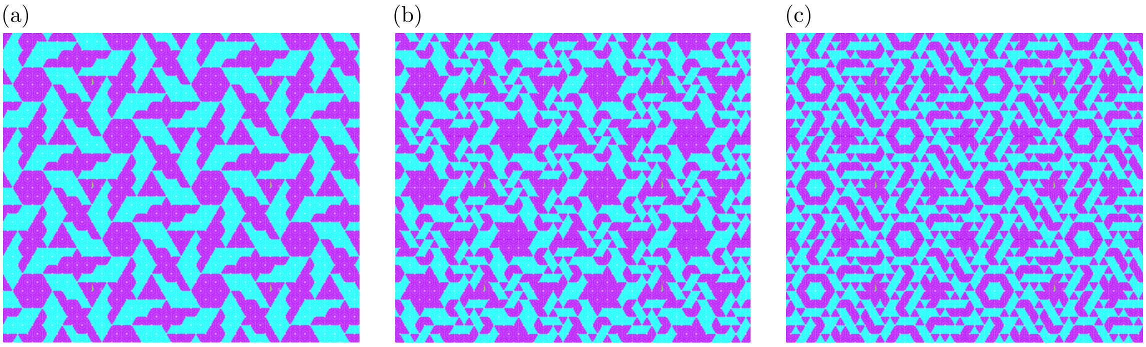

Fig. 10. Best configurations found for the 36 material domains base triangle – periodic model: (a) 1st best – greedy, $\nu = -0.152223$; (b) 2nd best – greedy, $\nu = -0.096786$; (c) 3rd best – PSO, $\nu = -0.074124$.

5. Conclusions

This study evaluates the performance of two optimization algorithms, greedy and PSO, in solving structural optimization problems. The evaluation focuses on metrics such as convergence speed, solution quality, computational efficiency, and robustness. The greedy algorithm demonstrates impressive convergence speed, making it computationally efficient and capable of finding good solutions with minimal cost. However, it has a notable limitation: its tendency to become stuck in suboptimal solutions, as it cannot explore solution spaces requiring intermediate steps through less favorable configurations. In contrast, PSO exhibits a higher success rate, reaching 84 % for the low-dimensional problem with 16 material domains. Both algorithms successfully attain the global maximum for this problem, but the computational efforts required by PSO are notably higher compared to greedy.

When scaling up to the more complex problem of 36 material domains, the differences between the two algorithms become more pronounced. PSO is more likely to encounter deadlocks in local minima, reducing its effectiveness for larger problems, whereas greedy shows greater resilience by consistently reaching a good solution. Although the solutions found by greedy may not always be the global optimum, they are achieved at a lower computational cost, making it a more practical choice for problems with constrained resources. On the other hand, PSO demonstrates its strength by producing higher-quality solutions when computational cost is less of a concern. Overall, the greedy algorithm is an effective choice for cost-efficient optimization, while PSO excels in scenarios where solution quality is prioritized over computational efficiency.

Acknowledgments

Iulian-Constantin Coropeţchi acknowledges the grant awarded by the Ministry of Education from Romania for completing his PhD studies under contract no. 06.19/05.10.2020.

References

1. Arjomandi, M.A., Mousavi Asl, S.S., Mosallanezhad, B., & Hajiaghaei-Keshteli, M. (2024). A metaheuristic-based comparative structure for solving discrete space mechanical engineering problem. *Annals of Operations Research.* https://doi.org/10.1007/s10479-024-06052-y
2. Bendsøe, M.P., & Sigmund, O. (2004). *Topology optimization. Theory, methods and applications* (2nd ed.). Berlin, Heidelberg: Springer-Verlag. https://doi.org/10.1007/978-3-662-05086-6
3. Casalotti, A., D'Annibale, F., & Rosi, G. (2020). Multi-scale design of an architected composite structure with optimized graded properties. *Composite Structures*, *252*, Article 112608. https://doi.org/10.1016/j.compstruct.2020.112608
4. Clerc, M. (2006). *Particle swarm optimization.* ISTE. https://doi.org/10.1002/9780470612163
5. Coropeţchi, I.C., Vasile, A., Sorohan, Ş., Picu, C.R., & Constantinescu, D.M. (2022). Stiffness optimization through a modified greedy algorithm. *Procedia Structural Integrity*, *37*, 755–762. https://doi.org/10.1016/j.prostr.2022.02.006
6. Engelbrecht, A.P. (2007). *Computational intelligence: An introduction.* John Wiley & Sons, Ltd. https://doi.org/10.1002/9780470512517
7. Ghiasi, H., Fayazbakhsh, K., Pasini, D., & Lessard, L. (2010). Optimum stacking sequence design of composite materials Part II: Variable stiffness design. *Composite Structures*, *93*(1), 1–13. https://doi.org/10.1016/j.compstruct.2010.06.001
8. Ghiasi, H., Pasini, D., & Lessard, L. (2009). Optimum stacking sequence design of composite materials Part I: Constant stiffness design. *Composite Structures*, *90*(1), 1–11. https://doi.org/10.1016/j.compstruct.2009.01.006
9. Gu, G.X., Chen, C.T., & Buehler, M.J. (2018a). *De novo* composite design based on machine learning algorithm. *Extreme Mechanics Letters*, *18*, 19–28. https://doi.org/10.1016/j.eml.2017.10.001

10. Gu, G.X., Chen, C.T., Richmond, D.J., & Buehler, M.J. (2018b). Bioinspired hierarchical composite design using machine learning: Simulation, additive manufacturing, and experiment. *Materials Horizons*, 5, 939–945. https://doi.org/10.1039/c8mh00653a
11. Harish, B., Eswara Sai Kumar, K., & Srinivasan, B. (2020). Topology optimization using convolutional neural network. In R.R. Salagame, P. Ramu, I. Narayanaswamy, D.K. Saxena (Eds.), *Advances in Multidisciplinary Analysis and Optimization. Proceedings of the 2nd National Conference on Multidisciplinary Analysis and Optimization* (pp. 301–307). Singapore: Springer. https://doi.org/10.1007/978-981-15-5432-2_26
12. Kumar, S., Tan, S., Zheng, L., & Kochmann, D.M. (2020). Inverse-designed spinodoid metamaterials. *npj Computational Materials*, *6*, Article 73. https://doi.org/10.1038/s41524-020-0341-6
13. Li, T., Liu, F., & Wang, L. (2020). Enhancing indentation and impact resistance in auxetic composite materials. *Composites Part B: Engineering*, *198*, Article 108229. https://doi.org/10.1016/j.compositesb.2020.108229
14. Luu, N.G., & Banh, T.T. (2023). A novel preconditioned conjugate gradient multigrid method for multi-material topology optimization. *arXiv*. https://doi.org/10.48550/arXiv.2301.07457
15. Pan, C., Han, Y., & Lu, J. (2020). Design and optimization of lattice structures: A review. *Applied Sciences*, *10*(18), Article 6374. https://doi.org/10.3390/app10186374
16. Perez, R.E., & Behdinan, K. (2007). Particle swarm approach for structural design optimization. *Computers and Structures*, *85*(19–20), 1579–1588. https://doi.org/10.1016/j.compstruc.2006.10.013
17. Ptochos, E., & Labeas, G. (2012). Elastic modulus and Poisson's ratio determination of micro-lattice cellular structures by analytical, numerical and homogenisation methods. *Journal of Sandwich Structures & Materials*, *14*(5), 597–626. https://doi.org/10.1177/1099636212444285
18. Sait, S.M., Mehta, P., Gürses, D., & Yildiz, A.R. (2023). Cheetah optimization algorithm for optimum design of heat exchangers. *Materials Testing*, *65*(8), 1230–1236. https://doi.org/doi:10.1515/mt-2023-0015
19. Sandhu, R. (1971). Parametric study of optimum fiber orientation for filamentary sheet. In *Technical Memorandum FBC-71-1*. Air Force Flight Dynamics Laboratory, Director of Laboratories, Air Force Systems Command, Wright Patterson Air Force Base, Ohio.
20. Sorohan, S., Constantinescu, D.M., Sandu, M., & Sandu, A.G. (2018). On the homogenization of hexagonal honeycombs under axial and shear loading. Part I: Analytical formulation for free skin effect. *Mechanics of Materials*, *119*, 74–91. https://doi.org/10.1016/j.mechmat.2017.09.003
21. Tavakoli, R. (2014). Multimaterial topology optimization by volume constrained Allen-Cahn system and regularized projected steepest descent method. *Computer Methods in Applied Mechanics and Engineering*, *276*, 534–565. https://doi.org/10.1016/j.cma.2014.04.005
22. Vasile, A., Coropețchi, I.C., Sorohan, Ș., Picu, C.R., & Constantinescu, D.M. (2022). A simulated annealing algorithm for stiffness optimization. *Procedia Structural Integrity*, *37*, 857–864. https://doi.org/10.1016/j.prostr.2022.02.019
23. Yoon, G.H. (2021). Multiphysics topology optimization scheme considering the evaporation cooling effect. *Computers & Structures*, *244*, Article 106409. https://doi.org/10.1016/j.compstruc.2020.106409
24. Yu, Y., Hur, T., Jung, J., & Jang, I.G. (2019). Deep learning for determining a near-optimal topological design without any iteration. *Structural and Multidisciplinary Optimization*, *59*(3), 787–799. https://doi.org/10.1007/s00158-018-2101-5
25. Zhang, Y., Peng, B., Zhou, X., Xiang, C., & Wang, D. (2019). A deep Convolutional Neural Network for topology optimization with strong generalization ability. *arXiv*. https://doi.org/10.48550/arXiv.1901.07761
26. Zhu, B., Zhang, X., Zhang, H., Liang, J., Zang, H., Li, H., & Wang, R. (2020). Design of compliant mechanisms using continuum topology optimization: A review. *Mechanism and Machine Theory*, *143*, Article 103622. https://doi.org/10.1016/j.mechmachtheory.2019.103622

Manuscript received December 9, 2024; accepted for publication February 1, 2025;
published online July 3, 2025.

JOURNAL OF THEORETICAL
AND APPLIED MECHANICS
63, 3, pp. 491–499, Warsaw 2025
https://doi.org/10.15632/jtam-pl/201313

ESTIMATING EQUIBIAXIAL STRESS-STRAIN RELATION BASED ON NON-HOMOGENEOUS BIAXIAL MEASUREMENT

Kristóf HAVASI, Attila KOSSA*

Department of Applied Mechanics, Faculty of Mechanical Engineering,
Budapest University of Technology and Economics, Műegyetem rkp. 3., H-1111 Budapest, Hungary
*corresponding author, *kossa@mm.bme.hu*

This study investigates the influence of geometry on stress distributions in equibiaxial testing of rubber-like materials using hyperelastic models. Two geometries were examined, characterized by parameters specifying configurations like corner angles and normalized radii. A finite element approach was employed to simulate deformation under equibiaxial stretching, revealing non-homogeneous stress states. Apparent stress ratios were derived to evaluate geometry-induced deviations from purely equibiaxial stress-strain behavior. Results highlight the significance of geometrical factors in stress distributions. The findings offer insights for optimizing specimen designs for equibiaxial material characterization and improving the accuracy of extracted material properties.

Keywords: equibiaxial testing; hyperelastic materials; specimen geometry; finite element analysis; stress-strain relationship.

1. Introduction

The execution of equibiaxial material testing for rubber-like materials remains a challenging task even today, whether involving symmetric or asymmetric biaxial measurements. Such tests frequently utilize so-called cruciform test specimens, but the exact geometry of these specimens remains a subject of debate. There is no consensus or standardized shape; thus, researchers typically design their own specimen geometries for their experiments. To illustrate the wide variety of specimen geometries reported in the literature, we highlight several characteristic designs in the following paragraph.

Perhaps the simplest design is a basic cruciform shape with rectangular arms (Labus & Puttlitz, 2016; Avanzini & Battini, 2016). A more complex variation involves angling the arms at a certain degree (Avanzini & Battini, 2016). However, the corners act as stress concentration regions, and localized rounding can help reduce high stresses in these domains (Bertin *et al.*, 2015). A further refinement involves continuous rounding between the arms, reducing stress concentration effects over a wider section (Jiang *et al.*, 2022; Chen *et al.*, 2013; Seibert *et al.*, 2014; Palacios, Pineda *et al.*, 2017; Avanzini & Battini, 2016; Silberstein *et al.*, 2011). Introducing a central cutout in the specimen allows larger and more visually apparent deformations to be measured (Hartmann *et al.*, 2018; Ranjan *et al.*, 2023). Extending these cutouts toward

---

Ministry of Science and Higher Education
Republic of Poland

The publication has been funded by the Polish Ministry of Science and Higher Education under the Excellent Science II programme "Support for scientific conferences".

The content of this article was presented during the 40th Danubia-Adria Symposium on Advances in Experimental Mechanics, Gdańsk, Poland, September 24–27, 2024.

the corners can create a more homogeneous stress field (Hartmann *et al.*, 2018; Makinde *et al.*, 1992). If the goal is to ensure that tensile loading is dominant along the arms, notches can be introduced to minimize deformation in the transverse direction (Avanzini & Battini, 2016; Kuwabara *et al.*, 1998). Another approach to reduce transverse deformation in the arms is to incorporate larger incisions rather than small notches (Zhao *et al.*, 2014). These can be combined with a central cutout extending toward the incisions (Hartmann *et al.*, 2018; Makinde *et al.*, 1992). To facilitate easier clamping, head sections can be added to the ends of the arms, tapering toward their intersection (Putra *et al.*, 2020). The tapering can also vary and need not form parallel arm edges in the geometry, potentially featuring a continuously changing shape that helps concentrate stresses in the central region (Palacios-Pineda *et al.*, 2017; Lamkanfi *et al.*, 2015). A middle-way solution involves adding cutouts to a continuously rounded design, focusing the effects more distinctly on the central region of the specimen (Morris *et al.*, 2020). An alternative method is to design the head sections with rounded edges instead of straight sides (Vitucci, 2024). For testing scenarios with low force measurements, thinner arms can be advantageous, as their stress distribution becomes less influential (Seibert *et al.*, 2014). Similar specimen designs can also be used for failure mode investigations, such as specimens with a central notch (Marano *et al.*, 2010) or a central hole to concentrate forces and stresses toward the corners (Oliveira *et al.*, 2021; Hamdoun & Mahnken, 2024). It should also be noted that asymmetric specimens can be used for testing purposes, not just symmetric ones (Chen *et al.*, 2023). The geometries found in the cited articles are illustrated in Fig. 1. For each specimen under biaxial loading the center region, often called a Region of Interest (ROI), shows a certain stress distribution typical for the specimen in use that approximates the pure equibiaxial stress-strain relationship (Chen *et al.*, 2013; Seibert *et al.*, 2014; Morris *et al.*, 2020). It can be concluded that the shapes of these specimens have a great impact on the exact stress fields forming in the material due to the applied loads, thus it would be possible to characterize the effects of the specimen geometries and use this information to grasp the equibiaxial behavior of the experiments carried out.

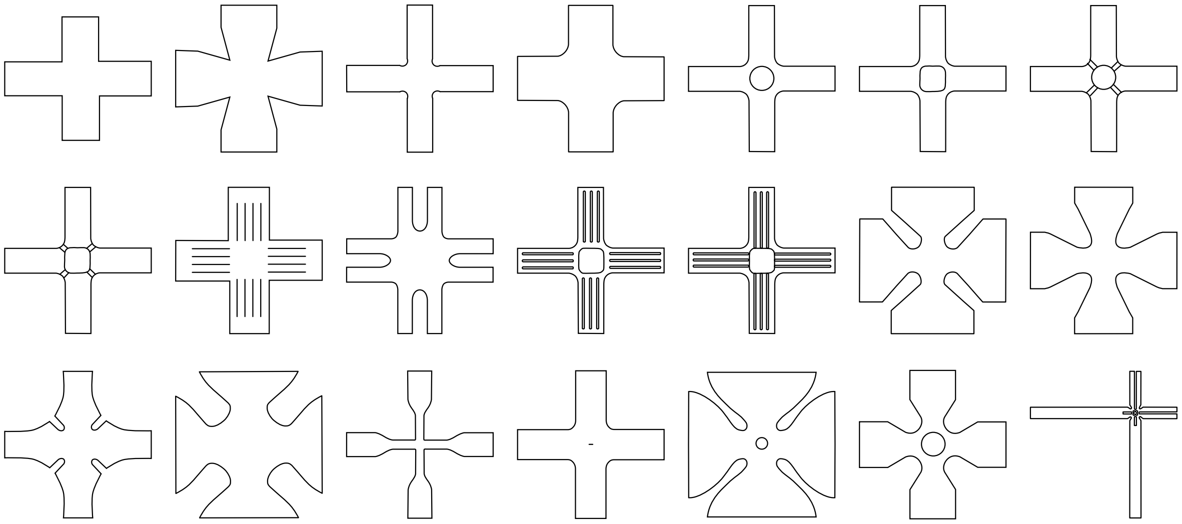

Fig. 1. Illustration of different biaxial test specimen geometries.

As demonstrated, a wide variety of test specimens can be proposed, each tailored to the experimental equipment available to the researcher and the specific properties to be measured. However, it is not possible to identify a globally optimal specimen design that universally satisfies all research needs. As a result, specially designed specimen geometries created to meet specific experimental needs are still widely used.

2. Description of the mechanical problem

In the present study, we investigate two distinct geometries of equibiaxial test specimens, as illustrated in Fig. 2. For both types, the overall dimensions of the specimen form a square with a side length of $3L$, while the ROI is defined by a square with a side length of L located at the center of the specimen. Both geometries are characterized by a single parameter. In the case of the specimen depicted in Fig. 2a, the defining parameter is the angle α as marked in the figure, whereas for the specimen shown in Fig. 2b, the characteristic geometrical parameter is the dimensionless ratio $\beta = R/L$. By varying the parameters α and β, we can generate specimens with different geometrical configurations. The thickness of all specimens is denoted as t. Given that thin specimens are examined, the stress distribution is assumed to be constant along the thickness direction, reducing the original three-dimensional problem to a two-dimensional analysis. For both geometric configurations, we investigate 10 distinct cases, which are identified using a specific coding scheme detailed in Table 1. This table also provides the characteristic geometrical dimensions associated with each code. It is noteworthy that for the geometry coded as B, the case $\beta = 0$ corresponds to case A00; therefore, it is not examined separately. In total, we analyze 20 different specimen geometries (see Fig. 3), enabling us to obtain a comprehensive understanding of how geometry influences the stress distribution in both configurations.

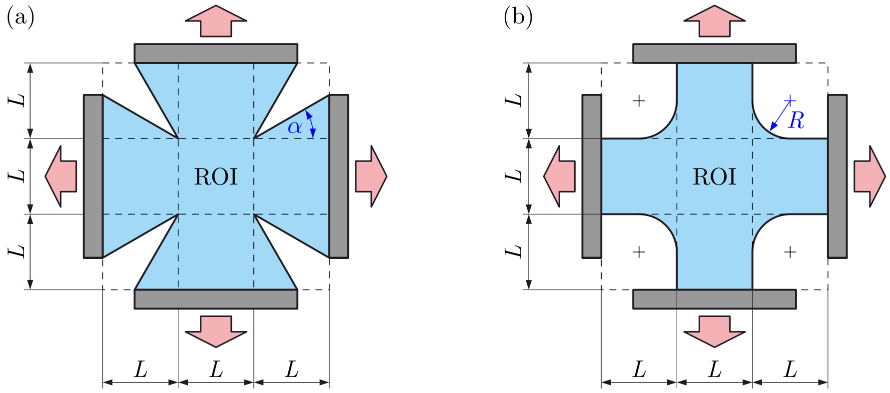

Fig. 2. The two examined geometrical configurations.

Table 1. Coding of the analyzed cases and their corresponding geometric parameters.

Case code	α [°]	Case code	$\beta = R/L$ [1]
A00	0	B01	0.1
A05	5	B02	0.2
A10	10	B03	0.3
A15	15	B04	0.4
A20	20	B05	0.5
A25	25	B06	0.6
A30	30	B07	0.7
A35	35	B08	0.8
A40	40	B09	0.9
A45	45	B10	1.0

The specimens are subjected to identical elongations in the horizontal and vertical directions. Due to the geometrical design, a non-homogeneous stress state develops within the specimens,

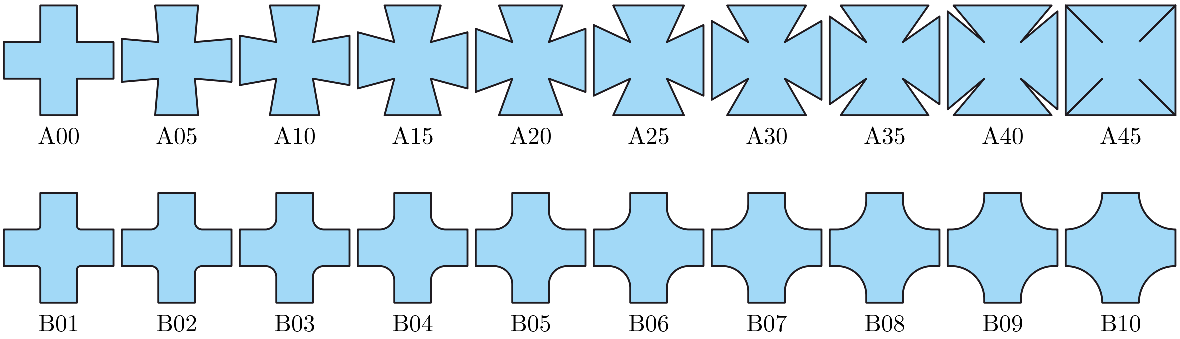

Fig. 3. Illustration of the 20 different geometries analyzed.

and only a single material point (located at the center of the specimen) experiences a purely equibiaxial stress state. Our objective is to determine how the geometrical configuration affects the stress distributions and how the equibiaxial stress-strain relationship, characteristic of the base material, can be extracted from the non-homogeneous stress state. To address these questions, finite element analyses are conducted. The finite element model is described in detail in the following section.

3. Finite element models

Since the aim is to examine purely elastic material behavior, the mechanical behavior of the test specimens is modeled using a hyperelastic material model. The theoretical framework of hyperelastic material modeling is extensively described in various textbooks and scientific articles (Holzapfel, 2010). Due to space constraints, this paper does not provide a detailed presentation of all equations; only the most essential relationships necessary for understanding the results are presented. For isotropic material behavior, the strain energy potential can be expressed using the principal stretches: $U = U(\lambda_1, \lambda_2, \lambda_3)$. The principal stretches are the eigenvalues of the left stretch tensor ($\mathbf{V}$) and the right stretch tensor ($\mathbf{U}$), which can be determined via the polar decomposition of the deformation gradient: $\mathbf{F} = \mathbf{RU} = \mathbf{VR}$. In the case of compressible materials, the Cauchy stress tensor is calculated as follows:

$$\boldsymbol{\sigma} = \sum_{i=1}^{3} \sigma_i \mathbf{n}_i \otimes \mathbf{n}_i = \sum_{i=1}^{3} \frac{\lambda_i}{J} \frac{\partial U}{\partial \lambda_i} \mathbf{n}_i \otimes \mathbf{n}_i, \tag{3.1}$$

where $J = \det\mathbf{F}$ represents the volume ratio, and $\mathbf{n}_i$ $(i = 1, 2, 3)$ are unit vectors in the principal directions of the current configuration. For incompressible materials $(J = 1)$, the hydrostatic stress component cannot be determined from the displacement field. In this case, the Cauchy stress tensor is expressed as

$$\boldsymbol{\sigma} = \mathrm{dev}\left[\sum_{i=1}^{3} \lambda_i \frac{\partial U}{\partial \lambda_i} \mathbf{n}_i \otimes \mathbf{n}_i\right] + \mathbf{p}, \tag{3.2}$$

where $\mathbf{p}$, the hydrostatic stress, is determined based on the boundary conditions of the specific problem. In our computations, we employ the Ogden incompressible hyperelastic material model, where the strain energy potential is defined as

$$U = \sum_{i=1}^{N} \frac{2\mu_i}{\alpha_i^2} \left(\lambda_1^{\alpha_i} + \lambda_2^{\alpha_i} + \lambda_3^{\alpha_i} - 3\right). \tag{3.3}$$

Note that the U function presented here corresponds to the version used by Abaqus (Dassault Systèms, 2022). The model's analytical stress solutions for uniaxial, equibiaxial, and planar loading conditions are given by the relations (Steinmann *et al.*, 2012):

$$P_{\text{uniaxial}}(\lambda) = \sum_{i=1}^{N} \frac{2\mu_i}{\alpha_i} \left(\lambda^{\alpha_i - 1} - \lambda^{-\alpha_i/2-1} \right),$$

$$P_{\text{equibiaxial}}(\lambda) = \sum_{i=1}^{N} \frac{2\mu_i}{\alpha_i} \left(\lambda^{\alpha_i - 1} - \lambda^{-2\alpha_i-1} \right), \tag{3.4}$$

$$P_{\text{planar}}(\lambda) = \sum_{i=1}^{N} \frac{2\mu_i}{\alpha_i} \left(\lambda^{\alpha_i - 1} - \lambda^{-\alpha_i-1} \right).$$

For the analysis presented in this manuscript, a third-order Ogden model was fitted to the Treloar data, which are among the most frequently cited experimental datasets in (Treloar, 1944; Steinmann *et al.*, 2012). During the fitting process, only values of $\lambda \leq 5$ were considered. Parameter fitting was conducted using the Wolfram Mathematica built-in NMinimize function to minimize the relative error. The fitted model parameters are as follows:

$$\begin{aligned} &\mu_1 = 0.0309526\,\text{MPa}, && \mu_2 = 0.352102\,\text{MPa}, && \mu_3 = 0.00646444\,\text{MPa}, \\ &\alpha_1 = 3.61341, && \alpha_2 = 0.871956, && \alpha_3 = -2.18698. \end{aligned} \tag{3.5}$$

The comparison between the fitted model and the experimental data is presented in Fig. 4b. The results show that the fitted model is accurate and closely follows the experimental data. The coefficient of determination (R^2) for the fit is 0.999471. A Drucker stability analysis was conducted for the fitted hyperelastic model using the Abaqus built-in module. The results indicate that the hyperelastic model is stable across the entire range.

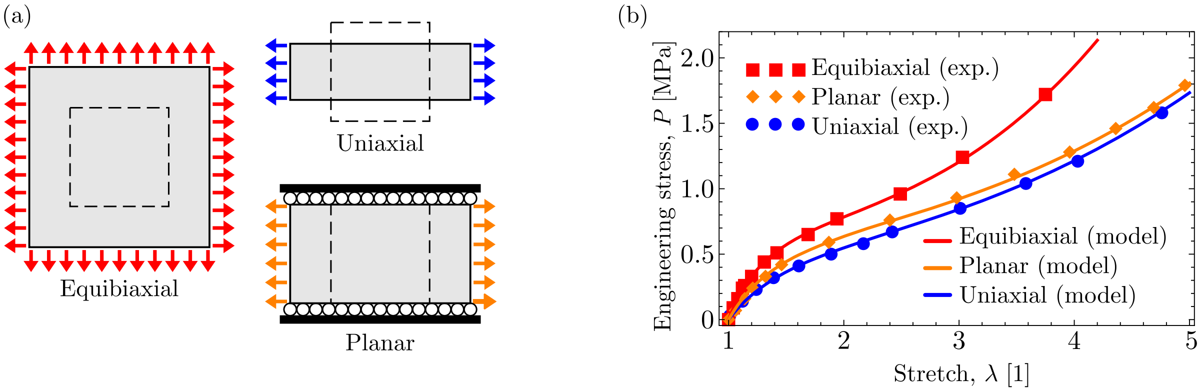

Fig. 4. (a) Illustration of homogeneous loading modes; (b) comparison of experimental data and the model for each loading case.

The finite element simulations were performed using Abaqus software. The test specimens were discretized using 8-node biquadratic plane stress quadrilateral elements (CPS8) with full integration scheme. Note that for plane stress element types, hybrid elements are not required to model incompressible material behavior. Prior to selecting the finite element meshes for analysis, a detailed mesh-independence study was conducted. A global element size was chosen such that the numerical results converged. Due to the symmetry of the geometries, only a quarter of each specimen was modeled with appropriate symmetric boundary conditions. While it would be possible to use an eighth model, for convenience, we opted for the quarter model, as it simplifies the application of boundary conditions. For all geometries, $L = 100\,\text{mm}$ was used with a global element size of 1 mm. To illustrate the finite element meshes, two cases are presented in Fig. 5. The codes shown in the figure correspond to those in Table 1. For these example cases, the number of elements and nodes are as follows: case A20: 16,616 elements and 50,511 nodes; case B05: 14,756 elements and 44,871 nodes.

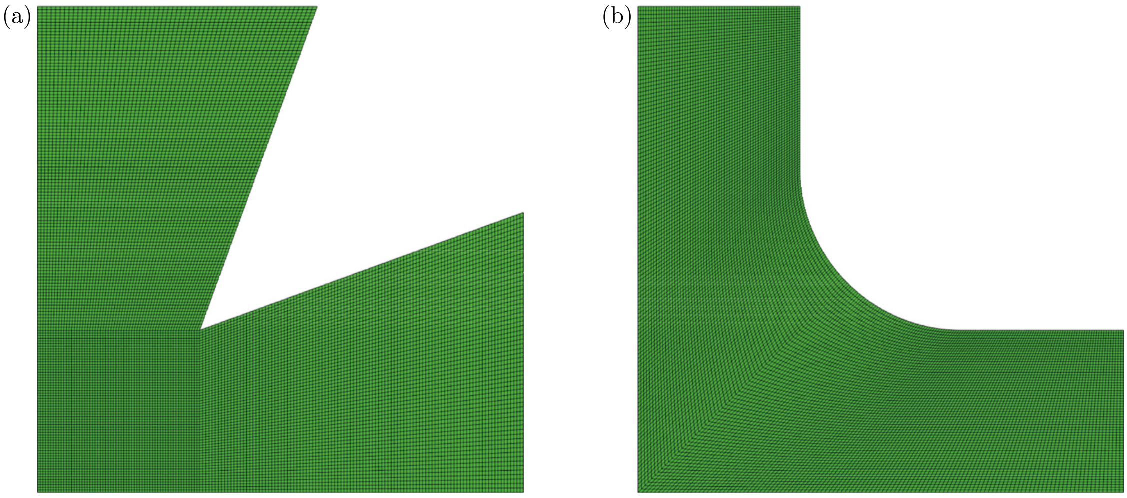

Fig. 5. Finite element meshes applied to the quarter models:
(a) geometry with A20 code; (b) geometry with B05 code.

The prescribed load was applied as displacements at the grips in the horizontal and vertical directions, based on the part of the specimen considered. Displacements perpendicular to the prescribed displacement were constrained, simulating ideal clamping conditions. A displacement value of $u = 600\,\mathrm{mm}$ was prescribed at the grips. At this magnitude, sufficiently large deformations are expected for all geometries. The applied boundary conditions are illustrated schematically in Fig. 6.

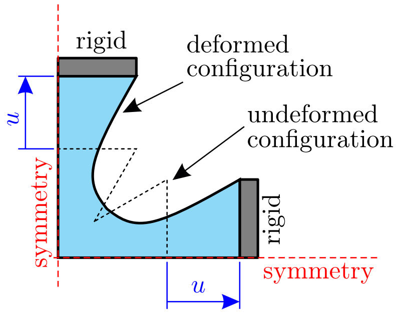

Fig. 6. Schematic illustration of the applied boundary conditions.

The problem was solved using the General Static procedure. The total load was applied in 500 equal increments, providing a sufficiently dense load distribution and reducing numerical errors. During the simulations, reaction forces at the grips were recorded to compute apparent stress values. Let $F/2$ denote the reaction force at the grips in the quarter model. For the investigated loading and geometries, an apparent stretch and nominal stress can be defined as follows:

$$\lambda = 1 + \frac{2u}{3L}, \qquad P = \frac{F}{Lt}, \tag{3.6}$$

where t is the thickness of the specimen. The resulting stretch and nominal stress values correspond to non-purely biaxial stress states, incorporating the influence of geometry. Plotting the nominal stress (P) as a function of λ reveals deviations from the purely equibiaxial solution valid for the material model. To characterize these deviations, a dimensionless stress ratio (or geometry factor) can be introduced:

$$\eta\left(\lambda\right) = \frac{P_{\mathrm{equibiaxial}}\left(\lambda\right)}{P\left(\lambda\right)}. \tag{3.7}$$

The resulting stress ratio (or geometry factor) reflects the influence of geometry on the stress distribution. Knowing η, the purely equibiaxial stress solutions can be computed by multiplying the measured P values by η. The solutions for each geometry are presented in the following section.

4. Results

First, we present the deformed configurations corresponding to each geometry at the end of loading in Fig. 7. Notably, despite the significant differences in initial configurations, the deformed shapes at the end of the applied large deformation appear very similar. More important than examining the deformed shapes is the variation in reaction forces and the apparent nominal stresses calculated from them. The engineering stress values computed for each specimen are presented in Fig. 8, with different cases distinguished by various colors. The figure also includes the stress solution derived under purely equibiaxial loading conditions, as per Eq. $(3.4)_2$.

Fig. 7. Deformed configurations obtained for the analyzed geometries.

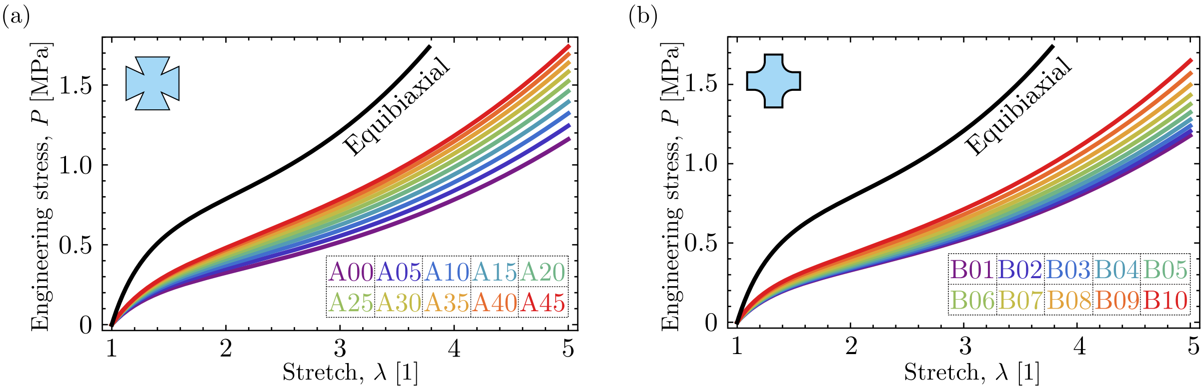

Fig. 8. Plots of the calculated stress values: (a) geometry with A coding; (b) geometry with B coding.

Using these stress solutions, we can compute the variation of the previously introduced η stress ratio as a function of λ. The results are shown in Fig. 9. Analyzing the results reveals that the geometry of the specimen has a significant impact on the value of the stress ratio.

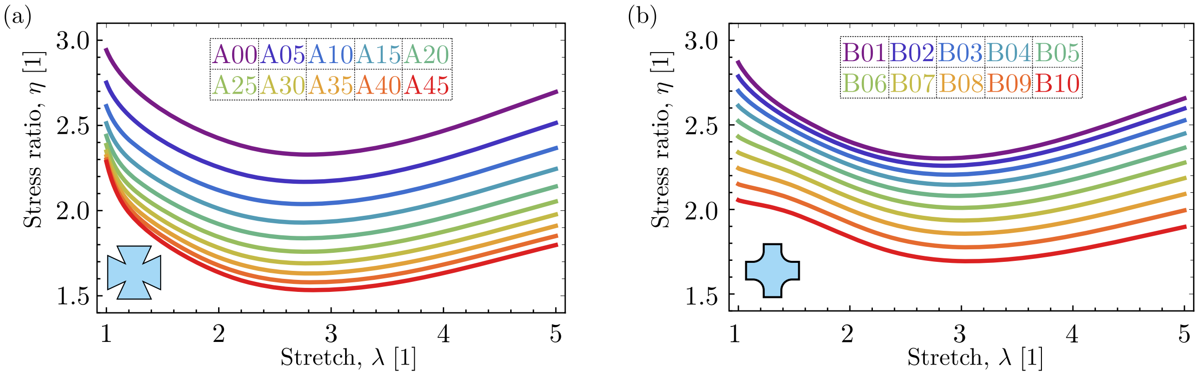

Fig. 9. Plots of the η stress ratio: (a) geometry with A coding; (b) geometry with B coding.

In all cases, the stress ratio depends on the stretch (λ) and consistently falls within the range of 1.5 to 3. If necessary, analytical functions can be fitted to the numerical values of η, but this aspect is beyond the scope of the present paper.

5. Conclusions

In this study, we present a comprehensive analysis of the influence of specimen geometry on the non-homogeneous stress state that develops during biaxial testing of rubber-like materials. Using finite element analysis, we examined a total of 20 configurations based on two characteristic geometries, modeling the base material with a third-order Ogden hyperelastic material model. Apparent stretch and nominal stress quantities were introduced, which can be directly calculated from the crosshead displacement and the measured force. We defined the dimensionless stress ratio, which is the ratio of the stress under purely equibiaxial loading of the base material to the apparent stress, interpreting it as a geometry-specific geometry factor. The stress ratio was calculated for all examined geometries. With the knowledge of the stress ratio, the mechanical behavior of the base material under purely equibiaxial loading conditions can be estimated for various geometries. The presented methodology is extendable to other geometries and materials.

Acknowledgments

This research was supported by the Hungarian National Research, Development and Innovation Office (FK 142457). This research was supported by the János Bolyai Research Scholarship of the Hungarian Academy of Sciences.

References

1. Avanzini, A., & Battini, D. (2016). Integrated experimental and numerical comparison of different approaches for planar biaxial testing of a hyperelastic material. *Advances in Materials Science and Engineering*, *2016*(1), Article 6014129. https://doi.org/10.1155/2016/6014129
2. Bertin, M., Hild, F., Roux, S., Mathieu, F., Leclerc, H., & Aimedieu, P. (2015). Integrated digital image correlation applied to elasto-plastic identification in a biaxial experiment. *Journal of Strain Analysis for Engineering Design*, *51*(2), 118–131. https://doi.org/10.1177/0309324715614759
3. Chen, S., Cai, D., Jiang, H., Li, G., & Cui, J. (2023). A new measurement technology for forming limit in aluminum alloy under biaxial dynamic loading. *Journal of Materials Processing Technology*, *317*, Article 117963. https://doi.org/10.1016/j.jmatprotec.2023.117963
4. Chen, Z., Scheffer, T., Seibert, H., & Diebels, S. (2013). Macroindentation of a soft polymer: Identification of hyperelasticity and validation by uni/biaxial tensile tests. *Mechanics of Materials*, *64*, 111–127. https://doi.org/10.1016/j.mechmat.2013.05.003
5. Dassault Systèmes, 2022, Abaqus version 2022.
6. Hamdoun, A., & Mahnken, R. (2024). Uniaxial and biaxial experimental investigation of glassy polymers. *Polymer*, *299*, Article 126981. https://doi.org/10.1016/j.polymer.2024.126981
7. Hartmann, S., Gilbert, R.R., & Sguazzo, C. (2018). Basic studies in biaxial tensile tests. *GAMM – Mitteilungen*, *41*(1), Article e201800004. https://doi.org/10.1002/gamm.201800004
8. Holzapfel, G.A. (2010). *Nonlinear solid mechanics: A continuum approach for engineering*, Wiley.
9. Jiang, M., Dai, J., Dong, G., & Wang, Z. (2022). A comparative study of invariant-based hyperelastic models for silicone elastomers under biaxial deformation with the virtual fields method. *Journal of the Mechanical Behavior of Biomedical Materials*, *136*, Article 105522. https://doi.org/10.1016/j.jmbbm.2022.105522
10. Kuwabara, T., Ikeda, S., & Kuroda, K. (1998). Measurement and analysis of differential work hardening in cold-rolled steel sheet under biaxial tension. *Journal of Materials Processing Technology*, *80–81*, 517–523. https://doi.org/10.1016/S0924-0136(98)00155-1

11. Labus, K.M., & Puttlitz, C.M. (2016). An anisotropic hyperelastic constitutive model of brain white matter in biaxial tension and structural–mechanical relationships. *Journal of the Mechanical Behavior of Biomedical Materials*, *62*, 195–208. https://doi.org/10.1016/j.jmbbm.2016.05.003
12. Lamkanfi, E., Van Paepegem, W., & Degrieck, J. (2015). Shape optimization of a cruciform geometry for biaxial testing of polymers. *Polymer Testing*, *41*, 7–16. https://doi.org/10.1016/j.polymertesting.2014.09.016
13. Makinde, A., Thibodeau, L., & Neale, K.W. (1992). Development of an apparatus for biaxial testing using cruciform specimens. *Experimental Mechanics*, *32*(2), 138–144. https://doi.org/10.1007/BF02324725
14. Marano, C., Calabrò, R., & Rink, M. (2010). Effect of molecular orientation on the fracture behavior of carbon black-filled natural rubber compounds. *Journal of Polymer Science. Part B: Polymer Physics*, *48*(13), 1509–1515. https://doi.org/10.1002/polb.22054
15. Morris, K., Rosenkranz, A., Seibert, H., Ringel, L., Diebels, S., & Talke, F.E. (2020). Uniaxial and biaxial testing of 3D printed hyperelastic photopolymers. *Journal of Applied Polymer Science*, *137*(8), Article 48400. https://doi.org/10.1002/app.48400
16. Oliveira, M.G., Thuillier, S., & Andrade-Campos, A. (2021). Evaluation of heterogeneous mechanical tests for model calibration of sheet metals. *The Journal of Strain Analysis for Engineering Design*, *57*(3), 208–224. https://doi.org/10.1177/03093247211027061
17. Palacios-Pineda, L., Perales-Martínez, I., Moreno-Guerra, M., & Elías-Zúñiga, A. (2017). An optimum specimen geometry for equibiaxial experimental tests of reinforced magnetorheological elastomers with iron micro- and nanoparticles. *Nanomaterials*, *7*(9), Article 254. https://doi.org/10.3390/nano7090254
18. Putra, K.B., Tian, X., Plott, J., & Shih, A. (2020). Biaxial test and hyperelastic material models of silicone elastomer fabricated by extrusion-based additive manufacturing for wearable biomedical devices. *Journal of the Mechanical Behavior of Biomedical Materials*, *107*, Article 103733. https://doi.org/10.1016/j.jmbbm.2020.103733
19. Ranjan, R., Murthy, H., Bhowmik, D., & Sadavarte, V.S. (2023). Behaviour of composite solid propellant under biaxial tensile loading. *Polymer Testing*, *124*, Article 108054. https://doi.org/10.1016/j.polymertesting.2023.108054
20. Seibert, H., Scheffer, T., & Diebels, S. (2014). Biaxial testing of elastomers – experimental setup, measurement and experimental optimisation of specimen's shape. *Technische Mechanik*, *34*(2), 72–89. https://doi.org/10.24352/UB.OVGU-2017-054
21. Silberstein, M.N., Pillai, P.V., & Boyce, M.C. (2011). Biaxial elastic–viscoplastic behavior of Nafion membranes. *Polymer*, *52*(2), 529–539. https://doi.org/10.1016/j.polymer.2010.11.032
22. Steinmann, P., Hossain, M., & Possart, G. (2012). Hyperelastic models for rubber-like materials: consistent tangent operators and suitability for Treloar's data. *Archive of Applied Mechanics*, *82*(9), 1183–1217. https://doi.org/10.1007/s00419-012-0610-z
23. Treloar, L.R.G. (1944). Stress-strain data for vulcanized rubber under various types of deformation. *Rubber Chemistry and Technology*, *17*(4), 813–825. https://doi.org/10.5254/1.3546701
24. Vitucci, G. (2024). Biaxial extension of cruciform specimens: Embedding equilibrium into design and constitutive characterization. *Experimental Mechanics*, *64*(4), 539–550. https://doi.org/10.1007/s11340-024-01052-2
25. Zhao, X., Berwick, Z.C., Krieger, J.F., Chen, H., Chambers, S., & Kassab, G.S. (2014). Novel design of cruciform specimens for planar biaxial testing of soft materials. *Experimental Mechanics*, *54*(3), 343–356. https://doi.org/10.1007/s11340-013-9808-4

Manuscript received December 3, 2024; accepted for publication February 11, 2025;

JOURNAL OF THEORETICAL
AND APPLIED MECHANICS
63, 3, pp. 501–510, Warsaw 2025
https://doi.org/10.15632/jtam-pl/202025

THE INFLUENCE OF THERMAL EFFECTS ON ELASTOPLASTIC PROPERTIES OF Ti/Cu BIMETAL BARS OBTAINED BY EXTRUSION

Robert UŚCINOWICZ

Department of Mechanics and Applied Computer Science, Faculty of Mechanical Engineering,
Bialystok University of Technology, Bialystok, Poland
r.uscinowicz@pb.edu.pl

The article presents the results of the study of the elastic-plastic properties of bimetallic titanium/copper rods subjected to short-term thermal action in the temperature range of 600 °C–900 °C. The study used the impulse vibration excitation technique and a quasi-static tensile test. The final stage of the study was a microscopic SEM analysis of the interface. Macroscopic observations of the destruction surface were also carried out. Short-term annealing of the Ti/Cu bimetal caused a decrease in strength and proof stress, as well as an increase in ductility and diffusion. The destructive and dangerous processes were mainly at a temperature of 900 °C.

Keywords: Ti/Cu bimetal; elastoplastic deformation; impulse excitation technique, failure.

1. Introduction

The answer to the current global energy crisis in the processing industry is a metal-layered composite with multifunctional physical properties. Technological progress in the methods for joining different metals has made their permanent connections with each other easy and possible. This way, a new functional metallic material is obtained with important technical significance and unique operational properties. Examples here are bimetallic Ti/Cu bars used as anodes and cathodes in electrolysis processes (Bockris, 1981; Chawla & Gupta, 1993; O'Brien *et al.*, 2007) or as bus-bars in high-temperature electrolytic cells (Xu *et al.*, 2007). They are made of a copper core surrounded by a titanium layer. The advantage of this solution is the excellent electrical conductivity of copper and the high corrosion resistance of titanium to the aggressive action of many chemical compounds, especially those originating from acidic and chloride environments (Sanjurjo *et al.*, 1991). The inseparable layered composition of copper and titanium is also used in cryogenic and heat exchanger devices for thermal partitions (Bateni *et al.*, 2001; 2003) or in medicine when producing bone implants where, in addition to titanium, a layer of copper is introduced, providing antibacterial properties (Mahmoudi *et al.*, 2022) and others.

Bimetallic Ti/Cu rods are often made by explosive welding (Paul *et al.*, 2020) or extrusion (Xu *et al.*, 2007), which is thermally activated. The hydrostatic extrusion process of titanium-copper alloy bimetal is described in (Matsushita *et al.*, 1988), where the viscoplastic extrusion technique was used. In addition, important information on Ti/Cu extrusion can be found in

---

Ministry of Science and Higher Education
Republic of Poland

The publication has been funded by the Polish Ministry of Science and Higher Education under the Excellent Science II programme "Support for scientific conferences".
The content of this article was presented during the 40th Danubia-Adria Symposium on Advances in Experimental Mechanics, Gdańsk, Poland, September 24–27, 2024.

(Lee *et al.*, 2007) and the co-extrusion process in (Xu *et al.*, 2007). The method of extrusion of rods intended for electrodes requires high loads and a correspondingly high temperature, which can cause the formation of intermetallic compounds at the interface of metal layers and thus reduce the bonding strength. During operation, the electrodes are exposed to thermal effects caused by the electric current flowing through them.

The risk of increased temperature in structural elements and installations made of Ti/Cu bimetal conducting high-density electrical current can cause an overheating effect, which results in a decrease in strength properties and may lead to premature destruction. The tests aimed to assess the effect of short-term exposure to a thermal medium in the temperature range of 600 °C–900 °C on the elastic-plastic properties of Ti/Cu bimetal rods. The condition of the Ti/Cu joint after annealing and the surface of the scrap samples after the tensile test were also evaluated. Research activities related to Ti/Cu bimetals should provide an answer to the question of how to reduce energy consumption, lower production costs in metallurgy, extend the service life, and protect bimetals against unforeseen results of thermomechanical effects. This work is based in part on the experimental data described in the research by Uścinowicz (2022) and extends them to include new research problems.

2. Material, specimens, and experimental setup

The research material was Ti/Cu bimetallic rods consisting of a copper core of ∅8.8 mm thickness and a titanium coating of 1.6 mm thickness distributed concentrically around the core circumference. The average volume fraction of the bimetal components was $f_{\mathrm{Ti}} = 46\,\%$, $f_{\mathrm{Cu}} = 54\,\%$. The chemical composition of the Ti/Cu bimetal components was determined by the Shenzhen Jia Ping Titanium Industry Co. Ltd, and it is presented in Table 1.

Table 1. Chemical composition of the titanium (Ti) and copper (Cu) layers.

<table>
<tr><td colspan="8">Titanium (Ti) layer [%]</td></tr>
<tr><td>Ti</td><td colspan="2">Fe</td><td>C</td><td>N</td><td>H</td><td>0</td><td>others</td></tr>
<tr><td>99.6</td><td colspan="2">0.002</td><td>0.003</td><td>0.002</td><td>0.0005</td><td>0.001</td><td>0.391</td></tr>
<tr><td colspan="8">Copper (Cu) layer [%]</td></tr>
<tr><td>Cu + Ag</td><td>Bi</td><td>Sb</td><td>As</td><td>Fe</td><td>Pb</td><td>S</td><td>others</td></tr>
<tr><td>99.9</td><td>0.03</td><td>0.002</td><td>0.004</td><td>0.005</td><td>0.004</td><td>0.005</td><td>0.05</td></tr>
</table>

Cylindrical samples of 110 mm length were made from Ti/Cu rods (Fig. 1). The geometric axis of the samples was consistent with the direction of the extrusion process. The test samples were divided into two groups. The first group contained samples without heat treatment, symbolically marked $T = 20\,^{\circ}\mathrm{C}$. Samples from the second group were independently heated in the furnace for 30 min to temperatures of 600 °C, 700 °C, 800 °C, and 900 °C, respectively. They were then annealed for 30 min and cooled in air to 20 °C.

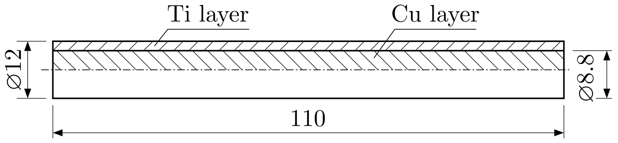

Fig. 1. Geometry of the Ti/Cu sample subjected to tensile tests and tests using the excitation impulse method.

The elastic properties of the tested bimetal were determined using the impulse excitation method (IME). The compact cylindrical shape of the Ti/Cu bimetal samples was helpful in measuring the elastic properties using an acoustic resonance frequency analyser (RFDA) from

IMCE NV. This (dynamic) method is described in the guide by Lord and Morrell (2006) and in the ASTM E1876-22 (2022) and ISO 12680-1 (2005) standards. With the help of this technique, Young's modulus E_d, the basic resonance frequencies χ_f, the internal friction parameters Q^{-1}, and the damping coefficient k were determined.

The essence of this method is to excite a mechanical impulse (impact with an impulse) and induce a mechanical wave (vibrations) in the tested sample subjected to 3-point bending. Induced vibrations have a frequency spectrum consistent with resonance frequencies and depend on the elastic properties of the material, its geometry, and density (mass). Next, with the help of an acoustic transducer (microphone), analog signals are transmitted to a computer and digitized. Unique mathematical algorithms using the Fourier transform calculate each frequency and attenuation from the detected frequency spectrum, assigning sinusoidal attenuated acoustic vibrations $x(t)$ to each frequency in the form:

$$x(t) = Ae^{-kt}\sin(2\pi\chi_f t + \varphi), \tag{2.1}$$

where A, φ – equation parameters, χ_f – basic resonance frequency during the bending mode, k – damping coefficient, t – time parameter. The selection of the appropriate value of the resonance frequency χ_f completed the process of determining the searched parameters.

The applied method experimentally confirmed the elastic constants of composites and other structurally complex materials (Uscinowicz, 2019; Song *et al.*, 2017; Stratigaki *et al.*, 2019; Yang *et al.*, 2012). The analysis of possible errors of this method is described in (Raggio *et al.*, 2010). This technique is so effective that it allows one to obtain quantitative information about the values of elastic constants and the integrity of samples (Roebben *et al.*, 1997).

Young's modulus for cylindrical Ti/Cu bimetallic samples with individually measured geometry and mass of specimen was determined from the following relationship (Lord & Morrell, 2006):

$$E_d = 1.6067 \cdot \left(\frac{L^3}{D^4}\right) m\,\chi_f^2\,H, \tag{2.2}$$

where E_d – Young's modulus, H – correction factor for flexural mode, m – sample mass, L, D – length and diameter of the cylindrical sample, respectively. Correction factor H was dependent on sample geometry and Poisson's ratio (Lord & Morrell, 2006). Young's modulus determined in the IME method was defined as dynamic and designated E_d.

The internal friction parameter was used to evaluate the energy balance in the above-described method and was defined by the following relationship:

$$Q^{-1} = \Delta W/2\pi W, \tag{2.3}$$

where W, ΔW – the energy stored and lost in a unit of the volume of the vibrating medium during one period, respectively. The following relationship was used to calculate it:

$$Q^{-1} = k/\pi\chi_f. \tag{2.4}$$

The elastic-plastic properties were determined from uniaxial tensile tests. The tests were carried out on an MTS 809.10 testing machine. Specimens' deformations were measured using the ARAMIS 3D 4M optical strain measurement system from GOM, which applied digital image correlation technology. The samples were loaded at a strain rate of $\dot{\varepsilon} = 2 \cdot 10^{-3}\,\mathrm{s}^{-1}$. Tensile tests were performed using the ASTM E8/E8M-22 (2022) technical standard on the same Ti/Cu bimetallic samples as on the RFDA device. The tests provided basic information on the elastic-plastic properties of the bimetal, i.e., Young's modulus E_s, the yield strength $R_{p0.2}$ corresponding to permanent deformations of 0.2%, tensile strength R_m and the values of the specific work of uniform plastic deformation L_p and elastic deformation L_e corresponding to uniform strains. The quantities defining the change in the dimensions of the diameter ε_d in tensile tests and the reduction of cross-sectional area after the fracture (Z) of bimetal components were also determined.

3. Results of tests and discussion

The values of elastic properties of the Ti/Cu bimetal obtained from tests using the impulse excitation technique depending on temperature are shown in Figs. 2 and 3 and Table 2.

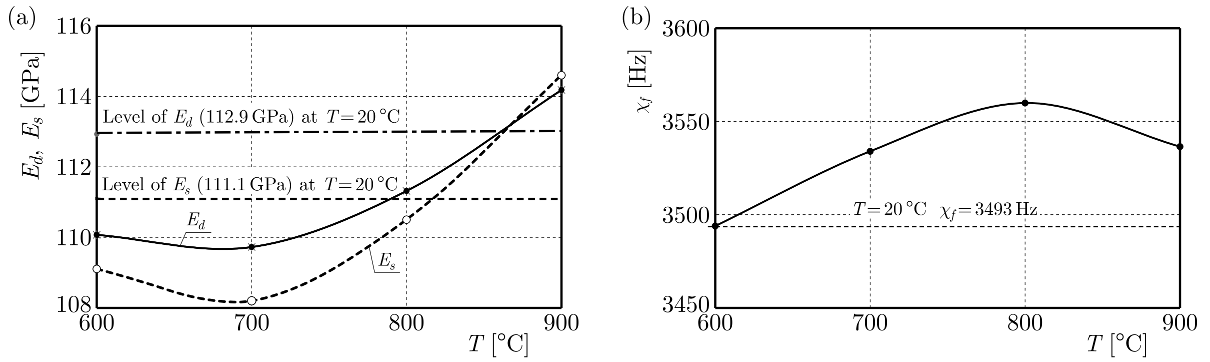

Fig. 2. Change of Young's modulus E_s and E_d (a) and resonance frequency χ_f (b) with increasing annealing temperature of the Ti/Cu bimetal.

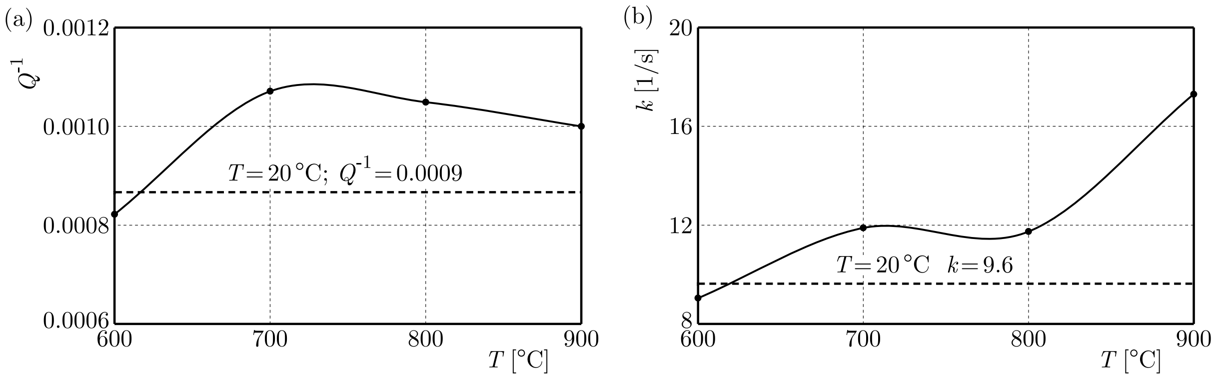

Fig. 3. Dependence of the internal friction parameter Q^{-1} (a) and the damping coefficient k (b) on the annealing temperature.

Table 2. Quantities determined for Ti/Cu bimetal using the impulse excitation method.

Temperature [°C]	E_d [GPa]	E_s [GPa]	χ_f [Hz]	Q^{-1} [–]	k [1/s]
20	112.9 ±0.4	111.1 ±4.5	3493 ±43	0.0009 ±0.0002	9.6 ±1.0
600	110.1 ±0.4	109.1 ±3.2	3494 ±17	0.0008 ±0.0001	9.0 ±0.5
700	109.7 ±0.4	108.2 ±2.1	3534 ±29	0.0011 ±0.0001	11.9 ±1.2
800	111.3 ±0.4	110.5 ±4.5	3560 ±36	0.0010 ±0.0002	11.7 ±1.9
900	114.2 ±0.4	114.6 ±5.6	3537 ±42	0.0010 ±0.0003	17.3 ±2.2

Figure 2a shows the variation of Young's moduli determined from the tensile test (E_s) and tests using the impulse excitation method (E_d). It was found that values of Young's modules within a tested temperature range differed by several GPa and were small in the tensile test cases. The highest values of Young's modulus of the Ti/Cu bimetal were $E_d = 114.2$ GPa and $E_s = 114.6$ GPa, recorded for the temperature of 900 °C. They were 3 GPa higher than for temperatures $T = 600$ °C, 700 °C. The values of the E_d moduli of the samples annealed at temperatures $T = 600$ °C and 700 °C were similar. Starting from the temperature of 700 °C, the values of Young's moduli increased in a parabolic manner (Fig. 2a). This was partly the result of structural changes in the titanium and copper layer and was associated with the formation of intermetallic brittle phases. It should be emphasized that the values of Young's moduli after annealing in the temperature range of 600 °C–900 °C compared to the unannealed ones were small.

A significantly different nature of the changes, with the increase in the annealing temperature, was observed for the resonance frequencies χ_f (Fig. 2b). In the case of χ_f, the highest frequency value was found for the temperature $T = 800\,^\circ\mathrm{C}$ and the range of frequency changes, for all temperatures, was small and covered only 50 Hz. It was noticed that the resonance frequencies for the unannealed samples ($T = 20\,^\circ\mathrm{C}$) and those annealed at 600 °C were identical.

Observation of the internal friction parameter Q^{-1}, related to energy losses in a given continuous medium subjected to impulsive loading, provides very important information about changes occurring in the internal structure of the Ti/Cu bimetal. They are helpful in assessing the cohesion of metal layers, but also provide information about the effects of processes in the structure during and after annealing. The parameter Q^{-1} reached its maximum value for samples annealed at a temperature of 700 °C, and the course of its variation in the tested temperature range was strongly non-linear (Fig. 3a). The values of Q^{-1}, for samples annealed at 600 °C and 20 °C, were very similar. It should be noted that high values of Q^{-1} are not recorded for metals. However, their noticeable increase with temperature can be attributed to processes occurring in the copper and titanium layers, i.e., the emergence of metallic phases at the interface as a result of diffusion. Puškár (2001) stated that there is no linear dependence of $Q^{-1} = f(T)$ when the temperature in metals exceeds the temperature by 50 %–60 % of the melting point, which is considered the limit.

It is commonly known that annealing at elevated and high temperatures can lead to an increase in grain size, structural reconstruction, changes in dislocation movements and a decrease in internal friction in the case of copper and titanium. The acquired strain of metals in the extrusion process can be thermally reduced, which results in a decrease in strength parameters and an increase in the ductility of bimetal components. However, in the case under study, internal friction slightly increases with temperature at 700 °C, and its causes can be sought in forming an intermetallic diffusion zone at the interface (third layer), which changes the reactivity of bimetal to a mechanical impulse.

Figure 3b shows the changes in the damping coefficient k. The increase in its value for the temperature of 900 °C and the simultaneous decrease in Q^{-1} can be attributed to the allotropic transformation of titanium, which significantly affects the elastic properties of Ti/Cu.

Based on the tensile tests, basic information was obtained about the elastic-plastic properties of the bimetal under monotonic quasi-static loading, i.e., the limit stresses $R_{p0.2}$ corresponding to permanent deformations of 0.2 %, tensile strength R_m, the course of which is shown in Figs. 4a and 4b. It should be noted that both the yield strength and the strength of the Ti/Cu bimetal were significantly decreased due to heat exposure compared to the analogous parameters for unannealed samples. The decrease in the $R_{p0.2}$ value was almost 3.5 times, while the strength R_m decreased 1.6 times. The increase in temperature from 800 °C to 900 °C caused a decrease in strength of only 20 MPa.

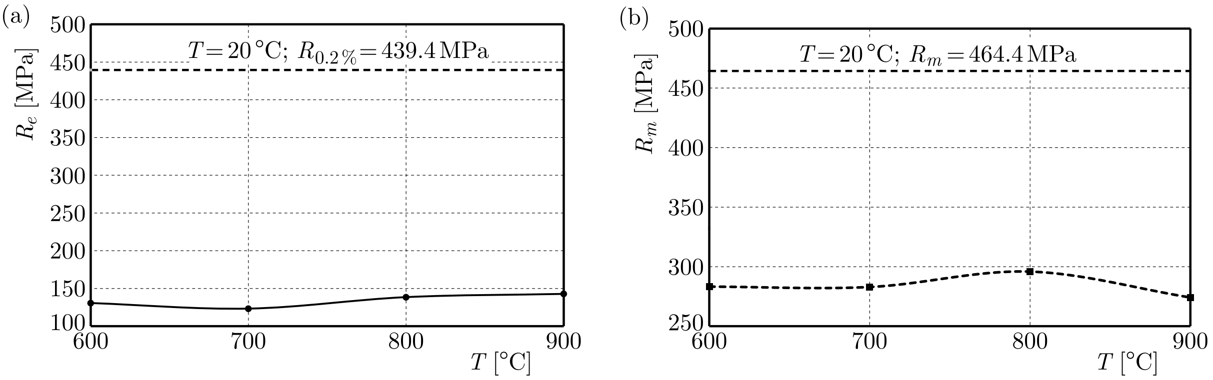

Fig. 4. Variation of the yield stress (a) and the strength (b) depending on the annealing temperature.

The effect of the decrease in strength due to annealing is the increase in the ductility of the bimetal, as evidenced by the increases in the value of the specific energy required for uniform plastic deformation of a unit of bimetal volume from 10.0 MJ/m^3 for $T = 20\,^\circ$C to 79.5 MJ/m^3 for $T = 700\,^\circ$C (Fig. 5b). The structural changes in the Ti/Cu bimetal samples at 900 °C caused a decrease in the L_p parameter almost 2.5 times compared to the value associated with the temperature of 800 °C. The values of basic mechanical properties determined from the tensile test are given in Table 3.

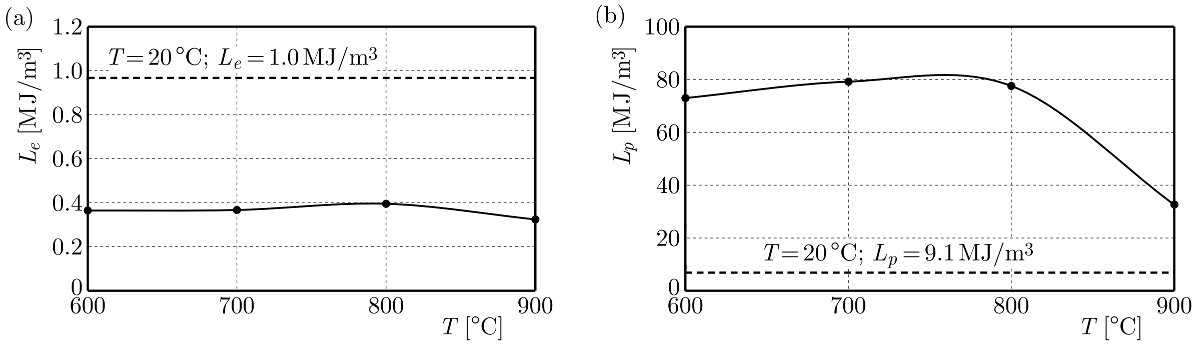

Fig. 5. Variation of the specific energy of the uniform elastic (a) and plastic (b) deformation depending on the annealing temperature.

Table 3. Average values of various mechanical properties obtained for Al/Cu bimetal.

Temperature [°C]	$R_{0.2}$ [MPa]	R_m [MPa]	L_p [MJ/m^3]	L_e [MJ/m^3]
20	464.4 ±6.4	464.4 ±9.6	9.1 ±1.5	0.96 ±0.15
600	283.2 ±5.3	283.2 ±6.9	73.0 ±5.3	0.36 ±0.06
700	283.9 ±4.1	283.9 ±6.0	79.2 ±6.9	0.37 ±0.04
800	295.9 ±5.9	295.9 ±7.4	77.5 ±6.2	0.40 ±0.03
900	274.1 ±7.2	274.1 ±8.5	36.6 ±4.3	0.32 ±0.05

In turn, when analysing the values of the specific energy of the elastic deformation L_e (Fig. 5a) necessary to deform a unit of volume, determined at the level of uniform deformation at the temperature $T = 20\,^\circ$C and in the temperature range of 600 °C–900 °C, it should be stated that also here, as a result of heat action, a decrease of this parameter by 68 % occurred. In the tested temperature range of 600 °C–900 °C, the L_e values differed slightly, which does not correlate well with the distribution of Young's modulus values in this range (Fig. 2a).

The deformation capacity of the Ti/Cu bimetal during the tensile test can be monitored by observing the changes in the transverse deformation of the sample expressed by the relative change in its diameter ε_d. The variability of this quantity is shown in Fig. 6. To facilitate the assessment of the scale of deformation and its course, the test duration was normalized

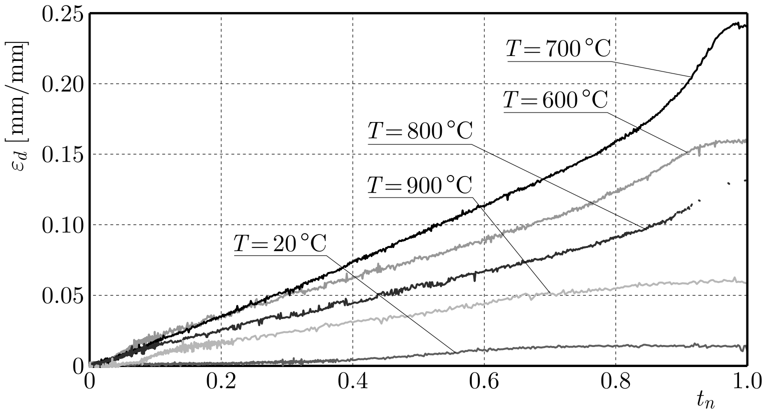

Fig. 6. Example variations of relative diameter deformation ε_d of Ti/Cu bimetallic samples throughout the tensile process.

by assuming the interval $\langle 0,1\rangle$ as the duration of the entire tensile process for tested samples. Assuming the same samples' deformation in the loading (axial) direction of the bimetal, including its Ti and Cu layers under different stresses in cross-sections, the most significant increase in elastic-plastic deformations of ε_d was observed in samples annealed at 700 °C; slightly lower values can be attributed to Ti/Cu samples for $T = 600\,^\circ\mathrm{C}$. Lower values ε_d with an increase in the normalized time t_n were observed in samples heated at $T = 800\,^\circ\mathrm{C}$ and 900 °C. This resulted from structural changes in the sample volume and the enlargement of the diffusion zone at the interface. Unannealed samples obtained the lowest ε_d values during stretching.

Important quantitative information allowing us to assess the influence of the annealing temperature on the tensile process and the destruction mechanism was the standard parameter Z [%] called the percentage maximum reduction of cross-sectional area after fracture. It described the change in the cross-sectional area of the samples at the fracture site related to the original area. The values of this parameter for the Ti/Cu bimetal components are shown in Fig. 7. The graph shows that the Ti/Cu bimetal components annealed at $T = 900\,^\circ\mathrm{C}$ are characterized by the minor reduction of the cross-section at the fracture site, which was about 41 % for copper and 45 % for titanium. It can, therefore, be assumed that the Ti and Cu components became more brittle after annealing at this temperature. In the 600 °C–800 °C temperature range, the Z constriction values for the individual bimetal components were similar and amounted to approximately 90 % for copper and 74 % for titanium, as observed. However, these values were higher than the corresponding Z values for the bimetal components for unannealed samples. In the case of titanium, this difference was 20 %. The more ductile metal in the composite was copper, which was the effect of final deformations just before the sample fracture.

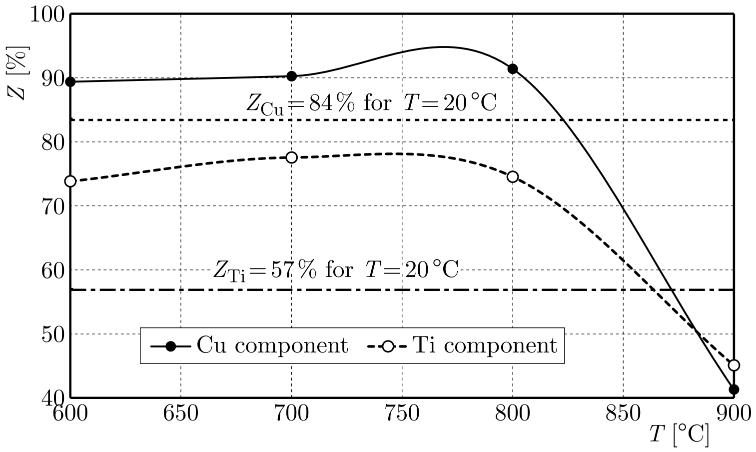

Fig. 7. Changes in the values of cross-sectional area Z after fracture of the titanium and copper layer depending on the annealing temperature measured on the sample scraps.

4. Microscopic and macroscopic observations of the Ti/Cu interface and fractures

For each sample tested, microscopic observations of the Ti/Cu bimetal layer connection zone were performed using a Phenom XL scanning microscope. At the same time, a linear analysis of its composition was performed immediately after annealing. The permanent connection of the copper and titanium layers in the Ti/Cu bimetal is crucial and has great significance for load transfer and operational task performance. No visible diffusion zone was observed in samples heated to 600 °C and 700 °C. However, in (Youn & Lee, 2020), the presence of a diffusion zone below 1 µm at a temperature of 450 °C was found. Only at 800 °C a narrow diffusion layer appeared (Fig. 8a) with an average thickness of 15.6 µm, which increased significantly at $T = 900\,^\circ\mathrm{C}$ (Fig. 8b) to a value of 31.7 µm. At temperatures of 800 °C and 900 °C, sporadic cracks appeared perpendicular to the interface (Fig. 8a). It seems that at annealing temperatures close to 900 °C the bond strength of the layers decreases significantly. This was accompanied

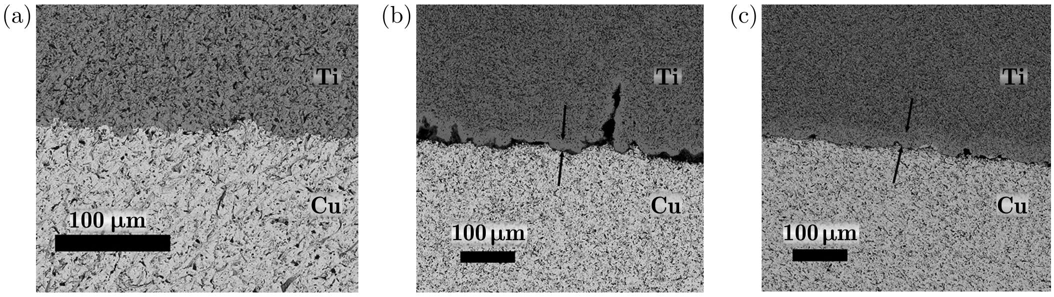

Fig. 8. Contact zone of titanium and copper in bimetal samples: (a) not annealed; (b) annealed at temperature $T = 800\,^\circ\mathrm{C}$; (c) annealed at temperature $T = 900\,^\circ\mathrm{C}$.

by an allotropic transformation of titanium, which changed from an HCP structure to a BCC structure, being more susceptible to diffusion processes. At this temperature, the tensile strength of the Ti/Cu bimetal decreased (Fig. 4b), making it less ductile (Fig. 5b). A similar nature of phenomena was observed by Lee *et al.* (2007) during the production of the Ti/Cu bimetal by the extrusion method.

Much information about the change in the plastic properties of the Ti/Cu bimetal due to annealing is provided by macroscopic observation of scrap samples created as a result of their rupture during tensile tests. Figure 9 presents photographs of characteristic traces of the scrap surface after the release of elastic energy due to destruction. The most severely degraded surface is the sample heated at 900 °C (Fig. 9e), where traces of the formed brittle Ti/Cu interphase layers are visible. The decomposition of the coating composed of titanium and intermetallic compounds could also be observed here. It had a different shade of grey and a characteristic fragmented structure, indicating brittleness. The mechanism of destruction in this case was different than for the unheated samples or those heated at temperatures of 600 °C and 700 °C. For these samples, it could be seen that the copper core, initially cylindrical, undergoes a ductile fracture (in a bundle), creating a characteristic cup and cone fracture. In the case of the bimetallic sample heated at 900 °C, the copper core was slippery (shear form), and the cross section was slightly deformed. The separating fracture had a mixed character in samples heated at $T = 800\,^\circ\mathrm{C}$.

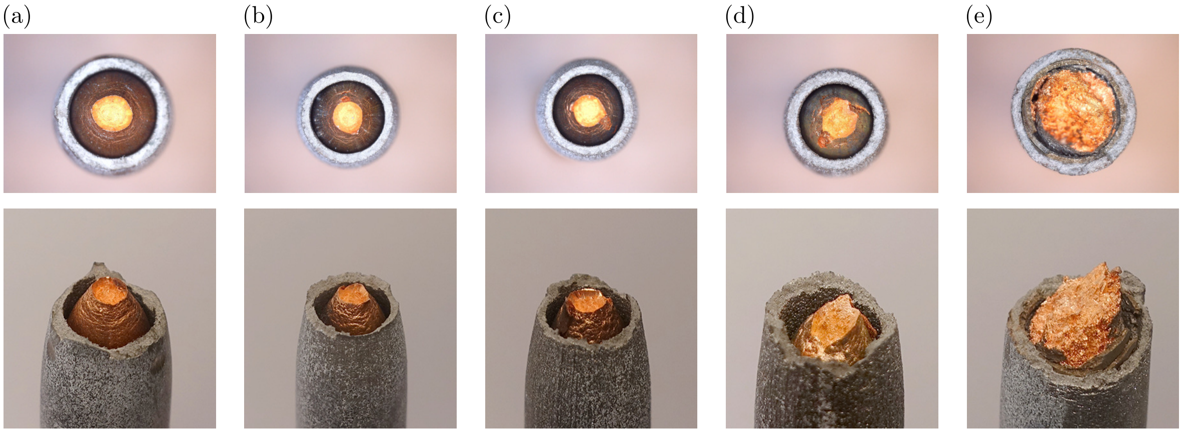

Fig. 9. Examples of surface zones of sample scraps formed as a result of the separation of samples during stretching after heating at the temperature: (a) 20 °C; (b) 600 °C; (c) 700 °C; (d) 800 °C; (e) 900 °C.

5. Conclusions

1) In the temperature range of 600 °C–800 °C, Young's modulus values determined for the Ti/Cu bimetal from tensile tests were slightly lower than the analogous values obtained from tests using the impulse excitation method and all oscillated in the range of 108 GPa–

111 GPa. The highest value of Young's modulus was found for samples annealed at $T = 900\,^{\circ}\mathrm{C}$ and amounted to over 114 GPa.

2) The increase in the value of internal friction Q^{-1} with increasing temperature (above 700 °C) can be attributed to the emerging of the diffusion zone at the boundary of the copper and titanium layers in the bimetal structure. The unannealed sample and the sample annealed at temperature $T = 600\,^{\circ}\mathrm{C}$ have similar Q^{-1} values. Annealing the Ti/Cu bimetal in the range of 600 °C–800 °C resulted in a multiple increase in the demand for energy for plastic deformation of a volume unit. For samples annealed at 900 °C, a significant decrease in this parameter was noted.
3) It was found that 30-minute heat exposure to Ti/Cu bimetal in the range of 600 °C–800 °C deteriorates strength properties, significantly lowering the yield point and increasing ductility, which reduces the bimetal's ability to work under load. The temperature of 900 °C threatens the safe use of bimetal, causing irreversible structural changes and accelerating processes leading to destruction.

Acknowledgments

This paper was prepared as a part of the research project no. WZ/WM-IIM/4/2023 of Bialystok University of Technology, financed by the Polish Ministry of Science and Higher Education, and research project no. 2019/35/B/ST8/03151, contract no. UMO−2019/35/B/ST8/03151, supported by the National Science Centre of Poland.

References

1. ASTM International. (2022). *Standard Test Methods for Tension Testing of Metallic Materials* (ASTM Standard No. E8/E8M-22). https://doi.org/10.1520/E0008_E0008M-22
2. ASTM International. (2022). *Standard Test Method for Dynamic Young's Modulus, Shear Modulus, and Poisson's Ratio by Impulse Excitation of Vibration* (ASTM Standard No. E1876-22). https://doi.org/10.1520/E1876-22
3. Bateni, M.R., Mirdamadi, S., Ashrafizadeh, F., Szpunar, J.A., & Drew, R.A.L. (2001). Formation of Ti–Cu intermetallic coatings on copper substrate. *Materials and Manufacturing Processes*, *16*(2), 219–228. https://doi.org/10.1081/AMP-100104302
4. Bateni, M.R., Szpunar, J.A., Ashrafizadeh, F., & Zandrahimi, M. (2003). The effect of novel Ti-Cu intermetallic compound coatings on tribological properties of copper. *Surfaces*, *10*(11), 55–62.
5. Bockris, J. O'M., Conway, B.E., Yeager, E., & White, R.E. (Eds.). (1981). *Comprehensive treatise of electrochemistry. Volume 2: Electrochemical processing.* Springer. https://doi.org/10.1007/978-1-4684-3785-0
6. Chawla, S.L., & Gupta, R.K. (1993). *Materials selection for corrosion control.* ASM International.
7. International Organization for Standardization. (2005). *Methods of test for refractory products – Part 1: Determination of dynamic Young's modulus (MOE) by impulse excitation of vibration* (ISO Standard No. 12680-1:2005). https://www.iso.org/standard/37670.html
8. Lee, J.S., Son, H.T., Oh, I.H., Kang, C.S., Yun, C.H., Lim, S.C., & Kwon, H.C. (2007). Fabrication and characterization of Ti–Cu clad materials by indirect extrusion. *Journal of Materials Processing Technology*, *187–188*, 653–656. https://doi.org/10.1016/j.jmatprotec.2006.11.144
9. Lord, J.D., & Morrell, R. (2006). Elastic modulus measurement. Measurement Good Practice Guide No. 98. *National Physical Laboratory.*
10. Mahmoudi, P., Akbarpour, M.R., Lakeh, H.B., Jing, F., Hadidi, M.R., & Akhavan, B. (2022). Antibacterial Ti–Cu implants: A critical review on mechanisms of action. *Materials Today Bio*, *17*, Article 100447. https://doi.org/10.1016/j.mtbio.2022.100447

11. Matsushita, T., Noguchi, M., & Arimura, K. (1988). Hot hydrostatic extrusion of Ti/Cu-alloy composite materials (in Japanese). *Journal of the Society of Materials Science, Japan*, *37*(413), 107–113. https://doi.org/10.2472/jsms.37.107
12. O'Brien, T.F., Bommaraju, T.V., & Hine, F. (2007). *Handbook of chlor-alkali technology. Volume II: Brine treatment and cell operation.* Springer Science & Business Media.
13. Paul, H., Chulist, R., Bobrowski, P., Perzyński, K., Madej, Ł., Mania, I., Miszczyk, M., & Cios, G. (2020). Microstructure and properties of the interfacial region in explosively welded and post-annealed titanium-copper sheets. *Materials Characterization*, *167*, Article 110520. https://doi.org/10.1016/j.matchar.2020.110520
14. Puškár, A. (2001). *Internal friction of materials.* Cambridge International Science Publishing Ltd.
15. Raggio, L.I., Etcheverry, J., Sánchez, G., & Bonadeo, N. (2010). Error analysis of the impulse excitation of vibration measurement of acoustic velocities in steel samples. *Physics Procedia*, *3*(1), 297–303. https://doi.org/10.1016/j.phpro.2010.01.040
16. Roebben, G., Bollen, B., Brebels, A., Van Humbeeck, J., & Van Der Biest, O. (1997). Impulse excitation apparatus to measure resonant frequencies, elastic moduli, and internal friction at room and high temperature. *Review of Scientific Instruments*, *68*(12), 4511–4515. https://doi.org/10.1063/1.1148422
17. Sanjurjo, A., Wood, B.J., Lau, K.H., Tong, G.T., Choi, D.K., McKubre, M.C.H., Song, H.K., & Church, N. (1991). Titanium-based coatings on copper by chemical vapor deposition in fluidized bed reactors. *Surface and Coatings Technology*, *49*(1–3), 110–115. https://doi.org/10.1016/0257-8972(91)90040-4
18. Song, W., Zhong, Y., & Xiang, J. (2017). Mechanical parameters identification for laminated composites based on the impulse excitation technique. *Composite Structures*, *162*, 255–260. https://doi.org/10.1016/j.compstruct.2016.12.005
19. Stratigaki, M., Pabst, W., Nečina, V., Hajíček, M., & Gotsis, A.D. (2019). Microstructure and mechanical properties study of slip-cast copper–alumina composites. *SN Applied Sciences*, *1*, Article 40. https://doi.org/10.1007/s42452-018-0037-4
20. Uscinowicz, R. (2019). Characterization of directional elastoplastic properties of Al/Cu bimetallic sheet. *Journal of Materials Engineering and Performance*, *28*(3), 1350–1359. https://doi.org/10.1007/s11665-019-03892-9
21. Uścinowicz, R. (2022). Effect of elevated temperature and annealing time on mechanical properties of Ti/Cu bimetal. *Materials*, *15*(23), Article 8707. https://doi.org/10.3390/ma15238707
22. Xu, F., Fredette, J.C., Holt, R.A., Rogge, R.B., Pickard, D., & Tuck, L. (2007). Investigation of residual stress in a bent Ti-clad Cu bus-bar by neutron diffraction and finite element modelling. *Journal of Neutron Research*, *15*(3–4), 259–266. https://doi.org/10.1080/10238160802449871
23. Yang, W.S., Biamino, S., Padovano, E., Fuso, L., Pavese, M., Marchisio, S., Vasquez, D., Vega Bolivar, C., Fino, P., & Badini, C. (2012). Microstructure and mechanical properties of short carbon fibre/SiC multilayer composites prepared by tape casting. *Composites Science and Technology*, *72*(6), 675–680. https://doi.org/10.1016/j.compscitech.2012.01.014
24. Youn, C.-S., & Lee, D.-G. (2020). Effects of post heat treatment on the mechanical properties of cold-rolled Ti/Cu clad sheet. *Metals*, *10*(12), Article 1672. https://doi.org/10.3390/met10121672

Manuscript received December 10, 2024; accepted for publication February 18, 2025;

JOURNAL OF THEORETICAL
AND APPLIED MECHANICS
63, 3, pp. 511–523, Warsaw 2025
https://doi.org/10.15632/jtam-pl/202124

MOMENT-CURVATURE RELATION FOR LASER-ASSISTED BENDING OF THIN INCONEL 718 BEAM

Jacek WIDLASZEWSKI[1*], Marcin NOWAK[2], Zdzisław NOWAK[1], Piotr KURP[3]

[1] *Institute of Fundamental Technological Research, Polish Academy of Sciences, Warsaw, Poland*
[2] *Institute of Structural Analysis, Poznan University of Technology, Poznan, Poland*
[3] *Center for Laser Technology of Metals, Kielce University of Technology, Kielce, Poland*
*corresponding author, *jacek.widlaszewski@ippt.pan.pl*

Moment-curvature relations for the thermo-mechanical bending of slender beams made of Inconel 718 in the factory-annealed state are determined in the study. The experimentally validated finite element method (FEM) model with the Johnson–Cook material model is used. For the considered conditions of thermo-mechanical processing, the final beam curvature can be estimated as a linear function of the curvature due to the elastic pre-stress. In processing 1 mm thick material, using laser power 500 W and feed rate 3.33 mm/s, a safe time distance of at least 5.4 minutes is estimated between the presence of high material temperature and the start of precipitation processes.

Keywords: thermo-mechanics; laser-assisted bending; Inconel 718; Johnson–Cook model; curvature.

1. Introduction

Materials with high-temperature strength may cause difficulties both in cold-shaping and hot-working. The interest in thermally-based forming is a response to the needs and challenges involved in the cost-effective and robust manufacturing of sheet metal based products. Local heating offers attractive characteristics for metal forming. The necessary forming force or pressure may be reduced with the desired temperature distribution and controlled heating rates. The thermally assisted processing offers reduced wear of forming tools and the reduction of the spring-back effect (Neugebauer *et al.*, 2006; Duflou & Aerens, 2006; Ponticelli *et al.*, 2018; Widłaszewski *et al.*, 2019). Heat-assisted bending of plates proved to be a flexible and cost-effective forming method for small batch situations (Wei *et al.*, 2021).

A laser beam is a heat source offering an exceptional opportunity to control heat input to the workpiece precisely both in time and space. Hence, laser-assisted manufacturing processes have gained ever increasing attention in recent years (Min *et al.*, 2023; Bammer, 2024; Liao *et al.*, 2024). They have been successfully introduced into stamping, bending, single-point incremental forming, spinning, stretch forming, roll profiling, deep drawing, wire drawing, hydroforming and other technologies (Kratky, 2007; Lauwers *et al.*, 2014). However, for successful development of new forming methods, the thermo-mechanics of the heat-assisted plastic deformation process should be thoroughly analysed and well understood. In parallel, thermal processing should retain

---

Ministry of Science and Higher Education
Republic of Poland

The publication has been funded by the Polish Ministry of Science and Higher Education under the Excellent Science II programme "Support for scientific conferences".
The content of this article was presented during the 40th Danubia-Adria Symposium on Advances in Experimental Mechanics, Gdańsk, Poland, September 24–27, 2024.

or establish the critical material properties, without adverse effects on its microstructure. A safe process window needs to be determined.

One of the recently studied thermo-mechanical bending methods consists in laser bending (Aher & Navthar, 2024) combined with mechanical preload. Fetene *et al.* (2018) used an artificial neural network in modelling the laser-assisted bending of a cantilever beam loaded with a force on the free end. The training and testing data set was obtained by a finite element method (FEM) model, which was validated by experiments. In research on bending and straightening of steel strips, Dutta *et al.* (2018) successfully applied laser scanning and external force generated with an electromagnet. Guo *et al.* (2020) proposed an analytical model to predict angular deformation due to the laser scanning of an elastically pre-stressed cantilever plate. The applied laser heating parameter values fostered the activation of the so-called buckling mechanism, which involves the thermally induced local buckling of a plate.

The present research concerns the thermo-mechanical behaviour of slender prismatic beams made of Inconel 718 alloy. Material selection was dictated by its wide application in structures and components operating at elevated temperatures, e.g., in the aerospace industry. Inconel 718 is a precipitation-hardenable nickel-based alloy having exceptionally high yield, tensile and creep-rupture properties at temperatures up to 700 °C (homologous temperature 0.63), combined with good oxidation resistance. The alloy is usually provided in the solution-annealed or the precipitation-hardened condition. The relatively slow precipitation hardening response of Inconel 718 permits annealing and welding without spontaneous hardening during heating and cooling, as well as repair welding, even in the aged condition. The outstanding resistance to post-weld cracking indicates the feasibility of laser-assisted forming application in manufacturing components made of the alloy. Fabrication of 3D complex components from Inconel 718 sheet metal is of great importance for the aerospace industry (Qu *et al.*, 2012; Prasad *et al.*, 2015; Hongbo & Gaochao, 2015; Tan *et al.*, 2018).

Numerical modelling using FEM is an effective tool to gain insight into the thermo-mechanic processes and the impact of processing parameters. In order to find moment-curvature relations in the considered problem, it is necessary to determine the beam curvature with high accuracy. Physical measurements of the curvature are prone to considerable errors and are difficult to perform, taking into account the application of a high power laser beam during experiments. Therefore, the present analysis is based on an experimentally validated numerical model.

2. Experiment

Experiments were conducted on beams made of commercial solution-annealed Inconel 718 with an average initial grain size of 17.5 μm. Specimens were laser-cut from a rolled sheet to minimize any introduction of residual stresses during material cutting. The chemical composition of the material is shown in Table 1.

Table 1. Chemical composition of Inconel 718 sheet [wt.%].

Ni	Cr	Mo	Nb	Co	Mn	Si	Fe	Al	Ti
52.9	19.83	3.12	4.83	0.05	0.29	0.14	Balance	0.60	1.04

A rectangular specimen 20 mm wide and 1 mm thick was clamped in a cantilever arrangement on the experimental stand, as shown in Fig. 1a. The thermo-mechanical loading is schematically presented in Fig. 1b.

Before heating by a moving laser beam, the specimen was pre-stressed in the elastic state. Mechanical load was introduced with gravity acting on weights mounted at the free end of the beam and on the mass of the specimen (Fig. 1). The vertical dead load F for the elastic pre-stress was 3.04 N. In the initial configuration, the distance between the force application point and the fixture was 175 mm.

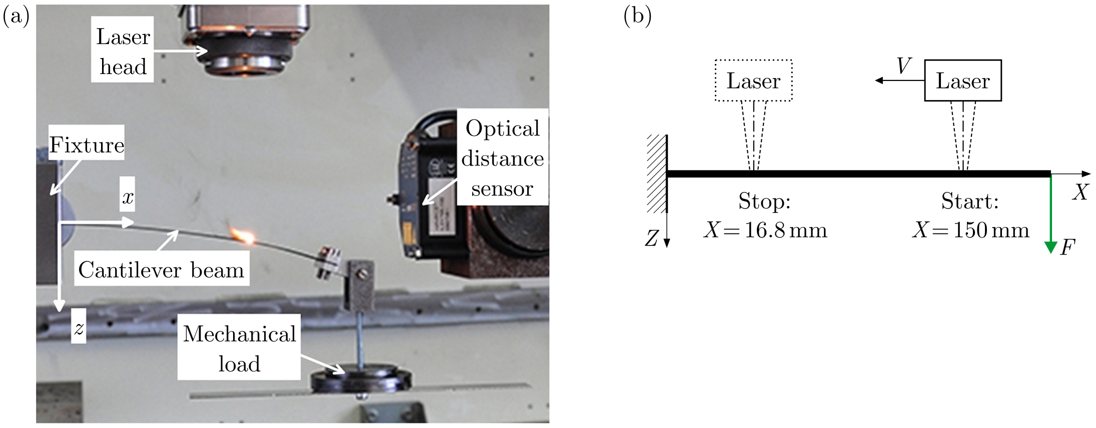

Fig. 1. Experimental setup: (a) a photograph, (b) thermo-mechanical loading scheme.

The pre-stressed beam was subjected to heating with a moving laser beam produced by the TruFlow6000 CO_2 laser which operated in the continuous-wave (CW) mode. A rectangular 20 mm × 2 mm laser spot was formed in the laser head using a facet mirror. The so-called mode shot in Fig. 2 shows a view of a plexiglass plate after short irradiation using the applied laser beam. The picture corresponds with the distribution of radiation power over the laser beam spot.

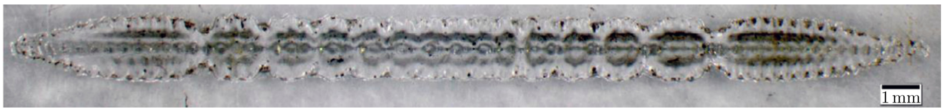

Fig. 2. Plexiglas plate after the mode shot performed with the applied laser beam.

The laser spot covered the whole width of the specimen and moved from the starting position $X = 150$ mm towards the final position $X = 16.8$ mm (Fig. 1b) with constant velocity. This scanning scheme minimized the unwanted influence of the laser beam divergence on laser spot dimensions.

The CO_2 laser radiation of the 10.6 μm wavelength incident at the right angle of the material surface is very poorly absorbed by perfectly clean, flat and smooth metal surfaces. The value of the radiation absorption coefficient rarely exceeds 0.1 for metals in such conditions.

An increase in absorptivity is observed with the increase in surface roughness and temperature. An improvement of energy transfer may be achieved by covering the processed material with an absorptive layer. Such a role can be played by oxides of the metal and various additional materials covering the surface in the form of powder or paint, e.g., graphite powder or a paint containing oxide pigments. Insulators generally have good absorptivity at long radiation wavelengths. Hence, coatings used in processing metallic materials with the CO_2 laser beam often contain dielectrics. A flat black paint is an excellent absorber but a flat white paint is also a highly effective absorber for the infrared radiation, despite its visual appearance.

Surface films may act as an anti-reflection coating due to the interference coupling. The destructive interference of the reflected ray occurs for the film thickness matched with the radiation wavelength. For the destructive interference of the CO_2 laser radiation, the film thickness value should be around 7.95 μm, 13.25 μm, 18.55 μm, and so on in the arithmetic progression.

The coating thickness should not be too large, as in the extreme conditions it can form a thermal barrier considerably affecting the heat flow to the underlying material. However, exothermic metal/oxide coatings may intensify heat input to the processed material. Too thin a coating may undergo a quick degradation without any noticeable effect on the radiation energy transfer. During laser irradiation the absorptive layer should be present at least till the rising temperature of the material surface starts playing a significant role in material absorptivity. Graphite spraying is used both to initially improve energy coupling and to prevent the excessive material surface temperature rise, the so-called thermal runaway, which impairs the thermal stability of processing. In order to achieve an effective laser treatment with high repeatability, it is necessary to ensure uniform and reproducible application of the absorptive coating to the workpiece surface.

The polished Inconel 718 subject to the CO_2 laser radiation in the air environment has absorptivity between 0.2 and 0.22 in the temperature range 227 °C–1227 °C. Specimens used in this study were covered with an absorptive layer of a black paint in order to improve and stabilize the transfer of laser beam energy into the material. The surface coating thickness was measured with a Mitutoyo Surftest SJ-301 device in a series of preliminary tests with X5CrNi18-10 stainless steel specimens (Kurp *et al.*, 2016). The average thickness of the coating was 8.13 µm with a standard deviation of 0.64 µm.

In order to determine the radiation absorption coefficient, the specimen surface temperature was measured using the OPTRIS CTL G5H CF2 pyrometer. The device operates at a 5.2 µm radiation wavelength and therefore is insensitive to the CO_2 laser radiation reflected from the specimen surface.

The free-end deflection of the specimen during thermo-mechanical loading and unloading processes was measured by a non-contact method. The optical displacement sensor MicroEpsilon LLT1700 measured the vertical displacement component of an auxiliary flat metal plate attached to the holder of weights.

A series of preliminary experiments was performed using laser beam velocity $v = 3.33\,\mathrm{mm/s}$ and laser power 200 W, 300 W, 350 W, 400 W, 500 W, 550 W, and 650 W. It was found that considerable bending deformation is produced using 500 W laser power. The plastic collapse of the processed beam occurred when applying higher laser power. Hence, laser beam velocity $v = 3.33\,\mathrm{mm/s}$ and the laser power 500 W were applied in the main thermo-mechanical bending experiments.

3. Numerical modelling

Spatial coordinates of material points in the initial (reference) configuration of the body are denoted by (X, Y, Z), while those of actual configuration, i.e., after deformation, are denoted by (x, y, z). The thermo-mechanical bending process was modelled in two sequentially coupled analyses, using the commercial FEM program ABAQUS, Version 2016. The symmetry of the object, load and boundary conditions allowed only a half of the considered beam, $0 \leq Y \leq 10\,\mathrm{mm}$, to be modelled, as shown in Fig. 3a. A regular mesh with hexahedral finite elements of dimensions $0.2\,\mathrm{mm} \times 0.5\,\mathrm{mm} \times 0.1\,\mathrm{mm}$ (in directions X, Y, and Z, respectively) was used.

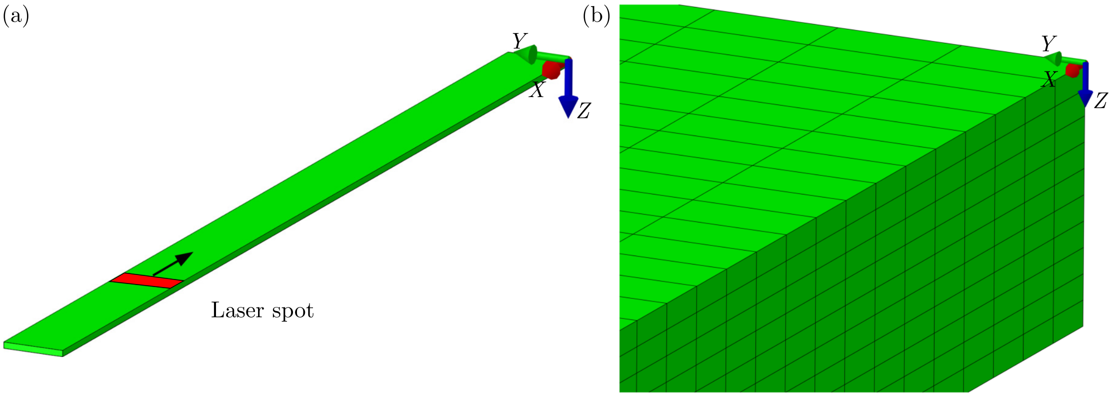

Fig. 3. Numerical model domain: (a) an overall view, (b) a detailed view of the finite element mesh.

The heat transfer analysis was performed in the initial configuration. The top-hat radiation energy distribution over the rectangular laser spot was assumed. A dedicated user subroutine DFLUX modelled the moving laser beam, treated as a surface heat source. The calculated temperature field and mechanical pre-stressing were subsequently used as thermo-mechanical loading in a quasi-static analysis.

Linear DC3D8 elements for the thermal problem and compatible C3D8 elements for the mechanical problem were applied. As the modelled laser spot had a dimension of 2 mm in the X-direction, the heat input from the moving laser beam was distributed over 10 rows of finite elements in the direction of laser scanning. Ten layers of elements were used in the material thickness direction (axis Z). Such a design of the finite element mesh enabled accurate, numerically-effective modelling of the temperature field and finally the bending effect due to the temperature gradient and mechanical pre-stressing. The regular mesh is also convenient for post-processing of simulation results.

The mesh consisted of 141600 elements and 163779 nodes. No strict mesh convergence study was performed, as numerical results were verified with experimental data. The complete computation time for both the thermal and mechanical analyses was 4 hours using 8-core processor operating at 3.6 GHz frequency.

The temperature dependence of material data was respected in simulations (Nowak *et al.*, 2019). A particular role in thermo-mechanical modelling is played by the application of a suitable material constitutive model with an accurate strain rate and temperature dependency of the yield stress σ_Y^T. The Johnson–Cook (JC) material model was applied in the study:

$$\sigma_Y^T\left(\varepsilon^{pl},\dot{\varepsilon}^{pl},T\right)=\left[A_{\mathrm{JC}}+B\cdot\left(\varepsilon^{pl}\right)^n\right]\left[1+C_{\mathrm{JC}}\cdot\ln\left(\frac{\dot{\varepsilon}^{pl}}{\dot{\varepsilon}_0}\right)\right]\left[1-(T^*)^m\right], \tag{3.1}$$

where ε^{pl} is the plastic strain component, $\dot{\varepsilon}_0$ ($0.001\,\mathrm{s}^{-1}$ in this work) is the reference strain rate, $T^*=(T-T_r)/(T_m-T_r)$, T_m is the melting temperature (1250 °C in this work) and the transition temperature T_r is assumed 20 °C in this work, A_{JC} is the yield stress under the transition temperature and the reference strain rate, B and n are strain hardening coefficient and exponent, respectively, C_{JC} describes strain rate hardening, and m stands for thermal softening effects.

The values of JC parameters are listed in Table 2 (Nowak *et al.*, 2019), while the assumed stress-strain-temperature behaviour for Inconel 718 is presented in Fig. 4.

Table 2. Parameters of the Johnson–Cook model.

A_{JC} [MPa]	B [MPa]	C_{JC}	m	n
450	2100.95	0.02	1.5	0.76

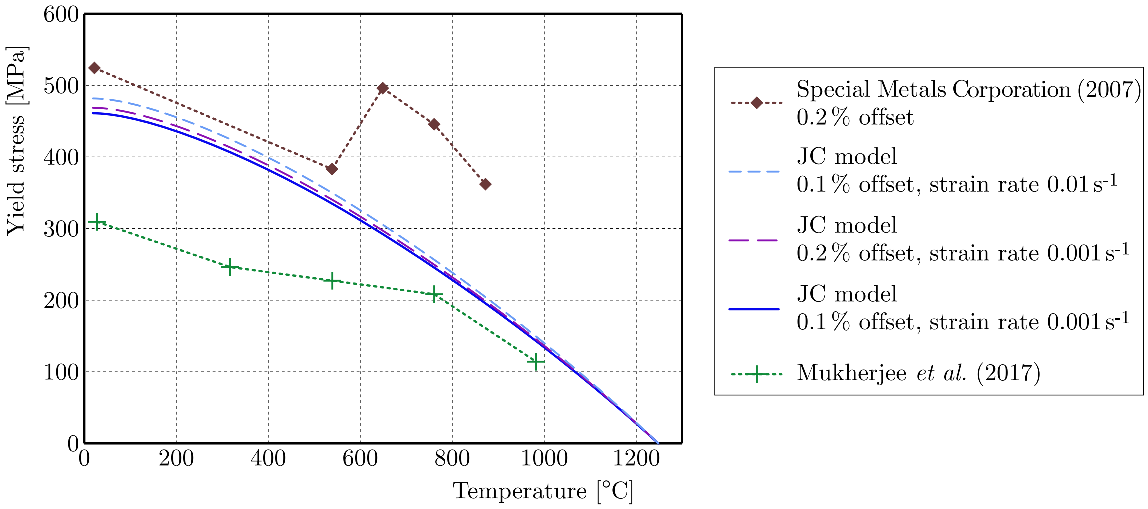

Fig. 4. Yield stress dependence of the annealed Inconel 718 on temperature.

The developed numerical model was used to simulate the thermo-mechanical behaviour of the Inconel 718 beam both with elastic pre-stress and without it. To account for large displacements, the geometric nonlinearity was respected in simulations and the parametric configuration representation was used in the post-processing of simulation results.

Experimental validation of the applied numerical model is crucial for the analysis value. The radiation absorption coefficient A and heat dissipation parameters were calibrated in a number of numerical simulations by comparing their results with the surface temperature measured in the experiment. A good agreement of results was obtained for $A = 0.37$, convection coefficient $5\,\mathrm{W/(m\cdot K)}$ and emissivity value 0.75 (Fig. 5). Strong oscillations visible in the temperature signal recorded during the experiment result from burning of the absorptive layer, as seen in the photograph in Fig. 1a.

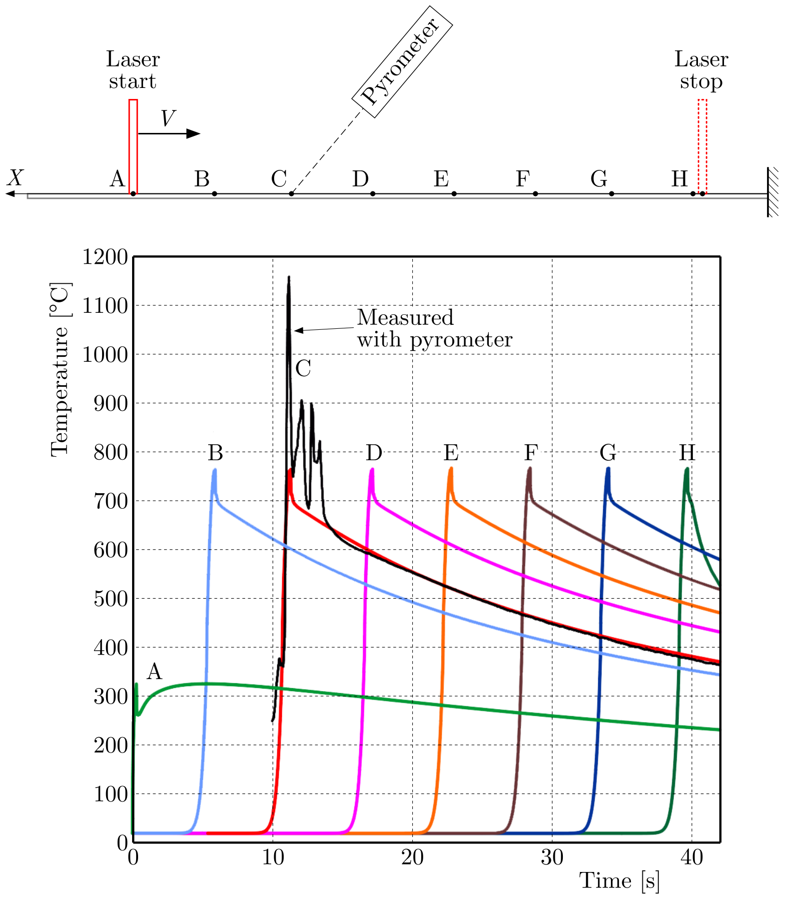

Fig. 5. Temperature variation at selected locations of the upper surface ($Y = 0$, $Z = 0$).

Experimental measurements and simulation results regarding the free-end deflection during laser scanning of the elastically pre-stressed beam are found to match well (Fig. 6). The reasonably close agreement of the temperature and deflection calculated in the simulations with experimental data is considered the numerical model validation.

4. Results

4.1. Temperature distribution and beam configuration

Figures 7 and 8 show the changes in surface temperature distribution and beam configuration for selected positions of the laser beam during scanning. Beam shapes (Fig. 8) present total deformation, i.e., due to the mechanical and thermal load, while the free-end deflection in Fig. 6 was measured starting from the mechanical pre-stressing configuration.

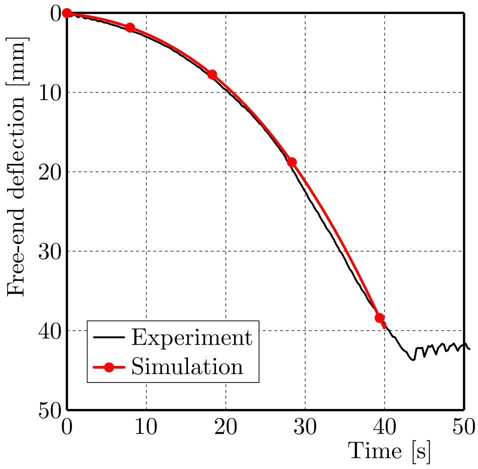

Fig. 6. Free-end deflection of the beam during thermo-mechanical bending.

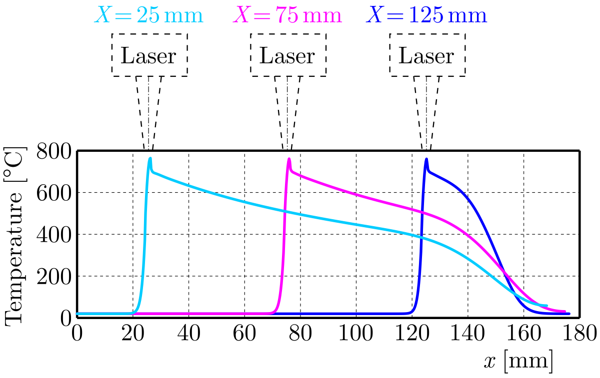

Fig. 7. Surface temperature distribution for laser beam positions $X = 125$ mm, 75 mm, and 25 mm ($Y = 0$, $Z = 0$).

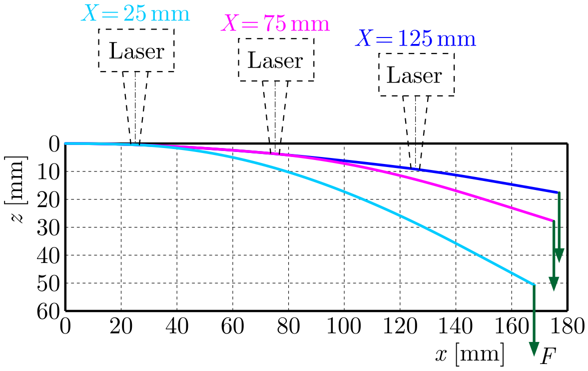

Fig. 8. Beam configurations for laser beam positions $X = 125$ mm, 75 mm, and 25 mm ($Y = 0$, $Z = 0$).

4.2. Thermal cycle

The determined temperature field variation enables the calculation of the thermal cycle which the processed material experiences during laser scanning. Figure 9 presents a typical evolution of temperature at the workpiece surface in relation to the time-temperature-transformation (T-T-T) diagram of Inconel 718. Localized heating with the moving laser beam results in a thermal cycle short enough to avoid the occurrence of unwanted microstructure changes. In the presented example, it offers a process window of over five-minute width, sufficient to induce plastic deformation and to cool down the material safely.

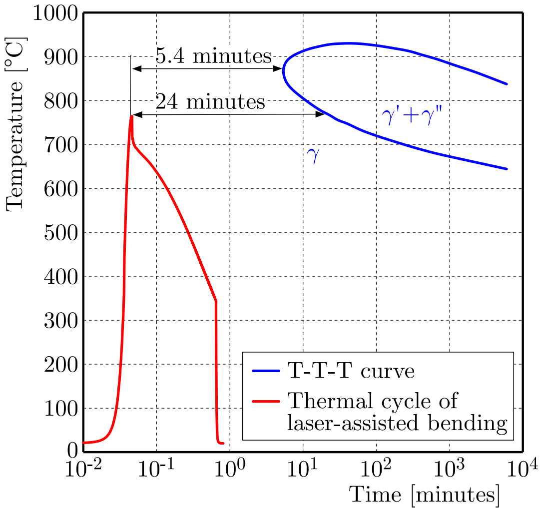

Fig. 9. Surface temperature cycle overlapped on the T-T-T diagram for Inconel 718 alloy (γ – metal matrix, γ' and γ'' – strengthening phases).

4.3. Curvature calculation

Determination of the moment-curvature relations in the considered problem requires the application of a curvature calculation method, which is capable of providing the necessary accuracy of results. Identification of the involved deformation mechanisms requires a careful separation of the contributing factors. Poor accuracy or excessive numerical noise of the calculated curvature values can make it impossible to draw meaningful conclusions from the moment-curvature relations in thermo-mechanical processing.

Two methods were applied to calculate beam curvature distributions after consecutive steps of the considered thermo-mechanical bending process. The first method is based on a discrete description of the beam axis as a 2-D curve. The second one uses the strain field linearization concept and strain values on the material boundary. While the first method involves numerical differentiation over some segment of the curve, the second method is based on the strain distribution over the considered cross-section of the material, and thus is more suitable to reveal local features of the curvature distribution.

4.3.1. Differential geometry approach

The beam axis ($Y = 0$, $Z = h/2$) is treated as a plane curve in the discrete parametric description $x = x(p)$, $z = z(p)$, where x, z are nodal coordinates, p is the parameter of the curve. The X-coordinate of a node in the initial configuration is used as the curve parameter ($p = X$).

The beam axis curvature C is calculated using the formula

$$C = \frac{|z''x' - x''z'|}{(x'^2 + z'^2)^{3/2}}, \tag{4.1}$$

where operators $(\,)'$ and $(\,)''$ denote the first and the second derivative with respect to the parameter p, respectively (Toponogov, 2006). For simplicity, the curvature and bending moment values are presented with the positive sign in this paper.

The finite difference method is used to calculate derivatives x' and z'. The symmetric difference quotient formula is applied for the first derivative:

$$f'(p) \approx \frac{f(p + \Delta p) - f(p - \Delta p)}{2\Delta p}, \tag{4.2}$$

where Δp is the numerical differentiation parameter of a possibly small value.

Similarly, the central difference approximation was used for the second derivatives x'' and z''

$$f''(p) \approx \frac{f(p+\Delta p) - 2f(p) + f(p-\Delta p)}{\Delta p^2}. \tag{4.3}$$

Numerical differentiation using a small value of parameter Δp is sensitive to errors resulting from the limited representation precision of numerical data, i.e., round-off errors. Low round-off and truncation errors were achieved using $\Delta p = 3\,\mathrm{mm}$, with $x(p)$, $z(p)$, and p expressed in millimetres.

4.3.2. Strain linearization approach

In general, the longitudinal strain across a section of the considered beam may be decomposed into the following components: (1) average membrane, (2) linear bending, and (3) peak strain. Figure 10 presents an example of the variation in the longitudinal strain component over the material thickness $\varepsilon_{xx}(Z)$ $(X = 100,\ Y = 0)$ after the consecutive steps of the process: (1) mechanical pre-stress, (2) laser heating, and (3) after cooling and removing of the mechanical load, i.e., in the final state. Dashed lines in the figure indicate linear approximations of the strain distribution. It is visible that the longitudinal strain component ε_{xx} may be fairly accurately treated as linear with respect to the coordinate Z. This conclusion justifies decomposing the through-thickness strain state into membrane and bending components.

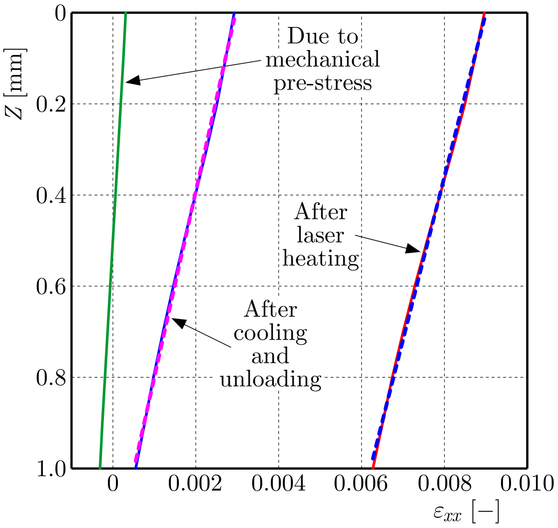

Fig. 10. Longitudinal strain distribution over material thickness $(X = 100,\ Y = 0)$.

The example of strain distribution over material thickness (Fig. 10) reveals that the considered thermo-mechanical processing may result in thermo-plastic stretching of material fibers over the whole thickness of the processed workpiece. In this case, the notion of the neutral axis can be related only to a theoretical line located out of the deformed material. It can no longer be identified with a real material fiber. Such a considerable "shift" of the neutral axis has to be respected in calculating the beam curvature based on the strain field.

By denoting longitudinal strain at the extreme points of a cross-section as $\varepsilon_{\mathrm{IN}}$ and $\varepsilon_{\mathrm{OUT}}$, for the inner and outer material fibers of the deformed beam, respectively, one can easily derive strain components of the decomposition and the curvature as

$$\varepsilon_b = \frac{\varepsilon_{\mathrm{OUT}} - \varepsilon_{\mathrm{IN}}}{2}, \quad \varepsilon_m = \frac{\varepsilon_{\mathrm{OUT}} + \varepsilon_{\mathrm{IN}}}{2}, \quad \frac{1}{R_0} = \frac{\varepsilon_{\mathrm{OUT}} - \varepsilon_{\mathrm{IN}}}{h}, \quad \frac{1}{R} = \frac{1}{1+\varepsilon_m}\frac{1}{R_0}, \tag{4.4}$$

where ε_b, ε_m are the bending and membrane strain components, respectively, $1/R_0$ is the curvature of the middle beam layer $(Z = h/2)$ for the case with no shift of the neutral axis $(\varepsilon_{\mathrm{OUT}} = -\varepsilon_{\mathrm{IN}})$, $1/R$ is the actual curvature when the neutral axis shift is present.

A comparison of the curvature calculated using both approaches is shown in Fig. 11. The strain linearization approach is more sensitive to such a local phenomenon as transient deformation due to temperature gradient over material thickness in the laser spot vicinity (see Fig. 11, vicinity of the laser track end at $X = 16.8\,\mathrm{mm}$). The curvature distribution obtained using the differential geometry approach has much smaller numerical noise, although it involves numerical differentiation. In general, the results of both calculation methods agree well with each other. On the basis of such verification, curvature calculated using the differential geometry approach is used in further analysis.

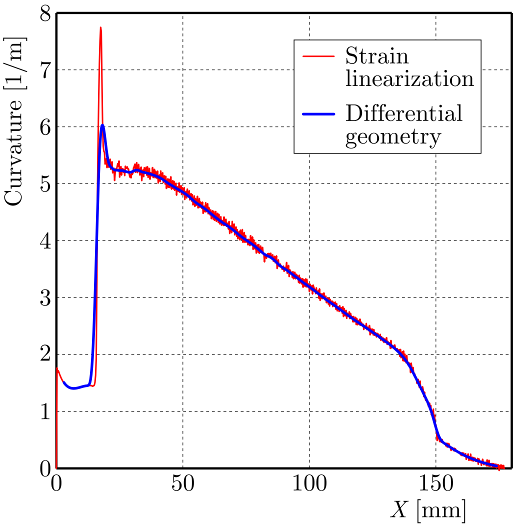

Fig. 11. Beam axis curvature immediately after the step of laser scanning ($Y = 0$, $Z = h/2$).

4.4. Curvature changes in thermo-mechanical processing

Figure 12 presents the following beam curvature characteristics: (1) after mechanical prestressing (marked as "elastic"), (2) after laser scanning followed by cooling the beam to the initial temperature (marked as "thermo-elastic-plastic"), and (3) after final unloading (marked as "plastic (final)"), calculated using the differential geometry approach. Three regions of thermo-elastic-plastic and plastic curvature characteristics can be distinguished. In the central region, from $X = 50$ to $X = 130$, the curvature practically depends linearly on the coordinate X. The other two regions, $X < 50$ and $X > 130$, include the start and stop positions of laser

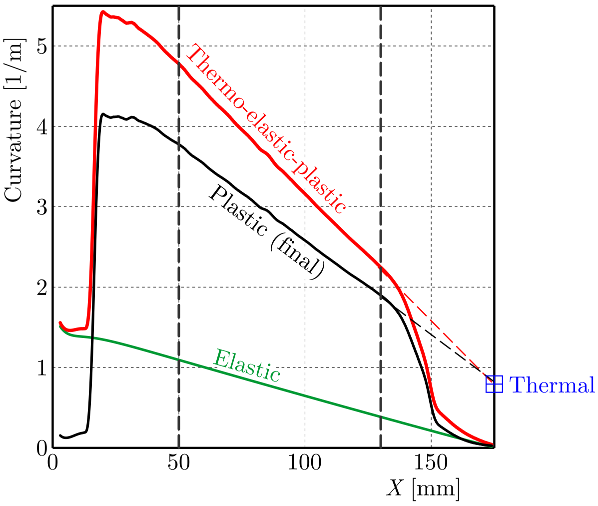

Fig. 12. Beam axis curvature distribution after specific processing steps.

scanning (cf. Figs. 1b and 5). Hence, the changes in thermal conditions greatly affect curvature characteristics in these regions.

Even without mechanical pre-stress ($F = 0$), the beam undergoes considerable plastic deformation, solely due to the load from a moving heat source. The related curvature is 0.797 (1/m) and in Figs. 12 and 13 is marked as "thermal". The so-called convex deformation occurred, such as when the heated material surface assumes the convex shape (Widłaszewski, 2022).

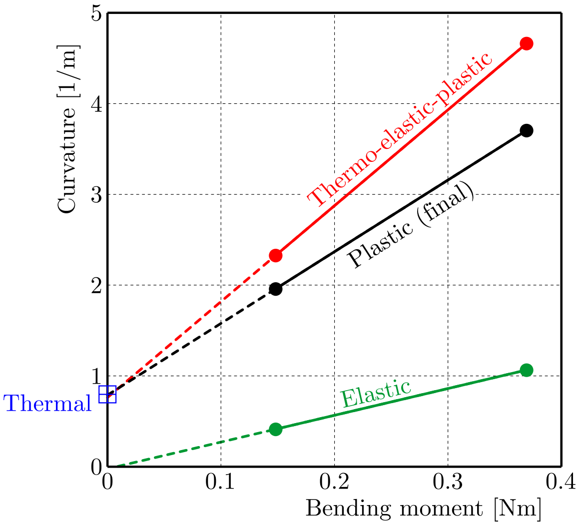

Fig. 13. Moment-curvature relations for specific steps of thermo-mechanical bending.

For the step of mechanical elastic pre-stressing, the calculated curvature agrees well with the analytical solution of the classical Euler-Bernoulli beam theory. Moment-curvature dependences shown in Fig. 13 were calculated for the central region of the beam, for $X = 50$ to $X = 130$. Curvature characteristics calculated after thermo-mechanical processing and after final unloading can be extrapolated up to the bending moment value 0, which corresponds to the pure thermal load case. The results of both extrapolations agree well with the curvature value determined in the simulation without pre-stress ($F = 0$).

Relations between the calculated curvatures can be characterized by the following dimensionless coefficients:

$$k_{\mathrm{TEP}} = \frac{(C_{\mathrm{TEP}} - C_T)}{C_E}, \qquad k_U = \frac{(C_{\mathrm{TEP}} - C_U)}{C_E}, \tag{4.5}$$

where C_T is the curvature due to purely thermal loading, C_E is the curvature after elastic pre-stressing, C_{TEP} is the curvature after thermo-elastic-plastic processing and cooling, still under mechanical load, C_U is the final curvature, i.e., after the final unloading.

The coefficient k_{TEP} represents the relation of the curvature change $(C_{\mathrm{TEP}} - C_T)$ resulting from thermo-mechanical processing to the curvature due to the initial elastic pre-stressing (C_E). The second coefficient, k_U, shows how the curvature change due to the final unloading $(C_{\mathrm{TEP}} - C_U)$ relates to the curvature after the initial elastic loading (C_E). Within the region $50 < X < 110$, the value of the coefficient k_{TEP} varies by less than 0.7 % of the mean value 3.64, while the value of the coefficient k_U changes by less than 1.3 % of the mean value 0.903. Hence, one can conclude that the curvature resulting from the considered thermo-mechanical processing can be estimated as a linear function of the curvature due to the elastic pre-stress:

$$C_{\mathrm{TEP}} = k_{\mathrm{TEP}} C_E + C_T, \qquad C_U = C_{\mathrm{TEP}} - k_U C_E. \tag{4.6}$$

The curvature change due to removal of the mechanical load describes the elastic response opposite to the deformation produced during pre-stressing. However, it concerns the beam with the residual stress field after considerable plastic deformation. Hence, the value of the coefficient k_U is not exactly 1.

5. Conclusions

Phenomenological moment-curvature relations for the laser-assisted bending of a slender Inconel 718 beam were formulated using the experimentally validated FEM model. For the analysed body and its thermal and mechanical loading conditions, the curvature after the laser-induced plastic deformation process can be estimated as a linear function of the curvature produced due to the elastic pre-stressing. The analysis revealed the presence of pure thermally induced deformation in the final change of the curvature. In processing 1 mm thick material, using laser power 500 W and feed rate 3.33 mm/s, a safe time distance of at least 5.4 minutes is estimated between the presence of high material temperature and the start of the precipitation processes. For the effective laser-assisted bending, the external mechanical load should be applied consistently with the deformation effect of the heat source alone, which under the considered conditions was the convex bending. The determined moment-curvature relations can be used in the design and optimization of thermo-mechanical processing.

Acknowledgments

The research reported herein was partly supported by a grant from the National Centre for Research and Development (no. PBS/A5/47/2015).

References

1. Aher, V., & Navthar, R.R. (2024). A comprehensive review on laser bending of advanced materials. *Lasers in Manufacturing and Materials Processing*, *11*(3), 814–852. https://doi.org/10.1007/s40516-024-00261-w

2. Bammer, F. (2024). Optimized heat distributions for laser-assisted forming. *Journal of Engineering*, *2024*(1), Article 9470839. https://doi.org/10.1155/2024/9470839

3. Duflou, J.R., & Aerens, R. (2006). Force reduction in bending of thick steel plates by localized preheating. *CIRP Annals*, *55*(1), 237–240. https://doi.org/10.1016/S0007-8506(07)60406-5

4. Dutta, P.P., Kalita, K., & Dixit, U.S. (2018). Electromagnetic-force-assisted bending and straightening of AH36 steel strip by laser irradiation. *Lasers in Manufacturing and Materials Processing*, *5*(3), 201–221. https://doi.org/10.1007/s40516-018-0062-6

5. Fetene, B.N., Shufen, R., & Dixit, U.S. (2018). FEM-based neural network modeling of laser-assisted bending. *Neural Computing & Applications*, *29*(6), 69–82. https://doi.org/10.1007/s00521-016-2544-9

6. Guo, Y., Shi, Y., Wang, X., Sun, R., & Bing, Z. (2020). An analytical model of laser bending angle under preload. *The International Journal of Advanced Manufacturing Technology*, *108*(7–8), 2569–2577. https://doi.org/10.1007/s00170-020-05521-5

7. Hongbo, D., & Gaochao, W. (2015). Effect of deformation process on superplasticity of Inconel 718 alloy. *Rare Metal Materials and Engineering*, *44*(2), 298–302. https://doi.org/10.1016/S1875-5372(15)30023-0

8. Kratky, A. (2007). Laser assisted forming techniques. *Proceedings Volume 6346, XVI International Symposium on Gas Flow, Chemical Lasers, and High-Power Lasers*, Article 634615. https://doi.org/10.1117/12.738146

9. Kurp, P., Mucha, Z., Mulczyk, K., Gradoń, R., & Trela, P. (2016). The influence of surface preparation on the absorption coefficient of laser radiation. *Proceedings Volume 10159, Laser Technology 2016: Progress and Applications of Lasers*, *10159*, Article 101590M. https://doi.org/10.1117/12.2257992

10. Lauwers, B., Klocke, F., Klink, A., Tekkaya, A.E., Neugebauer, R., & Mcintosh, D. (2014). Hybrid processes in manufacturing. *CIRP Annals*, *63*(2), 561–583. https://doi.org/10.1016/j.cirp.2014.05.003
11. Liao, W.-X., Lee, W.-T., Lin, C.-K., Tung, P.-C., & Ho, J.-R. (2024). Innovative laser-assisted glass bending approaches using a near-infrared continuous wave laser. *Optics and Lasers in Engineering*, *178*, Article 108162. https://doi.org/10.1016/j.optlaseng.2024.108162
12. Min, J., Wang, J., Lian, J., Liu, Y., & Hou, Z. (2023). Laser-assisted robotic roller forming of ultrahigh-strength steel QP1180 with high precision. *Materials*, *16*(3), Article 1026. https://doi.org/10.3390/ma16031026
13. Mukherjee, T., Zhang, W., & DebRoy, T. (2017). An improved prediction of residual stresses and distortion in additive manufacturing. *Computational Materials Science*, *126*, 360–372. https://doi.org/10.1016/j.commatsci.2016.10.003
14. Neugebauer, R., Altan, T., Geiger, M., Kleiner, M., & Sterzing, A. (2006). Sheet metal forming at elevated temperatures. *CIRP Annals*, *55*(2), 793–816. https://doi.org/10.1016/j.cirp.2006.10.008
15. Nowak, Z., Nowak, M., Pecherski, R.B., Wisniewski, K., Widłaszewski, J., & Kurp, P. (2019). Computational modeling of thermoplastic behavior of Inconel 718 in application to laser-assisted bending of thin-walled tubes. *International Journal for Multiscale Computational Engineering*, *17*(3), 317–338. https://doi.org/10.1615/IntJMultCompEng.2019029858
16. Oradei-Basile, A., & Radavich, J.F. (1991). A current T-T-T diagram for wrought alloy 718. In E.A. Loria (Ed.), *Superalloys 718, 625 and various derivatives* (pp. 325–335). The Minerals, Metals & Materials Society. Warrendale. https://doi.org./10.7449/1991/SUPERALLOYS_1991_325_335
17. Ponticelli, G.S., Guarino, S., & Giannini, O. (2018). A fuzzy logic-based model in laser-assisted bending springback control. *The International Journal of Advanced Manufacturing Technology*, *95*(9–12), 3887–3898. https://doi.org/10.1007/s00170-017-1482-8
18. Prasad, K.S., Kamal, T., Panda, S.K., Kar, S., Narayana Murty, S.V.S., & Sharma, S.C. (2015). Finite element validation of forming limit diagram of IN-718 sheet metal. *Materials Today: Proceedings*, *2*(4–5), 2037–2045. https://doi.org/10.1016/j.matpr.2015.07.174
19. Qu, F.S., Lu, Z., Xing, F., & Zhang, K.F. (2012). Study on laser beam welding/superplastic forming technology of multi-sheet cylinder sandwich structure for Inconel718 superalloy with ultra-fine grains. *Materials & Design*, *39*, 151–161. https://doi.org/10.1016/j.matdes.2012.02.002
20. Special Metals Corporation (2007). *Inconel Alloy 718*. Retrieved December 12, 2024, from https://www.specialmetals.com/documents/technical-bulletins/inconel/inconel-alloy-718.pdf
21. Tan, Y.B., Ma, Y.H., & Zhao, F. (2018). Hot deformation behavior and constitutive modeling of fine grained Inconel 718 superalloy. *Journal of Alloys and Compounds*, *741*, 85–96. https://doi.org/10.1016/j.jallcom.2017.12.265
22. Toponogov, V.A. (2006). *Differential geometry of curves and surfaces. A Concise Guide*. Boston: Birkhäuser.
23. Wei, B., Zhang, F., He, K., Zhou, C., & Du, R. (2021). Heat-assisted incremental bending of metal plates with unsymmetrical curvatures. *The International Journal of Advanced Manufacturing Technology*, *114*(11–12), 3437–3448. https://doi.org/10.1007/s00170-021-07067-6
24. Widłaszewski, J., Nowak, M., Nowak, Z., & Kurp, P. (2019). Laser-assisted thermomechanical bending of tube profiles. *Archives of Metallurgy and Materials*, *64*(1), 421–430. https://doi.org/10.24425/amm.2019.126268
25. Widłaszewski, J. (2022). Laser micro bending mechanism for high-precision adjustment in mechatronic systems. In J. Holnicki-Szulc, D. Wagg, & Ł. Jankowski (Eds.), *7th European Conference on Structural Control. Book of abstracts and selected papers* (pp. 262–269). Institute of Fundamental Technological Research and Committee on Mechanics, Polish Academy of Sciences. http://eacs2022.ippt.pan.pl/EACS%202022%20-%20Book.pdf

Manuscript received December 12, 2024; accepted for publication February 20, 2025;
published online June 23, 2025.

JOURNAL OF THEORETICAL
AND APPLIED MECHANICS
63, 3, pp. 525–534, Warsaw 2025
https://doi.org/10.15632/jtam-pl/202293

EVALUATION OF SHAPE TRANSFORMATION IN 4D PRINTED POLYLACTIC ACID USING COPPER WIRES

Raul-Mihai PETRAȘCU*, Sever-Gabriel RACZ, Eugen AVRIGEAN

Department of Industrial Machines and Equipment, Engineering Faculty, Lucian Blaga University of Sibiu, Sibiu 550025, Romania

*corresponding author, *raul.petrascu@ulbsibiu.ro*

This study explores the shape transformation of 4D printed polylactic acid (PLA) specimens activated by thermal stimulation above the glass transition temperature (T_g). Two methods were explored: (1) triggering shape transformation in a rectangular prism, "Flower", and "Spiderweb" designs via hot water immersion; and (2) inducing shape transformation through Joule heating using copper wires.

Keywords: polylactic acid; 4D printing; Joule heating; shape transformation; shape memory polymers.

1. Introduction

Fused filament fabrication (FFF), an extension of fused deposition modeling (FDM), is a 3D printing technique that builds objects layer-by-layer while extruding a semiliquid material through a nozzle (Ree, 2024). Material extrusion, or MEX, is a method that supports various thermoplastics, typically in the form of filaments. Polylactic acid (PLA) is biocompatible, ideal for usage in medical applications (DeStefano *et al.*, 2020), and biodegradable, which enables the development of environmentally friendly blends (Yousefi *et al.*, 2024).

Tibbits (2014) introduced the concept of 4D printing, which involves creating structures that modify their properties in response to external stimuli such as heat, light, magnetic fields, or pH changes. Smart materials which interact with stimuli can expand, contract, self-assemble, or self-heal, resulting in movements or structural adaptations (Petrașcu *et al.*, 2023). Shape memory polymers (SMPs) are of interest due to their shape memory effect (SME). The SME in SMPs refers to a material's ability to recover or transform into a programmed shape.

In 3D printing, a PLA sample is programmed for shape transformation after fabrication. The sample temperature (T_s) is raised above its glass transition temperature (T_g), which typically ranges from 44 °C to 63 °C (Crawford & Quinn, 2017). Above T_g, the material softens, which allows it to be deformed under an applied load into an intermediate shape. Under normal conditions, the sample retains this new shape due to the viscoelastic properties of the polymer until it is reheated above T_g, which triggers recovery to its programmed geometry, thus completing the SME cycle (Riley *et al.*, 2020).

Ministry of Science and Higher Education
Republic of Poland

The publication has been funded by the Polish Ministry of Science and Higher Education under the Excellent Science II programme "Support for scientific conferences".
The content of this article was presented during the 40th Danubia-Adria Symposium on Advances in Experimental Mechanics, Gdańsk, Poland, September 24–27, 2024.

In 4D printing, PLA sample programming is determined by printing parameters. The printed sample is considered an intermediate shape until T_s exceeds T_g, triggering the transformation into the programmed shape (Hosseinzadeh *et al.*, 2023). This transformation is driven by residual strain accumulated during the 3D printing process, influenced by temperature gradients and cooling rates. By adjusting printing parameters, such as printing speed, layer thickness and printing temperature, the amount of residual strain can be controlled (Wang & Li, 2020; Wu *et al.*, 2022). Figure 1 illustrates these programming approaches.

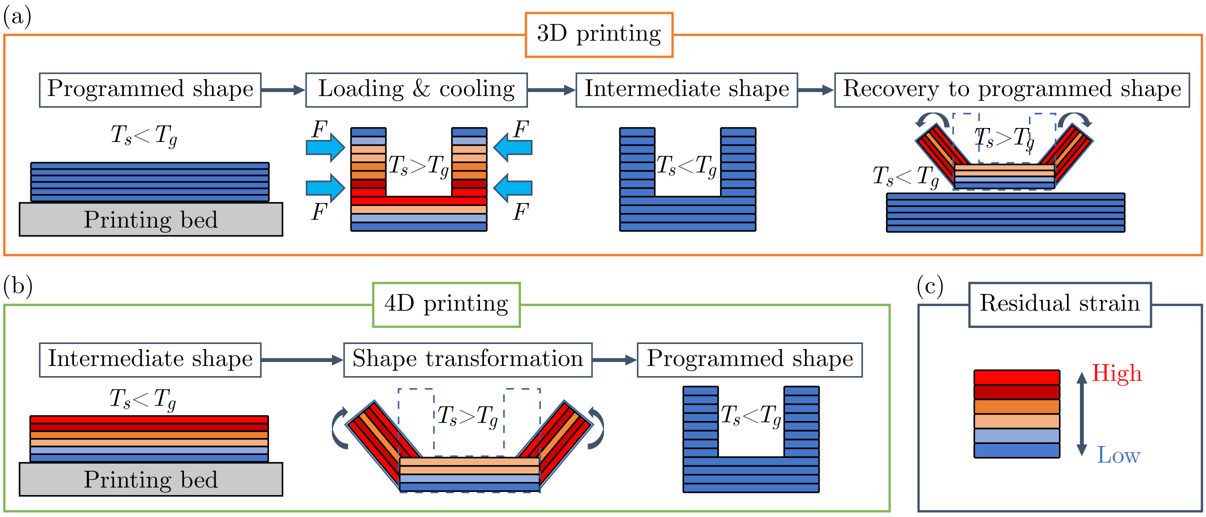

Fig. 1. Shape memory effect (SME): (a) 3D printing; (b) 4D printing; (c) residual strain levels [adapted from (Hosseinzadeh *et al.*, 2023)].

The activation of SME in PLA has been studied using various methods, including infrared radiation (Ren *et al.*, 2023), hot water immersion (Mehrpouya *et al.*, 2021), and conductive heating with resistive fillers like carbon black (Liu *et al.*, 2024), carbon nanotubes (Gholizadeh Ledari & Zolfaghari, 2025), and metal particles (Shao *et al.*, 2020). These fillers often require high voltage inputs; for example, Liu *et al.* (2019) used 70 V to activate a PLA-based gripper with carbon nanotubes.

Since higher filler content raises viscosity and necessitates more intensive mixing (Zhu *et al.*, 2021), its use presents challenges such as complex material preparation requiring uniform dispersion and strong interfacial bonding within the polymer matrix, as well as increased energy demands (Wang *et al.*, 2021). Moreover, PLA is inherently brittle, exhibits poor impact resistance, low heat tolerance, and limited dimensional stability at high temperatures (Wang *et al.*, 2024). To address these limitations, this study explores a simple and cost-effective approach to inducing shape transformation in 4D printed PLA specimens by embedding copper wires. Thermal activation above the T_g is applied in two ways: (1) in a water environment, where embedded copper wires control bending while mitigating the degradation of PLA's mechanical properties over time, and (2) in a non-fluid environment, where Joule heating of the embedded wires activates shape transformation.

The paper is structured as follows: Section 2 describes the sample design, printing parameters, and experimental setups for thermal stimulation using hot water immersion and Joule heating. It also details two configurations for embedding copper wires. Section 3 presents and discusses the results, starting with PLA's shape transformation in hot water, followed by the effects of embedded copper wires through Joule heating. Additionally, energy consumption is compared between configurations. Finally, Section 4 summarizes the study's findings.

2. Experimental section

2.1. Materials

Specimens were 3D printed using the FFF technique on an Ultimaker Connect 2+ 3D printer. The sample design is shown in Figs. 2a and 2c, with the corresponding printing parameters (Fig. 2b). Bell-shaped holes (Fig. 2d) were integrated to enable the post-printing insertion of copper wires. Two PLA filaments (2.85 mm diameter) were tested: red (Copper 3D) and blue (Ultimaker).

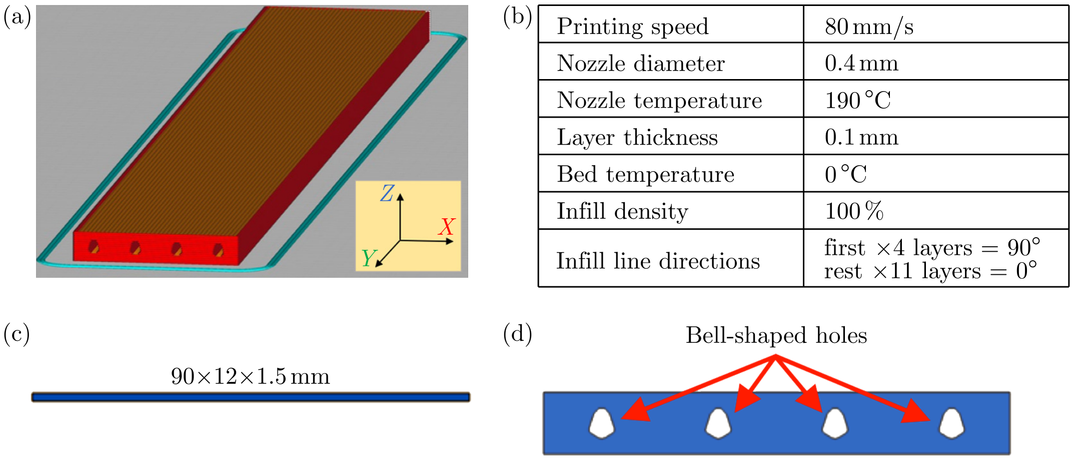

Printing speed	80 mm/s
Nozzle diameter	0.4 mm
Nozzle temperature	190 °C
Layer thickness	0.1 mm
Bed temperature	0 °C
Infill density	100 %
Infill line directions	first ×4 layers = 90° rest ×11 layers = 0°

Fig. 2. Sample design: (a) isometric view; (b) printing parameters; (c) lateral view, sample dimensions in millimeters, scale 1:2; (d) front view, bell-shaped holes, scale 1:16.

2.2. Testing procedure

Figure 3 presents the experimental setups designed to activate the shape transformation of PLA specimens in two different scenarios. In the first setup, specimens were immersed in hot water, with temperature regulated using a Zilan ZLN 4007 device, which employs a pump for fluid recirculation and a thermoplunger for heating. In the second setup, copper wires were embedded in the specimens and connected to a power supply delivering a constant 5 A current.

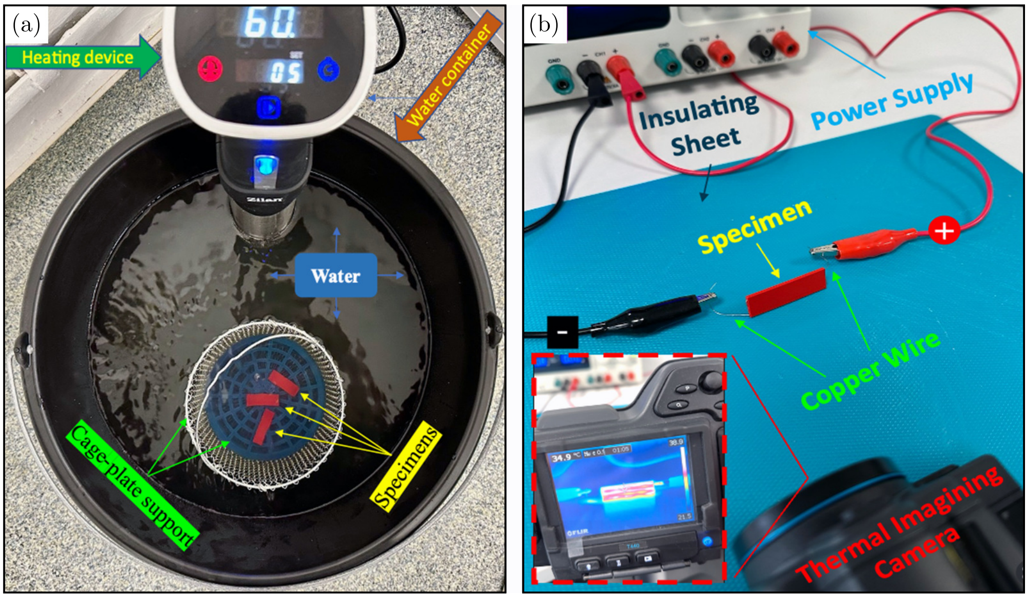

Fig. 3. Experimental setups: (a) immersion in hot water; (b) Joule heating.

Due to copper's negligible resistance, only the current required regulation. The temperature was monitored using a FLIR T440 thermal imaging camera.

The wire configurations are illustrated in Fig. 4. In the parallel configuration, four separate 100 mm wires were inserted individually, whereas the series configuration utilized a single continuous 400 mm wire. In both setups, after fabrication, 0.2 mm diameter copper wires were integrated into the specimens through bell-shaped holes.

Wire configuration	2D schematic representation
Parallel	
Series	

Fig. 4. 2D schematic of wire configurations and current flow pathways within the specimens.

3. Results and discussion

3.1. Shape transformation via hot water immersion

The first part of the study involves immersing 4D printed PLA specimens in hot water, which is a widely used method for activating shape transformation. Figure 5 illustrates the specimens' response in a water environment, where initially flat PLA samples undergo self-bending. At 65 °C, both specimens exhibit noticeable bending, while at 75 °C and 85 °C, they form coiled shapes. Notably, the red sample self-bends consistently, whereas the blue sample displays asymmetrical self-bending, likely due to variations in residual strain and filament color. The filament color affects PLA's thermal properties, while printing temperature plays a key role in achieving high crystallinity, which is essential for multiple SME cycles (Frunzaverde *et al.*, 2023; Cadete *et al.*, 2025).

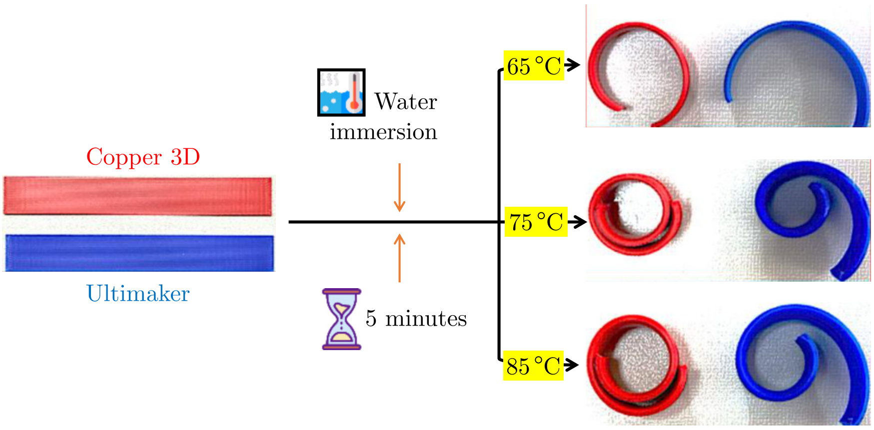

Fig. 5. Self-bending response of PLA specimens immersed in water at different temperatures.

The study further examines the shape transformations of PLA in hot water, focusing on more complex geometries. Figure 6 illustrates flat specimens transforming into concave, petal-like shapes when immersed at 70 °C. Similarly, Fig. 7 shows a spiderweb-shaped specimen undergoing the same transformation.

Figure 8 illustrates the self-bending deformation of 4D printed PLA specimens both without embedded wires (S_x) and with wires having a diameter of 0.2 mm (S_{02}), arranged in a parallel configuration.

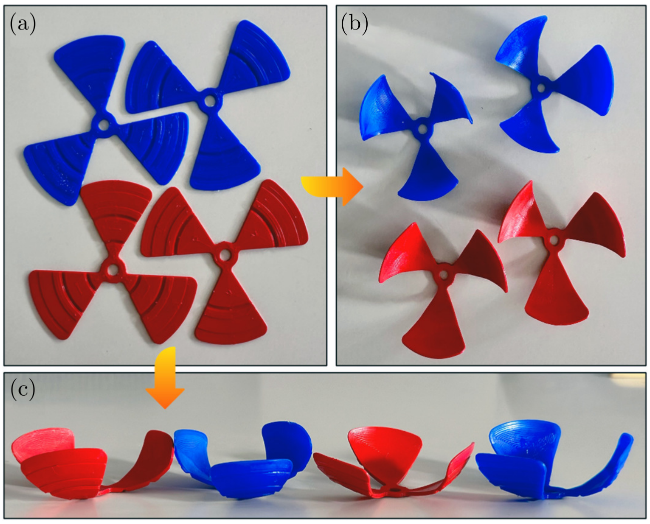

Fig. 6. Shape transformation of flower-shaped specimens: (a) 3D printed parts; (b) front view after thermal activation; (c) perspective view after thermal activation.

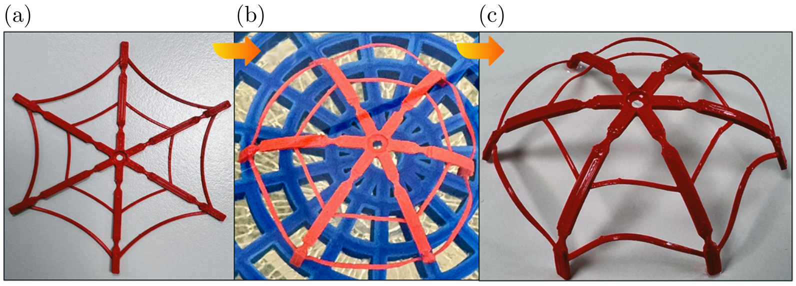

Fig. 7. Spiderweb sample shape transformation: (a) 3D printed part; (b) immersion in hot water; (c) perspective view after thermal activation.

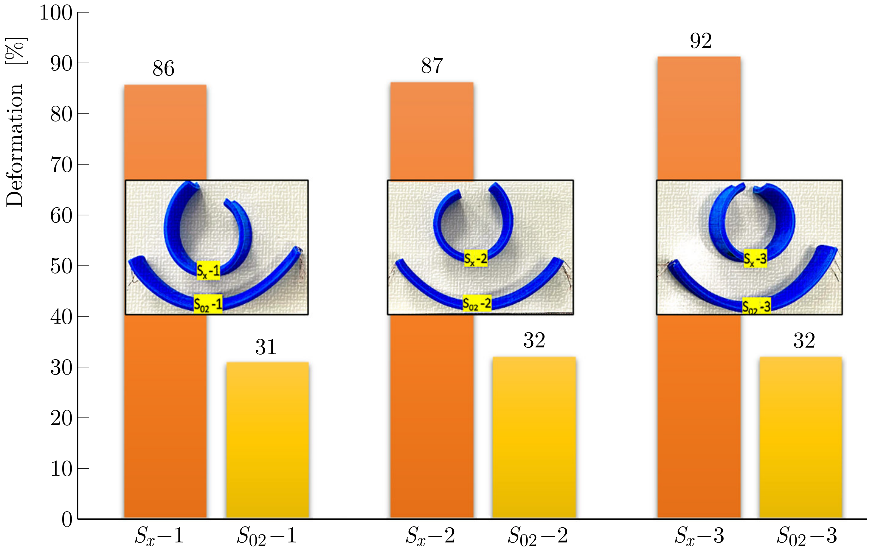

Fig. 8. Comparison of self-bending between specimens without integrated wires (S_x) and specimens with integrated copper wires (S_{02}).

The self-bending (S_b) for each specimen was calculated using Eq. (3.1), where L_0 represents the initial length and L_f the final length. Specimens without wires exhibited an average bending deformation of 88 %, consistent with findings by Ansaripour *et al.* (2024). In contrast, specimens with embedded copper wires exhibited a bending deformation of 56 %, reflecting a 32 % reduction. Each embedded wire contributed to an 8 % decrease in self-bending, indicating that copper wires can be utilized for controlled bending:

$$S_b = \frac{L_f - L_0}{L_0} \times 100. \tag{3.1}$$

Mechanical tests from the literature typically show a slight decline in material properties after multiple cycles of deformation and recovery (Ehrmann & Ehrmann, 2021). In this context, embedded wires can help preserve mechanical properties. In semi-crystalline PLA, heating times influence crystallinity when temperatures exceed T_g, with higher crystallinity enhancing shape fixity and recovery. This process is crucial for repeated deformation and recovery cycles, as it forms ordered, spring-like structures that interconnect polymer chains. However, over time, PLA can achieve sufficient crystallization through heat treatment (e.g., annealing), and this eliminates the need for further crystallization (Da Cunha *et al.*, 2023). Additionally, prolonged immersion in water allows PLA to absorb moisture due to its hydrophilic nature, which acts as a plasticizer, increasing macromolecular flexibility and lowering T_g, thereby facilitating shape recovery (Zhang *et al.*, 2020). These factors highlight the complex interplay between heat, environmental conditions, and PLA's shape memory response.

3.2. Shape transformation through Joule heating

3.2.1. Parallel configuration

In the first Joule heating scenario, four copper wires were embedded into a 3D printed sample (Fig. 2) in a parallel configuration (Fig. 4) and connected to a DC power source, supplying 5 A. Temperature measurements were recorded every 15 seconds for up to 60 seconds, as shown in Fig. 9. The results show a temperature increase from 26.4 °C to 33.3 °C over the entire interval, with a total rise of approximately 7 °C. Even so, since the internal temperature did not reach the T_g range, no shape transformation occurred. The highest temperature was recorded at the positive terminal due to electron accumulation at the circuit's exit, while the outer wires exhibited lower heating efficiency due to heat dissipation into the environment. However, reducing the wire length could enhance heating efficiency, making this setup more suitable for localized heating applications.

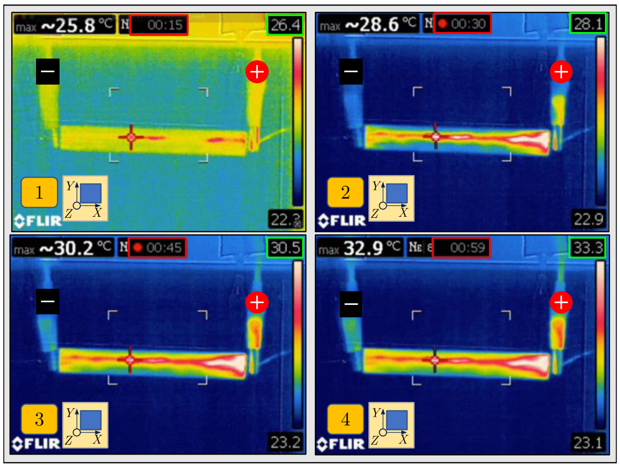

Fig. 9. Monitoring the temperature in parallel wires configuration.

3.2.2. Series configuration

In the second Joule heating scenario, a single copper wire was embedded into a 3D printed sample (Fig. 2) in a series configuration (Fig. 4) and connected to a DC power source, supplying 5 A. Temperature values recorded during the test are shown in Fig. 10. The results

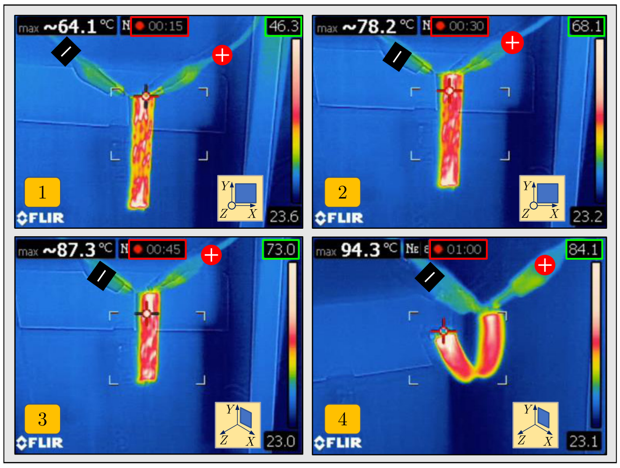

Fig. 10. Monitoring the Joule heating effect applied by integration of a single continuous copper wire.

indicate a faster temperature increase, from 46.3 °C to 84.1 °C, with a total increase of approximately 38 °C within 60 seconds. The highest temperatures were observed at the sample's ends, where the wire changed direction, leading to increased electron collisions.

In the first 15 seconds, the temperature reached 46.3 °C, which is below the T_g range of PLA and thus prevents any transformation. By 30 seconds, the temperature rose to 68.1 °C, surpassing T_g; however, the material's response was delayed. At 45 seconds, the temperature reached 73 °C, causing the unattached end of the sample to begin bending, which prompted a slight camera adjustment to capture the movement. By 60 seconds, the temperature reached approximately 84 °C, and the bending became more pronounced, with heat distribution appearing symmetrical within the sample.

Based on these findings, the series configuration may be effective for gripping applications. A similar study by (Shao *et al.*, 2020) used copper wires for localized heat transfer to activate a biomimetic flower-shaped gripper.

Figure 11 illustrates the energy consumption over time for both parallel and series configurations. The results indicate an estimated power dissipation of approximately 5.35 W. Since

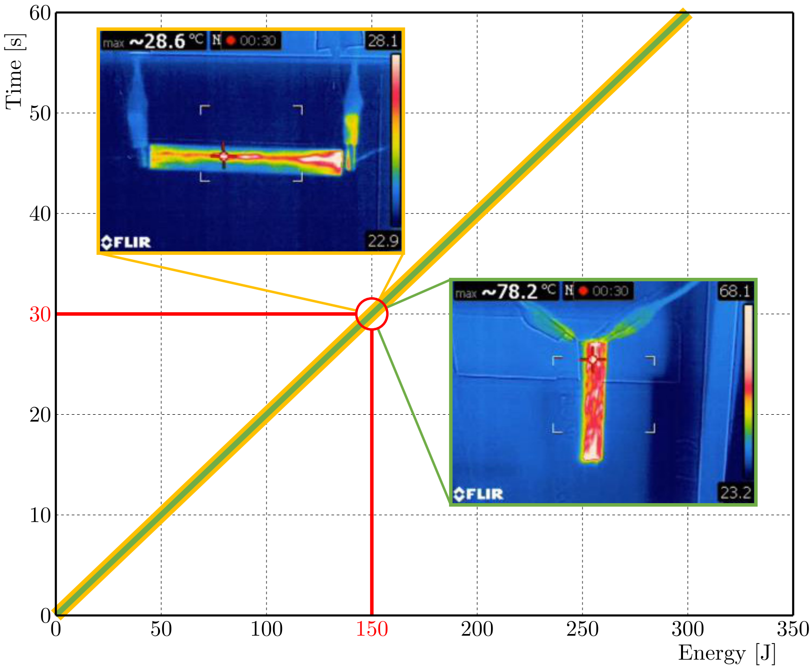

Fig. 11. Energy consumption over time for parallel and series configurations.

power directly influences the heating rate, the energy transferred increased linearly over time, reaching approximately 160 J at 30 seconds and peaking at 321 J by the end of the interval.

The inset thermal images highlight the differences in temperature distribution between the configurations. The parallel setup reached 28.6 °C, while the series configuration attained a significantly higher value 78.2 °C. In contrast, studies utilizing conductive composites typically require higher voltages, up to 60 V (Liu *et al.*, 2024) and 70 V (Liu *et al.*, 2019), due to their higher electrical resistance, which restricts current flow and reduces heating efficiency.

4. Conclusions

This study explores the shape transformation of 4D printed polylactic acid (PLA) specimens activated by thermal stimulation above the glass transition temperature (T_g) by two methods. The key findings:

1) Hot water immersion: 4D printed PLA specimens, including rectangular prism, “Flower”, and “Spiderweb” designs, exhibited shape transformation in hot water, highlighting potential applications in biomedical engineering and environmental science (Da Cunha *et al.*, 2023). Additionally, embedding copper wires in rectangular prisms can help control bending, and may mitigate the degradation of PLA’s mechanical properties over time.
2) Joule heating: Two wire configurations were tested in a rectangular prism sample: parallel, where separate wires were embedded, and series, where a single wire traversed the entire structure. A 5 A current was applied for 60 seconds, generating heat through Joule heating. The parallel configuration did not generate enough heat to induce shape transformation, as it required more time to reach the necessary temperature. Thus, this configuration may be suitable only with a reduced wire length, and so it is potentially useful for localized heating. In contrast, the series configuration produced bending similar to that observed in hot water, thus highlighting its potential for actuation applications such as gripping.

Further research should examine the mechanical properties after multiple SME cycles, test different wiring setups, and explore various wire material combinations. Additionally, localized heating using embedded wires could enable controlled shape transformation in specific areas.

Acknowledgments

The work was supported by the Learn. Inc 2021-1-RO01-KA220-HED-000031136 project.

References

1. Ansaripour, A., Heidari-Rarani, M., Mahshid, R., & Bodaghi, M. (2024). Influence of extrusion 4D printing parameters on the thermal shape-morphing behaviors of polylactic acid (PLA). *The International Journal of Advanced Manufacturing Technology*, *132*(3–4), 1827–1842. https://doi.org/10.1007/s00170-024-13470-6
2. Cadete, M.S., Gomes, T.E.P., Gonçalves, I., & Neto, V. (2025). Influence of 3D-printing deposition parameters on crystallinity and morphing properties of PLA-based materials. *Progress in Additive Manufacturing*, *10*(1), 127–137. https://doi.org/10.1007/s40964-024-00608-x
3. Crawford, C.B., & Quinn, B. (2017). *Physiochemical properties and degradation.* In Microplastic pollutants, (pp. 57–100). Elsevier. https://doi.org/10.1016/B978-0-12-809406-8.00004-9
4. Da Cunha, R.B., Pê, F.R., Agrawal, P., de Figueiredo Brito, G., & de Mélo, T.J.A. (2023). Influence of crystallization on the shape memory effect of poly (lactic acid). *Smart Materials and Structures*, *32*(8), 085016. https://doi.org/10.1088/1361-665X/ace226
5. DeStefano, V., Khan, S., & Tabada, A. (2020). Applications of PLA in modern medicine. *Engineered Regeneration*, *1*, 76–87. https://doi.org/10.1016/j.engreg.2020.08.002

6. Ehrmann, G., & Ehrmann, A. (2021). 3D printing of shape memory polymers. *Journal of Applied Polymer Science*, *138*(34), Article 50847. https://doi.org/10.1002/app.50847

7. Frunzaverde, D., Cojocaru, V., Bacescu, N., Ciubotariu, C.-R., Miclosina, C.-O., Turiac, R.R., & Marginean, G. (2023). The influence of the layer height and the filament color on the dimensional accuracy and the tensile strength of FDM-printed PLA specimens. *Polymers*, *15*(10), Article 2377. https://doi.org/10.3390/polym15102377

8. Gholizadeh Ledari, R., & Zolfaghari, A. (2025). 4D printing with the assistance of electrical stimulation on polylactic acid coated with carbon nanotubes. *Rapid Prototyping Journal*, *31*(4). https://doi.org/10.1108/RPJ-06-2024-0238

9. Hosseinzadeh, M., Ghoreishi, M., & Narooei, K. (2023). 4D printing of shape memory polylactic acid beams: An experimental investigation into FDM additive manufacturing process parameters, mathematical modeling, and optimization. *Journal of Manufacturing Processes*, *85*, 774–782. https://doi.org/10.1016/j.jmapro.2022.12.006

10. Liu, D., Zhu, L., Zhou, J., Xie, Y., Luo, X., & Evsyukov, S.A. (2024). Preparation and 3D printing parameters of thermo/electrically shape memory PLA/SEBS-g-MA/CB composites. *Polymer*, *313*, Article 127718. https://doi.org/10.1016/j.polymer.2024.127718

11. Liu, Y., Zhang, F., Leng, J., Fu, K., Lu, X.L., Wang, L., Cotton, C., Sun, B., Gu, B., & Chou, T. (2019). Remotely and sequentially controlled actuation of electroactivated carbon nanotube/shape memory polymer composites. *Advanced Materials Technologies*, *4*(12), Article 1900600. https://doi.org/10.1002/admt.201900600

12. Mehrpouya, M., Vahabi, H., Janbaz, S., Darafsheh, A., Mazur, T.R., & Ramakrishna, S. (2021). 4D printing of shape memory polylactic acid (PLA). *Polymer*, *230*, Article 124080. https://doi.org/10.1016/j.polymer.2021.124080

13. Petrașcu, R.M., Racz, S.-G., & Rusu, D.-M. (2023). Mapping smart materials' literature: An insight between 1990 and 2022. *Sustainability*, *15*(20), Article 15143. https://doi.org/10.3390/su152015143

14. Ree, B.J. (2024). Critical review and perspectives on recent progresses in 3D printing processes, materials, and applications. *Polymer*, *308*, Article 127384. https://doi.org/10.1016/j.polymer.2024.127384

15. Ren, L., Wang, Z., Ren, L., Liu, Q., Li, W., Song, Z., Li, B., Wu, Q., & Zhou, X. (2023). 4D printing of shape memory composites with remotely controllable local deformation. *Materials Today Chemistry*, *29*, Article 101470. https://doi.org/10.1016/j.mtchem.2023.101470

16. Riley, K.S., Ang, K.J., Martin, K.A., Chan, W.K., Faber, J.A., & Arrieta, A.F. (2020). Encoding multiple permanent shapes in 3D printed structures. *Materials & Design*, *194*, Article 108888. https://doi.org/10.1016/j.matdes.2020.108888

17. Shao, L.-H., Zhao, B., Zhang, Q., Xing, Y., & Zhang, K. (2020). 4D printing composite with electrically controlled local deformation. *Extreme Mechanics Letters*, *39*, Article 100793. https://doi.org/10.1016/j.eml.2020.100793

18. Tibbits, S. (2014). 4D printing: Multi-material shape change. *Architectural Design*, *84*(1), 116–121. https://doi.org/10.1002/ad.1710

19. Wang, X., Huang, L., Li, Y., Wang, Y., Lu, X., Wei, Z., Mo, Q., Zhang, S., Sheng, Y., Huang, C., Zhao, H., & Liu, Y. (2024). Research progress in polylactic acid processing for 3D printing. *Journal of Manufacturing Processes*, *112*, 161–178. https://doi.org/10.1016/j.jmapro.2024.01.038

20. Wang, Y., Desroches, G.J., & Macfarlane, R.J. (2021). Ordered polymer composite materials: challenges and opportunities. *Nanoscale*, *13*(2), 426–443. https://doi.org/10.1039/D0NR07547G

21. Wang, Y., & Li, X. (2020). An accurate finite element approach for programming 4D-printed self-morphing structures produced by fused deposition modeling. *Mechanics of Materials*, *151*, Article 103628. https://doi.org/10.1016/j.mechmat.2020.103628

22. Wu, P., Yu, T., Chen, M., & Hui, D. (2022). Effect of printing speed and part geometry on the self-deformation behaviors of 4D printed shape memory PLA using FDM. *Journal of Manufacturing Processes*, *84*, 1507–1518. https://doi.org/10.1016/j.jmapro.2022.11.007

23. Yousefi, M.A., Rahmatabadi, D., Baniassadi, M., Bodaghi, M., & Baghani, M. (2024). 4D printing of multifunctional and biodegradable PLA-PBAT-Fe_3O_4 nanocomposites with supreme mechanical and shape memory properties. *Macromolecular Rapid Communications*, *46*(2), Article 2400661. https://doi.org/10.1002/marc.202400661
24. Zhang, X.-J., Yang, Q.-S., Liu, X., Shang, J.-J., & Leng, J.-S. (2020). Atomistic investigation of the shape-memory effect of amorphous poly(*L*-lactide) with different molecular weights. *Smart Materials and Structures*, *29*(1), Article 015040. https://doi.org/10.1088/1361-665X/ab471c
25. Zhu, J., Abeykoon, C., & Karim, N. (2021). Investigation into the effects of fillers in polymer processing. *International Journal of Lightweight Materials and Manufacture*, *4*(3), 370–382. https://doi.org/10.1016/j.ijlmm.2021.04.003

Manuscript received December 5, 2024; accepted for publication February 24, 2025;
published online May 14, 2025.

JOURNAL OF THEORETICAL
AND APPLIED MECHANICS
63, 3, pp. 535–543, Warsaw 2025
https://doi.org/10.15632/jtam-pl/202686

RESPONSE OF SANDWICH STRUCTURES WITH NOVEL TPMS CORES UNDER CYCLIC UNIAXIAL COMPRESSION

Alexandru VASILE[1,2*], Iulian Constantin COROPEŢCHI[1,2], Andrei Ioan INDREŞ[1],
Dan Mihai CONSTANTINESCU[2,3], Ştefan SOROHAN[2], Dragoş Alexandru APOSTOL[2]

[1] *Faculty of Aircraft and Military Vehicles, Military Technical Academy "Ferdinand I", Bucharest, Romania*
[2] *Department of Strength of Materials, National University for Science and Technology POLITEHNICA Bucharest, Bucharest, Romania*
[3] *Institute of Solid Mechanics of the Romanian Academy, Bucharest, Romania*
*corresponding author, *alexandru.vasile@mta.ro*

This paper focuses on the compressive behavior of nine triply periodic minimal surface (TPMS) structures and one stochastic geometry, designed through an implicit modeling approach and fabricated using a stereolithography (SLA) technique. The compressive response is analyzed, with two topologies outperforming the well-known gyroid, in terms of rigidity and yield strength. Low cyclic testing at two strain levels highlights the good repeatability and stability of the proposed topologies, while comparing the specimens from an energy absorption performance and residual deformation perspective. The stochastic geometry exhibited the worst recovery rates, even though it had the second-best energy absorption capabilities for the single compression testing.

Keywords: TPMS; implicit modeling; sandwich structures; cyclic compression.

1. Introduction

Current literature provides many valuable observations regarding general mechanical properties, failure modes and possible applications of sandwich structures with metamaterial cores. From constant cross-sectional structures such as honeycombs or chiral topologies, to complex three-dimensional geometries such as cores based on interconnected ligaments, foams or foldable walls, all have been extensively studied and implemented in practical applications. However, with the advancements in additive manufacturing technologies, very complex topologies can now be generated and analyzed with methods involving an automated approach. A more detailed classification of existing types of sandwich structures with metamaterial cores is presented in (Feng *et al.*, 2020; Lu *et al.*, 2022; Yu *et al.*, 2018).

Recent studies have shown a growing interest in exploring thin-walled structures based on TPMS, particularly those produced using additive manufacturing techniques. Findings suggest that these structures outperform traditional topologies in terms of rigidity, compressive strength, energy absorption capabilities and mechanical behavior predictability (Al-Ketan *et al.*, 2019; Araya *et al.*, 2024). These characteristics make TPMS-based geometries particularly appealing for advanced engineering applications, including aerospace, automotive, and biomedical fields (Cresswell *et al.*, 2024; Gabrieli *et al.*, 2024). Their mathematically defined periodicity allows

---

Ministry of Science and Higher Education
Republic of Poland

The publication has been funded by the Polish Ministry of Science and Higher Education under the Excellent Science II programme "Support for scientific conferences".
The content of this article was presented during the 40th Danubia-Adria Symposium on Advances in Experimental Mechanics, Gdańsk, Poland, September 24–27, 2024.

for precise tailoring of mechanical properties, while advancements in additive manufacturing technologies have facilitated the fabrication of these complex geometries, opening new possibilities for optimizing material efficiency and structural resilience. Understanding and further developing TPMS structures is, therefore, critical for advancing next-generation materials and structural solutions.

Comprehensive investigations into the mechanical properties of commonly used TPMS structures, as highlighted by Gao *et al.* (2024), Ronca *et al.* (2019), Wei *et al.* (2024), Yang *et al.* (2023), offer valuable insights into the different domains where such topologies can be used. Adjusting the dimensions and orientation of the representative cell or employing a gradient-based design approach are methods for customizing the mechanical response of TPMS structures, including their energy absorption capacity and overall stability. Key articles that provide insights into how modifications to the fundamental geometry influence the mechanical properties include: Novak *et al.* (2022), Ramírez *et al.* (2024), Song *et al.* (2024), Viet *et al.* (2023).

Research on TPMS structures has largely focused on analyzing the properties and performance of predefined geometries, with little interest directed towards developing new types of topologies. Thus, this paper aims to present the compression behavior of sandwich structures with novel metamaterial cores, while understanding their mechanical properties, deformation mechanisms and energy absorption capabilities through low cyclic compressive testing.

2. Sample definition and fabrication

This study focuses on analyzing the behavior of ten types of sandwich structures. The first sample, the well-known gyroid, described initially by Schoen (1970), serves as a benchmark topology frequently encountered in relevant literature. Alongside it, nine additional geometries were proposed. The first eight are novel TPMS type topologies, based on continuous, self-supporting and non-intersecting surfaces. These are described by the equations presented by Vasile *et al.* (2024). The formulas are heuristically determined in order to obtain structures that do not need internal supports, allowing for scalability of the topology and avoiding the generation of enclosed chambers, which would be filled with resin or powder during the manufacturing process and modify the final characteristics of the geometry. At the same time, the functions were chosen in order to cover a broad range of topology types, that are currently being researched: bi-cameral geometries (S1, S3, S8), re-entrant type 3D structures (S2), designs with wall thickness gradient (S5), small feature topologies (S6), lattice 3D arrangements (S7), geometries with layers at an angle (S4, S9), foam-like structures (S10). Sample 10 is stochastically determined, with struts conditioned to align with the z-direction, defined as perpendicular to the two sandwich sheets, with an average distance between the ligaments of 3.5 mm and with an average number of ligaments intersecting at the same point being 6.

All the topologies were generated through an implicit approach method, using the *nTopology software* to generate thin-shelled cells. Each representative volume element was defined as a cube with 10 mm sides, which was multiplied to generate the metamaterial core. It incorporated $3 \times 3 \times 3$ such unit cells, to form a cube with 30 mm sides, which was placed between two 3 mm sheets as to obtain the final sandwich geometry. The cell wall thickness was adjusted to maintain a constant relative density of 0.3 across all the proposed samples.

All specimens were fabricated from the same material, in the form of a photosensitive polymer resin, Tough 1500v1, using a Formlabs Form L stereolithography printer, with a layer thickness of 50 µm. The post-cured average mechanical properties established by us through tensile testing are: ultimate tensile strength – 34.47 MPa, tensile Young's modulus – 1.29 GPa, and elongation at break – 26 %. Post-processing of the samples was performed using an automated washing and curing station. Details on the fabrication technique and geometry analysis of the samples are presented in (Vasile *et al.*, 2024). Figure 1 displays the printed samples after post-processing and removal of lateral supports.

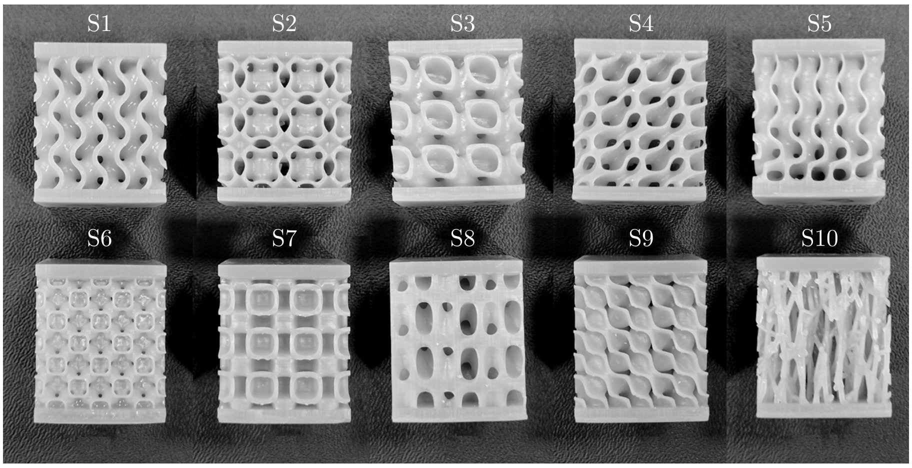

Fig. 1. Ten topologies of printed samples.

3. Low cyclic compression testing

First, quasi-static uniaxial compression tests were carried out on the architected samples, according to the ASTM D695 standard. Figure 2a highlights the compressive force as a function of deformation for the proposed structures. The tests are presented in detail in (Vasile *et al.*, 2024).

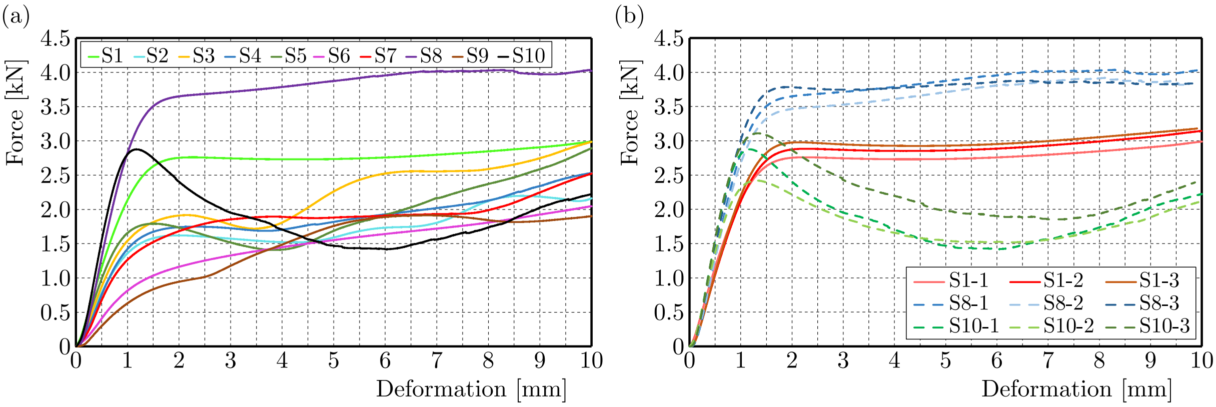

Fig. 2. (a) Variation of compressive force as a function of deformation for the proposed structures; (b) compressive force as a function of deformation for three tests carried out under identical conditions for S1, S8 and S10.

While most samples provided a similar response in terms of loading force, S1, S8 and S10 stand out as outliers. S10 the stochastic structure, proved to be the geometry with the greatest stiffness, exhibiting a higher yield force than the gyroid, but presenting an intense softening effect in the plastic region, due to fracture of the struts. This, in turn, greatly affects the energy absorption capabilities of the structure. Topology S8 exhibited a similar behavior to the gyroid, with values corresponding to the yield point up to 31 % higher than the gyroid counterpart. However, unlike the gyroid, it exhibited internal cracks at high deformations of approximately 23 % strain. These were observed in the outer surfaces of the specimen, but did not lead to premature generalized failure and are a result of the generated thin walls when confining the topology to a 30 mm cube domain.

In order to validate the repeatability of the results obtained experimentally, subsequent tests were carried out on the same type of specimens. Both the manufacturing and testing methods were maintained constant. Figure 2b shows the plots of the loading force versus the deformation for three tests for three of the proposed topologies. A similar behavior is observed in the elastic region, with limited variation in the plastic zone, the largest deviations occurring for the stochastic sample (S10), where the nature of the geometry generates lower repeatability. During S8 testing, the same fractures of the outer walls were visible. However, during the three tests, a maximum positive variation of up to 9 % in the force corresponding to yielding was observed, compared to the gyroid (S1) which had a maximum variation of only 7 %. This variation was attributed to insufficiently rigorous control following the printing procedure and during the sample washing and treatment processes.

Cyclic uniaxial compression tests were performed to evaluate the energy absorption capacity and recoverability of the proposed samples. Two complementary scenarios of loading and unloading cycles were considered, using the same testing set-up, at a speed of 1 mm/min.

In order to capture the behavior in the elastic region, the first scenario tested the samples for 100 cycles, up to a deformation of 0.15 mm (0.5 % strain) from the initial undeformed configuration. After the testing was concluded, another cycle was conducted after one hour, in order to study the recoverability of the specimens.

Figure 3a displays the compressive force as a function of deformation, for all 10 samples, for the 1st (C1), the 100th (C100), and the 101st (C101) cycles of loading-unloading. This additional cycle was captured, as already mentioned, one hour after the first 100 were finished, in order to observe the recovery rate of the specimens. The scale has been maintained constant in order to facilitate easier comparison between the samples. It can be seen that the evolutions are in accordance with the results shown in Fig. 2a, with the unloading curves following a different path, leading to hysteresis loops. These loops illustrate energy dissipation within the material, caused by internal mechanisms such as atomic rearrangements and nonlinear effects. Also, all the samples show a residual strain at the end of the cycle, which is due to the fact that the recovery rate is lower than the 1 mm/min speed used for tensile testing. The S10 stochastic structure shows the highest hysteresis loop area during the first cycle, pointing to a better energy absorption capability, while the structure S8 displays the highest stiffness.

It is noticeable that even though the loops continuously move towards lower values for loading force and higher residual strain, the behavior is stable, with both the loading and unloading cycles following similar patterns. The red curves which capture the additional cycle, overlap the first cycle in almost all the specimens, showing that all the TPMS have good recovery capabilities. An offset is visible in the case of S10, which means that the geometry did not fully return to the initial dimensions during the one-hour interval considered for recovery. This proves that the TPMS geometries exhibit better elastic recovery than the stochastic one, when subsequent tests are performed.

When comparing the residual deformation during the first 100 cycles, as shown in Fig. 3b, S8 proves to be the stiffest, with the lowest values of residual deformation, while S9 ranks first and the gyroid occupies the 4th position. This highlights how fast the force-deformation loops decrease in value, with S8 maintaining higher performance over a greater number of cycles.

Figure 3c shows the total amount of energy absorbed during loading for all the 100 cycles, along with the quantity of this energy that is dissipated through the hysteresis. On average, the hysteresis accounts for approximately 22 % of the loading energy, with S8 being an outlier, as only 18 % of its energy is dissipated internally due to its lower residual deformation values. It can be noticed that the stochastic topology S10 outranks the gyroid S1 in terms of energy absorption. Additionally, as an interesting observation, the S5 topology, which was designed with a wall thickness gradient along the axis of deformation (thickness being increased towards the bottom of the specimen), demonstrates very good energy absorption capabilities compared to the other specimens tested.

Figure 4a displays the energy absorption capabilities for the specimens during the 100 cycles considered. While all the samples show a descending trend, toward a value where the damage behavior stabilizes, it is clear that S10 (light-grey curve) has a slightly higher descending slope during the first cycles. The values are also in accordance with the variations displayed in Fig. 2a.

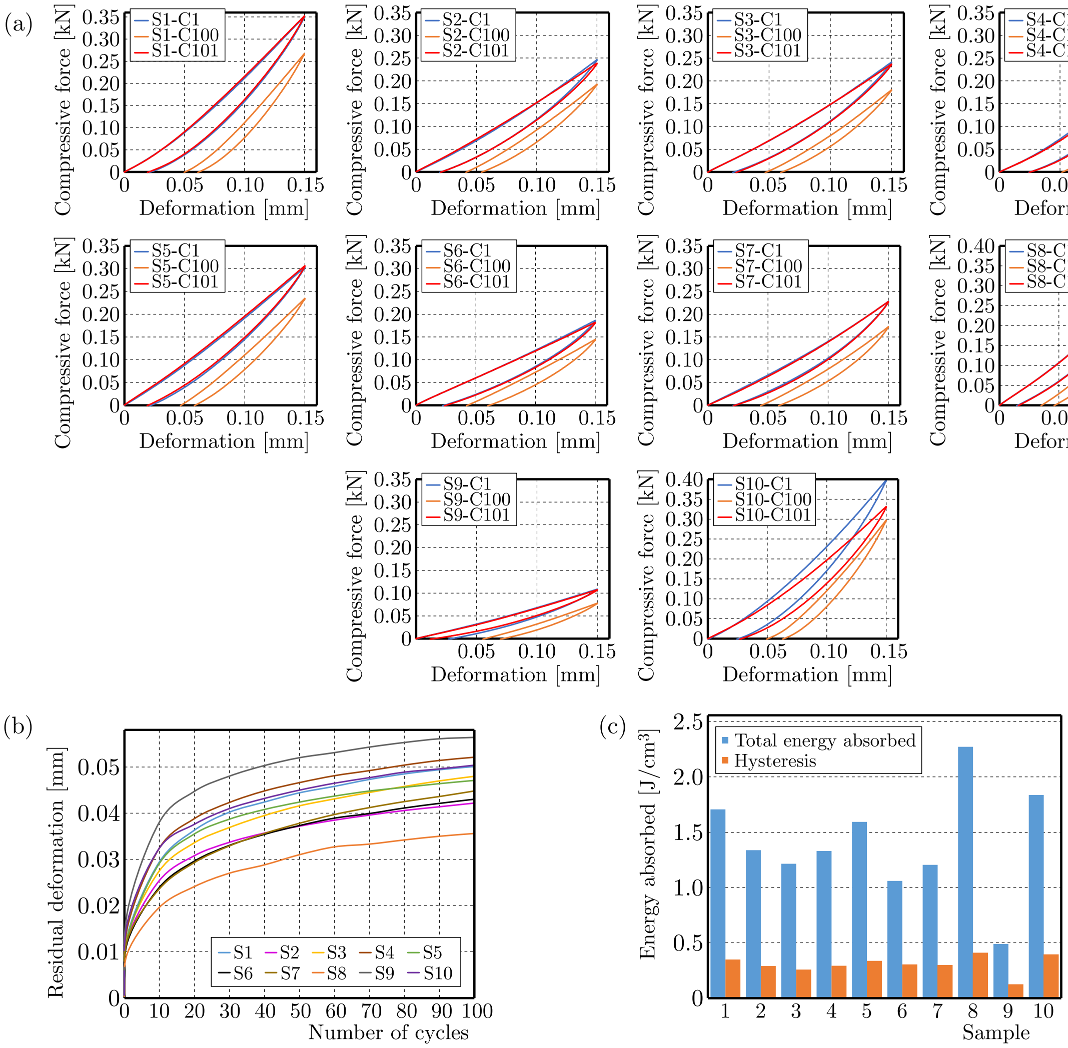

Fig. 3. (a) Cyclic compression results showing compressive force vs deformation plots for the 1st cycle (blue), the 100th cycle (orange) and an additional cycle after one hour of recovery time (red) for all topologies; (b) residual deformation accumulation during 100 cycles; (c) total energy absorbed and hysteresis for each topology during loading.

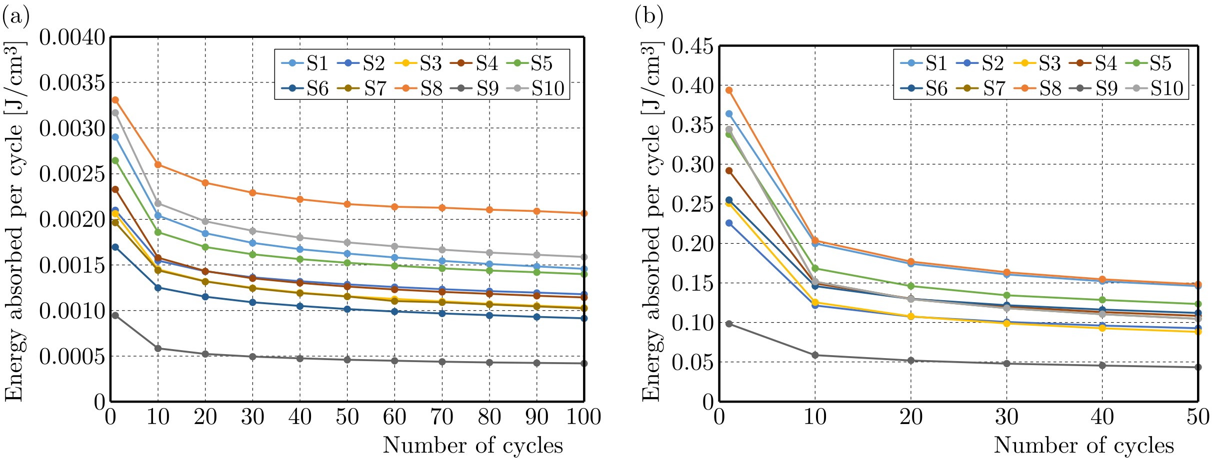

Fig. 4. Energy absorption variation during: (a) 100 cycles at 0.5 % strain; (b) 50 cycles at 5 % strain.

The second scenario presents the response of the samples over 50 cycles, up to a deformation of 1.5 mm (5 % strain), in order to capture the yielding and part of the plastic region.

To assess residual strain, two additional tests were conducted: one after one hour and one after 12 hours, to better understand the recovery behavior over time. Figure 5a displays the 1st (C1), the 50th (C50) cycle, and the two additional cycles for each sample. It can be noticed that the area of the hysteresis loop increases compared to the first scenario due to material loading in the plastic region, revealing higher plastic deformation. The decrease in force values with the number of performed cycles is also evident.

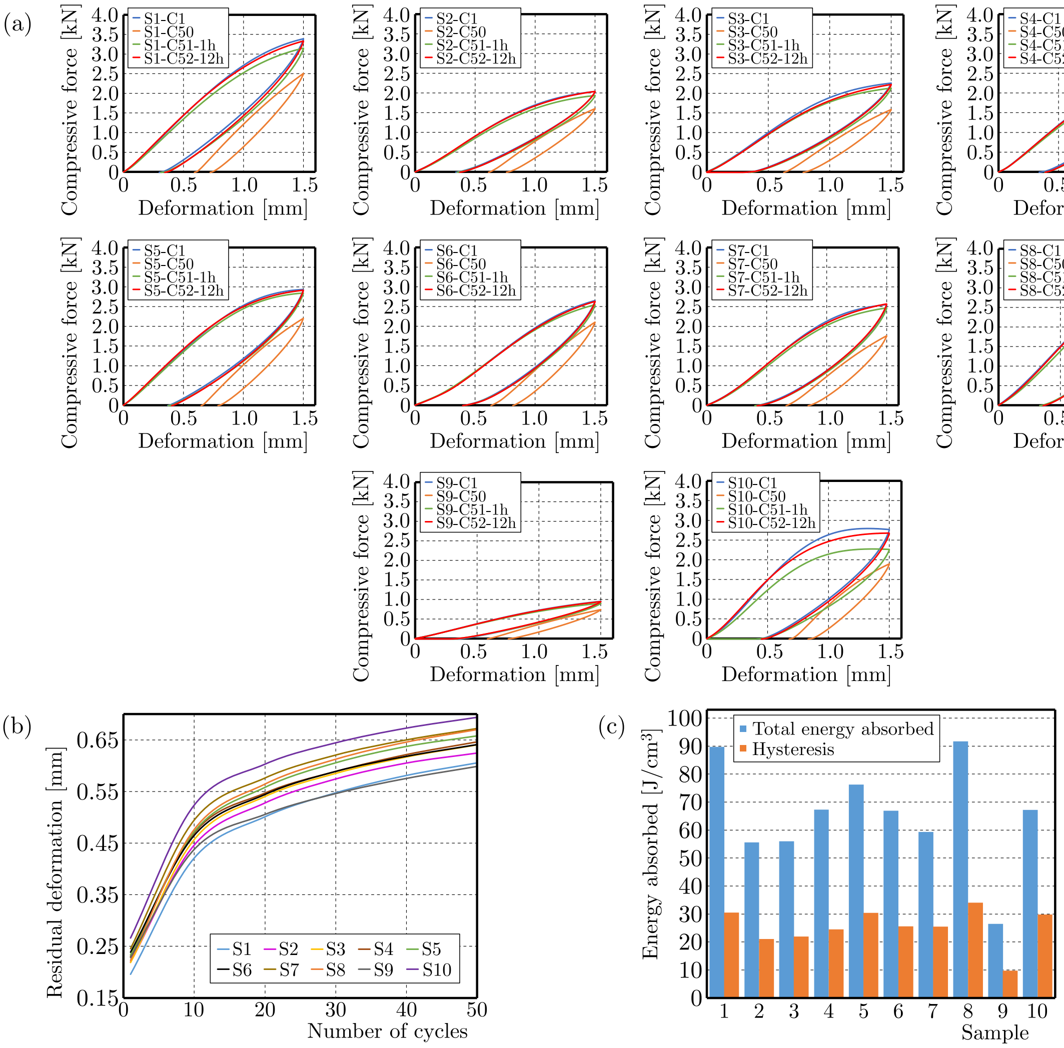

Fig. 5. (a) Cyclic compression results showing compressive force vs deformation plots for the 1st cycle (blue), the 50th cycle (orange) and two additional cycles after one hour of recovery time (green) and 12 h recovery time (red) for all topologies; (b) residual deformation accumulation during 50 cycles; (c) total energy absorbed and hysteresis for each sample during loading.

The green curve, representing the additional cycle performed after one hour (C51-1h), shows a lower compressive force, as the samples had not fully recovered to their initial shape. After 12 hours, however, most of the samples display similar evolutions to the first loading-unloading test, some even having slightly better performances. S6 demonstrates the smallest variation in performance among the 1st, the 51st (after 1 h), and the 52nd cycle (after 12 h) and the highest recovery rate, due to the geometry being architected from more cells of thinner walls that relax simultaneously. S10 exhibits the highest difference in recovery rates. A noticeable difference exists between the initial cycle and the force-deformation plot corresponding to the 51st cycle (C51-1h in Fig. 5). Even after 12 hours, the topology did not fully recover, given the fact that the red curve for the 52nd cycle (C52-12h) and the blue curve for the 1st cycle (C1) do not fully overlap. This shows that the continuous nature of the TPMS geometries provides better performances in terms of sample recovery and reusability.

Figure 5b shows that the stochastic geometry exhibits the highest value of residual deformation, followed by S7 and S8. Given the change of slope after the elastic region, most of the samples change their order compared to the first scenario. For example, the gyroid has a high level of residual deformation during the first scenario, but the rate at which it is accumulated decreases, so that during the second scenario it reaches the second-best position in terms of rigidity. However, this is not the case for S8, which accumulates strain with the fastest rate, changing from being the most rigid sample during the first scenario to the third-worst during the first 10 cycles of the second one.

Figure 5c displays the energy absorption capacity for each sample over 50 loading and unloading cycles, as well as the portion dissipated as hysteresis. It can be noticed that S8 maintains the best performance, while S10, which ranked second during the first scenario, dropped to the 5th place. This decline is attributed to the buckling of the struts, which causes premature softening and lower overall performance when more cycles are considered. Conversely, S6 exhibits improved performance, ranking 6th from the initial 9th position due to its lower residual strain accumulation. However, apart from S10 and S6, the ranking does not change, demonstrating the stability of the manufacturing process, material and topology response.

It can be noticed in Fig. 4b that the energy absorption capabilities exhibit a trend similar to that observed in the first scenario, where the damage behavior saturates after the first cycles. Here, however, the S10 sample does not rank so high, dropping from 3rd place to 6th place after the first 10 cycles. Also, S8 displays a steeper descending slope during the first 10 cycles, which coincides with the region where the sample accumulates the highest value of residual deformation. Beyond this region, the behavior stabilizes and the results are similar to the gyroid.

4. Conclusions

An implicit modeling approach was used to generate eight novel TPMS structures and one stochastic geometry, whose compressive behaviors were compared to the existing gyroid topology. Multiple samples were fabricated from a photo-polymeric resin, using an SLA technique.

Compressive testing revealed that topology S8 provided the best results in terms of yield strength and energy absorption capabilities, while displaying a deformation type very similar to the gyroid. Its yield strength values were up to 31 % higher than those of the gyroid, which ranked 3rd after the stochastic geometry. This topology, notated S10, demonstrated superior stiffness in the elastic deformation zone and approximately 6 % higher yield strength than the gyroid counterpart.

All the samples were tested following two scenarios: the first involved 100 cycles of loading and unloading up to 0.5 % strain at a speed of 1.5 mm/min, followed by one cycle after one hour of recovery. The second scenario consisted of 50 cycles at 5 % strain under the same loading speed, followed by two additional cycles after one hour and another after 12 hours of recovery. As expected, the hysteresis loops increased at higher strain values. During cyclic testing, these loops decreased in area, stabilizing at approximately 75 % of the loading force recorded during the first cycle. Topology S10 exhibited a different deformation mechanism due to the local buckling of the struts, which is also visible in the percentage of energy dissipated through hysteresis, only 44.4 % of the total energy being absorbed. In comparison, S8 registered a hysteresis dissipation percentage of 37 %, while the gyroid only 34.1 %.

From an energy absorption perspective, all the samples displayed a descendent trend that saturated after several cycles. Topology S8 showed the best results during both scenarios. However, the gyroid had a lower residual deformation at higher strain levels, leading to a more stable deformation over time, which improved the energy absorption capabilities when multiple cycles were considered. Overall, both S8 and the gyroid S1 displayed similar energy absorption capabilities after the first 10 cycles, when S8's behavior began to stabilize. The stochastic topology S10 demonstrated the second-best energy absorption capabilities for one-time compression or cyclic testing at low strain levels but ranked 6th during the second scenario due to the high residual strain and low recovery rate.

After the first 100 cycles at 0.5 % strain, the additional cycle performed after a recovery time of one hour showed a nearly identical behavior to the first loading cycle. The only outlier was the stochastic geometry which had a lower recovery rate than the TPMS specimens. Following the 50 cycles at 5 % strain, the samples recovered to approximately 95 % of the initial loading force after a one-hour recovery period and fully recovered after 12 hours. However, the stochastic topology recovered only 81 % of the initial loading force after one hour and 96 % after 12 hours.

Analyzing the results from all the cyclic tests performed, it was generally proven that TPMS topologies possess excellent loading-unloading repeatability, displaying a foam-type elastic behavior with a high recovery rate. Low cyclic compressive testing highlighted that the proposed TPMS topologies have a behavior showing high stability, and indicating their potential application as shock dampers and cushioning components.

Acknowledgments

Alexandru Vasile acknowledges the grant awarded by the Ministry of Education from Romania for completing his PhD studies under contract no. 06.87/05.10.2020.

References

1. Al-Ketan, O., Rowshan, R., Palazotto, A.N., & Abu Al-Rub, R.K. (2019). On mechanical properties of cellular steel solids with shell-like periodic architectures fabricated by selective laser sintering. *Journal of Engineering Materials and Technology*, *141*(2), Article 021009. https://doi.org/10.1115/1.4041874

2. Araya, M., Jaskari, M., Rautio, T., Guillén, T., & Järvenpää, A. (2024). Assessing the compressive and tensile properties of TPMS-Gyroid and stochastic Ti64 lattice structures: A study on laser powder bed fusion manufacturing for biomedical implants. *Journal of Science: Advanced Materials and Devices*, *9*(1), Article 100663. https://doi.org/10.1016/J.JSAMD.2023.100663

3. Cresswell, N.D., Ameri, A.A.H., Wang, J., Wang, H., Hazell, P., & Escobedo-Diaz, J.P. (2024). Characterization and modelling of triply periodic minimum surface (TPMS) lattice structures for energy absorption in automotive applications. In Z. Peng, *et al.* (Eds.), *Characterization of Minerals, Metals, and Materials 2024. TMS 2024. The Minerals, Metals & Materials Series* (pp. 295–305). Cham, Switzerland: Springer. https://doi.org/10.1007/978-3-031-50304-7_28

4. Feng, Y., Qiu, H., Gao, Y., Zheng, H., & Tan, J. (2020). Creative design for sandwich structures: A review. *International Journal of Advanced Robotic Systems*, *17*(3). https://doi.org/10.1177/1729881420921327

5. Gabrieli, R., Wenger, R., Mazza, M., Verné, E., & Baino, F. (2024). Design, stereolithographic 3D printing, and characterization of TPMS scaffolds. *Materials*, *17*(3), Article 654. https://doi.org/10.3390/MA17030654

6. Gao, T., Liu, K., Wang, X., Wei, K., & Wang, Z. (2024). Multi-level mechanism of biomimetic TPMS hybridizations with tailorable global homogeneity and heterogeneity. *Extreme Mechanics Letters*, *68*, Article 102136. https://doi.org/10.1016/J.EML.2024.102136

7. Lu, C., Hsieh, M., Huang, Z., Zhang, C., Lin, Y., Shen, Q., Chen, F., & Zhang, L. (2022). Architectural design and additive manufacturing of mechanical metamaterials: A review. *Engineering*, *17*, 44–63. https://doi.org/10.1016/J.ENG.2021.12.023

8. Novak, N., Borovinšek, M., Al-Ketan, O., Ren, Z., & Vesenjak, M. (2022). Impact and blast resistance of uniform and graded sandwich panels with TPMS cellular structures. *Composite Structures*, *300*, Article 116174. https://doi.org/10.1016/J.COMPSTRUCT.2022.116174

9. Ramírez, E.A., Béraud, N., Pourroy, F., Villeneuve, F., Amaya, J.L., & Museau, M. (2024). Design methodology of functionally graded cellular materials: Manipulating design parameters of triply periodic minimal surfaces through three-dimensional density distributions. *Computer-Aided Design*, *177*, Article 103778. https://doi.org/10.1016/J.CAD.2024.103778

10. Ronca, A., Rollo, G., Cerruti, P., Fei, G., Gan, X., Buonocore, G.G., Lavorgna, M., Xia, H., Silvestre, C., & Ambrosio, L. (2019). Selective laser sintering fabricated thermoplastic polyurethane/graphene cellular structures with tailorable properties and high strain sensitivity. *Applied Sciences*, *9*(5), Article 864. https://doi.org/10.3390/APP9050864

11. Schoen, A.H. (1970). Infinite periodic minimal surfaces without self-intersections. NASA Technical Note D-5541, Washington, D.C.: National Aeronautics and Space Administration.

12. Song, J., Wang, M., Li, D., & Zhang, J. (2024). Deformation and energy absorption performance of functionally graded TPMS structures fabricated by selective laser melting. *Applied Sciences*, *14*(5), Article 2064. https://doi.org/10.3390/APP14052064

13. Vasile, A., Constantinescu, D.M., Coropeţchi, I.C., Sorohan, Ş., & Apostol, D.A. (2024). Definition, fabrication, and compression testing of sandwich structures with novel TPMS-based cores. *Materials*, *17*(21), Article 5150. https://doi.org/10.3390/MA17215150

14. Viet, N.V., Waheed, W., Alazzam, A., & Zaki, W. (2023). Effective compressive behavior of functionally graded TPMS titanium implants with ingrown cortical or trabecular bone. *Composite Structures*, *303*, Article 116288. https://doi.org/10.1016/J.COMPSTRUCT.2022.116288

15. Wei, Y.P., Li, H.Q., Han, J.J., Ma, Y.C., Zhou, H.R., Cheng, J.C., Shi, J., Miao, Z.Q., Yu, B., & Lin, F. (2024). Mechanical and damping performances of TPMS lattice metamaterials fabricated by laser powder bed fusion. *China Foundry*, *21*(4), 327–333. https://doi.org/10.1007/S41230-024-4026-5

16. Yang, C., Wu, W., Fu, Z., & Zheng, H. (2023). Preparation and thermal insulation properties of TPMS 3Y-TZP ceramics using DLP 3D printing technology. *Journal of Material Science*, *58*(29), 11992–12007. https://doi.org/10.1007/S10853-023-08749-0

17. Yu, X., Zhou, J., Liang, H., Jiang, Z., & Wu, L. (2018). Mechanical metamaterials associated with stiffness, rigidity and compressibility: A brief review. *Progress in Materials Science*, *94*, 114–173. https://doi.org/10.1016/J.PMATSCI.2017.12.003

Manuscript received November 17, 2024; accepted for publication March 6, 2025;

JOURNAL OF THEORETICAL
AND APPLIED MECHANICS
63, 3, pp. 545–550, Warsaw 2025
https://doi.org/10.15632/jtam-pl/202689

COMPARISON OF FATIGUE RESISTANCE OF DOG-BONE AND HOURGLASS-SHAPED HARDOX 450 STEEL SPECIMENS

Denisa STRAKOVÁ*, František NOVÝ, Lukáš ŠIKYŇA, Miroslav NESLUŠAN

Faculty of Mechanical Engineering, University of Žilina, Žilina, Slovak Republic
*corresponding author, *denisa.strakova@uniza.sk*

This study compares the fatigue resistance of two standardized specimen geometries – dog-bone and hourglass-shaped – made from Hardox 450 high-strength steel. Rotating bending fatigue tests evaluated differences in fatigue durability. Strain gauge measurements and the FEM analysis showed hourglass specimens had more uniform stress distribution and lower concentration effects. Fatigue tests revealed an 8 % higher fatigue limit for the hourglass specimens, probably due to the lack of localized stress concentration at the transition between the radius and the cylindrical section. These findings contribute to understanding how standardized specimen geometries influence fatigue performance.

Keywords: fatigue testing; geometry; Hardox 450.

1. Introduction

High-strength steels play a critical role in industries such as construction, automotive, and aerospace, where their ability to withstand cyclic loading is essential for ensuring the long-term reliability and safety of structural components. Fatigue resistance, a key material property, directly impacts the performance and durability of components subjected to repeated loading. Among the many factors influencing fatigue performance, the geometry of the specimen plays a significant role in stress distribution and in the way cracks initiate and propagate during loading cycles. Understanding how different geometries affect fatigue behaviour is therefore crucial for optimizing the design and reliability of components (Chaurasiya *et al.*, 2023; Okuda *et al.*, 2019).

The shape and size of fatigue test specimens, such as dog-bone and hourglass geometries, can lead to variations in stress concentrations and gradients under cyclic loading. These differences can significantly influence the material's fatigue life and its susceptibility to crack propagation, which are of key importance to an engineering design. Fatigue testing provides valuable data on how materials perform under these conditions, but reliable testing methods are necessary to capture a comprehensive understanding of fatigue behaviour across a range of stress levels (Pan *et al.*, 2024; Hultgren & Barsoum, 2020).

This study aims to explore how the geometry of high-strength steel fatigue test specimens influences their ability to endure cyclic loading. By investigating the effects of specimen shape on stress distribution and fatigue life, this research aims to provide information to help design

---

Ministry of Science and Higher Education
Republic of Poland

The publication has been funded by the Polish Ministry of Science and Higher Education under the Excellent Science II programme "Support for scientific conferences".
The content of this article was presented during the 40th Danubia-Adria Symposium on Advances in Experimental Mechanics, Gdańsk, Poland, September 24–27, 2024.

more durable and efficient components. Accurate fatigue data is essential for guiding the material selection and component design, ensuring that structural elements perform optimally in demanding applications (McClung, 1994; Hehenberger & Nilsson, 1982).

2. Experimental material and methods

This study investigates the impact of specimen geometry on the fatigue resistance of Hardox 450 high-strength structural steel, whose chemical composition and mechanical properties are given in Table 1.

Table 1. Chemical composition and mechanical properties of Hardox 450 high-strength steel.

C [wt.%]	Si [wt.%]	Mn [wt.%]	Cr [wt.%]	Mo [wt.%]	Nb [wt.%]	B [wt.%]	E [GPa]	$R_{p0.2}$ [MPa]	R_m [MPa]	A [%]	KV_{-40} [J]	HB
0.2	0.39	0.8	0.45	0.01	0.05	0.001	210	1200	1400	10	40	420–475

The samples were fabricated from a 20 mm thick steel sheet via machining. The gauge sections were ground to a surface roughness of $R_a = 0.05\,\mu\text{m}$, followed by polishing to achieve a mirror-like finish, ensuring optimal surface quality for subsequent analysis. The surface stresses of hourglass-shaped and dog-bone-shaped test bars (Fig. 1) were analysed using a strain gauge (HBM 1-LY11-1.5/120). Critical radius tolerances were maintained within ±0.02 mm to ensure accurate stress distribution. The strain gauge was positioned at the central part of the gauge length on the opposite side of the applied bending moment. The test bars were subjected to a gradually increasing bending moment, starting from an initial value of $M_o = 2451.7$ Nmm and progressing incrementally up to a maximum of 26968.2 Nmm. The strain gauge detected the strain change, and the stress on the test bars' surface was calculated using DASYLab software. ANSYS Workbench software was used to create the finite element method (FEM) model of the test bars, set the boundary conditions, and carry out the meshing process. Rotating bending fatigue tests were conducted using a Rotoflex machine on two types of test bars: dog-bone and hourglass-shaped. The tests were performed at a loading frequency of $f = 30$ Hz.

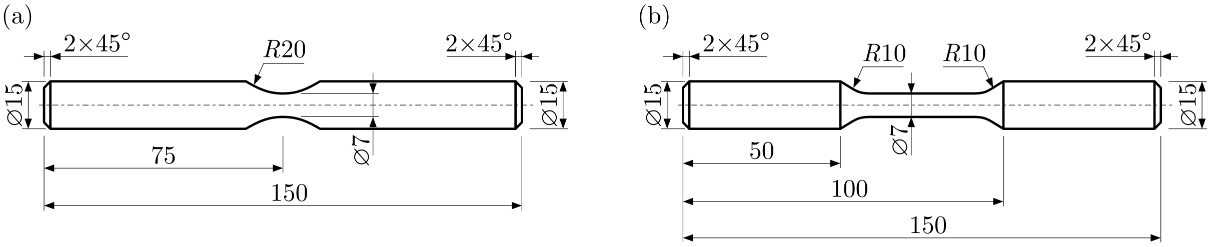

Fig. 1. Fatigue test bars with different geometry: (a) hourglass test bar; (b) dog-bone test bar.

3. Results

The FEM analysis identified the maximum stress concentration ($\sigma_{\max}$) of 76.3 MPa in the central area of the hourglass-shaped fatigue test bar under a bending load (M_o) of 2451.7 Nmm. The nominal stress at this bending moment was calculated to be 72.8 MPa allowing to calculate the stress concentration at the critical location, $K_t = 1.05$. In the FEM simulation of a dog-bone-shaped fatigue test bar under the same bending load (Fig. 2), the maximum stress of $\sigma_{\max} = 76.9$ MPa was found in the transition radius area. The stress concentration at this point is a little higher, $K_t = 1.06$.

Figure 3 compares stress changes in the gauge length of fatigue test bars. The stress changes were obtained by the strain gauge measurement (shown in blue) and by FEM analysis (shown

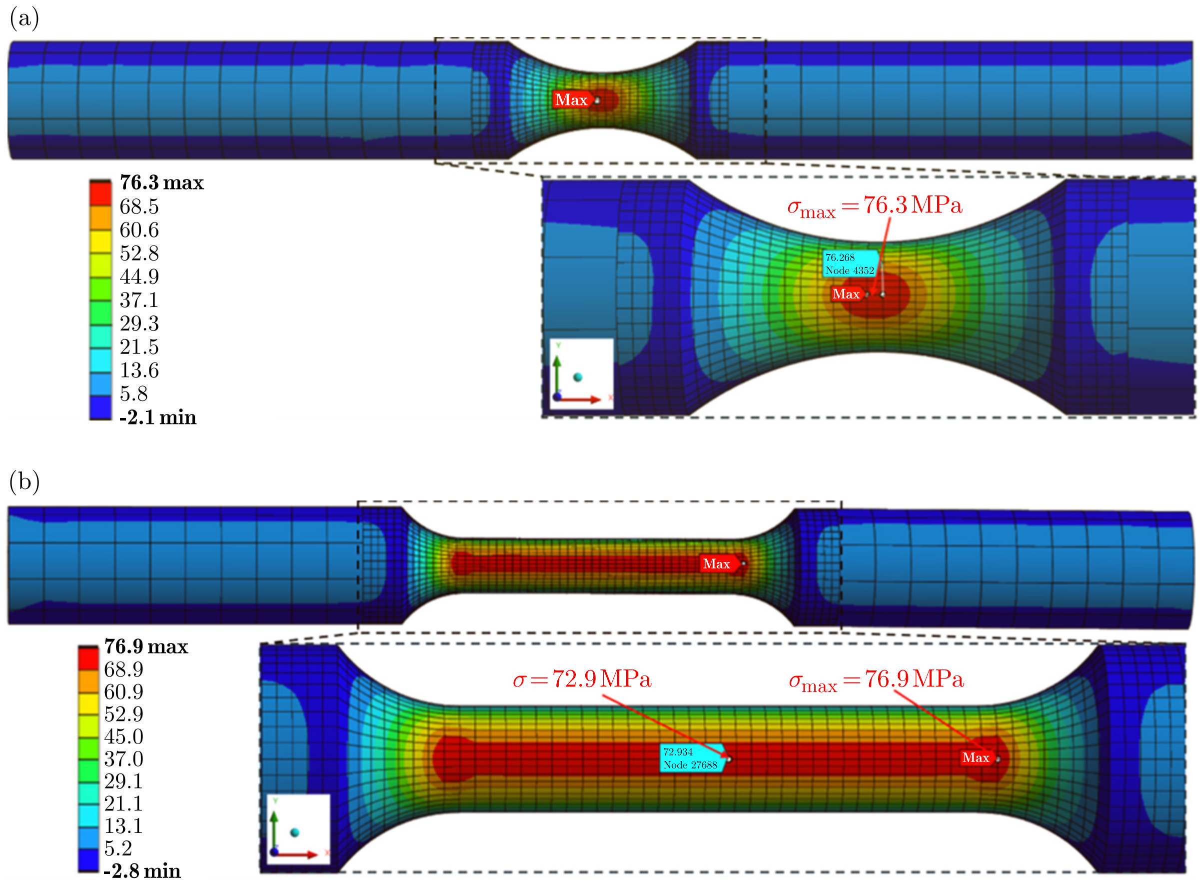

Fig. 2. Stress distribution and maximum concentration on the surface of fatigue test bars with different geometry.

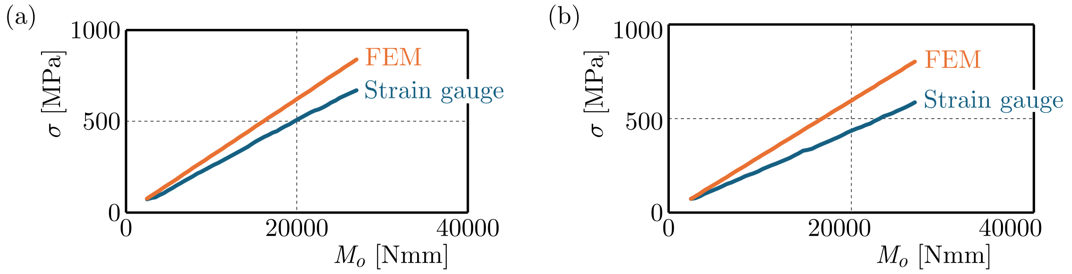

Fig. 3. Stress changes on the surface of the test bars (FEM – orange; strain gauge – blue): (a) hourglass fatigue test bar; (b) dog-bone fatigue test bar.

in orange). The results indicate that at the maximum bending load ($M_{o\,\max}$) of 26968.3 Nmm for the hourglass-shaped test bar, there was a 25 % difference. For the dog-bone test bar, there was a 37 % difference under the same bending load. The observed differences are probably caused by errors in the positioning of the strain gauge. Part of the error may result from the strain gauge being adhered at an angle, while another part may arise from the test specimen being slightly rotated during the measurement. This rotation could lead to a portion of the strain gauge's measuring base not being aligned with the lowest point of the presumed extreme fibre.

Based on the Wöhler curves depicted in Fig. 4, it is evident that the fatigue limit (denoted as σ_c) occurs at a specified number of cycles $N_f = 10^7$. For the hourglass-shaped fatigue test bar, the value of $\sigma_{c1} = 723$ MPa, and for the dog-bone-shaped test bar, the value of $\sigma_{c2} = 670$ MPa.

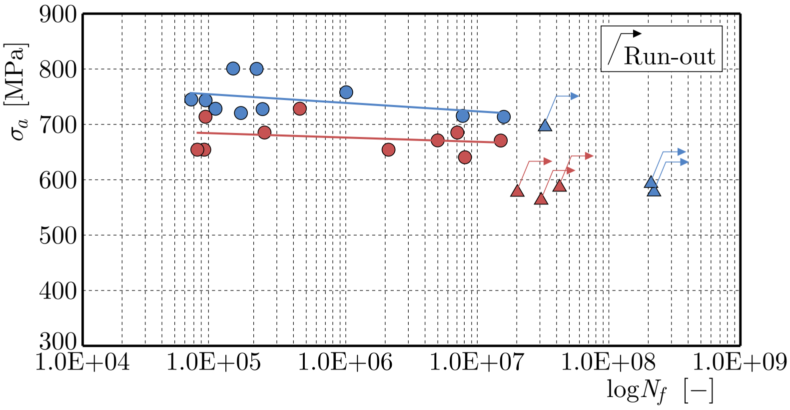

Fig. 4. Wöhler curves: blue – hourglass-shaped fatigue test bar; red – dog-bone-shaped fatigue test bar.

Hourglass fatigue test bars clearly showed a higher fatigue strength compared to dog-bone test bars. Compared to the study (Ulewicz *et al.*, 2017), which used the same experimental material, but under different testing conditions, the differences between results are likely attributed to differences in specimen geometry, surface preparation, and the specific test conditions, including loading frequency and cooling methods. These factors could influence the material's fatigue behaviour, thereby affecting the fatigue limits observed under different experimental setups.

Fatigue tests showed an 8 % higher fatigue limit for hourglass-shaped specimens compared to dog-bone-shaped specimens, primarily due to reduced stress concentration at the radius transition. Finite element analysis confirmed that fatigue failure occurred in the areas of maximum stress concentration: the central shaft for hourglass specimens and the transition radius for dog-bone specimens (Fig. 5). This highlights the significant role of specimen geometry in fatigue performance.

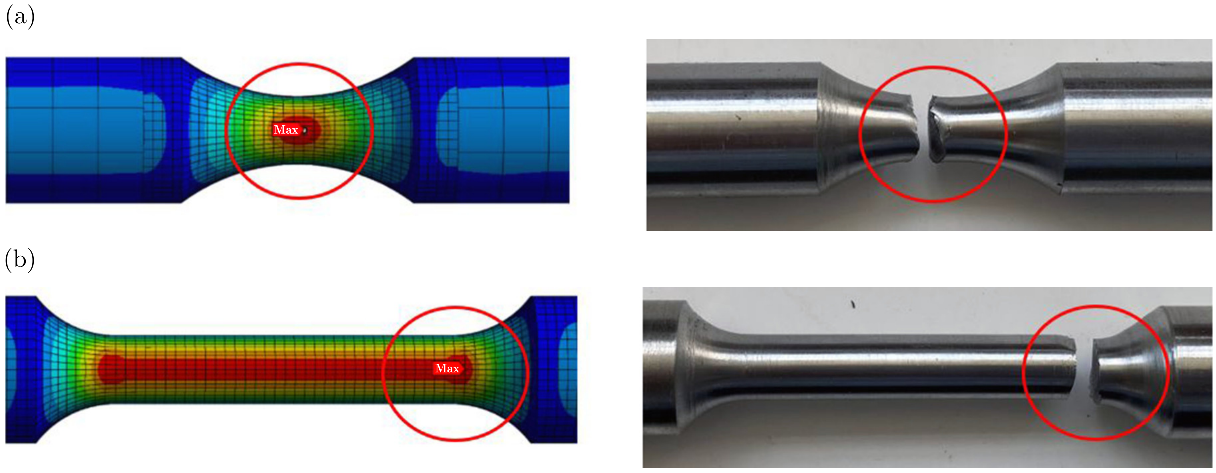

Fig. 5. Regions of maximum stress concentration and fatigue failure in test bars with different geometry: (a) hourglass test bar; (b) dog-bone test bar.

Fractographic analysis in Fig. 6 revealed subsurface fatigue crack initiation in hourglass-shaped specimens, while surface initiation was observed in dog-bone specimens. Both specimen types showed transcrystalline fatigue failure with striations and ductile fracture with fine dimple morphology in the final fracture zone.

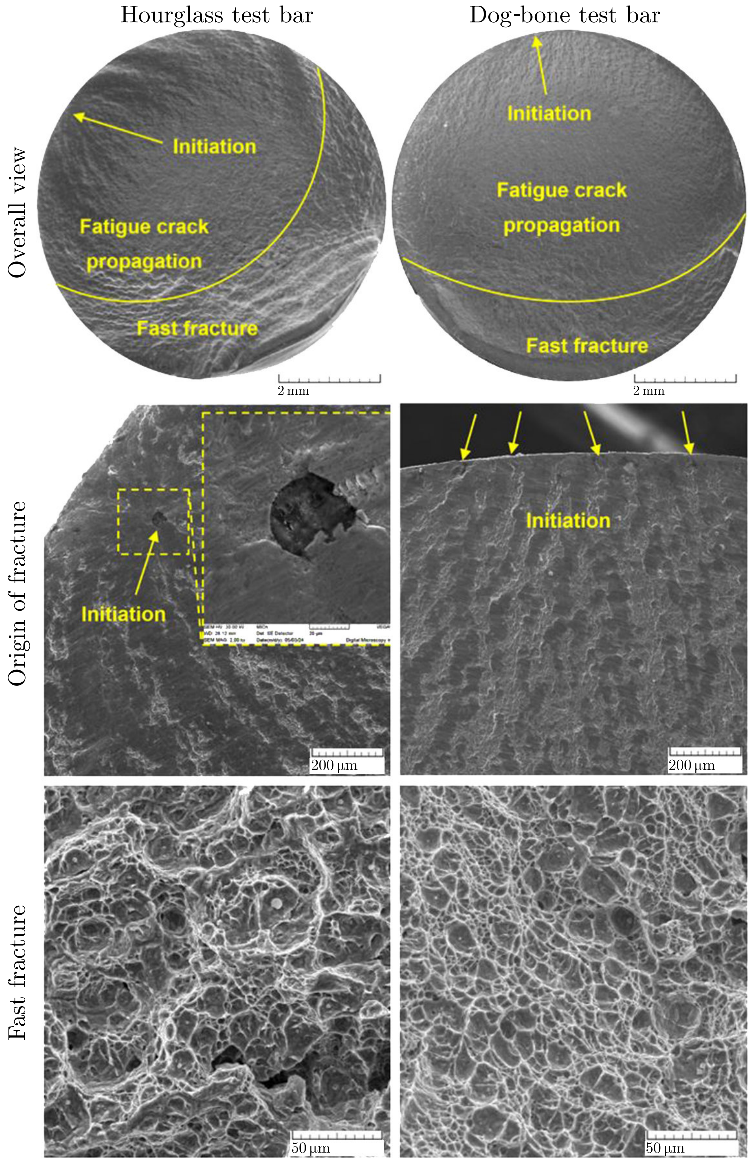

Fig. 6. Fractographic analysis of fractured surfaces after fatigue testing of test bars with different geometry.

4. Conclusions

This study highlights the influence of specimen geometry on the fatigue resistance of Hardox 450 high-strength structural steel. Based on the findings, the following conclusions can be drawn:

- experimental and computational evaluations revealed significant differences in stress concentration patterns between the two geometries. The hourglass test bar exhibited a more uniform and favourable stress distribution compared to the dog-bone counterpart, suggesting its superior design for reducing stress concentrations;
- the hourglass specimens exhibited an 8 % higher fatigue limit than the dog-bone specimens, primarily due to reduced local stress concentration at the radius transition. This highlights the significant impact of specimen geometry on fatigue performance;
- distinct crack initiation modes were observed: subsurface initiation in hourglass specimens and surface initiation in dog-bone specimens. Both exhibited transgranular fatigue failure with characteristic fine dimple fracture morphology, underlining consistent failure mechanisms across geometries.

While the standardized corner radii of both test specimens represent typical structural geometries, small variations could influence fatigue performance. A larger radius may reduce stress concentration and improve fatigue resistance, but the impact depends on other factors such as specimen size, loading conditions, and surface quality.

Acknowledgments

The Slovak Ministry of Education, Science, Research, and Sport's Scientific Grant Agency funded the research under contract VEGA no. 1/0741/21 and the Slovak Research and Development Agency under contract no. APVV-20-0427.

References

1. Chaurasiya, R., Maji, P., & Mukhopadhyay, G. (2023). High cycle fatigue behaviour of advanced high strength steel sheet (HS1000) in automotive application. *Materials Today: Proceedings* (in press). https://doi.org/10.1016/j.matpr.2023.09.120
2. Hehenberger, M., & Nilsson, J.O. (1982). A stress analysis of bending fatigue specimens using the finite element method. *International Compressor Engineering Conference*. Paper 381. https://docs.lib.purdue.edu/icec/381
3. Hultgren, G., & Barsoum, Z. (2020). Fatigue assessment in welded joints based on geometrical variations measured by laser scanning. *Welding in the World*, *64*(11), 1825–1831. https://doi.org/10.1007/s40194-020-00962-8
4. McClung, R.C. (1994). Finite element analysis of specimen geometry effects on fatigue crack closure. *Fatigue & Fracture of Engineering Materials & Structures*, *17*(8), 861–872. https://doi.org/10.1111/j.1460-2695.1994.tb00816.x
5. Okuda, K., Ogawa, K., Ichikawa, Y., Shiozaki, T., & Yamaguchi, N. (2019). Influence of microstructure on fatigue property of ultra high-strength steels. *Fracture and Structural Integrity*, *13*(48), 125–134. https://doi.org/10.3221/IGF-ESIS.48.15
6. Pan, M., Yang, L., Zheng, X., Mao, H., Kong, Y., & Du, Y. (2024). Numerical simulation of fatigue fracture in gradient high-strength steel: effects of carbides and gradient structure on stress–strain response and crack propagation behavior. *Journal of Materials Science*, *59*(27), 12757–12780. https://doi.org/10.1007/s10853-024-09907-8
7. Ulewicz, R., Szataniak, P., Novy, F., Trsko, L., & Bokuvka, O. (2017). Fatigue characteristics of structural steels in the gigacycle region of loading. *Materials Today: Proceedings*, *4*(5), 5979–5984. https://doi.org/10.1016/j.matpr.2017.06.081

Manuscript received December 5, 2024; accepted for publication March 6, 2025;

JOURNAL OF THEORETICAL
AND APPLIED MECHANICS
63, 3, pp. 551–556, Warsaw 2025
https://doi.org/10.15632/jtam-pl/202764

DIGITAL IMAGE CORRELATION IN MONITORING OF FATIGUE DAMAGE DEVELOPMENT OF MAR-M247 WITH ALUMINIDE COATING

Mateusz KOPEC

Institute of Fundamental Technological Research, Polish Academy of Sciences, Warsaw, Poland
mkopec@ippt.pan.pl

This study investigates the fatigue damage development in MAR-M247, a nickel-based superalloy with aluminide coating, using the digital image correlation (DIC) technique. The alloy's microstructures, including fine, coarse, and columnar grains, were analyzed to understand their influence on fatigue crack initiation and propagation. Fatigue tests were conducted at room temperature under controlled force, with strain evolution monitored through non-contact full-field DIC measurements. Results revealed that fine-grained MAR-M247 exhibited superior fatigue resistance due to uniform strain distribution, while coarse-grained and columnar structures showed pronounced strain localization and earlier crack initiation. The application of aluminide coatings did not significantly affect strain distribution across the different microstructures but highlighted complex interactions between coating and grain structure under cyclic loading. These findings provide critical insights into optimizing the performance of MAR-M247 for high-stress applications.

Keywords: fatigue; coatings; nickel alloys; digital image correlation.

1. Introduction

Nickel-based superalloys such as MAR-M247 are extensively used in high-performance applications, including gas turbine blades and aerospace components, due to their exceptional strength, thermal stability, and resistance to oxidation and corrosion at elevated temperatures (Kukla *et al.*, 2020). The complex, precipitation-strengthened microstructure of MAR-M247 is designed to maintain mechanical integrity under extreme conditions. However, the alloy's susceptibility to fatigue damage, especially under cyclic loading conditions, necessitates advanced techniques to monitor and predict failure mechanisms. One should highlight that the fatigue behavior of MAR-M247 is complex and highly dependent on temperature, stress conditions, and microstructural characteristics. At room temperature and intermediate temperatures, fatigue failure is typically dominated by crack initiation at microstructural defects such as casting pores, carbide particles, or inclusions (Kopec, 2023). These defects act as stress concentrators, leading to early crack formation. The propagation of fatigue cracks in this regime is mostly transgranular, following crystallographic slip planes due to the alloy's high strength and resistance to grain boundary sliding. At high temperatures (above 800 °C), fatigue behavior becomes

---

Ministry of Science and Higher Education
Republic of Poland

The publication has been funded by the Polish Ministry of Science and Higher Education under the Excellent Science II programme "Support for scientific conferences".
The content of this article was presented during the 40th Danubia-Adria Symposium on Advances in Experimental Mechanics, Gdańsk, Poland, September 24–27, 2024.

more influenced by environmental factors, particularly oxidation and creep (Šulák *et al.*, 2016). Oxidation-assisted fatigue leads to the formation of oxide layers along the crack path, which can accelerate crack growth by embrittling the surrounding material and reducing the effective load-bearing cross-section. Additionally, creep-fatigue interaction plays a crucial role, where sustained loads during cyclic loading allow time-dependent plastic deformation (creep) to contribute to crack growth, often leading to intergranular fracture as grain boundaries become weaker due to oxidation and the formation voids (Kopec, 2024a).

Digital image correlation (DIC) has emerged as a powerful tool for monitoring fatigue damage in metallic materials. By providing full-field, non-contact strain measurements, DIC enables precise tracking of strain localization, crack initiation, and propagation under various loading conditions. When applied to MAR-M247, DIC offers insights into how its microstructural characteristics influence fatigue behavior, particularly in the presence of protective aluminide coatings.

The microstructure of MAR-M247 can be tailored into fine-grained, coarse-grained, or columnar configurations, each offering distinct mechanical properties (Garimella *et al.*, 1997). Fine-grained structures are generally isotropic and exhibit improved resistance to crack initiation due to grain boundary strengthening. Coarse-grained structures, with larger grains, tend to concentrate strain at grain boundaries, making them prone to early crack initiation. Columnar structures, characterized by elongated grains aligned along the solidification direction, introduce significant anisotropy, affecting strain localization and fatigue performance. The addition of aluminide coatings further complicates this behavior. These coatings provide enhanced resistance to oxidation and hot corrosion but can introduce residual stresses and modify surface strain distributions (Kopec, 2024b). Investigating how these coatings interact with different microstructures during fatigue loading is critical to optimizing MAR-M247's performance in service.

This study employs DIC to examine the strain distribution and localization in fine-grained, coarse-grained, and columnar MAR-M247 during fatigue. Emphasis is placed on understanding how microstructural features influence fatigue crack initiation and propagation, as well as the role of aluminide coatings in altering strain evolution and fatigue life. By correlating DIC results with microstructural observations, this work aims to provide deeper insights into the complex interplay between material microstructure, surface coatings, and fatigue damage mechanisms.

2. Materials and methods

The initial microstructure of MAR-M247 of chemical composition presented in Table 1 varies based on casting conditions, producing fine, coarse, or columnar structures of the average grain size around 0.5 mm, 2.5 mm, and 5 mm, respectively (Fig. 1). In fine-grained forms, rapid cooling yields small, equiaxed grains with uniformly distributed gamma γ matrix and γ' precipitates (Fig. 1a), enhancing moderate-temperature strength and fatigue resistance. Coarse-grained structures, formed through slower cooling, feature larger grains (Fig. 1b) with an uneven precipitate distribution, improving high-temperature creep resistance but reducing fatigue performance. Columnar structures (Fig. 1c), common in directional solidification processes, exhibit elongated grains aligned along the growth direction, optimising creep and thermal fatigue properties in turbine blades due to reduced grain boundary sliding. Carbides and borides are present in all structures, influencing mechanical stability and crack resistance. Subsequently, aluminide coatings were applied through the Chemical Vapor Deposition (CVD) process with the optimized parameters (Kukla *et al.*, 2020) presented in Table 2.

Table 1. Chemical composition of MAR-M247 nickel based superalloy [wt.%].

C	Cr	Mn	Si	W	Co	Al	Ni
0.09	8.80	0.10	0.25	9.70	9.50	5.70	bal.

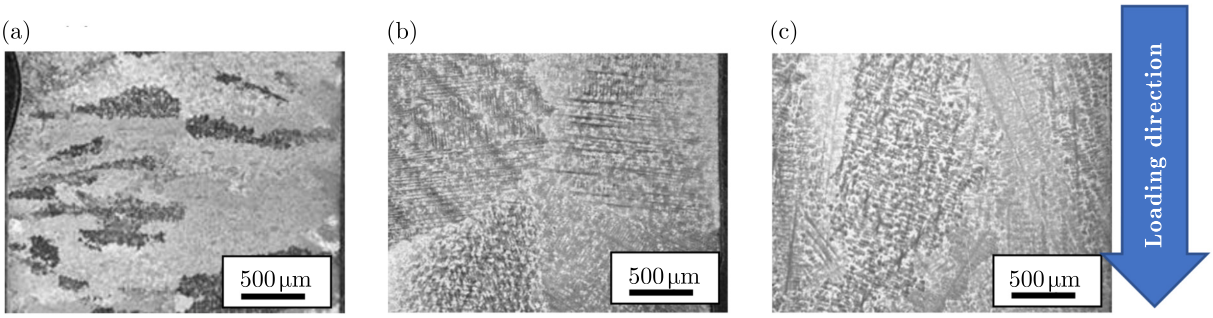

Fig. 1. Initial microstructures of MAR-M247: (a) fine; (b) coarse; (c) column-grained.

Table 2. CVD process parameters (Kukla *et al.*, 2020).

Deposition temperature	Internal pressure	Protective atmosphere	Deposition time	Coating thickness
1040 °C	150 mbar	hydrogen	8 hours	20 µm

Fatigue testing was conducted using the MTS 810 testing system (MTS System, Minnesota, USA) equipped with a standard MTS extensometer on specimens presented in Fig. 2. Uniaxial tensile evaluations were performed at a strain rate of $2 \times 10^{-4}\,\mathrm{s}^{-1}$ using five specimens. Fatigue assessments at room temperature (23 °C) were force-controlled with zero mean load, constant stress amplitude, and a frequency of 20 Hz. Each test was repeated at least twice to ensure consistent and reliable results. The stress amplitude range of 350 MPa to 650 MPa was determined based on the conventional yield strength derived from the tensile test. The strain evolution was monitored using DIC Aramis 12M setup.

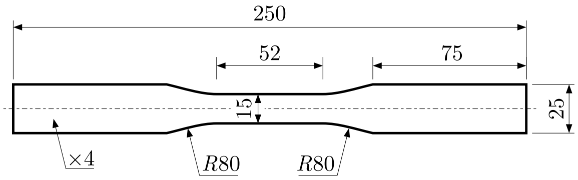

Fig. 2. Engineering drawing of coated MAR-M247 specimen for mechanical testing.

3. Results and discussion

The stress-strain curves for investigated MAR-M247 were presented in Fig. 3a. It was found, that all initial microstructures are characterized by similar yield strength of about 820 MPa, while

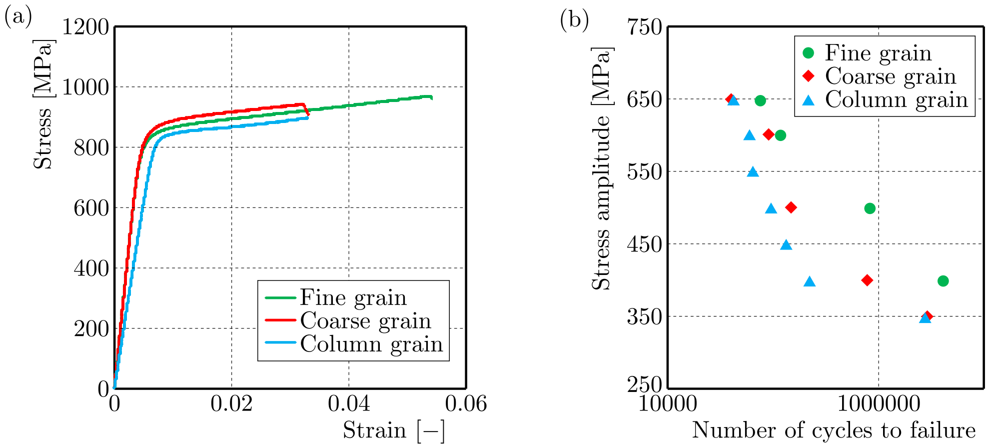

Fig. 3. Tensile (a) and fatigue (b) response of MAR-M247 alloy with three different initial microstructures and coating thickness of 20 µm.

the ultimate tensile strength and elongation are slightly higher for the fine grain. Subsequent fatigue testing revealed significantly improved response of fine-grained MAR-M247 reflected by the increased number of cycles to failure (Fig. 3b). The analysis of fatigue behavior at stress amplitude of 600 MPa using DIC revealed distinct strain distribution patterns associated with the alloy's initial microstructures (Fig. 4). Each microstructure displayed unique strain evolution

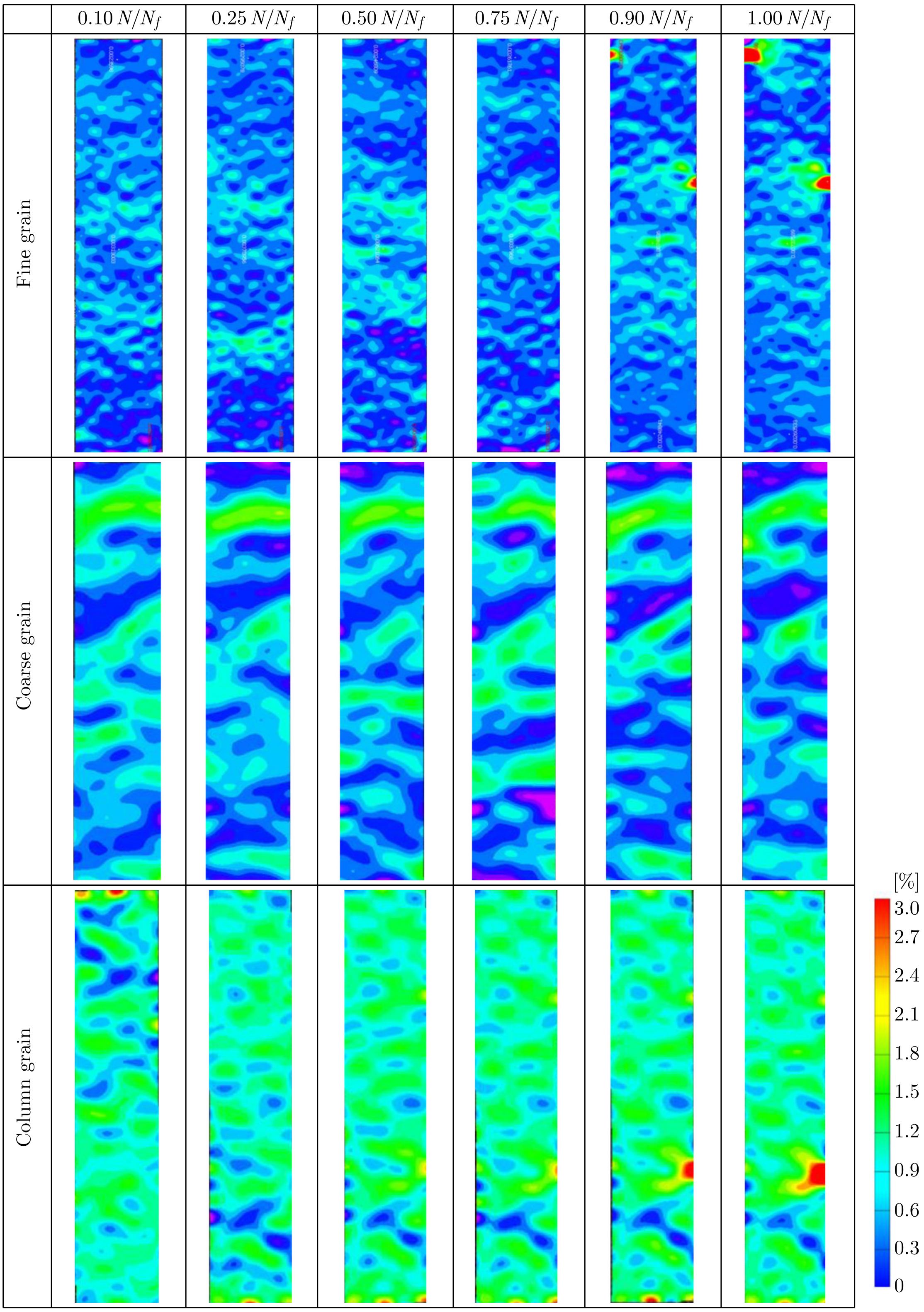

Fig. 4. Strain distribution in aluminized MAR-M247 subjected to stress amplitude of 600 MPa.

characteristics that significantly influenced fatigue crack initiation and propagation, underscoring the critical role of microstructure in determining the alloy's mechanical performance (Šulák & Obrtlík, 2025). Fine-grained MAR-M247 exhibited the most uniform strain distribution among the studied microstructures. DIC images showed minimal strain localization at early stages of cyclic loading. This behavior is attributed to the high density of grain boundaries in fine-grained structures, which act as barriers to dislocation motion, effectively distributing strain throughout the material. During fatigue loading, the delayed onset of localized strain bands and the lower severity of strain gradients contributed to prolonged resistance to crack initiation. These findings highlight the advantages of fine-grained MAR-M247 in applications where fatigue resistance is a priority. In coarse-grained MAR-M247, DIC captured pronounced strain localization more likely at grain boundaries. The larger grain size reduces the number of boundaries, concentrating strain in fewer locations and promoting early crack initiation. Strain maps revealed sharp gradients and isolated hotspots, corresponding to regions of microstructural discontinuity. These results align with the known anisotropic behavior of coarse-grained materials, where strain accumulation is less uniformly distributed, making them more susceptible to fatigue damage (Garimella *et al.*, 1997). The columnar microstructure presented a highly isotropic strain distribution, as observed in the DIC strain maps. Strain localization was strongly oriented along the grain aligned with the columnar grain growth direction which was also pararel to loading direction. One should highlight, however, that the application of aluminide coatings do not influence strain distribution across all microstructures as the strain areas represents directly grain interaction during cyclic loading.

The plastic strain accumulation capacity for each MAR-M247 microstructure significantly influences its fatigue life, as observed by the DIC analysis. Fine-grained MAR-M247 exhibited the highest plastic strain accumulation capacity due to its numerous grain boundaries, which effectively distributed strain and delayed localized deformation, resulting in superior fatigue resistance. Coarse-grained structures, with fewer grain boundaries, showed more pronounced strain localization, particularly at grain boundaries, leading to early crack initiation and reduced fatigue life. The columnar microstructure displayed anisotropic strain distribution, with strain localization aligning along the columnar grain growth direction, influencing fatigue performance depending on the loading orientation. The aluminide coatings did not significantly alter strain distribution across the different microstructures, indicating that the grain structure remains the dominant factor in fatigue behavior. Overall, fine-grained MAR-M247 demonstrated the best fatigue resistance due to its ability to accommodate plastic strain more uniformly, while coarse and columnar structures were more prone to early fatigue failure due to localized strain accumulation. A material with higher plastic strain accumulation capacity often has a lower service life because excessive plastic deformation accelerates fatigue damage mechanisms (Paul, 2025). Repeated plastic straining leads to localized stress concentrations, promoting early crack initiation at microstructural defects like grain boundaries and inclusions. Once cracks form, they propagate faster under cyclic loading, reducing fatigue life. Additionally, materials with high plastic strain tend to experience softening due to dislocation motion, making them more susceptible to failure (Paul, 2025). In high-temperature environments, accumulated strain also contributes to creep-fatigue interactions and oxidation-assisted crack growth, further diminishing durability. While beneficial in monotonic loading, excessive plastic strain in fatigue conditions accelerates microstructural deterioration, ultimately shortening service life.

4. Conclusions

The DIC data demonstrated that initial microstructure plays a critical role in determining strain evolution and fatigue behavior in MAR-M247. Fine-grained structures exhibited superior fatigue resistance due to their ability to distribute strain uniformly, while coarse-grained and columnar structures showed greater strain localization, leading to earlier crack initiation. The interaction of aluminide coatings with these microstructures introduced complex strain redistribution patterns, which require careful consideration when designing components and applying coatings.

Acknowledgments

The author would like to express his gratitude to the technical staff – M. Wyszkowski and A. Chojnacki for their kind help during the experimental part of this work. The methodological support of Prof. D. Kukla is also acknowledged.

References

1. Garimella, L., Liaw, P.K., & Klarstrom, D.L. (1997). Fatigue behavior in nickel-based superalloys: A literature review. *JOM*, *49*(7), 67–71. https://doi.org/10.1007/BF02914771
2. Kopec, M. (2023). Fatigue damage development in 14MoV6-3 steel for power plant pipes monitored by Digital Image Correlation. *Acta Mechanica Solida Sinica*, *36*(3), 405–417. https://doi.org/10.1007/s10338-023-00387-y
3. Kopec, M. (2024a). Effect of aluminide coating thickness on high-temperature fatigue response of MAR-M247 nickel-based superalloy. *Coatings*, *14*(8), Article 1072. https://doi.org/10.3390/coatings14081072
4. Kopec, M. (2024b). Recent advances in the deposition of aluminide coatings on nickel-based superalloys: A synthetic review (2019–2023). *Coatings*, *14*(5), Article 630. https://doi.org/10.3390/coatings14050630
5. Kukla, D., Kopec, M., Kowalewski, Z.L., Politis, D.J., Jóźwiak, S., & Senderowski, C. (2020). Thermal barrier stability and wear behavior of CVD deposited aluminide coatings for MAR 247 nickel superalloy. *Materials*, *13*(17), Article 3863. https://doi.org/10.3390/ma13173863
6. Kukla, D., Kopec, M., Wang, K., Senderowski, C., & Kowalewski, Z.L. (2021). Nondestructive methodology for identification of local discontinuities in aluminide layer-coated MAR 247 during its fatigue performance. *Materials*, *14*(14), Article 3824. https://doi.org/10.3390/ma14143824
7. Paul, S.K. (2025). A review on cyclic hardening and softening behavior of alloys. *Journal of Alloys and Metallurgical Systems*, *9*, Article 100153. https://doi.org/10.1016/j.jalmes.2025.100153
8. Šulák, I., & Obrtlík, K. (2025). Assessment of dwell-fatigue properties of nickel-based superalloy coated with a multi-layered thermal and environmental barrier coating. *International Journal of Fatigue*, *191*, Article 108693. https://doi.org/10.1016/j.ijfatigue.2024.108693
9. Šulák, I., Obrtlík, K., & Čelko, L. (2016). High-temperature low-cycle fatigue behaviour of HIP treated and untreated superalloy MAR-M247. *Kovove Materiály – Metallic Materials*, *54*(6), 471–481. https://doi.org/10.4149/km_2016_6_471

Manuscript received January 23, 2024; accepted for publication March 8, 2025;

JOURNAL OF THEORETICAL
AND APPLIED MECHANICS
63, 3, pp. 557–570, Warsaw 2025
https://doi.org/10.15632/jtam-pl/202820

EXPERIMENTAL IDENTIFICATION OF CP-Cu YIELD SURFACE AND ITS EVOLUTION DUE TO COMPLEX LOADING PRE-DEFORMATION

Ved Prakash DUBEY, Mateusz KOPEC*, Zbigniew L. KOWALEWSKI

Institute of Fundamental Technological Research, Polish Academy of Sciences, Warsaw, Poland
*corresponding author, *mkopec@ippt.pan.pl*

This study examines the yield surface evolution of technical copper (CP-Cu) under complex loading, focusing on monotonic tension and combined tension with cyclic torsion. Using biaxial testing, initial and pre-deformed yield surfaces were analysed. Results indicate kinematic hardening with tensile pre-strain, while cyclic torsion induces anisotropic hardening at lower amplitudes (±0.1 %) and softening at higher amplitudes (±0.2 %). Strain amplitude significantly impacts material response, while frequency has a minor effect.

Keywords: copper; pre-deformation; yield surface; biaxial.

1. Introduction

Copper, a versatile and highly conductive material, serves as a fundamental element in various engineering and industrial applications due to its exceptional mechanical, thermal, and electrical properties. Its alloys, such as bronze and brass, further expand its utility by enhancing characteristics such as strength, corrosion resistance, and wear resistance (Zhang *et al.*, 2024). Copper and its alloys are extensively used in sectors like electronics, electrical engineering, construction, automotive, and aerospace industries. The mechanical properties of copper, such as ductility, toughness, high thermal conductivity (400 W/m · K), high electrical conductivity (5.8×10^7 S/m), and low electrical resistivity ($1.72 \times 10^{-8}\ \Omega$), make it indispensable for manufacturing heat exchangers, electrical wires, printed circuit boards, and architectural elements (Vahedi Nemani *et al.*, 2024). However, understanding the mechanical behaviour of copper under different manufacturing conditions and loading situations is crucial for optimizing its performance and reliability in these applications. The mechanical properties of copper are closely related to its purity, microstructure, and the presence of alloying elements. Pure copper exhibits excellent ductility and thermal conductivity, with a tensile strength usually ranging between 200 MPa and 300 MPa and an elongation at break of up to 50 % in annealed conditions (Guschlbauer *et al.*, 2018; Li & Zinkle, 2012). Its yield strength is comparatively lower, approximately 70 MPa in a pure, annealed form, but can be significantly enhanced through alloying and work-hardening

---

Ministry of Science and Higher Education
Republic of Poland

The publication has been funded by the Polish Ministry of Science and Higher Education under the Excellent Science II programme "Support for scientific conferences".
The content of this article was presented during the 40th Danubia-Adria Symposium on Advances in Experimental Mechanics, Gdańsk, Poland, September 24–27, 2024.

(Guschlbauer *et al.*, 2018; Lai *et al.*, 2022). For example, copper-zinc alloys (brass) provide improved strength and machinability, with yield strengths reaching up to 600 MPa, while copper-tin alloys (bronze) are favoured for their corrosion resistance and higher tensile strength, reaching up to 700 MPa (Scudino *et al.*, 2015; Semih & Recep, 2023; Wu *et al.*, 2013).

Applications in the electrical industry demand high conductivity, which necessitates minimal alloying. In contrast, structural and mechanical applications prioritize strength and wear resistance, often achieved through alloying with elements like aluminium, titanium, silicon, or nickel (Czerwinski, 2024; Pingale *et al.*, 2021; Zhou *et al.*, 2023). The interplay of these properties underlines the need for a detailed understanding of the material's mechanical behaviour during various manufacturing processes.

Manufacturing techniques significantly influence the mechanical properties of copper and its alloys. Processes such as casting, forging, extrusion, rolling, and additive manufacturing introduce variations in grain size, texture, and residual stress, which affect yield strength and deformation behaviour (Jiang *et al.*, 2021; Zhang *et al.*, 2024). Several studies have investigated the impact of pre-deformation and manufacturing techniques on the mechanical properties of copper and its alloys. Pre-deformation, such as cold rolling or tension, modifies the microstructure of copper by inducing dislocations and work hardening. For example, Stepanov *et al.* (2012) demonstrated the effect of cold rolling on the microstructure and mechanical properties of copper processed via equal channel angular pressing (ECAP). It reveals that cold rolling transforms the equiaxed grains formed during ECAP into a lamellar structure. This process enhances yield strength by 100 MPa due to reduced boundary spacing, aligning with the Hall–Petch relationship. Additionally, dynamic restoration increases high-angle boundary fractions, reflecting microstructural refinement and strengthening. Sungar Singh Sivam *et al.* (2023) examined unidirectional rolling (UDR) and cross-rolling (CR) of pure copper, revealing distinct mechanical responses. UDR achieves higher tensile strength (324 MPa) and hardness (98.2 HV) compared to CR (310 MPa and 95.4 HV, respectively) at a true strain of 2.77. UDR induces elongated grains and higher stored energy (0.69 J/g), while CR forms equiaxed grains with reduced anisotropy and lower stored energy (0.54 J/g). These microstructural changes, driven by deformation modes, explain the variations in mechanical properties. Results of research conducted by Pan *et al.* (2023) revealed significant enhancement in mechanical properties of pure copper processed with low-angle dislocation boundaries (LADBs). Initial coarse-grained (CG) copper had a yield strength of 61 MPa, tensile strength of 231 MPa, and a fatigue endurance limit of 50 MPa (fatigue ratio 0.24). After LADBs introduction, dislocation-cell-structured (DC) copper exhibited a yield strength of 372 MPa, tensile strength of 374 MPa, and a fatigue endurance limit of 130 MPa (fatigue ratio 0.35). This improvement is attributed to nanoscale dislocation patterns, reducing surface roughening and enhancing cyclic loading resistance.

The study of yield strength and yield surface evolution in copper and its alloys has been an active area of research. The yield surface is a graphical representation of the stress states at which a material begins to deform plastically. The yield surface reflects anisotropy and hardening behaviour, providing insights into the material's deformation mechanisms under complex loading conditions. This analysis of copper enables the design of components that can withstand multiaxial stresses encountered in practical applications, such as piping systems, automotive heat exchangers, and structural elements in buildings. Mair and Pugh (1964) analysed thin-walled tubes of annealed copper pre-strained to the values of 1.3 %, 4.7 %, and 8.5 % in tension or 0.25 %, 1.5 %, and 3 % in torsion, respectively. The results demonstrated yield locus expansions and cross-effects in both cases, such that tensile pre-strain increased torsional yield stress and torsional pre-strain increased yield stress in tension, contrary to the expectations of isotropic hardening. The torsional pre-strain displayed a significant Bauschinger effect, with the magnitude increasing with the increase in the pre-strain level. Hecker (1971) investigated yield surface evolution in annealed OFHC copper subjected to biaxial stress. Specimens pre-strained via axial tension and internal pressure showed significant yield surface distortions and directional anisotropy at small proof strain (5 με) levels. The initial yield surface expanded and translated in the direction of pre-strain either in axial or circumferential pre-strain and, for biaxial pre-strains, distorted in the vicinity of the loading point. Larger proof strains (2000 με) mitigated these effects, resulting in isotropic expansion. Dietrich and Kowalewski (1997) explored the impact of pre-deformation on the yield surface of 99.9 % pure copper subjected to pre-strains of 5 % and 15 % of tension creep at 523 K and monotonic tension at ambient temperature. The investigations revealed that initial yield surfaces align with the isotropic Huber–von Mises criterion, but even minor plastic deformation introduces anisotropy. Pre-strain causes a disproportionate increase in yield surface axes, with monotonic loading inducing greater shifts than creep due to elevated-temperature exposure. Additionally, the major-to-minor axis ratio of the yield surface decreases significantly with small plastic pre-strain and stabilizes for higher pre-deformation for both pre-strain cases. These findings emphasize the role of deformation mechanisms in altering yield surface geometry and material anisotropy. This can be attributed to stress-induced texture development and subgrain formation that extended creep life and yield strength, with secondary creep rates reduced significantly for pre-strained copper. Helling *et al.* (1986) analysed multiaxial yield loci in 70:30 brass under torsional pre-strains ranging from 2.4 % to 32 %. Severe distortions and strong directional memory effects were observed, with yield surface translations of up to 80 % in comparison to the initial yield locus. Microstructural findings showed pronounced twin boundary motion and strain-induced grain refinement, contributing to yield locus shifts. The study also investigated the effects of directionality on yield surface distortion, i.e., the orientation of the flattened region on the yield locus. The results indicate that yield surface distortion is largely independent of the pre-stress path but is significantly influenced by the pre-strain path, with the final pre-strain direction exerting a dominant effect. A recent research conducted by Liu *et al.* (2023) investigates the yielding behaviour of TU00 pure copper under strain rates ranging from 10^{-3} s to 10^{3} s using a servo-hydraulic axial-torsional testing machine and a combined tension-torsion Hopkinson bar system for dynamic tension-torsion tests. Yield stress increased significantly with the strain rate, from 120 MPa to 190 MPa, highlighting the strain rate dependency. The modified Hill yield criterion, incorporating strain rate effects, provided the most accurate predictions of yield points, while emphasizing that strain rate hardening is anisotropic with notable differences in tensile and torsional responses. A universal strain rate hardening model integrating the Johnson–Cook constitutive framework effectively described the work hardening behaviour of copper under complex stress states, aligning well with experimental data and demonstrating the limitations of uniaxial tensile tests alone for describing the strain hardening behaviour of TU00 copper.

Although substantial progress has been made in understanding the mechanical behaviour and the yield surface evolution of copper and its alloys, still several gaps remain. The effects of complex pre-deformation and multiaxial stress loading on the yield surface evolution have not been fully studied. Therefore, the main aim of this paper is to determine experimentally the initial yield surface of CP-Cu alloy, followed by subsequent yield surfaces reflecting plastic pre-deformation. The pre-deformation was introduced by monotonic tension and combined monotonic tension – proportional cyclic torsion loadings. By advancing the understanding of the yield surface evolution, this research seeks to provide insights for optimizing the mechanical performance of copper in various engineering applications.

2. Materials and methods

The material used in this study was commercially pure copper (CP-Cu). The copper bars used in this study were obtained in the M1E-Z4 condition, which corresponds to the Cu-ETP (M1E; E-Cu58) state. The copper bars were machined into thin-walled tubular specimens with identical inner and outer surface finishes, using consistent turning parameters to ensure uniformity. The specimen geometry is illustrated in Fig. 1. Mechanical testing was conducted utilizing an MTS 858 servo-electrohydraulic biaxial testing machine at room temperature (23 °C). This system has a maximum axial force capacity of ±25 kN and a maximum torque of ±100 Nm. Uniaxial tensile tests were initially performed to determine the basic mechanical properties, including the conventional yield strength. Based on the stress-strain response, the pre-deformation criterion was defined.

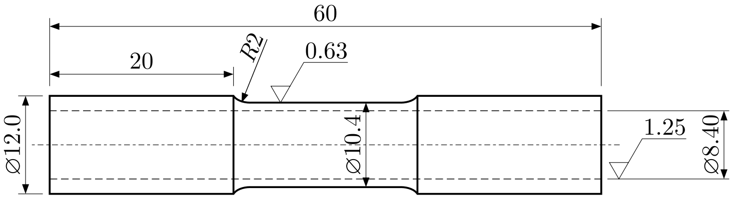

Fig. 1. Engineering drawing of the specimen.

Vishay 120 Ω strain gauges were affixed in the middle of the outer surface of the gauge section for the purpose of measuring and controlling strain components. Axial and shear strain components were recorded using a three-element 45° rectangular rosette (EA-05-125RA-120) with a 3.18 mm gauge length, while hoop strain was measured using a linear pattern rosette (EA-13-062AK-120) with a 1.57 mm gauge length. The strain gauges were bonded using M-Bond 610 adhesive, ensuring precise data acquisition. The three-element rosette configuration included a strain gauge aligned with the specimen's longitudinal axis for axial strain measurement, while the remaining two gauges, positioned at +45° and −45°, formed a half-bridge circuit to measure shear strain. The hoop strain was measured using a separate half-bridge circuit perpendicular to the longitudinal axis (Dubey *et al.*, 2023). This setup, directly integrated with the testing machine controller, enabled accurate strain monitoring and control throughout the experiments.

To determine the initial and subsequent yield surfaces of CP-Cu, a single-specimen sequential probing technique was employed under strain-controlled loading. The loading sequence began with tension and returned to the same direction after completing all predefined stress paths. Each loading path started from the zero stress state and continued until a limited plastic offset strain of 0.02 % was reached, after which stress-controlled unloading was performed until the zero stress state. Yield points were determined using the specified offset strain method, defining yield as the point where the equivalent stress-strain curve deviated by 0.01 % from the elastic response in each loading direction (Kopec *et al.*, 2024). The numerical computation of the yield surface was conducted using the Szczepiński anisotropic yield criterion, and experimental yield points were fitted to the yield equation using the least squares method to ensure accuracy in characterizing the anisotropic mechanical behaviour of CP-Cu. The Szczepiński yield criterion extends the von Mises and Hill models by incorporating linear stress terms to account for deformation-induced anisotropy and the Bauschinger effect, capturing the directional dependence of the yield strength.

The experimental study of CP-Cu was carried out in three stages following a structured methodology. Firstly, the fundamental mechanical properties of CP-Cu were characterized. Thereafter, plastic pre-deformation was introduced in the specimens through two approaches: (a) monotonic tension loading up to 1 % of permanent strain, and (b) a combination of monotonic axial tension up to the same strain level with proportional cyclic torsional loading. The cyclic torsional loading was performed at two strain amplitudes (±0.1 % and ±0.2 %) and two frequencies (0.5 Hz and 1 Hz), as CP-Cu achieved a very limited value of axial stress (15 MPa) at the 1 % axial pre-strain value at a higher strain amplitude equal to ±0.4 %, at a frequency of 0.5 Hz. Finally, the initial yield surface of the as-received CP-Cu was determined, along with the yield surfaces of the pre-deformed specimens.

3. Results and discussion

3.1. Mechanical properties of as-received material

Tensile tests were performed on solid tubular and thin-walled samples at room temperature at a constant strain rate of $0.005\,\mathrm{s}^{-1}$. Figure 2a shows the engineering stress-strain curve of CP-Cu, and its tensile properties are listed in Table 1. The minor variations in tensile results shown in Fig. 2a for both solid tubular and thin-walled specimens can be attributed to differences in specimen geometry, which may influence stress distribution and deformation characteristics. Comparing these findings with existing literature data is challenging, as the mechanical properties of commercially pure copper are highly sensitive to factors such as grain size, purity, processing, and heat treatment conditions. For reference, previous studies (Guschlbauer *et al.*, 2018; Jadhav *et al.*, 2021) report yield strengths ranging from 70 MPa to 300 MPa and tensile strengths between 150 MPa and 450 MPa, depending on these variables. The yield and tensile strength values obtained in this study fall within these ranges, suggesting consistency with established trends while also emphasizing the inherent variability in mechanical properties due to processing conditions. Figure 2b presents the effective stress-strain curves comparing the material behaviour of thin-walled specimens subjected to tension, tension-torsion, and pure torsion. The stress-strain curves for torsion and tension-torsion loading closely overlap, whereas the curve for tension loading deviates significantly from the other two loadings, which indicates that the same material exhibits distinct mechanical responses under different loading conditions. These variations can likely be attributed to the initial anisotropy introduced during the manufacturing process, which affects how the material accommodates different stress states. This anisotropy influences the deformation mechanisms, leading to differences in stress distribution and strain accumulation under various loading paths.

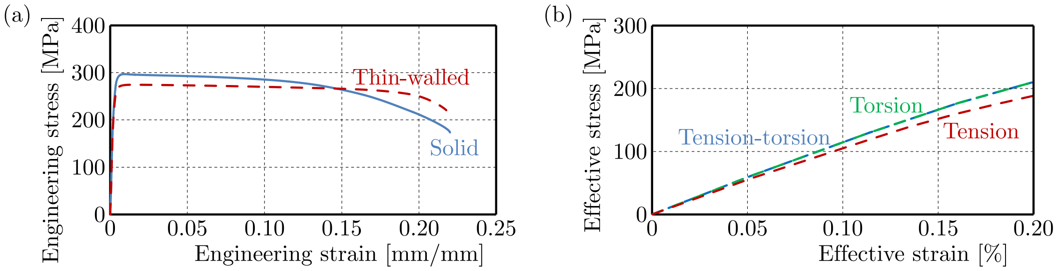

Fig. 2. (a) Tensile stress-strain response of solid and thin-walled CP-Cu specimens; (b) comparison of CP-Cu behaviour under various loading conditions.

Table 1. Mechanical properties of commercially pure copper.

	$R_{p0.2}$ [MPa]	R_m [MPa]	A [%]	E [GPa]
Solid specimen	286 (±2)	297 (±1)	22 (±1)	112 (±1)
Tubular specimen	264 (±2)	274 (±1)	21 (±1)	110 (±1)
ASTM standard (C11000) (Davis, 2001)	69–365	221–455	4–55	–

3.2. Mechanical response of CP-Cu under complex loading

The effect of the cyclic torsion with varying strain amplitudes and frequencies on the monotonic tensile behaviour of CP-Cu was investigated. The main aim was to induce plastic predeformation and examine changes in tensile characteristics under torsion-reverse-torsion cycling. Figures 3a and 3b demonstrate that the tensile characteristics of CP-Cu are significantly affected when tension is combined with cyclic torsion. A clear softening effect is observed, characterized by a decrease in axial stress as the cyclic strain amplitude increases. Additionally, an increase in

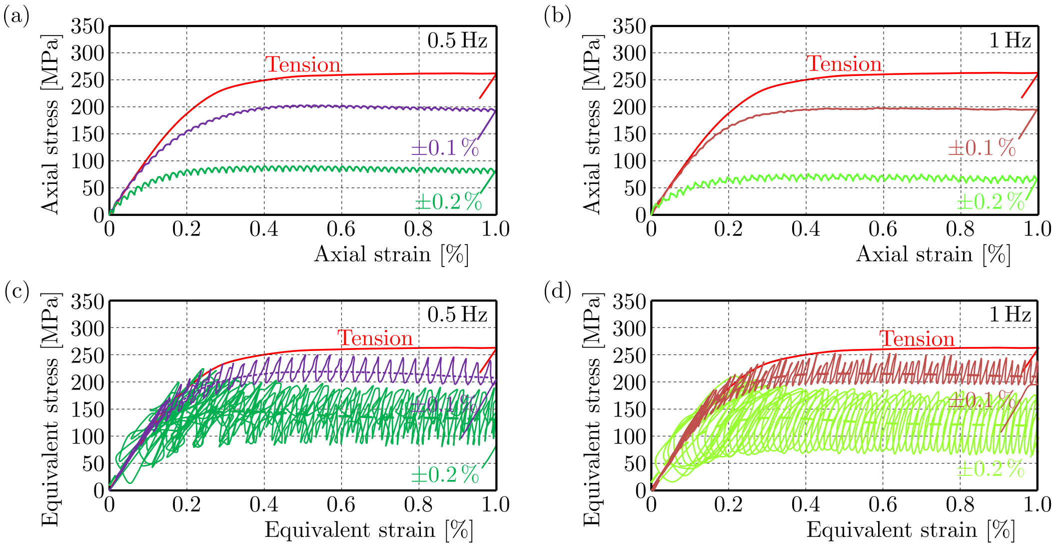

Fig. 3. Comparison of CP-Cu response in monotonic tension and tension with torsion-reverse-torsion at strain amplitudes of ±0.1 % and ±0.2 % for frequencies of 0.5 Hz (a, c) and 1 Hz (b, d).

cyclic torsion frequency further amplifies this decrease in the axial stress. For the cyclic torsion strain amplitude of ±0.1 % at the frequency of 0.5 Hz, the tensile stress at 0.2 % axial strain decreased from 188 MPa to 163 MPa. When the cyclic torsion strain amplitude increased to ±0.2 % at the same frequency, the decrease was more pronounced (80 MPa) at the same level of axial strain (Fig. 3a). The effect became even more significant at a higher frequency. For example, at ±0.2 % cyclic torsion strain amplitude and 1 Hz frequency, the tensile stress dropped from 188 MPa to 64 MPa, representing a 66 % reduction compared to the tension-only condition at 0.2 % axial strain (Fig. 3b).

This decrease in tensile stress is consistent with the influence of shear stress introduced during cyclic torsion. To better understand the effect of shear stress and evaluate the equivalence of stress under the three loading scenarios, Figs. 3c and 3d present the equivalent stress-strain curves. These curves provide a comprehensive representation of the material's response under combined tension and torsion loading. The equivalent stress-strain curves clearly demonstrate a pronounced softening effect in CP-Cu as the cyclic torsional strain amplitude increases. This trend aligns with the reduction in axial stress observed in Figs. 3a and 3b, suggesting that shear stress significantly alters the material's behaviour. The progressive reduction in equivalent stress at higher strain amplitudes highlights the combined effects of axial and torsional deformation, where shear stress introduces additional dislocation motion, enhancing plastic flow and reducing the material's load-bearing capacity.

The observed trend of decreasing tensile stress with increasing cyclic torsion is further illustrated in Fig. 4 for 0.5 % axial strain, evaluated across different cyclic torsion strain amplitudes and frequencies. Notably, the case of 0 % cyclic torsion strain amplitude corresponds to monotonic tension, serving as a baseline (Fig. 4a). The results clearly demonstrate a significant reduction in the tensile stress with the increasing cyclic torsion strain amplitude. In contrast, the impact of the increasing cyclic torsion frequency on tensile stress is comparatively less pronounced during combined loading (Fig. 4b). This suggests that the amplitude of torsional strain plays a dominant role in altering the stress state of copper by introducing additional shear deformation and facilitating plastic flow, whereas the role of frequency is primarily to modulate the rate at which these effects accumulate. The softening effect was also observed in CP-Ti with the increase in cyclic torsion strain amplitude and frequency during combined tension-torsion loading. These results indicate that the combination of cyclic torsion and tension leads to significant material softening, likely due to the accumulation of dislocation interactions and the

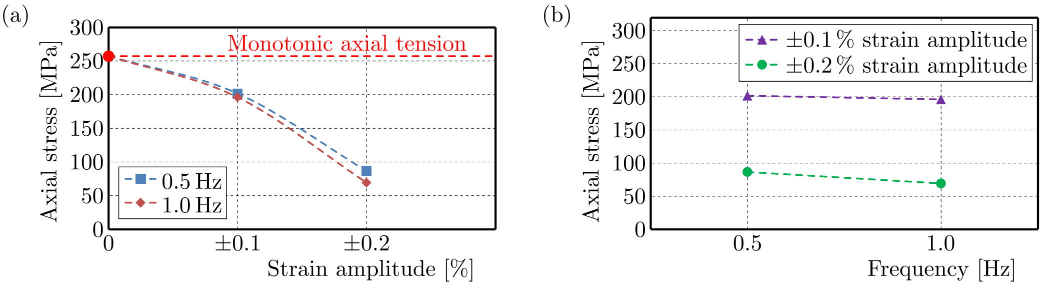

Fig. 4. Tensile stress variation at 0.5 % axial strain under combined tension-cyclic torsion for ±0.1 % and ±0.2 % (a) strain amplitudes and 0.5 Hz and 1 Hz (b) frequencies.

microstructural evolution under complex loading. The severity of the softening effect increases with both strain amplitude and frequency, emphasizing the need to account for such interactions when predicting the mechanical performance of CP-Cu in applications involving combined loading conditions.

3.3. Identification of the initial yield surface of CP-Cu

The yield surfaces of the CP-Cu in the as-received state were determined using a sequential loading procedure at offset strain values of 0.01 % and 0.005 %, as shown in Fig. 5a. These yield surfaces demonstrate a clear dependence on the chosen yield definition. After experimentally determining the yield points in various directions, ellipses were fitted using coefficients calculated via the least squares evaluation method. The primary parameters of these ellipses are summarized in Table 2, indicating that the centre of the yield surface is nearly aligned with the origin (0, 0) of the biaxial stress plane, with negligible rotation. Despite this alignment, some degree of initial anisotropy was evident, as the axis ratios of the yield surfaces were 1.34 and 1.37 – significantly lower than the isotropic value of 1.73 predicted by the Huber–von Mises yield criterion. This deviation highlights the anisotropic behaviour of the as-received material. While both yield definitions provided qualitatively similar yield surface shapes and anisotropic characteristics, the absolute values of the yield points and surface size differ, which emphasizes the need to carefully select the yield criterion based on the specific application. In applications requiring precise modelling of initial plastic yielding, a smaller offset may be more appropriate. However, for general engineering design, a larger offset is mostly selected.

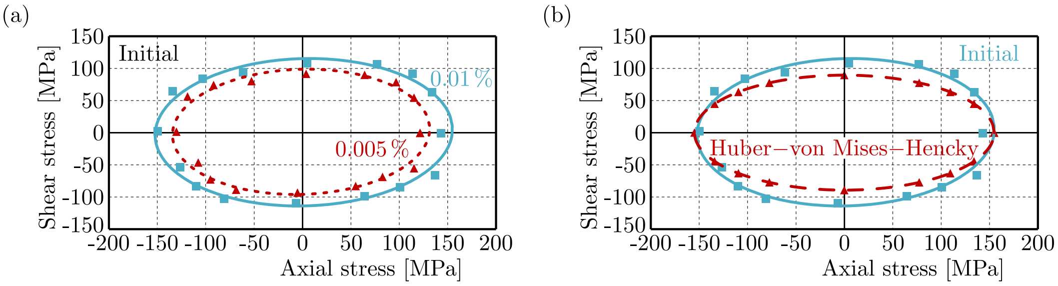

Fig. 5. Yield surfaces of as-received CP-Cu with yield points for 0.005 % (dotted red) and 0.01 % (continuous blue) offset strains (a); comparison of the initial yield surface with an isotropic yield surface (dashed red) (b).

Table 2. Ellipse parameters of the initial yield surfaces for CP-Cu.

	Centre (x_0, y_0) [MPa]	Rotation angle (Ø) [Radian]	Semi-axes (a, b) [MPa]	Axis ratio (a/b)
0.01 % offset strain	1.36, 0.60	0.07	153.78, 114.44	1.34
0.005 % offset strain	−1.45, 1.26	0.08	133.09, 97.17	1.37

To further investigate the material's initial anisotropy, the 0.01 % offset yield surface of CP-Cu was compared with an isotropic yield surface, anchored by the yield point in tension (direction 0). Figure 5b illustrates this comparison, showing that the axial yield stress of as-received CP-Cu aligns with the isotropic yield surface, while noticeable deviations occur in the shear stress direction. This discrepancy confirms the presence of initial anisotropy in the as-received material. The observed initial anisotropy is attributed to distinct hardening behaviour in shear strength, which likely results from the manufacturing processes applied to the material, such as the conversion of a solid specimen into a thin-walled tubular geometry or specific production methods used during material preparation. These processes induce microstructural variations, residual stresses, and texture development, which collectively contribute to the anisotropic response of CP-Cu.

3.4. Evolution of the CP-Cu yield surface due to pre-deformation

The effect of monotonic tension and a combination of monotonic tension with cyclic torsion pre-deformation on the mechanical properties of commercially pure copper was examined by studying changes in the initial yield surface. Pre-deformation tests were conducted until the specimens reached an axial strain of 1 %. Afterwards, the yield surfaces of the pre-deformed samples were determined using the same 0.01 % offset strain method as applied to the untreated specimen. Figure 6 presents the yield surface of CP-Cu following 1 % tensile pre-deformation in comparison to the initial yield surface. Although the overall shape remains consistent with the original yield surface, a distinct shift in the tensile direction is evident. This displacement suggests that monotonic tensile deformation has led to kinematic hardening along the direction of pre-strain. However, a decrease in the compressive direction and no change in the shear stress direction were observed. The increase in the tensile yield point is approximately 35 MPa, representing a 24 % enhancement over the initial yield point. This kinematic hardening effect can be attributed to the accumulation of dislocations and rearrangement of microstructural features during tensile pre-deformation, which results in an increase in material resistance to further plastic deformation in the pre-strain direction. The translation of the yield surface, rather than a uniform expansion, suggests that the material retains some degree of anisotropy following pre-deformation. This behaviour is consistent with the dislocation motion being predominantly oriented along the tensile direction, which reinforces the material's strength and shifts the yield surface correspondingly. The observed kinematic hardening in CP-Cu is crucial for metal forming processes, as pre-straining induces directional strengthening and it also influences fatigue performance in cyclic-loaded components by reducing reverse loading resistance.

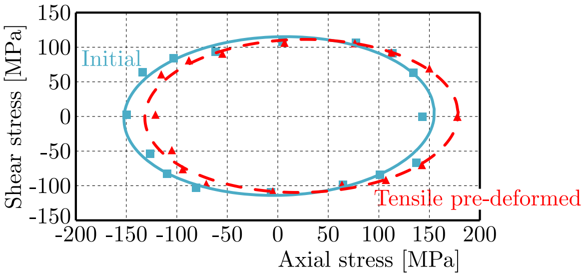

Fig. 6. Comparison of yield surfaces for pure copper: initial vs. after tensile pre-deformation.

Figure 7 illustrates the yield surfaces of CP-Cu following pre-deformation resulting from monotonic tension coupled with proportional torsion-reverse-torsion cyclic loading. These yield surfaces are evaluated against the initial yield surface of the material in its as-received condition (represented by a continuous line). The applied preloading leads to either anisotropic hardening or softening, influenced by the amplitude and frequency of the torsional strain during pre-deformation. For a torsional strain amplitude of ±0.1 % at a frequency of 0.5 Hz, the tensile

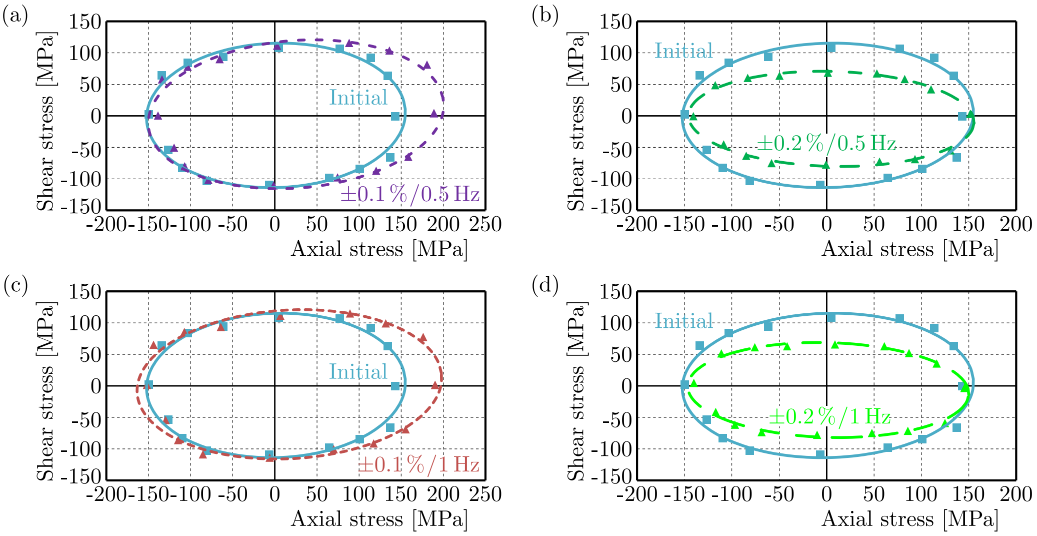

Fig. 7. Initial and pre-deformed yield surfaces of CP-Cu under combined tension and cyclic torsion (±0.1 % and ±0.2 % strain amplitudes, 0.5 Hz and 1 Hz frequencies).

yield stress increases by approximately 46 MPa compared to the initial yield surface, while yield stresses in other directions remain largely unchanged (Fig. 7a). The observed anisotropic hardening is likely linked to a more uniform dislocation distribution and the formation of low-energy dislocation structures, such as subgrain formation, which enhance resistance to plastic deformation in particular directions. This resulted in an expansion of the initial yield surface in the tensile direction, reflecting an increased yield strength across tensile dominated stress paths. A similar trend is observed when the frequency is increased to 1 Hz (Fig. 7c), suggesting that the low-amplitude cyclic torsion predominantly reinforces the material in the axial stress direction. Conversely, for a torsional strain amplitude of ±0.2 % at 0.5 Hz, the yield surface exhibits a reduction in the shear stress direction by 32 MPa–38 MPa, while axial stress values remain comparable to those of the initial yield surface (Fig. 7b). The observed anisotropic softening can be associated with shear band formation, dislocation glide along specific planes, and localized microstructural rearrangements due to large shear strains (Gazder *et al.*, 2006), which may reduce the material's resistance to shear loading. Increasing the frequency to 1 Hz produces similar results, with a decrease in shear stress and a negligible change in the axial stress (Fig. 7d). This indicates that higher torsional strain amplitudes primarily weaken the material in the shear direction without significantly affecting axial properties. When the frequency increases from 0.5 Hz to 1 Hz for either torsional strain amplitude (±0.1 % or ±0.2 %), the yield surface changes remain consistent, emphasizing that the cyclic torsion strain amplitude has a more pronounced impact on the yield surface evolution than the frequency. Regardless of the pre-deformation conditions, the compressive yield stress values exhibit minimal variation compared to the initial state, thus indicating that the compressive response is less sensitive to the combined tension-cyclic torsion pre-deformation.

These findings highlight the complex interplay of the strain amplitude, the frequency, and the stress direction in determining the anisotropic evolution of the yield surface. The behaviour of CP-Cu under combined preloading reflects its unique response, which may be influenced by factors such as dislocation interactions, texture development, and a strain path. Although similar studies have explored the yield surface evolution in different materials, variations in material properties, microstructures, and loading conditions make direct comparisons challenging. This highlights the importance of tailored investigations for specific materials and preloading scenarios to fully understand their mechanical responses.

The coefficients of the Szczepiński yield equation were calculated using the least squares method to fit the experimental data and describe the elliptical yield surface of the tested material.

This approach minimizes the sum of squares of the distances between the experimental yield points and the approximation curve, ensuring an optimal representation of the yield surface. Table 3 summarizes the fitting errors for each yield surface determined during the analysis. The fitting error values were minimal across all cases, demonstrating a high degree of accuracy in matching the experimental data with the fitted ellipses. These low errors validate the reliability and precision of the Szczepiński anisotropic yield criterion in approximating the yield behaviour of the material. The accuracy of the fitting not only confirms the robustness of the Szczepiński model but also highlights its ability to account for the material's anisotropy effectively. By closely representing the experimental data, the model captures the features of the yield surface evolution, such as the influence of pre-deformation, stress directionality, and anisotropic hardening or softening effects. This agreement further highlights the suitability of the Szczepiński criterion for characterizing the complex mechanical behaviour of the tested material under multiaxial stress states, providing a reliable foundation for predictive modelling and material design.

Table 3. Yield surfaces fitting errors for CP-Cu in as-received state and after pre-deformation.

As-received	Monotonic tension deformed	±0.1 % at 0.5 Hz deformed	±0.2 % at 0.5 Hz deformed	±0.1 % at 1 Hz deformed	±0.2 % at 1 Hz deformed
1.95E-01	1.01E-01	1.58E-01	7.18E-02	1.63E-01	8.77E-02

Figure 8 highlights the evolution of the elliptical parameters representing the yield surface (YS) of CP-Cu in the pre-deformed state compared to the as-received state. Pre-deformation through monotonic tension, represented by 0 % cyclic torsion strain amplitude, shows minimal deviations in the axis ratio relative to the yield surface of the material in the as-received state (1.34). However, the combined tension-cyclic torsion pre-deformation significantly alters

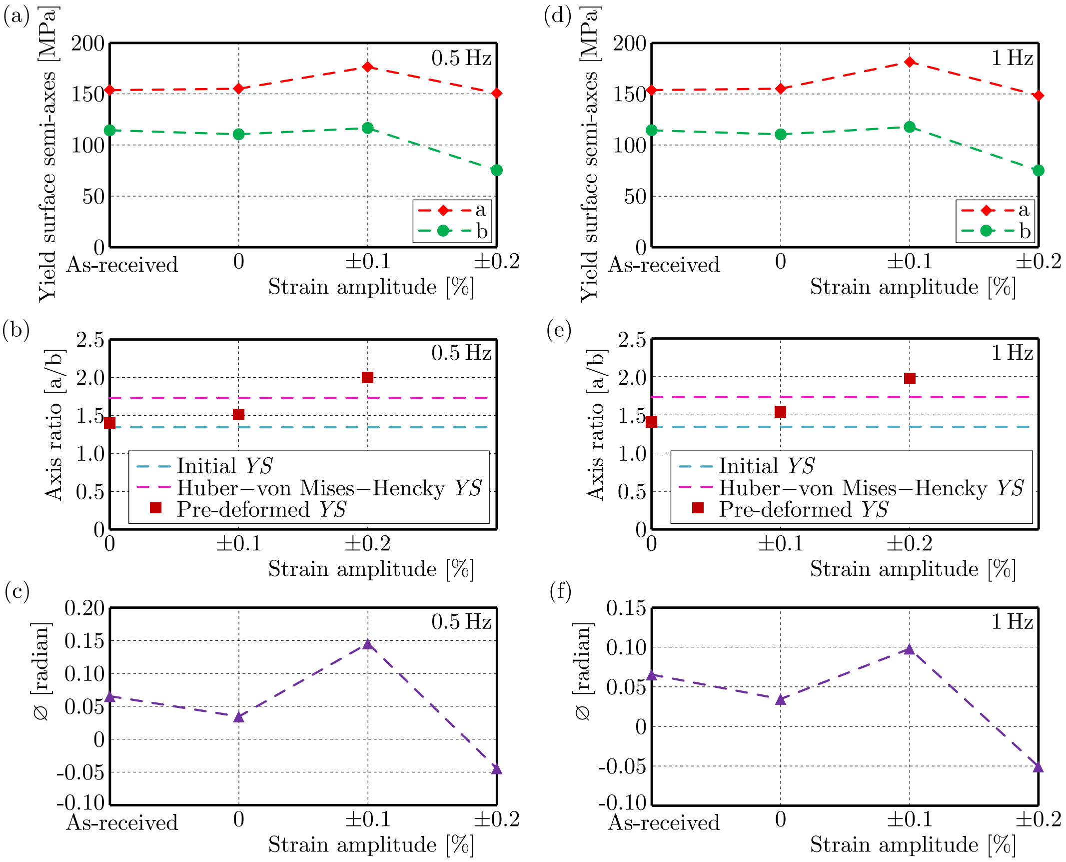

Fig. 8. CP-Cu yield surface parameters evolution caused by tension and combined tension-cyclic torsion pre-deformation (±0.1 % and ±0.2 % strain amplitudes, 0.5 Hz and 1 Hz frequencies).

the axis ratio, with higher values observed at both 0.5 Hz and 1 Hz cyclic torsion frequencies (Figs. 8b and 8e). The highest axis ratio, reaching 2, occurs after pre-deformation with a cyclic torsion strain amplitude of ±0.2 % at 0.5 Hz, indicating substantial anisotropic behaviour.

The rotation angle (Ø) of the YS-axes with respect to the (σ_{xx}, τ_{xy}) coordinate system further reflects the influence of pre-deformation. As shown in Figs. 8c and 8f, monotonic tension pre-deformation results in near-zero rotation, signifying minimal distortion in the YS orientation. In contrast, the combined tension-cyclic torsion pre-deformation induces distinct rotations: positive angles (counter-clockwise) for a cyclic torsion strain amplitude of ±0.1 % and negative angles (clockwise) as the strain amplitude increases to ±0.2 % at both 0.5 Hz and 1 Hz frequencies. These rotations highlight the directional sensitivity of anisotropic behaviour induced by cyclic torsion and its dependence on strain amplitude.

Figure 9 presents a further analysis of the YS centre positions, emphasizing the role of back stress components in pre-deformed materials. In the as-received state, the YS centre aligns closely with the origin, reflecting minimal back stress. However, pre-deformation through monotonic tension and combined tension-cyclic torsion at ±0.1 % strain amplitude shows a significant shift in the YS centre, indicating elevated back stress. In contrast, the combined tension-cyclic torsion at higher strain amplitudes (±0.2 %) results in minimal back stress, suggesting a redistribution of internal stresses. The observed back stress arises from dislocation interactions, including the accumulation of geometrically necessary dislocations (GNDs) and their ability to impede further dislocation motion. These interactions create localized high-stress regions that influence the material's plastic behaviour. The findings emphasize the interplay between dislocation structures, strain amplitude, and the stress state in shaping the yield surface evolution of CP-Cu.

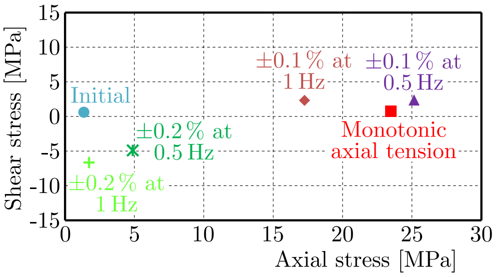

Fig. 9. Centre of yield surfaces of CP-Cu in as-received and pre-deformed states.

Figure 10 presents a comprehensive visualization of the evolution of the initial yield surface in the axial-shear stress space, derived from experimental data following material pre-deformation at frequencies of 0.5 Hz and 1 Hz. The results reveal distinct yield surface shapes and significant variations in their dimensions depending on the pre-deformation loading conditions. For monotonic tension combined with cyclic torsion at a strain amplitude of ±0.1 %, the yield surfaces at both frequencies exhibit the largest dimensions among all loading conditions. This indicates that even at a low strain amplitude, cyclic torsion induces pronounced hardening effects in the material.

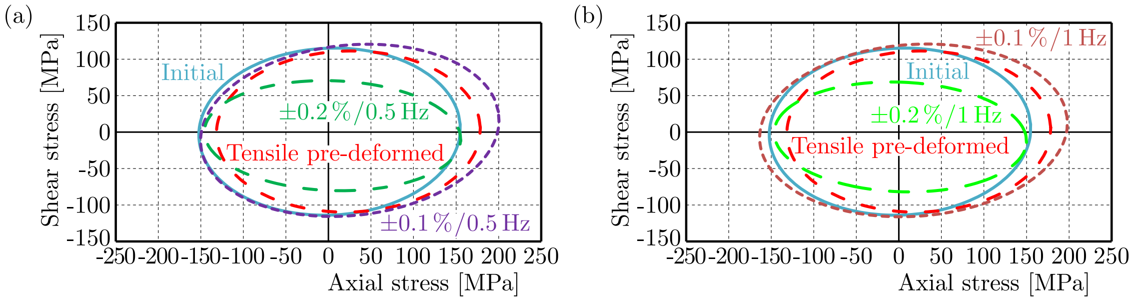

Fig. 10. Comparison of CP-Cu yield surfaces in as-received state and after pre-deformation.

A detailed examination of the yield surfaces highlights two primary hardening mechanisms: kinematic and isotropic. After the monotonic tension pre-deformation, the yield surface shifts in the direction of axial pre-deformation. This translation indicates kinematic hardening, which reflects the material's increased resistance to plastic flow in the pre-deformation direction, likely due to the accumulation of dislocations and directional stress-induced anisotropy. On the other hand, when cyclic torsion (±0.1 % strain amplitude) is introduced during monotonic tensile pre-deformation, nearly isotropic hardening is observed in comparison to the monotonic tensile pre-deformed yield surface. This is demonstrated by the expansion of the yield loci compared to those resulting from monotonic tension alone. The presence of a small cyclic torsion facilitates a more distributed microstructural rearrangement, leading to an overall increase in the material strength across all stress directions. This effect is consistent across both frequencies (0.5 Hz and 1 Hz), emphasizing that the strain amplitude, rather than the frequency, is the dominant factor influencing isotropic hardening.

Furthermore, the analysis of yield surface shapes highlights a clear dependency on the preloading direction. The directional nature of pre-deformation, whether purely axial or combined with torsional components, governs the stress distribution and subsequent yield surface dimensions. The axial preloading emphasizes anisotropic hardening effects, while the addition of small torsional components promotes more uniform strengthening across stress states. However, a larger torsional component during axial preloading led to anisotropic softening. These findings emphasize the complex relationships between preloading conditions, the strain path, and the resulting hardening/softening mechanisms. Understanding these effects is essential for modelling the mechanical behaviour of CP-Cu accurately and optimizing its performance in applications involving multiaxial loading and pre-deformed states. While the explanation of hardening or softening behaviour of the yield surface of CP-Cu is supported by deformation theories and previous research, microstructural investigations will be essential for further validation in subsequent studies.

4. Concluding remarks

The comprehensive investigation into the yield surface evolution of commercially pure copper under monotonic tension and combined tension-cyclic torsion loading has provided insights into its mechanical response and hardening/softening behaviour. The key findings are summarized as follows:

- Pre-deformation, whether through monotonic tension or combined tension-cyclic torsion, significantly changes the shape, size, and position of the yield surface. Monotonic tension induces kinematic hardening, translating the yield surface in the pre-strain direction, while combined tension-cyclic torsion (±0.1 % strain amplitude) introduces anisotropic hardening, in comparison to the initial yield loci. Higher torsional strain amplitude during pre-deformation (±0.2 %) leads to anisotropic softening, especially in the shear stress direction, reflecting the complex interplay between the loading direction and the strain path.
- The cyclic torsion strain amplitude significantly impacts the material's mechanical response, with higher amplitudes (±0.2 %) causing pronounced softening effects, maybe due to increased dislocation interactions and microstructural rearrangements. Conversely, the cyclic torsion frequency has a comparatively lesser impact, with the yield surface evolution remaining consistent across frequencies (0.5 Hz and 1 Hz). This underscores strain amplitude as the dominant factor influencing the hardening or softening mechanisms in CP-Cu.
- The initial yield surface of the as-received copper at 0.01 % and 0.005 % offset strain demonstrates anisotropic behaviour, as indicated by deviations from the isotropic Huber–von Mises–Hencky (HMH) criterion. Additionally, the yield surface is influenced by the

specific definition of the yield used. This anisotropy is likely a result of the material's manufacturing process or specimen machining, which can introduce crystallographic textures, residual stresses, and microstructural inconsistencies. Further evidence of elastic anisotropy is seen in the variations of Young's modulus across different loading directions, highlighting the need to account for these factors when modelling the material's behaviour.

- The Szczepiński anisotropic yield criterion, fitted using the least squares method, effectively captured the experimental yield surfaces with minimal fitting errors. This model accurately represents anisotropic and isotropic hardening behaviours, providing a robust framework for predicting the mechanical response of CP-Cu under multiaxial stress states.

Acknowledgments

The authors would like to express their gratitude to the technical staff Mr M. Wyszkowski and Mr A. Chojnacki for their kind help during the experimental part of this work.

This work has been supported by the National Science Centre through the Grant No 2019/35/B/ST8/03151.

References

1. Czerwinski, F. (2024). Aluminum alloys for electrical engineering: a review. *Journal of Materials Science*, *59*(32), 14847–14892. https://doi.org/10.1007/s10853-024-09890-0
2. Davis, J.R. (2001). *Copper and copper alloys*. In J.R. Davis (Ed.), Alloying: Understanding the basics (pp. 457–494). ASM International. https://doi.org/10.31399/asm.tb.aub.t61170457
3. Dietrich, L., & Kowalewski, Z.L. (1997). Experimental investigation of an anisotropy in copper subjected to predeformation due to constant and monotonic loadings. *International Journal of Plasticity*, *13*(1–2), 87–109. https://doi.org/10.1016/S0749-6419(97)00002-8
4. Dubey, V.P., Kopec, M., Łazińska, M., & Kowalewski, Z.L. (2023). Yield surface identification of CP-Ti and its evolution reflecting pre-deformation under complex loading. *International Journal of Plasticity*, *167*, Article 103677. https://doi.org/10.1016/j.ijplas.2023.103677
5. Gazder, A.A., Dalla Torre, F., Gu, C.F., Davies, C.H.J., & Pereloma, E.V. (2006). Microstructure and texture evolution of bcc and fcc metals subjected to equal channel angular extrusion. *Materials Science and Engineering: A*, *415*(1–2), 126–139. https://doi.org/10.1016/j.msea.2005.09.065
6. Guschlbauer, R., Momeni, S., Osmanlic, F., & Körner, C. (2018). Process development of 99.95% pure copper processed via selective electron beam melting and its mechanical and physical properties. *Materials Characterization*, *143*, 163–170. https://doi.org/10.1016/j.matchar.2018.04.009
7. Hecker, S.S. (1971). Yield surfaces in prestrained aluminum and copper. *Metallurgical Transactions*, *2*(8), 2077–2086. https://doi.org/10.1007/BF02917534
8. Helling, D.E., Miller, A.K., & Stout, M.G. (1986). An experimental investigation of the yield loci of 1100-0 aluminum, 70:30 brass, and an overaged 2024 aluminum alloy after various prestrains. *Journal of Engineering Materials and Technology*, *108*(4), 313–320. https://doi.org/10.1115/1.3225888
9. Jadhav, S.D., Goossens, L.R., Kinds, Y., Van Hooreweder, B., & Vanmeensel, K. (2021). Laser-based powder bed fusion additive manufacturing of pure copper. *Additive Manufacturing*, *42*, Article 101990. https://doi.org/10.1016/j.addma.2021.101990
10. Jiang, Q., Zhang, P., Yu, Z., Shi, H., Wu, D., Yan, H., Ye, X., Lu, Q., & Tian, Y. (2021). A review on additive manufacturing of pure copper. *Coatings*, *11*(6), Article 740. https://doi.org/10.3390/coatings11060740
11. Kopec, M., Dubey, V.P., Pawlik, M., Wood, P., & Kowalewski, Z.L. (2024). Experimental identification of yield surface for additively manufactured stainless steel 316L under tension–compression-torsion conditions considering its printing orientation. *Manufacturing Letters*, *41*, 28–32. https://doi.org/10.1016/j.mfglet.2024.07.003

12. Lai, Z., Mai, Y., Song, H., Mai, J., & Jie, X. (2022). Heterogeneous microstructure enables a synergy of strength, ductility and electrical conductivity in copper alloys. *Journal of Alloys and Compounds*, *902*, Article 163646. https://doi.org/10.1016/j.jallcom.2022.163646

13. Li, M., & Zinkle, S.J. (2012). 4.20 – Physical and mechanical properties of copper and copper alloys. *Comprehensive Nuclear Materials*, *4*, 667–690. https://doi.org/10.1016/B978-0-08-056033-5.00122-1

14. Liu, C., Yang, X., Ding, Y., Li, H., Wan, S., Guo, Y., & Li, Y. (2023). The yielding behavior of TU00 pure copper under impact loading. *International Journal of Mechanical Sciences*, *245*, Article 108110. https://doi.org/10.1016/j.ijmecsci.2023.108110

15. Mair, W.M., & Pugh, H.Ll.D. (1964). Effect of pre-strain on yield surfaces in copper. *Journal of Mechanical Engineering Science*, *6*(2), 150–163. https://doi.org/10.1243/JMES_JOUR_1964_006_025_02

16. Pan, Q., Jing, L., & Lu, L. (2023). Enhanced fatigue endurance limit of Cu through low-angle dislocation boundary. *Acta Materialia*, *244*, Article 118542. https://doi.org/10.1016/j.actamat.2022.118542

17. Pingale, A.D., Owhal, A., Katarkar, A.S., Belgamwar, S.U., & Rathore, J.S. (2021). Recent researches on Cu-Ni alloy matrix composites through electrodeposition and powder metallurgy methods: A review. *Materials Today: Proceedings, 3rd International Conference on Advances in Mechanical Engineering and Nanotechnology*, *47*(Part 11), 3301–3308. https://doi.org/10.1016/j.matpr.2021.07.145

18. Scudino, S., Unterdörfer, C., Prashanth, K.G., Attar, H., Ellendt, N., Uhlenwinkel, V., & Eckert, J. (2015). Additive manufacturing of Cu–10Sn bronze. *Materials Letters*, *156*, 202–204. https://doi.org/10.1016/j.matlet.2015.05.076

19. Semih, Ö., & Recep, A. (2023). Investigation of microstructure, machinability, and mechanical properties of new-generation hybrid lead-free brass alloys. *High Temperature Materials and Processes*, *42*(1), Article 20220263. https://doi.org/10.1515/htmp-2022-0263

20. Stepanov, N.D., Kuznetsov, A.V., Salishchev, G.A., Raab, G.I., & Valiev, R.Z. (2012). Effect of cold rolling on microstructure and mechanical properties of copper subjected to ECAP with various numbers of passes. *Materials Science and Engineering: A*, *554*, 105–115. https://doi.org/10.1016/j.msea.2012.06.022

21. Sundar Singh Sivam, S.P., Rajendran, R., & Harshavardhana, N. (2023). An investigation of stored energy in uniaxial and biaxial directional rolling on mechanical properties and microstructure of pure copper. *Mechanics Based Design of Structures and Machines*, *51*(5), 2831–2843. https://doi.org/10.1080/15397734.2021.1909484

22. Vahedi Nemani, A., Ghaffari, M., Sabet Bokati, K., Valizade, N., Afshari, E., & Nasiri, A. (2024). Advancements in additive manufacturing for copper-based alloys and composites: A comprehensive review. *Journal of Manufacturing and Materials Processing*, *8*(2), Article 54. https://doi.org/10.3390/jmmp8020054

23. Wu, X.X., San, X.Y., Gong, Y.L., Chen, L.P., Li, C.J., & Zhu, X.K. (2013). Studies on strength and ductility of Cu–Zn alloys by stress relaxation. *Materials & Design*, *47*, 295–299. https://doi.org/10.1016/j.matdes.2012.12.020

24. Zhang, W.-J., Huang, L., Mi, X.-J., Xie, H.-F., Feng, X., & Ahn, J.H. (2024). Researches for higher electrical conductivity copper-based materials. *cMat*, *1*(1), e13. https://doi.org/10.1002/cmt2.13

25. Zhou, M., Geng, Y., Zhang, Y., Ban, Y., Li, X., Jia, Y., Liang, S., Tian, B., Liu, Y., & Volinsky, A.A. (2023). Enhanced mechanical properties and high electrical conductivity of copper alloy via dual-nanoprecipitation. *Materials Characterization*, *195*, Article 112494. https://doi.org/10.1016/j.matchar.2022.112494

Manuscript received January 26, 2025; accepted for publication March 10, 2025;
published online July 7, 2025.

JOURNAL OF THEORETICAL
AND APPLIED MECHANICS
63, 3, pp. 571–582, Warsaw 2025
https://doi.org/10.15632/jtam-pl/202927

3D STABILITY ANALYSIS OF THE POKER CHIP DETACHMENT PROBLEM

András Levente HORVÁTH*, Attila KOSSA

Department of Applied Mechanics, Faculty of Mechanical Engineering,
Budapest University of Technology and Economics, Műegyetem rkp. 3., H-1111, Budapest, Hungary
*corresponding author, *levente.horvath@mm.bme.hu*

Dry adhesives utilizing the Van der Waals forces are the focus of many applications. Detachment phenomena are especially important to explore in this field. Most previous research was done using axisymmetric models. However, several important cases cannot be analyzed with this simplification. In this work, we build a 3D model to examine the classical "poker chip" problem. We analyze the propagation stability for detachments initiating at the edge of the chip. Novel stability maps are presented for the investigated non-axisymmetric cases. The effect of compressibility and propagation front shape are presented as well.

Keywords: poker chip; adhesion; stability; energy release rate; finite element analysis.

1. Introduction

Throughout history, people have used different types of adhesives. Most commonly, these connect two surfaces by chemical or mechanical bonding mechanisms (Bricotte *et al.*, 2024). In recent decades, another type, called "dry adhesion", has gained the interest of several researchers. This type of adhesion is based on the Van der Waals forces, for which two surfaces need to get in extremely close contact. This type of adhesive has several practical benefits compared to other types. These are well presented by numerous species of animals – mostly reptiles and insects – which utilize this effect (Gorb & Varenberg, 2007; Autumn *et al.*, 2002; Arzt *et al.*, 2003). Among them, the gecko has the largest body mass and remarkable climbing abilities. Geckos are able to rapidly climb smooth and rough vertical surfaces, even when the surface is wet. Their feet strongly bond to the surface, but they can also quickly and reversibly detach from the surface. Animals achieve this by having hierarchical spatula-like hair structures on their feet, allowing them to get sufficiently close to the other surface to exploit the Van der Waals forces. These structures are well visualized in (Varenberg *et al.*, 2010) where several images of various animals are presented using a scanning electron microscope.

Artificial structures mimicking gecko-like adhesion are mostly manufactured from polymer-like materials. These structures have simpler geometry compared to the gecko's feet, utilizing patterns made of pillars. The shape of the contact geometry has a notable effect on adhesion strength and has been studied by many researchers. Hensel *et al.* (2018) studied the effect of the

---

Ministry of Science and Higher Education
Republic of Poland

The publication has been funded by the Polish Ministry of Science and Higher Education under the Excellent Science II programme "Support for scientific conferences".
The content of this article was presented during the 40th Danubia-Adria Symposium on Advances in Experimental Mechanics, Gdańsk, Poland, September 24–27, 2024.

shape of artificial pillars on adhesion in such structures. Almost all previous research assumes axisymmetric geometry. Hao *et al.* (2024) investigated the importance of considering the effect of nonlinear material behavior and compressibility depending on layer thickness with such a model.

To understand these structures, a better description of the underlying mechanical phenomena is needed. In general, adhesion has been studied using numerical and analytical tools. Both approaches often used the toolset of linear fracture mechanics (Schneider & Swain, 2015; Benvidi & Bacca, 2021). The FEM is well suited for calculating the stored strain energy (U) in the system for arbitrary geometry and material parameters.

Gent and Lindley's (1957) work from the last century is often considered to be the first important contribution regarding the "poker chip" problem. Their research was concerned with material failure, showing that under tensile load, rubber specimens fail under surprisingly low loads due to the triaxial stress state. A decade later Lindsey (1967) published analytical approximations to the normal stress distribution. Since then, several other approximate solutions have been developed, but all of them rely on significant assumptions, like the chip being "thin" and the material being perfectly incompressible (Movchan *et al.*, 2021). They are also limited to axisymmetric cases only. Several other researchers used numerical tools to investigate the internal cracks and cavitation in the material.

The poker chip problem is commonly used to investigate adhesive phenomena. In this case, the interfacial debonding is considered. The poker chip arrangement (see Fig. 1) was used in numerous studies focusing on separation as one of the simplest geometries. Despite being seemingly simple, this setup shows strongly nonlinear behavior regarding, e.g., stress distributions and stored elastic energy. Many more complex geometries (e.g., mushroom, funnel-tip) are used in practice. Their behavior is expected to be even more complex. Thus, it is important to understand the simplest available case as well as possible.

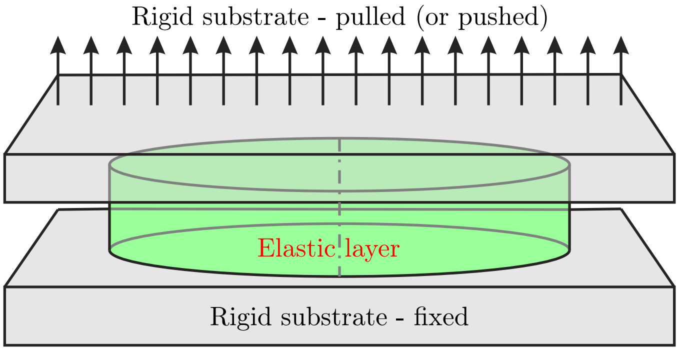

Fig. 1. Poker chip setup.

The most important aspect of previous results for this paper is the importance of the chip thickness and Poisson's ratio regarding detachment stability. The importance and effect of these two parameters are analyzed in detail in (Horváth & Kossa, 2024), where they used an axisymmetric model. They presented stability maps for the axisymmetric edge and center detachment cases. It was shown that the region of stable detachment is narrowed as the thickness of the chip is increased, and there exists a critical thickness above which no stable detachment occurs. Increasing volumetric compressibility slightly decreased the size of the stable zone in these cases.

Local detachment initiated on the outer edge of the poker chip often does not propagate in an axisymmetric way in reality. This can also be observed on the measurements made by Balijepalli *et al.* (2017). In their work, two cases are shown where the detachment initiates from the edge of the chip. In one case the detachment front resembles a circle-like shape, in the other it is closer to straight line. This cannot be investigate with axisymmetric models, which are used in previous studies. The aim of our work is to explore three-dimensional detachment cases initiated on the edge of the poker chip. We created a 3D numerical model to investigate these previously unexplored cases. We present three stability maps, demonstrating the effect of compressibility as well as shape of the propagating detachment. These basic crack front shapes reveal the previously unknown fundamentals of 3D detachments. Our presented methodology can be extended for more complex, arbitrary detachment propagation fronts.

Section 1 of this article provides an introduction to the topic and summarizes the related literature. Section 2 presents the poker chip problem and the quantities important for our investigation. Section 3 describes the created numerical model and the process used to determine stability. The topic of automated mesh generation is touched upon as well. In Section 4 the obtained novel results are presented, most importantly the stability maps for the investigated cases. Section 5 summarizes the new results. Additionally, the distribution of normal stresses along the contact interface is illustrated in the Appendix at the end of the manuscript.

2. Problem description

The poker chip setup involves a cylindrical elastic solid layer, which is fixed between stiff plates. In real measurements, the elastic layer is made of some polymer, and the plates (substrate) are made of steel. The plates are moved axially, either compressing or pulling the elastic specimen – most research is concerned with the tension case. As the plates are pulled apart, the elastic material may fail due to void nucleation and growing internal cracks. Several papers discussed this in great detail, our work is not concerned with these phenomena (Asp *et al.*, 1995; Kumar & Lopez-Pamies, 2021).

Alternatively, the elastic layer can start to detach from the substrate due to interfacial failure. This scenario is adopted by numerous researchers to study adhesion-related phenomena (Balijepalli *et al.*, 2016). Our work is concerned with this case as well, with detachment propagation stability in the focus. We utilize linear fracture mechanics to study this phenomenon; thus, detachment is modeled as a crack. This approach has been used in multiple previous studies (Antunes *et al.*, 1999; Millwater *et al.*, 2016). The concept of energy release rate is applied. The energy release rate (G) is defined as the decrease of potential energy (π) per unit of contact area (A) decrease:

$$G = \frac{\partial \pi}{\partial A}. \tag{2.1}$$

Note that some papers write G using derivative according to the crack length (which is denoted by a in some papers). This causes the sign of the expression to change. However, in this paper we follow the form adopted by the researchers concerned with detachment and define the energy release rate as per Eq. (2.1).

As a critical value of G is reached (the specific value depends on the strength of the adhesive bond between the surfaces), crack propagation is initiated. Stability analysis is used to determine whether additional external work is needed for the detachment to propagate further. If the detachment process is stable, then additional energy is needed. If the detachment is unstable, the decrease of potential energy will cover the energetic cost of creating the new surface. Thus, the detachment propagates further without the need for additional external work. Stability is determined by the partial derivative of the energy release rate. Importantly, detachment stability does not depend on the type and strength of adhesion between the poker chip and the rigid plate. We investigate a displacement-driven case, thus the potential energy (π) will be equal to the stored strain energy in the system (U). For this reason, investigating the strain energy is sufficient for all of our calculations. Thus, the condition for stable detachment propagation in the displacement-driven case is

$$0 < \frac{\partial G}{\partial A} = \frac{\partial^2 \pi}{\partial A^2} = \frac{\partial^2 U}{\partial A^2}. \tag{2.2}$$

Most previous research focuses on axisymmetric detachments, as this considerably simplifies numerical as well as analytical calculations. In this paper, however, we will not use this assumption, and we will investigate two more general detachment cases. In both cases, detachment is initiated at a single point on the outer edge of the poker chip. In the first case, the detachment propagation front is a straight line. In the second case, the detachment front is circular.

We investigate this problem with numerical tools – FEM specifically. This allows us to investigate quantities that are difficult (or impossible) to measure during experiments. The stored strain energy (U) is easily obtained with FE calculations, making stability evaluation possible.

Our approach matches the method widely adopted by the researchers of adhesion. This makes our results easier to compare to other studies. Detachment is modeled as a crack, but more complex methods, like XFEM or the cohesive zone mode, are not needed for our investigation.

3. Numerical model

Previous research shows that the governing parameters for stability are the relative chip thickness and Poisson's ratio. The polymers used to create artificial structures with dry adhesive properties are usually nearly incompressible. For this reason, many researchers used incompressible models ($\nu = 0.5$). In this paper, the effect of slight compressibility is analyzed as well. The radius of the poker chip is denoted by a. The thickness of the chip is given relative to the radius and it is denoted by h/a. The detachment is characterized by its length along the axis of symmetry in both cases; this length is also compared to the radius and denoted by c/a. The radius is chosen to be $a = 1\,\text{mm}$ during our calculations. The parameters of the model are visualized in Fig. 2. "A" denotes the detachment initiation point, "B" is the last point to detach, and "C" marks the current intersection of the detachment front with the axis of symmetry.

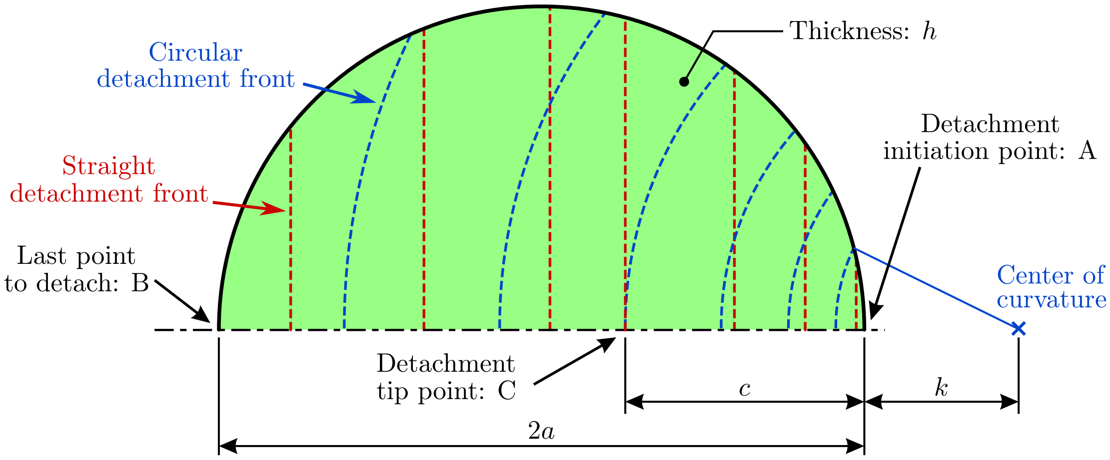

Fig. 2. Model parameters.

As mentioned previously, we consider a case with a straight detachment front and a case with a circular detachment front. Detachment is initiated from the outer edge of the chip. We can describe a circular front with an arbitrary radius using parameter k/a, denoting the dimensionless distance between the detachment initiation point and the center of the circular detachment front. According to the geometry, $0 \leq k/a \leq \infty$. The straight front corresponds to the $k/a = \infty$ limit case. The other investigated case will be the $k/a = 0$ limit, where the initiation point coincides with the center of the circular front.

The chip is modeled with an isotropic linear elastic material, as material nonlinearities can be neglected due the presence of only small strains and deformations in the system. Note that Young's modulus acts as a constant multiplier on U. As derivatives are taken according to Eq. (2.2), it has no influence on the stability properties. During our simulations, we chose $E = 1\,\mathrm{MPa}$.

The non-detached part of the interface is assumed to be perfectly bonded to the rigid substrate – this assumption is also commonly used in the literature to model dry (or other types of) adhesive contact. The substrate material is assumed to be rigid, as commonly used in the literature. The no-slip boundary condition is applied to the non-detached part of the elastic material, which represents perfect bonding to the substrate. The detached part is free to deform, thus no boundary condition is applied there. As the contact with the substrate is well-modeled by the boundary condition and the substrate is assumed to be rigid, it can be fully omitted from the FE model. The meshed model is illustrated in Fig. 4.

The upper interface is prescribed to move by $\overline{u}$ vertically (see Fig. 1). The particular value has no effect on stability, and it is chosen to be $\overline{u} = h/100$ in all simulations.

We built our 3D finite element model in ABAQUS (Dassault Systèmes, 2022). Multiple element types are available for modeling structural 3D problems. After evaluating the options, we predominantly used hex-shaped C3D8(H) elements, but in some cases a few wedge-shaped C3D6(H) elements were also needed to create a well structured mesh. These are general purpose, deformation based linear elements with 8 or 6 nodes respectively. As per ABAQUS recommendations, hybrid formulation was used if Poisson's ratio was greater or equal to 0.495. The problem has planar symmetry, thus a half-model is used to reduce computational costs.

In ABAQUS, our calculation is realized in two simulation steps. The initial step defines the symmetry boundary condition (corresponding to the half model) as well as the no-slip (fixed 0 displacement and rotation) boundary condition on the non-detached part of the interface. These boundary conditions are propagated to the second step, where the prescribed $\overline{u}$ displacement is applied to the top interface.

3.1. Stability calculation

Stability is determined according to Eq. (2.2). The value of U is obtained at several values of detachment length (c/a). Assuming $a = 1$, the contact area (A) is calculated from the detachment length as

$$A = \begin{cases} \dfrac{1}{4}\left(-\sin\left(2\,\mathrm{acos}\,(1-c)\right) + 2\,\mathrm{acos}\,(1-c)\right) & \text{if } \ c \le 1, \\ \dfrac{1}{4}\left(\sin\left(2\,\mathrm{acos}\,(c-1)\right) - 2\,\mathrm{acos}\,(c-1)\right) + \pi & \text{if } \ c > 1, \end{cases} \tag{3.1}$$

for the straight detachment front and as

$$A = \frac{\pi c^2}{3} - 0.5\sqrt{c^2 \cdot (2-c)(c+2)} + \mathrm{acos}\left(1 - \frac{c^2}{2}\right), \tag{3.2}$$

for the circular detachment front (assuming $k/a = 0$).

From these relations, the value of $U(A)$ is determined at a series of points. This needs to be differentiated twice to investigate stability. Although several approaches are available to do this, we chose to fit a spline of sufficiently high order on the points of $U(A)$, then carried out the differentiation step on the spline. The exact method for interpolation does not have a notable effect on the obtained values.

These numerical differentiation steps generate small numerical "noise" by nature. This causes the investigated function to oscillate. To mitigate this issue, we applied a Savitzky–Golay filter to the 2nd derivative. After the filtering, the dataset becomes sufficiently smooth for stability evaluation.

The process of stability evaluation is illustrated in Fig. 3 for one particular case (straight detachment front, $h/a = 0.1$, $\nu = 0.5$). $\overline{U}$ and $\overline{G}$ denote the normalized stored strain energy and energy release rate, calculated as

$$\overline{U} = \frac{U}{U_{\max}} \quad \text{and} \quad \overline{G} = \frac{G}{G_{\max}}. \tag{3.3}$$

Stable regions are denoted by a green background, and unstable regions are shown in red.

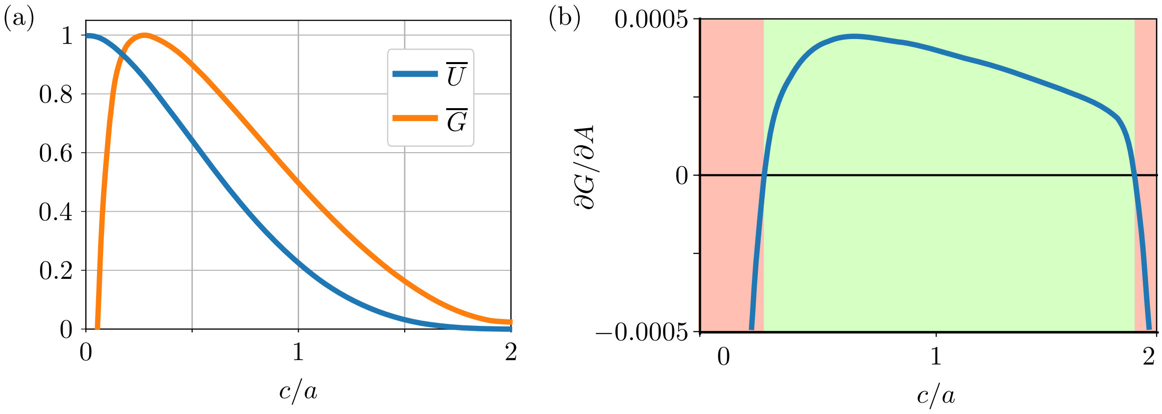

Fig. 3. Illustration of the stability evaluation process (straight detachment front, $h/a = 0.1$, $\nu = 0.5$): (a) normalized strain energy and energy release rate; (b) stability map, green is stable, red is unstable.

3.2. About mesh generation

For creating stability maps with sufficient resolution, several thousands of simulations were needed. For this reason, it was necessary to fully automate mesh generation. The parameters, which influence mesh generation are summarized in Table 1.

Table 1. Parameters describing individual simulations.

Parameter	Possible value
Detachment front shape	Straight or circular
Chip thickness (h/a)	0.01 ... 1.5
Poisson's ratio (ν)	0.5 or 0.48
Detachment length (c/a)	0 ... 1.99

In ABAQUS, the user can control the generated mesh by "seeding" the edges. The following principles were used during the development of the meshing strategy:

– a mesh was characterized by two numbers, one related to the minimum and one to the maximum edge length near the detachment front. These numbers are kept constant for each combination of front shape and h/a;
– the region near the detachment front needs to be the most refined, a smooth transition is needed from the mesh far away from the detachment front;
– the mesh should be well-structured near the detachment front. This means nearly brick-shaped elements with edges parallel/orthogonal to the crack front.

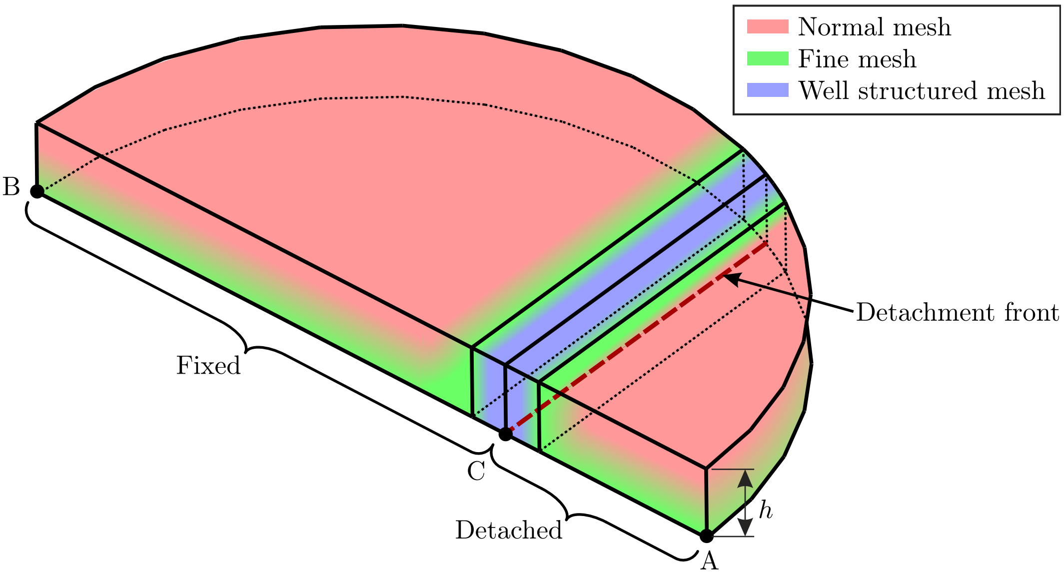

Fig. 4. Illustration of FE model and meshing strategy.

The structure of the mesh is illustrated in Fig. 4. The mesh is well structured in the vicinity of the propagation front, where smaller elements are needed to capture the nonlinear stress distributions.

It is not trivial to fulfill these requirements for the entire range of parameters. In both straight and circular front cases, the main source of problems is the intersection of the detachment front and outer edge of the elastic material. These lines intersect at very shallow angles if c/a is either too small or too large. This leads to highly distorted elements being generated or even failure to generate any mesh – both lead to errors during simulation.

While, in some cases, sharp angles cannot be avoided in the immediate vicinity of the intersection point, these alone did not lead to major issues. Some methods were applied to eliminate mesh generation issues. The meshing strategy was changed based on the value of c/a. If the detachment was very short, the entire detached area was meshed with a uniform dense mesh. As c/a got larger, the entire detached area was meshed as a transition zone. As c/a got sufficiently large, the meshing structure shown in Fig. 4 was used. As cases with almost full detachment were investigated, a similar strategy was applied to those at low values of c/a. First, the left transition zone is extended to the entire non-detached area; then, as full detachment is almost reached, the entire non-detached area is meshed with a uniform dense mesh.

The meshing parameters are chosen so a limit node number is not exceeded by any mesh for a given detachment front shape and h/a. This ensures that computational costs are kept reasonable. Some examples are shown in Table 2.

Table 2. Example node and element numbers for some cases.

Front type	h/a	c/a	Number of nodes	Number of elements
Circular ($k/a = 0$)	0.2	1.6	186802	176505
Circular ($k/a = 0$)	0.2	1.9	188716	178206
Circular ($k/a = 0$)	1.0	0.4	100672	95675
Straight ($k/a = \infty$)	0.4	1.75	99840	93467
Straight ($k/a = \infty$)	0.4	0.15	76470	70876
Straight ($k/a = \infty$)	0.7	0.3	90720	85120

4. Results

Three main cases were investigated. These are a straight detachment front with incompressible material ($\nu = 0.5$) and slightly compressible material ($\nu = 0.48$), then a circular detachment front with incompressible material. The effect of compressibility and shape of the detachment front will be investigated by comparing their respective simulations to the case with the straight detachment front and incompressible material.

The stability map obtained for the straight detachment front and incompressible material case is presented in Fig. 5. Each line for any chip thickness (h/a) is made from 200 simulations; this resolution is sufficiently dense to be drawn as a continuous line. Blue dashed lines denote the interpolated boundary of the stable domain.

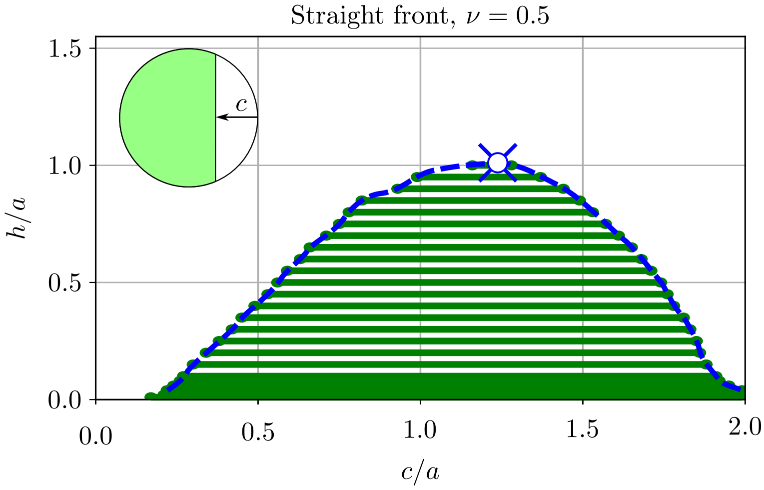

Fig. 5. Stability map for the straight detachment front and incompressible material.

We can see that for any thickness value, detachment propagates in an unstable way after initiation. This unstable region may be followed by a stable segment, and then the final part of the detachment process is unstable once again. For thin chips, the stable region covers almost the whole detachment process. As the chip gets thicker, the stable region starts later and ends sooner. After a critical value of thickness (visible as a blue “X” with a white middle point on the boundary), no stable region exists. This thickness value is denoted by h_{cr}/a, and the corresponding value of detachment length is denoted as c_{cr}/a. Based on the interpolated boundaries, we can calculate the critical values. In the current case $h_{cr} = 1.006$ and $c_{cr}/a = 1.233$. Overall, the limit points of stability follow relatively simple, monotonous trends.

The stability map for the slightly compressible case ($\nu = 0.48$) is presented in Fig. 6. Compared to the previous case, the most noticeable difference is for low thickness values ($h/a \leq 0.3$). A “dent” forms in the stable region and the trend of stability limit points is no longer monotonous. For very thin chips, stability is hard to evaluate, leading to discontinuity in the stable region. The rest of the stable region is qualitatively similar to the incompressible case but quantitatively gets smaller in every direction. This includes a decrease in critical thickness, for this case $h_{cr}/a = 0.957$ and $c_{cr}/a = 1.233$.

The stability map for the circular detachment front case is presented in Fig. 7. The general trends are the same as with the straight detachment front. The stable region is generally quantitatively smaller, but the difference is marginal. The critical thickness changes to $h_{cr}/a = 0.963$ and $c_{cr} = 1.193$. At extremely small thickness values, the stable region is wider. Overall, the change in the propagation front shape results in a surprisingly small difference regarding the stability maps.

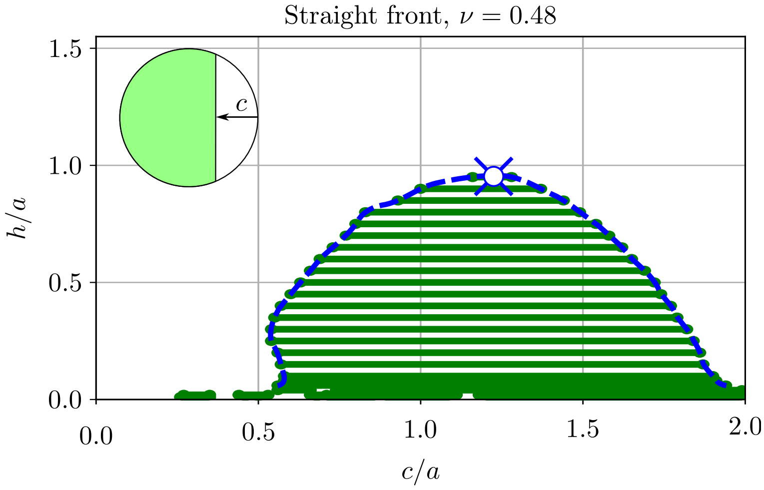

Fig. 6. Stability map for the straight detachment front and slightly compressible material.

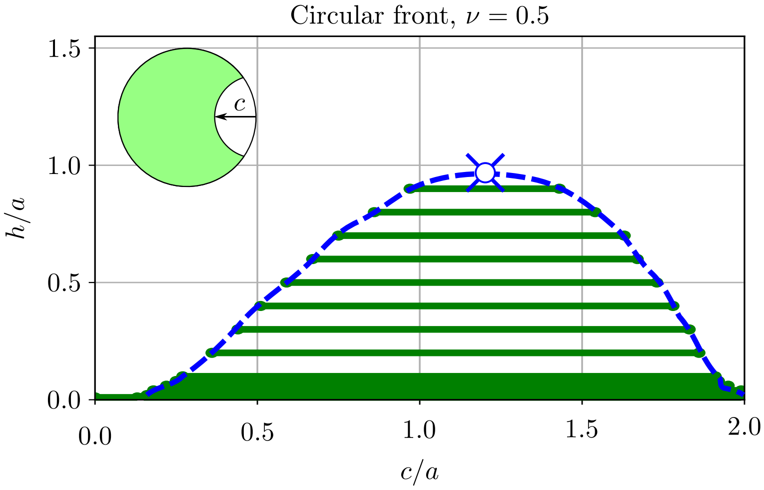

Fig. 7. Stability map for the circular detachment front and incompressible material.

4.1. Stress distributions

The stress distribution is easily obtained from the built model. The mesh is most refined near the detachment front, making the areas with the highest stress gradients the most resolved. The main focus of this paper is detachment stability, not stress distributions. However, we show some of the stress results as well to demonstrate the nonlinearities in the normal stress distributions.

Stresses are normalized by $\overline{\sigma}$, which is the average stress along the contact area. Due to the prescribed vertical displacement $\overline{u}$ on the upper rigid plate, the strain energy U stored in the elastic body is induced. In the absence of energy dissipation, this energy equals the work done by the external force system. With this, the reaction force F generated during loading can be calculated from the strain energy, from which the average normal stress along the contact surface can be calculated as

$$U = \frac{1}{2} F \overline{u} \quad \rightarrow \quad F = \frac{2U}{\overline{\sigma}} \quad \rightarrow \quad \overline{\sigma} = \frac{F}{A}, \tag{4.1}$$

where A is calculated as per Eqs. (3.1) or (3.2).

One illustration of the stress distributions is shown in Fig. 8. We can see that the shape of the crack front has no significant impact on the normal stresses along the symmetry line. The normal stress distributions along the entire contact interface are included in the Appendix.

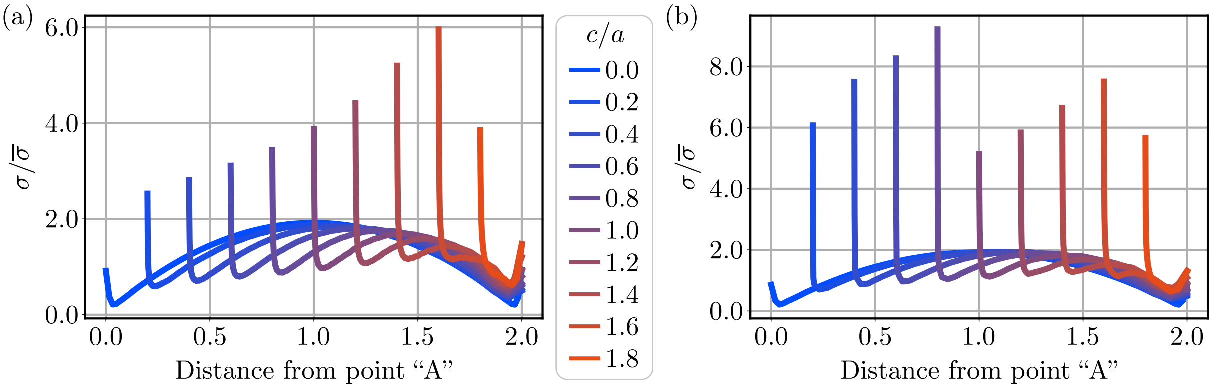

Fig. 8. Illustration of normalized normal stress distributions along the C-B line of symmetry (see Fig. 2), contact interface ($h/a = 0.2$ and $\nu = 0.5$): (a) straight detachment front; (b) circular detachment front.

5. Discussion

The detachment stability of the poker chip problem was investigated in detail using a fully 3D FE model built in ABAQUS. This allowed us to study detachment phenomena, which had previously not been investigated in the literature. In all of the cases considered, the detachment initiated from a point on the edge of the chip. In one case, the detachment front propagated as a straight line. The effect of slight compressibility was also demonstrated using this scenario. In the second case, a circular propagation front was considered.

We analyzed two different crack front shapes: straight and circular. The difference in crack front shape had only a minor effect on the stability maps – the stable region got slightly smaller for the circular front case. These can be considered as two extreme cases: the circular front's center of curvature matches the detachment initiation point. The straight front can be viewed as a circle with an infinite radius, and the center of curvature is infinitely far from the detachment initiation point. Thus, we hypothesize that a circular crack front with an arbitrary center of curvature will produce similar results and have only a minor quantitative effect on the stability of the detachment.

In all the investigated cases, the detachment was initially unstable. This unstable region may be followed by a stable region. The detachment turned unstable once again, nearing complete detachment. The width of the stable region is determined by the chip thickness (h/a). Generally, the thicker the chip gets, the narrower the stable region becomes. For very thin chips, almost the entire detachment process is stable. Above a critical thickness value (h_{cr}/a), no stable region can exist, and the detachment is fully unstable.

The effect of slight compressibility is presented. At low ($h/a \leq 0.3$) thickness values, a noticeable "dent" forms on the stability map – detachment gets stable later. This effect may be relevant for practical applications, as materials that are used to manufacture structures with dry adhesive properties show little, but not negligible, volumetric compressibility. If $h/a > 0.3$, the stable zone shrinks by a small amount.

Appendix – Example: normal stress distribution

The distribution of normal stress on the bottom interface is shown in Fig. 9. In this case $h/a = 0.2$ and $\nu = 0.5$ (these contour plots are not normalized with average stress $\overline{\sigma}$).

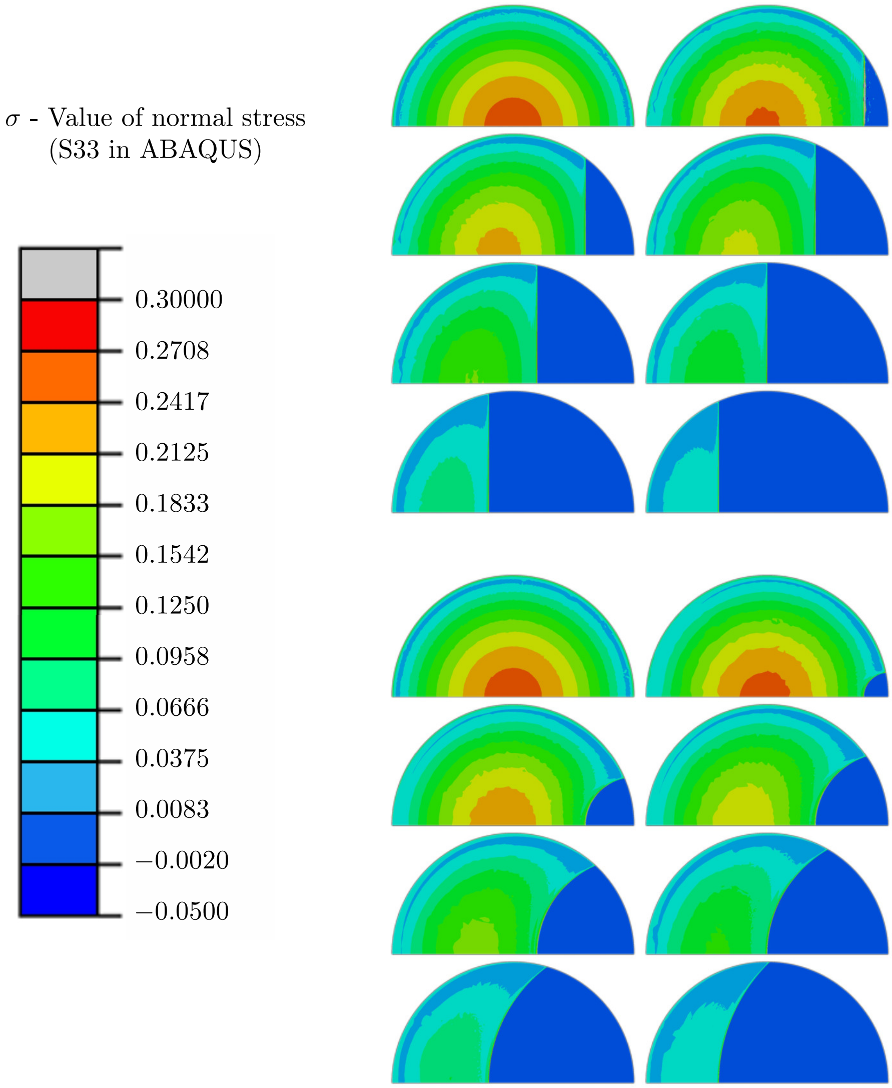

Fig. 9. Normal stress distribution for straight and circular detachment fronts, $h/a = 0.2$, $\nu = 0.5$.

Acknowledgments

This research was supported by the Hungarian National Research, Development and Innovation Office (FK 142457). This research was supported by the János Bolyai Research Scholarship of the Hungarian Academy of Sciences.

References

1. Antunes, F.V., Ferreira, J.M., & Byrne, J. (1999). Stress intensity factor calculation based on the work of external forces. *International Journal of Fracture*, *98*(1), 1–14. https://doi.org/10.1023/A:1018684932071

2. Arzt, E., Gorb, S., & Spolenak, R. (2003). From micro to nano contacts in biological attachment devices. *Proceedings of the National Academy of Sciences*, *100*(19), 10603–10606. https://doi.org/10.1073/pnas.1534701100

3. Asp, L.E., Berglund, L.A., & Gudmundson, P. (1995). Effects of a composite-like stress state on the fracture of epoxies. *Composites Science and Technology*, *53*(1), 27–37. https://doi.org/10.1016/0266-3538(94)00075-1

4. Autumn, K., Sitti, M., Liang, Y.A., Peattie, A.M., Hansen, W.R., Sponberg, S., Kenny, T.W., Fearing, R., Israelachvili, J.N., & Full, R.J. (2002). Evidence for van der Waals adhesion in gecko setae. *Proceedings of the National Academy of Sciences*, *99*(19), 12252–12256. https://doi.org/10.1073/pnas.192252799
5. Balijepalli, R.G., Begley, M.R., Fleck, N.A., McMeeking, R.M., & Arzt, E. (2016). Numerical simulation of the edge stress singularity and the adhesion strength for compliant mushroom fibrils adhered to rigid substrates. *International Journal of Solids and Structures*, *85–86*, 160–171. https://doi.org/10.1016/j.ijsolstr.2016.02.018
6. Balijepalli, R.G., Fischer, S.C.L., Hensel, R., McMeeking, R.M., & Arzt, E. (2017). Numerical study of adhesion enhancement by composite fibrils with soft tip layers. *Journal of the Mechanics and Physics of Solids*, *99*, 357–378. https://doi.org/10.1016/j.jmps.2016.11.017
7. Benvidi, F.H., & Bacca, M. (2021). Theoretical limits in detachment strength for axisymmetric bimaterial adhesives. *Journal of Applied Mechanics*, *88*(12), Article 121007. https://doi.org/10.1115/1.4052107
8. Bricotte, L., Chougrani, K., Alard, V., Ladmiral, V., & Caillol, S. (2024). Adhesion theories: A didactic review about a century of progress. *International Journal of Adhesion and Adhesives*, *132*, Article 103673. https://doi.org/10.1016/j.ijadhadh.2024.103673
9. Dassault Systèmes (2022). Abaqus version 2022.
10. Gent, A.N., & Lindley, P.B. (1957). Internal flaws in bonded cylinders of soft vulcanized rubber subjected to tensile loads. *Nature*, *180*, 912–913. https://doi.org/10.1038/180912a0
11. Gorb, S.N., & Varenberg, M. (2007). Mushroom-shaped geometry of contact elements in biological adhesive systems. *Journal of Adhesion Science and Technology*, *21*(12–13), 1175–1183. https://doi.org/10.1163/156856107782328317
12. Hao, S., Huang, R., & Rodin, G.J. (2024). Constitutive models for confined elastomeric layers: Effects of nonlinearity and compressibility. *Mechanics of Materials*, *190*, Article 104912. https://doi.org/10.1016/j.mechmat.2024.104912
13. Hensel, R., Moh, K., & Arzt, E. (2018). Engineering micropatterned dry adhesives: From contact theory to handling applications. *Advanced Functional Materials*, *28*(28), Article 1800865. https://doi.org/10.1002/adfm.201800865
14. Horváth, A.L., & Kossa, A. (2024). Stability maps for the slightly compressible poker chip detachment problem. *Finite Elements in Analysis and Design*, *242*, Article 104257. https://doi.org/10.1016/j.finel.2024.104257
15. Kumar, A., & Lopez-Pamies, O. (2021). The poker-chip experiments of Gent and Lindley (1959) explained. *Journal of the Mechanics and Physics of Solids*, *150*, Article 104359. https://doi.org/10.1016/j.jmps.2021.104359
16. Lindsey, G.H. (1967). Triaxial fracture studies. *Journal of Applied Physics*, *38*(12), 4843–4852. https://doi.org/10.1063/1.1709232
17. Millwater, H., Wagner, D., Baines, A., & Montoya, A. (2016). A virtual crack extension method to compute energy release rates using a complex variable finite element method. *Engineering Fracture Mechanics*, *162*, 95–111. https://doi.org/10.1016/j.engfracmech.2016.04.002
18. Movchan, A.B., Rebrov, K.R., & Rodin, G.J. (2021). Axisymmetric deformation of compressible, nearly incompressible, and incompressible thin layers between two rigid surfaces. *International Journal of Solids and Structures*, *214–215*, 61–73. https://doi.org/10.1016/j.ijsolstr.2020.12.002
19. Schneider, G.A., & Swain, M.V. (2015). The Schwickerath adhesion test: A fracture mechanics analysis. *Dental Materials*, *31*(8), 986–991. https://doi.org/10.1016/j.dental.2015.05.007
20. Varenberg, M., Pugno, N.M., & Gorb, S.N. (2010). Spatulate structures in biological fibrillar adhesion. *Soft Matter*, *6*, 3269–3272. https://doi.org/10.1039/C003207G

Manuscript received December 15, 2024; accepted for publication March 13, 2025;

JOURNAL OF THEORETICAL
AND APPLIED MECHANICS
63, 3, pp. 583–588, Warsaw 2025
https://doi.org/10.15632/jtam-pl/203353

ASSESSMENT OF ALUMINIDE COATING INTEGRITY BY USING ACOUSTIC EMISSION

Mateusz KOPEC*, Dominik KUKLA, Zbigniew L. KOWALEWSKI

Institute of Fundamental Technological Research, Polish Academy of Sciences, Warsaw, Poland
*corresponding author, *mkopec@ippt.pan.pl*

Coatings are essential for protecting high-temperature components in aerospace and power generation industries. This study evaluates the integrity of aluminide coatings on MAR-M247, a nickel-based superalloy, under uniaxial tensile loading using acoustic emission (AE). Aluminide coatings, deposited via chemical vapor deposition (CVD), provide oxidation and corrosion resistance but are prone to damage under operational stresses. AE monitoring, a nondestructive evaluation method, detects transient elastic waves associated with damage events such as crack initiation and delamination. By analyzing AE signal characteristics like amplitude and energy, this research identifies acoustic signatures indicative of coating degradation. The findings highlight AE's potential for real-time damage assessment, enabling early detection and predictive maintenance strategies in high-temperature applications.

Keywords: coatings; acoustic emission; nickel alloys; nondestructive testing.

1. Introduction

Thermal barrier coatings (TBCs) are indispensable in high-temperature applications, particularly in industries such as aerospace and power generation, where components are subjected to extreme thermal and mechanical loads (Barwinska, 2023). These coatings serve as protective layers that insulate and shield the underlying metallic substrates from excessive heat, oxidation, and corrosion. By doing so, they enhance the durability, performance, and operational efficiency of critical components such as turbine blades and combustion chamber liners. Among the various substrate materials used in such applications, MAR-M247 – a nickel-based superalloy – is a prominent choice due to its superior mechanical strength, creep resistance, and thermal stability at elevated temperatures (Kopec, 2024b).

Aluminide coatings are applied to MAR-M247 to provide additional protection against oxidation and high-temperature corrosion (Kopec, 2024a). These coatings, often produced via processes such as chemical vapor deposition (CVD) or pack cementation, form a stable alumina or chromium oxide layer upon exposure to high temperatures, which acts as a barrier to oxygen diffusion. Despite their excellent protective properties, aluminide-based coatings are susceptible to damage due to thermal cycling, mechanical loading, and prolonged exposure to extreme environments (Kukla, 2020). Such damage manifests itself in various forms, including

---

Ministry of Science and Higher Education
Republic of Poland

The publication has been funded by the Polish Ministry of Science and Higher Education under the Excellent Science II programme "Support for scientific conferences".
The content of this article was presented during the 40th Danubia-Adria Symposium on Advances in Experimental Mechanics, Gdańsk, Poland, September 24–27, 2024.

cracking, delamination, and spallation, which compromise the coating's integrity and lead to potential component failure. The ability to monitor and assess the integrity of coating systems in real time is crucial for preventing unexpected failures and optimizing maintenance schedules (Kukla, 2021a). Conventional inspection techniques, such as eddy current, visual examination, microscopy, and ultrasonic testing, are often time-consuming, invasive, or limited in their ability to detect early-stage damage (Kukla, 2021b). In contrast, acoustic emission (AE) monitoring has emerged as a powerful nondestructive evaluation (NDE) method for detecting and characterizing damage processes in real-time. AE monitoring involves the detection and analysis of transient elastic waves generated by the rapid release of localized energy within a material, typically associated with events such as crack initiation, crack propagation, or interfacial delamination (Andrews & Taylor, 2000). This study investigates the application of AE monitoring to evaluate the integrity of aluminide coatings deposited on MAR-M247 when subjected to uniaxial tensile loading. Uniaxial tension serves as a simplified mechanical loading condition to simulate the stresses that coating systems may encounter during service, particularly those associated with mechanical deformation, thermal gradients, and operational vibrations. By correlating AE signal features – such as amplitude, frequency, and energy – with the progression of damage, this work aims to identify characteristic acoustic signatures that can serve as indicators of the coating degradation. The integration of AE monitoring with traditional post-mortem analysis methods, such as scanning electron microscopy (SEM) and metallographic evaluation, provides a comprehensive approach to understanding the failure mechanisms in coating systems. The findings of this study hold significant implications for industries reliant on high-temperature components, where the early detection of coating failure is essential to ensure reliability, safety, and cost-effectiveness. By advancing the understanding of AE monitoring in the context of aluminide-coated MAR-M247, this research contributes to the broader effort of implementing advanced NDE methods for predictive maintenance and life-cycle management of critical engineering systems.

2. Materials and methods

MAR-M247 nickel superalloy specimens were produced using a conventional casting technique (Fig. 1a). Aluminide coatings were applied through the chemical vapor deposition (CVD) process. The deposition was carried out at a temperature of 1040 °C and an internal pressure of 150 mbar, utilizing optimized CVD parameters in a hydrogen-protective atmosphere, with deposition durations of 8 and 12 hours (Kopec, 2024b). A representative cross-section of a MAR-M247 specimen with a 40 μm coating is shown in Fig. 1a. The microstructure exhibits a two-layer configuration: a homogeneous zone of a secondary solid solution β (NiAl) phase and a heterogeneous NiAl matrix (dark gray) containing dispersions of a Ni_3Al phase (light gray). Acoustic emission assessment was conducted to evaluate its applicability to identifying the cracking of the coating layer based on the acoustic effect associated with the crack propagation. The tests were performed on a specimen subjected to static tension, using four measurement sensors mounted at the lower and upper parts of the specimen, on both sides (Fig. 1b). This sensor arrangement made it possible to separate the acoustic emission signals from the gripping sections of the specimen from those from the measurement area, where crack propagation in the coating was expected. The measurements were carried out using the AMSY-5 M6-2 Acoustic Emission System from Vallen and VS-150 type sensors with a preamplifier (Fig. 1b). The tests were based on the assumption that cracks initiated in the brittle aluminide layer would generate an acoustic emission signal in the form of an elastic wave propagating through the specimen material. The AE sensors detect and convert the waves into electrical signals, while the measurement channel of the AE system parameterizes the signal and records its progression. The tests were performed during tensile tests with a traverse speed of 0.05 mm/sec.

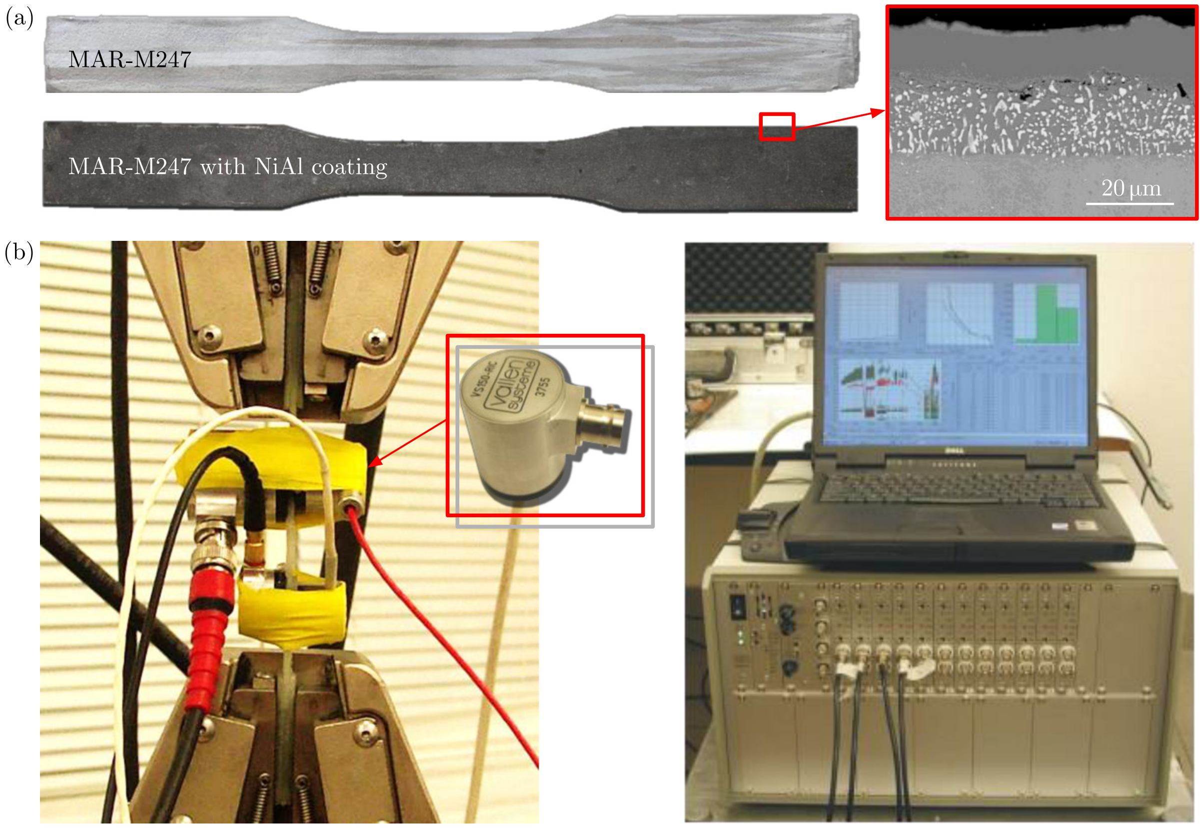

Fig. 1. (a) General view of casted MAR-M247 specimen and the same specimen with aluminide coating with additional magnification of coating cross-section; (b) specimen fixed in the grips of the testing machine with VS-150 type AE sensors and a preamplifier.

3. Results and discussion

The results indicate a significant increase in the number of acoustic hits as well as their energy and amplitude in the tensile specimen with the coating (Figs. 2a and 2b). It can be inferred from other research conducted on materials and structures under load that signals with the highest energy may be associated with coating failure in the specimen. Since the specimens only differed in the presence of the coating (with the same core structure), the noticeable changes in the obtained results are solely related to surface effects.

In addition to crack formation, acoustic effects related to the loss of coherence between the coating and the substrate may also occur, which is a result of differences in the susceptibility of the two materials to plastic deformation (Fig. 2c). It could be further confirmed by the distribution of the parameter D, which represents a duration of a specific event in microseconds and was categorized by different ranges: $0 \leq D < 500\,\mu\mathrm{s}$ (green points); $500 \leq D < 1000\,\mu\mathrm{s}$ (red points); $1000 \leq D < 10000\,\mu\mathrm{s}$ (yellow points). Shorter times ($0\,\mu\mathrm{s}$–$500\,\mu\mathrm{s}$) correspond to weaker or less severe events, while longer times ($1000\,\mu\mathrm{s}$–$10000\,\mu\mathrm{s}$) indicate stronger emissions related to significant material changes. One could observe that AE is a highly effective NDT technique for monitoring and detecting cracks during tensile testing, particularly for complex materials like MAR-M247 with an aluminide coating. The combined structural integrity of both the substrate and the coating is vital during tensile testing, as failure can occur in either phase or at the interface between them. AE can provide a detailed and real-time assessment of the material's behavior under stress, which is crucial for understanding how cracks initiate, propagate, and affect the overall performance of the material. During tensile testing, the deformation of the material generates microstructural events such as the formation of dislocations, crack initiation,

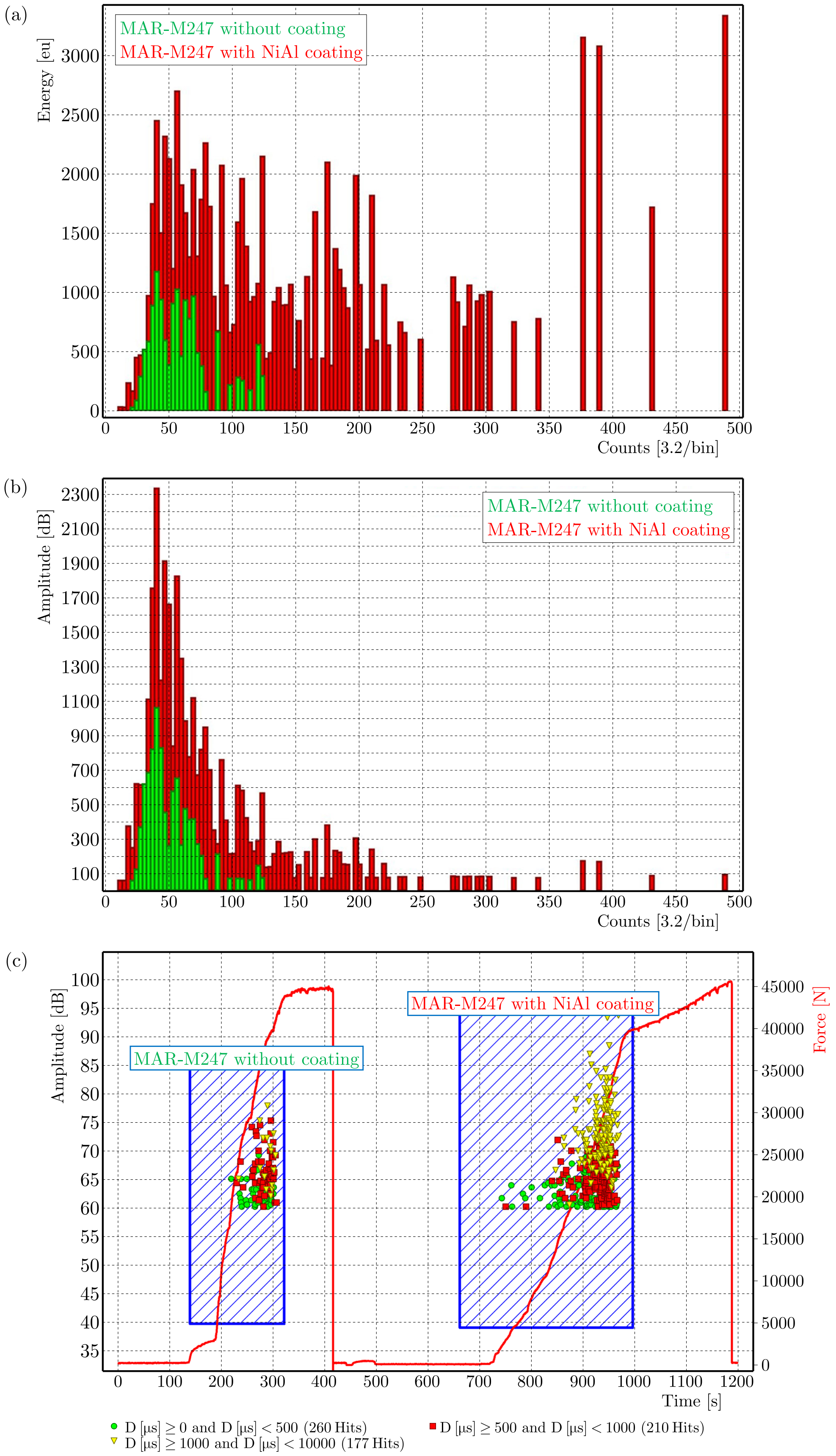

Fig. 2. Dependence of signal energy (a) and amplitude (b) of acoustic emission on their count, recorded during the tensile testing of specimens with and without the coating. Amplitudes of acoustic emission signals recorded during the tensile testing of specimens with and without the coating, along with the tensile curve (c).

and the growth of these cracks into larger fractures. AE detects the high-frequency sound waves or “pings” that are emitted when these energy-releasing events occur. When a crack forms, it generates a burst of elastic waves that travel through the material. AE sensors positioned on the surface of the material can detect these waves, thus enabling early identification of the damage, before it becomes visually detectable. The ability of AE to pick up these emissions provides critical insight into the initiation of cracks at stress concentration points, such as grain boundaries, inclusions, or other microstructural imperfections, which are common in materials like MAR-M247. This early detection is invaluable because it enables timely intervention, potentially preventing catastrophic failures. AE is also particularly useful in monitoring crack propagation during tensile testing. As cracks grow, they emit higher intensity AE signals, and the frequency and amplitude of these signals can be correlated with the size and rate of crack propagation. In the case of MAR-M247, the evolution of cracks can occur in both the aluminide coating and the base alloy, and AE can help differentiate the sources of emissions. For instance, cracks in the aluminide coating might produce different acoustic signatures compared to cracks in the nickel-based alloy due to the differences in their mechanical properties, such as stiffness and hardness. AE can also detect any delamination or debonding at the interface between the aluminide coating and the MAR-M247 substrate, which is crucial for understanding the behavior of coated materials under stress. This ability to monitor both phases of the material in real-time provides a more comprehensive understanding of the material’s failure modes, particularly in materials that are prone to complex failure mechanisms, like those with coatings. Furthermore, AE can assist in the assessment of localized damage in regions where the aluminide coating might be subject to plastic deformation or cracking due to the mismatch in the thermal expansion between the coating and the substrate. The AE from these localized cracks in the coating may differ from that in the substrate, and this enables a more detailed analysis of the performance of the aluminide coating under tensile stress. AE can thus be used not only to detect cracks but also to monitor their growth and to assess the potential for catastrophic failure, providing valuable information about the durability and reliability of materials like MAR-M247 with an aluminide coating. The ability to track damage evolution in real-time, especially in critical aerospace applications, is one of the key advantages of AE, as it provides immediate feedback that can be used to make decisions about material behavior, design improvements, and failure prevention strategies.

4. Conclusions

AE monitoring has proven to be a highly effective nondestructive evaluation technique for assessing the integrity of aluminide coatings on MAR-M247 nickel-based superalloys under tensile loading. The study demonstrated that AE can reliably detect and characterize damage mechanisms such as crack initiation, propagation, and delamination, providing real-time insights into coating degradation. The distinct acoustic signatures of the coating and substrate failures highlight AE’s capability to differentiate between damage sources, offering a detailed understanding of the failure mechanisms. These findings emphasize AE’s potential for industrial applications, particularly in the aerospace and energy sectors, where the early detection of coating damage is critical for ensuring component reliability and safety. By facilitating timely intervention and supporting predictive maintenance strategies, AE monitoring enhances the operational efficiency and life-cycle management of high-temperature components.

References

1. Andrews, D.J., & Taylor, J.A.T. (2000). Quality control of thermal barrier coatings using acoustic emission. *Journal of Thermal Spray Technology*, *9*(2), 181–190. https://doi.org/10.1361/105996300770349908

2. Barwinska, I., Kopec, M., Kukla, D., Senderowski, C., & Kowalewski, Z.L. (2023). Thermal barrier coatings for high-temperature performance of nickel-based superalloys: A synthetic review. *Coatings*, *13*(4), Article 769. https://doi.org/10.3390/coatings13040769
3. Kopec, M. (2024a). Recent advances in the deposition of aluminide coatings on nickel-based superalloys: A synthetic review (2019–2023). *Coatings*, *14*(5), Article 630. https://doi.org/10.3390/coatings14050630
4. Kopec, M. (2024b). Effect of aluminide coating thickness on high-temperature fatigue response of MAR-M247 nickel-based superalloy. *Coatings*, *14*(8), Article 1072. https://doi.org/10.3390/coatings14081072
5. Kukla, D., Kopec, M., Kowalewski, Z.L., Politis, D.J., Jóźwiak, S., & Senderowski, C. (2020). Thermal barrier stability and wear behavior of CVD deposited aluminide coatings for MAR 247 nickel superalloy. *Materials*, *13*(17), Article 3863. https://doi.org/10.3390/ma13173863
6. Kukla, D., Kopec, M., Sitek, R., Olejnik, A., Kachel, S., & Kiszkowiak, Ł. (2021a). A novel method for high temperature fatigue testing of nickel superalloy turbine blades with additional NDT diagnostics. *Materials*, *14*(6), Article 1392. https://doi.org/10.3390/ma14061392
7. Kukla, D., Kopec, M., Wang, K., Senderowski, C., & Kowalewski, Z.L. (2021b). Nondestructive methodology for identification of local discontinuities in aluminide layer-coated MAR 247 during its fatigue performance. *Materials*, *14*(14), Article 3824. https://doi.org/10.3390/ma14143824

Manuscript received January 8, 2025; accepted for publication March 25, 2025;

JOURNAL OF THEORETICAL
AND APPLIED MECHANICS
63, 3, pp. 589–599, Warsaw 2025
https://doi.org/10.15632/jtam-pl/203583

THE INFLUENCE OF INDUSTRIAL AND ENVIRONMENTAL FACTORS ON THE POLYOXYMETHYLENE

Olivia-Laura PETRAȘCU, Dan-Mihai RUSU*, Adrian Marius PASCU

Department of Industrial Machines and Equipment, Faculty of Engineering, "Lucian Blaga" University, Sibiu, Romania
*corresponding author, *dan-mihai.rusu@ulbsibiu.ro*

This paper analyzes the influence of industrial environmental factors on the mechanical and physical characteristics of polyoxymethylene (POM), a semicrystalline polymer commonly used in industrial applications due to its strength and dimensional stability. The study exposed POM samples to four specific test media (distilled water, cooling oil, UV-C radiation and saline solution), following the relevant ISO standards for measuring liquid absorption and mechanical behavior. Uniaxial tensile tests were conducted to assess the influence of various factors on characteristics, such as maximum normal stress, maximum strain, and elastic modulus. The results indicated that all four media negatively impacted the mechanical properties of POM. However, the most severe effect was attributed to UV-C radiation, this factor markedly diminished both strength and maximum strain. Because of this, the material exhibited a notable tendency toward embrittlement, although one might consider other influences as well. In contrast, saline and cooling oil caused increases in the maximum strain, suggesting an increase in the ductility of the material. The influences on liquid absorption and elastic modulus were also varied, with cooling oil having the least impact on the latter value.

Keywords: polyoxymethylene (POM); tensile tests; mechanical characteristics; liquid absorption.

1. Introduction

POM (polyoxymethylene, also known as polyacetal) is a widely used crystalline polymer. This material stands out for its superior strength and exceptional dimensional stability and very good machinability. Due to its very high degree of crystallinity, POM exhibits the lowest wear level among all thermoplastics (Berer *et al.*, 2018). This characteristic makes it ideal for applications such as wheels and gears, as well as in any other field requiring sliding friction properties without special additives (Sun *et al.*, 2008). Applications in the connector and switch sector, as well as in the machinery construction industry, complete the range of uses for POM (Hsissou *et al.*, 2021).

POM is classified as a crystalline polymeric material, with a crystallinity of over 70 %, has stable chemical compositions and excellent mechanical properties including high strength, stiffness, impact and creep resistance and long-term durability (He *et al.*, 2021; Mao *et al.*, 2019). Widely used in the manufacture of equipment, light industrial products and tools, POM gained attention in the 1970s and 1980s as a high-performance material (Nakagawa *et al.*, 1985).

Ministry of Science and Higher Education
Republic of Poland

The publication has been funded by the Polish Ministry of Science and Higher Education under the Excellent Science II programme "Support for scientific conferences".
The content of this article was presented during the 40th Danubia-Adria Symposium on Advances in Experimental Mechanics, Gdańsk, Poland, September 24–27, 2024.

The outstanding characteristics of this polymer, such as stiffness, allow the design of parts with large surface areas and thin cross-sections, high tensile strength and creep resistance over a wide range of temperature and humidity conditions, as well as the fatigue strength and elasticity required in applications requiring toughness and elasticity. Polyacetal has gained importance in various applications due to its excellent balance of properties. There are two types of acetals available: a homopolymer with superior mechanical properties, higher end-use temperatures and a higher melt flow index, and a copolymer, which offers superior processing characteristics and an impact strength (Campo, 2006; Pascu, 2018).

However, like any material, the mechanical properties of POM can be influenced by environmental factors. Exposure to varying conditions of temperature, humidity, and chemical agents can affect the performance and durability of this polymer (Chen *et al.*, 2020). For instance, thermal variations can lead to changes in crystallinity, while humidity can impact dimensional stability and wear resistance (Kneissl *et al.*, 2023). In this context, it is essential to thoroughly investigate and understand how these environmental factors influence the mechanical properties of POM to ensure its efficient use in critical applications and improve the performance of final products. This article aims to explore in detail the impact of environmental factors on POM and provide recommendations for optimizing the use of this polymer under various operating conditions.

In our previous studies, we conducted similar tests on elastomeric materials used in soft robotics (Rusu *et al.*, 2023). In this study, we aim to observe changes in the mechanical characteristics of polymeric materials, such as POM, following exposure to chemical and physical factors. Our goal is to better understand how these external influences affect the performance and durability of these materials.

2. Materials and methods

One of the methods for identifying the impact that a particular environment has on a particular material is addressed in (International Organization for Standardization [ISO], 2008), which establishes a clear methodology for determining the fluid absorption of materials. Based on this standard and ISO (2012) standard used to determine the tensile behavior of plastics, the impact that four specific industrial media (distilled water, synthetic cooling oil, saline solution and UV radiation type C) have on polymeric materials was analyzed. POM material was used in the analysis, specimens were made by the water jet extrusion process. The shape and dimensions of the specimens used, according to the standard, are shown in Fig. 1a, and the 10 test specimens of POM material in the test lanes in Fig. 1b.

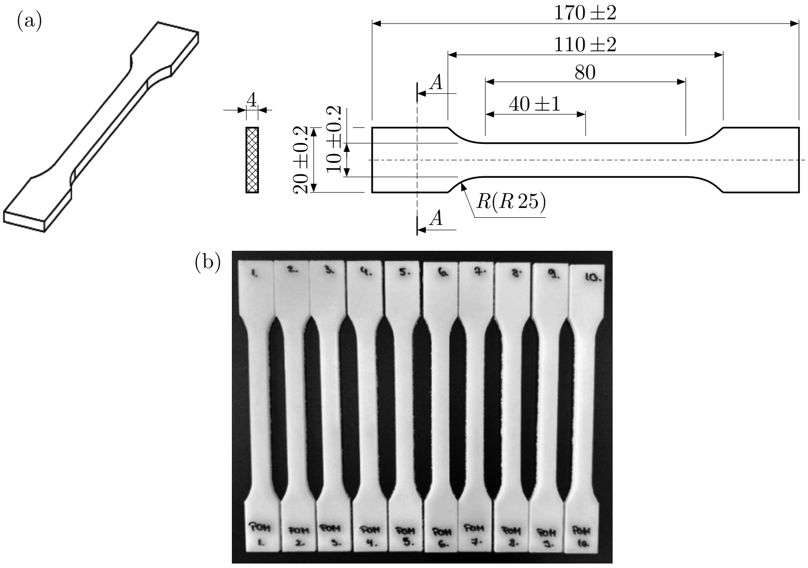

Fig. 1. (a) Specimen dimensions (in mm); (b) specimens made of POM before testing.

To ensure the best possible positioning/orientation of the specimens in the testing machine grips, as well as to achieve coaxially with the vertical axes of the machine trays and consistent specimen placement between the grips, a specimen orientation device was designed, realized and used (Fig. 2). This device was essential to position the specimen axis coinciding with the central axis of the testing machine grips, thus reducing the possibility of eccentric stretching stresses on the specimen, which would have led to additional bending stresses that could have negatively influenced the results obtained. It should be noted that the device used for specimen positioning/orientation was 3D printed and did not influence the experimental results in any way, because after the specimen was correctly aligned with the grips, this device was removed.

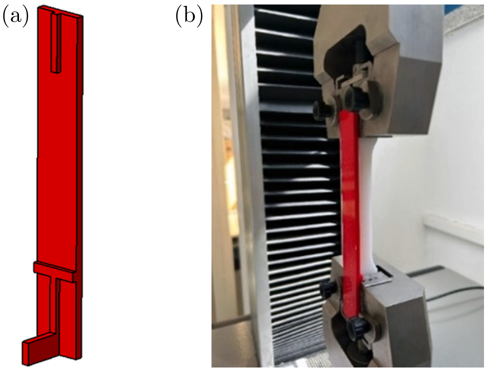

Fig. 2. (a) Device for orienting specimens between trays; (b) test specimen attached to the test machine using the device.

Uniaxial tensile tests under laboratory conditions are fundamental to polymeric materials for several reasons and these were performed on the Galdabini Quasar 25 universal testing machine, at a temperature of 23 °C ±5 °C and the test speed was 5 mm/min. This test speed was maintained for all tests performed in all the environment conditions.

Firstly, they allow the determination of mechanical properties necessary to compare results from different working environments. Through these tests, direct comparisons can be made between different polymeric materials or polymer formulations, which is essential for engineers in selecting the optimal material for specific applications.

The second test medium was distilled water. Distilled water was supplied by the Simplu Quality Products brand and it was used to immerse the test specimens. This water is used in various industrial applications, such as dilution of antifreeze and windshield washer fluids, topping up the electrolyte level in electric batteries, as a spray liquid for electric irons, cooling of internal combustion engines, etc. The distilled water used had a pH between 6 and 7.5 and a density of 1 g/cm^3 at 20 °C.

The third test medium chosen for this study is the cooling oil supplied by the Azur-Cut 602.01 M-15 brand. This is a combination of mineral oil and additives specifically designed to operate at high pressures and to cope with the intense machining regimes that occur in mechanical machining with material removal. The oil has a viscosity of 15 mm^2/s at 40 °C and is a synthetic coolant oil for industrial uses.

The fourth test medium used was ultraviolet type C (UV-C) radiation. Testing polymeric materials to UV-C radiation is essential to assess the durability and resistance of polymeric materials under conditions of intense exposure to UV-C radiation. UV-C radiation, which has a wavelength between 100 and 280 nanometers, is known for its ability to degrade polymeric materials by photochemical processes. These tests allow the identification of potential changes in the physical and mechanical properties of polymers, such as embrittlement, loss of elasticity, discoloration, or decrease in mechanical strength. By exposing materials to UV-C, we can determine the lifetime and performance of various polymeric materials in applications where they are subjected to such intense UV radiation, thus ensuring the reliability and safety of the final products.

The fifth medium used was saline solution, and in this case, we used the standard ISO (2023), with the following specifications: water salinity of 25 %, pH = 2.162, and an immersion temperature of 0.5 °C. The saline solution consisted of 25 l of demineralized water, 8.34 kg of salt, and 30 ml of hydrochloric acid.

The successive steps required for the study were shown graphically in Fig. 3. The specimens were measured to avoid introducing errors into the process, then dried in an oven at a constant temperature of 50 °C for 24 hours. After drying, specimens were weighed and immersed in the media of interest (distilled water, cooling oil, and saline solution) and exposed to the UV-C light for 24 hours. Subsequently the specimens were again weighed to determine, according to ISO (2008), the amount of absorbed liquid applied to distilled water, cooling oil, and saline solution only. Finally, uniaxial tensile tests were carried out until breakage with a test speed of 5 mm/min at room temperature. In step 5, after drying, the specimens were re-weighed to calculate the quantity of liquid absorbed. To calculate liquid uptake, the formula was used:

$$c = \frac{m_2 - m_1}{m_1} \times 100\,\%. \tag{2.1}$$

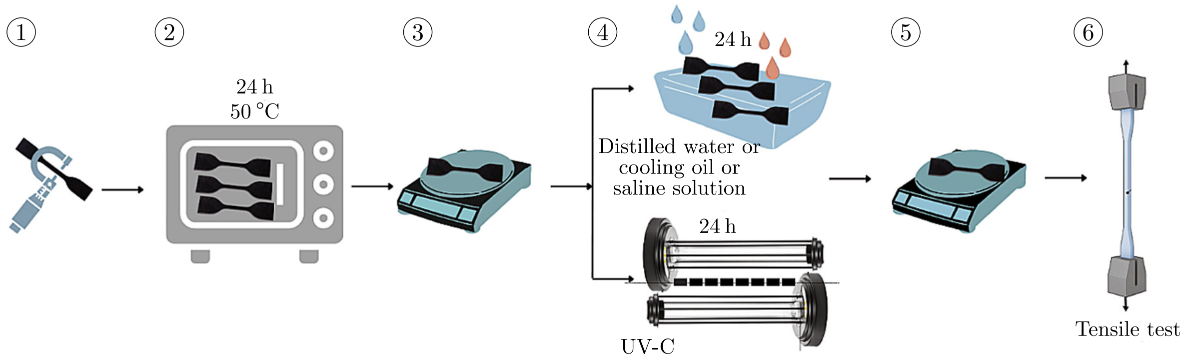

Fig. 3. Steps to perform the analysis: 1 – measuring the specimens, 2 – oven drying, 3 – weighing after drying, 4 – immersion/exposure to the medium of interest, 5 – absorption weighing, 6 – uniaxial tensile test.

3. Results

In the initial phase, specimens made of POM were tested in uniaxial tension, in quasi-static mode (speed = 5 mm/min, this speed being maintained for all tensile tests), in an ambient environment (laboratory conditions). To ensure the best possible reproducibility of results, ten specimens were tested.

The results after testing in all five environments are presented in Table 1, where only the mean values of stress, strain and modulus of elasticity (E) are found. Tables A1–A5 are found in Appendix, where the results of the basic statistical analysis such as arithmetic mean, standard

Table 1. Mean values for experimental results for POM specimens tested in five different environments.

Environment type	Mean values				
	$F_{\max}$ [N]	$\Delta_{L_{\max}}$ [mm]	$\sigma_{\max}$ [MPa]	$\varepsilon_{\max}$ [%]	E [MPa]
Ambient environment	1737.74	13.77	57.15	17.25	1847.97
Distilled water	2272.88	13.42	55.97	16.44	1734.89
Cooling oil	1619.54	15.28	52.98	19.10	1755.67
UV-C	1399.35	7.97	46.18	9.97	1699.41
Saline solution	2184.49	20.50	53.64	25.62	1662.91

deviation, minimum and maximum values are also presented. Also, in these tables we present the results of statistical analysis, using Minitab 18 from two perspectives: the Outliers test and the Normality test, where two tests were applied: the Anderson–Darling test to check the normal distribution of the data and the Grubbs test to eliminate outliers.

In the case of the tests performed in saline, we used the non-parametric Kolmogorov–Smirnov test instead of the Anderson–Darling normality test, because normality tests check not only symmetry but also how the data are distributed with respect to the mean. If the distribution is too "flat" or too "sharp" compared to a normal distribution, the test may reject the hypothesis of normality, and in some cases our data were too concentrated.

It can be observed that in the case of the AD/KS test, the values of AD/KS and p for $F_{\max}$, $\Delta_{L_{\max}}$, $\sigma_{\max}$, $\varepsilon_{\max}$, and E fall in ranges of values greater than 0.05 and the same is true in the case of the Grubbs test, the values of G and p for $F_{\max}$, $\Delta_{L_{\max}}$, $\sigma_{\max}$, $\varepsilon_{\max}$, and E fall in ranges of values greater than 0.05, all of these confirming that the results obtained are showing a normal distribution of the data, which is also confirmed by the values of p, greater than 0.05.

Based on the experimental results, characteristic curves – engineering stress vs. engineering strain – were plotted for each of the ten test sets in all five environments. For each environment, a mean curve, made on the basis of all the curves plotted for all the samples tested in each case, is presented in Fig. 4.

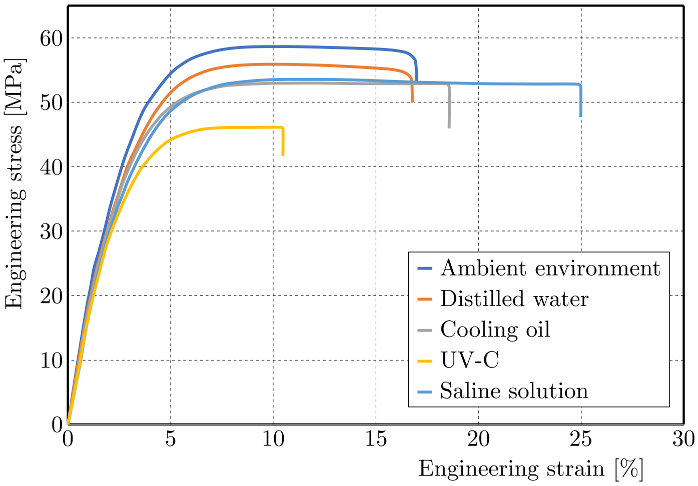

Fig. 4. Mean engineering stress-strain curves for tensile testing of POM material in five different media.

Figure 5 shows a comparative plot of the mean values of the maximum engineering stress obtained for the five studied environments.

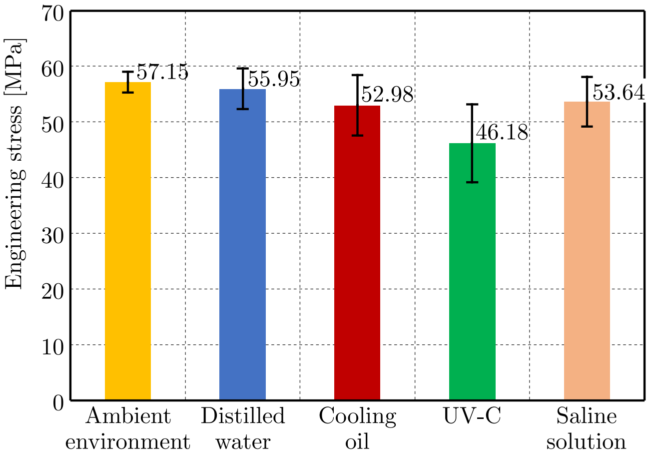

Fig. 5. Mean values of the maximum engineering stress for POM specimens obtained for all five studied environments.

It can be seen from this graph that, taking as a baseline the results obtained when specimens were tested in an ambient environment without any external factor, for all the other four cases where specimens were previously tested with an external factor (distilled water, cooling oil, UV-C radiation, and saline solution), the maximum engineering stress decreases. Thus, in the case of specimens immersed in distilled water, there is a decrease in this maximum engineering stress of 2.11 %; in the case of specimens immersed in saline solution, the decrease is 6.54 %; in the case of specimens immersed in cooling oil, the decrease is somewhat more pronounced, being 7.87 %; and in the case of specimens subjected to UV-C radiation, the decrease is the most significant, 23.75 %.

Therefore, it can be concluded that all four media (distilled water, cooling oil, UV-C radiation, and saline solution) have a negative influence on the tensile strength of POM samples, with UV-C radiation having the highest influence and distilled water having the lowest influence. The saline solution has the lowest degree of absorption in the material, followed by distilled water and cooling oil, as can be seen in Fig. 6.

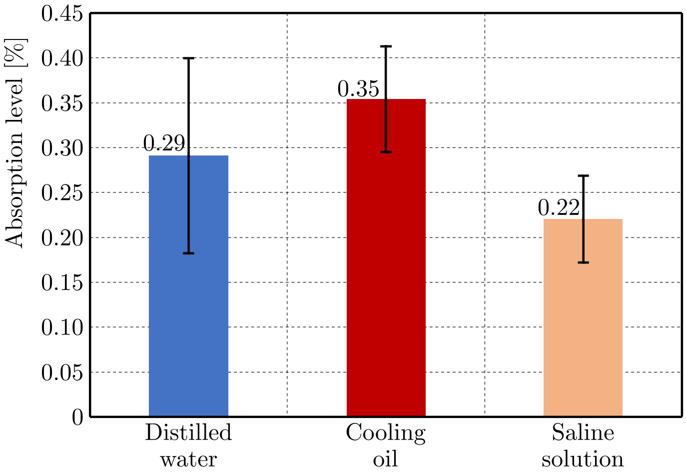

Fig. 6. Mean absorption level in POM specimens for all three liquids studied.

In this case too, changes can be observed in the values of the maximum engineering strain compared to the values recorded for the specimens tested in an ambient environment and not previously subjected to any external factor, for all the other four cases in which the specimens were previously subjected to an external factor (distilled water, cooling oil, UV-C radiation, and saline solution). The results are shown in Fig. 7. Thus, in the case of specimens immersed in distilled water, the (smallest) decrease in the maximum engineering strain is 4.93 %, and in the case of specimens subjected to UV-C radiation, we have the most significant decrease, 73.02 %. In the case of the other two studied media (cooling oil and saline solution), an increase of the maximum values for the specific strain is observed; thus, in the case of cooling oil, we have an increase of 10.72 %, and in the case of saline solution, an increase of 48.52 %.

It can therefore be concluded that UV-C radiation has the most negative influence on the maximum engineering strain of the specimens made of POM, with the maximum elongation being reduced by 73.02 % compared to specimens tested in an ambient environment and not previously subjected to any external factor. It can therefore be said that UV-C radiation tends to make the POM material brittle. There are also two environments that lead to an increase in the maximum engineering strain value of POM specimens, namely cooling oil and saline solution, the latter making POM specimens more ductile by approx. 24 % than specimens tested in ambient environments and not previously exposed to any external factors.

Also, in this case of the elastic modulus (Fig. 8), decreases in the values of the maximum engineering strain can be observed compared to the values recorded for the specimens tested in an ambient environment and not previously subjected to any external factor, for all the other

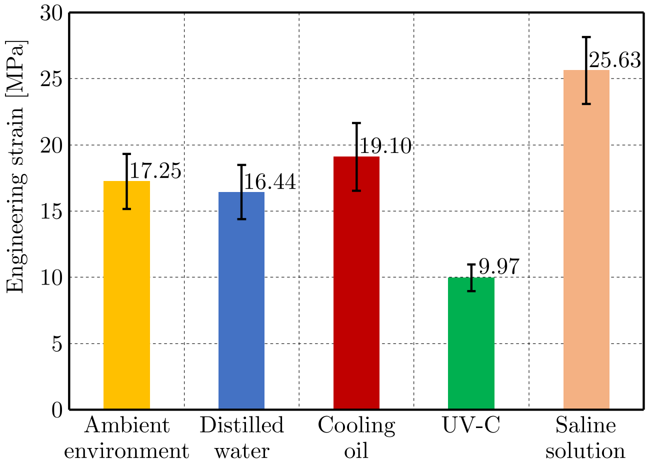

Fig. 7. Mean values of maximum engineering strain for POM specimens obtained for all five studied environments.

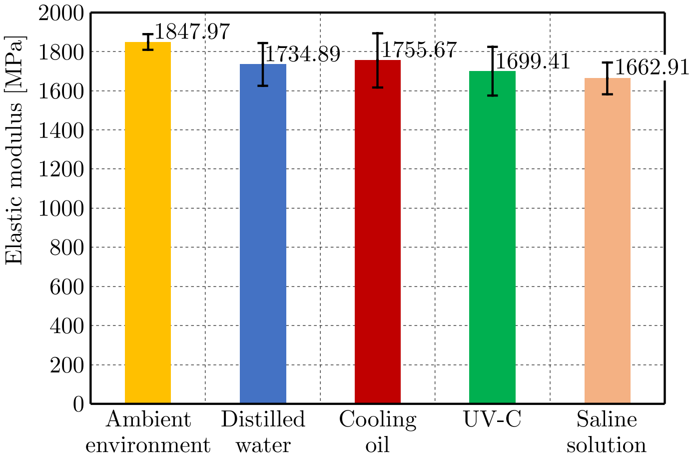

Fig. 8. Mean values of the elastic modulus for POM specimens obtained for all five studied environments.

four cases where the specimens were previously subjected to an external factor (distilled water, cooling oil, UV-C radiation, and saline solution). It can be seen from this graph that, taking as a baseline the results obtained when specimens were tested in an ambient environment without any external factor, for all the other four cases where specimens were previously tested with an external factor (distilled water, cooling oil, UV-C radiation, and saline solution), the elastic modulus decreases. Thus, the specimens immersed in cooling oil show the smallest decrease in this characteristic, 5.26 %. In second place are the specimens immersed in distilled water with a decrease of 6.52 %, and in the case of specimens subjected to UV-C radiation, the decrease is 8.74 %. The largest decrease in the value of the elastic modulus is 11.13 % and was obtained for specimens immersed in saline solution.

It can therefore be concluded that all four media (distilled water, cooling oil, UV-C radiation, and saline solution) have a negative influence on the elastic modulus of POM specimens, the highest influence being the saline solution and the lowest the cooling oil, which has the highest degree of absorption in the material of all three liquid media studied, as can be seen in Fig. 6.

4. Conclusions

The study findings highlight the significant influence that industrial and environmental factors have on the mechanical properties of POM. Of the four environments analyzed, UV-C radiation was found to have the greatest negative effect on the characteristics of material, leading to a considerable reduction in its strength by 23.75 % and a decrease in its maximum engineering strain by 73.02 %, indicating embrittlement. Also, the saline solution produced the largest decrease in the elastic modulus, with a decrease of 11.13 %, suggesting a significant impairment of the stiffness of the material.

On the other hand, saline and cooling oil led to increases in the ductility of the polymer, manifested by significant increases in the maximum engineering strain, with saline contributing an increase of up to 48.52 %. Cooling oil, although it had the least effect on the elastic modulus, influenced the mechanical properties through a slight improvement in ductility. According to the results, the aggressive environments analyzed have a significant effect on the POM material, effects that in commercial or industrial applications can cause a number of problems. However, these effects of the aggressive media can be ameliorated by additives, stabilizers, fillers to be added into the material structure. Chemical protective coatings can also be used to reduce the impact on the material.

In conclusion, the research emphasizes the importance of understanding the effects of industrial and environmental environments on POM, highlighting the need to take these factors into account in the design and use of components made of this material. This approach can help to optimize the performance and durability of manufactured products, ensuring efficient use in industrial applications.

Appendix

Table A1. Experimental results and statistical analysis for POM specimens tested in ambient environment.

Specimen no.	$F_{\max}$ [N]	$\Delta_{L_{\max}}$ [mm]	$\sigma_{\max}$ [MPa]	$\varepsilon_{\max}$ [%]	E [MPa]
#1	1728.2	15.25	56.3	19.06	1792.2
#2	1769	12.72	58	15.9	1860.51
#3	1796.38	14.26	58.9	17.83	1875.56
#4	1722.88	11.88	56.3	14.85	1841
#5	1705	16.04	55.9	20.05	1850.02
#6	1780	10.71	58.44	13.39	1855.2
#7	1733.13	15.44	56.9	19.3	1855.12
#8	1753.88	14.5	60.22	18.13	1921.94
#9	1651.13	13.48	53.43	16.85	1779.96
#10	1737.5	13.68	57.15	17.1	1848.16
Mean	**1737.74**	**13.77**	**57.15**	**17.25**	**1847.97**
Median	**1735.32**	**13.97**	**57.03**	**17.46**	**1852.57**
Standard deviation	**41.32**	**1.65**	**1.88**	**2.08**	**39.84**
Minimum	**1651.13**	**10.71**	**53.43**	**13.39**	**1779.96**
Maximum	**1796.38**	**16.04**	**60.22**	**20.05**	**1921.94**
AD value	**0.24**	**0.18**	**0.208**	**0.18**	**0.55**
p-value (AD)	**0.7**	**0.9**	**0.811**	**0.9**	**0.12**
G-value	**2.1**	**1.85**	**1.98**	**1.85**	**1.86**
p-value (Grubbs)	**0.15**	**0.42**	**0.25**	**0.42**	**0.41**

Table A2. Experimental results and statistical analysis for POM specimens tested in distilled water.

Specimen no.	$F_{\max}$ [N]	$\Delta_{L_{\max}}$ [mm]	$\sigma_{\max}$ [MPa]	$\varepsilon_{\max}$ [%]	E [MPa]
#1	2080.38	13.16	51.27	16.45	1644.63
#2	2399.5	13.62	59.7	17.03	1827.32
#3	2406	13.33	59.12	16.66	1760.79
#4	2043.75	12.67	49.79	15.84	1585.99
#5	2318.88	15.4	56.84	19.25	1692.06
#6	2327.75	11.69	57.22	14.61	1706.68
#7	2151.63	11.45	53.26	14.31	1672.96
#8	2425	13.5	59.23	16.88	1726.95
#9	2201.63	13.42	54.02	13.42	1981.08
#10	2374.25	15.93	59.06	19.91	1750.45
Mean	**2272.88**	**13.42**	**55.97**	**16.44**	**1734.89**
Median	**2323.32**	**13.38**	**57.03**	**16.56**	**1716.81**
Standard deviation	**142.06**	**1.41**	**3.64**	**2.05**	**108.99**
Minimum	**2043.75**	**11.45**	**49.79**	**13.42**	**1585.99**
Maximum	**2425**	**15.93**	**59.87**	**19.91**	**1981.08**
AD Value	**0.5**	**0.44**	**0.48**	**0.28**	**0.38**
p-value (AD)	**0.16**	**0.23**	**0.18**	**0.56**	**0.32**
G-value	**1.61**	**1.8**	**1.7**	**1.7**	**2.26**
p-value (Grubbs)	**0.88**	**0.52**	**0.69**	**0.69**	**0.06**

Table A3. Experimental results and statistical analysis for POM specimens tested in cooling oil.

Specimen no.	$F_{\max}$ [N]	$\Delta_{L_{\max}}$ [mm]	$\sigma_{\max}$ [MPa]	$\varepsilon_{\max}$ [%]	E [MPa]
#1	1680.38	18.56	53.20	23.20	1739.05
#2	1529.63	14.67	48.2	18.34	1647.41
#3	1647.5	16.42	51.79	20.53	1694.67
#4	1613.25	12.37	51.66	15.46	1723.19
#5	1692.75	14.45	59.26	18.06	1959.69
#6	1579.75	14.62	50.33	18.28	1698.88
#7	1617.88	16.89	51.16	21.11	1694.94
#8	1378	17.58	43.73	21.98	1541.77
#9	1736.63	14.68	59.28	18.35	1897.87
#10	1719.63	12.58	61.18	15.73	1959.25
Mean	**1619.54**	**15.28**	**52.98**	**19.1**	**1755.67**
Median	**1632.69**	**14.68**	**51.73**	**18.34**	**1711.03**
Standard deviation	**106.26**	**2.04**	**5.46**	**2.55**	**138.54**
Minimum	**1378**	**12.37**	**43.73**	**15.46**	**1541.77**
Maximum	**1736.63**	**18.56**	**61.18**	**23.2**	**1959.69**
AD value	**0.4**	**0.32**	**0.39**	**0.32**	**0.57**
p-value (AD)	**0.29**	**0.46**	**0.31**	**0.46**	**0.1**
G-value	**2.27**	**1.6**	**1.69**	**1.6**	**1.54**
p-value (Grubbs)	**0.06**	**0.9**	**0.7**	**0.9**	**1**

Table A4. Experimental results and statistical analysis for POM specimens tested at UV-C rays.

Specimen no.	$F_{\max}$ [N]	$\Delta_{L_{\max}}$ [mm]	$\sigma_{\max}$ [MPa]	$\varepsilon_{\max}$ [%]	E [MPa]
#1	1664.88	8.37	54.99	10.46	1839.07
#2	1657.75	7.54	54.99	9.43	1868.27
#3	1601.13	7.93	52.48	9.91	1796.77
#4	1482.75	8.66	49.01	10.83	1768.5
#5	1240.38	7.42	40.94	9.28	1603.88
#6	1363.75	9.73	44.94	12.16	1693.29
#7	1328.38	6.81	44.04	8.51	1675.99
#8	1247.25	8.04	40.95	10.05	1575.51
#9	1406.25	7.43	46.5	9.29	1705.4
#10	1001	7.81	32.93	9.76	1467.45
Mean	**1399.35**	**7.97**	**46.18**	**9.97**	**1699.41**
Median	**1385**	**7.87**	**45.72**	**9.84**	**1699.35**
Standard deviation	**210.39**	**0.81**	**6.99**	**1.01**	**125.24**
Minimum	**1001**	**6.81**	**32.93**	**8.51**	**1467.45**
Maximum	**1664.88**	**9.73**	**54.99**	**12.16**	**1868.27**
AD value	**0.23**	**0.32**	**0.23**	**0.32**	**0.17**
p-value (AD)	**0.74**	**0.46**	**0.76**	**0.46**	**0.91**
G-value	**1.9**	**2.17**	**1.9**	**2.17**	**1.85**
p-value (Grubbs)	**0.36**	**0.1**	**0.36**	**0.1**	**0.42**

Table A5. Experimental results and statistical analysis for POM specimens tested in saline solution.

Specimen no.	$F_{\max}$ [N]	$\Delta_{L_{\max}}$ [mm]	$\sigma_{\max}$ [MPa]	$\varepsilon_{\max}$ [%]	E [MPa]
#1	2010	22.07	49.31	27.59	1596.67
#2	1985.13	22.21	49.23	27.76	1577.56
#3	1973.88	20.78	48.14	25.98	1539.81
#4	2393.75	18.93	58.38	23.66	1744.09
#5	2371.88	19.93	58.02	24.91	1737.22
#6	2030.63	17.76	49.48	19.7	1596.77
#7	2294.63	21.44	56.91	26.8	1719.81
#8	2347.5	21.71	57.76	27.14	1727.39
#9	2103.13	22.26	51.35	27.83	1644.6
#10	2334.38	19.9	57.84	24.88	1745.18
Mean	**2184.49**	**20.5**	**53.64**	**25.62**	**1662.91**
Median	**2198.88**	**21.11**	**54.13**	**26.39**	**1682.21**
Standard deviation	**177.92**	**2.01**	**4.45**	**2.52**	**80.15**
Minimum	**1973.88**	**15.76**	**48.14**	**19.7**	**1539.81**
Maximum	**2393.75**	**22.26**	**58.38**	**27.83**	**1745.18**
AD value	**0.23**	**0.19**	**0.26**	**0.19**	**0.26**
p-value (KS)	**0.13**	**0.15**	**0.05**	**0.15**	**0.05**
G-value	**1.18**	**2.12**	**1.3**	**2.22**	**1.54**
p-value (Grubbs)	**1**	**0.14**	**1**	**0.08**	**1**

References

1. Berer, M., Halb, M., Feuchter, M., Pacher, G., & Pinter, G. (2018). Fatigue fracture properties and morphology of polyoxymethylene (POM) plates produced under moderate processing conditions, *International Journal of Polymer Science*, *2018*(1), Article 7410925. http://doi.org/10.1155/2018/7410925

2. Campo, E.A. (2006). *The complete part design handbook.* Munich, Germany: Hanser.

3. Chen, C., Zhang, Z., Zhao, X., & Ye, L. (2020). Polyoxymethylene/graphene oxide-perfluoropolyether nano-composite with ultra-low friction coefficient fabricated by formation of superior interfacial tribofilm. *Composites Part A: Applied Science and Manufacturing*, *132*, Article 105856. https://doi.org/10.1016/j.compositesa.2020.105856

4. He, J., Wang, Q., Yao, B., & Ho, J. (2021). Mechanical properties of high strength POM-FRCC and its performance under elevated temperatures. *Construction and Building Materials*, *290*, Article 123177. https://doi.org/10.1016/j.conbuildmat.2021.123177

5. Hsissou, R., Seghiri, R., Benzekri, Z., Hilali, M., Rafik, M., & Elharfi, A. (2021). Polymer composite materials: A comprehensive review. *Composite Structures*, *262*, Article 113640. https://doi.org/10.1016/j.compstruct.2021.113640

6. International Organization for Standardization (2008). *Plastics – Determination of water absorption* (ISO Standard No. 62:2008). https://www.iso.org/standard/41672.html

7. International Organization for Standardization (2012). *Plastics – Determination of tensile properties. Part 2: Test conditions for moulding and extrusion plastics* (ISO Standard No. 527-2:2012). https://www.iso.org/standard/56046.html

8. International Organization for Standardization (2023). *Road vehicles – Environmental conditions and testing for electrical and electronic equipment. Part 4: Climatic loads* (ISO Standard No. 16750-4:2023). https://www.iso.org/standard/77580.html

9. Kneissl, L.M., Gonçalves, G., Joffe, R., Kalin, M., & Emami, N. (2023). Mechanical properties and tribological performance of polyoxymethylene/short cellulose fiber composites. *Polymer Testing*, *128*, Article 108234. https://doi.org/10.1016/j.polymertesting.2023.108234

10. Mao, K., Greenwood, D., Ramakrishnan, R., Goodship, V., Shrouti, C., Chetwynd, D., & Langlois, P. (2019). The wear resistance improvement of fibre reinforced polymer composite gears. *Wear*, *426–427*(Part B), 1033–1039. https://doi.org/10.1016/j.wear.2018.12.043

11. Nakagawa, K., Konaka, T., & Yamakawa, S. (1985). Production of ultrahigh modulus polyoxymethylene by drawing under dielectric heating. *Polymer*, *26*(1), 84–88. https://doi.org/10.1016/0032-3861(85)90060-6

12. Pascu, A.M. (2018). *Mechanical behavior of materials* (in Romanian). “Lucian Blaga” University Publishing House Sibiu.

13. Rusu, D.M., Petrașcu, O.L., Pascu, A.M., & Mândru, S.D. (2023). The influence of industrial environmental factors on soft robot materials. *Materials*, *16*(8), Article 2948. https://doi.org/10.3390/ma16082948

14. Sun, L.H., Yang, Z.G., & Li, X.H. (2008). Study on the friction and wear behavior of POM/Al_2O_3 nanocomposites. *Wear*, *264*(7–8), 693–700. https://doi.org/10.1016/j.wear.2007.06.005

*Manuscript received December 14, 2024; accepted for publication March 31, 2025;
published online June 4, 2025.*

JOURNAL OF THEORETICAL
AND APPLIED MECHANICS
63, 3, pp. 601–606, Warsaw 2025
https://doi.org/10.15632/jtam-pl/203598

ASSESSMENT OF MICROSTRUCTURAL CHANGES IN S235 STEEL AFTER COLD ROLLING USING EDDY CURRENT TESTING

Dominik KUKLA, Zbigniew L. KOWALEWSKI, Mateusz KOPEC*

Institute of Fundamental Technological Research, Polish Academy of Sciences, Warsaw, Poland
*corresponding author, *mkopec@ippt.pan.pl*

This study investigates the eddy current testing (ECT) technique to assess microstructural changes in S235 low carbon steel after cold rolling. Specimens of varying thicknesses (12 mm, 8 mm, and 6 mm) were analyzed to evaluate the impact of deformation on such properties as dislocation density, grain texture, and hardness. Metallographic studies using light microscopy were performed, supplemented by dislocation density measurements via transmission electron microscopy (TEM). The ECT results demonstrated that microstructural changes, particularly cold-work hardening and grain elongation, significantly influenced the phase angle of impedance. Lower penetration depths were more sensitive to surface changes, highlighting the capacity of ECT for detecting near-surface deformation. This work establishes a robust, non-destructive methodology for characterizing manufacturing-induced microstructural changes in heat-resistant steels, with applications in quality control and material performance evaluation.

Keywords: cold rolling; eddy current; microstructure.

1. Introduction

Structural steels, such as S235, play a pivotal role in industries that demand materials capable of maintaining structural integrity under extreme operating conditions (Brnic, 2021). Applications in power generation, aerospace, petrochemical processing, and other high-temperature environments require materials that can withstand prolonged exposure to thermal and mechanical stresses without compromising their mechanical properties or dimensional stability. S235 has emerged as a preferred material for these demanding applications. However, processing techniques such as cold rolling, while essential for achieving desired mechanical and dimensional parameters, inevitably introduce microstructural changes that can influence the material's long-term performance.

Cold rolling is a widely used manufacturing process for refining grain structure, improving mechanical properties, and achieving dimensional precision (Ueji, 2002). However, it also induces localized plastic deformation, leading to microstructural variations, and as a consequence, to strain hardening, dislocation density increase, and possible changes in grain size and morphology. These changes directly affect key properties like strength, ductility, and resistance to corrosion and fatigue. Therefore, understanding and quantifying these microstructural changes are essential for ensuring the reliability and safety of components made of S235 steel.

Ministry of Science and Higher Education
Republic of Poland

The publication has been funded by the Polish Ministry of Science and Higher Education under the Excellent Science II programme "Support for scientific conferences".
The content of this article was presented during the 40th Danubia-Adria Symposium on Advances in Experimental Mechanics, Gdańsk, Poland, September 24–27, 2024.

Traditional techniques for microstructural changes evaluation, including optical and electron microscopy, X-ray diffraction, Magnetic Barkhausen Noise and hardness testing, provide detailed information. However, they have notable limitations (Makowska, 2024). These methods often require destructive sampling, extensive preparation, and significant time investment, making them less practical for routine quality control or in-service inspections. In contrast, non-destructive testing (NDT) methods offer the potential for rapid, cost-effective, and non-invasive assessment of material properties. Among these, eddy current testing (ECT) has gained prominence due to its sensitivity to microstructural and compositional variations (Kukla, 2021).

Eddy current testing operates on the principle of electromagnetic induction, where alternating current in a probe coil induces eddy currents within the conductive material being tested. The interaction between the eddy currents and material's microstructure affects the impedance of the probe, which can be measured and analyzed. Changes in material properties such as electrical conductivity, magnetic permeability, and surface roughness, often associated with microstructural transformations, lead to measurable variations of ECT signals (Kukla, 2022). This makes ECT particularly well-suited for detecting deformation-induced changes, including those resulting from cold rolling processes.

This study explores the feasibility and effectiveness of using eddy current testing to assess microstructural changes in S235 steel subjected to cold rolling. By correlating ECT signals with metallurgical parameters such as dislocation density, grain structure, and phase composition, this research seeks to develop a reliable, non-destructive approach to evaluating the impact of manufacturing processes on material properties. The insights gained from this work have a potential to enhance the understanding of microstructural evolution in S235 steel and facilitate the broader adoption of NDT techniques for quality control and material characterization in industrial settings.

2. Materials and methods

S235 steel specimens with different degrees of deformation were used in this study. The initial specimen (S) was a 12 mm thick hot rolled sheet. It was then cold rolled into 8 mm and 6 mm thick sheets and designated as S1W and S2W, respectively. Metallographic examinations and stereological analysis were performed using a NIKON light microscope and were prepared with the standard metallographic techniques (mechanical polishing) and etched with 10 % Nital. Subsequent studies included the assessment of dislocation density based on transmission electron microscopy (TEM) observations of thin foil samples obtained by electrolytic thinning, on JEOL JEM 1200 EX. Microstructure images were used to estimate the density dislocation on samples S, S1W, and S2W. The intersection of dislocation and lines was counted based on 5 lines inserted into the images. Analyzed areas were observed with 50000× and 100000× magnification. Dislocation density was estimated from the equation:

$$\rho = N/LrT, \tag{2.1}$$

where N – the number of dislocations measured through line intersection, Lr – the total length of all lines, T – sample thickness (established $T = 200\,\text{nm}$).

The last stage involved the analysis of the eddy current signal on various surfaces of S235 steel specimens with various degrees of deformation. The impact of cold-work hardening on the value of the impedance phase angle was analyzed.

3. Results

The microstructure of rolled sheets exhibited a strong texture, which is visible in the cross-sectional view (Fig. 1). Its presence could be also confirmed based on the results of stereological

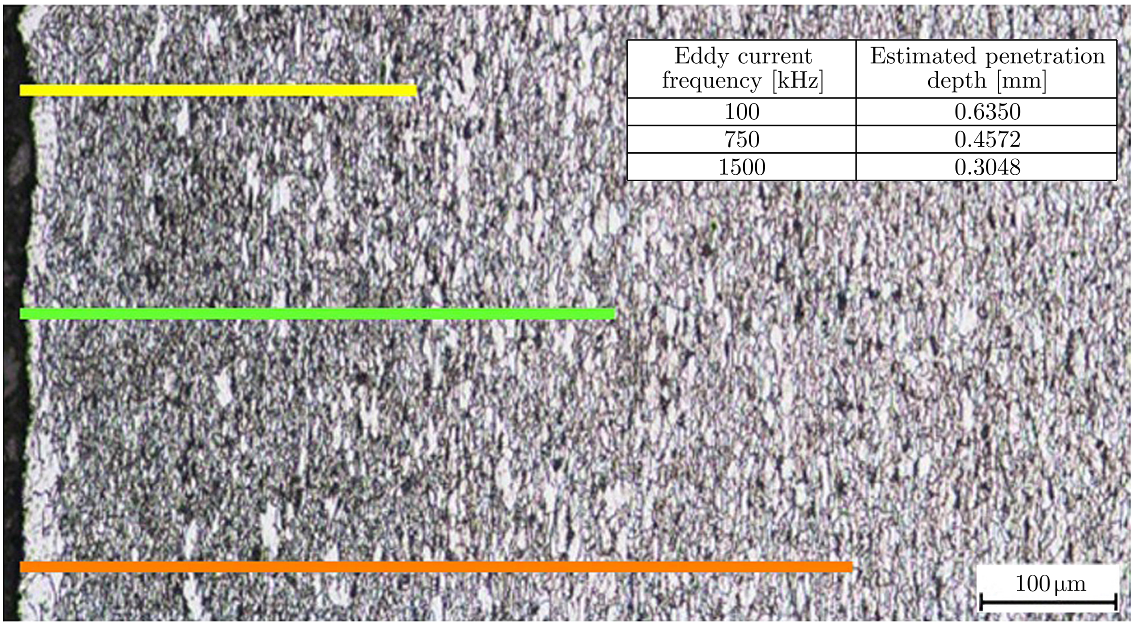

Eddy current frequency [kHz]	Estimated penetration depth [mm]
100	0.6350
750	0.4572
1500	0.3048

Fig. 1. Microstructure of the cross-section of the rolled sample S2W with estimated penetration depths of eddy currents for different induction frequencies.

tests, including a quantitative assessment of grain elongation. Figure 1 shows the estimated penetration depths of eddy currents for three values of the excitation frequency that were selected for testing. The impedance phase angle was measured on the surfaces of rolled specimens with different deformations and cross-sections in transverse and longitudinal directions to the rolling. It was observed that the most notable differences were found for the lowest penetration depth (Fig. 2). Such behavior was related to the highest deformation degree of the surface due to cold-work hardening. The deeper the measurement frequency was, the lower the recorded differences were. It was directly connected with the microstructural changes that occurred below the surface (Fig. 1).

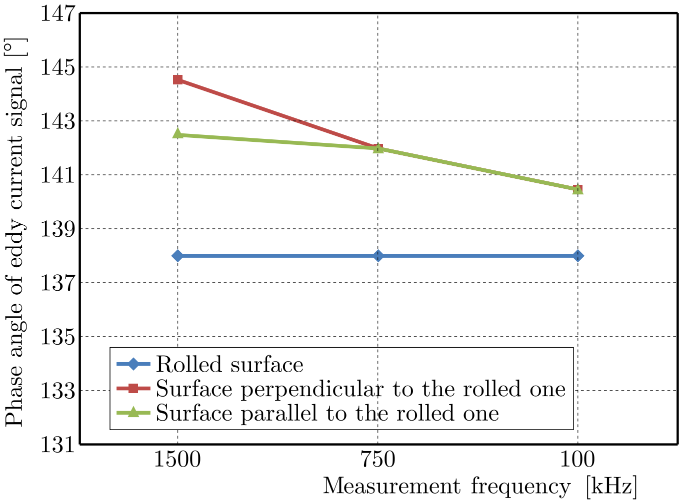

Fig. 2. Changes in the phase angle as a function of frequency for three surfaces of the sheet with a thickness of 6 mm.

The results of impedance measurements performed on surfaces with various degrees of deformation were compared with dislocation density measurement, as shown in Table 1. Example images of the dislocation structures and measurement lines are shown in Fig. 3. The numbers of estimated dislocation for the analyzed samples are shown in Table 1.

Table 1. Mean value for dislocation density in specimen S, S1W, and S2W.

Specimen	Dislocation density
S (initial state, 12 mm thick)	$5.50 \times 10^{12}\,\mathrm{m}^{-2}$
S1W (cold rolled, 8 mm thick)	$9.14 \times 10^{12}\,\mathrm{m}^{-2}$
S2W (cold rolled, 6 mm thick)	$1.10 \times 10^{13}\,\mathrm{m}^{-2}$

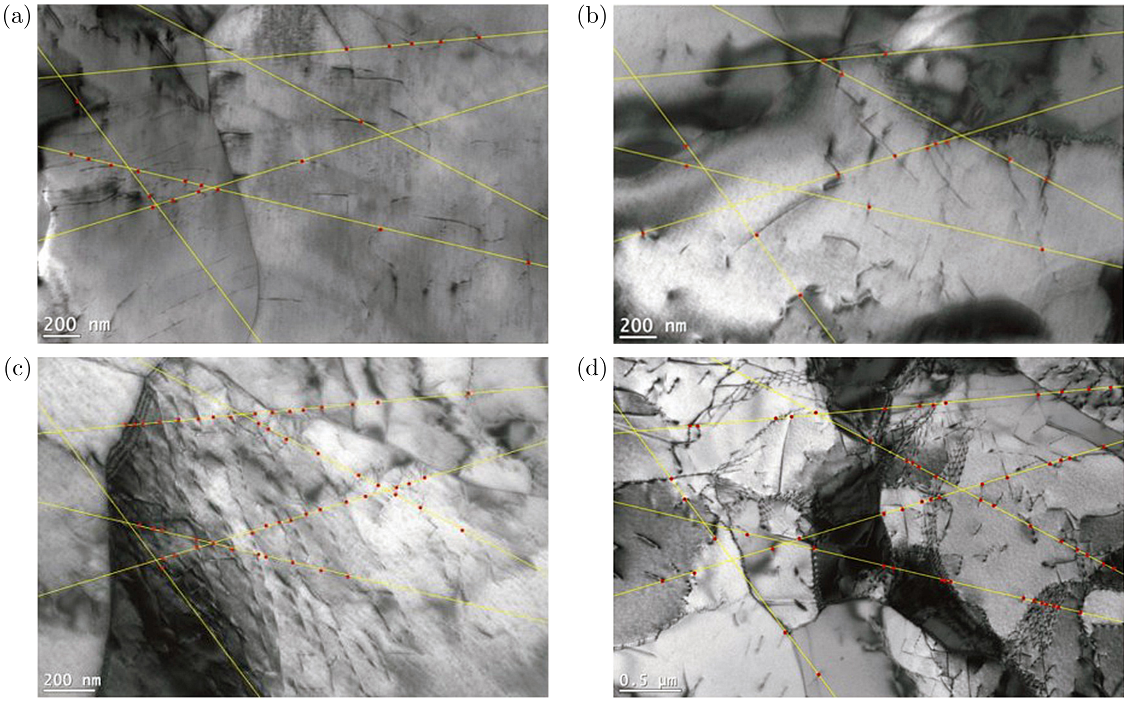

Fig. 3. Dislocation structure of S235 (sample S) with visible dislocation and measurement lines, the number of intersections is 21 for image (a) and 17 for image (b); dislocation structure of S235 after cold rolling (sample S2W) with visible dislocation and measurement lines, the number of intersections is 48 for image (c) and 51 for image (d).

Such comparison clearly indicates an increase in dislocation density for specimens after cold rolling in comparison to the initial state. The higher the dislocation density was, the more material hardening was introduced.

The results clearly show an increase in the dislocation number for samples after cold rolling in comparison to the initial state. However, a higher number of observed dislocations was expected. This fact can be explained by the low dimension of the analyzed area (TEM sample) which can make the analyzed volume of the material insufficient for proper estimation of dislocation density. Another explanation is the possible annihilation of dislocation being a result of residual stress relaxation during TEM sample preparation.

The variation of the eddy current parameter as a function of dislocation density measured for samples after various degrees of deformation, with different penetration depths, is shown in Fig. 4. It is easy to notice that the same deformation degree represented by the specific dislocation density value can be more precisely detected for higher measurement frequency applied.

The experimental results highlight the intricate relationship between the microstructural changes due to cold-rolling and corresponding ECT signals. As shown in the cross-sectional microstructures, the deformation process caused a pronounced grain elongation and texture development. This was quantitatively confirmed through stereological and TEM analyses. The differences in crystallographic texture between the initial state and cold-rolled states underscore the significant alterations in the material's internal structure.

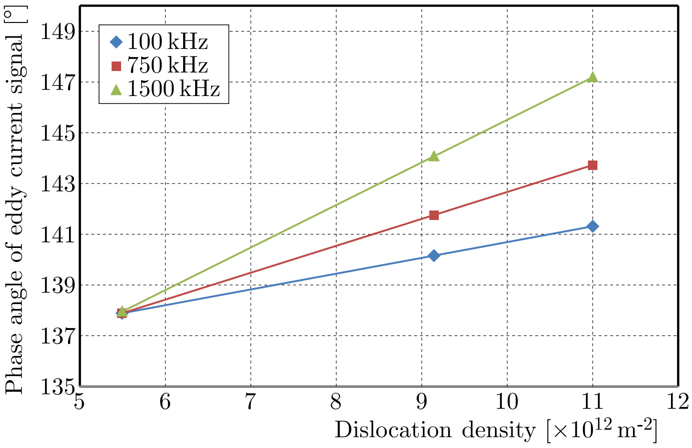

Fig. 4. Influence of dislocation density on the phase angle for different ET penetration depths.

The phase angle of impedance, measured at various ECT penetration depths, revealed distinct trends tied to the degree of deformation. At the lowest penetration depth, the most substantial differences in the phase angle were observed, correlating with the pronounced surface deformation induced by cold rolling. This behavior reflects the higher sensitivity of shallow measurements to surface changes, where cold-work hardening and increased dislocation density are predominant. In contrast, deeper penetration depths exhibited attenuated differences, as the subsurface regions experienced comparatively less deformation. The correlation between dislocation density and the phase angle further elucidates the role of cold rolling in modification of the steel's microstructure. Dislocation density, which increased from $5.50 \times 10^{12}\,\mathrm{m}^{-2}$ in the initial state to $1.10 \times 10^{13}\,\mathrm{m}^{-2}$ in the 6-mm thick rolled specimen, aligned with progressive material hardening. This increase was directly mirrored in the ECT data, where higher dislocation densities corresponded to more pronounced changes in the impedance phase angle. Notably, these effects were most discernible at higher excitation frequencies, which enhanced the detection precision for specific deformation degrees.

The results also underscore the efficacy of ECT in distinguishing microstructural gradients within the material. By leveraging varying penetration depths, ECT demonstrated its capability to detect surface versus subsurface changes. This feature is particularly valuable for assessing surface treatments or identification of the localized deformation zones that may impact material performance.

4. Conclusions

This study successfully demonstrated the utility of ECT in evaluating microstructural changes in S235 heat-resistant steel subjected to cold rolling. Key conclusions include:

- ECT effectively detected changes in grain elongation, crystallographic texture, and dislocation density induced by cold rolling. These microstructural alterations significantly influenced the impedance phase angle, particularly at lower penetration depths;
- the highest sensitivity to deformation-induced changes was observed at shallow penetration depths, making ECT a powerful tool for surface-level assessments where cold-work hardening is predominant;
- a strong correlation between increased dislocation density and changes in the ECT phase angle was established, providing a quantitative link between microstructural changes and ECT signal variations;
- the results highlight the potential of ECT as a non-destructive technique for the characterization of manufacturing-induced microstructural changes in heat-resistant steels. The

method is applicable to quality control processes and can aid in predicting material performance in service.

Future work should focus on extending the methodology to other materials and deformation processes, as well as exploring the integration of ECT with other non-destructive techniques for comprehensive microstructural evaluations.

Acknowledgments

The authors would like to express their gratitude to M. Wyszkowski for his kind help during the experimental part of this work.

References

1. Brnic, J., Brcic, M., Balos, S., Vukelic, G., Krscanski, S., Milutinovic, M., & Dramicanin, M. (2021). S235JRC+C steel response analysis subjected to uniaxial stress tests in the area of high temperatures and material fatigue. *Sustainability*, *13*(10), Article 5675. https://doi.org/10.3390/su13105675
2. Kukla, D., Kopec, M., & Gradzik, A. (2022). Identification and characterization of the grinding burns by eddy current method. *Open Engineering*, *12*(1), 1046–1050. https://doi.org/10.1515/eng-2022-0382
3. Kukla, D., Kopec, M., Wang, K., Senderowski, C., & Kowalewski, Z.L. (2021). Nondestructive methodology for identification of local discontinuities in aluminide layer-coated MAR 247 during its fatigue performance. *Materials*, *14*(14), Article 3824. https://doi.org/10.3390/ma14143824
4. Makowska, K., & Kowalewski, Z.L. (2024). Evaluation of microstructure and mechanical properties of ferromagnetic structural steels using Barkhausen noise. *Journal of Theoretical and Applied Mechanics*, *62*(3), 587–599. https://doi.org/10.15632/jtam-pl/191444
5. Ueji, R., Tsuji, N. Minamino, Y., & Koizumi, Y. (2002). Ultragrain refinement of plain low carbon steel by cold-rolling and annealing of martensite. *Acta Materialia*, *50*(16), 4177–4189. https://doi.org/10.1016/S1359-6454(02)00260-4

*Manuscript received January 10, 2025; accepted for publication March 31, 2025;
published online July 10, 2024.*

**JOURNAL OF THEORETICAL
AND APPLIED MECHANICS**
63, 3, pp. 607–621, Warsaw 2025
https://doi.org/10.15632/jtam-pl/203600

FIELD PATH DETECTION FOR TRACTORS BASED ON ACCELERATION MEASUREMENTS AND MULTIBODY SYSTEM SIMULATIONS

Wilhelm FUCHS[1], Gernot JEDINGER-PAUSCHENWEIN[1], Helmut J. HOLL[2*]

[1] *AVL List GmbH, Tech-Center Steyr, Austria*
[2] *Institute of Technical Mechanics, Johannes Kepler University, Linz, Austria*
*corresponding author, *helmut.holl@jku.at*

A process is described that allows the identification of the road profile traversed by a tractor based only on acceleration signals measured in the field. The objective of this identification process is to obtain a field path profile that, when simulated, produces accelerations in the tractor as close as possible to those generated by the original profile, thereby causing similar damage values to the structure of the tractor. This process requires an accurate multibody system model of the vehicle with a sophisticated tire model. Under these considerations a method has been developed making it possible to invert the dynamic problem and to determine the field path profile, which can subsequently be used for simulations of arbitrary tractors.

Keywords: vehicle; multibody system; Adams; inverse dynamics; identification.

1. Introduction

Virtual development of tractors requires an accurate load case definition with a reasonable correspondence between simulation and real-world field conditions, which is the fundamental prerequisite for the strength and mechanical fatigue analysis (see (Renius, 2020)). The predominantly used input load parameters are the forces at the wheel hubs and excitations caused by the field path profile.

A well-established method to measure the forces at the wheel hubs is to use measurement rims (see Fig. 1), although this approach is time consuming (Ferhadbegović, 2008).

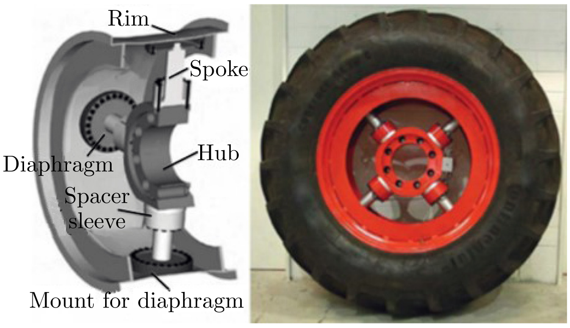

Fig. 1. Measurement rim.

Ministry of Science and Higher Education
Republic of Poland

The publication has been funded by the Polish Ministry of Science and Higher Education under the Excellent Science II programme "Support for scientific conferences".
The content of this article was presented during the 40th Danubia-Adria Symposium on Advances in Experimental Mechanics, Gdańsk, Poland, September 24–27, 2024.

Moreover, these forces are specific to one particular parameter set, whereby even a minor change (e.g., adjusting ballast mass, using another implement, etc.) makes these measured forces unusable for further simulations with the established tractor model.

Therefore, parameters are needed which are independent of the specific tractor configuration. Since the field path profile fulfills this requirement, it emerges as a promising approach (also see (Gattringer, 2023)).

2. Field path detection based on measured accelerations

An accurate multibody system simulation model of the tractor including a high sophisticated tire model is the prerequisite for field path detection, which has been elaborated in (Fuchs & Pauschenwein, 2019; Jedinger-Pauschenwein *et al.*, 2024).

For setting up the multibody system (see (Schrattbauer, 2024)), the software system Adams, version 2022.2.0, has been used in combination with FTire. Adams is a multibody dynamics simulation software system (see (Adams)), whereas FTire is used for modeling tires (see (Gipser, 2007; Leister, 2009; Oertel, 2007; FTire)).

The method presented here allows the identification of the road profile traversed by a tractor based solely on measuring accelerations.

The target is to derive a profile that, when simulated, generates accelerations in the tractor as closely as possible to those generated by the original profile. As a result, the identification of the road profile excitations on basis of measured accelerations is an inverse problem.

Considering an inverse problem, a simplified model with a reduced number of degrees of freedom seems to be advantageous. Therefore, such a model is derived from the complex nonlinear tractor model in Adams replicating the dynamic behavior of the real tractor very accurately. Referring to Schiller (2018) comparative simulations proved that a reasonable reduction of degrees of freedoms has a negligible influence on the accelerations (e.g., fixing cabin rigidly to the tractor body, etc.). Furthermore, the high sophisticated FTire model is replaced by a spring damper system, and further simplifications of the inverse problem are achieved by linearization.

2.1. Mathematical framework

Linear time-invariant mechanical systems are characterized by the differential equation:

$$\mathbf{M}\ddot{\mathbf{s}} + \mathbf{D}\dot{\mathbf{s}} + \mathbf{K}\mathbf{s} = \mathbf{f}. \tag{2.1}$$

Description of the parameters and the variables:

q	– number of degrees of freedom,	$\mathbf{M} \in \mathbb{R}^q \times \mathbb{R}^q$	– mass matrix,
$\mathbf{s} \in \mathbb{R}^q$	– generalized displacement vector,	$\mathbf{D} \in \mathbb{R}^q \times \mathbb{R}^q$	– damping matrix,
$\dot{\mathbf{s}} \in \mathbb{R}^q$	– generalized velocity vector,	$\mathbf{K} \in \mathbb{R}^q \times \mathbb{R}^q$	– stiffness matrix,
$\ddot{\mathbf{s}} \in \mathbb{R}^q$	– generalized acceleration vector,	$\mathbf{f} \in \mathbb{R}^q$	– external forces vector.

Using the substitution $\dot{\mathbf{s}} = \mathbf{v}$ and adjusting the notation such that $\mathbf{M}^{-1}\mathbf{f} = \widehat{\mathbf{B}}\mathbf{u}$ leads to a first order system of linear differential equations:

$$\begin{bmatrix} \dot{\mathbf{s}} \\ \dot{\mathbf{v}} \end{bmatrix} = \underbrace{\begin{bmatrix} \mathbf{0} & \mathbf{E} \\ -\mathbf{M}^{-1}\mathbf{K} & -\mathbf{M}^{-1}\mathbf{D} \end{bmatrix}}_{\mathbf{A}} \begin{bmatrix} \mathbf{s} \\ \mathbf{v} \end{bmatrix} + \underbrace{\begin{bmatrix} \mathbf{0} \\ \widehat{\mathbf{B}} \end{bmatrix}}_{\mathbf{B}} \mathbf{u}. \tag{2.2}$$

Introducing the state vector $\mathbf{x}^{\mathrm{T}} = \left[\mathbf{s}^{\mathrm{T}}, \mathbf{v}^{\mathrm{T}}\right]$, the linear time-invariant (LTI) system results in a more compact form, whereby the wheel hub forces are collected in the input vector $\mathbf{u}$:

$$\dot{\mathbf{x}} = \mathbf{A}\mathbf{x} + \mathbf{B}\mathbf{u} \quad \text{with} \quad \mathbf{y} = \mathbf{C}\mathbf{x} + \mathbf{D}_T\mathbf{u}. \tag{2.3}$$

Description of the matrices:

$\mathbf{A} \in \mathbb{R}^n \times \mathbb{R}^n$ – system matrix
$\mathbf{C} \in \mathbb{R}^k \times \mathbb{R}^n$ – output matrix
$\mathbf{B} \in \mathbb{R}^n \times \mathbb{R}^m$ – input matrix
$\mathbf{D}_T \in \mathbb{R}^k \times \mathbb{R}^m$ – direct transmission matrix.

This LTI system comprises matrices $\mathbf{A}$, $\mathbf{B}$, $\mathbf{C}$, $\mathbf{D}_T$, state vector $\mathbf{x} \in \mathbb{R}^n$ (positions and velocities), input vector $\mathbf{u} \in \mathbb{R}^m$, and output vector $\mathbf{y} \in \mathbb{R}^k$.

Since in this study the direct transmission matrix $\mathbf{D}_T$, not to be confused with the damping matrix $\mathbf{D}$, is consistently zero, the output vector (measured variables) can be expressed as

$$\mathbf{y} = \mathbf{C}\mathbf{x}. \tag{2.4}$$

Differentiating Eq. (2.4) and substituting the vector $\dot{\mathbf{x}}$ from Eq. (2.3), $\dot{\mathbf{y}}$ becomes

$$\dot{\mathbf{y}} = \mathbf{C}\mathbf{A}\mathbf{x} + \mathbf{C}\mathbf{B}\mathbf{u}. \tag{2.5}$$

Reorganizing the terms to isolate the input vector $\mathbf{u}$ leads to

$$\mathbf{u} = (\mathbf{C}\mathbf{B})^{-1} \cdot \left[\dot{\mathbf{y}} - \mathbf{C}\mathbf{A}\mathbf{C}^{-1}\mathbf{y}\right]. \tag{2.6}$$

Generally, matrix $\mathbf{C}$ possesses dimensions $k \times n$ while matrix $\mathbf{B}$ has $n \times m$. Upon multiplying these matrices, the resulting dimensions of $\mathbf{CB}$ are $k \times m$. If m is equal to k, and assuming $\mathbf{CB}$ is regular, it could be conventionally inverted. However, for non-square $\mathbf{CB}$ matrices, the equation has to be modified to (see (Freund & Hoppe, 2007)):

$$\mathbf{u} = (\mathbf{C}\mathbf{B})^{+} \cdot \left[\dot{\mathbf{y}} - \mathbf{C}\mathbf{A}\mathbf{C}^{-1}\mathbf{y}\right], \tag{2.7}$$

with the so-called Moore–Penrose pseudo-inverse for non-square matrices $\mathbf{CB}$, which is described in (Freund & Hoppe, 2007):

$$(\mathbf{C}\mathbf{B})^{+} = \left[\mathbf{B}^{\mathrm{T}}\mathbf{C}^{\mathrm{T}}\mathbf{C}\mathbf{B}\right]^{-1}\mathbf{B}^{\mathrm{T}}\mathbf{C}^{\mathrm{T}}. \tag{2.8}$$

Using the abbreviation $\mathbf{S} = \mathbf{B}^{\mathrm{T}}\mathbf{C}^{\mathrm{T}}\mathbf{C}\mathbf{B}$, the pseudo-inverse becomes

$$(\mathbf{C}\mathbf{B})^{+} = \mathbf{S}^{-1}\mathbf{B}^{\mathrm{T}}\mathbf{C}^{\mathrm{T}}, \tag{2.9}$$

and Eq. (2.7) transforms to

$$\mathbf{u} = \mathbf{S}^{-1}\mathbf{B}^{\mathrm{T}}\mathbf{C}^{\mathrm{T}} \cdot \left[\dot{\mathbf{y}} - \mathbf{C}\mathbf{A}\mathbf{C}^{-1}\mathbf{y}\right]. \tag{2.10}$$

Matrix $\mathbf{S}$ must be invertible for this algorithm's application. This necessitates matrix $\mathbf{C}$ to be regular. Considering this relationship, the input variables of an LTI-system can be deduced, and this research indicates that, in general, the addressed problem is a pseudo-inverse one.

A significant merit of this approach is the elimination of frequency domain transformations which are normally used for inversion by virtual iteration (see (Gattringer, 2023; Reichl, 2011; Witteveen, 2023)). Furthermore, matrix $\mathbf{S}$ requires only one single inversion, regardless of the computed time steps, as it comprises fixed values.

Since the second derivation of the positions is measurable (accelerations), only signal integration is required to obtain $\dot{\mathbf{y}}$ and $\mathbf{y}$, which is a stable numerical procedure. In this special case it has been chosen for simplicity without loss of generality that $\dot{\mathbf{y}} = \dot{\mathbf{x}}$ and $\mathbf{y} = \mathbf{x}$.

Knowing the forces $\mathbf{u}$, the state vector $\mathbf{x}$, tire stiffness and damping, a differential equation is applied to deduce the field path profile (ground elevation $\mathbf{x}_G$) considering the geometry referring to the tire radius.

2.2. Identification of wheel center point displacement

The system description (2.2) and (2.3), along with its inverted variant (2.10), is relevant only for systems that have forces as their inputs, but field path detection requires a further relation between forces and displacements which will be the final inputs.

To establish the relationship between force and displacement, a single-mass oscillator composed of a spring and damper is utilized, as depicted in Fig. 2. In this context, the linear spring/damper model approximates the complex stiffness and damping properties of the tire. Consequently, the values for the spring constant k and the damping coefficient d can be derived from parameters of the FTire-model.

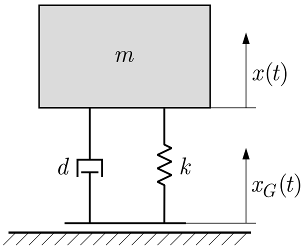

Fig. 2. One-mass-oscillator.

The equation of motion for the mass in Fig. 2 is

$$m\ddot{x} = -d(\dot{x}_G - \dot{x}) - c(x_G - x), \tag{2.11}$$

where x and $\dot{x}$ represent the vertical position and velocity of the wheel center point (WCP). Both state variables are obtained from the simulation directly or from integration of the sensor signal. The force F, which is identical to the right side of Eq. (2.11), has been determined by the inverse algorithm to identify the wheel hub forces. As a result, it becomes feasible to determine x_G by solving the differential equation:

$$\dot{x}_G = \frac{c(x - x_G) + d\dot{x} + F}{d}. \tag{2.12}$$

In simulations with different profiles, it is not ensured that, even with otherwise unchanged simulation parameters, the average speed remains the same. This implies that when comparing two simulation results over the time parameter, a reliable comparability of the state variables cannot be guaranteed.

However, as part of the iteration process, it is essential to compare and link state variables from different simulations with varying track profiles. For the before mentioned reason, the dependence on time is transformed into a dependence on distance $s(t)$. By introducing

$$v(t) = \frac{\mathrm{d}s(t)}{\mathrm{d}t} \tag{2.13}$$

and applying the chain rule

$$\frac{\mathrm{d}x(s(t))}{\mathrm{d}t} = \frac{\mathrm{d}x(s(t))}{\mathrm{d}s}v(t) \to \frac{\mathrm{d}x(s)}{\mathrm{d}s} = \frac{\mathrm{d}x(t)}{\mathrm{d}t}\frac{1}{v(t)}. \tag{2.14}$$

Equation (2.12) results in

$$\frac{\mathrm{d}x_G(s)}{\mathrm{d}s} = \frac{c(x(s) - x_G(s)) + d\dot{x}(s) + F(s)}{d}\frac{1}{v(s)}. \tag{2.15}$$

To transform the simulation data from the time domain to the space domain, the variable x_{td} (traveled distance) was introduced. This variable integrates the longitudinal velocity component of the chassis center of mass, storing the distance covered at each sample time point (the traveled distances of the wheel hub centers should be identical with x_{td} of the chassis center of mass). By replacing the time vector with the resulting displacement vector, the state variable data can be transformed into the space domain.

Generally, it is important to realize that traversing a road profile in reality involves a tire with a non-zero radius, as sketched in Fig. 3.

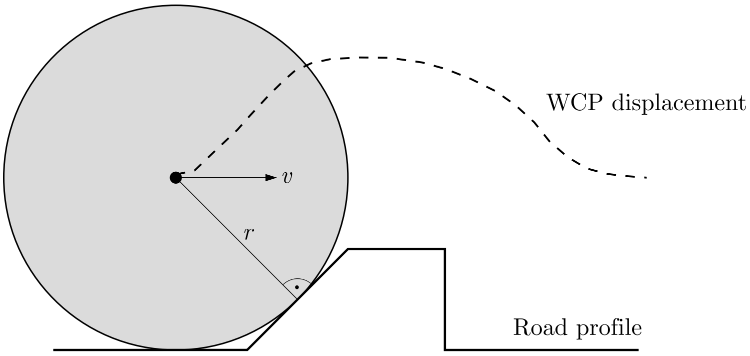

Fig. 3. Merry-go-round profile.

The line connecting the point of contact to the wheel center is supposed to remain always approximately normal to the road profile. This implies that the resulting movement of the wheel center will not represent the geometry of the traversed profile. Therefore, it becomes essential to construct the road profile from the determined displacements of the wheel center points.

Moreover, it is crucial to recognize that the determination of wheel center point movements, based on the differential Eq. (2.2), presupposes that the tire's contact with the road occurs precisely at a single point vertically below the wheel center point. However, this is an idealized simplification, because multi-point contacts as illustrated in Fig. 3 can occur as well as tire's compression at edges (see Fig. 4). Due to these multi-point contacts and extreme tire deflections the field path profile cannot be captured accurately within this section.

Fig. 4. Tire compressed by edge.

Regarding the influence of tire radii on the quality of identification, this study aims to demonstrate that an identified profile achieves satisfactory accelerations even when traversed with tires of larger radii. As a result, re-identification is not necessary when using tires with larger radii.

Another point to consider is that during the simulation or during the field test, one or more wheels may lift off the roadway. It is impossible for the identification algorithm to distinguish between an actual lift off and a touching road profile. In addition, tires starting to skid can cause another problem: since the identified profiles will always differ from the original profile, these effects will never occur at the same time, with the same duration, or at the same place in subsequent simulations of an iteration.

As a result, there can be phase shifts in the acceleration signals of different simulations. All these real-world effects influence the identified road profile, whereby a geometrically precise identification of the road profile using this method seems to be unattainable.

For future investigations it may be expected that AI-methods incorporate potential for further improvements concerning the identification and inversion process.

Nevertheless, it must be emphasized that the highest accuracy is not the primary aim, anyway. The goal is to ensure that the accelerations resulting from the identified road profile sufficiently approximate the accelerations caused by the original road profile, because in this case the damage values referring to the identified road profile can be expected satisfactorily close related to those caused by the original road profile, see (Fuchs *et al.*, 2024).

2.3. Road generation

The unknown track profile can be generated from the identified wheel center point deflections using geometrical considerations. As already explained in the preceding section, the wheel center point deflections arise approximately by following the line always perpendicular to the track with a length of the constant tire radius r as illustrated in Fig. 3.

The track profile can now be determined in the opposite manner. The derivative of the wheel center point deflection p_{WCP} defines $g(s)$ as

$$\frac{\mathrm{d}p_{\mathrm{WCP}}(s)}{\mathrm{d}x} = g(s), \tag{2.16}$$

and the gradient of the deflection curve is

$$\mathbf{g}(s) = \begin{pmatrix} 1 \\ g(s) \end{pmatrix}. \tag{2.17}$$

By rotating the gradient by 90° clockwise, one obtains

$$\acute{\mathbf{g}}(s) = \begin{pmatrix} g(s) \\ -1 \end{pmatrix}. \tag{2.18}$$

As a unit vector multiplied by the tire radius r_W, the desired vector

$$\mathbf{g}_r(s) = \frac{1}{|\acute{\mathbf{g}}(s)|}\acute{\mathbf{g}}(s) r_W \tag{2.19}$$

is obtained, pointing from the current wheel center point position to the corresponding contact point or point on the track. Adding the wheel center point position and the vector (Eq. 2.19) yields the absolute position of the current track point.

Adding the tire radius in the z-direction (vertical) ensures that the track coordinate in the z-direction starts at 0:

$$\mathbf{p}_R(s) = \mathbf{p}_{\mathrm{WCP}}(s) + \mathbf{g}_r(s) + \begin{pmatrix} 0 \\ r_W \end{pmatrix}. \tag{2.20}$$

Since the longitudinal components of the tire contact forces are known from the Adams simulation, and the longitudinal stiffnesses k_{Long} of the tires are available, the determined position of the current contact point can be further corrected in the x-direction by estimating

$$c(s) = \frac{F_{\mathrm{Long}}(s)}{k_{\mathrm{Long}}(s)} \tag{2.21}$$

as an additional shift:

$$\mathbf{p}(s) = \mathbf{p}_{\mathrm{WCP}}(s) + \mathbf{g}_r(s) + \begin{pmatrix} c(s) \\ r_W \end{pmatrix}. \tag{2.22}$$

A significant observation is that the road created using this method cannot generally be directly utilized. This stems from the fact that it cannot be assumed that in the identified wheel center point movements, all local radii of curvature are greater than or equal to the idealized tire radius as already mentioned (see Fig. 4).

If the radii of curvature are smaller than the tire radius, a track profile can emerge that self-penetrates, resulting in road points whose x-coordinates have multiple z-coordinates.

This phenomenon is illustrated in Fig. 5, which exemplifies such a generated road.

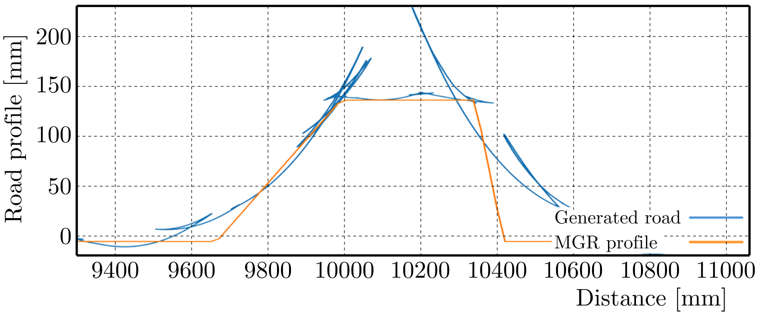

Fig. 5. Generated road profile from identified wheel center point movements.

Realistically, such tracks cannot be either created or traversed. Addressing these issues requires additional considerations. A sorting of all the generated track points according to their x-coordinates has been conducted. This sorting ensures a track with a unique x/z mapping. Figure 6 displays the track that results from sorting the track shown in Fig. 5.

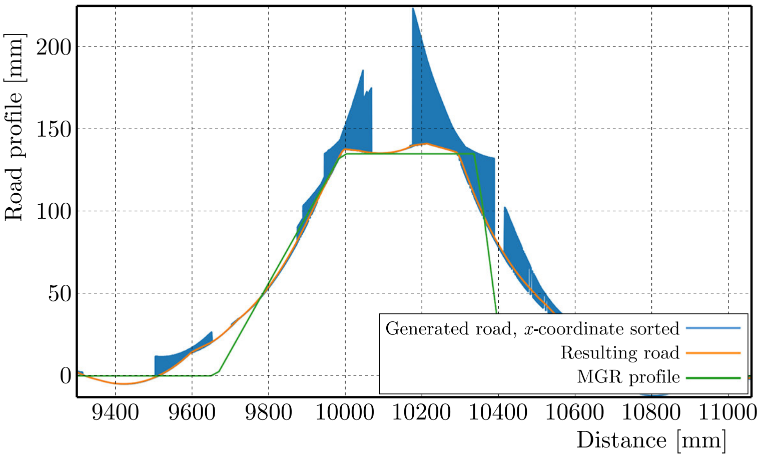

Fig. 6. Generated road profile with sorted x-coordinates.

Having achieved a unique x/z mapping, the next step involves eliminating the peaks that arose during the sorting process. This elimination is executed via a search algorithm. Starting from the current point, the algorithm searches for the first point in the x-direction such that the connecting line between the points does not exceed a predetermined maximum gradient value.

This newly identified point then serves as the starting point for subsequent searches. The final profile generated through this process is depicted in Fig. 6. This methodical approach ensures a road profile that can be used in subsequent simulations.

A summarizing description of the identification algorithm is described in Fig. 7.

The original accelerations refer to a complex nonlinear model, especially in view of the highly sophisticated tire model. Since identifications are carried out with the simplified LTI models, the identified profiles deviate from the original one. Therefore, a virtual iteration process in the time domain has been developed so that the identified solutions should converge to the original profiles (see Fig. 8).

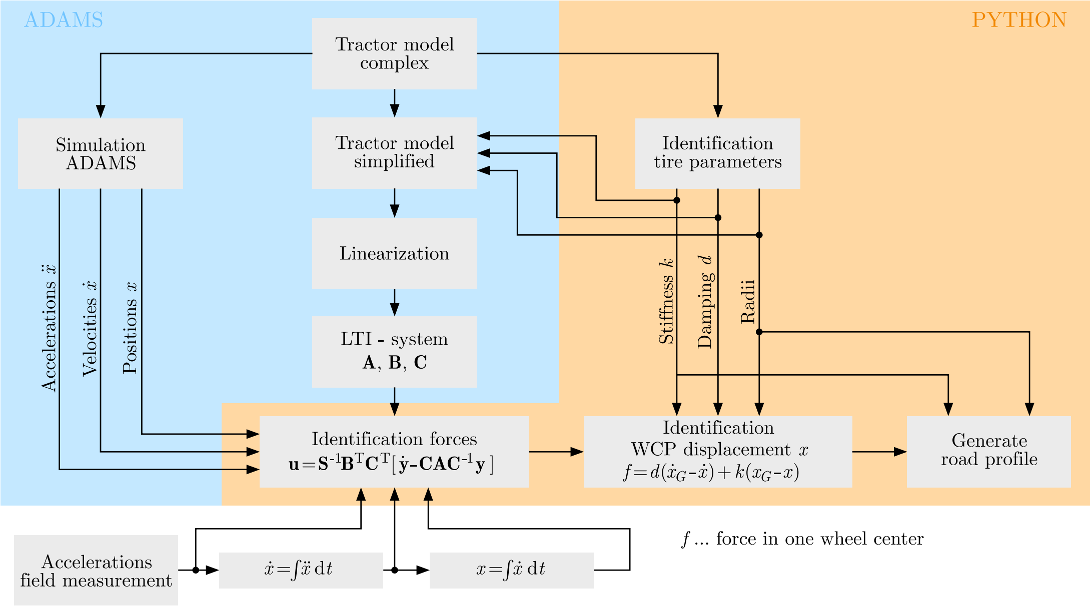

Fig. 7. Identification algorithm.

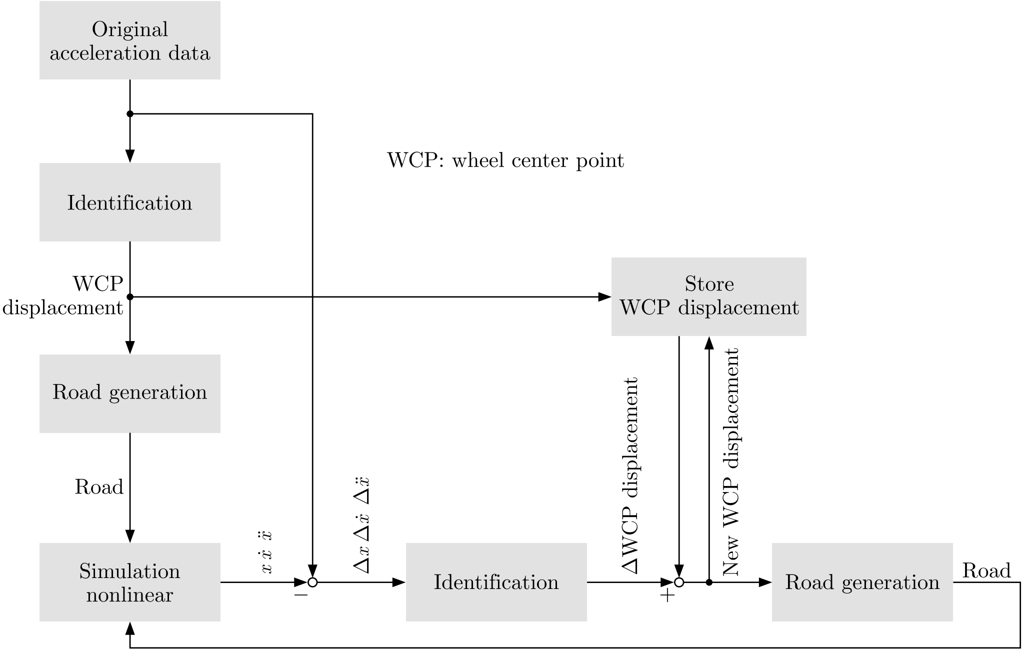

Fig. 8. Iteration process for road identification.

However, it must be emphasized that convergence cannot be warranted, and it has to be checked with a keen eye whether the process is successful and whether the iterated accelerations are sufficiently close to the original ones.

2.4. Simplified model for inversion

It is crucial to select an appropriate number of degrees of freedom and, consequently, an adequate number of state variables (see (Popp & Schiehlen, 2010; Shabana, 2013)). Typically, a rigid body possesses six degrees of freedom, encompassing movements in the x-, y-, and z-directions, and rotations about these axes. An additional degree of freedom arises from the front axle, which can rotate about the longitudinal axis independently of the main chassis in the case presented here.

In the context of the simplified model, movement in the longitudinal direction is not considered, and the model is fixed in this direction at the center of gravity. Additionally, the movement of the center of gravity in the lateral direction and its rotation about the vertical axes have been selected as the fifth and sixth degrees of freedom.

Consequently, the following six degrees of freedom remain:

1) movement of chassis in vertical direction;
2) movement of chassis in lateral direction;
3) rotation of chassis about vertical axis;
4) rotation of chassis about longitudinal axis;
5) rotation of chassis about lateral axis;
6) rotation of front axle about longitudinal axis of chassis.

These six degrees of freedom can be expressed via transformations of the six state variables (X_1, X_2, X_3, X_4, X_5, X_6), as seen in Fig. 9, where also the chosen combination of state variables and boundary conditions is illustrated.

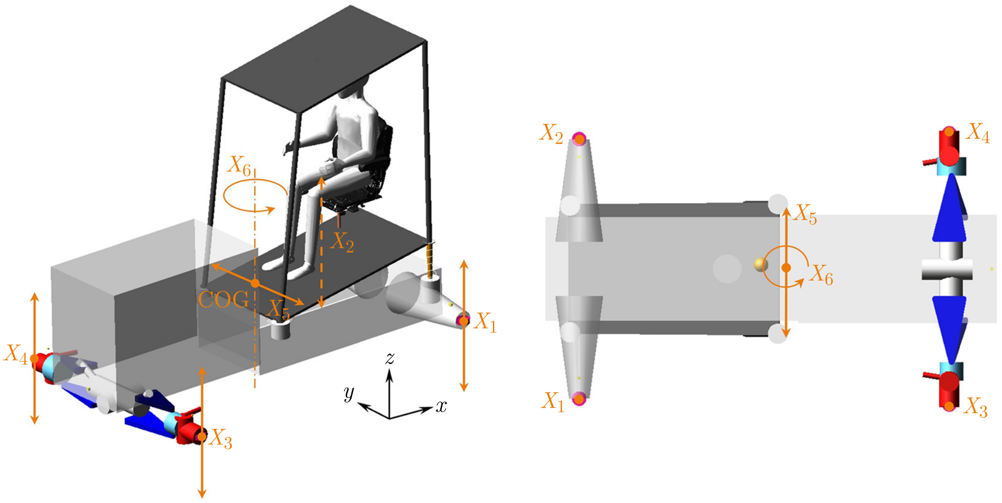

Fig. 9. Simplified model, state and boundary condition.

The four sensor locations from the nonlinear model, depicted in Fig. 10, are selected, whereby all sensors can measure accelerations in x-, y-, and z-directions. Without loss of generality, the sensor positions have been virtually shifted to the wheel center points, which requires transformations of the measured acceleration signals.

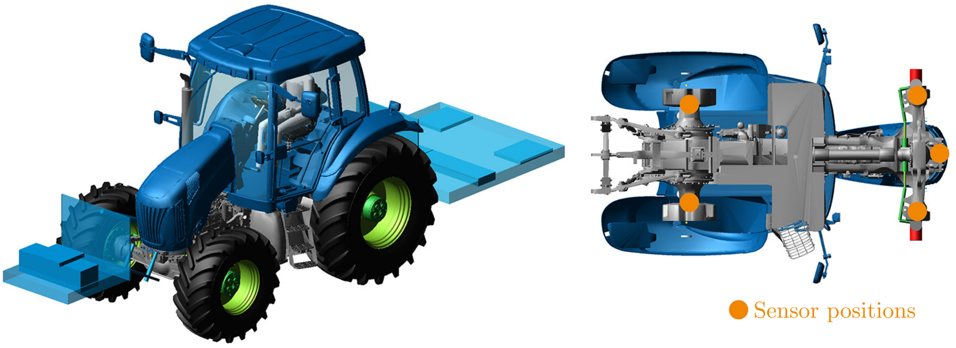

Fig. 10. Tractor, position of acceleration sensors.

All these transformations serve to reduce potential error sources during development, as the movement of the wheel center points is integral to the identification process.

Fortunately, this system comprises six degrees of freedom and six input parameters which are four vertical and two lateral forces (one lateral force per axle). As a result, in this case a direct inversion of the matrix **CB** is possible. If a swing arm at the front axle is to be considered, the number of degrees of freedom will be greater than the number of input parameters, which requires the application of the Moore-Penrose pseudo-inversion.

3. Examples for field path detection

General remark: references to measurement details (tractor manufacturer, test location) cannot be provided because of confidentiality agreements with AVL's customer.

3.1. Merry-go-round test

The merry-go-round test (MGR) is specifically designed to test the durability and resilience of vehicles when exposed to real or simulated working conditions, whereby periodical excitations due to obstacles as shown in Figs. 11 and 12 are to be considered. In literature it is also referred to as a bump test track circuit with obstacles (see (Renius, 2020)).

Fig. 11. Merry-go-round test.

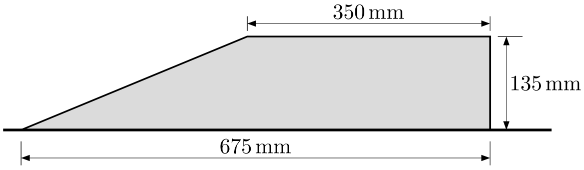

Fig. 12. Obstacle in detail.

A tractor was tested with a speed of 7.5 km/h. Based on accelerations measured close to the wheel hub centers, the obstacle shape has been identified, as seen in Fig. 13.

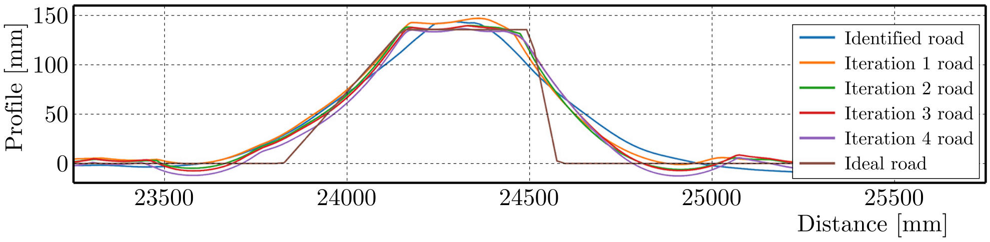

Fig. 13. MGR, 7.5 km/h, path profile.

However, the comparison between Figs. 12 and 13 indicates that the iterated profile does not match the original one exactly. The reason for the deviations can be explained by the following example.

For simplicity, a stiff disc is considered instead of an elastic tire, and furthermore, it is assumed that there will be no loss of contact between the profile and the disc. Even with these extremely simplified conditions it gets obvious that the red profile in Fig. 14 will cause the same vertical wheel center movement as the original black one, which means that in some cases the road profile cannot be uniquely determined on the basis of acceleration measurements.

In reality contact loss and multi-point contacts can additionally occur as well as compression of the tires at edges (see Fig. 4). It is impossible for the identification algorithm to distinguish between an actual lift off and a slight touching of the road profile. This is an illustrative explanation that convergence cannot be warranted. Therefore, it always must be checked if the iterated accelerations are sufficiently close to the original ones.

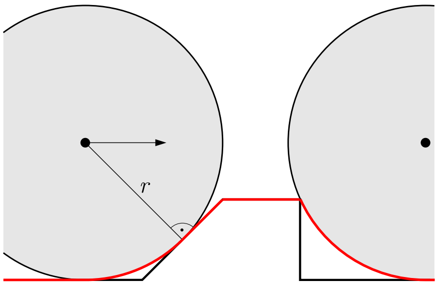

Fig. 14. Different road profiles achieving the same acceleration at wheel center point.

Nevertheless, Figs. 15 and 16 indicate that the acceleration results achieved with the identified profile correspond very well with the acceleration achieved with the original one. This is the most important condition for the simulation to present a realistic dynamic behavior of the tractor, also in view of subsequent strength and mechanical fatigue analyses.

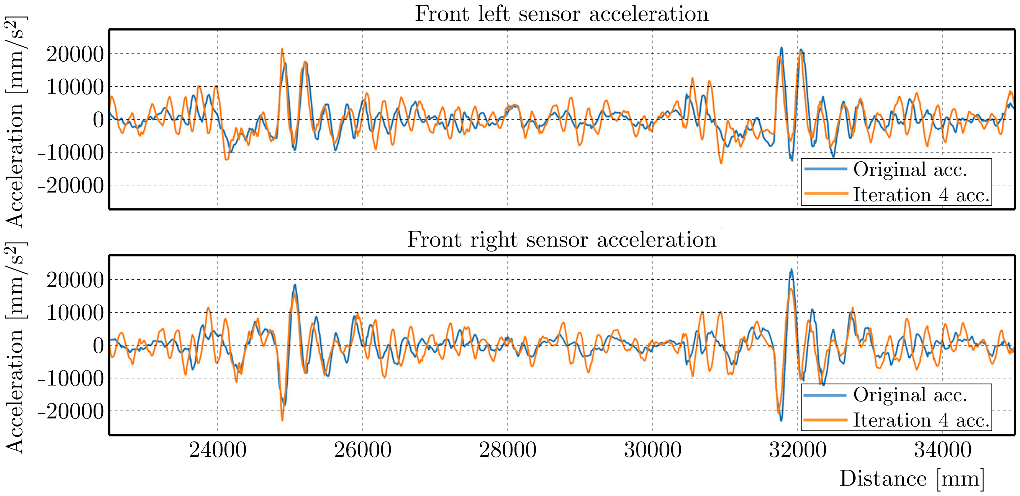

Fig. 15. MGR, 7.5 km/h, front acceleration.

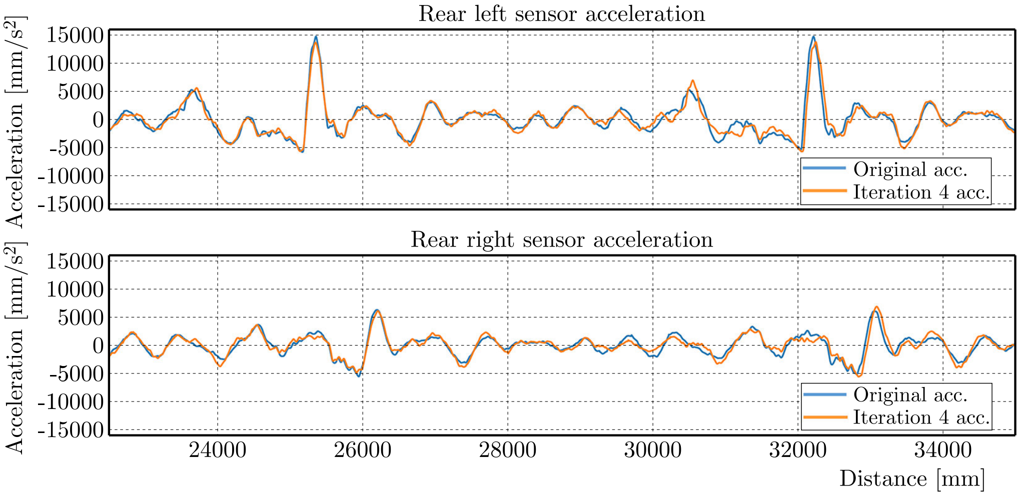

Fig. 16. MGR, 7.5 km/h, rear acceleration.

3.2. ISO 5008 track

The second test track was modeled on the basis of the ISO 5008 rougher road course (see (Wiesebrock, 2016)), the so-called Holperbahn-35 (jolting path or “Sturzacker”) as seen in Fig. 17.

Fig. 17. ISO 5008, rougher road course in reality.

This road course was traversed unballasted at a speed of 7.5 km/h.

Although the ISO 5008 profile challenges the inversion algorithm with its instances of multiple-point tire contacts and several sharp edges, Fig. 18 indicates that the original and the identified field path profiles correspond very well.

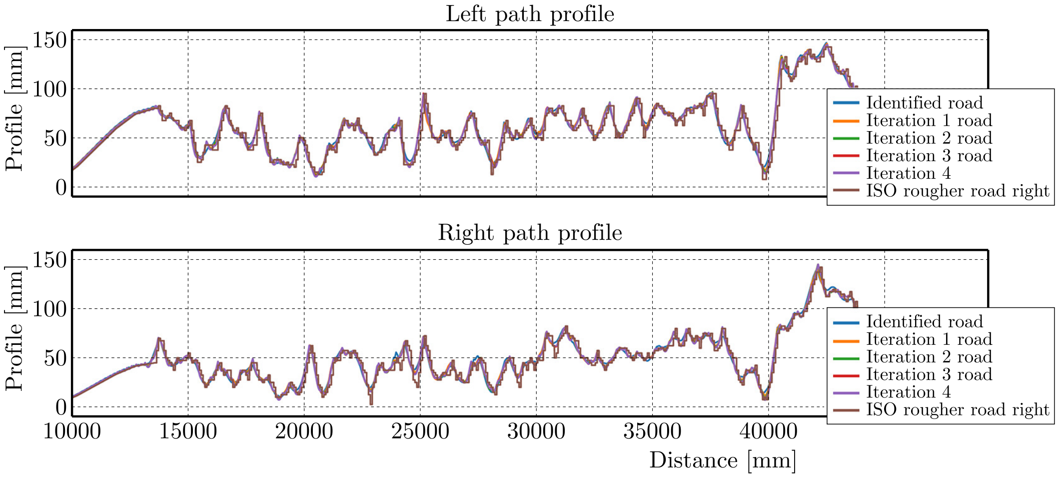

Fig. 18. ISO 5008, rougher road, path profile.

Nevertheless, a geometric match is not the ultimate objective, because the goal is to achieve vertical accelerations when traversing, which closely resemble the original ones. This must be verified by conducting another simulation using the identified track, and as seen in Figs. 19 and 20, the accelerations correspond sufficiently accurately with those achieved with the original profile, so that a satisfactory lifetime prediction should be possible.

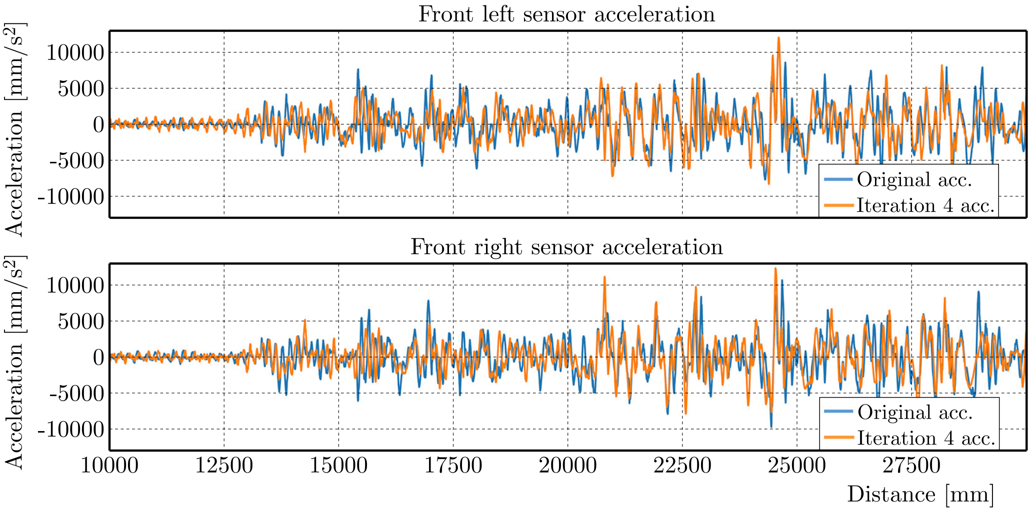

Fig. 19. ISO 5008, rougher road, 7.5 km/h, unballasted, front acceleration.

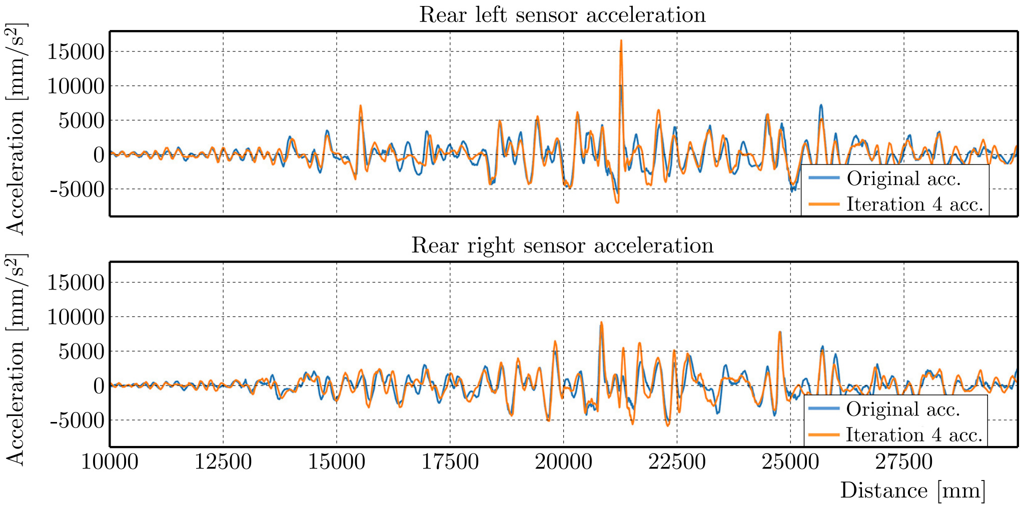

Fig. 20. ISO 5008, rougher road, 7.5 km/h, unballasted, rear acceleration.

3.3. Four-poster test rig

The four-poster test rig is designed to simulate working conditions in the field. It consists of four hydraulic actuators, each positioned under a wheel of the vehicle (see also (Reichl, 2011)). The objective is to achieve the same vertical accelerations as measured in the field. The presented inversion algorithm provides the input signals for the actuators, also for random and long test tracks. The simplified model is adjusted to the boundary conditions at the test bed, which means that the lateral degree of freedom is fixed by two bars at one front/rear wheel, as shown in Fig. 21. This measure and the fact that multiple tire contact surfaces cannot occur at the four-poster test rig accelerate the convergence.

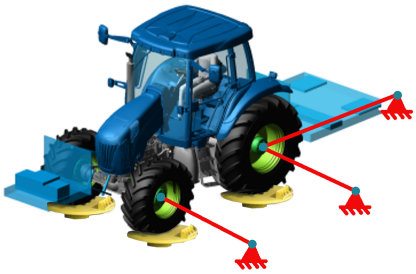

Fig. 21. Boundary conditions at four poster test rig.

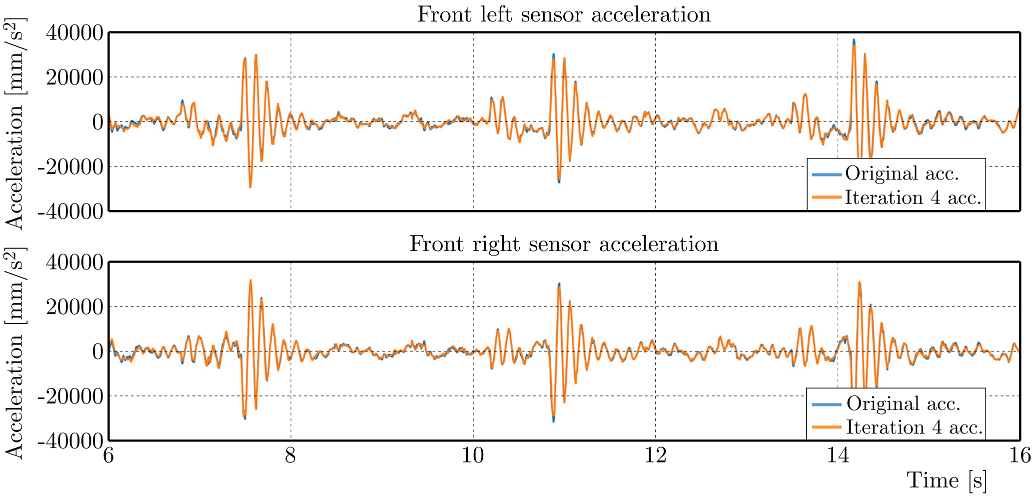

Fig. 22. Four-poster, MGR, 7.5 km/h, ballasted, front acceleration.

Using the merry-go-round test as example, Figs. 22 and 23 indicate that the target of reproducing the original acceleration on the test rig is met very well.

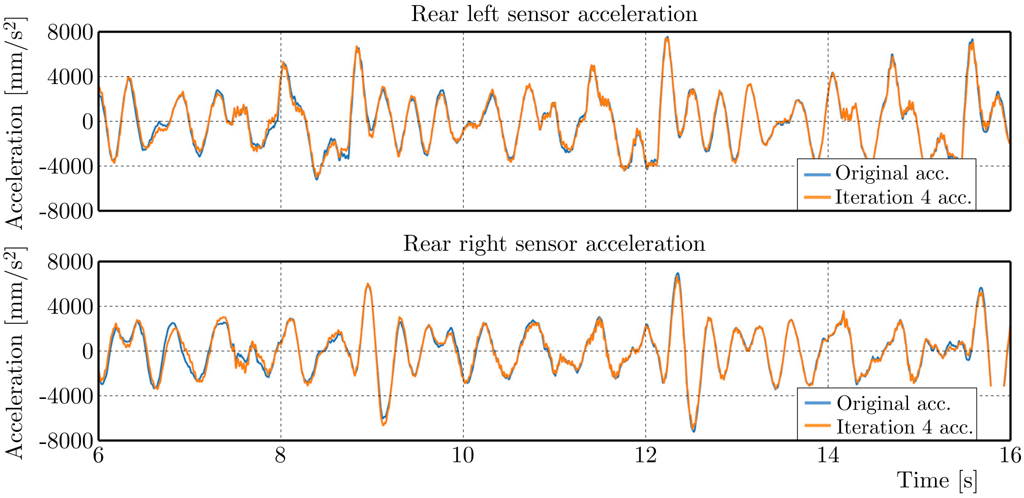

Fig. 23. Four-poster, MGR, 7.5 km/h, ballasted, rear acceleration.

4. Conclusions

An iterative method in the time domain has been established for field path detection based on measured accelerations. This method is cost-effective and sufficiently accurate as can be seen in the examples carried out.

Furthermore, in contrast to wheel hub forces, field path profiles do not depend on a certain set of tractor parameters, and therefore, they are outstandingly suitable for setting up an input data base for tractor multibody system simulations, also in view of different countries and farmlands.

Based on reliable input data, these tractor multibody system simulations will deliver sufficiently accurate load cases for the finite element analysis and mechanical fatigue life prediction, which is a prerequisite for the weight optimized tractor design.

For the future it may be expected that AI methods will provide further potential for process improvements.

Acknowledgments

The authors are grateful to Michael Schrattbauer for contributions with respect to the contents of the present paper.

References

1. Adams. Version v2021.0.1. Retrieved July 13, 2025, from https://hexagon.com/products/product-groups/computer-aided-engineering-software/adams.
2. Ferhadbegović, B. (2008). *Development and application of a transient tire model for the vehicle dynamics simulation of agricultural tractors* (in German), [Doctoral dissertation, Institut für Agrartechnik], Shaker Verlag Aachen.
3. Freund, R.W., & Hoppe, R.W. (2007). *Stoer/Bulirsch: Numerical Mathematics 1* (in German). Springer.
4. Fuchs, W., Jedinger-Pauschenwein, G., & Holl, H. (2024, September 24–27). *Field path detection for tractors based on acceleration measurements and virtual multibody system simulations* [Conference presentation]. 40th Danubia-Adria Symposium on Advances in Experimental Mechanics, Gdańsk, Poland.

5. Fuchs, W., & Pauschenwein, G. (2019). From field path profile detection to component testing. *ATZheavy duty worldwide*, *12*(2), 50–55. https://doi.org/10.1007/s41321-019-0022-x

6. FTire. Version 2021-1. Retrieved July 13, 2025, from https://www.cosin.eu.

7. Gattringer, O. (2023). *Virtual road for loads in concept phase using MBS and FEMFAT LAB, engineer vehicle dynamics analysis* [Conference presentation]. Magna ECS Simulation Conference, Linz.

8. Gipser, M. (2007). FTire – the tire simulation model for all applications related to vehicle dynamics. *Vehicle System Dynamics*, *45*(sup1), 139–151. https://doi.org/10.1080/00423110801899960

9. Jedinger-Pauschenwein, G., Fuchs, W., & Holl, H. (2024, September 24–27). *Virtual load case definition for off-road vehicles: Methodology based on multibody system simulation* [Conference presentation]. 40th Danubia-Adria Symposium on Advances in Experimental Mechanics, Gdańsk, Poland.

10. Leister, G. (2009). *Tire and chassis development: strategy, methods, tools, and applications* (in German). ATZ-MTZ Fachbuch, Vieweg und Teubner.

11. Oertel, C. (2007). *Tire modeling in full vehicle simulation: from real-time models to load spectrum analysis* (in German). Haus der Technik.

12. Popp, K., & Schiehlen, W. (2010). *Ground vehicle dynamics*. Springer.

13. Reichl, S. (2011). *Inverse dynamics and trajectory tracking of underactuated multibody systems* [Doctoral dissertation, Vienna University of Technology].

14. Renius, K.T. (2020). *Fundamentals of tractor design*. Springer.

15. Schiller, S. (2018). *Tractor global loading, method optimization* [Master's thesis, University of Applied Sciences]. Upper Austria.

16. Schrattbauer, M. (2024). *Field path profile detection for tractors* [Unpublished master's thesis, Johannes Kepler University]. Linz, Austria.

17. Shabana, A.A. (2013). *Dynamics of multibody systems* (4th ed.). Cambridge University Press.

18. Wiesebrock, A. (2016). *A generic road surface model for vehicle dynamics simulation* (in German). Springer Fachmedien Wiesbaden.

19. Witteveen, W. (2023). *Iterative method for the coupling of arbitrarily many spatially distributed simulations and/or test rigs to a dynamic overall system* [Conference presentation]. Magna ECS Simulation Conference, Linz, Austria.

Manuscript received December 31, 2024; accepted for publication March 31, 2025;
published online July 15, 2025.

JOURNAL OF THEORETICAL
AND APPLIED MECHANICS
63, 3, pp. 623–636, Warsaw 2025
https://doi.org/10.15632/jtam-pl/

ANALYSIS OF NOTCH STRAINS COMBINING ELECTRONIC SPECKLE PATTERN INTERFEROMETRY AND DIGITAL IMAGE CORRELATION

Thomas LEHMANN*, Jörn IHLEMANN

Chemnitz University of Technology, Chair of Solid Mechanics, Chemnitz, Germany
*corresponding author, *thomas.lehmann@mb.tu-chemnitz.de*

In this contribution, electronic speckle pattern interferometry (ESPI) and digital image correlation (DIC) are combined for strain analysis around a notch. The investigations are demonstrated using an epoxy notched cantilever bending beam. For the evaluation of the experimental raw data a special method is used, which includes parametrization of the notch surrounding region and optimized smoothing. Thus, the determination of more precise results of the ESPI and DIC analyses is enabled compared to standard evaluation procedures. The deformation measurement methods complement each other profitably, considering the respective limitations and potentials of the ESPI and DIC.

Keywords: electronic speckle pattern interferometry; digital image correlation; strain; smoothing.

Nomenclature

Symbols

a – coordinate (general),
B, $\overline{B}$ – matrices of the fast Fourier transform,
C – correlation coefficient,
c – subpixel shift resolution,
d – diameter,
f – objective function,
I – intensity,
k – aperture number (f-number),
l – length (width, height), size,
M – magnification,
n – number of pixels,
R, r – radius,
s – parameter of the annulus,
Tol – smoothing parameter (tolerance),
T – thickness
t – parameter of the annulus,
u – displacement,
x, $\overline{x}$, y, $\overline{y}$ – coordinates,
Δ – difference,

Subscripts/superscripts

i – frame number,
j – condition,
ij – matrix indices,
m – modulated,
p – punch,
res – resulting,
s – speckle,
u – displacement,
0 – basic,
$1, 2, 3, \ldots$ – condition, frame number.

Abbreviations

C – camera,
DG – diffraction grating,
DIC – digital image correlation,
EO – expansion optics,
ESPI – electronic speckle pattern interferometry,
FFT – fast Fourier transform,
LS – light source,
M – mirror,

Ministry of Science and Higher Education
Republic of Poland

The publication has been funded by the Polish Ministry of Science and Higher Education under the Excellent Science II programme "Support for scientific conferences".

The content of this article was presented during the 40th Danubia-Adria Symposium on Advances in Experimental Mechanics, Gdańsk, Poland, September 24–27, 2024.

ε – strain,
η – error measure,
θ – beam angle,
λ – wavelength of the laser,
φ, ϕ – phase,
ψ – angle of the annulus.

O – object,
PO – parallelization optics,
Pz – piezo actuator,
ROI – region-of-interest,
S – shutter.

1. Introduction

The determination of inhomogeneous deformations is of particular importance in experimental mechanics. Examples of such analyses can be found in experimental deformation and stress analyses of structures. Furthermore, it may be required in the verification and validation of simulation models of complex structures with inhomogeneous strain and stress states. Other examples of analyzing inhomogeneous strain fields are the characterization of materials, parameter identification for material models (high information density due to the inhomogeneous strain distribution) and measurements with component-oriented specimens. In order to meet the high requirements of such analyses, powerful field measurement methods are used. In experimental deformation analysis, two measuring methods have become established, which are also particularly suitable for inhomogeneous strains. These are electronic speckle pattern interferometry (ESPI) and digital image correlation (DIC) which operate on completely different physical and mathematical principles and in different measuring ranges (the basics to the methods are given for ESPI in (e.g., Jacquot, 2008; Dudescu, 2015) and for DIC in (e.g., Sutton *et al.*, 2009)). The basis of the ESPI principle is interference of coherent light wave trains with evaluation of the intensity of the speckle pattern formed through interference. In contrast, DIC is based on the correlation of gray value distributions of the surface by a matching algorithm. By both methods 2D and also 3D displacement fields of optically accessible surfaces can be determined. However, the measuring ranges are very different depending on the method. ESPI has an upwardly limited measuring range regarding one-step analysis due to the physical basic principle. However, the precision of this method is very high for small deformations. DIC, on the other hand, can be very well used to measure large deformations, but shows limited precision in the lower deformation range due to the lower sensitivity of the method depending on the respective parameters (setup, conditions, DIC and strain evaluation algorithm). These limitations resulting from the measuring principles cannot or can only hardly be influenced by improving the device technology and the evaluation method. A combination of both measuring methods, in which ESPI is used in the lower deformation range and DIC for larger deformations, would enable an increase in measurement opportunities and precision. In the framework of this paper, the corresponding 2D techniques are used. The analysis of surface contours is not possible by means of these measurement methods. Therefore, e.g., surface topography investigations cannot be carried out in this way. Examples of such analyses can be found in (Macek *et al.*, 2023; Kobayashi & Shockey, 2010).

In ESPI as well as DIC analyses the displacement fields are measured, which can be further processed. On the basis of the displacements, strains can be determined by various methods, which is independent of the measuring method. The frequently used standard strain evaluation method is based on local evaluations using measured coordinates of adjacent points, e.g., for DIC in (Carl Zeiss GOM, 2016). However, when this standard evaluation method is used, the precision of the analysis will be particularly limited in the respective range of the measuring method. This can be observed for example using standard strain evaluation tools of commercial DIC software. Due to the noisy raw data, smoothing is recommended or can be required. One way is the use of filters such as spatial mean or median filters in the vicinity of a point (see (Sun & Qu, 2014)). Another method is strain calculation based on smoothing of the displacement data using the finite element method (FEM), as a global approach that can be found in (e.g., Avril *et al.*, 2008). A further global approach to calculate strains is based on the approximation of raw data by functions. For example, polynomials (cf. Kirbach *et al.* (2015), Pierron *et al.* (2007)) or B-splines can be used for this purpose. Basics of B-spline approximation can be found in (Hoschek & Lasser, 1992) and a selection of application examples are given in (Lehmann *et al.*, 2018; 2019; Peretzki *et al.*, 2022; Lehmann & Ihlemann, 2022; Kanzenbach *et al.*, 2022). Using an approximation-based method, strains are easily determined by derivatives and smoothing is achieved by the continuous mathematical description due to the functions (in most cases the displacement). However, using polynomials, overshooting effects at the edges can occur producing significant errors. This can be reduced or at best avoided by using B-splines, which also enables an improved smoothing control, which is shown in (Lehmann *et al.*, 2018). Though, following this approach, errors can occur near sections where no data is available (e.g., notches, holes). In order to avoid these effects, a parameterization of the surrounding region (near these boundaries) can be used to improve the accuracy of the strain evaluation, demonstrated for a notch in (Lehmann *et al.*, 2019). Furthermore, approximation using B-splines may be improved by analyzing the occurring noise, which enables the optimization of the smoothing control parameter shown in (Lehmann & Ihlemann, 2022; Kanzenbach *et al.*, 2022).

In the present paper, both measuring methods – 2D ESPI with phase shifting technique and 2D DIC – are evaluated regarding their resolution and measuring range. A combination of both methods in one setup is presented. The in-plane deformation analysis at a notch is performed by parametrization of the surrounding region and approximation of the raw ESPI and DIC data by B-splines. Furthermore, an optimization of the smoothing is performed considering the characteristic noise properties of the data in the approximation process.

2. Preliminary considerations regarding displacement resolution and largest detectable displacement of the measurement methods

2.1. 2D ESPI with phase shifting

Using the phase shifting technique in ESPI, the resolution of the basic method is increased. The principle is based on a shift (change) of the phase φ in a speckle pattern due to displacement of points in two loading conditions $j = 1, 2$ (e.g., unloaded, loaded). The speckle patterns are formed by interference of two laser object beams (coherent light). A precondition is a diffuse reflecting object surface. Considering the resulting intensity I_{res} of the speckle pattern, given by:

$$I_{\mathrm{res}}(x,y) = I_0(x,y) + I_m(x,y)\cos\varphi(x,y), \tag{2.1}$$

the phase φ cannot be calculated directly. This is caused by the unknown basic and modulated intensity I_0 and I_m. Using temporal phase shifting technique, a minimum of 3 additional phase shifts (angles) are necessary for the determination of the phase φ. In order to increase the data base, 4 additional phase shifts are implemented. In the contribution presented, an appropriate 4-frame-algorithm is used with the phase shifts 0, $\frac{\pi}{2}$, π, $\frac{3}{2}\pi$ resulting in 4 different intensities $I_{\mathrm{res}\,i}$. The phase in the two conditions ($j = 1, 2$) is determined by:

$$\varphi_j(x,y) = \arctan\frac{I_{\mathrm{res}\,4j}(x,y) - I_{\mathrm{res}\,2j}(x,y)}{I_{\mathrm{res}\,1j}(x,y) - I_{\mathrm{res}\,3j}(x,y)}. \tag{2.2}$$

Finally, the phase difference $\Delta\varphi(x,y)$ is defined by:

$$\Delta\varphi(x,y) = \varphi_2(x,y) - \varphi_1(x,y). \tag{2.3}$$

These calculations are carried out for the directions x and y. Due to the basic equations, $\Delta\varphi$ is discontinuous ($\Delta\varphi \in (-\pi,\pi]$) with a phase modulo of 2π, which results in the respective phase maps. Thus, unwrapping the distribution $\Delta\varphi$ is required to obtain the associated continuous phase difference $\Delta\phi$ used for displacement determination. The displacement fields u_a with $a = x, y$ are calculated by:

$$u_a(x,y) = \frac{\lambda}{4\pi \cdot \sin\theta} \cdot \Delta\phi_a(x,y), \tag{2.4}$$

where λ is the wavelength of the laser and θ the beam angle of the object beams. Furthermore, the appropriate sign needs to be considered according to the coordinate axis definition. As aforementioned, between the phase edges a phase difference of 2π occurs in the phase maps, which is usually represented in the gray value distribution. For an example with the parameters $\lambda = 532\,\mathrm{nm}$ and $\theta = 39.67^\circ$ the displacement step using Eq. (2.4) is 417 nm. Using 8 bit resolution for the displayed grey scale distribution, 256 grey values are provided. This leads to a theoretical minimum detectable displacement in x- and y-directions of $\Delta u_{\min a} = 1.6\,\mathrm{nm}$ representing a theoretical resolution of ESPI with phase shifting for this example. In practical analyses, the variance error of a measuring sequence in the same load condition can be considered to determine the noise and thus the approximated practical achievable resolution. It depends, in addition to the determining influencing parameters, on the actual conditions of the respective experimental setup. Hence, the practical minimum detectable displacement values will increase.

For displacement of object points, displacements in the speckle pattern occur in addition to the desired phase shift. The ESPI theory is based only on intensity changes of the speckle. Therefore, in experimental applications of the method it is assumed that the speckles shift and deform only very slightly, which leads to a considerable limitation of the measuring range upwards. This concerns the measurement in one step. The restriction of displacement depends on the speckle size. Experimental experiences show that stable phase maps cannot be calculated, when the displacement (absolute value) exceeds approximately $0.25 \ldots 0.4 \cdot d_s$. Hereby, d_s is the approximated speckle diameter. It results from the wavelength as well as the imaging conditions and is determined at the object by the following equation (cf. Rohrbach (1989), Cloud (2007)):

$$d_s \approx 1.2\,\lambda\,k\left(1 + \frac{1}{M}\right). \tag{2.5}$$

Herein, k is the aperture number (f-number) and M is the magnification given by the optical system. For an example of $\lambda = 532\,\mathrm{nm}$, $k = 11$, and $M = 0.3$ the speckle size d_s is approximately 30 µm. Thus, for this example, the maximum approximately detectable absolute displacement value in one step at the object is $\Delta u_{\max} \approx 8 \ldots 12\,\mu\mathrm{m}$ under the above condition.

2.2. 2D DIC

The principle of 2D DIC is based on correlation of grey scale distributions with the consideration of point environment defined by a subset of pixels in the digital images. The coordinates in a second condition (e.g., loaded) are determined using a matching algorithm. As DIC is a well-known and meanwhile frequently used method, the basics are not given in detail here. The principle and examples are well described in the literature (e.g., Sutton *et al.*, 2009).

The minimum detectable displacement $\Delta u_{\min a}$ as displacement resolution depends strongly (linear dependency) on the subpixel shift resolution c. Typical values for c are between 0.1 and 0.25 pixel and depend on the actual experimental conditions influencing the quality of the images acquired and the matching algorithm. For special conditions, values of $c = 0.01$ pixel even can be reached. The value c is multiplied by the image scale l_a/n_a in mm/pixel as it is given by:

$$\Delta u_{\min a} = \frac{l_a}{n_a} c, \tag{2.6}$$

where l_a is the width or height of the measuring field (field-of-view) and n_a is the number of pixels at the camera chip in the respective direction. For an example with the image scale $l_a/n_a = 0.01\,\mathrm{mm/pixel}$ and with an estimated value $c = 0.1$ pixel, according to Eq. (2.6) the minimum detectable displacement is $\Delta u_{\min a} = 1\,\mu\mathrm{m}$.

On the other hand, generally large displacements and strains can be measured with DIC. Depending on the calculation options and the algorithm of the DIC system, an approach to limitation in the form of the theoretical maximum detectable displacement in one step can be (approximately):

$$\Delta u_{\max a} \approx l_a - l_{\mathrm{subset}}, \tag{2.7}$$

considering the subset size l_{subset} as well as the field-of-view size l_a. Following this approach, for an example with $l_x = 24.7\,\mathrm{mm}$ and $l_{\mathrm{subset}} = 0.25\,\mathrm{mm}$, a value of $\Delta u_{\max x} \approx 24.45\,\mathrm{mm}$ is calculated. That is approximately the dimension l_x.

3. Experimental setup and procedure

3.1. Setup

The experimental setup is complex due to the general requirements of the in-plane ESPI method. Additionally, it is extended by the application of DIC. The principle of the setup is given in Fig. 1. Beyond, the real experimental setup is depicted in Figs. 2 and 3.

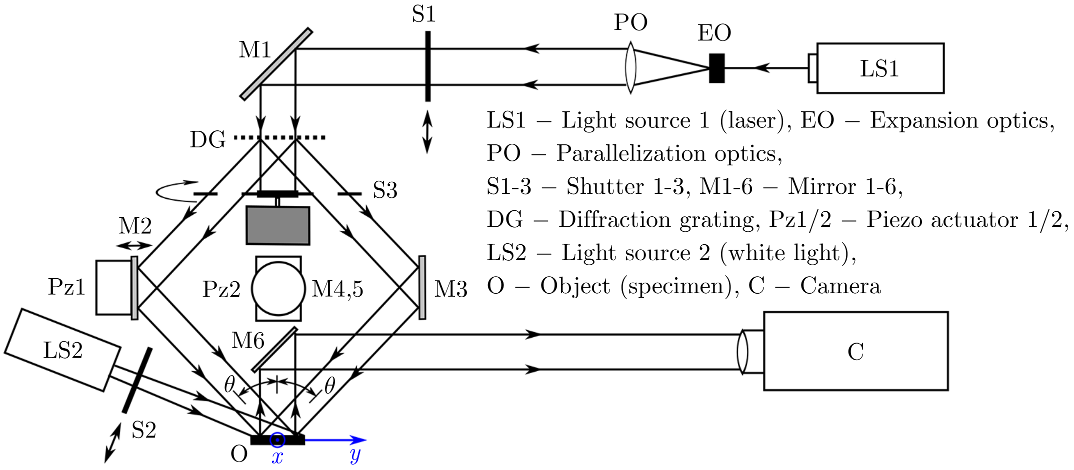

Fig. 1. Principle of the experimental setup including ESPI (based on Lehmann *et al.* (2019)) and DIC equipment.

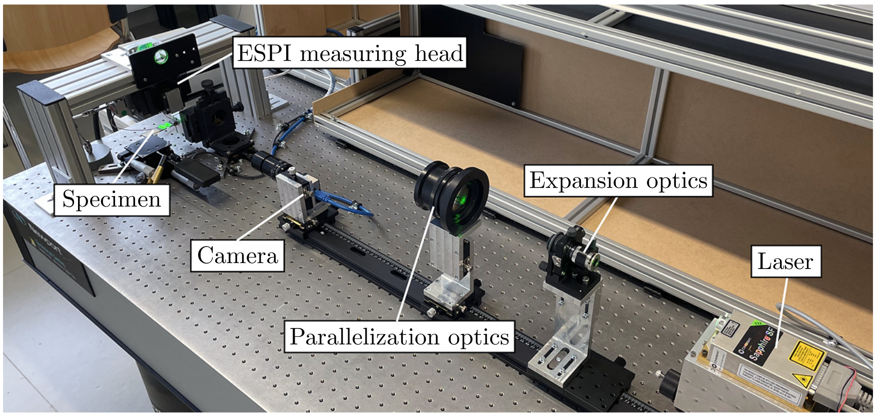

Fig. 2. Real experimental setup including ESPI and DIC equipment.

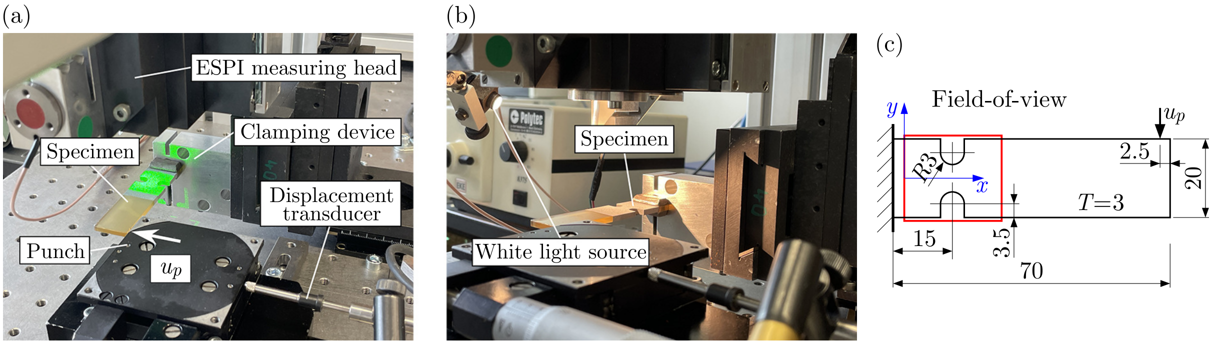

Fig. 3. Details of the experimental setup – specimen and surrounding components: a) during ESPI analysis (green laser light); b) during DIC analysis (white light); c) specimen geometry and load case (based on Lehmann *et al.* (2019)).

The basis of the setup is a self-developed 2D ESPI device including an optically pumped semiconductor laser from Coherent, of the type Sapphire 532 SF with a wavelength of $\lambda = 532\,\mathrm{nm}$, LS1. The focused beam is expanded by the expansion optics EO with a pinhole. The next step is the parallelization using the optical paralleling lens PO, which includes an aperture for limitation adjustment of the beam diameter. Then, from horizontal direction, the expanded and parallelized beam is deflected to the vertical direction by reflection at a mirror M1 which is arranged in a 45° angle. The beam is divided by a diffraction grating DG (cross grating for the two directions with 1200 lines per mm), so that the orders -1 and 1 are symmetrically guided within the ESPI measuring head (see also Figs. 2 and 3) to further mirrors M2/M3 (for the y-direction) and M4/M5 (for the x-direction), respectively. The two beams are reflected and symmetrically radiated to the object O (specimen) under the beam angle $\theta = 39.67^\circ$. Finally, the reflected and interfering laser light is reflected by an additional 45° arranged mirror M6 and observed by the camera C (Baumer, type VCXU-50M, CMOS camera with resolution of 5 megapixels). For the temporal phase shifting technique, the additional phase shifts are applied using piezo actuators Pz1 (for the y-direction) and Pz2 (for the x-direction). Shutter S3, which can be rotated by a stepper motor, covers the direction not currently being analyzed by the respective angle position. To perform the ESPI analyses, the shutter S2, which blocks the white light source LS2 (cold light source with fiber optic cable, see Fig. 3b), is closed in order to use only the laser light.

In contrast, the shutter S1 is closed for the DIC analyses in order to block the laser light. Furthermore, the shutter S2 is open enabling illumination of the specimen (object) with white light. The light reflected at the object is then deflected by the mirror M6 to provide the horizontal direction of the light path. Thus, for acquisition of the DIC images, the same camera C is used as in the ESPI measurement.

A notched cantilever bending beam made of epoxy resin is used as the object, see Figs. 2 and 3. For the DIC measurement, a fine speckle pattern was produced by coating using black and white spray paint at the surface of the specimen. The properties of the coating are such that a diffusely reflecting surface with corresponding roughness is created, which is also suitable for the ESPI analysis. The specimen is fixed by a clamping device and the bending load is applied by a manually adjustable linear unit acting as a punch (punch displacement u_p measured by an incremental displacement transducer, Heidenhain MT 25). The specimen geometry and the field-of-view (dimensions 24.7×20.7, width × height in mm) observed by the camera are given in Fig. 3c.

3.2. Test procedure

The specimen was loaded by punch displacement in steps of $u_p = 15\,\mu\mathrm{m}$, $30\,\mu\mathrm{m}$, $60\,\mu\mathrm{m}$, and $120\,\mu\mathrm{m}$. In each load step, grey scale images were acquired successively to apply both methods, ESPI and DIC. A reference state was adjusted with a preload to obtain defined initial conditions and to ensure that the punch is in contact with the specimen. Image acquisition for ESPI (automatically within the phase shifting 4-frame-algorithm with piezo and shutter control) and for the DIC analysis was performed using a self-developed ESPI software. In the reference state, 4 ESPI phase shift images (for both directions x and y) and 1 DIC image were recorded. In the deformed state (relative to the reference state), a set of ESPI images (4×4 images per direction) and 4 DIC images were taken, that is a repetition of image acquisition in the same condition was carried out. These images are used as a basis for the noise analysis and deformation calculation.

For the 2D ESPI measurements with phase shifting, calculations are carried out using the aforementioned self-developed measurement software. The primary results calculated by the software are the phase maps according to Eqs. (2.2) and (2.3). In the following step the raw phase map data is processed using a filter to obtain sharp phase edges and suitable grayscale distributions in the final phase map, which is used for calculation in further steps. For the DIC procedure, the respective images acquired were analyzed by the DIC inspection software GOM Correlate Professional. For the conversion of the data in mm, the image scale was determined and implemented. The DIC correlation algorithm was performed regarding the first image with subset (facet) size of 25 pixels (0.25 mm) and a step size of 20 pixels (0.20 mm). The primary results are the coordinates, which were provided as data for further processing.

4. Evaluation method

The displacement and strain calculation were performed using a post processing procedure in MATLAB for both measurement methods. The individual process steps are presented in the following.

4.1. Determination and processing of displacements

As described in Subsection 2.1, in the ESPI analysis the discontinuities of the phase difference $\Delta\varphi_a$ must be dissolved by an unwrapping algorithm. The continuous phase difference $\Delta\phi_a$ is determined in this paper by unwrapping with a procedure implemented in MATLAB, given by Herráez *et al.* (2002) and Kasim (2017). Furthermore, by Eq. (2.4) the ESPI displacement fields u_x and u_y are obtained. However, this displacement raw data is noisy to a certain extent, so that the accuracy of further calculations can be improved by smoothing. Regarding DIC, in this contribution, the displacements as raw data were calculated within the post processing procedure based on the coordinates (by difference calculation) in the different loading conditions instead of using the direct software displacement results. Because the DIC data is noisy, smoothing is here required too.

Besides displacement evaluation over the whole field-of-view based on the raw ESPI and DIC data, the surrounding region around the upper notch root is considered as a special region-of-interest (ROI) for further analysis. Due to the characteristic of strain analysis at notch edges described in Section 1, this annulus region is analyzed implementing a parametrization. This approach was first demonstrated in a similar way by the authors and tested for ESPI analyses including comparison with numerical simulation in (Lehmann *et al.*, 2019). To this end, normalized parameters s and t considering an angle ψ are introduced as follows, cf. Fig. 4:

$$\begin{aligned} &s(\psi = 0^\circ) = 0, \qquad s(\psi = 180^\circ) = 1, \\ &t(r = r_{\min}) = 0, \qquad t(r = r_{\max}) = 1. \end{aligned} \tag{4.1}$$

In the presented analyses, $r_{\min}$ is defined at a distance of approximately 0.2 mm from the edge of the notch, as error-influenced raw data occurs directly at this edge. Furthermore, as shown in Fig. 4, in addition to the xy-coordinate system, local coordinates $\overline{x}$ and $\overline{y}$ are used. By the

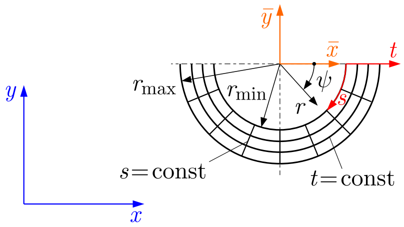

Fig. 4. Parametrization of the notch surrounding region.

parameters s and t, which are functions which depend on the coordinates $\overline{x}$ and $\overline{y}$, a dimensionless 1×1 square is formed. The relations are based on the geometry and are given by:

$$s(\overline{x},\overline{y}) = \frac{\arctan\left(-\overline{y}/\overline{x}\right)}{\pi} \qquad \text{and} \qquad t(\overline{x},\overline{y}) = \frac{\sqrt{\overline{x}^2+\overline{y}^2}-r_{\min}}{r_{\max}-r_{\min}}. \tag{4.2}$$

Hence, in the defined parametrized notch ROI, approximation can be performed with all existing measuring data to obtain the displacement functions $u_a(s,t)$.

The approximation of the ESPI and DIC displacements is carried out using cubic B-splines considering characteristic noise properties (referred to as the approximation-based method). Within this algorithm, the smoothing parameter Tol_{u_a}, representing a controlling parameter for the displacement approximation, is determined by an optimization procedure. Basics of the optimization method are given by Lehmann and Ihlemann (2022) and Kanzenbach *et al.* (2022). The principle is depicted in Fig. 5.

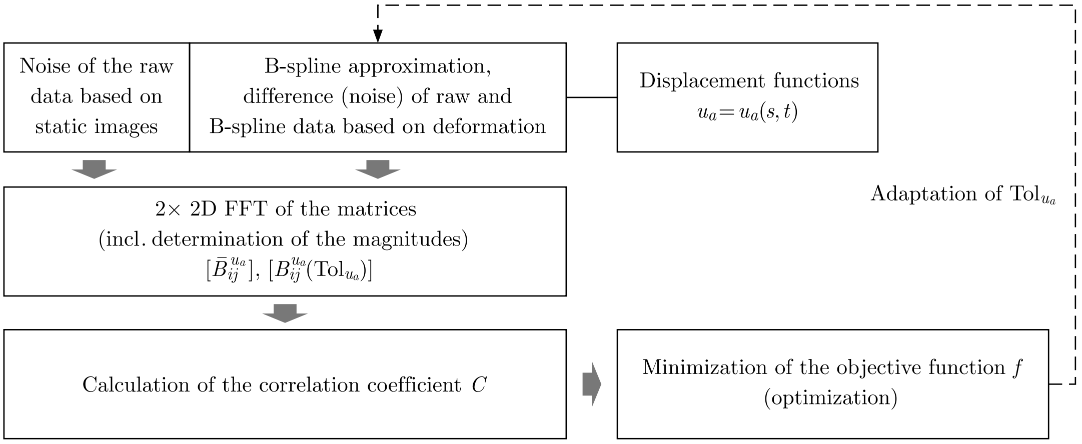

Fig. 5. Displacement approximation with optimized smoothing.

The spatial noise of the raw data is analyzed based on static images, that is in a loading condition without changes of the load and without movement of the specimen. Since the algorithm should also be suitable for ESPI measurements based on characteristic phase maps, the deformed state was selected for this noise analysis of the raw data. Hence, the database is a sequence of resulting static ESPI phase maps or DIC images in the deformed state. The noise of the raw data is defined by the difference between two displacement fields based on the noise images. If necessary, components with significantly lower spatial oscillation (long-wave variation) within the noise database are filtered out by a mean filter additionally. Furthermore, the displacements in the deformed state are analyzed as a difference to the reference state and approximated by B-splines as described. Here, the difference between the raw and B-spline data based on deformation represents the resulting noise. The object of optimizing the smoothing parameter Tol_{u_a} is to achieve good correlation of the noise characteristics. For this purpose, a first 2D fast Fourier transform (FFT) of the matrices (field data of the noise analysis) with calculation of the magnitudes is performed. Tests have shown that the noise properties show good correlation based on optimization, if the FFT is performed twice. Hence, by a second 2D FFT the matrices $[\overline{B}_{ij}^{u_a}]$ (based on static images) and $[B_{ij}^{u_a}]$ (based on deformation) are obtained. As a similarity measure of the noise analysis, the Pearson correlation coefficient C (cf. Profillidis and Botzoris (2019)) is calculated and used for the optimization. Finally, suitable tolerances Tol_{u_a} are found by an optimization using the Nelder–Mead simplex algorithm with minimization of the objective function f:

$$\min_{\mathrm{Tol}_{u_a}} f(\mathrm{Tol}_{u_a}) = \min_{\mathrm{Tol}_{u_a}} \Big(1 - C\Big(\Big[\overline{B}_{ij}^{u_a}\Big], \Big[B_{ij}^{u_a}\left(\mathrm{Tol}_{u_a}\right)\Big]\Big)\Big). \tag{4.3}$$

4.2. Calculation of strains

The strains are determined based on the functions $u_a(s,t)$. This requires the partial derivatives of the displacements with respect to the parameters and the partial derivatives of the parameters (based on Eqs. (4.2)) with respect to the coordinates. As an example, the strain ε_x, relevant for the investigations demonstrated, is defined by:

$$\varepsilon_x = \frac{\partial u_x}{\partial x} = \frac{\partial u_x}{\partial \overline{x}} = \frac{\partial u_x}{\partial s}\frac{\partial s}{\partial \overline{x}} + \frac{\partial u_x}{\partial t}\frac{\partial t}{\partial \overline{x}}. \tag{4.4}$$

5. Results

The results presented are limited to the evaluation of the x-direction, as the deformation analysis for this load case is relevant in this direction. The evaluation is performed using the procedures described in Section 4.

5.1. Phase maps and displacements

For the ESPI analyses, at first the wrapped phase maps are assessed, as these already provide an indication of the quality of the measurement. The load steps with punch displacement $u_p = 15\,\mu\mathrm{m}$ (cf. Fig. 6a) and $30\,\mu\mathrm{m}$ (cf. Fig. 7a) show plausible phase differences $\Delta\varphi_x$ (inclu-

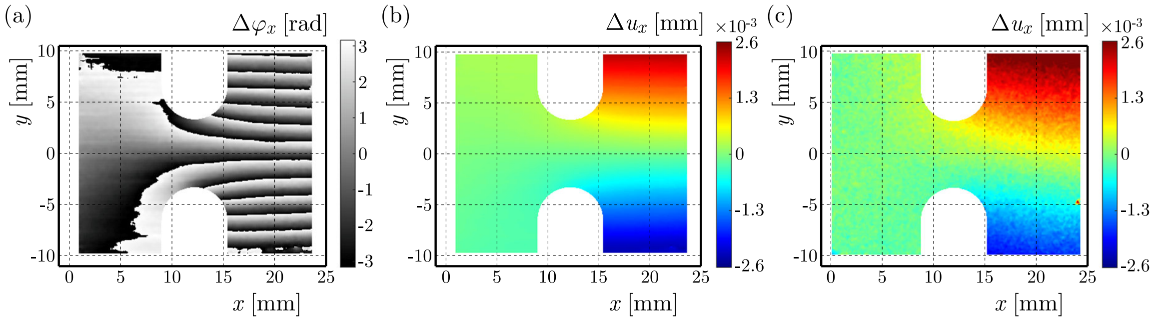

Fig. 6. (a) Phase map $\Delta\varphi_x$; (b) ESPI displacement field Δu_x; (c) DIC displacement field Δu_x – for punch displacement 15 µm.

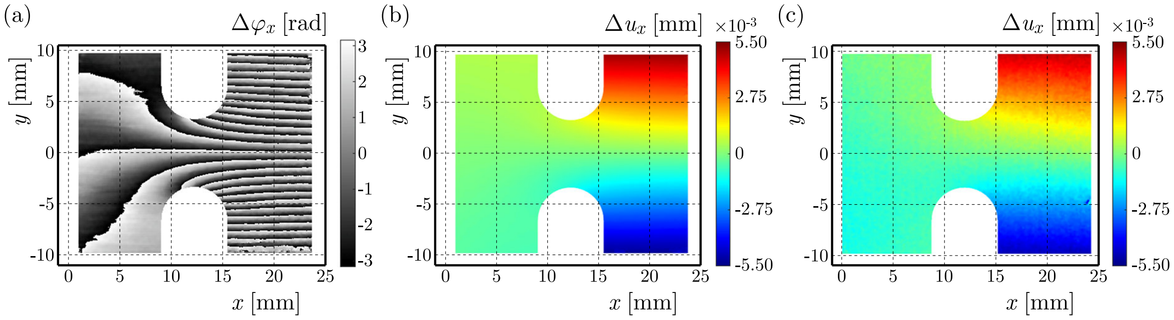

Fig. 7. (a) Phase map $\Delta\varphi_x$; (b) ESPI displacement field Δu_x; (c) DIC displacement field Δu_x – for punch displacement 30 µm.

ding the discontinuities) with the typical distribution of this load case considering the notched cantilever bending beam.

In the case of the higher load steps of $u_p = 60\,\mu\mathrm{m}$ (cf. Fig. 8a) and $120\,\mu\mathrm{m}$ (cf. Fig. 9a), the limitation of the algorithm takes effect, as the displacements of the speckles are too large and exceed the critical value. This is for $u_p = 60\,\mu\mathrm{m}$ in the region on the right side of the notches (over the full specimen height) and for $u_p = 120\,\mu\mathrm{m}$ approximately in the right half of the field-of-view. By unwrapping, the ESPI displacement fields Δu_x for the lower load steps are obtained, cf. Figs. 6b and 7b. This is expressed as displacement difference regarding the point at the left boundary at $y = 0$ (at this point the displacement is defined as zero). This approach is the same for the DIC displacements, cf. Figs. 6c, 7c, 8b, and 9b. The ESPI results show an almost symmetrical displacement distribution for the evaluable load steps and the DIC results for the load steps except $u_p = 15\,\mu\mathrm{m}$. Thus, for $u_p = 30\,\mu\mathrm{m}$ the distributions of ESPI and DIC measurement show good agreement. In the lower load levels (see Figs. 6c and 7c) significantly more noise is observed in the DIC data due to the limited sensitivity of the method.

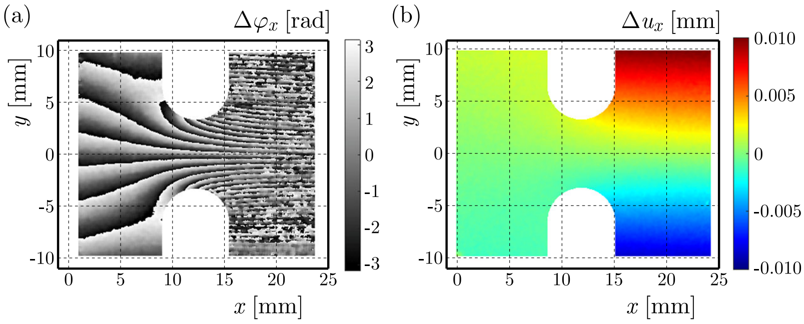

Fig. 8. (a) Phase map $\Delta\varphi_x$; (b) DIC displacement field Δu_x – for punch displacement $60\,\mu\mathrm{m}$.

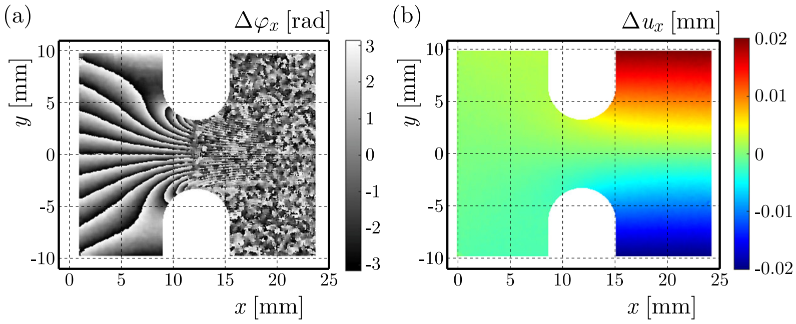

Fig. 9. (a) Phase map $\Delta\varphi_x$; (b) DIC displacement field Δu_x – for punch displacement $120\,\mu\mathrm{m}$.

The special ROI is the annulus region surrounding the upper notch root, which is parametrized according to the described evaluation method. In Fig. 10, a representative example of the noise analysis, showing the database of $u_p = 30\,\mu\mathrm{m}$, is given. The noise Δu_x based on static images (analyzed by an image sequence in the deformed state without change of loading), cf. Figs. 10a and 10c, generally show small values, but with different characteristic of the noise distribution for the ESPI and DIC methods. In this example, the noise floor – defined as the spatial standard deviation – is $1.2 \cdot 10^{-2}\,\mu\mathrm{m}$ for ESPI and $6.8 \cdot 10^{-2}\,\mu\mathrm{m}$ for DIC. The higher precision of the ESPI method is clearly obvious. Furthermore, a small offset value is observed in the noise plot, which indicates that small displayed rigid body shifts occur due to error influences. The comparison with the resulting noise based on deformation (as difference of the raw data and the B-spline approximation) with optimized smoothing (cf. Figs. 10b and 10d) shows good agreement regarding the criterion. Due to the optimization of the smoothing parameter Tol_{u_a}, the noise characteristic is appropriately similar.

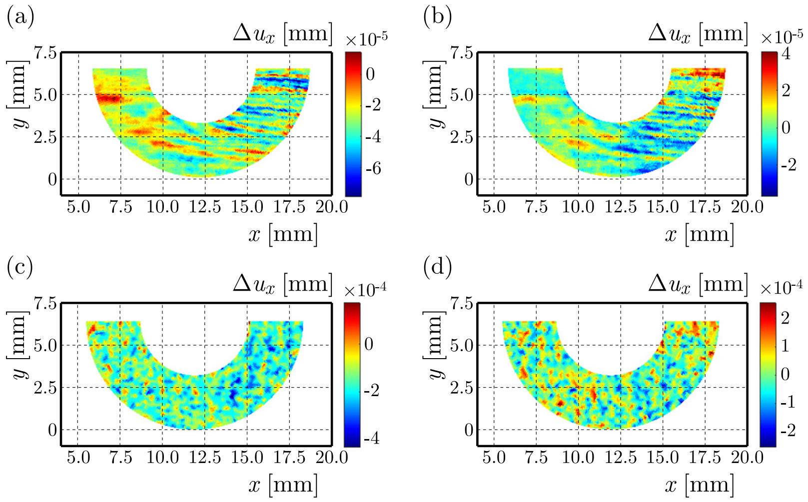

Fig. 10. Comparison of noise distribution Δu_x in the deformed state: (a) ESPI deviation based on static images; (b) ESPI deviation based on deformation; (c) DIC deviation based on static images; (d) DIC deviation based on deformation – for punch displacement 30 μm.

5.2. Strains

The strains are based on the parametrization of the notch root surrounding region and approximation of displacements providing suitable functions. All the described extensive evaluations essentially serve the purpose of strain analysis. The strain ε_x is finally obtained by calculation using Eq. (4.4). In Fig. 11 the ESPI and DIC strains are compared for the lowest load step with $u_p = 15\,\mu\text{m}$. Here, significant differences between the results of the methods occur. The ESPI strain shows a more plausible and precise distribution with typical gradients at the notch root.

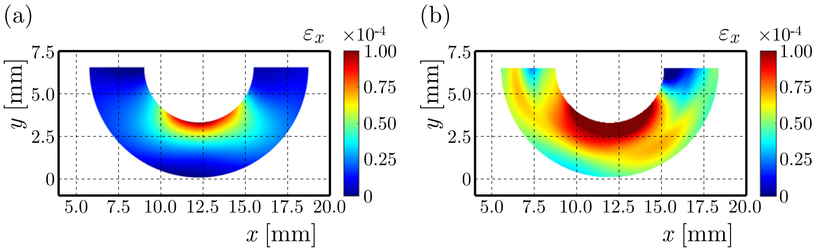

Fig. 11. Strain field ε_x: (a) ESPI result; (b) DIC result – for punch displacement 15 μm.

Figure 12 shows good correlation between the strains results of the two measurement methods in the load step with $u_p = 30\,\mu\text{m}$. For a better quantitative evaluation of the deviations, an error measure η_x is introduced:

$$\eta_x = \frac{\varepsilon_x^{\text{DIC}} - \varepsilon_x^{\text{ESPI}}}{|\varepsilon_x^{\text{ESPI}}|_{\text{max}}}. \tag{5.1}$$

Therein, strain differences regarding the maximum absolute value of the ESPI strain $|\varepsilon_x^{\text{ESPI}}|_{\text{max}}$ are considered, where $\varepsilon_x^{\text{DIC}}$ and $\varepsilon_x^{\text{ESPI}}$ are the strains obtained by the respective methods. The largest deviations occur in the left region of the ROI (annulus). The more precise result is represented by the ESPI strain due to the higher sensitivity, which leads to good suitability of the method for measuring these small strains. It should be noted that this deviation evaluation is one example. Generally, small deviations between the measurements performed at different times at the same load occur for both methods (based on the image sequence in the deformed state). Since the loading was not changed during the step, this is due to errors in the test setup and conditions.

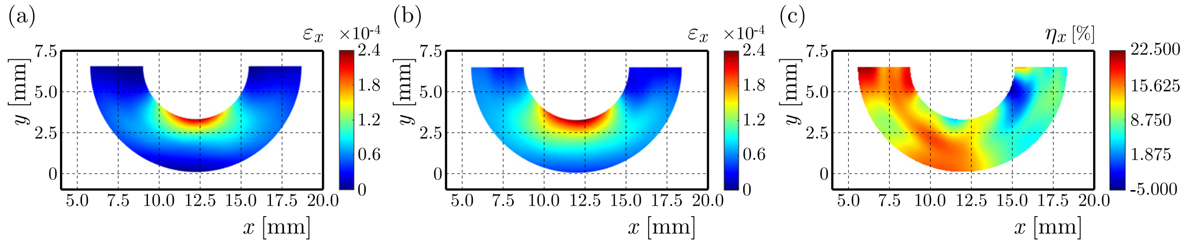

Fig. 12. (a) ESPI strain field ε_x; (b) DIC strain field ε_x; (c) local error measure field η_x (relative deviation between DIC and ESPI) – for punch displacement 30 μm.

At the higher load steps, the strain cannot be determined by the ESPI method, as the displacements are too large for the algorithm (cf. Figs. 8a and 9a). The DIC strains of the higher load steps are determined by the described approximation-based method with parametrization and additionally by the standard method (without filter), which is provided by the DIC software GOM Correlate Professional and are depicted in Fig. 13 (for $u_p = 60$ μm) and Fig. 14 (for $u_p = 120$ μm). The approximation-based method with parametrization (cf. Figs. 13a and 14a) shows more precise results of the strain distribution compared to the standard method (cf. Figs. 13b and 14b). The reason can be found in the basically noisy raw data. It influences the local approach used in the standard method resulting in visible noise of the strain. Smoothing could be achieved by a filter, but with occurring bias at the edges. The higher the strain, the more precise the standard method becomes.

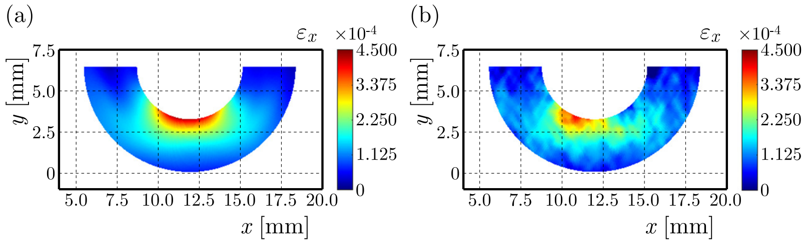

Fig. 13. (a) DIC strain field ε_x using the approximation-based method with parametrization; (b) DIC strain field ε_x using the standard method – for punch displacement 60 μm.

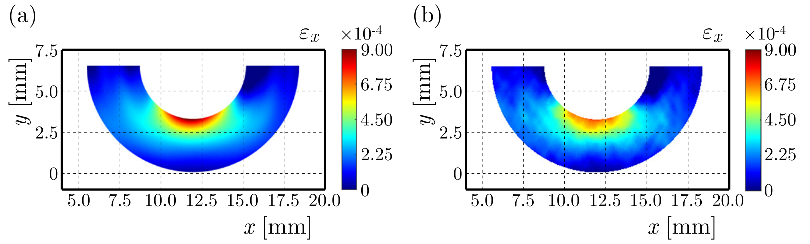

Fig. 14. (a) DIC strain field ε_x using the approximation-based method with parametrization; (b) DIC strain field ε_x using the standard method – for punch displacement 120 μm.

6. Conclusions

In this paper, a test setup for deformation analysis combining ESPI and DIC is introduced. The setup enables the measurement of displacement fields with both methods in the same load step. This is demonstrated by a bending load case using an epoxy notched cantilever bending beam. The combined ESPI and DIC measurements were successfully performed for different loads. Regarding the basic displacement determination, the following can be concluded:

- The higher sensitivity of the ESPI method leads to more precise results of the displacements demonstrated at the lower load steps (punch displacement $u_p = 15$ μm and 30 μm) compared to DIC. Nevertheless, due to the occurring noise floor ($1.2 \cdot 10^{-2}$ μm for an evaluation example), the theoretical displacement resolution of ESPI described in Subsection 2.1 cannot be reached. Furthermore, the fundamental limitations regarding sensitivity of DIC were confirmed. However, the short-wave characteristic noise of the DIC displacements shows good results (noise floor of $6.8 \cdot 10^{-2}$ μm for an evaluation example) providing a positive impact on the resolution.

- At the higher load steps large regions – that is the region on the right side of the notches for $u_p = 60$ μm and the right half of the field-of-view for $u_p = 120$ μm – cannot be analyzed by ESPI due to too large displacements of the speckles. Hence, the limitation of the applicability of ESPI regarding increasing displacements was demonstrated. In contrast, the results confirm that the DIC method is well applicable with larger displacements.

Furthermore, strain evaluation was carried out, which is concluded as follows:

- A special approximation-based evaluation method considering characteristic noise properties with parametrization of the notch root surroundings (developed by the authors) was adapted and advantageously applied. For both measurement methods, the characteristic spatial noise of the raw data based on static images in the deformed state was used as the basis for the optimized smoothing. In that way, good correlation of the resulting noise based on deformation with the noise based on static images is provided. The obtained functions are used for strain determination.
- In the smallest load step ($u_p = 15$ μm, maximum strain $\varepsilon_x \approx 1 \cdot 10^{-4}$) the precision of the DIC is not sufficient. In contrast, ESPI provides precise results with plausible distribution due to the high sensitivity of the method. In the load step with $u_p = 30$ μm (maximum strain $\varepsilon_x \approx 2.4 \cdot 10^{-4}$) the results of both methods show good correlation of the strain. Here too, the precision of the ESPI result can be classified as higher.
- Due to the limitations of ESPI mentioned before, strain analysis at the higher load steps could not be performed. However, the DIC shows very plausible and precise results for $u_p = 60$ μm and 120 μm (maximum strains $\varepsilon_x \approx 4.5 \cdot 10^{-4}$ and $9 \cdot 10^{-4}$). Compared to standard evaluation, the approximation-based method with parametrization shows more precision in the results.

Finally, we can conclude that based on the experiments presented, the ESPI and DIC methods complement each other very well in one test setup and enable the extension of the deformation measuring range. Generally, the evaluation method demonstrated in this contribution provides advantages resulting in more precision of the deformation analysis compared to other algorithms, independent of the measuring method used (ESPI or DIC). The possibility of extending the DIC measuring range to smaller strains using the special evaluation method is particularly noteworthy. Occurring influences, which have an impact on the variance on the displacements and strains over time, especially with the used test setup, must be analyzed in future investigations to improve the results. This will also improve the comparison of both measurement methods.

References

1. Avril, S., Feissel, P., Pierron, F., & Villon, P. (2008). Estimation of the strain field from full-field displacement noisy data. *European Journal of Computional Mechanics*, *17*(5–7), 857–868. https://doi.org/10.3166/remn.17.857-868
2. Carl Zeiss GOM (Gesellschaft für Optische Messtechnik) Metrology GmbH (2016). *Aramis tutorial: DIC strain computation basics.*
3. Cloud, G. (2007). Optical methods in experimental mechanics, Part 27: Speckle size estimates. *Experimental Techniques*, *31*(3), 19–22. https://doi.org/10.1111/j.1747-1567.2007.00201.x
4. Dudescu, M.C. (2015). *Optical methods in experimental mechanics of solids* [Habilitation thesis, The Technical University of Cluj-Napoca], Cluj-Napoca, Romania. https://www.utcluj.ro/media/documents/2015/Habilitation_Thesis_-_Dudescu_Cristian.pdf

5. Herráez, M.A., Burton, D.R., Lalor, M.J., & Gdeisat, M.A. (2002). Fast two-dimensional phase-unwrapping algorithm based on sorting by reliability following a noncontinuous path. *Applied Optics*, *41*(35), 7437–7444. https://doi.org/10.1364/AO.41.007437
6. Hoschek, J., & Lasser, D. (1992). *Fundamentals of geometric data processing* (in German). Teubner. https://doi.org/10.1007/978-3-322-89829-6
7. Jacquot, P. (2008). Speckle interferometry: A review of the principal methods in use for experimental mechanics applications. *Strain*, *44*(1), 57–69. https://doi.org/10.1111/j.1475-1305.2008.00372.x
8. Kanzenbach, L., Lehmann, T., & Ihlemann, J. (2022). Digital image correlation based characterization of rubber material at large shear deformations in an extended temperature range. *GAMM-Mitteilungen*, *45*(3–4), Article e202200009. https://doi.org/10.1002/gamm.202200009
9. Kasim, M.F. (2017). Fast 2D phase unwrapping implementation in MATLAB. https://github.com/mfkasim91/unwrap_phase/
10. Kirbach, C., Lehmann, T., Stockmann, M., & Ihlemann, J. (2015). Digital image correlation used for experimental investigations of Al/Mg compounds. *Strain*, *51*(3), 223–234. https://doi.org/10.1111/str.12135
11. Kobayashi, T., & Shockey, D.A. (2010). Fracture surface topography analysis (FRASTA)–Development, accomplishments, and future applications. *Engineering Fracture Mechanics*, *77*(12), 2370–2384, https://doi.org/10.1016/j.engfracmech.2010.05.016
12. Lehmann, T., & Ihlemann, J. (2022). DIC deformation analysis using B-spline smoothing with consideration of characteristic noise properties. *Materials Today: Proceedings*, *62*(Part 5), 2549–2553. https://doi.org/10.1016/j.matpr.2022.03.368
13. Lehmann, T., Müller, J., & Ihlemann, J. (2018). DIC deformation analyses of Mg specimens at elevated temperatures. *Materials Today: Proceedings*, *5*(13, Part 2), 26778–26783. https://doi.org/10.1016/j.matpr.2018.08.151
14. Lehmann, T., Stockmann, M., & Ihlemann, J. (2019). A method for strain analyses of surfaces with curved boundaries based on measured displacement fields. *Materials Today: Proceedings*, *12*(Part 2), 200–206. https://doi.org/10.1016/j.matpr.2019.03.114
15. Macek, W., Branco, R., Podulka, P., Kopec, M., Zhu, S.-P., & Costa, J.D. (2023). A brief note on entire fracture surface topography parameters for 18Ni300 maraging steel produced by LB-PBF after LCF. *Engineering Failure Analysis*, *153*, Article 107541. https://doi.org/10.1016/j.engfailanal.2023.107541
16. Peretzki, E., Lehmann, T., & Ihlemann, J. (2022). Adaption of the hole drilling method for residual stress analysis inside plastic parts. *Materials Today: Proceedings*, *62*(Part 5), 2523–2527. https://doi.org/10.1016/j.matpr.2022.03.114
17. Pierron, F., Green, B., & Wisnom, M.R. (2007). Full-field assessment of the damage process of laminated composite open-hole tensile specimens. Part I: Methodology. *Composites Part A: Applied Science and Manufacturing*, *38*(11), 2307–2320. https://doi.org/10.1016/j.compositesa.2007.01.010
18. Profillidis, V.A., & Botzoris, G.N. (2019). *Chapter 5 – Statistical methods for transport demand modeling*. In *Modeling of transport demand* (pp. 163–224). Elsevier Inc. https://doi.org/10.1016/B978-0-12-811513-8.00005-4
19. Rohrbach, C. (1989). *Handbook for experimental stress analysis* (in German). Springer. https://doi.org/10.1007/978-3-642-48659-3
20. Sun, X.X., & Qu, W. (2014). Comparison between mean filter and median filter algorithm in image denoising field. *Applied Mechanics and Materials*, *644–650*, 4112–4116. https://doi.org/10.4028/www.scientific.net/AMM.644-650.4112
21. Sutton, M.A., Orteu, J.J., & Schreier, H.W. (2009). *Image correlation for shape, motion and deformation measurements*. Springer. https://doi.org/10.1007/978-0-387-78747-3

Manuscript received December 15, 2024; accepted for publication April 9, 2025;
published online June 9, 2025.

JOURNAL OF THEORETICAL
AND APPLIED MECHANICS
63, 3, pp. 637–645, Warsaw 2025
https://doi.org/10.15632/jtam-pl/204360

FRICTIONLESS EDGE SUPPORT FOR THREE-POINT BENDING TESTS IN THE NONLINEAR REGION

Péter MÁTÉ*, András SZEKRÉNYES

Department of Applied Mechanics, Faculty of Mechanical Engineering,
Budapest University of Technology and Economics, Budapest, Hungary
*corresponding author, *peter.mate@mm.bme.hu*

In this article, a newly developed support type is presented for three-point bending in the nonlinear region. The support can keep the contact point's location static during the loading process, thus imitating an edge-like support with theoretically no radius and friction. The support can be used for measurements in the region of large deflections without having to consider the displacement of the contact point or dissipative forces. The support was tested on fiber reinforced composite and steel beams. During the measurements, the movement of the supports and the beam shape was monitored using digital image processing.

Keywords: three-point bending; large deflection; digital image processing; material testing.

1. Introduction

Three-point bending tests are widely used in the industry for easy and relatively cheap material testing. They are reliable and are less demanding than proper tensile tests in terms of instrumentation. Three-point bending tests feature loads usually only in the linear region, where the rotation of the beam at the supports is negligible. Thus, the linearized solution for the beam deflection holds true. If one exceeds these boundaries and increases the beam deflection to the point where the specimen starts slipping on the supports, the solution used for the test evaluation cannot be applied, because the reaction forces are not parallel anymore (Arnautov, 2005; Batista, 2015; Mujika, 2006; West, 1964).

For bending tests in the nonlinear region, the supports are usually cylindrical and running on bearings to decrease the frictional forces (Batista, 2015; Mujika, 2006; West, 1964). Although it makes friction negligible, it induces new nonlinearities into the system. As the deflection increases, the contact point of the rollers and the beam changes location, as shown in Fig. 1a (Arnautov, 2005; Batista, 2015; Máté & Szekrényes, 2020). Using simple edges as a support to fix the contact point (as presented in Fig. 1b) would induce larger and unpredictable frictional forces, especially for softer materials like polymers. It is also shown by Pandit and Srinivasan (2017) that for the cases when the deflection is comparable to the roller size, the displacement of the contact point must be considered. In their work, they showed that an increasing roller radius can have a non-negligible stiffening effect.

Ministry of Science and Higher Education
Republic of Poland

The publication has been funded by the Polish Ministry of Science and Higher Education under the Excellent Science II programme "Support for scientific conferences".
The content of this article was presented during the 40th Danubia-Adria Symposium on Advances in Experimental Mechanics, Gdańsk, Poland, September 24–27, 2024.

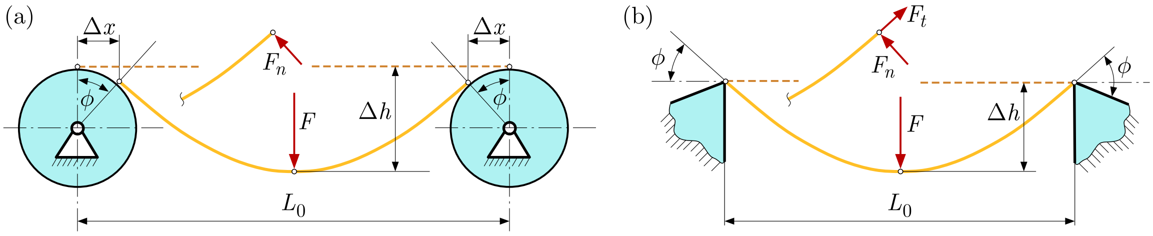

Fig. 1. Three-point bending support solutions: (a) rollers on bearings; (b) simple edge supports.

In this manuscript, a novel support type is proposed, which functions as a frictionless edge. It not only eliminates friction between the support and the specimen, but also fixes the point of contact, which can make the mechanical modeling easier, as it eliminates a source of nonlinearity. Furthermore, as later presented, one can choose theoretically any supporting pin diameter, which may be used to reduce contact pressure, if needed.

2. Experimental device

The schematic drawing of the support is presented in Fig. 2. The specimen (A) is sitting on a rolling axle (B), which is supported on both ends by deep-groove ball bearings (C). The bearings can freely roll on a cylindrical surface (D) that is machined into an aluminum supporting block (E). The supporting block (E) is milled in such a way that the specimen ends may undergo rotations up to 90°. The cylindrical surface on which the bearings roll should have a diameter that is twice the diameter of the bearings (C) and the axle (B) as follows:

$$D = d + d_b. \tag{2.1}$$

With this setup (if one neglects the weight of the axle and bearings), the beam (A) will always push the axle (B) in a position where the contact forces go through the center of the cylinder (D) and axle (B). This, together with Eq. (2.1) implies that the contact point must always coincide with the center point. The bearings (C) ensure that the frictional forces remain negligible.

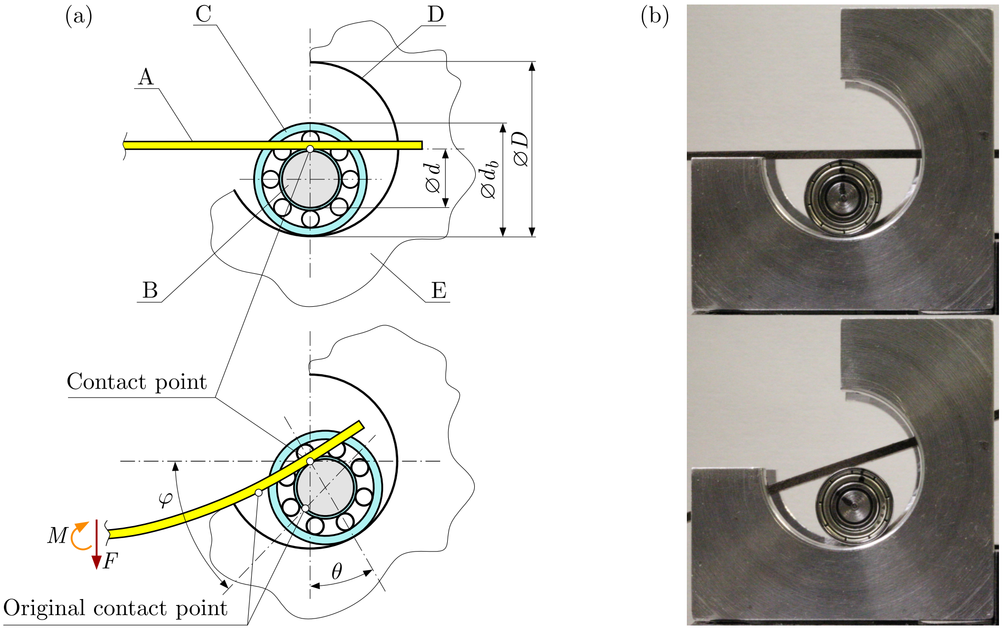

Fig. 2. Proposed solution and the working principle of a frictionless edge support (a), and the realized support during a measurement (b).

A demonstration of the support during a measurement is presented in Fig. 2b in a loaded and in an unloaded state.

For a better visibility of the beam during the loading process, one can equate the bearing and axle diameters. Thus:

$$d = d_b = \frac{D}{2}. \tag{2.2}$$

While theoretically the contact point always coincides with the center of the circular track, with the gravitational force acting on the rollers this is not always the case. For a deeper insight into the behavior of the support, the reader is referred to Fig. 3, which shows the free-body diagram of the roller.

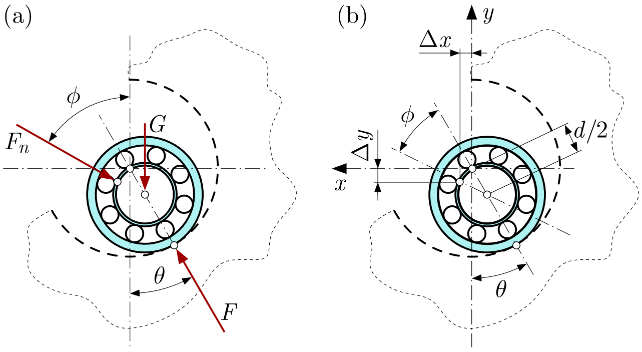

Fig. 3. Free-body diagram of the roller with gravitational force (a), and the important dimension parameters (b).

Solving the equilibrium of three forces yields the contact angle θ and contact force F as functions of the normal force on the beam (F_n) and the beam end's tangent angle (ϕ) as follows:

$$\theta = \operatorname{acot}\left(\cot\phi + \frac{G}{F_n \sin\phi}\right), \qquad F = \sqrt{F_n^2 + G^2 + 2\,G\,F_n\cos\phi}. \tag{2.3}$$

Given the nature of the cotangent function and the fact that both G and F_n are positive numbers, the contact angle θ will always "fall behind" the beam end's rotation angle. The angular difference results in a shifted contact point, as presented in Fig. 3. The contact point's displacement can be given for the x- and y-directions as the following:

$$\Delta x = \frac{d}{2}\left(\sin\phi - \sin\theta\right), \qquad \Delta y = \frac{d}{2}\left(\cos\phi - \cos\theta\right). \tag{2.4}$$

For any F_n and θ combination, the contact angle and the contact point displacement can be calculated. However, the latter changes the beam length that undergoes bending, which in return changes the $F_n\phi$ pair in the equilibrium state. The equilibrium for a given F_n normal force can be obtained iteratively. For a given F_n value, the iteration goes as follows: start by assuming that the support points are at their nominal locations (at a distance of L_0) and find the rotation of the beam end. For the beam end rotation ϕ_i, find the contact angle θ_i and the expected contact point displacement in the x direction (Δx_i) by using Eqs. $(2.3)_1$ and $(2.4)_1$. Based on the Δx estimate, update the support span by setting $L_{i+1} := L_i - \Delta x_i$, and solve the beam equilibrium for the new support span, with the same F_n shear force on the beam end. In the simulations, a convergence criterion of $|\Delta x_i - \Delta x_{i-1}| < 10^{-5}$ mm was used. In our experience, this iteration converges in 4–5 steps. These calculations were repeated for several shear force values to obtain the behavior of the beam in a nonlinear three-point flexural test with the frictionless edge supports. The shape of the elastica curve was found by using a numerical method developed earlier for numerical simulation of the three-roll bending process (Máté & Szekrényes, 2020).

3. Measurement and proof of concept

A modular three-point bending device was manufactured at the Applied Mechanics Department of the Budapest University of Technology, which can be operated by any suitable tensile testing machine. This device can be configured for three- and four-point bending tests, and it can incorporate the above-mentioned support type. During the tests, an Instron 3345 universal testing machine was used. The former was used while capturing the movement of the bearings and the shafts, simply because there was enough space for the camera setup (as presented later, the movement of the bearings is obtained from photographs via simple DIC algorithms similar to the algorithm developed by Sutton *et al.* (1983).

In the manufactured version of the support, the axle had a diameter of $d = 13\,\mathrm{mm}$ (with $D = 26\,\mathrm{mm}$), and the bearings were of type 618 (Koyo Jtekt, 2024). The bearings and the shaft have the same diameter, as it can also be seen in Fig. 2. It is emphasized here that the beam's centerline actually rolls on a virtual roller of radius $R_1 = t/2$ (where t is the specimen thickness) if the shaft perimeter touches the track's center point. In our setup, this was the case. However, one can design supports with a modified Eq. (2.1), which includes the specimen thickness and reduces the radius of the virtual roller to zero:

$$D = d_b + d + t. \tag{3.1}$$

The weight of the axle-bearing assembly plays a crucial role in the contact point's displacement. A reduced weight of the shaft helps in reducing the contact point displacement. The manufactured shaft, together with the bearings, weighs 48.7 g. Thus, $G = 0.478\,\mathrm{N}$.

The measurement setup was tested on two slender composite beams and a thin steel strip. The data for these specimens and the measurement setup is given in Table 1.

Table 1. Specimen and three-point bending test data.

Specimen	b [mm]	t [mm]	L_0 [mm]	Material	Flexural modulus of elasticity [GPa]
Composite 1	25.1	1.22	148.2	8-ply Hexply M92 55 % 220	13.81
Composite 2	25.2	2.43	148.2	16-ply Hexply M92 55 % 220	14.02
Steel	30.15	1.54	301	Spring-grade steel	200.00

All three specimen types listed in Table 1 were tested both on the novel frictionless edge support and on simple, smoothed edge supports. The measurement setup is shown with the Composite 1 specimen under testing in Fig. 4. In the first two photographs, the measurement can be seen with the frictionless edge support mounted on the testing jig. The third photograph shows the simple edge realized by two 8 mm thick steel blocks mounted instead of the new support type. Before measurement, the laser cut edge was deburred with sandpaper in order not to cut into the beam, especially in the case of the composite specimens.

The measurement results were compared to the simulation results obtained by the iterative solution presented in Section 2, based on (Máté & Szekrényes, 2020). The measurement results for the displacement-force characteristics for the three specimens are presented in Fig. 5. In the plot legends, "F.E." stands for "frictionless edge support", while "S.E." stands for "simple edge support". It is important to emphasize that the simulation results here are for the actual setup, where the shaft and bearing assembly has weight. The beam's own weight was considered negligible.

The composite beam's flexural modulus of elasticity was measured with classical three-point flexural tests, and in the simulations these beams were treated as if they were made of linear, isotropic materials. As can be seen in Fig. 5, the thicker composite beam's hysteretic behavior cannot be neglected anymore, as it undergoes relatively large deformations. To ensure that the

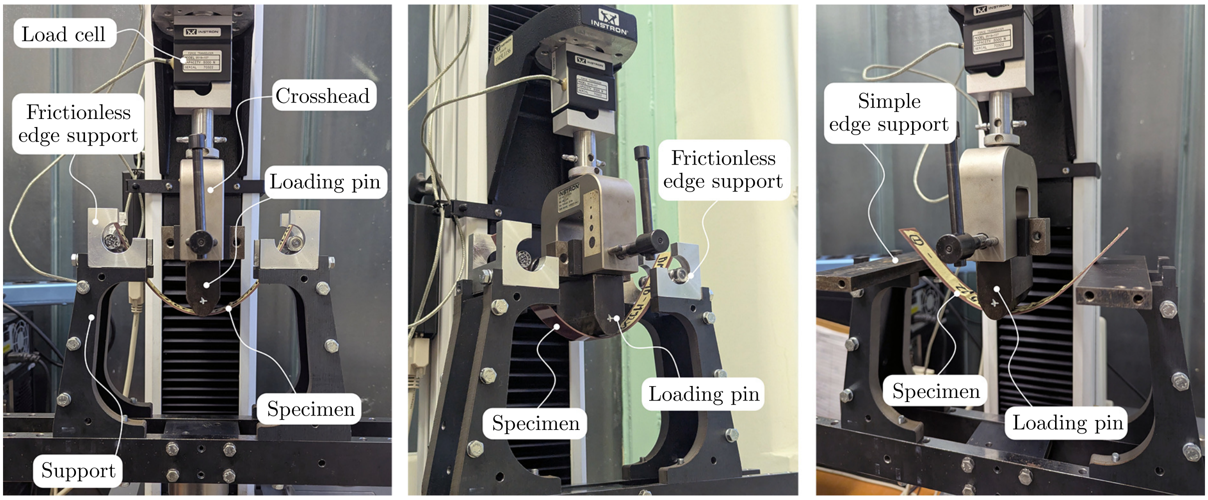

Fig. 4. Measurement setup shown with the frictionless edge support (left and middle) and with the simple edge support (right).

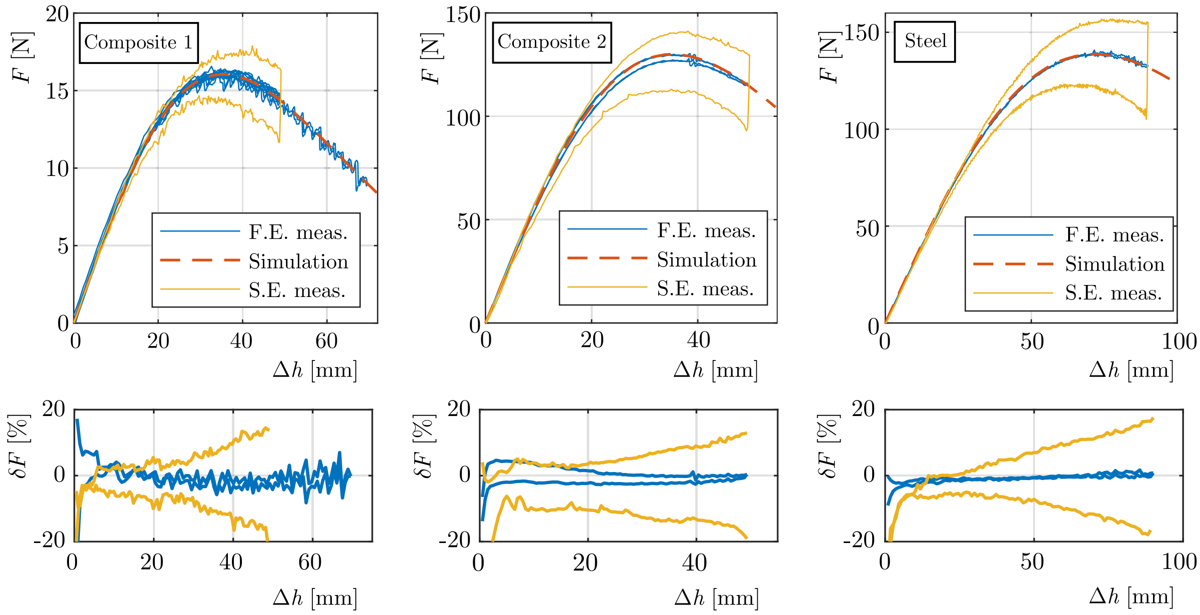

Fig. 5. Comparison of the measured and simulated deflection-force characteristics for the three specimens (upper row), along with the relative difference of the measurements to the simulations (lower row).

measurements were conducted in the elastic region, both the loading and unloading cycles are shown in the figures. To show that the hysteresis that can be seen in the measurements made with the simple edge support is not caused by the beam material or the bearing friction, a total of six load cycles are plotted in Fig. 5 for the Composite 1 specimen in the case of measurements made with the simple edge support. These consist of five shorter (50 mm displacement) and a longer cycle (70 mm displacement). The composite beam follows the same path each time it is cycled, showing that the material hysteresis and the bearing friction are negligible. In the case of the steel beam, the match between the simulation and the measurements is remarkable. The repeatability of the measurement was exceptional for all specimen types. The lower row of Fig. 5 shows the relative difference of the measured force to the simulation in percentage as a function of the displacement Δh.

It is also important to examine the deviation of the realistic loading characteristics (which consider the shaft weight) from the ideal ones (with stationary contact point, i.e. simulation results with $G = 0\,\mathrm{N}$). To quantify the imperfection of the frictionless edge support, the simulations, also visible in Fig. 5, were conducted for the weightless, ideal case too. The relative difference is given in Fig. 6 as

$$\delta F(\Delta h) = 100\left(\frac{F^r(\Delta h)}{F^i(\Delta h)} - 1\right), \tag{3.2}$$

where $F^r(\Delta h)$ denotes the loading characteristic obtained from simulations which consider the shaft's weight (also plotted in Fig. 5), while $F^i(\Delta h)$ stands for the results of the ideal case (i.e. simulation result with stationary contact point). As Fig. 6 shows, the imperfection in the loading characteristic of the new support type caused by the roller weight can be considered negligible if the test specimen is stiff enough. For example, there is almost an order of magnitude difference between the two composite specimens, only because of the difference in bending stiffness (similar support span). The oscillatory characteristic of the relative difference functions in Fig. 6 is caused both by the inaccuracies of the numerical simulations and the fact that the resulting $F^r(\Delta h)$ and $F^i(\Delta h)$ functions were resampled using a cubic spline interpolation to get their value at the same Δh locations. The theoretical contact point displacement can also be extracted from the simulations. The Δx and Δy values as functions of deflection Δh for the three specimens are displayed in Fig. 7.

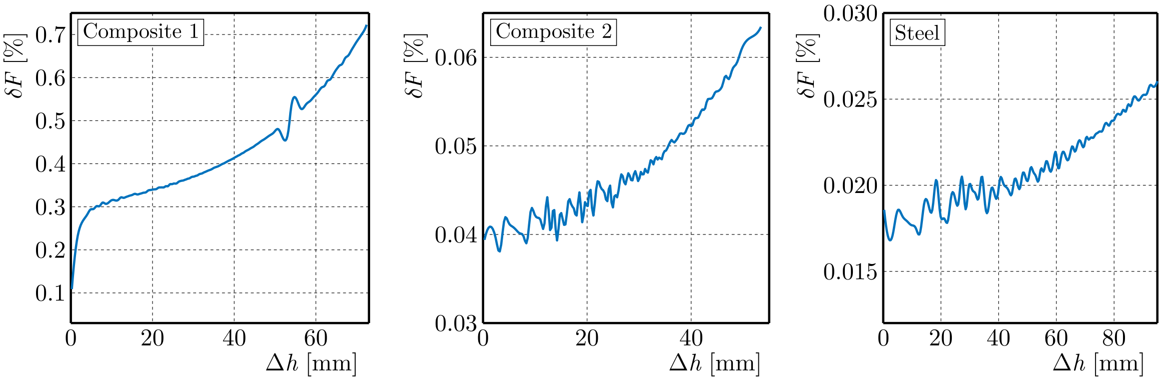

Fig. 6. Relative error of the "measured" force F, when gravity acts on the roller assembly, compared to the ideal case, with weightless rollers.

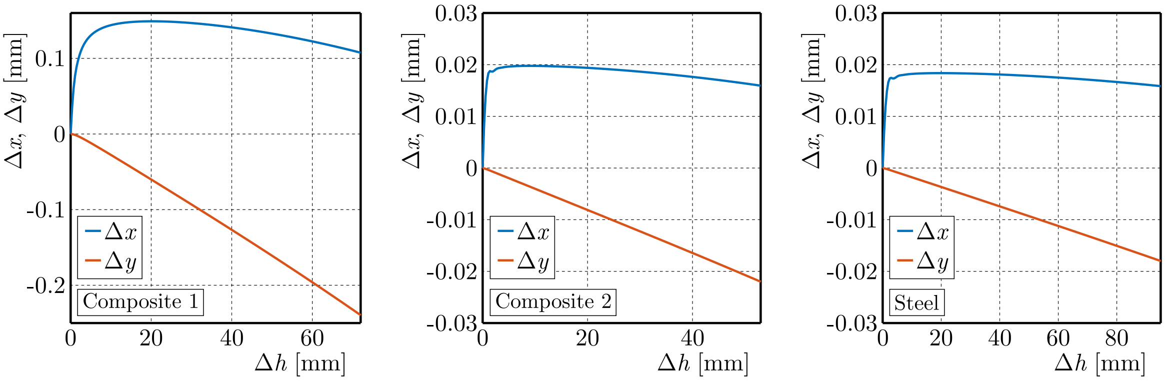

Fig. 7. Expected, theoretical displacement of the contact point for the three specimen types.

As Fig. 7 shows, the displacement of the contact point is expected to be very small, even for the Composite 1 specimen with the lowest flexural rigidity. These values can be lowered further either by using either a smaller shaft diameter, according to Eq. (2.4), or by reducing the rolling element's weight. Note that the simulation results in Fig. 7 are the contact point displacements compared to a simple edge support with zero radius, and do not consider the fact that the centerline of the beam rolls on a virtual roller with a radius of $t/2$. However, if needed, unique designs may be created based on Eq. (3.1) for given specimen thicknesses, which ensure that the support of the centerline becomes stationary.

To compare the shape of the simulated elastica curve and the measurements, the testing jig was transferred to an Alfred J. Amsler & Co. tensile testing machine so that photographs could have been taken from a proper distance. This ensures that the central projection of the camera gets as close as possible to the parallel projection, making the photograph suitable for accurate measurements. Then, the elastica curve was calculated for the measured deflection and plotted onto the photograph, as shown in Fig. 8.

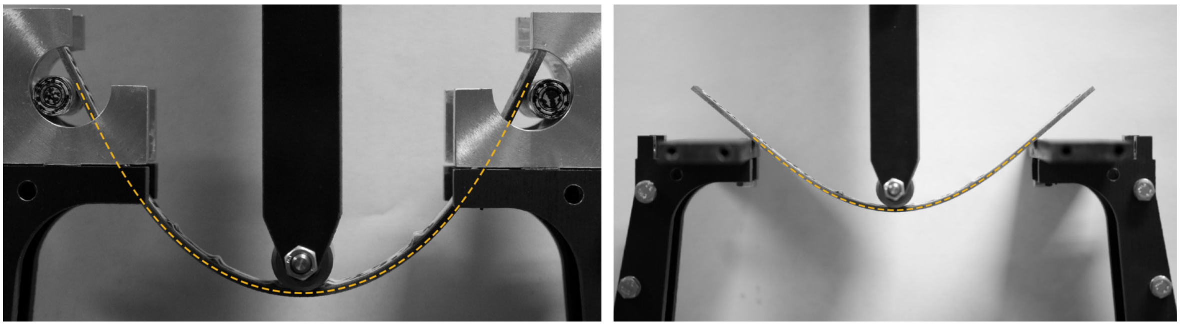

Fig. 8. Comparison of the elastica curve (dashed yellow line) with the actual measurement of a composite beam both on the frictionless edge (left) and the simple edge (right).

This was done for the Composite 2 specimen. The images in Fig. 8 were taken at $\Delta h = 68\,\mathrm{mm}$ with the frictionless edge, and at $\Delta h = 37\,\mathrm{mm}$ with the simple edge support. The simulated results (simulation was done without considering friction) represented by the dashed curve match remarkably well with the curve on the photograph. While some deviation can be observed between the elastica curve and the deformed shape of the beam when using simple edge supports, this difference is hardly noticeable.

4. Measurement of the shaft and bearing rotation

The previously presented setup was used for a further analysis of the supports. An investigation was led on whether slip occurs in the system, by capturing the rotation of the shafts and the bearings on the camera. Several photographs were taken during a full load cycle about the supports (also shown in Fig. 9) at 21 load levels. The black random pattern on the axle and the bearing seen in Fig. 9 is there to show the rotation of the shaft and bearing outer ring.

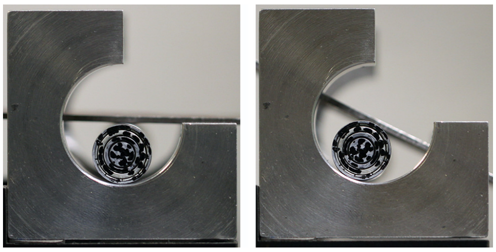

Fig. 9. Pattern on the roller assembly used to track the rotation of the shaft and bearing outer ring.

The rotational angle of the shaft and outer ring (φ and θ in Fig. 2) was traced with the help of a custom MATLAB Digital Image Correlation algorithm. The displacement of the loading pin was determined based also on digital image processing. The measured rotations are given in the left side of Fig. 10, for the Composite 2 test specimen. Here, the yellow continuous curve shows the theoretical outer ring rotation θ (calculated with weightless rollers). The measurements show that, as expected, the outer ring rotation θ is smaller than the rotation in the ideal, weightless case. The discrete data contains a full load cycle. To check whether there is a slip in the system, one can calculate the increment in the beam specimen's working length (arc-length between the two contact points with the supports). The arc-length increment between the contact point with the rollers can be given as a function of the rotation angles as

$$\Delta L = \frac{d+t}{2}(\varphi_l + \varphi_r - \theta_l - \theta_r), \tag{4.1}$$

where the subindices "l" and "r" refer to the left and the right side, respectively. In the right side of Fig. 10 the expected theoretical increment is plotted together with the increment calculated with Eq. (4.1), based on the measured angle values, also presented in the left part of Fig. 10. The figure also shows the relative difference between the measurements and the theoretical calculations in the bottom plots. These show that the errors present in the beginning fade away with increasing displacement Δh. The bottom left plot of Fig. 10 also shows that the two supports behaved identically during the measurements.

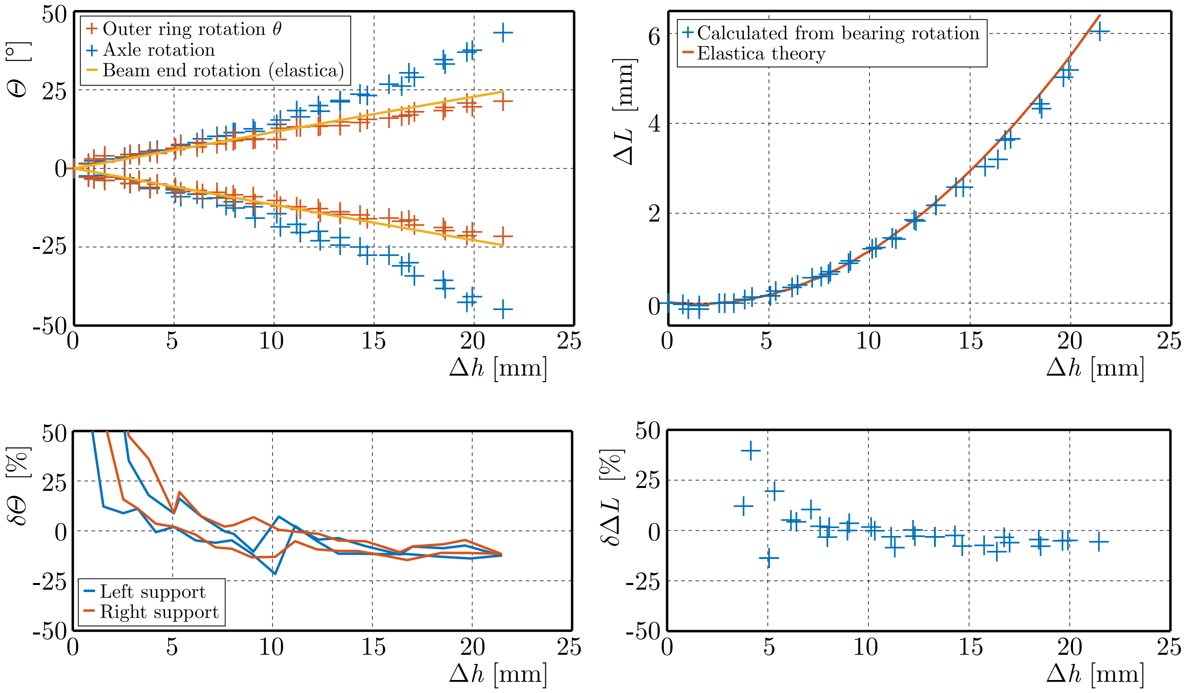

Fig. 10. Rotation of the axle and outer ring (left), and the working beam length increment calculated from the measured bearing and axle rotations (right), along with relative difference of the measurements compared to calculations from the elastica theory, shown in the bottom plots.

5. Conclusions

In this paper, a novel support is proposed, which can simulate a frictionless edge in the case of the three- and four-point bending tests. The mechanical analysis of the support was performed, and a support prototype was manufactured. Multiple tests conducted on several steel and composite beam specimens proved that the concept functions as expected, with negligible friction and contact point displacement. In the theoretical analysis, the bearing friction was neglected, but the effect of the roller's weight was considered. The measurement results revealed that the bearing friction is truly negligible, and that the supports function perfectly, as expected, without a significant contact point displacement. We compared the force-displacement load characteristics obtained from simulations with measurement results. The results were in exceptional agreement with the numerical calculations. We also measured the shaft and bearing rotation by using our simple DIC algorithm, on whose basis the arc-length increment was calculated.

The arc-length increment also follows the theoretical prediction and shows negligible hysteresis, meaning that there is no significant slip between the rollers, the beam, and the track.

Acknowledgments

This work has been supported by the National Research, Development and Innovation Office (NRDI) under grant no. 134303. The research reported in this paper has been supported by project no. TKP-6-6/PALY-2021 provided by the Ministry of Culture and Innovation of Hungary from the National Research, Development and Innovation Fund, financed under the TKP2021-NVA funding scheme.

We would also like to thank Aurél Horváth and the BME Suborbitals competition team for providing the composite beam specimens.

References

1. Arnautov, A.K. (2005). The method of three-point bending in testing thin high-strength reinforced plastics at large deflections. *Mechanics of Composite Materials*, *41*(5), 467–476. https://doi.org/10.1007/s11029-005-0072-2
2. Batista, M. (2015). Large deflections of a beam subject to three-point bending. *International Journal of Non-Linear Mechanics*, *69*, 84–92. https://doi.org/10.1016/j.ijnonlinmec.2014.11.024
3. Koyo Jtekt, Ball & Roller Bearing catalog. Retrieved December 15, 2024, from https://koyo.jtekt.co.jp/en/support/catalog-download/
4. Máté, P., & Szekrényes, A. (2020). Numerical modelling of the three-roll bending process of a thin plate. *Műszaki Tudományos Közlemények*, *13*, 133–136. https://doi.org/10.33894/mtk-2020.13.24
5. Mujika, F. (2006). On the difference between flexural moduli obtained by three-point and four-point bending tests. *Polymer Testing*, *25*(2), 214–220. https://doi.org/10.1016/j.polymertesting.2005.10.006
6. Pandit, D., & Srinivasan, S.M. (2017). Large elasto-plastic deflection of thin beams with roller support contact. *Procedia Engineering*, *173*, 1079–1084. https://doi.org/10.1016/j.proeng.2016.12.188
7. Sutton, M.A., Wolters, W.J., Peters, W.H., Ranson, W.F., & McNeill, S.R. (1983). Determination of displacements using an improved digital correlation method. *Image and Vision Computing*, *1*(3), 133–139. https://doi.org/10.1016/0262-8856(83)90064-1
8. West, D.C. (1964). Flexure testing of plastics. *Experimental Mechanics*, *4*(7), 185–190. https://doi.org/10.1007/BF02323649

Manuscript received December 16, 2024; accepted for publication April 24, 2025;

JOURNAL OF THEORETICAL
AND APPLIED MECHANICS
63, 3, pp. 647–656, Warsaw 2025
https://doi.org/10.15632/jtam-pl/204804

INVESTIGATION INTO RESISTANCE FORCES FROM THE WHEEL-RAIL INTERFACE OF A FOUR-AXLE RAILWAY VEHICLE IN CURVED TRACK

Máté M. SZŰCS*, Zoltán ZÁBORI

Department of Railway Vehicles and Vehicle System Analysis, Budapest University of Technology and Economics, Budapest, Hungary

*corresponding author, *m.szucs.mate@kjk.bme.hu*

This study focuses on the resistance forces resulting from the wheel-rail contact in a four-axle railway vehicle operating on curved tracks of varying radii and quality. Using a dynamic simulation tool, the research analysed over 900 simulations to compute energy dissipation and specific resistance forces. The findings reveal that curve resistance decreases with larger curve radii, whereas deteriorating track quality leads to higher resistance and increased deviation. The results emphasize the significant impact of track quality on resistance forces, particularly for larger curve radii. Future research aims to refine regression models and explore the deviation reduction in resistance for small-radius curves.

Keywords: wheel-rail contact; energy dissipation; resistance force; curve resistance force; dynamical simulation.

1. Introduction

Resistance forces are important to consider in the design and operation of rail vehicles and need to be studied in more depth for several reasons. Determining resistance forces is relevant for predicting wheel and rail wear, for using longitudinal dynamic models, for obtaining the maximum hauled train load, for simulating the energy consumption of train movements (Garg & Dukkipati, 1984; Jerrelind *et al.*, 2021). The main part of resistance forces is the force resulting from the inevitable loss of energy due to the wheel-rail rolling contact (Tkachenko *et al.*, 2016). In general, this loss is difficult to estimate because multiple parameters are involved, and this process becomes more complex considering movements on curved track sections. Resistance forces in curves remain a significant research area today, both with simulation and experimental approaches (Michálek *et al.*, 2024; Semenov *et al.*, 2023; Wu *et al.*, 2020).

The lateral movement of the vehicle on the track has a strong influence on the energy loss. Due to lateral track irregularities, the lateral displacement impacted of the vehicle; the track quality therefore influences the resistance forces (Iwnicki *et al.*, 2015; Tunna & Urban, 2009). However, previous studies have not comprehensively examined this phenomenon in terms of resistance forces.

This paper is the investigation of energy dissipation from wheel-rail contact based on dynamic simulation of curved track sections and different specifications with stochastic lateral track irregularities and their comparative analysis.

Ministry of Science and Higher Education
Republic of Poland

The publication has been funded by the Polish Ministry of Science and Higher Education under the Excellent Science II programme "Support for scientific conferences".
The content of this article was presented during the 40th Danubia-Adria Symposium on Advances in Experimental Mechanics, Gdańsk, Poland, September 24–27, 2024.

2. Computation method

The computational method is based on simulation using a lateral dynamic model of a four-axle, two-bogie railway vehicle in the excited lateral dynamics in arbitrary curving and the wear (ELDACW) program system developed by the Department of Railway Vehicles and Vehicle System Analysis (TU Budapest) (Szabó *et al.*, 1994). The program system was specifically designed for the investigation of dynamic interaction between the wheel and rail interface, thereby enabling a detailed analysis of the resistance forces arising from the wheel-rail contact (Zobory, 1997).

Figure 1 illustrates the flowchart of the calculation method. By simulating the vehicle motion, the dissipated power $W(t)$ from the wheel-rail contact is calculated over time t:

$$W(t) = \int_0^t P(\tau)\,\mathrm{d}\tau, \tag{2.1}$$

where P is the power dissipated in wheel-rail contact, with the time variable τ.

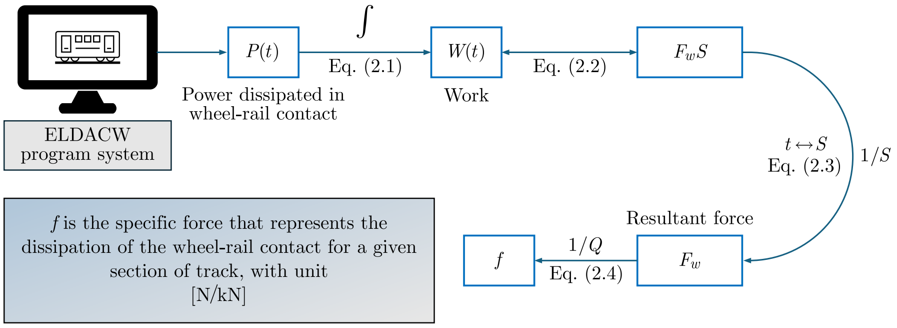

Fig. 1. Flowchart of the calculation method.

A force of constant magnitude can be defined that does the same work W on a given section of road:

$$W(t) = \int_0^S F_w^*(s)\,\mathrm{d}s = \int_0^t P(\tau)\,\mathrm{d}\tau = F_W S, \tag{2.2}$$

where $F_w^*(s)$ is the resultant force at the wheel-rail contact of the variable magnitude for a given section of track, depending on the travelled distance s, F_W is the force of constant magnitude associated with the total travelled distance S, with a work equal to the work $W(t)$. The resistance force calculated from the loss of wheel-rail contact on a given section of track can be determined by the following formula:

$$F_W = \frac{W(t)}{S}. \tag{2.3}$$

Dividing the resistance force in Eq. (2.3) by the vehicle's weight Q gives the specific drag force per unit weight, in [N/kN]:

$$f = \frac{1}{Q} F_W = \frac{\int_0^S F_w^*(s)\,\mathrm{d}s}{SQ}. \tag{2.4}$$

The specific resistance force f in expression (2.4) is used to describe the loss due to wheel-rail contact for the vehicle on a given section of track. It depends on the vehicle's motion whether the specific resistance force f is nearly constant after a distance. If the distance is too short, the result may be unreliable; the value may refer to a particular section of track or to the transient motion of the vehicle, while if the distance is too long, the computational requirements of the simulations increase (M. Szűcs, 2024).

3. Dynamical model

The complete vehicle-track dynamic model incorporates a total of 34 degrees of freedom (DoFs). These include the vehicle body, two bogie frames, two bogie bolsters, four wheels, and the equivalent track-masses placed under the individual wheels to represent the inertia of the track. Each of these components is modelled as a rigid mass. The main features of the model are:

- all rigid bodies, except for the equivalent track-masses, possess lateral displacement, and rotation around the vertical (z) axis (yaw movement) (2 DoFs $\times$ 9 components). The wheelsets have two additional DoFs: rotation around their own axes and longitudinal displacement. These are necessary to include in the model for calculating creep forces (2 DoFs $\times$ 4 wheelsets). The 8 equivalent track-masses have lateral displacement, allowing the representation of track flexibility in the lateral direction (1 DoF $\times$ 8 components). The total DoFs of the model is 34;
- the program system incorporates equations corresponding to all degrees of freedom of the rigid bodies, based on Newton's second law applied to acceleration and momentum, used for translational and rotational movement;
- the lateral deviations of rails from their nominal position, in the form of track-unevenness functions can be taken into consideration;
- the wheel-rail force at the wheel tread is modelled as a creep-dependent force, where the relationship between creep and the friction coefficient is nonlinear (Zobory, 2008);
- the flange contact is considered as a lateral, linearly elastic, and damped connection linking the wheel to the mass representing the track in the case where the contact point is on the wheel flange.

In the simulation, the parameters of a reference UIC Z passenger car were considered for modelling the four-axle rail vehicle. Table 1 contains the main characteristics of the standard gauge passenger car, and the vehicle model is shown in Fig. 2.

Table 1. Main characteristic of the passenger car.

Maximum speed of the vehicle during the simulation	120	km/h
Mass of vehicle body (m_{sz})	34800	kg
Mass of bogie (m_f)	3800	kg
Mass of wheelset (m_k)	1600	kg
Mass of bolster (m_h)	200	kg
Yaw inertia of the vehicle body (Θ_{sz})	20 000 000	$\mathrm{kg \cdot m^2}$
Yaw inertia of the bogie (Θ_f)	4500	$\mathrm{kg \cdot m^2}$
Pitch inertia of the wheelset (Θ_{ky})	110	$\mathrm{kg \cdot m^2}$
Yaw inertia of the wheelset (Θ_{kz})	820	$\mathrm{kg \cdot m^2}$
Yaw inertia of the bolster (Θ_h)	150	$\mathrm{kg \cdot m^2}$
Bogie centre base distance (l_f)	19	m
Bogie wheelbase (l_k)	2.5	m
Height of the centre of gravity of the vehicle body (h_s)	1.7	m
Friction torque on a wheelset axle	100	Nm
Wheel load – each wheel (Q)	60.09	kN

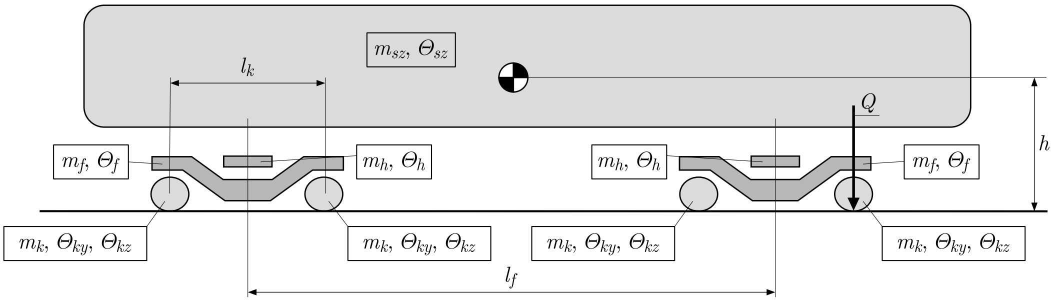

Fig. 2. Passenger car's main dimensions and masses.

4. The generation of track lateral irregularity

The lateral track irregularities are approximated by the realisation of a weakly stationary stochastic process defined along the track length. In this context, a stochastic process refers to a random function which has statistical properties (i.e., mean, deviance) remaining constant over space (i.e., along the track). The realisations are constructed using one-sided spectral density functions derived from measured data (Frederich, 1984). Simulations are conducted for three track quality levels: ideal (category I) without irregularities, good (category II), and medium (category III) from (Frederich, 1984).

The main track geometric parameters affecting the lateral position of the vehicle are track gauge and alignment. The deviations of the right and left rails from the geometric ideal are the combined effect of the track gauge and the alignment, which are generated by random number realisation generation (Szabó & Zobory, 1998). From the spectral density functions, 150–150 different realisations of each track category were generated for the simulation and used to define track irregularities in different curved track sections, with 75 m length. The total length of the track sections corresponding to the given curve and quality level is 11.25 km (M. Szűcs & Zábori, 2024).

Figure 3 illustrates the realisation of a typical category II lateral track irregularity for the right and left rails.

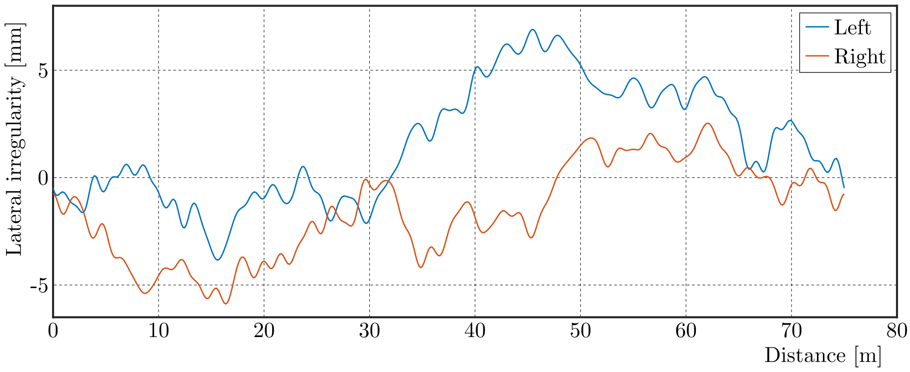

Fig. 3. Lateral track irregularity realisation.

The simulations were performed for six different curve radii in addition to the two quality categories mentioned above (category II and III) and for an ideal track without track irregularity (category I).

The initial values of the simulation are calculated in a preliminary step by ELDACW. To prevent computational errors in the approximate initial values from affecting the final simulation results, the summation of the dissipation from the wheel-rail contact was started after a certain distance travelled by the vehicle. Based on the preliminary simulation results, the length of this section used in the study is 40 % (30 m) of the 75 m base wavelength of the track irregularity.

5. Details of track lateral irregularity

The EN 13848 standard family (Railway applications – Track – Track geometry quality) recommends a wavelength range of 3–70 m for the geometric classification of railway tracks. Rail vehicle dynamics are usually evaluated at frequencies between 0.4 Hz and 20 Hz. The selected track irregularity has a base wavelength of 75 m and a minimum wavelength of 1.5 m. The frequency range for the maximum speed of 120 km/h is 0.44 Hz–22.22 Hz for wavelengths between 1.5 m–75 m. In curves with small radius, the speed needs to be limited, for lower speeds this range shifts to lower values.

The standard sets three different limits for different types of track defects, which are derived from experimentation/experience. These are the following:

- immediate action limit – IAL;
- intervention limit – IL;
- alert limit – AL.

The relation between them:

$$\mathrm{IAL} > \mathrm{IL} > \mathrm{AL}. \tag{5.1}$$

The realisations of track gauges are mainly of zero mean value. In the category III, there may be realisations where the gauge narrowing is more than the value that still ensures the lateral positioning of the wheel without "locking" (−8.1 mm). Therefore, in these realisations, both rails are shifted "outwards" – the left rail to the left, the right rail to the right – symmetrically by a value that ensures that the track gauge error does not exceed −8.1 mm. This adjustment does not represent standard maintenance practice but rather serves as a computational strategy to ensure stability of the simulation. Importantly, all adjustments have been kept within the intervention limit (IL) thresholds specified in EN 13848, ensuring that our track geometry remains representative of acceptable real-world conditions. We have verified that this technical simplification does not meaningfully impact our results, as the primary dynamic interactions remain governed by the same physical principles.

The parameters of the tracks from categories II and III used for the simulations in relation to these limits are given in Table 2 in terms of track gauge and alignment, to compare to the values in the standard. Explanation of the rows in the table from the EN 13848 standard family:

- TG – ID: track gauge – AL/IL/IAL – isolated defects – nominal track gauge to peak value;
- TG – NTG: track gauge – AL/IL/IAL – nominal track gauge to mean track gauge (over 100 m);
- AM – ID: alignment – AL/IL/IAL – isolated defects – zero to a peak value (D1 3 m–25 m, D2 N/A);
- AM – SD: alignment – standard deviation – (wavelength 3 m–25 m).

Table 2. Parameters used for simulation of category II and III tracks compared to the limits of the EN 13848 standard family – minimum, maximum and expected values (EV).

	Limits in EN 13848 $80 < V$ [km/h] ≤ 120 [mm]	Category II [mm]	Category III [mm]
TG – ID	IL: MIN −9 | MAX +30	MIN −8.1 | MAX 6.6	MIN −8.1 | MAX 27.1
TG – NTG	AL: MIN −5 | MAX +16	MIN 0 | MAX 0	MIN 0 | MAX 13.4
AM – ID	IAL: MAX 17	EV 2.25 | MAX 4.26	EV 8.72 | MAX 16.52
AM – SD	Class from B to E	EV 0.93 | MAX 1.71	EV 3.51 | MAX 6.31

6. Results

The simulation results are shown in Table 3, for six different curve radii, categories I, II, and III.

Table 3. Simulation results.

Cases	$R = 300\,\mathrm{m}$	R400	R600	R900	R1500	R3000
	A	B	C	D	E	F
V [km/h]	60	80	100	120	120	120
h [mm]	80	128	136	128	52	56
τ [m/s^2]	0.40	0.40	0.40	0.40	0.40	0
I. f	1.90	1.41	1.01	0.71	0.37	0.10
II. f_{II}	1.92 +1 %	1.45 +3 %	1.00 −1 %	0.68 −4 %	0.42 +13 %	0.25 +144 %
III. f_{III}	2.00 +5 %	1.60 +14 %	1.27 +25 %	1.14 +59 %	1.06 +182 %	1.01 +897 %
II. d	0.00	0.01	0.01	0.01	0.02	0.03
d [%]	0	0	1	1	4	14
III. d	0.03	0.05	0.09	0.13	0.15	0.17
d [%]	2	3	7	12	15	17

In Table 3, V is the constant speed of the vehicle, h is the cant of the curve and τ is the unbalanced lateral acceleration. f is the value obtained on the ideal track in category I, and the expected value of the simulation is based on the realisation of 150 different realisations in categories II and III. The value d is calculated for each case and represents the standard deviation normalised to the given f in %.

For validation purposes, Table 4 presents a comparison between resistance forces derived from detailed theoretical formulations found in the literature and the results obtained for the ideal track (Schramm, 1963), clearly demonstrating the similarity between them.

Table 4. Simulation results of category I compared to literature values [N/kN].

Cases	A	B	C	D	E	F
I. f	1.90	1.41	1.01	0.71	0.37	0.10
Schramm $\frac{160 l_k + 162}{R}$	1.87	1.41	0.94	0.62	0.37	0.19

Based on Tables 3 and 4, it can be stated that the resistance forces decrease with increasing curve radius, in accordance with simulation (Wu *et al.*, 2020) and experimental (Lukaszewicz, 2008; Schmidt, 1927) results in the literature, and as derived from theoretical considerations. This trend is also found for categories II and III. However, the literature shows that the resistance forces calculated from empirical and theoretical formulas exhibit significant variability (Wu *et al.*, 2020).

In terms of track quality, it can be concluded that the lower the quality, the higher the resistance force. The difference increases for a larger curve radius compared to the ideal track. This phenomenon was also detected in simulations by (Bailey & Hedrick, 1988; Tunna & Urban, 2009) and the results align with the previous findings provided by the referred literature (Michálek *et al.*, 2024).

Figure 4 shows the standard deviation for categories II and III.

The standard deviation of the resistance values for each realisation shows a similar trend for both track qualities: a larger curve radius is associated with a larger standard deviation and hence a larger range. The results for the six curve radii are shown in Fig. 5.

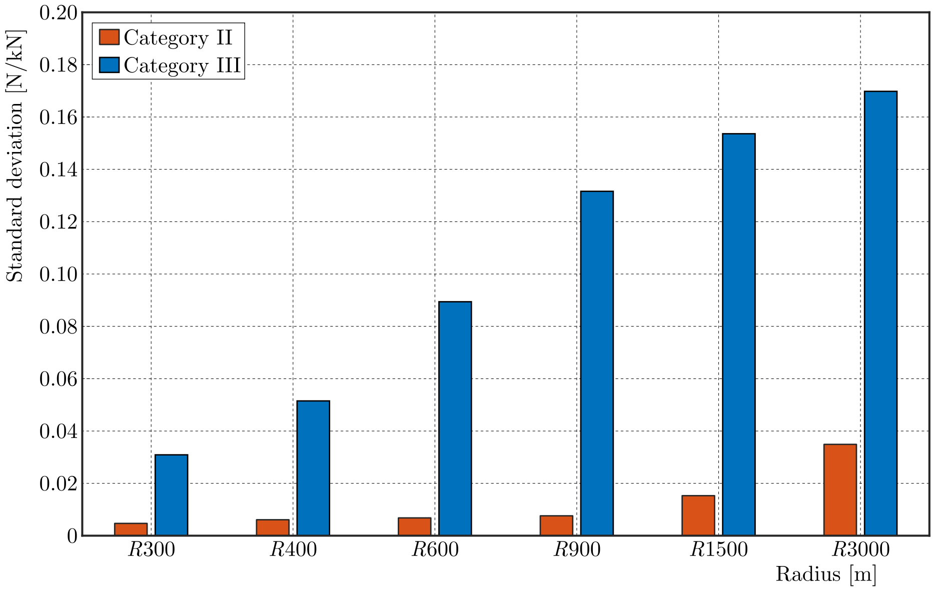

Fig. 4. Standard deviation of resistance forces for categories II and III.

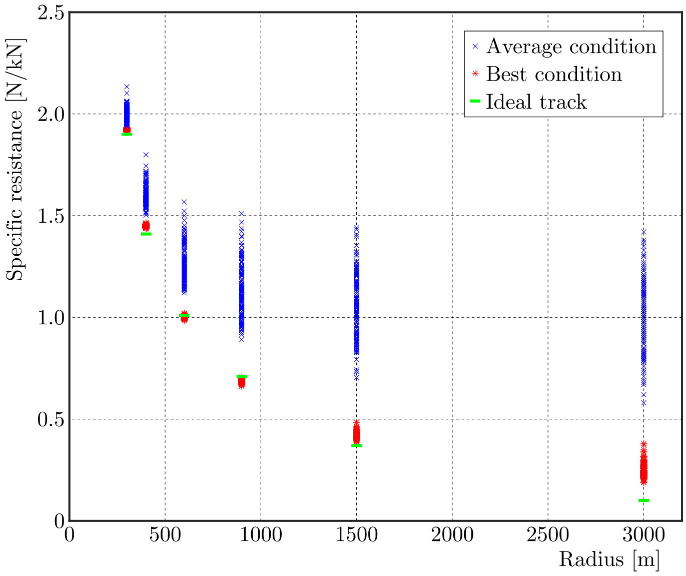

Fig. 5. Results for the six curve radii.

While for category II there is no overlap between the results for different curve radii, for category III the higher resistance forces overlap largely in the cases C to F for the adjacent curve radius. Thus, although the expected values are well separated in each curve (Table 3, f, f_{II}, and f_{III}), the resistive forces associated with each track section under stochastic track irregularity are loaded with great uncertainty.

In Fig. 6, beyond showing the expected values, we have included the 95% confidence intervals calculated using the t-distribution for each track quality category, which appropriately addresses the varying standard deviations and unknown distributions in our results. Simple linear connections between different curve radius points effectively illustrate how potential regression models would differ depending on track quality. Table 5 shows the lower and upper limits of categories II and III.

Figures 7 and 8 show the results for categories II and III, represented by boxplots and histograms (Danz, 2024). These figures illustrate the large difference in the range of values for categories II and III caused by the quality of the track. Compared to the expected values of the

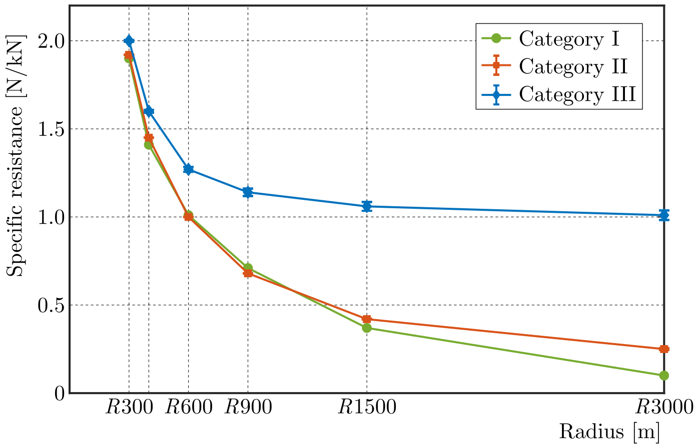

Fig. 6. 95 % confidence intervals calculated using t-distribution.

Table 5. 95 % confidence intervals calculated using *t*-distribution for categories II and III [N/kN].

Cases		A	B	C	D	E	F
II.	lower	1.919	1.449	0.999	0.679	0.418	0.244
	upper	1.921	1.451	1.001	0.681	0.422	0.256
III.	lower	1.995	1.592	1.256	1.119	1.035	0.983
	upper	2.005	1.608	1.284	1.161	1.085	1.037

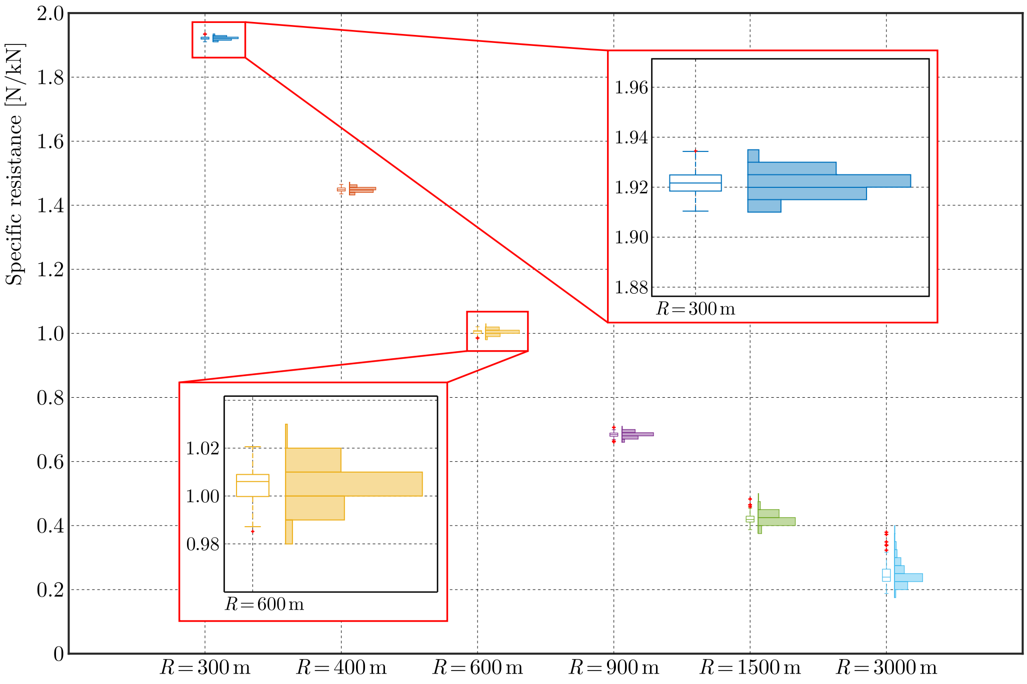

Fig. 7. Distribution of specific resistance values using boxplot and histogram, category II.

specific resistances, the standard deviation is almost negligible for category II. Figure 6 shows the highlighted details of the 300 and 600 metre radii. In contrast, for category III with higher curve radii, the difference between the maximum and minimum values is comparable to the expected value. For larger curve radii and lower track quality, there is a large uncertainty in the resistance values.

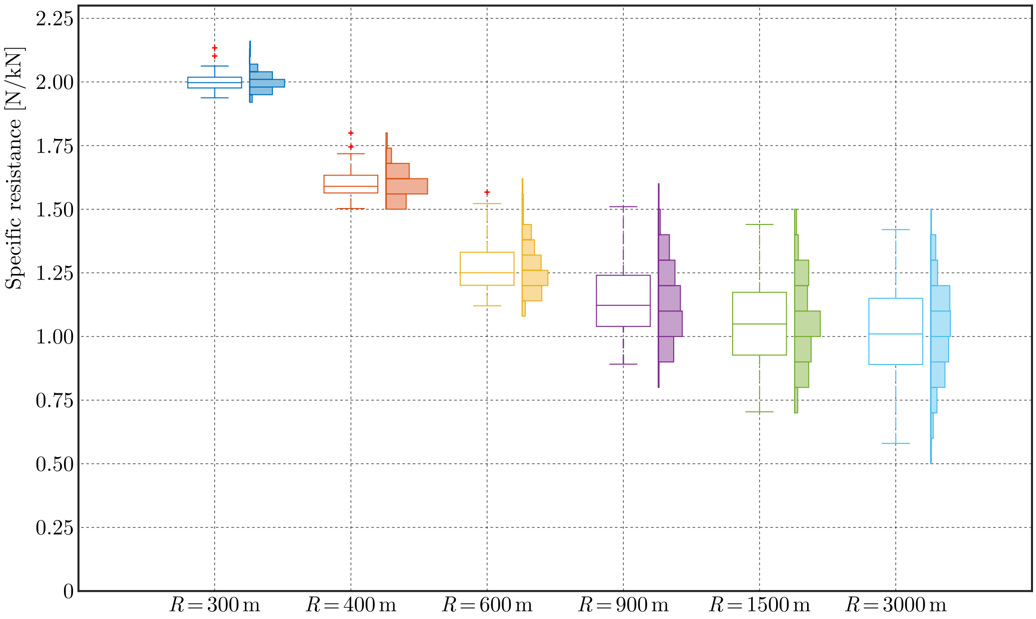

Fig. 8. Distribution of specific resistance values using boxplot and histogram, category III.

7. Conclusion

This article presents the curve resistance forces computation determined by computer-based simulation from the wheel-rail contact of a 4-axle railway vehicle moving at a constant speed on track sections with different curve radii and quality. Based on a total of more than 900 simulation results, the conclusions can be summarised as follows:

- effect of curve radius on expected curve resistance: the simulation reveals a decreasing trend in the expected curve resistance value as the track curve radius increases;
- expected curve resistance and track quality: the expected curve resistance value can be determined from the computer simulation of a stochastic dynamic process dependent on the track quality. This aligns with previous findings in the literature and highlights the sensitivity of wheel-rail contact forces against track irregularities;
- decreasing dependency with deteriorating track quality: the effect of track quality on curve resistance becomes less significant as the curve radius decreases, because the lateral movement of the vehicle is more likely determined by the geometry of the smaller radius curve;
- standard deviation and track condition: the poorer track quality, the higher the standard deviation of curve resistance, indicating larger range of the wheel-rail contact force changes;

In practice, the curve resistance forces are described by the closed-form expression, e.g., Schramm's expression. It is recommended to take into account the phenomena observed during the simulation by modifying the formulas used in practice. Different expressions can be used to describe the effect of track quality on forces of curve resistance.

A research direction could be to define a regression curve reflecting different track qualities, that can be practically useful. Further subject of research is deeper exploration of the revealed reasons for the smaller standard deviation of curve resistance at smaller track radii values and investigation of speed-dependent trends in conjunction with track superelevation to analyse their combined impact on resistance forces.

References

1. Bailey, J.R., & Hedrick, J.K. (1988). Rail vehicle energy dissipation due to lateral vehicle/track interactions. *Vehicle System Dynamics*, *17*(sup 1), 29–40. https://doi.org/10.1080/00423118808969238

2. Danz, A. (2024). boxplotGroup. *MATLAB Central File Exchange.* Retrieved December 10, 2024, from https://www.mathworks.com/matlabcentral/fileexchange/74437-boxplotgroup
3. EN 13848 standard family, *Railway applications – Track – Track geometry quality*, Part 1 2019, Part 2 2020, Part 3 2021, Part 4 2011, Part 5 2017, Part 6 2014, *European Standard.*
4. Frederich, F. (1984). Effect of track geometry on vehicle performance (in German). *ZEV-Glasers Annalen*, 12, 355–362.
5. Garg, V.K., & Dukkipati, R.V. (1984). *Dynamics of railway vehicle systems* (pp. 343–362). Elsevier. https://doi.org/10.1016/B978-0-12-275950-5.50014-6
6. Iwnicki, S.D., Stichel, S., Orlova, A., & Hecht, M. (2015). Dynamics of railway freight vehicles. *Vehicle System Dynamics*, *53*(7), 995–1033. https://doi.org/10.1080/00423114.2015.1037773
7. Jerrelind, J., Allen, P., Gruber, P., Berg, M., & Drugge, L. (2021). Contributions of vehicle dynamics to the energy efficient operation of road and rail vehicles. *Vehicle System Dynamics*, 59(7), 1114–1147. https://doi.org/10.1080/00423114.2021.1913194
8. Lukaszewicz, P. (2008). Running resistance and energy consumption of ore trains in Sweden. *Proceedings of the Institution of Mechanical Engineers, Part F: Journal of Rail and Rapid Transit*, 223(2), 189–197. https://doi.org/10.1243/09544097JRRT233
9. M. Szűcs, M., & Zábori, Z. (2024). Investigation of resistance forces from the wheel-rail interface of a four-axle railway vehicle in straight and curved track (in Hungarian). In *XIV. International Conference on Transport Sciences Győr*, 687–697.
10. Michálek, T., Kohout, M., Šlapák, J., Vágner, J., & Pulda, J. (2024). Curving and running resistance of freight trains: current experience with on-track measurements. *Vehicle System Dynamics*, 1–15. https://doi.org/10.1080/00423114.2024.2398003
11. Schmidt, E.C. (1927). Freight train curve resistance on a one-degree curve and on a three-degree curve. *University of Illinois Engineering Experiment Station*, *24*(45), Bulletin No. 167.
12. Schramm, G. (1963). Curve resistance. *Monthly Bulletin of the International Railway Congress Association*, *40*(7), 483–491.
13. Semenov, S., Mikhailov, E., Kovtanets, M., Sergienko, O., Dižo, J., Blatnický, M., Gerlici, J., & Kostrzewski, M. (2023). Kinematic running resistance of an urban rail vehicle undercarriage: a study of the impact of wheel design. *Scientific Reports*, *13*, Article 10856. https://doi.org/10.1038/s41598-023-37640-w
14. Szabó, A., Sostarics, G. & Zobory, I. (1994). Optimum axle-box guidance stiffnesses for traditional running gears operating on a given railway line. *International Journal of Vehicle Design*, 15(3–5), 484–493. https://doi.org/10.1504/IJVD.1994.061877
15. Szabó, A., & Zobory, I. (1998). On deterministic and stochastic simulation of wheel and rail profile wear process, *Periodica Polytechnica Transportation Engineering*, *26*(1–2), 3–17.
16. Tkachenko, V.P., Sapronova, S.Y., Maliuk, S.V., & Kulbovskyi, I.I. (2016). Studying the structure of railway rolling stock resistance. *Metallurgical and Mining Industry*, *11*, 30–36.
17. Tunna, J., & Urban, C. (2009). A parametric study of the effects of freight vehicles on rolling contact fatigue of rail. *Proceedings of the Institution of Mechanical Engineers, Part F: Journal of Rail and Rapid Transit*, 223(2), 141–151. https://doi.org/10.1243/09544097JRRT228
18. Wu, Q., Wang, B., Spiryagin, M., & Cole, C. (2020). Curving resistance from wheel-rail interface. *Vehicle System Dynamics*, *60*(3), 1018–1036. https://doi.org/10.1080/00423114.2020.1843689
19. Zobory, I. (1997). Prediction of wheel/rail profile wear. *Vehicle System Dynamics*, *28*(2–3), 221–259. https://doi.org/10.1080/00423119708969355
20. Zobory, I. (2008). On stochastic field model of the wheel/rail rolling/sliding contact force transfer. In *Proceedings of the 10th Mini Conference on Vehicle System Dynamics, Identification and Anomalies*, 95–116. Budapest University of Technology and Economics, Budapest, Hungary.

Manuscript received December 15, 2024; accepted for publication May 7, 2025;

JOURNAL OF THEORETICAL
AND APPLIED MECHANICS
63, 3, pp. 657–672, Warsaw 2025
https://doi.org/10.15632/jtam-pl/205163

EXPLOITATION PARAMETERS OF DEFORMED HIGH-STRENGTH STEEL ASSESSED BY THE BARKHAUSEN NOISE METHOD

Katarzyna MAKOWSKA[1]*, Tadeusz SZYMCZAK[2], Zbigniew L. KOWALEWSKI[3]

[1] *Faculty of Mechatronics, Armament and Aerospace, Military University of Technology, Warsaw, Poland*
[2] *Department of Vehicle Type-Approval & Testing, Motor Transport Institute, Warsaw, Poland*
[3] *Department of Experimental Mechanics, Institute of Fundamental Technological Research, Polish Academy of Sciences, Warsaw, Poland*

*corresponding author, *katarzyna.makowska@wat.edu.pl*

The elastic limit, yield point, strain hardening component, and strength coefficient of martensitic steel were determined after monotonic tensile loading. The monotonic tension test of 41Cr4 steel was conducted for selected values of deformation. The specimen was unloaded after each pre-strain. The parameters from destructive tests were compared with those from the Barkhausen noise (BN) method obtained. It turned out that the magnetic Barkhausen effect can be helpful in the diagnostics of structural steel components and devices. Linear relationships between the elastic limit/yield point and parameters coming from the rms voltage of Barkhausen noise envelope were found.

Keywords: yield point; elastic limit; strain hardening component; strength coefficient; magnetic Barkhausen noise.

1. Introduction

Assessment of mechanical properties is crucial from an engineering point of view especially in situations requiring a high level of operational safety of responsible structures. The elastic limit and yield point are the basic mechanical properties that affect limits of material behaviour during its exploitation. On the other hand, the strain hardening exponent (n) and strength coefficient (K) are usually required for the accurate design analysis of components and engineering structures (Li *et al.*, 2019). It is well known that a long-term usage of objects connected even with a small increase in monotonic load generates a difference in working conditions. An unexpected load may produce additional deformation of materials and significantly affect the safety of structures. Among many types of deformation, the plastic flow may be treated as a major reason for components failure in several branches of industry (Kashefi *et al.*, 2023). As a consequence, the main objective of this work is to propose an effective method for determining the variation in mechanical properties using a non-destructive method based on the Barkhausen noise (BN) effect applied after tensile monotonic loading. This technique is proposed instead of destructive tests that require cutting parts from the structure to prepare specimens for subsequent testing. The BN offers an attractive tool for detecting a degree of deformation within the ferromagnetic materials (Kleber & Vincent, 2004). It enables the testing of materials in four stages: perfectly

---

Ministry of Science and Higher Education
Republic of Poland

The publication has been funded by the Polish Ministry of Science and Higher Education under the Excellent Science II programme “Support for scientific conferences”.
The content of this article was presented during the 40th Danubia-Adria Symposium on Advances in Experimental Mechanics, Gdańsk, Poland, September 24–27, 2024.

elastic, micro-yielded, macro-yielded, and after progressive plastic deformation (Vaidyanathan *et al.*, 1999). Therefore, it can be suitable to evaluate a condition of the structural components and devices in service and help to find places where potential cracks may occur.

2. Theoretical background

The BN method is based on the magnetic Barkhausen effect. The BN effect represents the irreversible movement of domain walls during a magnetization cycle (Cullity & Graham, 2009). The movements appear discontinuously, because the domain walls are temporarily pinned by microstructural barriers, such as dislocation tangles, precipitations, grain boundaries, and voids, and subsequently, they are released abruptly in the changing magnetic field (Cullity & Graham, 2009). The stepwise breakaway of domain walls from the obstacles changes the magnetization state locally. Then, local changes in magnetization induce pulsed eddy currents, which activate electrical voltage pulses that may be detected by a searching coil or magnetic receiving head (Cullity & Graham, 2009). Stupakov *et al.* (2007) found that BN is sensitive to dislocation tangles introduced by plastic deformation. This also means that BN can also be sensitive to the applied stress. Such a phenomenon was explained by (Kleber & Vincent, 2004) at the level of the crystallographic network using pure iron as an example.

In the case of unloaded material, the magnetic moments of domains are oriented along the easy direction of magnetization. In the case of iron, the [100] represents the easy direction of magnetization. A tensile stress causes a change in the direction of easy magnetization. Both the magnetic domains and magnetic moments become parallel to the axis of stress action – they are locally privileged and grow at the expense of others. The privileging of domain walls results from the equation defining the magnetoelastic energy

$$E_m = -1.5 \cdot \lambda_s \cdot \cos^2(\phi), \tag{2.1}$$

where E_m – magnetoelastic energy of isotropic material, λ_s – magnetostriction constant for isotropic material $\lambda_{100} = \lambda_{111} = \lambda_s$, ϕ – the angle between the direction of stress $\boldsymbol{\sigma}$ and the direction of the vector local magnetization $\mathbf{J}_s$.

Since either the tensile stress or magnetostriction constants for iron are positive, their multiplication product also takes the positive value. The magnetoelastic energy reaches a minimum when the moments of magnetic domains are arranged to each other in a parallel way. As a consequence, the angle between the direction of local magnetization vector $\mathbf{J}_s$ and the direction of stress $\boldsymbol{\sigma}$ equals 0.

The Barkhausen signal decreases due to the appearance of the induced anisotropy of the material after exceeding the critical stress value. The sign of the magnetostriction constant for the iron changes from positive to negative for the magnetic field strength of about $16\,\mathrm{kAm}^{-1}$ (Cullity & Graham, 2009). Simultaneously, the easy magnetization direction of iron crystal changes from [100] to [111] (Kleber & Vincent, 2004). Magnetic domain walls are arranged lengthwise in the [111] easy magnetization direction, differently from the stress direction (Anglada-Rivera *et al.*, 2001). The influence of external tensile stress on the changes in the domain structure and in the BN level was also discussed in (Anglada-Rivera *et al.*, 2001). Moreover, the effect of compressive stress on domain walls behaviour was studied in (Stewart *et al.*, 2004).

In the case of compressive stress, the domains of the materials with a positive magnetostriction contrast and having their magnetic moments perpendicular to the axis of the applied stress become energetically favourable (Kleber & Vincent, 2004). Then, the magnetoelastic energy of the ferromagnetic material achieves a minimum. As a consequence, the angle between the direction of local magnetization vector $\mathbf{J}_s$ and the direction of stress $\boldsymbol{\sigma}$ equals 90°. The 90° domain walls enlarge at the expense of other domains (Kleber & Vincent, 2004). In this case, the BN signal decreases. Stupakov *et al.* (2007) studied CSN12013 low-carbon steel ($C = 0.03\,\%$) subjected to plastic deformation up to 23 %. It was found that the effective stress of the Barkhausen emission initially increases (up to approximately 2.5 %) with an increase in plastic deformation and then decreases. Similar results were found in (Piotrowski *et al.*, 2009) for CSN12021 steel tested up to 18.2 %. The highest BN amplitude was obtained for the specimen deformed to 1.9 %.

The problem of elastic tensile or compressive stresses effect on the magnetic BN is well recognized. However, the correlation between BN and plastic deformation is still a matter of intense investigation. From the microstructural point of view, the dislocations create different consequences during plastic deformation. In the early stage of the deformation process, they are distributed randomly and independently (Kashefi *et al.*, 2023). In the further stages of the deformation process, dislocations form sub-grains consisting of dislocation cells of hard density in the case of cell walls and lower density for the cell interior (Kashefi *et al.*, 2023). The soft and hard dislocation regions are responsible for a formation of the residual internal stress of type II after unloading of the previously plastically deformed material (Hong *et al.*, 2018). Dislocation tangles and cells interact with domain walls as the pinning sites and affect the BN signal (Cullity & Graham 2009). As a result, a change in the magnetic anisotropy may occur (Cullity & Graham 2009), and therefore, a change in the BN level can be observed.

According to the available literature, plastic deformation affects significantly the mechanical properties of materials. This research aims to find an answer to the questions how large changes in mechanical parameters are, and whether they can be determined using the BN technique. The elastic limit, yield point, strain hardening coefficient and strength coefficient were determined based on the relationships between parameters coming from monotonic tensile tests and the BN method. To date, the BN analysis has not been performed on a material subjected to repeated plastic deformation. The experiment demonstrates the possibilities of estimating material properties in worn-out structural parts involved in service downtime.

3. Material and experimental procedure

41Cr4 steel was selected for tests due to its wide application in automotive components, e.g., crankshafts, steering components, gears, front axle bearings. The steel is still an attractive structural material due to its high strength and qualified toughness (Celtik *et al.*, 2023). However, as of now, there are still some areas of knowledge requiring further thorough studies devoted to an influence of stress on mechanical parameters of plastically deformed zones (Romanowicz *et al.*, 2020).

The experimental procedure contained two main steps: monotonic tensile tests up to the selected values of deformation and the BN measurements. Mechanical tests were carried out at room temperature using flat specimens on the 8802 Instron servo-hydraulic testing machine. Strain was measured by means of the 2630 Instron uni-axial extensometer. The width, gauge length and thickness of the specimen were 10 mm, 25 mm, and 3 mm, respectively. The total length of the specimen was 174.5 mm (Fig. 1). The specimens were loaded monotonically under strain control with loading velocity of 0.005 mm/mm. The following levels of deformation were applied: 1 %, 2 %, 3 %, 4 %, 6 %, 8 %, 10 %, 12 %, 14 %. After each pre-strain, the specimen was unloaded. The yield point (YP), elastic limit (EL), strain hardening exponent (n), and strength coefficient (K) were determined for each loading process.

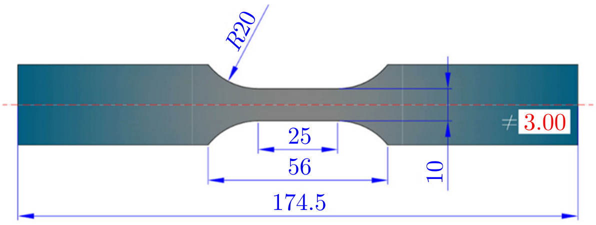

Fig. 1. Dimensions of specimen used in the experiment.

The BN measurements were performed using an MEB-4C defectoscope with a head consisting of a U-shaped core of electromagnets wrapped in the wound excitation coil. The pick-up coil was built into the sensor. In the pick-up coil, a voltage signal was induced. A triangular waveform was used. The fast-variable component was separated using a high-pass filter $f = (0\text{–}500)\,\text{Hz}$. The analysis of this component provided information on the strain level degree of the steel tested. The envelopes of magnetic BN were calculated as rms value U_b according to the following equation (Makowska *et al.*, 2024):

$$U_b = \sqrt{\frac{1}{\tau}\int\limits_0^{\tau} U_{tb1}^2(t)\,\mathrm{d}t}, \tag{3.1}$$

where U_b – root mean square (rms) of the coil output voltage [V], U_{tb1} – fast-variable component defining voltage separated using the high-pass filter from the induced voltage in the pick-up coil [V], τ – integration time [s].

Then, the amplitude of BN ($U_{b\,pp}$), defined as the voltage difference between the maximum peak value of the magnetic BN (U_b) and the background noise (U_{tb}), was determined. Moreover, the integral of the half-period voltage signal of MBN was calculated (Makowska *et al.*, 2024):

$$\mathrm{Int}(U_b) = \int\limits_{-Ug\max}^{+Ug\max} U_{sb}\,\mathrm{d}U_g, \tag{3.2}$$

where U_{sb} – rms of the Barkhausen emission voltage after correction with respect to the background noise [V], U_{tb} – rms of the background voltage [V], U_g – generator voltage [V].

The last step of the experimental programme was to find relationships between such mechanical parameters as elastic stress, yield point, maximal axis stress, stain hardening coefficient and parameters coming from rms of the BN envelope.

4. Results and analysis

The 41Cr4 steel stress-strain curves after various pre-strains are presented in Fig. 2. Important differences in tensile curves were found in the range from 0 % to 1 %. It was observed that the yield point and elastic limit increased with the pre-strain level (Fig. 3).

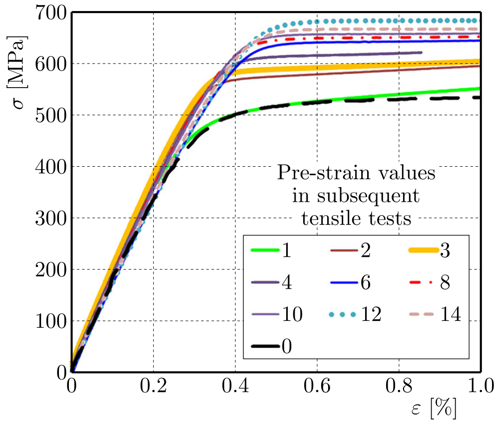

Fig. 2. Comparison of the tensile curve in the initial range of deformation for 41Cr4 in the as-received state to characteristics determined after the subsequent 9 steps of the loading-unloading process.

The greatest strengthening was achieved for an initial deformation of 0.12 mm/mm. The maximum value of the yield point was 690 MPa for the pre-strain level of 12 %, whereas the maximum

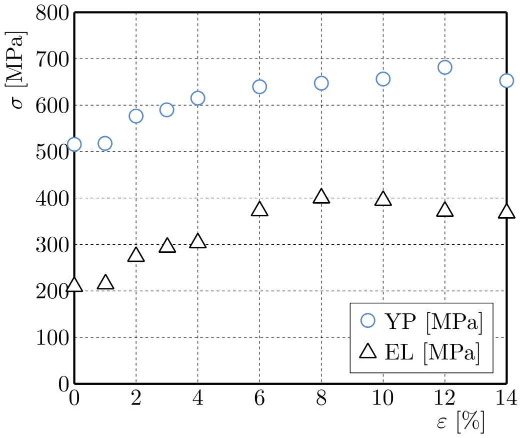

Fig. 3. Elastic limit (EL) and yield point (YP) versus total axial strain achieved during subsequent loading steps.

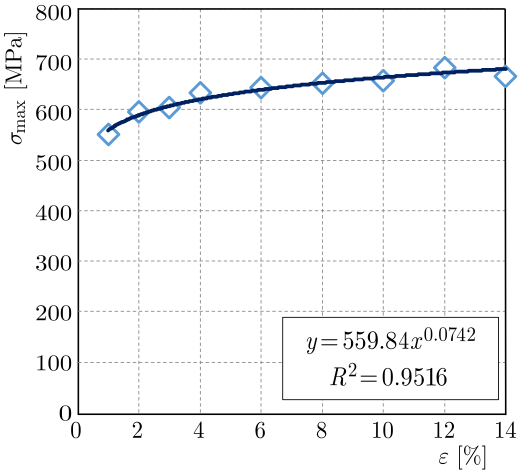

Fig. 4. Maximum value of axial stress versus total axial strain achieved during subsequent loading steps.

value of the elastic limit was 400 MPa for pre-strain of 8 % (Fig. 3). It means that 41Cr4 steel is sensitive to prior deformation and its mechanical parameters after loading to achieve 12 % pre-strain were almost 200 MPa higher than those for the same material in the as-received state obtained. The hardening was stabilized for the higher deformation reflected by similar values of the yield point and elastic limit. One can conclude that the pre-straining created almost a perfect elasto-plastic material with a little hardening effect. Also variations of the strain hardening exponent that was equal almost to zero for the highest strain level confirm such behaviour (Fig. 5). As is shown in Fig. 4, the maxiumum value of axial stress versus total axial strain increased

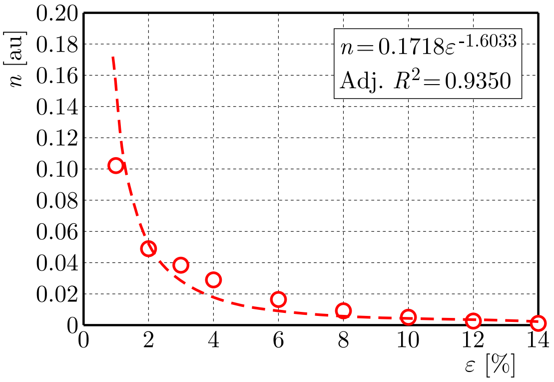

Fig. 5. Strain hardening exponents versus total axial strain achieved during subsequent loading steps.

during subsequent loading steps. Changes in the strength coefficient decreased asymptotically up to the constant level with an increase in the total axial strain (Fig. 6). The power-law work hardening equations for various values of the total strain are presented in Table 1. The true stress-plastic strain relationship is described by the equation $\sigma = K\varepsilon^n$ (Li *et al.*, 2019), where σ is the true stress, ε is the true plastic strain, K is the strength coefficient, and n is the strain hardening coefficient.

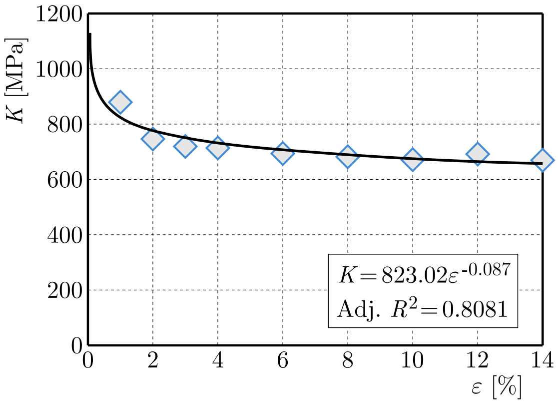

Fig. 6. Changes in strength coefficient versus total axial strain achieved during subsequent loading steps.

Table 1. Power-law work hardening equations for the total axial strain achieved during subsequent loading steps for 41Cr4 steel.

Total axial strain	Power-law hardening equation
1 %	$\sigma = 882.41\varepsilon^{0.1018}$
2 %	$\sigma = 743.44\varepsilon^{0.849}$
3 %	$\sigma = 719.37\varepsilon^{0.0383}$
4 %	$\sigma = 713.05\varepsilon^{0.0291}$
6 %	$\sigma = 695.29\varepsilon^{0.0165}$
8 %	$\sigma = 679.31\varepsilon^{0.0091}$
10 %	$\sigma = 673.69\varepsilon^{0.0052}$
12 %	$\sigma = 690.86\varepsilon^{0.0025}$
14 %	$\sigma = 669.28\varepsilon^{0.001}$

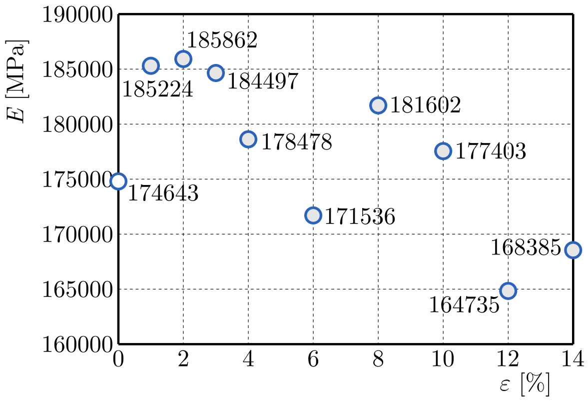

Fig. 7. Young's modulus versus total axial strain achieved during subsequent loading steps.

The effect of plastic deformation was also observed using the BN non-destructive method. It was found that the rms BN envelopes are sensitive to the pre-strain level (Fig. 9). The amplitude (Fig. 10) and the integral of BN (Fig. 11) decrease up to 6 % of plastic pre-strain. For its higher levels, both parameters take the constant value. For a better interpretation of the BN results, the points representing subsequent levels of prior deformation were introduced on the tensile curve of 41Cr4 steel (Fig. 8).

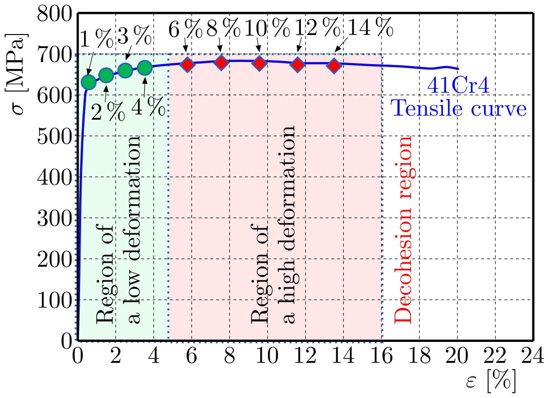

Fig. 8. Tensile curve of 41Cr4 steel with points illustrating the total strain values achieved during subsequent loading steps.

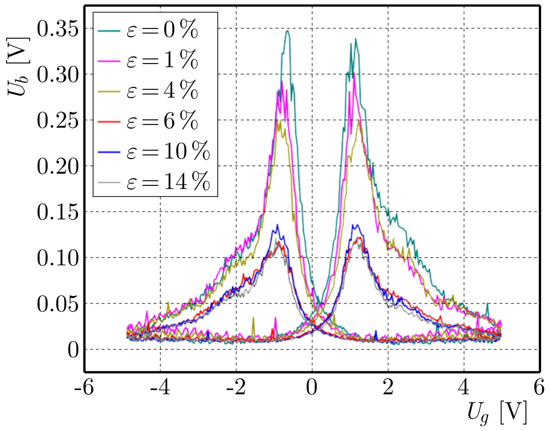

Fig. 9. Envelopes of rms BN before and after prior deformation.

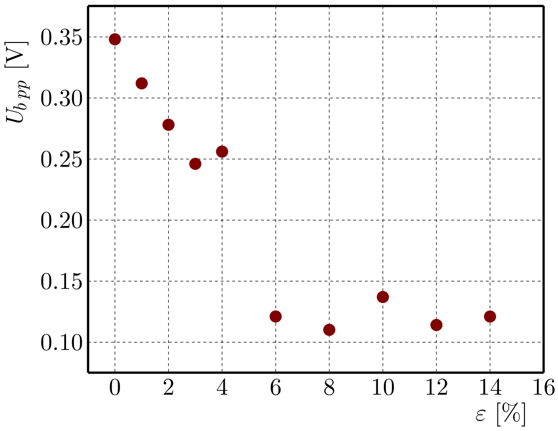

Fig. 10. Amplitude of rms BN envelopes versus total axial pre-str.

Figures 11 and 14 show that the BN is most sensitive in the elastic range of stress characteristic. In this case, the dislocation line length does not change significantly and the BN depends on changes in the crystal lattice. As a consequence, a rearrangement of the magnetic moments in magnetic domains through magnetoelastic energy takes place. In the elastic range, dislocations bow out and create a zig-zag segment structure. It indicates that the intergranular dislocation slip started before the initial plastic stage (Wang *et al.*, 2020). These are early

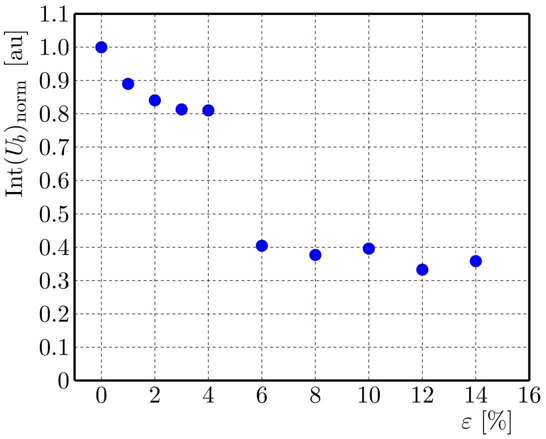

Fig. 11. Normalized $\mathrm{Int}(U_b)$ versus total axial pre-strain.

signs of plastic deformation also called micro-yielding. Generally, dislocations are likely to be generated first in the grain boundary regions during micro-yielding (Stefanita, 1999). As the grain slip process occurs partially, the plastic flow starts to appear in the material. The Barkhausen noise signal decreases with the plastic strain until the material becomes fully macro-yielded.

If the yield point is reached, then dislocations can be formed in the grain interior and the macroscopic yielding can occur by a massive generation of dislocations motion. In consequence, dislocation density becomes similar in boundary regions and inside the grain (Stefanita, 1999).

The dislocation tangles of high dislocation density create pinning sites during the further plastic deformation process. Forming dislocation configurations hinders the movement of the domain walls and the BN signal decreases.

This means that the Domain Walls (DWs) movements are hindered by defects of larger geometrical size (He *et al.*, 2019). According to (He *et al.*, 2019), magnetic domains are stuck between the micro-defects. Plastic deformation over 1 % introduced through the single-cycle loading process changes material isotropic orientation to the unique orientation of magnetic domains. Conversely, plastic deformation lower than 0.5 % and introduced by several loading processes leads to the cataclastic domain structures with weak orientation (He *et al.*, 2019).

When the specimen is stretched to 3 %, a dislocation density increases and distributes homogeneously. According to Mughrabi's composite model, the structure with dislocation-rich cell walls and dislocation-rich walls is created (Dannoshita *et al.*, 2023). Edge dislocations create dislocation cell walls, whereas screw dislocations are the main components of the cell interiors (Dannoshita *et al.*, 2023).

Dislocation tangles develop with plastic strain and dislocation lines intertwined with each other. Within the range of strain $\varepsilon = 10\,\%$–$14\,\%$, dislocation pile-up occurred and dislocation net structures consisted of high-density dislocation tangles developed (Wang *et al.*, 2020). Moreover, the formation of voids under tensile stress can be observed (Wang *et al.*, 2020). The voids are created in both regions of high dislocation density as well as the precipitated phase vicinity, and they serve as the demagnetization areas that contribute to the BN signal reduction.

An interesting feature can be observed by the analysis of Young's modulus variations due to subsequent steps of prior deformation. Studies of Young's modulus as a function of strain were repeatedly undertaken in (Roca *et al.*, 2014). A decrease in Young's modulus after plastic deformation was noticed in the low-carbon steel delivered in the form of sheets. It varied from 215 GPa, 200 GPa, 195 GPa for pre-strain of 0 %, 10 % and 15 %, respectively (Yamaguchi *et al.*, 1998). It was also observed that Young's modulus of the low-carbon steel sheet could be recovered to the value of undeformed sheet by subsequent annealing (Yamaguchi *et al.*, 1998). Researchers presumed that a decrease in Young's modulus came mainly from the microscopic debonding at the interface between inclusions or 2nd-phase particles and matrix (Yamaguchi *et al.*, 1998).

Similar tendency was obtained for a ductile iron by Berdin and HauŠild (2002). In this case, a debonding at the interface between graphite nodules and metallic matrix was responsible for Young's modulus lowering. In (Rutecka *et al.*, 2020), debonding between SiC particles and aluminium matrix was observed in the form of small microstructural discontinuities and cracks around SiC particles. It led to a decrease in Young's modulus with plastic deformation (Rutecka *et al.*, 2020). However, in the case of 41Cr4 steel tested in this research, Young's modulus seems to be insensitive to prior deformation (Fig. 7). From the microstructural point of view, Young's modulus values could be attributed to certain categories depending on the strain range. One can indicate the first range if $\varepsilon = 1\,\%$–$3\,\%$, the second one if $\varepsilon = 3\,\%$–$10\,\%$, and the third one if $\varepsilon = 10\,\%$–$14\,\%$. As it was mentioned earlier, the first range corresponds either to micro-yielding or macro-yielding where there are no significant material inhomogeneities, so E = 185 GPa–186 GPa. The second range represents an increase in inhomogenously distributed dislocations. Dislocations increase and interact with each other inside the crystal in the homogenous plastic region. A threshold of the slip process is increased by the hardening of the material. So, E = 172 GPa–182 GPa. In the third range ($\varepsilon = 10\,\%$–$14\,\%$), voids in the material occur near very high dislocation tangles. The steel structure becomes very inhomogeneous, so Young's modulus drops below 170 GPa (takes values between 165 GPa and 168 GPa). An influence of dislocation density on Young's modulus was discussed in (Benito *et al.*, 2005). The authors noticed that Young's modulus of pure iron decreased after plastic deformation from the original mean value of 210 GPa to 196 GPa at $\varepsilon = 0.060$. Next, a slight recovery occurred and Young's modulus increased to 198 GPa until the neck appeared at $\varepsilon = 0.100$ (Benito *et al.*, 2005). An explanation of such behaviour is based on Mott's model (Benito *et al.*, 2005). It was proposed that the assumed dislocations can bow out in their glide planes, giving an extra elastic strain, and thus, a decrease in Young's modulus. According to Mott's theory, the first steps of deformation in pure iron lower Young's modulus due to the dislocation density and the extra elastic strain increase (Benito *et al.*, 2005). Hence, when the cellular dislocation structure has formed during plastic deformation at higher strains (between $\varepsilon = 0.060$ and 0.080), the dislocations in cell interiors may give an extra elastic strain (Benito *et al.*, 2005). In the early stages of deformation, the cell structure is not able to develop, so the dislocation density in cell interiors is lower than that in the first deformation stage observed. It causes the slight recovery of Young's modulus measured at the strain ranges considered. Finally, for the higher strain values than $\varepsilon = 0.080$, no changes of dislocation density in cell interiors are observed and the values of Young's modulus are stabilized (Benito *et al.*, 2005).

The change in parameters coming from the BN envelope can be considered separately for low and high degrees of prior deformation. The linear relationship between the BN amplitude and pre-strain was found (Fig. 12). Exponential dependence was observed in the case of the BN integral and prior deformation (Fig. 14). However, both BN parameters are insensitive to higher levels of pre-strain (Fig. 13 and Fig. 15).

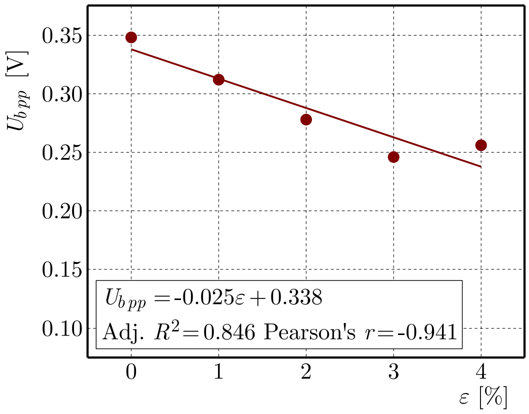

Fig. 12. Amplitude of rms BN envelopes versus low total axial pre-strain.

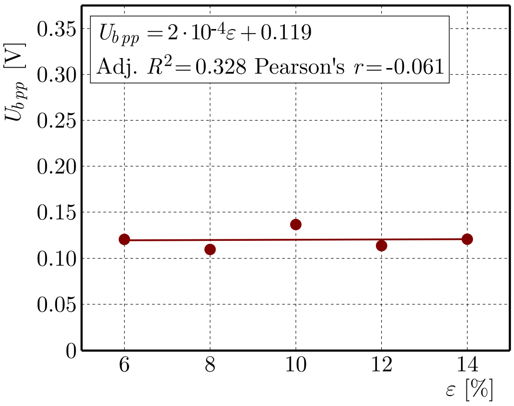

Fig. 13. Amplitude of rms BN envelopes versus high total axial pre-strain.

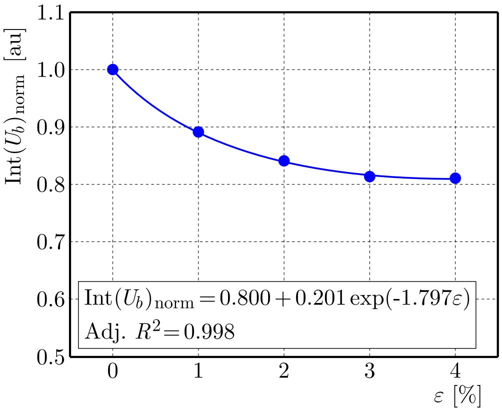

Fig. 14. Normalized BN integral versus low total axial pre-strain.

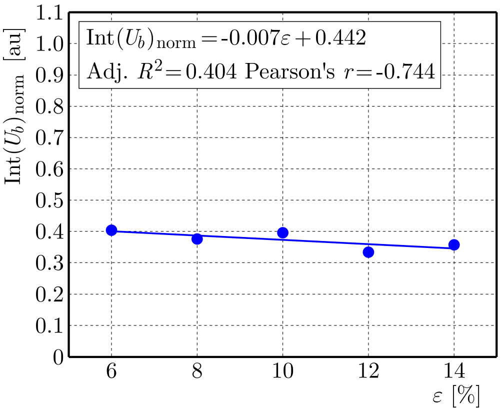

Fig. 15. Normalized BN integral versus high total axial pre-strain.

The BN signal depends strongly on dislocation density. In (Li *et al.*, 2024), the dislocation density was measured for similar medium carbon steel with martensitic structure for different levels of strain. The results were shown in the form of a dislocation density diagram versus strain (Fig. 16) (Li *et al.*, 2024).

Dislocation densities at specific strains can be calculated using the Williamson–Hall equation based on the X-ray diffraction (Deutges *et al.*, 2025): $\beta \cdot \cos(\theta) = 0.9\lambda/D + \varepsilon \cdot 2\sin(\theta)$, where θ – Bragg angle, λ – wavelength of the X-ray beam, β – full width at half maximum (FWHM) of the Bragg peaks, D – grain size, ε – lattice strain.

The term of equation $0.9\lambda/D$ is considered to be negligibly small when the effective average grain size that affects dislocation density calculations of the martensitic substructure is not smaller than 1 µm (Deutges *et al.*, 2025).

The relationship between strain and dislocation density ρ and ε can be given by the equation: $\rho = \frac{k \cdot \varepsilon^2}{b^2}$, where ε – lattice strain, b – Burger vector, k – geometrical constant ($k = 14.4$ for body-centred cubic materials) (Deutges *et al.*, 2025).

The dislocation density variations presented in Fig. 16 enable to indicate a decrease in the amplitude and integral values of the half-period BN voltage signal. Dislocation density values for the deformation range from 1 % to 4 % and are located near 21×10^{14} [1/mm^2]. However, for a strain level of 7 %, the dislocation density increases rapidly up to 26.85×10^{14} [1/mm^2]. Also, a rapid change in the amplitude and the normalized BN integral can be noticed for the strain range from 1 % to 6 %. The normalized Int(U_b) values changed from 0.81–0.89 in the 1 %–4 % strain range to 0.37–0.40 in the strain range of 4 %–6 %. The values of the BN amplitude changed from 0.31 V–0.24 V in the 1 %–4 % strain range and attained a value equal to 0.11–0.13 after pre-strain exceeding $\varepsilon = 4$ %. Thus, a sudden increase in the dislocation density causes a sharp decrease in the parameters of the BN. It was observed that the greater magnetic results diversity was obtained at the higher values of the BN amplitude. This is due to the greater sensitivity of this parameter to the microstructure features. It seems that the microstructural forms, like dislocations, change the stress levels in micro-regions of material, for example.

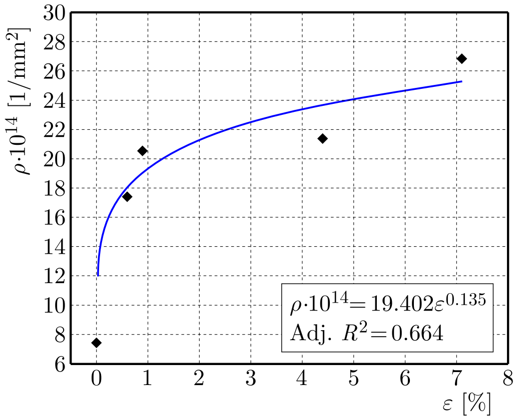

Fig. 16. Dislocation density of the martensitic medium-carbon specimens, based on (Li *et al.*, 2024).

The experimental points representing dislocation density in Fig. 16 were approximated to describe a character of dislocation density variation. In Fig. 17, the relationship between dislocation density and the normalized BN integral of the half-period voltage signal Int(U_b) was elaborated. Dislocation density values for the pre-strain levels considered in this research are included in Table 2. Figure 17 shows that the Int(U_b) related to the dislocation density of about 21×10^{14} [1/mm^2] corresponds to the deformation value equal to 2 %.

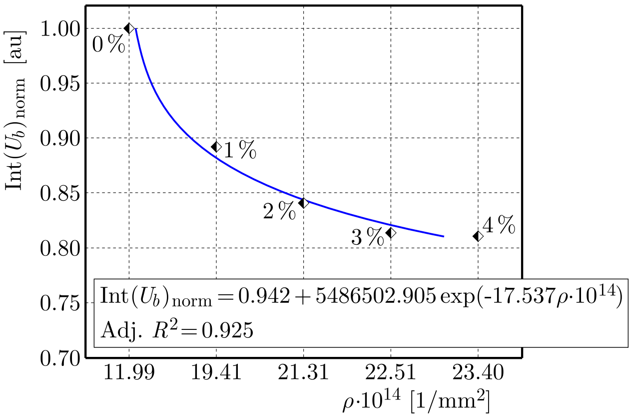

Fig. 17. Relationship between the dislocation density and normalized BN integral of the half-period voltage signal Int(U_b).

Table 2. Dislocation density values determined on the basis of approximation line from the graph in Fig. 16.

Strain level ε [%]	Dislocation density ρ [$\times 10^{14}$ 1/mm^2]
0	11.990
1	19.407
2	21.312
3	22.512
4	23.398
6	24.717

Strength and strain hardening coefficients versus the BN amplitude and integral are presented in Figs. 18–21. Both BN parameters variations, $U_{b\,pp}$ and $\mathrm{Int}(U_b)$, enable to identify n and K that correspond to a stress region close to the yield point. The point representing pre-strain equal to 1 % can be assigned to the elastic stress section of the tensile curve and dislocation density of about 20×10^{14} [1/mm^2]. Plastic deformation of a metal or metallic alloys begins at a stress lower than the yield strength. Plastic deformation does not occur simultaneously throughout the entire specimen volume in polycrystalline materials. A transition from the elastic stress range to the plastic one is smooth. In practice, the elastic limit is considered to be the normal stress at which the plastic deformation is still very small but measurable, from 0.001 % to 0.05 % (Dębski *et al.*, 1990). The next strain range that covers values from 2 % to 4 % is already connected with the early plastic deformation where the dislocation density is about 21×10^{14} [1/mm^2] for

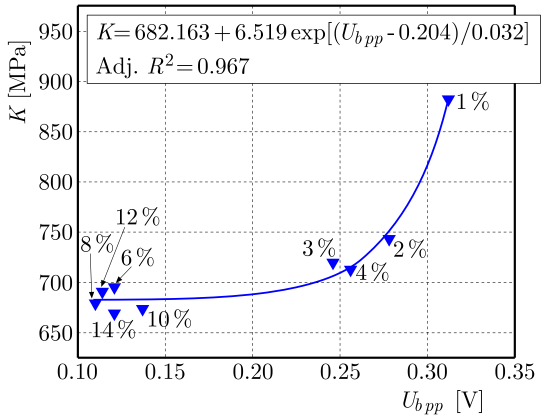

Fig. 18. Strength coefficient versus amplitude of BN.

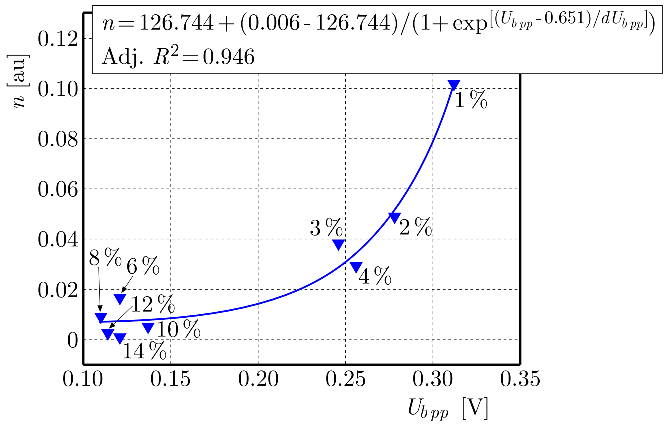

Fig. 19. Strain hardening coefficient versus amplitude of BN.

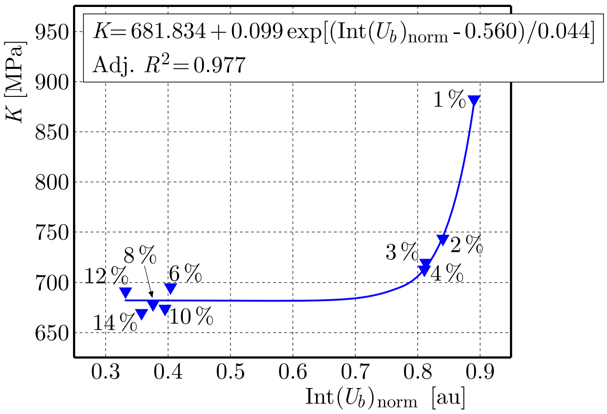

Fig. 20. Strength coefficient versus integral of BN.

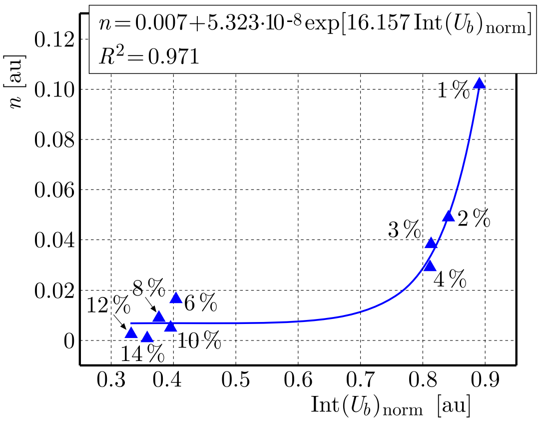

Fig. 21. Strain hardening coefficient versus integral of BN.

pre-strains equal either to 3 % or 4 %. As a consequence, both these points are next to each other on the graphs, especially in Fig. 20.

The points representing the pre-strain range from 6 % to 14 % are located close to each other on the graphs presented in Figs. 18–21 due to the insensitivity of $U_{b\,pp}$ and $\mathrm{Int}(U_b)$ parameters on the higher total pre-strain.

Figures 22 and 23 indicate that $U_{b\,pp}$ and $\mathrm{Int}(U_b)$ can be helpful in the prediction of the elastic stress and yield point of 41Cr4 after deformation in the range of 1 %–4 %. Linear relationships between the yield point/elastic limit and the amplitude/integral of the half-period voltage signal of magnetic BN were obtained in the case of low pre-strain values (Figs. 22 and 23). The pre-

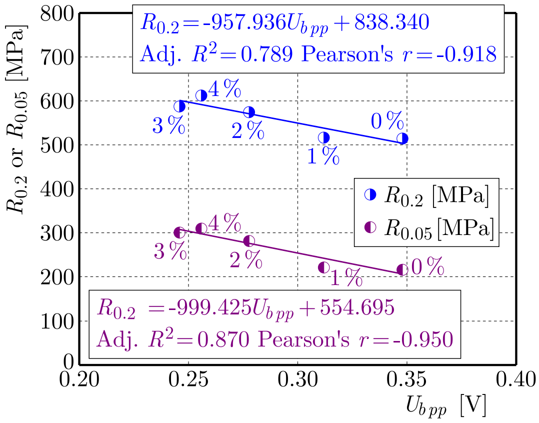

Fig. 22. Yield point and elastic limit versus amplitude of BN.

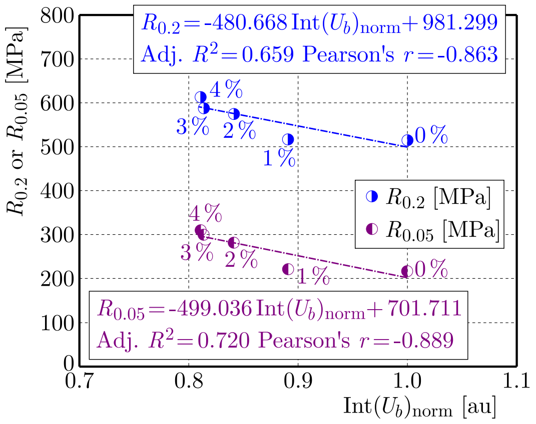

Fig. 23. Yield point and elastic limit versus integral of BN.

strain level of 1 % did not change the value of the yield point and elastic limit in comparison to the specimen before loading. On the contrary, both magnetic parameters represented a completely different character of behaviour. The changes in values of the magnetic parameters at the strain range of 1 %-–4 % are related to the material elastic region, and therefore, the stress state of 41Cr4 steel tested came back to its initial state.

5. Conclusions

Plastic deformation leads to local changes in mechanical parameters of the material tested in this study. This paper has indicated the possibility for simple identification of selected mechanical parameters of the steel subjected to prior deformation from tensile tests. This is a particularly important issue, because defects may appear during material exploitation that could change significantly its response to further loading programmes. Linear relationships were found between the stress limit/yield point and parameters determined from the BN method for low pre-strain values (0 %–4 %). The amplitude and integral of the BN were insensitive to deformations above 6 %. However, the same parameters may be successfully applied for identification of the strength and strain hardening coefficient values of ferromagnetic materials deformed up to the stress corresponding to the yield point. In conclusion, one can indicate the BN as a method that may provide effective technical support for devices inspection and structural parts diagnostics.

Acknowledgments

This work was financed by the Military University of Technology under research project 742/2004 “Modern technologies and research of modern materials used in armament technology”.

References

1. Anglada-Rivera, J., Padovese, L.R., & Capó-Sánchez, J. (2001). Magnetic Barkhausen Noise and hysteresis loop in commercial carbon steel: influence of applied tensile stress and grain size. *Journal of Magnetism and Magnetic Materials*, *231*(2–3), 299–306. https://doi.org/10.1016/S0304-8853(01)00066-X

2. Benito, J.A., Jorba, J., Manero, J.M., & Roca, A. (2005). Change of Young’s modulus of cold-deformed pure iron in a tensile test. *Metallurgical and Materials Transactions A*, *36*(12), 3317–3324. https://doi.org/10.1007/s11661-005-0006-6

3. Berdin, C., & HauŠild, P. (2002). Damage mechanisms and local approach to fracture. Part I: Ductile fracture. In I. Dloughý (Ed.), *Transferability of fracture mechanical characteristics* (pp. 167–180). NATO Science Series, vol. 78. Springer, Dordrecht. https://doi.org/10.1007/978-94-010-0608-8_12
4. Celtik, C., Ayhan, I.I., & Yurekturk, Y. (2023). Effect of double austenization and pre-annealing heat treatment on the microstructural and mechanical properties of QT 41Cr4 steel. *Transactions of the Indian Institute of Metals*, *76*(10), 2845–2855. https://doi.org/10.1007/s12666-023-02975-5
5. Cullity, B.D., & Graham, C.D. (2009). Introduction to magnetic materials (2nd ed.). Wiley-IEEE Press. https://doi.org/10.1002/9780470386323
6. Dannoshita, H., Hasegawa, H., Higuchi, S., Matsuda, H., Gong, W., Kawasaki, T., Harjo, S., & Umezawa, O. (2023). Effects of dislocation arrangement and character on the work hardening of lath martensitic steels. *Scripta Materialia*, *236*, Article 115648. https://doi.org/10.1016/j.scriptamat.2023.115648
7. Deutges, M., Barth, H.P., Chen, Y., Borchers, C., & Kirchheim, R. (2015). Hydrogen diffusivities as a measure of relative dislocation densities in palladium and increase of the density by plastic deformation in the presence of dissolved hydrogen. *Acta Materialia*, *82*, 266–274. https://doi.org/10.1016/j.actamat.2014.09.013
8. Dębski, A., Michałowski, J., Wiśniewski, S., & Wojciechowski, W. (1990). Construction materials in armament. Laboratory exercises (in Polish). Wydawnictwo Wojskowej Akademii Technicznej, Warszawa, Poland.
9. He, M., Matsumoto, T., Uchiomoto, T., Takagi, T., Chen, H., Xie, S., & Chen, Z. (2019). Caution to apply Magnetic Barkhausen Noise method to nondestructive evaluation of plastic deformation in some ferromagnetic materials. *Chinese Journal of Mechanical Engineering*, *32*, Article 104. https://doi.org/10.1186/s10033-019-0420-0
10. Hong, Y., Li, S., Li, H., Li, J., Sun, G., & Wang, Y.-D. (2018). Development of intergranular residual stress and its implication to mechanical behaviors at elevated temperatures in AL6XN austenitic stainless steel. *Metallurgical and Materials Transactions A*, *49*(8), 3237–3246. https://doi.org/10.1007/s11661-018-4655-7
11. Kashefi, M., Krause, T.W., Underhill, P.R., & Wowk, D. (2023). On the combined effect of elastic and plastic strain on Magnetic Barkhausen Noise signals. *Journal of Nondestructive Evaluation*, *42*(2), Article 55. https://doi.org/10.1007/s10921-023-00970-w
12. Kleber, X., & Vincent, A. (2004). On the role of residual internal stresses and dislocations on Barkhausen noise in plastically deformed steel. *NDT & E International*, *37*(6), 439–445. https://doi.org/10.1016/j.ndteint.2003.11.008
13. Li, J., Qiu, Y.-Y., Wang, H.-D., & Wang, Z.-X. (2019). Estimation of the strength coefficient and strain hardening exponent from monotonic tensile properties of steels. *International Journal of Steel Structures*, *19*(6), 1951–1968. https://doi.org/10.1007/s13296-019-00256-w
14. Li, J., Zhang, J.-z., Zeng, L.-y., Wang, S., Song, X.-y., Chen, N.-I., Zuo, X.-w., & Rong, Y.-h. (2024). Revealing dislocation activity modes during yielding and uniform deformation of low-temperature tempered steel by acoustic emission. *Journal of Iron and Steel Research International*, *31*(12), 3022–3036. https://doi.org/10.1007/s42243-024-01253-y
15. Makowska, K., Szymczak, T., & Kowalewski, Z.L. (2024). Fatigue behaviour of medium carbon steel assessed by the Barkhausen noise method. *Acta Mechanica et Automatica*, *18*(1), 40–47. http://doi.org/10.2478/ama-2024-0005
16. Piotrowski, L., Augustyniak, B., Chmielewski, M., & Tomáš, I. (2009). The influence of plastic deformation on the magnetoelastic properties of the CSN12021 grade steel. *Journal of Magnetism and Magnetic Materials*, *321*(15), 2331–2335. https://doi.org/10.1016/j.jmmm.2009.02.028
17. Roca, A., Villuendas, A., Mejía, I., Benito, J.A., Llorca-Isern, N., Llumà, J., & Jorba, J. (2014). Can Young's modulus of metallic alloys change with plastic deformation? *Materials Science Forum*, *783–786*, 2382–2387. https://doi.org/10.4028/www.scientific.net/MSF.783-786.2382
18. Romanowicz, P.J., Szybiński, B., & Wygoda, M. (2020). Application of DIC method in the analysis of stress concentration and plastic zone development problems. *Materials*, *13*(16), Article 3460. https://doi.org/10.3390/ma13163460

19. Rutecka, A., Kursa, M., Pietrzak, K., Kowalczyk-Gajewska, K., Makowska, K., & Wyszkowski, M. (2020). Damage evolution in AA2124/SiC metal matrix composites under tension with consecutive unloadings. *Archives of Civil and Mechanical Engineering*, *20*(4), Article 135. https://doi.org/10.1007/s43452-020-00134-x

20. Stefanita, C.-G. (1999). *Surface magnetic Barkhausen noise response to plastic yield of steel.* [Doctoral dissertation, Queen's University of Kingston], Ontario, Canada.

21. Stewart, D.M., Stevens, K.J., & Kaiser, A.B. (2004). Magnetic Barkhausen noise analysis of stress in steel. *Current Applied Physics*, *4*(2–4), 308–311. https://doi.org/10.1016/j.cap.2003.11.035

22. Stupakov, O., Pal'a, J., Tomáš, I., Bydžovský, J., & Novák, V. (2007). Investigation of magnetic response to plastic deformation of low-carbon steel. *Materials Science and Engineering: A*, *462*(1–2), 351–354. https://doi.org/10.1016/j.msea.2006.02.475

23. Vaidyanathan, S., Moorthy, V., Kalyanasundaram, P., Jayakumar, T., & Raj Baldev (1999). Effect of different stages of tensile deformation on micromagnetic parameters in high-strength, low-alloy steel. *Metallurgical and Materials Transactions A*, *30*(8), 2067–2072. https://doi.org/10.1007/s11661-999-0017-9

24. Wang, X., Chen, J.-G., Su, G.-F., Li, H.-Y., & Wang, C. (2020). Plastic damage evolution in structural steel and its non-destructive evaluation. *Journal of Materials Research and Technology*, *9*(2), 1189–1199. https://doi.org/10.1016/j.jmrt.2019.11.046

25. Yamaguchi, K., Adachi, H., & Takakura, N. (1998). Effects of plastic strain and strain path on Young's modulus of sheet metals. *Metals and Materials*, *4*(3), 420–425. https://doi.org/10.1007/BF03187802

Manuscript received December 20, 2024; accepted for publication May 14, 2025;
published online July 19, 2025.

JOURNAL OF THEORETICAL
AND APPLIED MECHANICS
63, 3, pp. 673–678, Warsaw 2025
https://doi.org/10.15632/jtam-pl/205162

THE VIRTUAL LOAD CASE DEFINITION FOR OFF-ROAD VEHICLES: METHODOLOGY BASED ON MULTIBODY SYSTEM SIMULATION

Gernot JEDINGER-PAUSCHENWEIN[1], Wilhelm FUCHS[1], Helmut J. HOLL[2]*

[1] *AVL List GmbH, Tech-Center Steyr, Austria*
[2] *Institute of Technical Mechanics, Johannes Kepler University, Linz, Austria*
*corresponding author, *helmut.holl@jku.at*

The methodology for setting up a multibody system for a tractor, incorporating an advanced tire model is presented and discussed. The goal is to obtain precise load and boundary conditions for the finite element analysis, which in turn aids in predicting fatigue life. Additionally, the generated loads and boundary conditions are used to define a test procedure with hydraulic actuators, aiming to replicate field damage values for the relevant components as precisely as possible. As a result, a consistent simulation process extended from the early design stage to the prototype test phase is presented in this contribution. Furthermore, all the results achieved with this methodology are confirmed by measurements.

Keywords: vehicle; multibody system; Adams; fatigue load.

1. Introduction

Defining virtual and accurate load cases is a critical challenge in modern off-road vehicle development to ensure proper dimensions and lightweight design at an early stage of development. Focusing on accurate load cases, AVL (AVL List GmbH) attempted to establish a simulation methodology comprehensively supporting the whole development process.

An agricultural tractor with a tare mass of approximately 6 tons from serial production was selected as the test object for this research (see (Jedinger-Pauschenwein *et al.*, 2024)). Unfortunately, more information about the vehicle cannot be provided because of confidentiality agreement with AVL's customer.

All simulations were conducted using simulations without considering any flexibility of the tractor body, as its rigid structure has eigenfrequencies well above the excitation spectrum of the tested road profile (<20 Hz).

Fully integrated simulation process:

- The setup of a complex multibody system model is carried out in Adams which is a multibody dynamics simulation software system (see (Adams)). The model includes an air suspended cabin with a sprung driver seat, front axle suspension incorporating the behavior of the hydraulic suspension, lashes at the rear lift hinges, elasticities in powertrain, and other details. The first parametrization of the module FTire, which is used for modelling tires (see (Gipser, 2007; FTire)), is based on approximate and scaled values.

Ministry of Science and Higher Education
Republic of Poland

The publication has been funded by the Polish Ministry of Science and Higher Education under the Excellent Science II programme "Support for scientific conferences".
The content of this article was presented during the 40th Danubia-Adria Symposium on Advances in Experimental Mechanics, Gdańsk, Poland, September 24–27, 2024.

- Fine tuning of the tire parameters is an iterative process with multibody system simulations, whereby the parameters are adapted via measurements from the tractor testing in the field.
- Based on the fine-tuned multibody system model, traversing a field path defined by the customer is simulated with Adams. The results (accelerations, forces, etc.) are the input data (loads and boundary conditions) for the subsequent finite element analysis.
- The strength analysis with the nonlinear finite element method delivers deformations, stresses, contact behavior in the flanges, etc. A subsequent mechanical fatigue analysis provides safety factors or damage values, respectively.
- Finally, the setup of the test bed is derived from the simulation methodology and its results. It includes the arrangement of the hydraulic cylinders, the definition of the fixation of the tractor body on the test bed, and the loads and their referring cycles to achieve the same damage values at certain components as it is expected in the whole tractor lifetime.

The outstanding feature of the presented methodology is the consistent, virtual support of the development process from a design stage until prototype testing, which is not existing practice.

2. Vehicle multibody system simulation model

A vehicle multibody system (VMBS) simulation model is established (see (Popp & Schiehlen, 2010; Shabana, 2013)), including the following rigid bodies: chassis frame, rigid (pendulum) axle, cabin, and implements. The model accounts for lashes in the rear hitch, among other factors. The front axle is locked, allowing only the rotation about the longitudinal axis of the hinge as an additional degree of freedom. Springs and dampers with both linear and nonlinear characteristics are incorporated for the cabin suspension and the front/rear hitches. Various ballasting scenarios are also considered.

Tire parameters significantly impact the dynamic behavior of the entire mechanical system. To accurately account for the tires, the FTire module was utilized with initial parameter estimates provided by company cosin (see (Bayerischen Transformations- und Forschungsstiftung, 2021; FTire)) who are the software manufacturer of FTire.

For fine-tuning, acceleration measurements at the wheel hubs taken in the field (several short-wave road profiles, i.e.: cleats, see Fig. 1) have been evaluated and analyzed. The comparison with the virtually achieved simulation results formed the basis for fine adjustment of the tire parameters.

Fig. 1. Cleat obstacles for tire parametrization.

For this fine-tuning ten main parameters were varied, whereby the focus was to achieve the same acceleration signals during cleat traversing at the metering points near the wheel hubs in simulation, in the time domain as well as in the frequency domain (the Fourier spectrum) (Fig. 2).

To proof the new methodology, a merry-go-round (MGR) test track (as seen in Fig. 3) is built-up in the field. This track is specifically designed to test the durability and resilience of vehicles when exposed to real or simulated working conditions, whereby periodical excitations due to obstacles as shown in Fig. 3 are to be considered. In literature it is also referred to as a bump test track circuit with obstacles (see (Renius, 2020)).

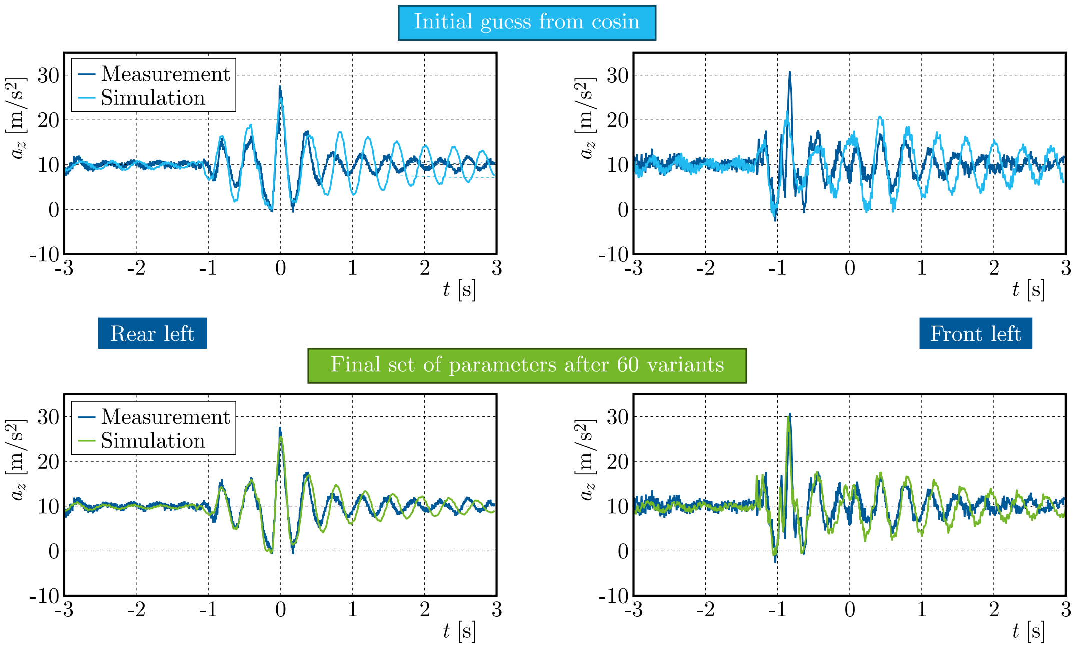

Fig. 2. Accelerations in time domain.

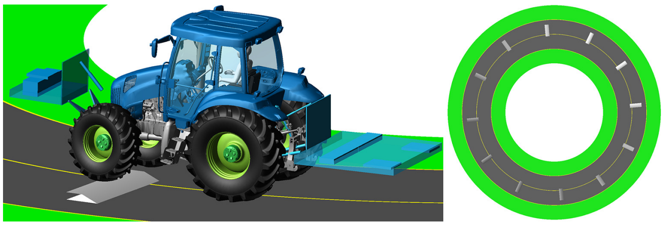

Fig. 3. Merry-go-round test.

To check the reliability of the simulation, the acceleration signals at the wheel hubs are measured again, and virtual simulations are performed with the fine-tuned model in parallel. As a result, the comparison between measured and simulated signals indicated a strong correspondence, which justifies the conclusion that a virtual multibody system simulation delivers a sufficiently accurate basis for the load case definition (see Fig. 4).

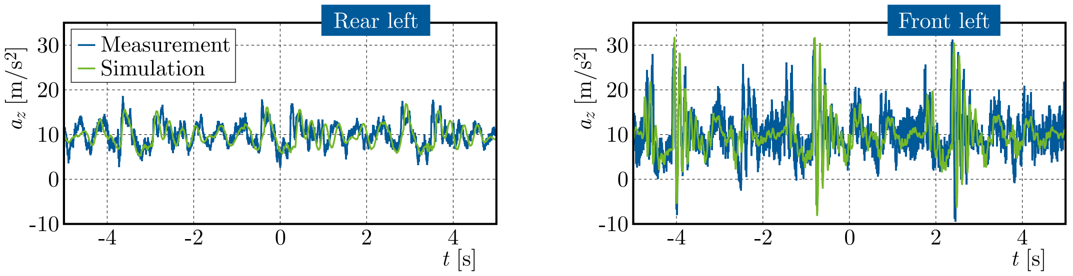

Fig. 4. Accelerations near wheel hubs in time domain during MGR test.

Additionally, these simulations enable the definition of internal forces and accelerations for all components, including those where mounting measurement sensors are impractical. Measuring intermediate/connecting forces between components directly in the field can be a quite challenging task in general, which is why the AVL "Marker Method" (Fuchs & Pauschenwein, 2019; Schiller, 2018) is a practical way to obtain them through simulation.

Because of their extent, mathematical details are not shown in the short communication paper.

3. Loads and boundary conditions

3.1. Dynamic conditions for finite element analysis

Using the validated model, loads and boundary conditions (LBC) for the finite element analysis (FEA) can now be derived from VMBS simulation results. The FEA is carried out with the software tool Abaqus (see (Abaqus)). While the straightforward approach would be to replicate the exact loading conditions from VMBS in the FE-model, this is only practical for singular events, such as accidents involving (front) wheel impacts. For durability loads under seemingly random rough road conditions, statistical methods like Rainflow counting must be applied (see (Fuchs & Pauschenwein, 2019)). However, for the periodic conditions of the MGR test track, identifying the relevant time steps within one period is more suitable.

To achieve this, the first step is to narrow down the set of all variables (forces, torques, accelerations) to a small set of relevant observables. Experience and observation have shown that the vertical forces from implements and on the axles define the critical conditions for the structural components.

This results in the desired set of forces and loads as depicted in Fig. 5.

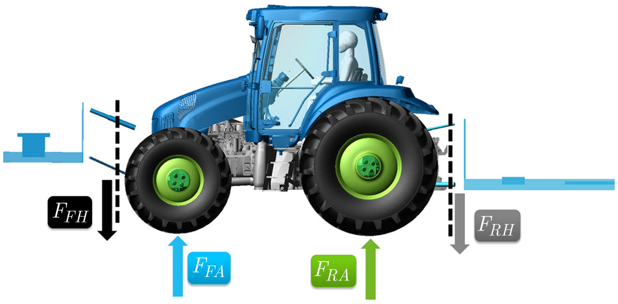

F_{FA}: front axle load
F_{RA}: rear axle load
F_{FH}: vertical force from front hitch
F_{RH}: vertical force from rear hitch

Fig. 5. Relevant observables (forces) at the chassis.

After condensing all simulated obstacle traversals into a single representative period (for all variables), the next step is to identify all local maxima and minima for the four dominant loads, combining time points that are close to each other. This selection is depicted in Fig. 6, where shock factors ($F_{\text{dynamic}}/F_{\text{static}}$) instead of forces are utilized for better visualization. Then, using the beam as an example, for each final time, the loads on the part (e.g., forces in the suspensions, rear wheel hub loads, etc.) are extracted applying the following rule: If a local extremum is nearby, the extremum is used; otherwise, the value at the specified time is used.

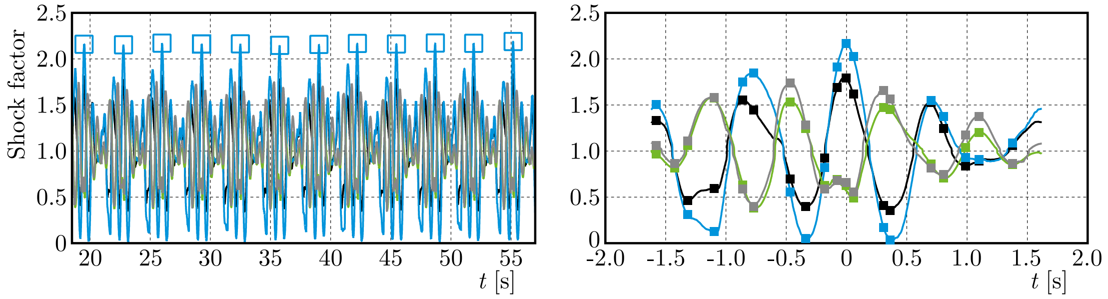

Fig. 6. Shock load factors for main forces; one full round (left), representative period (right).

All the defined load points are to be applied to the FE-model, and inertia relief warrants equilibrium of forces. Considering the constructed representative cycle, a succeeding analysis with FEMFAT/TRANS MAX obtains the damage of one period. FEMFAT is a software tool for the mechanical fatigue analysis (see (FEMFAT)). Multiplying this value with the number of cycles appearing in the whole tractor lifetime predicts the damage value.

3.2. Static conditions for hydro-pulse system and FEA

Severe load cases (e.g., pendulum impact, one-sided impact at the front wheel, etc.) require test beds with hydraulic actuators, as four-poster test beds can only apply vertical forces at the tire treads. Additionally, these test rigs with hydraulic cylinders are more cost-efficient. Therefore, a procedure has been developed to simulate the MGR test using hydraulic actuators, as shown in Fig. 7. Of course, it is not possible to determine load and boundary conditions at the test bed for the whole vehicle, but only for selected components to be investigated, because dynamic boundary conditions (i.e., accelerations) cannot be applied. Nevertheless, the hydraulic forces can be determined in a way that they are expected to cause the same damage values in the referring component as simulated in the finite element analysis described in Subsection 3.1, as the simulation results in Fig. 8 show.

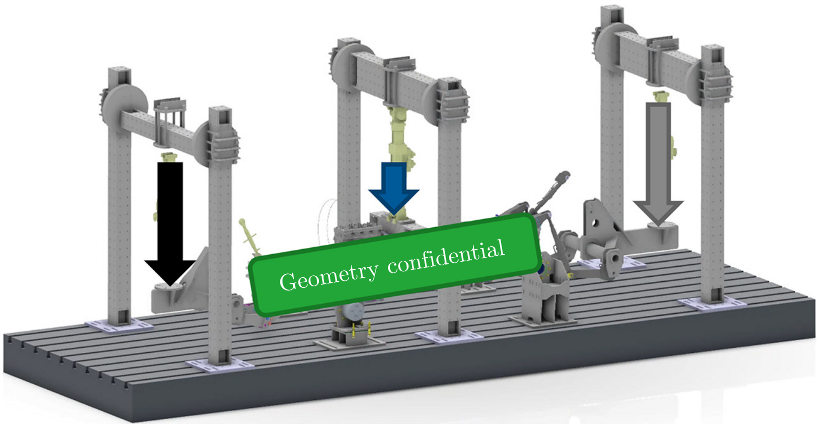

Fig. 7. Test rig with hydraulic actuators.

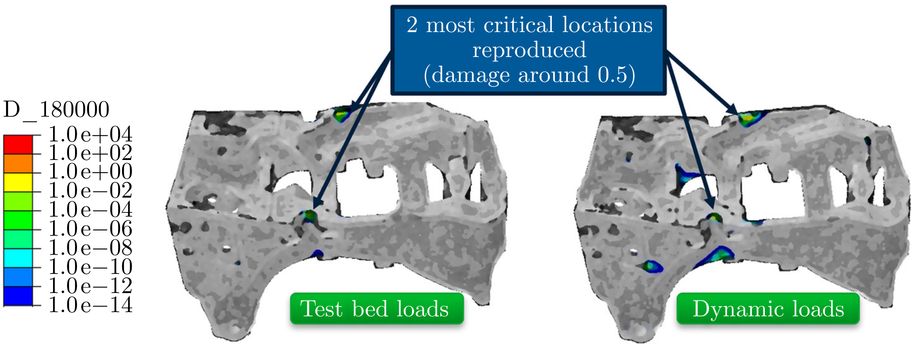

Fig. 8. Damage values test bed/dynamic loads.

4. Conclusions

A method has been developed for accurate tractor tire parametrization without a tire test-rig, which is based on measured accelerations during traversing cleat obstacles. It has been validated by a merry-go-round test track.

Moreover, a fully integrated, virtual methodology has been elaborated which supports the whole development process consistently from early design stage until prototype testing.

Although the simulation effort increases, it leads to a significant reduction in the total development costs and speeds-up the development process, as well as more accurate dimensioning of parts compared to conventional, estimated loads. It also provides valuable insight into the dynamic behavior of the tractor and allows cost-efficient optimization of parameters. Furthermore, the field conditions referring to the tractor lifetime can be precisely derived for the test bed.

Appendix. Overview of complexity levels of simulation processes

Standard simulation process (existing practice)

LBCs for FEA based on experience	Probably too severe → oversized design.
LBCs for FEA based on force measurements with similar vehicle → Lowest simulation complexity	Measurements refer to one parameter set. Parameter changes (e.g., additional mass) make LBCs unusable. In most cases test bed represents field conditions poorly.

Advanced simulation process

LBCs based on VMBS simulation, and tire parametrization is based on *approximate values* from tire database. → Elevated simulation complexity	VMBS-results deliver inferior accuracy of LBCs → mediocre accuracy of FEA-results. Inferior insight into dynamic behavior. Test bed represents field conditions with limitations.

Integrated simulation process (presented in this contribution)

LBCs based on VMBS simulation and tire parametrization with *fine-tuned values* based on measurements. → High simulation complexity	Accurate LBCs for FEA → precise FE-results. Good understanding of dynamic behavior. Test bed represents field conditions well.

References

1. Abaqus. Version: V2021FP2346. Retrieved July 13, 2025, from https://www.3ds.com/products/simulia/abaqus.
2. Adams. Version: v2021.0.1. Retrieved July 13, 2025, from https://hexagon.com/products/product-groups/computer-aided-engineering-software/adams.
3. Bayerische Transformations- und Forschungsstiftung (2021). *Traction on demand* (in German). https://www.forschungsstiftung.bayern.de/projekt/traction-on-demand/
4. FEMFAT. Version: 2022.1. Retrieved July 13, 2025, from https://femfat.magna.com.
5. FTire. Version: 2021-1. Retrieved July 13, 2025, from https://www.cosin.eu.
6. Fuchs, W., & Pauschenwein, G. (2019). From field path profile detection to component testing. *ATZheavy duty worldwide*, *12*(2), 50–55. https://doi.org/10.1007/s41321-019-0022-x
7. Gipser, M. (2007). FTire – the tire simulation model for all applications related to vehicle dynamics. *Vehicle System Dynamics*, *45*(sup 1), 139–151. https://doi.org/10.1080/00423110801899960
8. Jedinger-Pauschenwein, G., Fuchs, W., & Holl, H. (2024, September 24–27). *Virtual load case definition for off-road vehicles: Methodology based on multibody system simulation* [Conference presentation]. 40th Danubia-Adria Symposium on Advances in Experimental Mechanics, Gdańsk, Poland.
9. Popp, K., & Schiehlen, W. (2010). *Ground vehicle dynamics*. Springer.
10. Renius, K.T. (2020). *Fundamentals of tractor design*. Springer.
11. Schiller, S. (2018). *Tractor global loading, method optimization* [Master's thesis, University of Applied Sciences]. Upper Austria.
12. Shabana, A.A. (2013). *Dynamics of multibody systems* (4th ed.). Cambridge University Press.

Manuscript received December 31, 2024; accepted for publication May 14, 2025; published online July 15, 2025.

JOURNAL OF THEORETICAL
AND APPLIED MECHANICS
63, 3, pp. 679–690, Warsaw 2025
https://doi.org/10.15632/jtam-pl/205304

IMPROVED HYPERELASTIC MATERIAL CHARACTERIZATION USING MEASUREMENT DATA PRE-PROCESSING

Zoltan KOVACS[1], Andras ANINGER[1]*, Szabolcs BEREZVAI[2]

[1] *eCon Engineering Ltd, Budapest, Hungary*
[2] *Department of Applied Mechanics, Faculty of Mechanical Engineering,*
Budapest University of Technology and Economics, Budapest, Hungary
*corresponding author, *andras.aninger@econengineering.com*

Mechanical characterization of elastomers is a long-studied but still challenging area. Finite element solvers offer a great variety of hyperelastic models; however, no straightforward selection process is provided. This paper presents a methodology for high-fidelity hyperelastic parameter fitting tailored for elastomers. One of its main components is a pre-processing module, which helps select the most suitable model based on all information extractable from the measured stress-strain curves. In this contribution, the concept of the pre-processing module is presented, while its efficiency is demonstrated through benchmark fitting processes using the Treloar dataset and an experimental dataset of an nitril butadiene rubber (NBR) specimen.

Keywords: hyperelasticity; elastomers; parameter-optimization.

1. Introduction

The mechanical characterization of elastomers and rubber-like materials is a long-researched but still challenging area in the field of solid mechanics. These materials exhibit large strains and displacements during loading, while the stress-strain curve can be highly nonlinear (Bergström, 2015; Treloar, 2005). For the constitutive modelling of the elastic behavior of elastomers, the so-called hyperelastic constitutive models can be adopted. This modelling approach is a phenomenological approach, where a suitable strain energy function is to be fitted simultaneously to the experimental data from various load cases (Holzapfel, 2010; Doghri, 2000).

The history of hyperelastic constitutive models is strongly connected to rubbers since the first hyperelastic strain energy functions were formulated by Mooney (1940) and Rivlin and Saunders (1951) to describe the behaviour of filled rubbers as the generalization of the Hooke's law for finite strains. Since then, a great variety of hyperelastic potentials were developed. Some rely on only mathematical considerations (e.g., the polynomial model family), while others are based on the micromechanical or microstructural description of the strongly crosslinked elastomers. Recently, He *et al.* (2022) summarized a total number of 85 formulations of hyperelastic strain energy potential both for incompressible (pure deviatoric) and for volumetric compression cases. Furthermore, concerning the fitting of the parameters of these models, the generalized Mooney space (GMS) approach for some specific hyperelastic potentials was recently proposed which

---

Ministry of Science and Higher Education
Republic of Poland

The publication has been funded by the Polish Ministry of Science and Higher Education under the Excellent Science II programme "Support for scientific conferences".
The content of this article was presented during the 40th Danubia-Adria Symposium on Advances in Experimental Mechanics, Gdańsk, Poland, September 24–27, 2024.

transforms the material testing curve into a polynomial space, where the fit can be performed more efficiently (Anssari-Benam *et al.*, 2022).

In the commercial finite element solvers (Ansys, Abaqus, Ls-Dyna), a great variety of hyperelastic models are available. However, no straightforward selection process is provided for the users. Since hyperelastic modelling and parameter fitting is a complex task, dedicated software solutions (e.g., MCalibration (Bergström, 2015), Hyperfit) are available as well to fit a suitably chosen hyperelastic strain energy potential to the material testing data. However, none of these dedicated software applications provides the user with constitutive model decision support, which is an essential decision in the material modeling process to be made prior to the fitting. In addition, industrial practice shows that the available measurement data are often incomplete and contradictory, and the average user does not have the expertise to confidently filter the data containing information about the complex material behaviour.

The research project "2020-1.1.2-PIACI-KFI-2021-00314" aims to develop a high-fidelity material parameter fitting methodology tailored for rubber-like material characterized by hyperelastic constitutive models. One of the main components of the fitting procedure is an automatic pre-processing module, which helps users select the most suitable material model using all information extractable from the measured stress-strain curves for different load cases and further available mechanical test data using techniques based on the theory of hyperelasticity.

In this paper, the concept of the pre-processing module is presented. Section 2 summarizes the theoretical background of hyperelasticity and the investigated hyperelastic models. Section 3 presents the concept of the pre-processing module and the applied methods. Section 4 is dedicated to the case studies, including 1) the classical Treloar dataset and 2) a self-made dataset for NBRs, including uniaxial tension and compression, planar tension and simple shear tests. Finally, the main findings of the case studies are presented in Section 5.

2. Theoretical background

The theory of hyperelasticity is based on the finite strain material formulation of kinematics, where a polyconvex scalar function $W(\mathbf{F})$ can be introduced expressing the stored strain energy per unit reference volume as the function of deformation gradient $\mathbf{F}$ or the right Cauchy–Green deformation tensor $\mathbf{C}$, namely $W(\mathbf{C})$. From this, the first Piola–Kirchhoff stress tensor ($\mathbf{P}$) can be directly derived from the strain energy function using

$$\mathbf{P} = \frac{\partial W(\mathbf{F})}{\partial \mathbf{F}}, \qquad \text{or} \qquad \mathbf{P} = 2\mathbf{F}\frac{\partial W(\mathbf{C})}{\partial \mathbf{C}}. \tag{2.1}$$

2.1. Isotropic hyperelastic models

In the case of isotropic material, the strain energy function can be expressed by either the function of the principal invariants of $\mathbf{C}$ (I_1, I_2, and I_3) or the principal stretches (λ_1, λ_2, and λ_3), namely $W(I_1, I_2, I_3)$ or $W(\lambda_1, \lambda_2, \lambda_3)$ (Holzapfel, 2010). The scalar invariants of $\mathbf{C}$ are defined as

$$I_1 = \operatorname{tr}(\mathbf{C}), \qquad I_2 = \frac{1}{2}\left(I_1^2 - \operatorname{tr}(\mathbf{C}^2)\right), \qquad I_3 = \det \mathbf{C} {=} J^2, \tag{2.2}$$

which can also be expressed using the principal stretches (λ_1, λ_2, and λ_3) as

$$I_1 = \lambda_1^2 + \lambda_2^2 + \lambda_3^2, \qquad I_2 = (\lambda_1\lambda_2)^2 + (\lambda_1\lambda_3)^2 + (\lambda_2\lambda_3)^2, \qquad I_3 = (\lambda_1\lambda_2\lambda_3)^2. \tag{2.3}$$

In this case, the Cauchy (σ_k) and the first Piola–Kirchhoff (P_k) principal stresses can also be expressed in a compact form as

$$\sigma_k = \frac{\lambda_k}{J}\frac{\partial W}{\partial \lambda_k}, \qquad P_k = \frac{\partial W}{\partial \lambda_k}, \qquad k = 1, 2, 3. \tag{2.4}$$

2.2. Incompressible hyperelastic model

Elastomers are commonly modeled as incompressible materials because their bulk modulus is extremely high, while the volumetric deformation is negligible. Assuming a perfectly incompressible material, where the volume is constant during loading, for the entire deformation

$$\det \mathbf{F} = J \equiv 1 \qquad \text{and} \qquad I_3 \equiv 1 \tag{2.5}$$

holds. Consequently, the strain energy potential simplifies to $W(I_1, I_2, I_3) = W(I_1, I_2)$. In this case, the stress tensor can be derived using the deviatoric and volumetric split as

$$\boldsymbol{\sigma} = \mathbf{s} + \mathbf{p}, \tag{2.6}$$

where $\mathbf{s} = \operatorname{dev}\boldsymbol{\sigma}$ is the deviatoric part and $\mathbf{p} = p\mathbf{I}$ is the volumetric stress term. In this case, the deviatoric stress can be derived from the $W(I_1, I_2)$ strain energy functions using the derivations in Eq. (2.4), while the unknown pressure p should be expressed from the boundary conditions (e.g., stress-free transverse stresses). Therefore, the principal stresses for the incompressible case simplify to

$$\sigma_k = \lambda_k \frac{\partial W}{\partial \lambda_k} + p, \qquad P_k = \frac{\partial W}{\partial \lambda_k} + \frac{p}{\lambda_k}, \qquad k = 1, 2, 3. \tag{2.7}$$

2.3. Strain energy functions

In the literature, a great variety of incompressible hyperelastic potentials are available (He *et al.*, 2022). However, in commercial finite element solvers, the number of models is limited. Some models are defined only using the first invariant I_1, and the strain energy potential can be expressed as $W(I_1)$. These models are the Neo–Hookean (NH) (Mooney, 1940), the Yeoh (Y) (Yeoh, 1990), the Arruda–Boyce (AB) (Arruda & Boyce, 1993), and the Gent models (G) (Gent, 1996; Gent & Thomas, 1958). The corresponding strain energy functions are defined as

$$W^{\mathrm{NH}} = C_{10}\left(I_1 - 3\right), \tag{2.8}$$

$$W^{\mathrm{Y}} = C_{10}\left(I_1 - 3\right) + C_{20}\left(I_1 - 3\right)^2 + C_{30}\left(I_1 - 3\right)^3, \tag{2.9}$$

$$W^{\mathrm{AB}} = \mu\left[\frac{I_1 - 3}{2} + \frac{I_1^2 - 9}{20\lambda_m^2} + \frac{11\left(I_1^3 - 27\right)}{1050\lambda_m^4} + \frac{19\left(I_1^4 - 81\right)}{7000\lambda_m^6} + \frac{519\left(I_1^5 - 243\right)}{673750\lambda_m^8}\right], \tag{2.10}$$

$$W^{\mathrm{G}} = C_0 \ln\left(1 - \frac{I_1 - 3}{I_m - 3}\right), \tag{2.11}$$

Some other models are also dependent on the second invariant I_2. Therefore, the hyperelastic potential in this form can be expressed as $W(I_1, I_2)$. These models are the Mooney–Rivlin (MR) (Rivlin & Saunders, 1951), the polynomial (P), and the Ogden (O) (Ogden, 1972):

$$W^{\mathrm{MR}} = C_{10}\left(I_1 - 3\right) + C_{01}\left(I_2 - 3\right), \tag{2.12}$$

$$W^{\mathrm{P}} = \sum_{i+j=1}^{N} C_{ij}\left(I_1 - 3\right)^i \left(I_2 - 3\right)^j, \tag{2.13}$$

$$W^{\mathrm{O}} = \sum_{i=1}^{N} \frac{2\mu_i}{\alpha_i^2}\left(\lambda_1^{\alpha_i} + \lambda_2^{\alpha_i} + \lambda_2^{\alpha_i} - 3\right). \tag{2.14}$$

It should be noted that some models are based on pure mathematical considerations (e.g., polynomial, Ogden, Yeoh), while others rely on statistical or micromechanical models (e.g., Gent, Arruda–Boyce). On the other hand, these models are not independent since by selecting the material constants properly, the models reduce to each other. The hyperelastic models and their relations are summarized in Fig. 1.

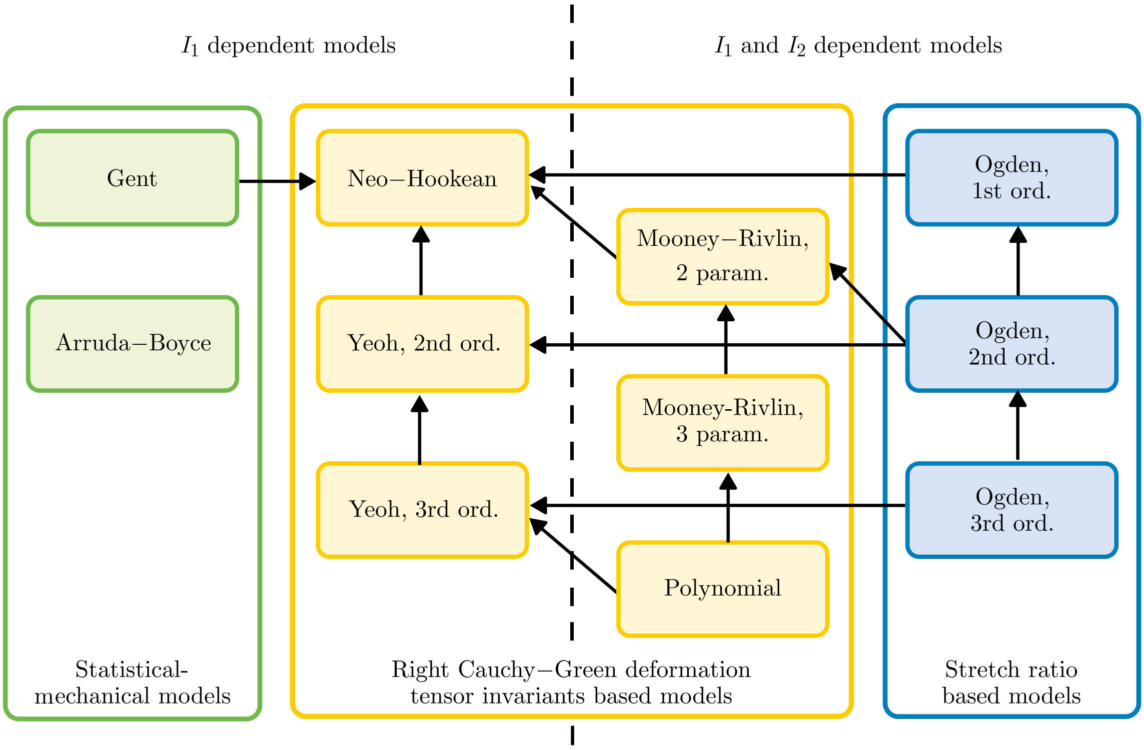

Fig. 1. Summary of the hyperelastic models available in the commercial finite element solvers.

2.4. Load cases

The hyperelastic potentials contain many material parameters that need to be fitted based on experimental data. For incompressible materials, four different load cases are distinguished: uniaxial (UA), biaxial (BA), planar (PL) and simple shear (SS). For these loading cases, the deformation gradient tensor **F**, the volume ratio J and the first Piola–Kirchhoff stress tensor **P** or the Cauchy stress tensor $\boldsymbol{\sigma}$ can be obtained as:

- uniaxial tension/compression (UN):

$$\mathbf{F}^{\mathrm{UN}} = \begin{bmatrix} \lambda & 0 & 0 \\ 0 & \lambda_T & 0 \\ 0 & 0 & \lambda_T \end{bmatrix}, \qquad J^{\mathrm{UN}} = \lambda\lambda_T^2, \qquad \mathbf{P}^{\mathrm{UN}} = \begin{bmatrix} P & 0 & 0 \\ 0 & 0 & 0 \\ 0 & 0 & 0 \end{bmatrix}, \tag{2.15}$$

- biaxial tension/compression (BA):

$$\mathbf{F}^{\mathrm{BA}} = \begin{bmatrix} \lambda & 0 & 0 \\ 0 & \lambda & 0 \\ 0 & 0 & \lambda_T \end{bmatrix}, \qquad J^{\mathrm{BA}} = \lambda^2\lambda_T, \qquad \mathbf{P}^{\mathrm{BA}} = \begin{bmatrix} P & 0 & 0 \\ 0 & P & 0 \\ 0 & 0 & 0 \end{bmatrix}, \tag{2.16}$$

- planar tension/compression (PL):

$$\mathbf{F}^{\mathrm{PL}} = \begin{bmatrix} \lambda & 0 & 0 \\ 0 & 1 & 0 \\ 0 & 0 & \lambda_T \end{bmatrix}, \qquad J^{\mathrm{PL}} = \lambda\lambda_T, \qquad \mathbf{P}^{\mathrm{PL}} = \begin{bmatrix} P_1 & 0 & 0 \\ 0 & P_2 & 0 \\ 0 & 0 & 0 \end{bmatrix}, \tag{2.17}$$

– simple shear (SS):

$$\mathbf{F}^{\mathrm{SS}}=\begin{bmatrix}1&\gamma&0\\0&1&0\\0&0&1\end{bmatrix},\qquad J^{\mathrm{SS}}=1,\qquad \boldsymbol{\sigma}^{\mathrm{SS}}=\begin{bmatrix}\sigma_{11}&\sigma_{12}&0\\\sigma_{12}&\sigma_{22}&0\\0&0&0\end{bmatrix}. \tag{2.18}$$

3. Concept of data pre-processing

For modelling rubber-like elastomers, a large number of material models and parameter fitting procedures are available in the literature. However, all these methods assume that the user has a precise knowledge of the constitutive model they wish to fit to the existing measurement data. Industrial practice, however, shows that the available measurement data are often incomplete and contradictory, and the user does not have an advanced knowledge of the exact material behaviour.

The main goal of the pre-processing module (Fig. 2) is not only to select the suitable material models for fitting but also to provide information about the model parameters (min/max values and initial values) to speed up and improve the accuracy of the model fitting.

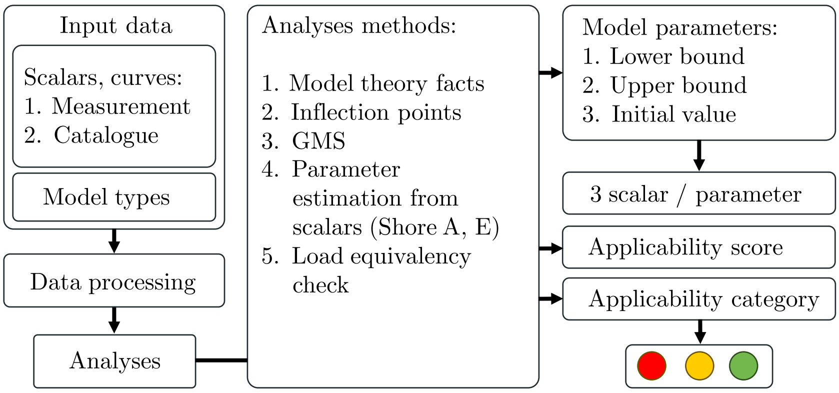

Fig. 2. Flowchart of the proposed data pre-processing module.

3.1. Analyses methods

The pre-processing module is based on the following five methods: 1) theoretical model properties; 2) inflection check; 3) GMS transformation; 4) parameter estimation from scalars, and 5) load equivalency check.

3.1.1. Theoretical model properties

In this module, the theoretical suitability of each material model is examined. Based on the previous list (see Subsection 2.3), it can be seen that the strain energy potential of some hyperelastic models is only a function of the invariant I_1, while other models also depend on the invariant I_2. As a general rule, it is assumed that

- for I_1-dependent material models, it is sufficient to fit for a single load case; the measured data from the other load cases will not provide additional information;
- for I_1- and I_2-dependent material models, it is necessary to fit at least two load cases. In this case, one of the measurements that is particularly recommended is the biaxial load curve since this will be the most dominant of the basic load cases for the I_2.

Furthermore, this module also includes the estimation of the parameter's initial values based on theoretical considerations, e.g., the requirement of positive initial moduli, consistency with Hooke's law and any further constraints related to the model definition. Based on this analysis, both initial values and boundaries are defined for the model parameters.

3.1.2. Inflection

In this module, the convexity and the number of inflection points of the theoretical models and the measurement datasets are analyzed and compared. Spline interpolation is applied to each measurement curve in the datasets to reduce the effect of noisy measurement data from which the convexity, inflection points, and their location can be determined analytically. After the analysis of the measurement curve, the hyperelastic models are then evaluated to decide whether or not they are capable of describing a measurement curve with such inflection properties. Based on the analysis of the theoretical model curves, it can be concluded that

- Neo–Hooke, Mooney–Rivlin models can be excluded if inflections are present in any curve;
- Arruda–Boyce, 1-order Ogden models can be excluded if inflections are found in the compression range, in simple shear, or if more than one inflection is seen in the tensile regime.

3.1.3. Generalized Mooney space transformation

The GMS transformation is a method developed recently by Anssari-Benam *et al.* (2022) as an extension of the Mooney–Rivlin plot. For the simpler hyperelastic models (Neo–Hookean, Mooney–Rivlin, Yeoh, Gent), the stress-strain curve $(P(\lambda) \to \mathcal{G}(\eta))$ can be transformed to a GMS of the material model, where the stress-strain curve for the simpler material models can be rewritten in a polynomial form. For the pre-processing module, this method is used in several ways.

Firstly, it allows for checking the suitability of the model to characterize the measurements. This can be easily checked using the polynomial space transformation, where the applicability of simpler models can be examined. If the GMS transform of the measurement curve matches the nature of the theoretical curve, the model can be adequate, i.e., it should be recommended for fitting. If the GMS transform of the measurement curve contradicts the nature of the theoretical curve, the given model will be excluded from the list of suitable strain energy functions.

Moreover, parameter fitting in a polynomial space is also much more reliable and robust. As a result, after transforming each material model into a GMS, a fast polynomial fitting can be used to estimate the initial value of the material parameters. The drawback of this method is that GMS transformation is not available for complex material models.

3.1.4. Parameter estimation from scalars

In addition to the measurement curves performed from material testing, the mechanical behaviour of the investigated elastomer can also be characterized by scalar parameters, which are often available as catalogue data, e.g., on the material data sheet. Such scalar values may be the modulus at 100 % elongation E_{100}, the modulus at 200 % elongation E_{200} or the modulus at 300% elongation E_{300}, which are commonly used in polymer technology. These quantities can be easily converted to material parameter relationships by evaluating the stress solutions at the given stretch level, respectively, to the given elongation level. In the proposed pre-processing module, we can use these scalar modulus values to estimate the initial values of the material parameters. Another important metric in the field of elastomers is the Shore A hardness, an easy-to-perform measurement that is often available in catalogue data. Using Qi's model (Qi *et al.*, 2003), which relates the Shore A hardness H_A and the elastic modulus as

$$\lg E = 0.0253 \cdot H_A - 0.6403 \qquad \text{for} \qquad 20 < H_A < 80, \tag{3.1}$$

we can estimate the initial elastic modulus of the material, from which we can also estimate the initial value of the model parameters using the above relationships.

3.1.5. Load equivalency check

It can be shown that due to the incompressibility, some load cases can be considered equivalent from a theoretical viewpoint since by adding or removing any hydrostatic pressure (see Eq. (2.6)), the deformation of the specimen does not change. Therefore, the load case pairs of uniaxial tension – biaxial compression and uniaxial compression – biaxial tension can be considered as equivalent load cases. Furthermore, this also means that if both tension and compression data are available for uniaxial or biaxial load cases, one already has two non-equivalent measurements. In this module, the load equivalency is analyzed. This module is used to analyze equivalent load cases, i.e., to check the consistency of the data from the cases considered equivalent. In the case of a discrepancy above a threshold value, the user is warned.

3.2. Evaluation of the pre-processing

By utilizing the methods mentioned above, the pre-processing module will provide: a) lower and upper bounds for the model parameters, b) initial values for some of the parameters, and c) an evaluation of model suitability using the traffic light marking system. Based on the pre-processing results, this classifies the available material models into the following categories:

- red – there is a discrepancy between the material model and the uploaded measurement data. This material model is not recommended for fitting;
- yellow – there is no inconsistency between the material model and the uploaded measurement data, but the uploaded data is incomplete for adequate fitting;
- green – no inconsistency between the given material model and the measurement data.

As a last step in the pre-processing module, a quick fitting is performed for each curve separately in order to quantify the accuracy of the model. Based on the preliminary single-curve fitting results and all the further pre-processing results, an applicability score is generated for each material model in the range of [0, 10], where 10 indicates the perfect match.

4. Case-studies

In order to highlight the benefits of the proposed pre-processing algorithm, two case studies were performed, including 1) the well-known Treloar dataset (Treloar, 1944) for unfilled rubber and 2) a self-made measurement dataset for a NBR specimen.

4.1. Measurement data I – Treloar-data

The first set of measurement data was the well-known Treloar dataset (Treloar, 1944) for unfilled rubber, which includes mechanical tests for three different load cases, namely uniaxial (UA), biaxial (BA) and planar (PL) tension. The $P - \lambda$ engineering stress (forces-per-initial cross-sectional area) – stretch dataset is depicted in Fig. 3.

4.2. Case study II – NBR

The second dataset (eCon measurement) contains measurements conducted at the test laboratory of eCon Engineering Ltd. The test specimens were made out of NBR. The four different load cases in the measurement set were: a) uniaxial tension (UT), b) uniaxial compression (UC), c) planar tension (PT), and d) simple shear (SS). The uniaxial tensile measurement was carried out according to the ASTM 412 standard (see Fig. 4) using an INSTRON 8801 servo-hydraulic Material Testing System equipped with a Dynacell 2527-111 100 kN load cell. The uniaxial compression test was performed according to ASTM D395. The specimen measured was made up of 3 rubber disks piled on each other, as shown in Fig. 4. For the planar tension test, there were no standards to follow, but a fairly common approach is to use a "wide enough", thin, rectangular specimen with both of its ends fastened in a test frame as displayed in Fig. 4. A uniaxial test

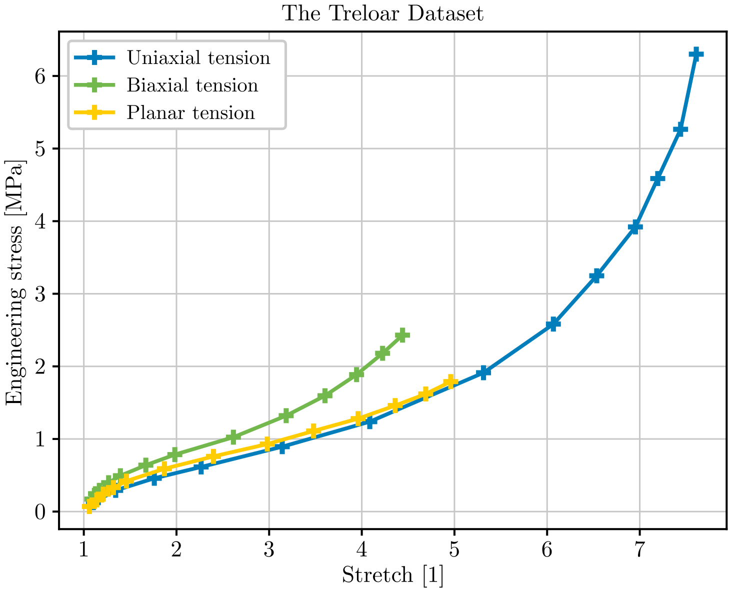

Fig. 3. $P-\lambda$ engineering stress (force-per-initial cross-sectional area) – stretch curves of uniaxial, biaxial and planar tension data from the Treloar dataset (Treloar, 1944).

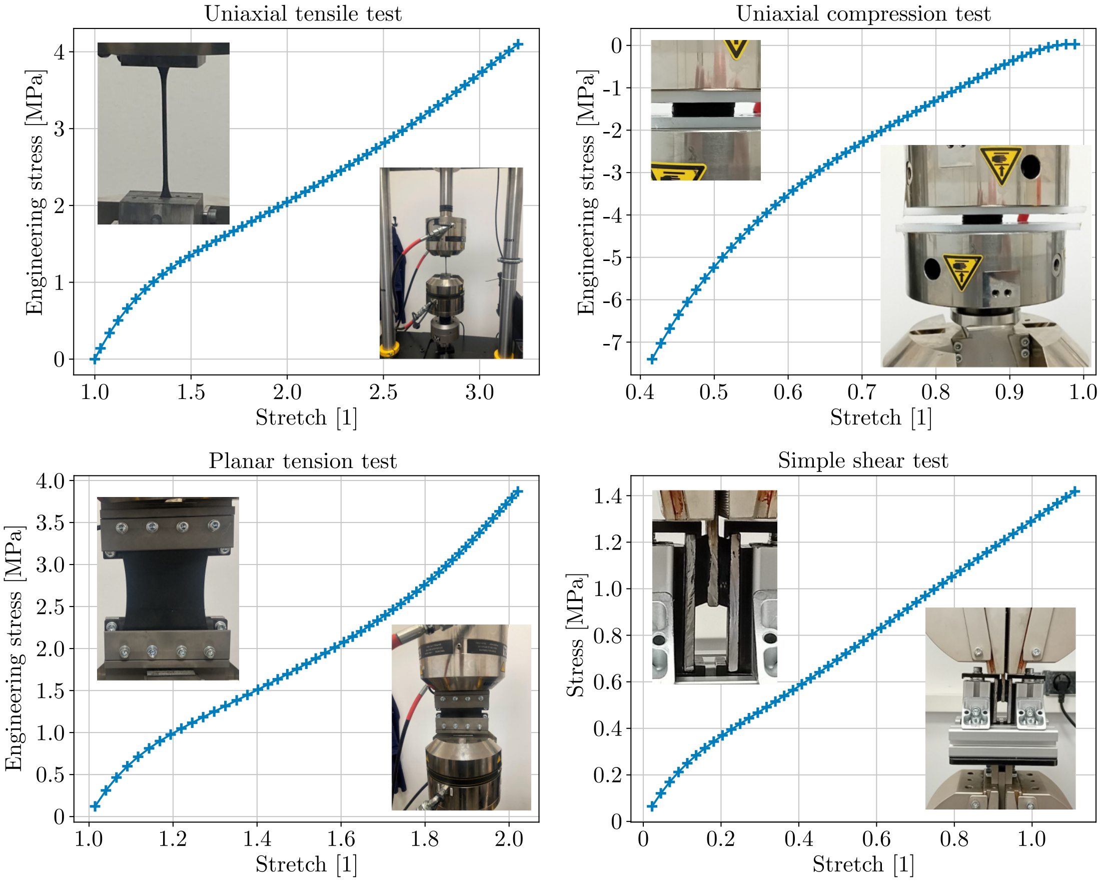

Fig. 4. Uniaxial tension, uniaxial compression, planar tension and simple shear measurement curves for the investigated NBR specimen.

machine can then pull the frame at both ends. Finally, a simple shear test according to ASTM D945 was also performed using a H&P universal testing machine with H&P 50 kN load cell, as shown in Fig. 4. The planar and simple shear measurements were performed using custom designed and manufactured grippers.

4.3. Parameter fitting scenarios

Both the pre-processing algorithms and the fitting tool were implemented in Python, the latter software component relying heavily on the “lmfit” Python package (Newville *et al.*, 2024). The possible benefits of using our pre-processor were examined by comparing the obtained fitted results, initializing all parameters with a) the constant value of 1 (Inits:1) or b) random numbers (Inits: rnd).

For the demonstration of the capabilities of the proposed algorithms, five different models from three different model families (see Fig. 1) were used with both datasets. These were the stretch ratio-based 2nd and 3rd-order Ogden models (O2 and O3), the Neo–Hookean (NH) and 3rd-order polynomial (PL3) and the Arruda–Boyce (AB) model from the statistical-mechanical model family. All five models were fitted on both datasets with constant 1 (Inits:1) and randomly generated numbers (Inits: rnd) as starting model parameter initial values and with and without using the pre-processing algorithms.

4.4. Fitting results

The remaining residuals after the fitting are displayed for all models at the top of Fig. 5 for the Treloar dataset and Fig. 6 for the eCon measurements. The colour of the circles above the residual bar charts indicates whether the pre-processor found the model applicable or not. The scores next to the circles show how good the fitting quality will be, based on the algorithm’s estimation before the actual fit happens.

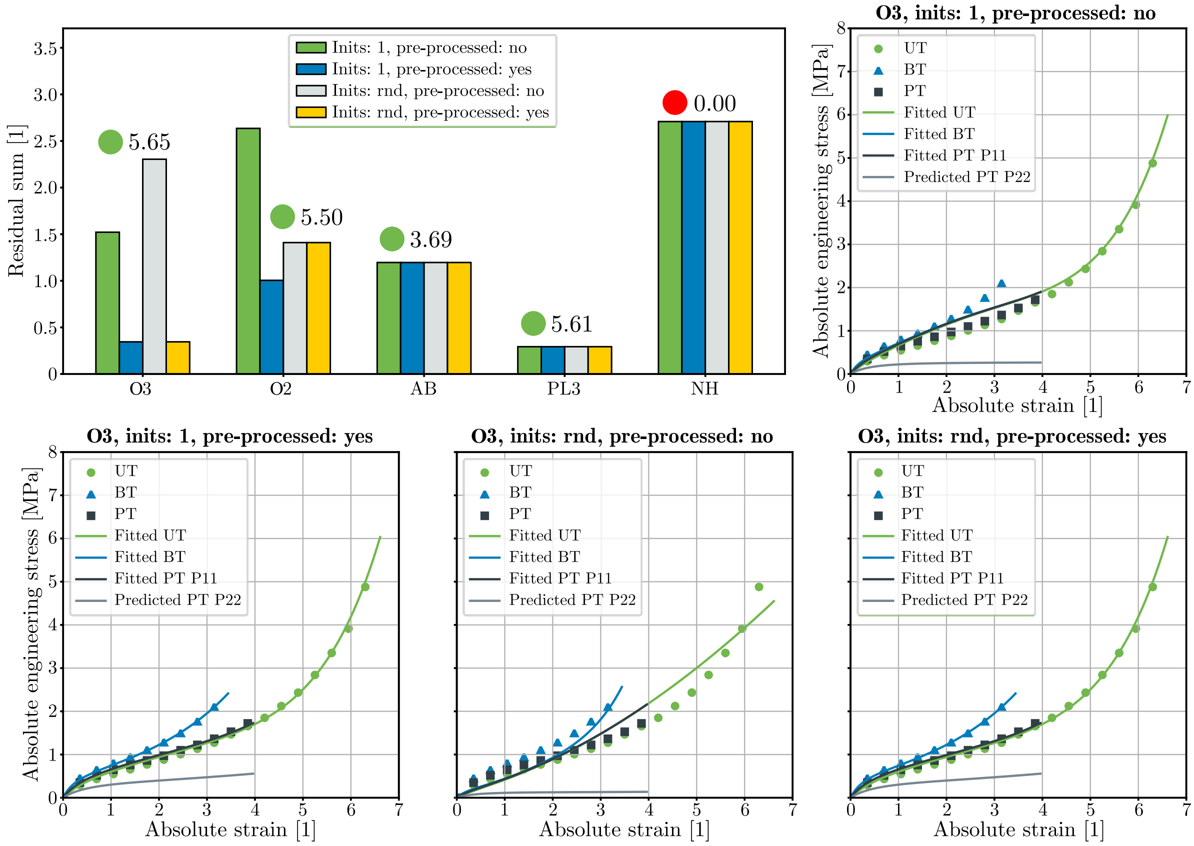

Fig. 5. Fitting results for the Treloar dataset using four fitting scenarios including the 2nd and 3rd-order Ogden models (O2 and O3), the Neo–Hookean (NH) and 3rd-order polynomial (PL3) and the Arruda–Boyce (AB) models.

As the summaries of the residual plots show, the applicability scores from the pre-processor show great agreement with the residual sums after the complete fitting procedure with one ex-

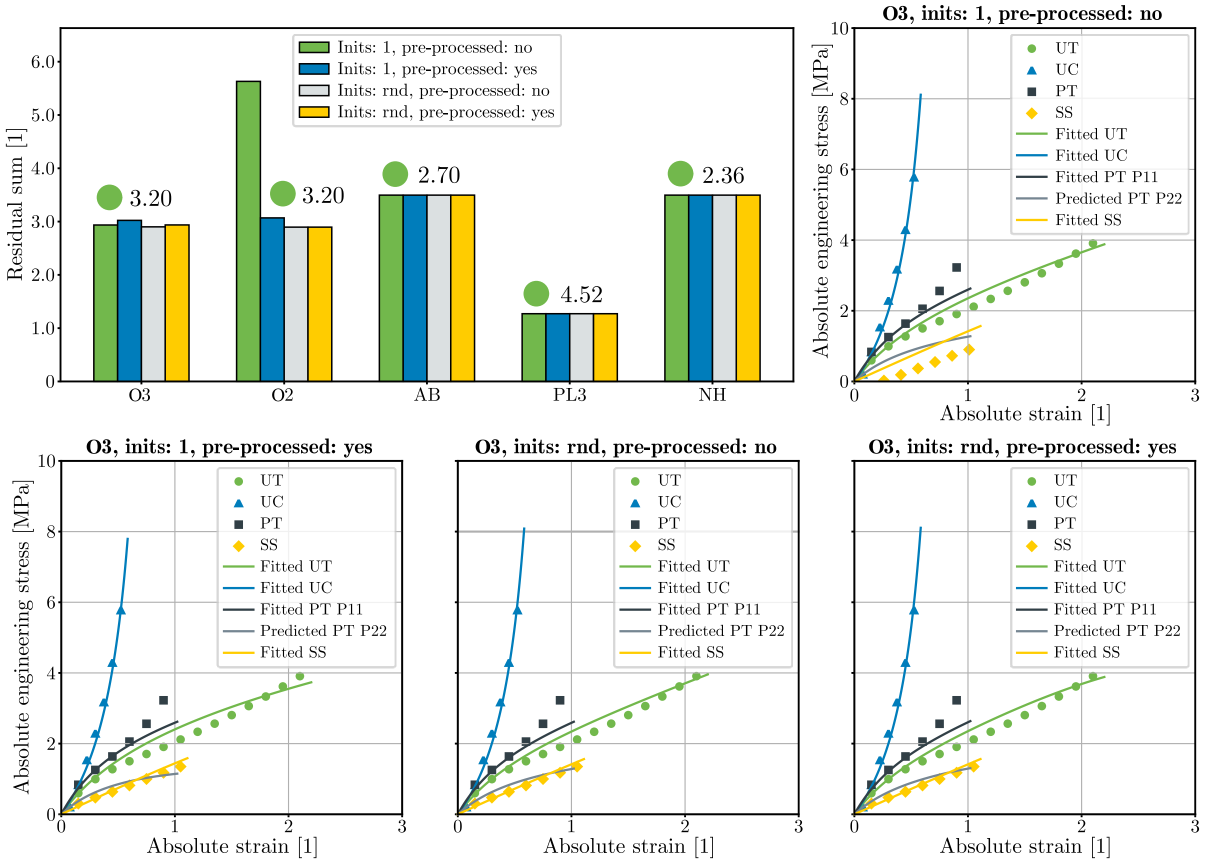

Fig. 6. Fitting results for the eCon dataset using four fitting scenarios including the 2nd and 3rd-order Ogden models (O2 and O3), the Neo–Hookean (NH) and 3rd-order polynomial (PL3) and the Arruda–Boyce (AB) models.

ception: in the case of the Treloar dataset, the 2nd order Ogden model ended up with a higher remaining residual value than the Arruda–Boyce model when the model parameters were randomly initialized. The Neo–Hookean model was also correctly identified as non-applicable (red circle) in the case of the Treloar dataset since it could not describe the inflections present in the measured curves.

Considering the effect of the initial values provided by the pre-processing algorithms, it was found that for models where the model redundancy was high (parameters can take each other's role), e.g., in the case of the 3rd order Ogden model, the suggested initial values for the parameters were able to improve the fitting accuracy. For this model, the obtained curves and the measurement data were plotted against each other on the bottom part of Fig. 5 and Fig. 6. for all four fitting scenarios. As one can see, the improvements in the fit quality in the Treloar dataset case were high. For the other models, the differences between the pre-processed and simple fits were not significant in any of the scenarios.

5. Conclusion

This paper presents a pre-processing procedure for incompressible hyperelastic fitting of rubber-like materials. The proposed method, based on the analysis of the measurement curves and the theoretical background of each hyperelastic model, not only provides an estimate of the initial values and bounds of the model parameters but also evaluates the adequacy of each material model. This provides the user with a tool to assist in choosing a material model. The performance of the method is illustrated via two case studies using the Treloar dataset and an NBR dataset.

As detailed in the previous section, the proposed pre-processing algorithms provided a very decent, although not completely errorless, assessment of the different models' applicability and expected fit quality upfront. Furthermore, the offered initial values significantly improved the final quality of the fit in some cases. However, they did not lead to significantly faster fitting times. For hyperelastic models with a high number of parameters, the minimization of the objective function can result in multiple solutions with similar goodness (local minima) due to the redundancy of the terms in such constitutive models. With a good choice of initial values, i.e., with physically consistent initial values, such redundancy of fitting results, and thus the uncertainty of the fitting can be reduced. Such initial values can usually be defined for the parameters related to the lower terms in the strain energy function. Therefore, in the case of models with a higher number of parameters (e.g., 3rd-order polynomial (PL3), 3rd-order Ogden models (O3)) specifying constraints and initial values to improve the uniqueness of the fit is still a challenge to be solved in future research.

It was also found that the pre-processing step greatly improved the fitting accuracy for models where the model redundancy was high (parameters can take each other's role), e.g., in the case of the 3rd-order Ogden model. For less complex models, the differences were not significant. The initial values provided by the pre-processor are close to the values obtained after the fitting process. However, this did not bring significant improvements in the fitting runtimes for the examined models. The randomly initialized cases were executed without noticeable differences. However, having good initial guesses can significantly improve runtimes in more complex models (e.g., compressible or viscoelastic models).

Acknowledgments

This research activity has been completed with the grant from the National Research, Development and Innovation Office. The project title is as follows: Precision Characterization of Nonlinear Mechanical Behaviour of Reinforced and Unreinforced Polymeric Materials for Numerical Simulations (project number: 2020-1.1.2-Piaci-KFI-2021-00314). Szabolcs Berezvai has been supported by the Hungarian National Research, Development and Innovation Office (NKFIH NKKP STARTING 149473) and the Janos Bolyai Research Scholarship of the Hungarian Academy of Sciences.

References

1. Anssari-Benam, A., Bucchi, A., Destrade, M., & Saccomandi, G. (2022). The generalised Mooney space for modelling the response of rubber-like materials. *Journal of Elasticity*, *151*(1), 127–141. https://doi.org/10.1007/s10659-022-09889-1
2. Arruda, E.M., & Boyce, M.C. (1993). A three-dimensional constitutive model for the large stretch behavior of rubber elastic materials. *Journal of the Mechanics and Physics of Solids*, *41*(2), 389–412, https://doi.org/10.1016/0022-5096(93)90013-6
3. Bergström, J. (2015). *Mechanics of solid polymers. Theory and computational modeling.* William Andrew.
4. Doghri, I. (2000). *Mechanics of deformable solids. Linear and nonlinear, analytical and computational aspects.* Springer Berlin Heidelberg. https://doi.org/10.1007/978-3-662-04168-0
5. Gent, A.N. (1996). A new constitutive relation for rubber. *Rubber Chemistry and Technology*, *69*(1), 59–61. https://doi.org/10.5254/1.3538357
6. Gent, A.N., & Thomas, A.G. (1958). Forms for the stored (strain) energy function for vulcanized rubber. *Journal of Polymer Science*, *28*(118), 625–628. https://doi.org/10.1002/pol.1958.1202811814
7. He, H., Zhang, Q., Zhang, Y., Chen, J., Zhang, L., & Li, F. (2022). A comparative study of 85 hyperelastic constitutive models for both unfilled rubber and highly filled rubber nanocomposite material. *Nano Materials Science*, *4*(2), 64–82. https://doi.org/10.1016/j.nanoms.2021.07.003

8. Holzapfel, G.A. (2010). *Nonlinear solid mechanics: a continuum approach for engineering*. Wiley.
9. Mooney, M. (1940). A theory of large elastic deformation. *Journal of Applied Physics*, *11*(9), 582–592. https://doi.org/10.1063/1.1712836
10. Newville, M., Otten, R., Nelson, A., Stensitzki, T., Ingargiola, A., Allan, D., Fox, A., Carter, F., Michał, Osborn, R., Pustakhod, D., Weigand, S., lneuhaus, Aristov, A., Glenn, Mark, mgunyho, Deil, C., Hansen, A.L.R., ... Persaud, A. (2024). lmfit/lmfit-py: 1.3.2 (1.3.2). Zenodo. https://doi.org/10.5281/zenodo.12785036
11. Ogden, R.W. (1972). Large deformation isotropic elasticity – on the correlation of theory and experiment for incompressible rubberlike solids. *Proceedings of the Royal Society A. Mathematical, Physical and Engineering Sciences*, *326*(1567), 565–584. https://doi.org/10.1098/rspa.1972.0026
12. Qi, H.J., Joyce, K., & Boyce, M.C. (2003). Durometer hardness and the stress-strain behavior of elastomeric materials. *Rubber Chemistry and Technology*, *76*(2), 419–435. https://doi.org/10.5254/1.3547752
13. Rivlin, R.S., & Saunders, D.W. (1951). Large elastic deformations of isotropic materials VII. Experiments on the deformation of rubber. *Philosophical Transactions of the Royal Society A. Mathematical, Physical and Engineering Sciences*, *243*(865), 251–288. https://doi.org/10.1098/rsta.1951.0004
14. Treloar, L.R.G. (1944). Stress-strain data for vulcanised rubber under various types of deformation. *Transactions of the Faraday Society*, *40*, 59–70. https://doi.org/10.1039/tf9444000059
15. Treloar, L.R.G. (2005). *The physics of rubber elasticity* (3rd ed.). Oxford Classic Texts in the Physical Sciences. Oxford University Press.
16. Yeoh, O.H. (1990). Characterization of elastic properties of carbon-black-filled rubber vulcanizates. *Rubber Chemistry and Technology*, *63*(5), 792–805. https://doi.org/10.5254/1.3538289

Manuscript received December 14, 2024; accepted for publication May 19, 2025;

JOURNAL OF THEORETICAL
AND APPLIED MECHANICS
63, 3, pp. 691–700, Warsaw 2025
https://doi.org/10.15632/jtam-pl/205727

IMPACTS OF IMPLEMENTING STOCHASTIC EXCITATION TO ASSESS ANOMALIES ON RAILWAY VEHICLE DYNAMIC MODEL

Péter FERENCZ[1]*, Gergő FODOR[2]

[1] *Department of Railway Vehicles and Vehicle System Analysis,*
Faculty of Transportation Engineering and Vehicle Engineering,
Budapest University of Technology and Economics, Budapest, Hungary
[2] *Department of Applied Mechanics, Faculty of Mechanical Engineering,*
Budapest University of Technology and Economics, Budapest, Hungary
*corresponding author, *ferencz.peter@kjk.bme.hu*

This paper investigates the effects of incorporating stochastic features into the simulation of a dynamic suspension system. The study is motivated by a real-world anomaly phenomenon observed in railway vehicles, where changes in the stiffness of rubber springs during operation can lead to irregular motion. A series of tests were conducted to characterize these stiffness variations and their dynamic behavior under stochastic excitation. Using a simplified, symmetrically structured model, the study demonstrates that such changes can initiate system anomalies, accelerating the deterioration of the system's technical state and potentially leading to a significant reduction in component lifetime.

Keywords: stochastic process; system anomaly; technical state deterioration; Euler–Maruyama technique.

1. Introduction

Railway vehicle dynamics are profoundly influenced by the mechanical properties and performance of suspension components. In this study, we investigate a specific anomaly in the secondary suspension system of an electric locomotive type. In practice, intensive asymmetric wheel profile wear appeared during the long-time operation of these types of vehicles (Ferencz, 2010), meaning that the wheels on one side were subjected to larger degradation than on the other side of one wheelset. The problem originated from deviations in the stiffness properties of the suspension's rubber-to-metal spring (secondary spring) components, which were identified as the primary cause of the anomaly (Ferencz, 2010).

First, we explain the secondary spring measurements and their outcomes, then the six-degree-of-freedom mechanical model of the railway vehicle is introduced. We add independent track excitations on the left and the right side of the vehicle to include track irregularities, and thus the mathematical model of the system is a stochastic differential equation (SDE), as similarly used by Bruni *et al.* (2011) and Knothe and Stichel (2017).

Numerical techniques are used to simulate the motion of the vehicle, and from the simulation results we calculate the deformation distribution of the secondary springs during the steady-state

---

Ministry of Science and Higher Education
Republic of Poland

The publication has been funded by the Polish Ministry of Science and Higher Education under the Excellent Science II programme "Support for scientific conferences".
The content of this article was presented during the 40th Danubia-Adria Symposium on Advances in Experimental Mechanics, Gdańsk, Poland, September 24–27, 2024.

operation. Based on this distribution we can calculate the probability of critical operation (PCO) if we define a certain critical limit of operation (CLO). This critical limit in our case is a large secondary spring deformation we consider to be harmful and that might cause degradation and failure in the stiffness characteristics.

If the secondary spring stiffness changes due to critical operation, the model is not symmetric anymore. We show that in terms of PCO values the emerging asymmetric secondary spring structure is much more dangerous than a symmetric structure.

2. The subject

2.1. Suspension component tests

Anomalies in the suspension system parameters of railway vehicle structures (such as unexpected deviations between the secondary springs) can lead to unexpected reductions in component lifespan and accelerated deterioration of the system's technical condition.

In 2006, a detailed analysis was conducted on a set of layered rubber-to-metal spring units to evaluate their vertical stiffness characteristics after a significant number of system anomalies, e.g., asymmetric wheel wear was observed in practice. To further investigate the long-term behavior of these springs, new measurements were carried out in 2024 (as illustrated in Fig. 1). The analysis included units still in operation and others dismantled after approximately 5–6 years of use.

Fig. 1. Test bench set to measure spring characteristics.

The results revealed significant deviations in the stiffness parameters of the tested secondary spring components.

The measured stiffness characteristics were evaluated using the classical least squares regression method, providing statistical representations of the data. On the basis of the optimization parameters an average function can be calculated as drawn with red line. These characteristics could be compared to the nominal design characteristics (as illustrated in Fig. 2) drawn black, with the approach assumption that the spring units were accepted with prescribed tolerances at operation start time according to the assembly by manufacturer technical requirements.

The tested spring units that had been in operation for 5–6 years show substantial deviations in stiffness, particularly at the nominal design load point at displacement of 4 mm.

In the figure two units showed unexpectedly softness, considered as outliers due to a possible material defect. Leaving out these from the further calculations a corrected average function was obtained. The range of the considered calculated spring stiffness values is as follows:

$$r = \max\{s_i\} - \max\{s_i\} = 16.137\,\frac{\mathrm{kN}}{\mathrm{mm}} - 10.175\,\frac{\mathrm{kN}}{\mathrm{mm}} = 5.9622\,\frac{\mathrm{kN}}{\mathrm{mm}}. \tag{2.1}$$

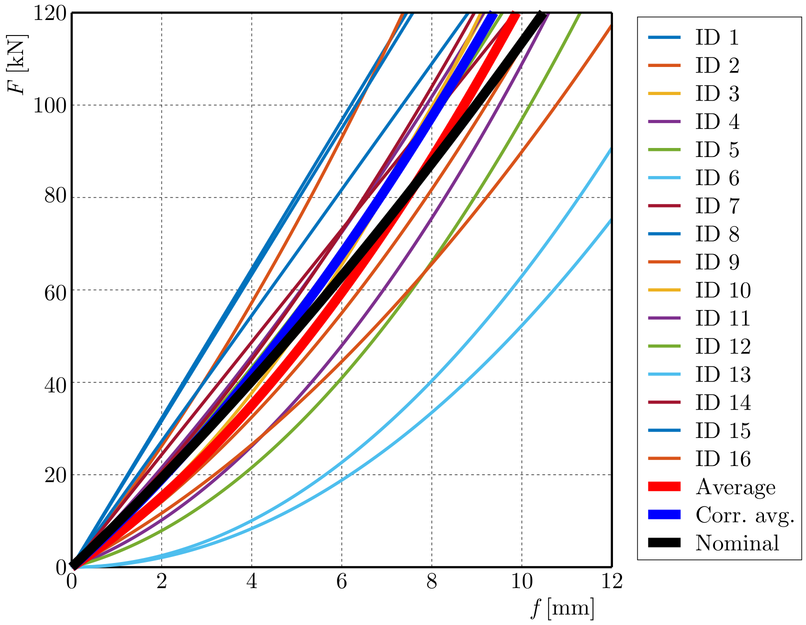

Fig. 2. Calculated vertical spring stiffness characteristics based on the measurements.

Statistical data from these measurements were incorporated into the mechanical model presented in Section 3, along with the specific mass and moment of inertia values of the locomotive under study.

2.2. System anomaly

An anomaly is when a certain system parameter exceeds its permitted in-operation maximum or minimum limit. From the measurements we conclude that during operation the secondary spring characteristics change due to such anomalies in the system. In the next section, we introduce a mechanical model of railway vehicles with random track ("road" contact surface) excitation that aims to explain an anomaly regarding the deformation of the secondary springs.

The actual phenomena can be described by the stochastic deterioration process $D(t, w)$ curve shown in Fig. 3. The curve shows with increasing operation time an increasing standard deviation banding around the expectation function indicated by $ED(t, w)$. It describes the natural physical process of normal material and structural damage, as the stochastic process of deterioration, as shown in Fig. 3 (Ferencz, 2023) over the time axis.

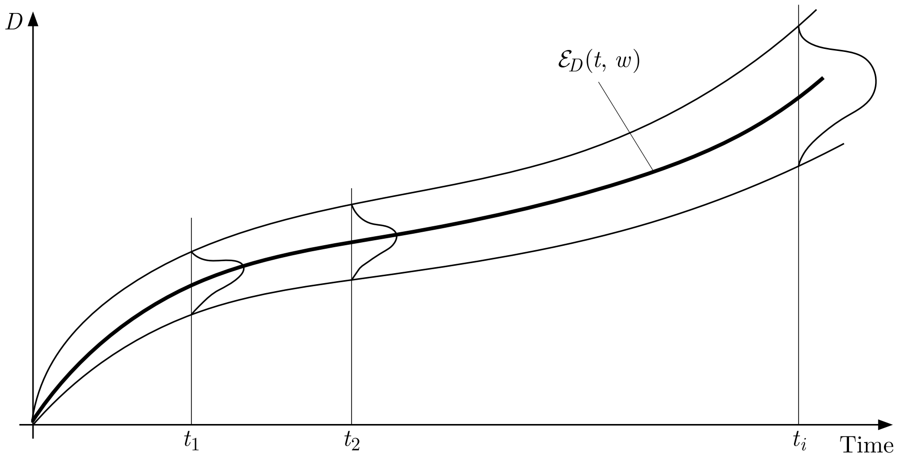

Fig. 3. Band characteristics of the deterioration process vs. time.

The natural degradation of spring stiffness change can be considered accordingly. Possible individual realization curves running within the bandwidth consist of two main sections divided by an inflexion point. The estimated speed of technical condition deterioration is exactly defined by the time-derivative process of $D(t, w)$, that depends on time t and on the elementary event w.

3. The mechanical model

In this study, a simplified six-degree-of-freedom mechanical model is utilized. The model as shown in Fig. 4, represents the cross section of the railway vehicle with three mass elements: half of a bogie and a quarter of a carbody structure over one wheelset.

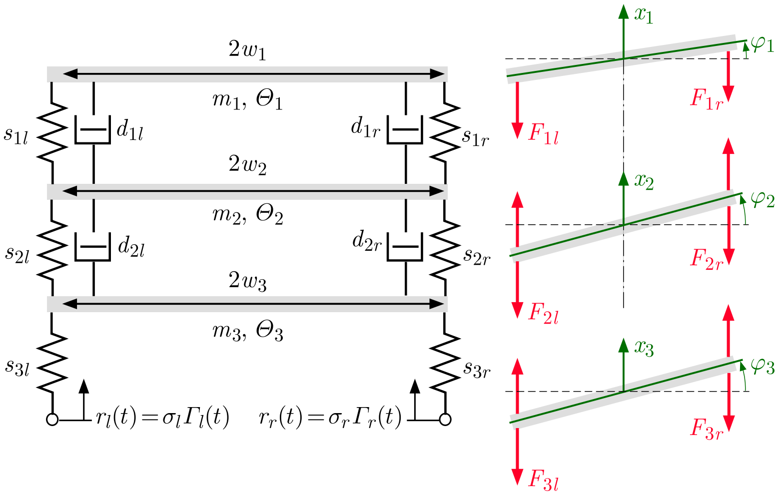

Fig. 4. Mechanical model.

The s parameters are spring stiffnesses, the d parameters represent damping, m, Θ and w are the mass, mass moment of inertia and half width of the different bodies, respectively. We presented the forces acting between the bodies on the right side of Fig. 4. The model focuses only on the behavior of the three components (half of a bogie and a quarter of a carbody structure over one wheelset) subjected to stochastic track excitation denoted by $r_l(t)$ and $r_r(t)$ (directly impacting the wheels) to highlight the statistical features and possible threats during operation.

The track excitation represents the irregularities of track rail lines on each side. The state vector is taken as follows: $\mathbf{y} = [x_3\ \dot{x}_3\ \varphi_3\ \dot{\varphi}_3\ x_2\ \dot{x}_2\ \varphi_2\ \dot{\varphi}_2\ x_1\ \dot{x}_1\ \varphi_1\ \dot{\varphi}_1]^{\mathrm{T}}$. The vector elements are the considered movements and their derivatives as velocity parameters.

The probabilistic nature of the excitation is captured by two separate white noise processes: $W_l(t)$ on the left side and $W_r(t)$ on the right.

The following forces are acting on the bodies:

$$\begin{aligned}
F_{1l} &= s_{1l}(x_1 - w_1\sin(\varphi_1) - x_2 + w_2\sin(\varphi_2)) + d_{1l}(\dot{x}_1 - \dot{\varphi}_1 w_1\cos(\varphi_1) - \dot{x}_2 + \dot{\varphi}_2 w_2\cos(\varphi_2)),\\
F_{1r} &= s_{1r}(x_1 + w_1\sin(\varphi_1) - x_2 - w_2\sin(\varphi_2)) + d_{1r}(\dot{x}_1 + \dot{\varphi}_1 w_1\cos(\varphi_1) - \dot{x}_2 - \dot{\varphi}_2 w_2\cos(\varphi_2)),\\
F_{2l} &= s_{2l}(x_2 - w_2\sin(\varphi_2) - x_3 + w_3\sin(\varphi_3)) + d_{2l}(\dot{x}_2 - \dot{\varphi}_2 w_2\cos(\varphi_2) - \dot{x}_3 + \dot{\varphi}_3 w_3\cos(\varphi_3)),\\
F_{2r} &= s_{2r}(x_2 + w_2\sin(\varphi_2) - x_3 - w_3\sin(\varphi_3)) + d_{2r}(\dot{x}_2 + \dot{\varphi}_2 w_2\cos(\varphi_2) - \dot{x}_3 - \dot{\varphi}_3 w_3\cos(\varphi_3)),\\
F_{3l} &= s_{3l}(x_3 - w_3\sin(\varphi_3)),\\
F_{3r} &= s_{3r}(x_3 + w_3\sin(\varphi_3)).
\end{aligned} \tag{3.1}$$

The stochastic track excitations are taken as

$$r_l(t) = \sigma_l \mathit{\Gamma}_l(t), \qquad r_r(t) = \sigma_r \mathit{\Gamma}_r(t), \tag{3.2}$$

where $\mathit{\Gamma}_l(t)$ and $\mathit{\Gamma}_r(t)$ represent independent white noise processes modeling the random irregularities of the track with noise intensities σ_l and σ_r on the left and right side, respectively. The equation of motion of the system is a stochastic differential equation (SDE) (Sun, 2006) written in an incremental form:

$$\mathrm{d}\mathbf{y} = \mathbf{f}(\mathbf{y})\,\mathrm{d}t + \mathbf{g_l}(\mathbf{y})\,\mathrm{d}W_l + \mathbf{g_r}(\mathbf{y})\,\mathrm{d}W_r, \tag{3.3}$$

where the elements of the deterministic part $\mathbf{f}(\mathbf{y})$ are as follows:

$$\begin{aligned}
f_1(\mathbf{y}) &= \dot{x}_1, & f_2(\mathbf{y}) &= -g + \frac{1}{m_1}(-F_{1l} - F_{1r}),\\
f_3(\mathbf{y}) &= \dot{\varphi}_1, & f_4(\mathbf{y}) &= \frac{1}{\mathit{\Theta}_1}(F_{1l} - F_{1r}) w_1 \cos(\varphi_1),\\
f_5(\mathbf{y}) &= \dot{x}_2, & f_6(\mathbf{y}) &= -g + \frac{1}{m_2}(-F_{2l} - F_{2r} + F_{1l} + F_{1r}),\\
f_7(\mathbf{y}) &= \dot{\varphi}_2, & f_8(\mathbf{y}) &= \frac{1}{\mathit{\Theta}_2}(F_{2l} - F_{2r} - F_{1l} + F_{1r}) w_2 \cos(\varphi_2),\\
f_9(\mathbf{y}) &= \dot{x}_3, & f_{10}(\mathbf{y}) &= -g + \frac{1}{m_3}(-F_{3l} - F_{3r} + F_{2l} + F_{2r}),\\
f_{11}(\mathbf{y}) &= \dot{\varphi}_3, & f_{12}(\mathbf{y}) &= \frac{1}{\mathit{\Theta}_3}(F_{3l} - F_{3r} - F_{2l} + F_{2r}) w_3 \cos(\varphi_3).
\end{aligned} \tag{3.4}$$

The stochastic effects of the track excitation are given on the left side by the vector $\mathbf{g_l}(\mathbf{y})$ and the corresponding Wiener-process increment $\mathrm{d}W_l$, and on the right side $\mathbf{g_r}(\mathbf{y})$ and $\mathrm{d}W_r$. The elements of the vectors are

$$\begin{aligned}
g_{l10}(\mathbf{y}) &= -\frac{s_{3l}}{m_3}\sigma_l, & g_{l12}(\mathbf{y}) &= \frac{s_{3l}}{\mathit{\Theta}_3} w_3 \sigma_l \cos\varphi_3,\\
g_{r10}(\mathbf{y}) &= -\frac{s_{3r}}{m_3}\sigma_r, & g_{r12}(\mathbf{y}) &= -\frac{s_{3r}}{\mathit{\Theta}_3} w_3 \sigma_r \cos\varphi_3.
\end{aligned} \tag{3.5}$$

The not listed elements of $\mathbf{g_l}(\mathbf{y})$ and $\mathbf{g}_r(\mathbf{y})$ are zeros. The $\mathrm{d}W_l$ and $\mathrm{d}W_r$ increments are random variables of independent normal distributions with zero expected values and $\mathrm{d}t$ variance. The system's behavior is investigated based on numerical simulations.

4. Results

Our main interest lies in understanding what happens with the secondary springs (characterized by s_{1l} and s_{1r} on the left and right sides below the carbody) during long-time operation. For that, relatively long simulations are performed to have enough data to estimate the steady-state distribution of the deformation (length change) Δl in the springs. The deformation is calculated at each time step from the state variables:

$$\Delta l = \sin(\varphi_2) w_2 - \sin(\varphi_1) w_1. \tag{4.1}$$

In expectation, the springs are compressed by about 4 mm nominally. The Δl is the deformation of the left secondary spring about this expected compression value. Note that the deformation of the right secondary spring would be $-\Delta l$. From the simulations we can calculate the distribution of this deformation during the steady-state operation. If we set a critical limit of operation (CLO), which means that at certain deformation the springs are subjected to weakening or potential failure, we can calculate the probability of critical operation (PCO) in the steady state.

4.1. Simulations

In practice, SDEs are investigated mainly utilizing numerical solvers, since exact analytical solutions only exists for a handful of simple examples.

The simulations presented in this paper are acquired by using an implicit Euler–Maruyama scheme built into the DifferentialEquations.jl package of The programming language Julia. Explicit schemes struggle to converge properly for stiff problems, and since the spring stiffnesses are large in our system, the performance of implicit schemes is much better (Rackauckas & Nie, 2020).

First, we consider the system to be symmetric, i.e., $s_{1l} = s_{1r} = s_1$, $d_{1l} = d_{1r} = d_1$, $s_{2l} = s_{2r} = s_2$, $d_{2l} = d_{2r} = d_2$, $s_{3l} = s_{3r} = s_3$, and $\sigma_l = \sigma_r = \sigma$. Only the noise processes differ on the two sides. In this case, the simulations are carried out using the parameters in Table 1. This study focused on the variability of the stiffness parameters. It is to be mentioned that the energy dissipation characteristics of these spring units after a certain deteriorated technical state are an object of further investigations. Table 1 shows special damping parameter figures cited from calculations of the certain locomotive type structural nominal design parameters (Ferencz, 2010). The indicated stiffness values were by purpose chosen to avoid possible numerical distortion in the solver process. With this possibility, the influence of the noise and the real asymmetricity of the focused secondary suspension system elements could be qualitatively examined.

Table 1. Simulation system parameters.

Parameter	Value	Unit	Parameter	Value	Unit	Parameter	Value	Unit
m_1	10450	kg	m_2	4305	kg	m_3	3640	kg
Θ_1	104 250	$\mathrm{kg \cdot m^2}$	Θ_2	8 610	$\mathrm{kg \cdot m^2}$	Θ_3	7280	$\mathrm{kg \cdot m^2}$
w_1	1	m	w_2	1	m	w_3	1	m
s_1	12 746 000	N/m	s_2	1 035 000	N/m	s_3	2 070 000	N/m
d_1	1409	Ns/m	d_2	2000	Ns/m	σ	0.001	1

Figure 5 shows the simulation results of state variables over time in relation to their respective expected solutions. The expected solution is when the noise is removed from the system in this

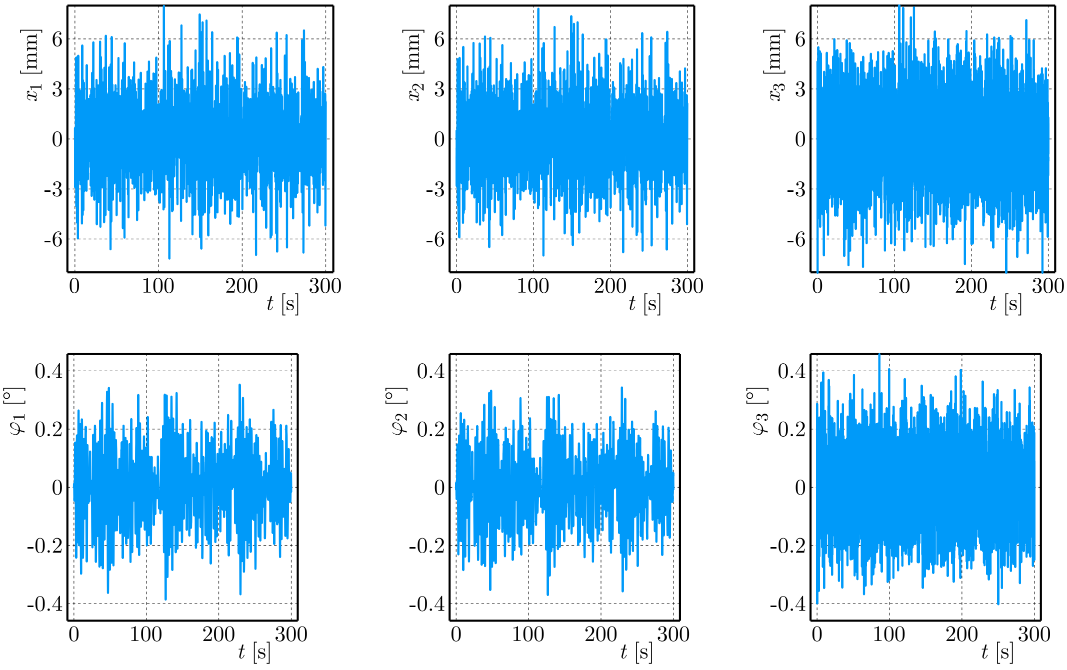

Fig. 5. Simulations results of state variables, plotted about their steady-state solution.

case. For example, the expected solution of the rotational movement angles of the bodies φ_1, φ_2, φ_3 are zero, because the system is symmetric. However, the stochastic excitation forces the bodies to move randomly, and the rotational angles constantly deviate from the expected zero value.

4.2. Probability of critical operation (PCO)

Hypothetically an anomaly process can appear on the basis of an operation with critical considered parameters within the system. This acts as the necessary first criteria to exist and to step toward, to "detour the system" toward an anomaly process. To model this, we can use the empirical density function values of the spring characteristic features to calculate the secondary spring deformation Δl changes from the state variables in each time step. The distribution is shown in Fig. 6.

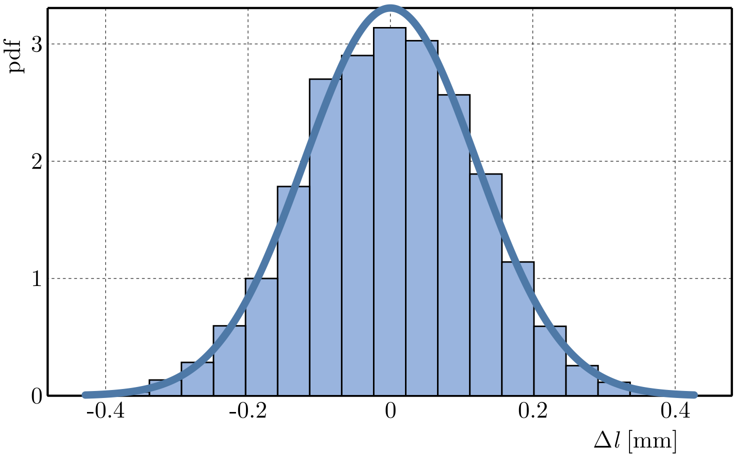

Fig. 6. Secondary spring deformation distribution during steady-state operation.

If we set a critical limit of operation (CLO), i.e., a $\pm\Delta l$ value for which the process is considered unsafe, we can calculate the PCO based on this distribution.

Figure 7 displays the connection between the CLO and the PCO values in the case of a symmetric secondary spring structure. For example, if we set the critical limit to zero, the probability that we have larger deformations is equal to 100 %. The larger CLO, the lesser gets PCO. According to the measurements explained in Section 2, there is a significant deviation in the secondary spring stiffness values s_1. We calculated the PCO for a symmetric case, when the secondary springs on the left and right sides are identical.

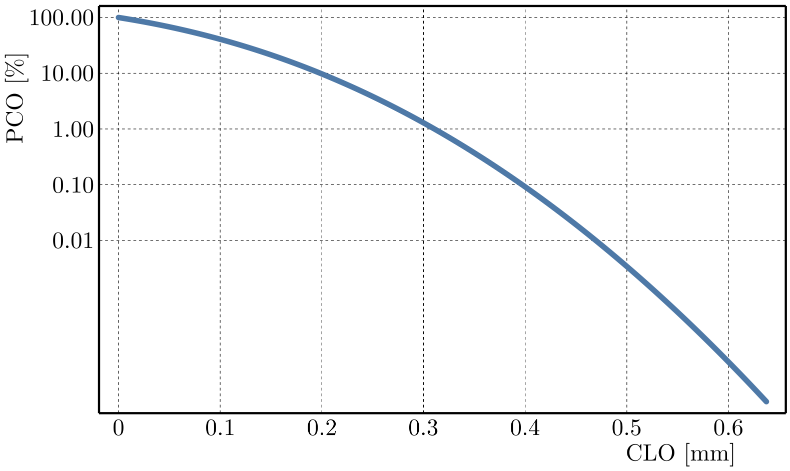

Fig. 7. Probability of critical operation (PCO) as a function of the critical limit of operation (CLO).

We considered two asymmetric cases: 1 % asymmetry means the s_{1r} is 99 % and s_{1l} is 101 % of the nominal value. Second, 5 % asymmetry is when s_{1r} is 95 % and s_{1l} is 105 %. Figure 8 shows the steady-state distribution of the secondary spring deformation Δl in the symmetric and asymmetric cases. In asymmetric cases the expected rotation movement angle of the carbody φ_1 is no longer zero, i.e., there is a steady-state tilt. If the expected value of φ_1 is not zero, then the expected value of Δl also differs from zero. Figure 8 displays how the Δl distributions shift depending on the measure of secondary spring asymmetry. For larger asymmetry values, the distribution is centered further aligned from zero value.

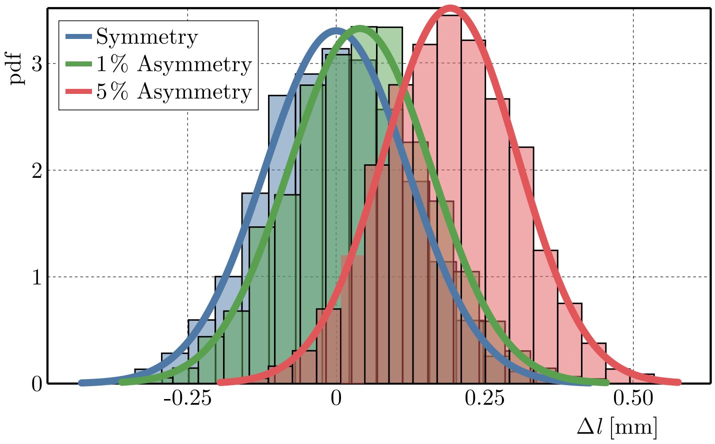

Fig. 8. Symmetric and asymmetric steady-state distribution of Δl.

Figure 9 presents the PCO values for the symmetric and asymmetric cases. For a certain CLO value, e.g., 0.4 mm, the symmetric probability is around 0.7 %, the 1 % asymmetric probability is slightly larger than 0.1 %, close to the symmetric case, but the 5 % asymmetric probability is more than 4 %. This essentially means that larger asymmetry causes high probability for the vehicle system itself to be in critical operation.

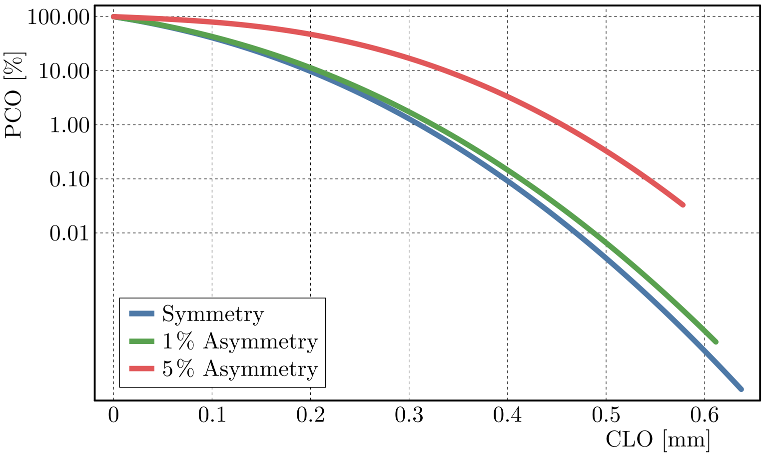

Fig. 9. PCO as a function of CLO for symmetric and asymmetric cases.

If we specify the operation time (OT) to be, e.g., 10000 hours, we can transform the PCO into critical operation time (COT):

$$\mathrm{COT} = \mathrm{PCO} \times \mathrm{OT}. \tag{4.2}$$

Table 2 presents the COT values for different cases. Note that as the CLO increases for a certain case, i.e., we allow larger deformation of these secondary springs, the COT values decrease. However, if we fix the CLO value at 0.5 mm and focus on the effect of asymmetry,

Table 2. COT in different cases.

	CLO [mm]	PCO [%]	COT [hours]
Sym	0.4	0.07	7.03
1 % Asym	0.4	0.107	10.7
5 % Asym	0.4	4.09	409.9
Sym	0.5	0.0022	0.22
1 % Asym	0.5	0.00426	0.426
5 % Asym	0.5	0.407	40.7

we see that out of 10000 hours the symmetric springs spend 0.22 hours in critical operation, which seems low, but the 5 % asymmetric springs spend 40.7 hours.

5. Conclusions

This paper provides an opportunity to assess the impacts of stochastic excitation on symmetrically and asymmetrically structured models of a railway vehicle. The results indicate that, even under nominal structural conditions, the system can exhibit anomalies when subjected to random forcing. The noise may drive the system into unexpected motions, especially during asymmetric operation conditions.

One can consider a symmetric case: the left and right secondary spring stiffness is the same. Even in a symmetric case the probability of critical operation is not zero in the presence of stochastic track excitation. After some time, one of the springs gets damaged due to operating above its intended limit. Its stiffness changes, and now the system is asymmetric because the stiffnesses of the secondary springs are different on the two sides. The PCO is larger in the asymmetric case, therefore the system spends even more time in critical operation than before, which means that an anomaly process develops with high probability.

Acknowledgments

Hereby as authors of this article, we express our special thanks to tutors Professor András Szabó, Professor Lajos Borbás, and Professor Vince Nagy.

References

1. Bruni, S., Meijaard, J., Rill, G., & Schwab, A.L. (2020). State-of-the-art and challenges of railway and road vehicle dynamics with multibody dynamics approaches. *Multibody System Dynamics*, *49*(1), 1–32. https://doi.org/10.1007/s11044-020-09735-z

2. Bruni, S., Vinolas, J., Berg, M., Polach, O., & Stichel, S. (2011). Modelling of suspension components in a rail vehicle dynamics context. *Vehicle System Dynamics*, *49*(7), 1021–1072. https://doi.org/10.1080/00423114.2011.586430

3. DifferentialEquations.jl: Efficient differential equation solving in Julia. https://docs.sciml.ai/DiffEqDocs/stable/

4. Ferencz, P. (2010). Investigation into wheel profile wear processes influenced by parameter anomalies in suspension characteristics of electro-locomotive bogies. In I. Zobory (Ed.), *Proceedings of the 8th International Conference on Railway Bogies and Running Gears* (pp. 201–212). Department of Rolling Stock, Budapest, Hungary.

5. Ferencz, P. (2023, September 26–29). *Investigation into impacts of dynamic system anomalies on railway vehicle wheel wear propagation* [Conference poster presentation]. 39th Danubia-Adria Symposium on Advances in Experimental Mechanics, Siófok, Hungary.

6. Knothe, K., & Stichel, S. (2017). *Rail vehicle dynamics*, Springer. https://doi.org/10.1007/978-3-319-45376-7
7. Rackauckas, C., & Nie, Q. (2020). Stability-optimized high order methods and stiffness detection for pathwise stiff stochastic differential equations. In *2020 IEEE High Performance Extreme Computing Conference (HPEC)*, Waltham, MA, USA, (pp. 1–8). https://doi.org/10.1109/HPEC43674.2020.9286178
8. Sun, J.Q. (2006). Stochastic dynamics and control. *Monograph Series on Nonlinear Science and Complexity* (vol. 4). Elsevier Science & Technology. https://doi.org/10.1016/S1574-6917(06)04001-3
9. The Julia Programming Language. https://julialang.org/
10. Zobory, I. (1997). Prediciton of wheel/rail profile wear. *Vehicle System Dynamics*, *28*(2–3), 221–259. https://doi.org/10.1080/00423119708969355

Manuscript received December 15, 2024; accepted for publication May 29, 2025;

JOURNAL OF THEORETICAL
AND APPLIED MECHANICS
63, 3, pp. 701–710, Warsaw 2025
https://doi.org/10.15632/jtam-pl/208250

MONITORING OF STRUCTURAL STIFFNESS DEGRADATION AND IMPACT DAMAGE DETECTION BY CARBON FIBER SENSORS

Nikola SCHMIDOVÁ, Milan RŮŽIČKA, Karel DOUBRAVA, David BLAHA

Department of Mechanics, Biomechanics and Mechatronics, Faculty of Mechanical Engineering,
Czech Technical University in Prague, Prague, Czech Republic
*corresponding author, *nikola.schmidova@cvut.cz*

This paper presents findings on the sensing capabilities of carbon fiber sensors (CFSs) for detecting impact damage in composite structures. New insights are provided into the correlation between stiffness degradation after impact and the measured response of integrated CFSs, placing both recent and previous data in a broader context. The results demonstrate the potential of CFSs for predicting structural stiffness loss and enabling effective impact damage monitoring. An experimental program focused on structural health monitoring (SHM) was carried out using CFSs embedded within flat specimens made of glass-fiber-reinforced polymer composites. The influence of cyclic loading on sensor response was investigated both before and after impact damage initiation during bending tests.

Keywords: carbon fiber sensor; SHM; electrical resistance; damage detection; composites.

1. Introduction

Long fiber reinforced polymer (FRP) composites are widely used in industries such as aerospace, automotive, manufacturing, and civil engineering. These materials are valued for their high strength, stiffness, low weight, and excellent resistance to fatigue. They are also used in infrastructure, such as bridges and roofs, where safety is critical. However, unlike traditional materials like steel, aluminum, or concrete, long FRP composites often fail without showing clear signs of damage. This makes it difficult to detect damage in time and highlights the need for advanced methods to monitor these materials.

Current inspections of FRP components often rely on scheduled visual checks, but these can easily miss hidden damage. While non-destructive testing (NDT) methods like C-scan, X-ray, thermography, and eddy current testing are more sensitive, they are time-consuming and usually require removing parts from service (Tabatabaeian *et al.*, 2022; Klute *et al.*, 2015; Gardiner, 2015; Kostroun & Dvořák, 2021). To overcome these challenges, structural health monitoring (SHM) systems are being developed. SHM allows for continuous monitoring of materials during use, providing real-time information about their condition. Originally developed for aerospace applications, SHM is now gaining attention in other industries to improve safety and reduce maintenance costs.

Ministry of Science and Higher Education
Republic of Poland

The publication has been funded by the Polish Ministry of Science and Higher Education under the Excellent Science II programme "Support for scientific conferences".
The content of this article was presented during the 40th Danubia-Adria Symposium on Advances in Experimental Mechanics, Gdańsk, Poland, September 24–27, 2024.

This work focuses on a specific method for SHM in FRP composites: the use of carbon fiber rovings for damage detection. This method takes advantage of the electrical properties of carbon fibers, which are conductive and piezoresistive. This means that their electrical resistance changes when they are stressed. These properties have been extensively studied, and different types of carbon fibers (e.g., PAN-based, graphite) are known to exhibit different levels of resistivity and piezoresistive behavior (Horoschenkoff & Christner, 2012; Wang & Chung, 1997; Scholle & Sinapius, 2021; Blazewicz *et al.*, 1997). Since individual carbon fibers are very thin (about 7–8 µm in diameter) and difficult to handle, bundles of fibers, called rovings, are often used instead. These rovings can contain thousands of fibers (e.g., 1 K, 3 K or 12 K), which makes them more practical for applications, but also introduces complexities in stress distribution and conductivity (Huang *et al.*, 2012; Huang & Wu, 2012).

For carbon fiber rovings to work as sensors, it is essential that good electrical contacts are prepared. Ideally, all fibers in the roving should contribute to the electrical signal. Poor contact can lead to inaccuracies caused by transverse resistance (Schulte & Baron, 1989). Methods to improve contact include the use of conductive paints, adhesives, metal splices or nickel coatings (Häntzsche *et al.*, 2013; Kalashnyk *et al.*, 2017; Gajda, 1978). The arrangement of these sensors is also important. They can be organized in simple meshes (Horoschenkoff & Christner, 2012) or in more complex arrangements (Park & Roh, 2021; Kunadt *et al.*, 2010) in which several rovings work together.

This study summarizes investigations regarding carbon fiber rovings to act as self-sensing materials for impact damage detection. Carbon fiber sensors (CFSs) can be successfully used as strain sensors. The sensors can be used as integrated sensors within a composite laminate, or they can be attached to the surface. It was shown that CFSs can be utilized also for impact damage detection (Schmidová *et al.*, 2018; 2022; 2023; 2024). CFSs were embedded in glass fiber composite plates. The sensors response to cyclic loading in the pristine state and after impact is described.

For practical applications, it would be beneficial to use longer sensors to monitor a larger area. For this reason, the influence of the length of the sensors on the possibility of impact damage detection using CFSs was also investigated.

The study also examined whether the amount of damage and the structural response could be predicted from the change in electrical resistance measured by CFSs.

Consider a beam of a manipulator with a working head drive. Different working heads with different masses move within the beam. We need to consider the variable loading of the beam. During the operation of the manipulator, a collision can occur, potentially reducing the beam's maximum load capacity due to damage. The detection of such collisions and the prediction of the residual strength of the structure would be useful.

A summary of current knowledge should contribute to the development of reliable and cost-effective SHM solutions.

2. Experimental campaign

Three experimental campaigns were conducted to evaluate the suitability of CFSs for impact damage detection, which provides a solid foundation for further applications:

- campaign 1: initial feasibility (Schmidová *et al.*, 2018);
- campaign 2: investigation of sensor positioning within the composite layup (Schmidová *et al.*, 2022);
- campaign 3: study of sensor length and correlation between sensor response and structural post-impact behavior (Schmidová *et al.*, 2023; 2024).

The basic evaluation of the individual experimental campaigns has been published in articles: (Schmidová *et al.*, 2018; 2022; 2023; 2024). In this paper, we analyze the relationships and interconnections among the individual experimental campaigns. The comparison of the change in electrical resistance after impact for different lengths of CFSs will follow as well as detailed discussion regarding correlation between stiffness degradation after impact and the measured response of integrated CFSs.

2.1. Materials and specimen preparation

In the first experimental campaign, hand lamination was used for specimen preparation. The specimens were composed of two unidirectional layers of glass non-crimp fabric oriented in the [0]2 lay-up. CFSs were placed on one side of the fabric before curing. In the second and third experimental campaigns, specimens were manufactured using autoclave technology from prepreg sheets used in the aerospace industry. A $[+45/0/-45/90]_{\mathrm{sym}}$ laminate lay-up was used for the specimens. The specimens with integrated CFSs underwent the curing process: 125 °C for 90 minutes under the pressure of 6 bar.

Specimens were fabricated using glass fiber reinforced polymers and glass woven fabric prepregs. CFSs made from various types of carbon fiber rovings, including PAN-based and pitch-based fibers, were embedded within the specimens. Specimens underwent curing and were cut into strips for mechanical testing. Sensor integration and electrical connections were meticulously prepared to ensure reliable measurements.

2.2. Carbon fiber sensors

The CFSs were prepared from different carbon fiber rovings, see Table 1. The same methodology of CFS manufacturing was used as described in (Horoschenkoff & Christner, 2012). The ends of each roving were coated with a nickel electrolyte. A thin copper wire was then used to make electrical connections, as shown in Fig. 1.

Table 1. Overview of carbon fiber rovings used for CFS preparation.

	A	B	C	D	70A	95A
Label of the fiber [–]	T300 1000–50A	HTS40 A23 12K 1420TEX MC	HTS 40 MC	CN-80-30S	YSH-70A-30A	YSH-95A-30A
Type [–]	EX-PAN	EX-PAN	EX-PAN	EX-PITCH	EX-PITCH	EX-PITCH
Producer	Toray	Toho Tenax	Toho Tenax	Nippon Graphite Fibre Corporation		
Number of filaments used [–]	1000	7720	6000	3000	3000	3000
Metalization [–]	–	Nickel	–	–	–	–
E [GPa]	230	215	230	780	714	693
Elongation at break [%]	1.5	1.28	1.3	0.5	0.5	0.3

2.3. Mechanical loading – bending test

In all the experimental campaigns, the specimens were subjected to cyclic bending tests, followed by impact loading, and subsequently to cyclic bending tests again. In the first and second experimental campaigns, the specimens underwent three-point bending tests. In the third experimental campaign, a four-point bending (4PB) test was adopted, see Fig. 2. Switching the loading configuration from 3PB to 4PB resulted in a larger area of constant deformation under maximal loading. During all the tests, the maximum loading parameter corresponded to a maximum strain of 3.000 μm/m in the area of maximal loading.

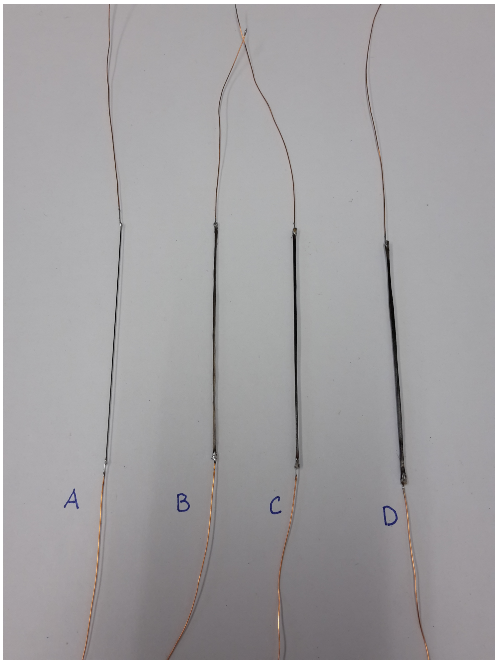

Fig. 1. CFSs prepared from different materials according to Table 1.

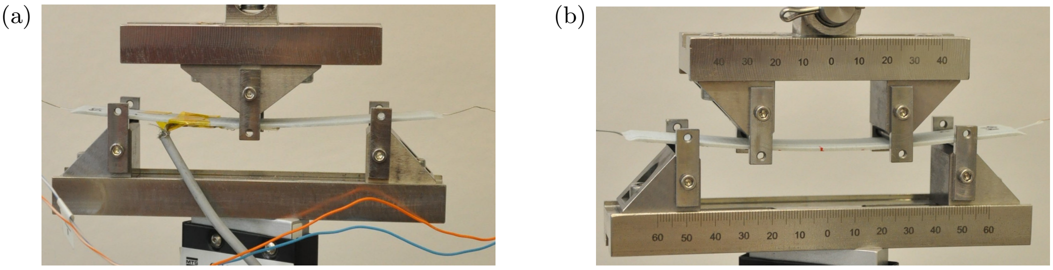

Fig. 2. Configuration of (a) three-point bending cyclic mechanical test during experimental campaign 1 and (b) four-point bending test cyclic mechanical test during experimental campaign 2.

2.4. Impact testing

Impact damage was induced using a drop weight impactor with energies ranging from 2 J to 4 J. An impactor with the diameter of 16 mm with the weight of 410 g was used. Electrical resistance measurements were recorded before and after impact loading to assess sensor performance. The impact energy of 2 J resulted in barely visible impact damage (BVID), see Fig. 3.

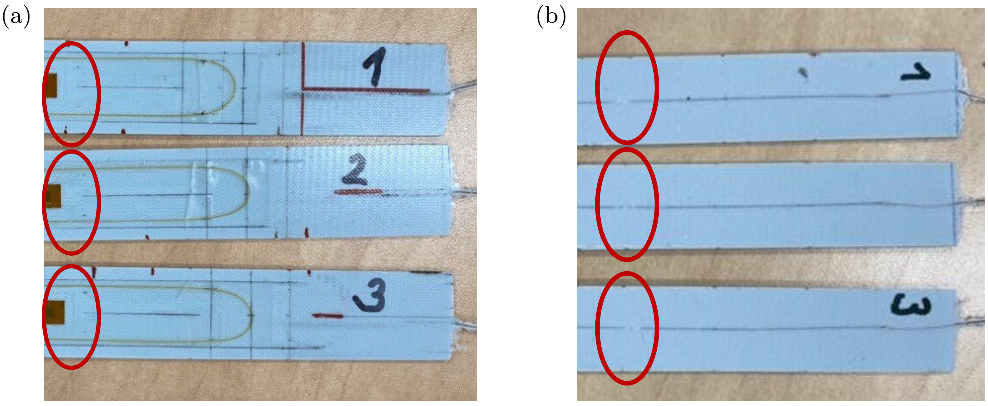

Fig. 3. Specimens from experimental campaign 3 after 2 J impact. CFSs are made of carbon fiber roving A (see Table 1) with the length equal to 140 mm. An impacted side (mold side of the specimen) in the section (a), bottom side of the specimen (b). The red circle indicates the impacted area.

In the third experimental campaign, three specimens were impacted also by the energy of 3 J and one specimen by the energy of 4 J. The energy of 4 J resulted in a crack of the specimen.

3. Results and discussion

Test results of each experimental campaign have added new information regarding sensing capabilities of CFSs. For the further usage of CFSs, this paper aims to put the information gained in greater context.

In the first experimental campaign, it was shown that CFSs are sensitive to impact damage detection. Cyclic mechanical loading causes the biggest difference in measured electrical resistance change to the most brittle material. On the other hand, the least brittle material showed the most stable behavior regarding cyclic loading.

The second experimental campaign included more specimens to broaden the statistics and to investigate the influence of positioning of the sensor within the lay-up. In the second experimental campaign, it was shown that brittle materials are much more difficult to handle during sensors preparation and even though they are more sensitive to impact damage, due to the difficulties associated with handling brittle fibers they are currently not suitable for further research. It was shown that thermographic inspection is suitable for CFSs integrated in glass reinforced composites and can serve for localization of the impact within the sensor's length. The CFSs response to temperature was described in the range of temperature levels 20 °C to 120 °C. It was revealed for all types of CFSs that the best position for impact damage detection within the lay-up is close to the opposite site to the impact and close to the impacted side.

In the third experimental campaign, CFSs made of Toray T300 1000-50A material were investigated, see Table 1. They were integrated between the 7th and 8th layer of the composite lay-up opposite to the impacted side of the specimen. The specimens were prepared using the same material and autoclave curing technology as during the second experimental campaign, but the length of the sensors was set to 140 mm.

During this experimental campaign, extensive cyclic testing was performed. Three specimens were first subjected to 1000 loading cycles, followed by a 2 J impact. Subsequently, the specimens underwent additional 1000 loading cycles. The increase in the number of loading cycles showed stable behavior of the sensor even for 1000 loading cycles, see Fig. 4. The relative electrical resistance change of the CFSs during cyclic loading was calculated according to Eq. (3.1), $R_{\text{max (loading CYCLE X)}}$ is equal to maximal electrical resistance of the CFS measured during the loading cycle, $R_{\text{min loading (CYCLE X)}}$ is equal to minimal electrical resistance measured during the loading cycle, $R_{\text{after implementation}}$ is equal to electrical resistance of the integrated CFS measured after implementation to the specimen:

$$\frac{\Delta R}{R} = \frac{R_{\text{max (loading CYCLE X)}} - R_{\text{min loading (CYCLE X)}}}{R_{\text{after implementation}}} \cdot 100\,[\%]. \tag{3.1}$$

The change in measured relative electrical resistance change of the sensor during cyclic loading before and after impact loading is more than 300 %. It is important to note that the size of the impact was so small that there were no signs of damage on the impacted side of the specimen, see Fig. 3a. According to this observation, it should be possible to detect impact damage of the CFS during scheduled inspections of the composite structure, which is necessary in many applications.

Because the same material for specimen preparation was used in the second and the third experimental campaign, it is possible to compare the response of sensors with the length of 70 mm and 140 mm, see Fig. 5. The analysis shows that the absolute changes in electrical resistance were identical for both sensor lengths. However, this indicates that the relative change in resistance is smaller for the longer sensors.

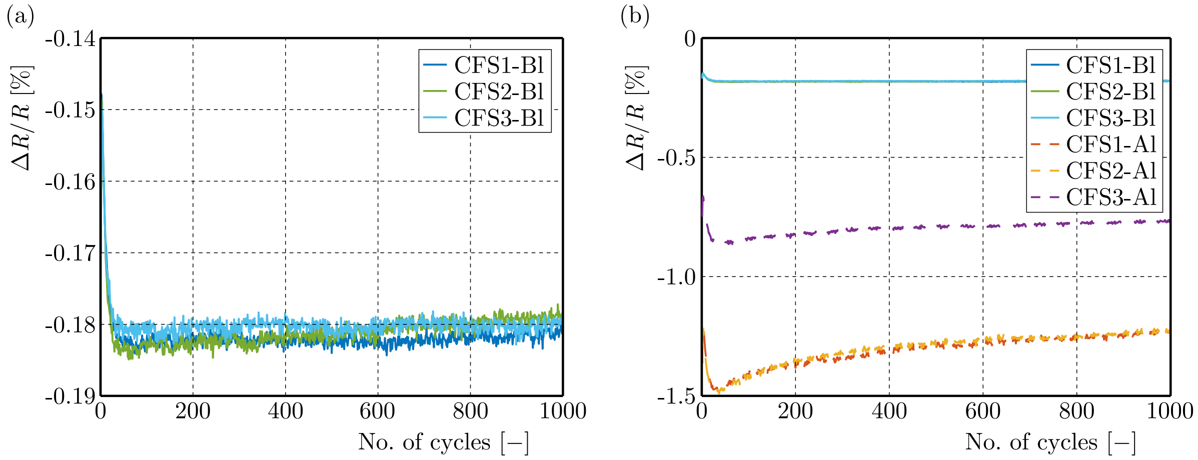

Fig. 4. Relative electrical resistance of the CFSs during cyclic test: (a) before impact (BI) for specimens CFS1, CFS2, and CFS3; (b) BI loading and after impact (AI) loading.

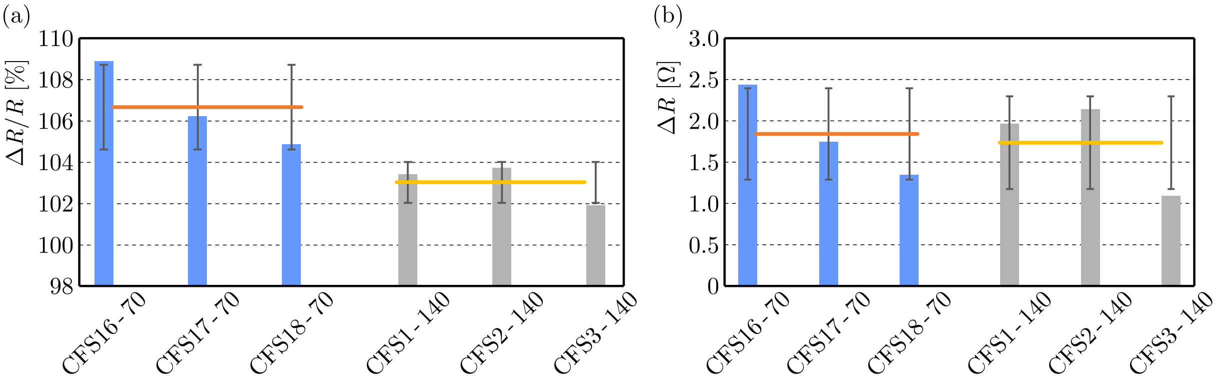

Fig. 5. (a) Relative electrical resistance change after BVID impact of 2 J of sensors with length of 70 mm and 140 mm; (b) absolute values of electrical resistance change of integrated CFS after BVID impact of 2 J.

This comparison enables better insight into the measurement preparation for more complex applications. When designing an application involving longer CFSs, it is necessary to consider the increased requirements for the measuring equipment, as it will be necessary to measure higher nominal resistance values. At the same time, the system must be capable of detecting small changes in electrical resistance resulting from impact events. Figure 6 shows extrapolated data for different possible lengths of CFSs up to the length of 1000 mm.

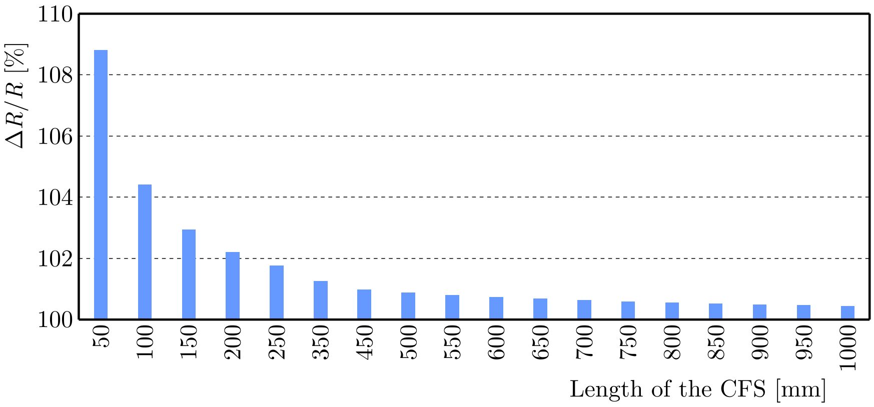

Fig. 6. Extrapolated relative electrical resistance change after BVID impact of 2 J for sensors with length from 50 mm to 1000 mm.

3.1. Correlation between stiffness degradation after impact and response of integrated CFSs

Furthermore, in the third experimental campaign, the change in measured electrical resistance during mechanical loading was investigated as a function of displacement of the specimen and force applied to the specimen before and after impact loading. These experimental data have not yet been presented in their full complexity; therefore, detailed information is provided here.

Figures 7 and 8 present the changes in the measured electrical resistance of the integrated CFSs in specimens exposed to different levels of impact loading (0 J, 2 J, 3 J, and 4 J). Following the impact loading, the specimens were subjected to four-point bending (4PB) tests.

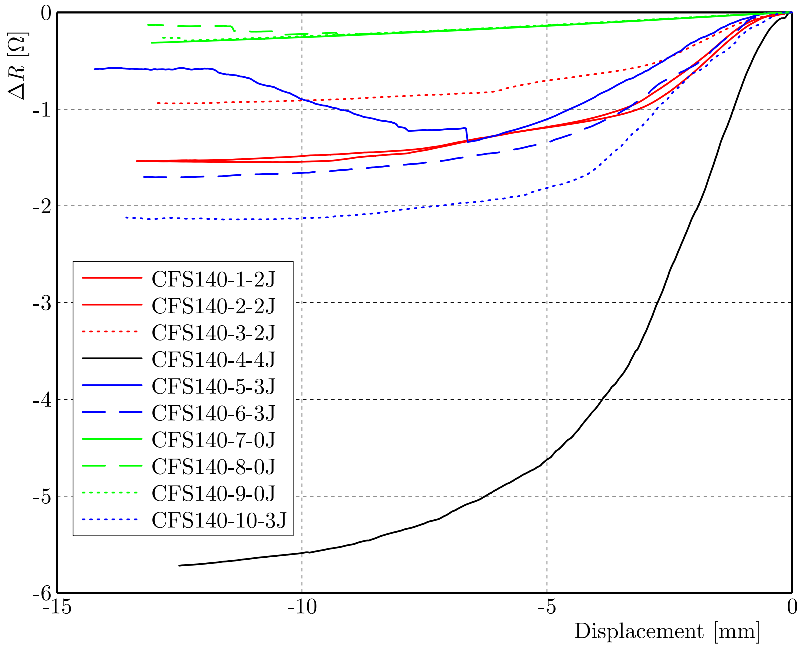

Fig. 7. Change of electrical resistance of the integrated CFS depending on applied displacement during 4PB.

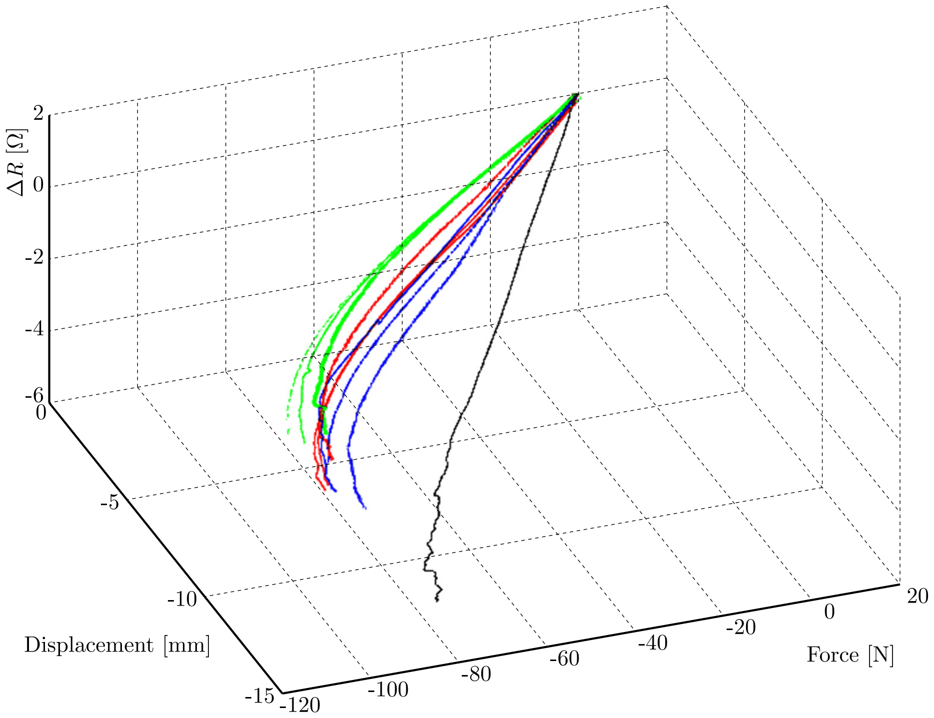

Fig. 8. 3D force-displacement-ΔR from integrated CFS during 4PB test.

The initial plan was to load the specimens until the final rupture; however, they proved to be too flexible. Despite setting the loading span to 20 mm and the support span length to 70 mm to achieve the maximum bending moment, only the specimen impacted with 4 J ultimately failed.

The configuration of the 4PB test was selected so that the applied loading force in both types of 4PB tests (loading/support spans of 20 mm/70 mm for the static test and 50 mm/100 mm for the cyclic test) produced equivalent bending moments and, consequently, the same strain levels. The loading limits for the cyclic tests were set to achieve a maximum strain of 3000 µm/m. This strain corresponds to a loading force of 30 N and a displacement of 2.65 mm.

Figure 7 shows data of the change in measured electrical resistance for each specimen, which was calculated according to the equation:

$$\Delta R = R_{\text{at the beginning of loading (deflection = 0 mm)}} - R_{(\text{deflection}=x\,\text{mm})}. \tag{3.2}$$

According to the 3D graph showing the relationship between ΔR, deflection, and force in Fig. 8, greater deflection amplifies the effect of stiffness loss caused by impact damage. The influence of increasing impact energy is relatively minor when comparing specimens impacted with 2 J and 3 J. However, the increase in impact energy from 3 J to 4 J results in a significant effect. This is likely due to the presence of different damage mechanisms in the specimen impacted with 4 J.

As shown in Fig. 7 and Fig. 8, it is difficult to distinguish between 2 J and 3 J impacts based on the data from the tested specimens alone. However, when comparing the measured data across all specimens (no impact, 2 J, 3 J, and 4 J impacts), there is a clear correlation between reduced stiffness (lower force required for the same level of deflection) and greater changes in the electrical resistance of the CFS induced by the impact. Specifically, higher impact energies result in lower forces required for the same displacement of the sensor and greater changes in the measured electrical resistance during loading.

Figures 7 and 8 also show that the relationship between the observed quantities is not uniform across the load range. Two distinct areas of slope can be identified in the load curve and a transitional area.

Figure 9 demonstrates that the decrease in the force required to achieve a defined displacement of the specimen (or structure) can be predicted both from the change in electrical resistance measured during loading and from the resistance change recorded before and after impact on the unloaded structure. The measured data provides a basis for predicting the structural behavior following impact events. Although the specimens were not loaded to complete fracture, it can be inferred that the force necessary to cause final failure correlates with both the impact energy and the magnitude of the measured change in electrical resistance of the integrated CFSs.

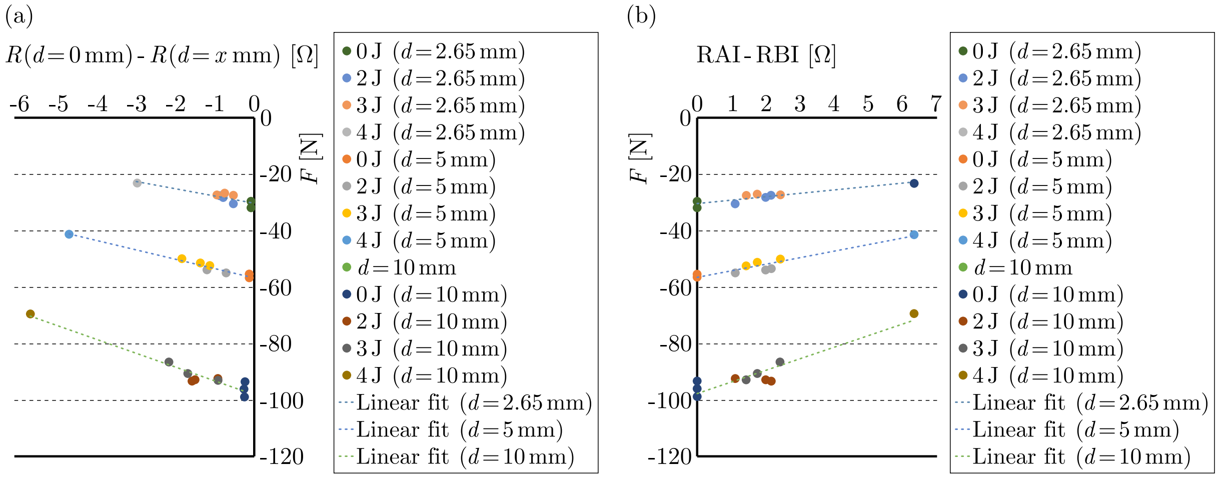

Fig. 9. Graph of force – change of measured electrical resistance for different impact energies and displacements (a) during loading ($d = x$ mm); (b) AI and BI.

4. Conclusions

Experimental measurements have been made using CFSs integrated into the glass composite. They showed that CFSs are promising tools for impact damage detection in composite structures.

A recommendation regarding the material used for carbon fiber roving in sensor preparation was made. The influence of temperature change and cyclic mechanical loading on the measured signal was described. It was shown that thermographic inspection can be used for the inspection of CFSs and for closer focusing of the impact position within the length of the sensor, also applicable for BVID.

The change in electrical resistance of CFSs after impact loading at identical energy levels is comparable, even for sensors twice the length. This suggests that longer sensors are suitable for detecting small impact damage, facilitating the mapping of impact events over larger component areas.

CFSs show stable responses to cyclic mechanical loading, with consistent $\Delta R/R$ values observed for all three sensors tested. Following impact loading, the sensor response increases significantly during subsequent loading, with measured $\Delta R/R$ values more than three times greater than those recorded prior to impact.

The results indicate that impact damage in a structure subjected to specific loading cycles can be detected by measuring the sensor response during operational shutdowns.

A strong correlation was found between the change in electrical resistance of the integrated CFSs and the reduction in stiffness of the specimens caused by impact loading. This relationship allows for the prediction of stiffness reduction in the structure using two different approaches:

- by measuring the change in electrical resistance of the built-in sensors during load cycles;
- by comparing the electrical resistance of the sensors before and after the impact.

These results highlight the potential of CFSs for monitoring impact damage and predicting the loss of structural stiffness, providing valuable tools for assessing the condition of in-service components.

Acknowledgments

This work has been supported by project No. FW06010296 of the Technological Agency of the Czech Republic.

References

1. Blazewicz, S., Patalita, B., & Touzain, Ph. (1997). Study of piezoresistance effect in carbon fibers. *Carbon*, *35*(10–11), 1613–1618. https://doi.org/10.1016/S0008-6223(97)00120-6
2. Gajda, W.J. (1978). *A fundamental study of the electromagnetic properties of advanced composite materials*. https://api.semanticscholar.org/CorpusID:136838814
3. Gardiner, G. (2015). Structural health monitoring: NDT-integrated aerostructures. *Composites World*. https://www.compositesworld.com/articles/structural-health-monitoring-ndt-integrated-aerostructures-enter-service
4. Häntzsche, E., Matthes, A., Nocke, A., & Cherif, Ch. (2013). Characteristics of carbon fiber based strain sensors for structural-health monitoring of textile-reinforced thermoplastic composites depending on the textile technological integration process. *Sensors and Actuators A: Physical*, *203*, 189–203. https://doi.org/10.1016/j.sna.2013.08.045
5. Horoschenkoff, A., & Christner, C. (2012). Carbon fibre sensor: Theory and application. In N. Hu (Ed.), *Composites and Their Applications* (pp. 219–242). InTech. https://doi.org/10.5772/50504
6. Huang, H., & Wu, Z.S. (2012a). Static and dynamic measurement of low-level strains with carbon fibers. *Sensors and Actuators A: Physical*, *183*, 140–147. https://doi.org/10.1016/j.sna.2012.06.006

7. Huang, H., Yang, C., & Wu, Z. (2012b). Electrical sensing properties of carbon fiber reinforced plastic strips for detecting low-level strains. *Smart Materials and Structures*, *21*(3), Article 035013. https://doi.org/10.1088/0964-1726/21/3/035013

8. Kalashnyk, N., Faulques, E., Schjødt-Thomsen, J., Jensen, L.R., Rauhe, J.C.M., & Pyrz, R. (2017). Monitoring self-sensing damage of multiple carbon fiber composites using piezoresistivity. *Synthetic Metals*, *224*, 56–62. https://doi.org/10.1016/j.synthmet.2016.12.021

9. Klute, S.M., Metrey, D.R., Garg, N., & Rahim, N.A.A. (2015). In-situ structural health monitoring of composite-overwrapped pressure vessels. *Luna Innovations Incorporated.* Retrieved June 5, 2023, from https://lunainc.com/sites/default/files/assets/files/resource-library/36_Klute_2015_Luna_InSituSHM_COPV_final.pdf

10. Kostroun, T., & Dvořák, M. (2021). Application of the pulse infrared thermography method for nondestructive evaluation of composite aircraft adhesive joints. *Materials*, *14*(3), Article 533. https://doi.org/10.3390/ma14030533

11. Kunadt, A., Heinig, A., Starke, E., Pfeifer, G., Cherif, C., & Fischer, W.-J. (2010). Design and properties of a sensor network embedded in thin fiber-reinforced composites. In *2010 IEEE Sensors* (pp. 673–677). https://doi.org/10.1109/ICSENS.2010.5690085

12. Park, Y.-B., & Roh, H.D. (2021). Electromechanical analysis of CFRP for real-time structural self-sensing and non-destructive evaluation. In *Nondestructive Characterization and Monitoring of Advanced Materials, Aerospace, Civil Infrastructure, and Transportation XV* (Article 11710). SPIE. https://doi.org/10.1117/12.2582669

13. Schmidová, N. (2024). *Electrical resistance measurement for structural health monitoring of composite materials* [Doctoral dissertation, Czech Technical University in Prague, Faculty of Mechanical Engineering].

14. Schmidová, N., Horoschenkoff, A., & Růžička, M. (2018). Investigation of the electrical resistivity of damaged carbon fibers sensors with regard to SHM. In *Proceedings of the ECCM18.* https://www.academia.edu/69240591/Investigation_of_the_Electrical_Resistivity_of_Damaged_Carbon_Fibers_Sensors_with_Regard_to_SHM

15. Schmidová, N., Macken, J., Horoschenkoff, A., Sedláček, R., Kostroun, T., Šimota, J., & Růžička, M. (2022). Impact damage detection of a glass fabric composite using carbon fiber sensors with regard to mechanical loading. *Applied Sciences*, *12*(3), Article 1112. https://doi.org/10.3390/app12031112

16. Schmidová, N., Sedláček, R., Kratochvíl, A., & Růžička, M. (2023). Behavior of carbon fiber sensors under cyclic loading and impact damage. In *Proceedings of the 33rd Workshop of Applied Mechanics* (pp. 1–3). Czech Technical University in Prague, Faculty of Mechanical Engineering.

17. Scholle, P., & Sinapius, M. (2021). A review on the usage of continuous carbon fibers for piezoresistive self strain sensing fiber reinforced plastics. *Journal of Composites Science*, *5*(4), Article 96. https://doi.org/10.3390/jcs5040096

18. Schulte, K., & Baron, C. (1989). Load and failure analyses of CFRP laminates by means of electrical resistivity measurements. *Composites Science and Technology*, *36*(1), 63–76. https://doi.org/10.1016/0266-3538(89)90016-X

19. Tabatabaeian, A., Liu, S., Harrison, P., Schlangen, E., & Fotouhi, M. (2022). A review on self-reporting mechanochromic composites: An emerging technology for structural health monitoring. *Composites Part A: Applied Science and Manufacturing*, *163*, Article 107236. https://doi.org/10.1016/j.compositesa.2022.107236

20. Wang, X., & Chung, D.D.L. (1997). Electromechanical behavior of carbon fiber. *Carbon*, *35*(5), 706–709. https://doi.org/10.1016/S0008-6223(97)86644-4

Manuscript received December 15, 2024; accepted for publication July 14, 2025;
published online July 22, 2025.

Contents